PAUL SCHERRER INSTITUT

PSI Proceedings 95-02
November 1995
ISSN 1019-6447

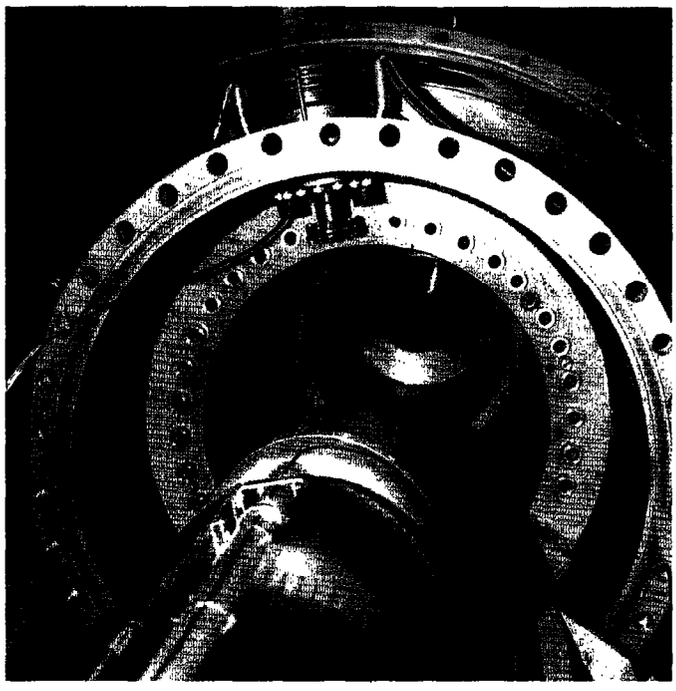

ICANS-XIII

Proceedings of the Meetings ICANS-XIII and ESS-PM4 – Volume II –

Villigen PSI, Switzerland, Oktober 11 - 14, 1995 and
Weinfelden, Switzerland, October 16 - 19, 1995

PAUL SCHERRER INSTITUT

PSI-Proceedings 95-02
November 1995

ICANS-XIII

Joint Proceedings of the
13th meeting of the
International Collaboration on Advanced Neutron Sources
held at Paul Scherrer Institut
October 11 - 14, 1995
and the
4th Plenary Meeting of the
European Spallation Source Project, ESS,
held at Weinfelden
October 16 - 19, 1995

Volume II

Editors

G.S. Bauer
R. Bercher

Paul Scherrer Institut, CH-5232 Villigen PSI

PSI-Proceedings 95-02
ISSN 1019-6447
November 1995

Photographs:
A. Lehner (cover)
A. Müller
G. Bauer

This publication is available from:
Paul Scherrer Institut, PSI
Renate Bercher
Würenlingen and Villigen
CH-5232 Villigen PSI
Switzerland
Telephone: +41 56 310 3402
Telefax +41 56 310 3131
E-mail Renate.BERCHER@PSI.CH

PREFACE

It was a pleasure to host ICANS-XIII at the Paul Scherrer Institut from October 11 to 14, 1995. It was particularly rewarding to see that, besides the old friends we have shared our interest in new neutron sources with for many years, several young people have entered the scene and were able to make important contributions to the field.

The topic of new sources could be seen to be as acute as ever. Several important events since ICANS-XII made this meeting a particularly exciting one: The AUSTRON-study has been completed and both, ANL and LANL have produced impressive documents on upgrade options for their respective facilities. Crucial decisions were taken in Japan concerning the future of the KEK-accelerating complex which lead to a complete rethinking of the KENS-II-project. Also the European Spallation Source Study had finally received funding from the EU which gave the project work a significant boost. To acknowledge this and to make information exchange as intense as possible without requiring excessive duplication of presentations, ICANS-XIII and the 4th General Meeting of the ESS-project group were moved close together (in time and location). In this spirit it was decided to make these proceedings joint ones between ICANS-XIII and ESS-PM4 in order to give everyone the opportunity to have his paper included, irrespective of where it was presented.

The new interest in the long pulse option which has developed steadily since ICANS-XII reflected itself in a significant number of contributions to this topic, not all of which were received in written form, however.

Finally, the probably most decisive event, the negative decision on the ANS project in the US, which deprived the world neutron scattering community of its hope to have a next generation neutron source soon, had an immediate effect also on the ICANS-group of laboratories:
Oak Ridge National Laboratory as the preferred alternative site for the US spallation neutron source project study has applied and was warmly welcomed as a new member of the collaboration. We all wish them success in the duty they have taken on and will be happy to share our knowledge and experience in very possible way.

Last but not least, I would like to thank all the authors of the papers in these proceedings for complying with the deadlines we had to set in order to ensure speedy publication. The work presented at the ICANS-meetings traditionally represents latest results, often forwarded for discussions and critism. This is only possible, if the written documents become available soon after the meeting. We made every effort to accomplish this. The papers are published unreviewed and their form and contents are exclusively in the responsibility of the authors. Thanks again, for the co-operation!

Günter Bauer
Head
Spallation Neutron Source Division
Paul Scherrer Institut
November 2, 1995

ICANS XIII

Groups/Topics/Time zone/Papers/ Chairman

Session	Topics/Groups	Date	Start	End	Duration	Papers	min/p	Chairperson	Local assistan	Tel. Int.
N	News from existing ICANS facilities	11.Oct				5		Bauer Watanabe		
O1	Ongoing projects	12.Oct	08,00	10,30	02,30	5		Ikeda		
O2	Ongoing projects	12.Oct	11,00	12,30	01,30	5		Carpenter		
O3	Ongoing projects	12.Oct	15,30	16,30	01,00	2		Pynn	Y.Takeda	3568
R	Review talks					3		Furrer Taylor Aksenov		
G1A	Target-moderator system : Neutronics	13.Oct	10,30	12,30	02,00	6	20,00	Russell	E.Lehmann	2963
G1B	Target-moderator system : Target concepts	13.Oct	15,30	18,30	03,00	9	20,00	Filges	F. Atchison	3256
G1C	Target-moderator system : Moderators general	11.Oct	17,50	18,30	00,40	2	20,00	Broome	W.Wagner	2517
G1D	Target-moderator system : Cold moderators	13.Oct	08,00	10,00	02,00	6	20,00	Broome	W.Wagner	2517
G2A	Scattering methodology : Instrument components	13.Oct	08,00	10,00	02,00	6	20,00	Conrad	J. Schefer	3066
G2B	Scattering methodology : Elastic scattering	13.Oct	15,30	18,00	02,30	7	21,26	Cser	D.Clemens	2925
G2C	Scattering methodology : Inelastic scattering	13.Oct	10,30	12,30	02,00	5	24,00	Steigenberger	J. Mesot	4029
G3	Science in Q'w?	13.Oct	08,00	10,00	02,00	4	30,00	Arai	A. Dönni	4007
G4A	Source concepts : Instrumentations	13.Oct	10,30	12,30	02,00	5	24,00	Johnson	W. Marti	4044
G4B	Source concepts : Source	11.Oct	15,30	17,50	02,20	7	20,00	Hjelm	M. Gutmann	2092
T3	Fourier and correlation techniques	11.Oct	15,30	17,50	02,20	6	23,20	Aksenov	G. Boettger	2091
T4	Computational methods	11.Oct	15,30	17,50	02,20	6	23,20	Seeger	P. Allenspach	2527
S1	Summary : G1, G4, T4	13.Oct	08,00	10,00	02,00			Appleton		
S2	Summary : G2, G3, T3	13.Oct	10,30	12,00	01,30			Leadbetter		
S	Conference Summary : Carpenter	13.Oct	12,00	13,00	01,00			Fischer		
P	Poster	11.Oct	08,00			7				

Table of Contents

Volume I

Session Summaries 1

S-1 Science with Neutrons 3
J. Arai

S-2 Methods in Inelastic Scattering 5
L. Cser

S-3 Instrumentation for Inelastic Scattering Experiments 7
U. Steigenberger

S-4 Fourier RTOF Diffractometers 9
V. Aksenov

S-5 Target-Moderator-System: Target Concepts 11
D. Filges

S-6 Target-Moderator-Systems: Components 13
T. Broome

S-7 Computational Methods 15
P.A. Seeger

S-8 Source Concepts 17
R. Hjelm

S-9 Target Moderator System-Neutronics 19
G.J. Russell

S-10 Scattering Methodology: Instrument components 20
H. Conrad

General 22

G-1 ICANS on the World Wide Web 22
J.M. Carpenter, J.P. Harnmonds

News from Existing ICANS-Facilities 29

N-1 ISIS: The First 10 Years 31
A. Taylor

N-2 News From IPNS 35
B.S. Brown

N-3 Progress On The PSR/LANSCE Upgrade 44
R.J. Macek

N-4 News From KENS 52
H. Ikeda

N-5 News From IBR-2 56
V.L. Aksenov

N-6 Spallation Neutron Sources at the INR RAS: Present Status and Prospects 63
Y.Y. Stavissky

N-7 SINQ A Continuous Spallation Neutron Source (An Approach to 1 Mwatt of Beam Power) 75
W.E. Fischer

Instruments, Methods and Components 85

I-1 Setup and Operation Mode of a Pulsed White Beam Angle-Dispersive ToF-Texture-Diffractometer 87
W. Schäfer, E. Jansen, W. Kockelmann, H. Tietze-Jaensch, K. Will

I-2 Neutron Time-of-Flight Diffractometer for Investigations of Microsamples under High External Pressure 93
V.L. Aksenov, A.M. Balagurov, S.L. Platonov, B.N. Savenko, D.V. Sheptyakov, V.P. Glazkov, V.P. Naumov, V.A. Somenkov, G.F. Syrykh

I-3 The New Small-Angle Diffractometer SAND at IPNS 99
R.K. Crawford, P. Thiyagarajan, J.E. Epperson, F. Trouw, R. Kleb, D. Wozniak, D. Leach

I-4 Novel Tendencies in Developing Small-Angle Neutron Scattering Methods for Studying the Structure of Biological Macromolecules 118
I. Serdyuk

I-5 SURF - A Second Generation Neutron Reflectometer 123
D.G. Bucknall, J. Penfold, J.R.P. Webster, A. Zarbakhsh, R.M. Richardson, A. Rennie, J.S. Higgins, R.A.L. Jones, P. Fletcher, R.K. Thomas, S. Roser, E. Dickinson

I-6 Evaluation of ROTAX 130
H. Tietze-Jaensch, W. Schmidt, R. Geick, G. Will

I-7 FOCUS: A New Time of Flight Spectrometer at the Neutron Spallation Source SINQ/CH 150
J. Mesot, S. Janssen, L. Holitzner, M. Prager, D. Richter, R. Hempelmann

I-8 Inelastic Neutron Scattering Spectrometer for the IN-06 Neutron Source at the Moscow Meson Factory 155
V.Y. Kazimirov, A.V. Belushkin

I-9 Future Opportunities and Present Possibilities for Coherent Inelastic Single Crystal Measurements on Pulsed Neutron Sources 164
M. Hagen, U. Steigenberger, C. Petrillo, F. Sacchetti

I-10 Pulsed Magnetic Fields and Pulsed Neutron Sources 164
U. Steigenberger, K. McEwen

I-11 Time Collimation for Elastic Neutron Scattering at a Pulsed Source 165
V.L. Aksenov, Yu.V. Nikitenko

I-12 Deconvoluting Source Pulse Broadening in Pulsed Source Time of Flight Measurements 175
J.M. Carpenter

I-13 Improvements in Resolution Calculation for Triple Axis and Time-of-Flight 184
W. Schmidt, H. Tietze-Jaensch, R. Geick, H. Grimm, G. Will

I-14	The MCLIB Library: Monte Carlo Simulation of Neutron Scattering Instruments *P.A. Seeger*	194
I-15	Development of the FLNP Measurement- and Computational Complex *Yu.A. Astakhov, A.A. Bogdzel, F.V. Levchanovsky, B. Michaelis, V.E. Novozhilov, A.I. Ostrovnoy, V.I. Prikhodko, V.E. Rezaev, V.E. Sirotin, G.A. Sukhomlinov, Yu.A. Volkov*	213
I-16	Principles of Reverse Time of Flight Method and Fourier Technique *P. Hiismäki*	228
I-17	Performance of the High Resolution Fourier Diffractometer at the IBR-2 Pulsed Reactor; Latest Results *V.L. Aksenov, A.M. Balagurov, V.A. Trounov, P. Hiismäki*	235
I-18	The Fourier RTOF Neutron Diffractometer FSS at the 5 MW Research Reactor FRG-I *H.G. Priesmeyer*	240
I-19	M.SFINKS Diffractometer at the Gatchina Reactor *V.A. Trounov*	247
I-20	Some Pecularities of RTOF Method and Calibration of Diffratometer "MINI-SFINKS" *D.Y. Chernyshov*	261
I-21	Wide Band Devices *L. Cser*	267
I-22	Morphology of Glass Surfaces: Influence On the Performance of Supermirrors *P. Böni, D. Clemens, H. Grimmer, H. Van Swygenhoven*	279
I-23	Neutron Composite Germanium Monochromators for Diffraction Instruments at SINQ *J. Schefer, S. Fischer, M. Medarde, R. Thut, M. Koch, P. Fischer, U. Staub, A. Dönni, G. Böttger, M. Horisberger*	288
I-24	Julios Detectors Combined to a PC-Based Data Acquisition System *E. Jansen, W. Schäfer, G. Will, R. Engels, R. Reinartz, K.D. Müller*	294
I-25	Proposal for a 30-T Pulsed Magnet Suitable for Neutron Scattering Experiments *R.A. Robinson, Y.M. Eyssa, H.J. Schneider-Muntau, H.J. Boenig*	300
I-26	A User-Friendly, Graphical Interface for the Monte Carlo Neutron Optics Code MCLIB *T. Thelliez, L. Daemen, P.A. Seeger, R.P.Hjelm*	307
I-27	Remanent Multilayers for Polarized Neutron Instrumentation *D. Clemens, W. Hahn, A. Vananti, P. Schubert-Bischoff, P. Böni, M. Horisberger*	312

The Long Pulse Option 321

L-1 Performance of Long-Pulse Source Reference Target-Moderator-Reflector Configurations 323
E. Pitcher, G. Russell, P.A. Seeger, P.D. Ferguson

L-2 The Performance of Neutron Spectrometers at a Long-Pulse Spallation Source 330
R. Pynn, L. Daemen

L-3 Instrument Options for Long Pulse Neutron Sources 339
G.S. Bauer

L-4 On Proton Pulse Lengths and Rep Rates with Emphasis on SANS 355
H. Conrad

L-5 Small-Angle Scattering Instruments on a 1 MW Long Pulse Spallation Source 370
G.A. Olah, R.P. Hjelm, P.A. Seeger

L-6 The Performance of Reflectometers at Continuous Wave and Pulsed-Neutron Sources 381
M.R. Fitzsimmons, R. Pynn

L-7 Monte Carlo Study of the Performance of a Time-of-Flight Multichopper Spectrometer 388
L.L. Daemen, J. Eckert, R. Pynn, P.A. Seeger

L-8 Complementarity of Long Pulse and Short Pulse Spallation Sources 400
F. Mezei

Volume II

Targets, Moderators and Handling Devices 429

T-1 Computation Methods for Neutron, Heat and Radiation Damage Properties of Pulsed Neutron Sources 431
A.V. Dementyev, S.G. Lebedev, O.N. Smirnova, N.M. Sobolevsky, Y.Y. Stavissky

T-2 Measurements of Spallation Neutrons from a Thick Lead Target Bombarded with 0.5 and 1.5 GeV Protons 442
S. Meigo, H. Takada, S. Chiba, T. Nakamoto, K. Ishibashi, N. Matsufuji, K. Maehata, N. Shigyo, Y. Wakuta, Y. Watanabe, M. Numajiri

T-3 Multiplying Target for a High-Intensity Spallation Neutron Source 454
V.G. Miroshnichenko, S.F. Sidorkin, Y.Y. Stavissky, V.F. Kolesov, E.P. Shabalin, Y.N. Likhachev

T-4 Tungsten and Uranium Targets for the Moscow Meson Factory 461
A.V. Dementyev, V.G. Miroshnichenko, S.F. Sidorkin, N.M. Sobolevsky, Y.Y. Stavissky, I.I. Konovalov, A.A. Maslov, I.T. Tretyakov, V.I. Trushkin, A.D. Rogov

T-5	The AUSTRON-Target: The Neutron Flux of Decoupled and Poisoned Moderators *G. Muhrer, W. Ninaus, E. Schachinger*	480
T-6	Radioactive Halogen Yields from the Tungsten Target Irradiated by High-Energy Protons *S.V. Ignatiev, D.V. Pankratov, E.I. Yefimov*	487
T-7	Coupled Moderator Neutronics *G.J. Russell, E. Pitcher, P. Ferguson*	495
T-8	Reference Moderator Calculated Performance for the LANSCE Upgrade Project *P. Ferguson, G.J. Russell, E. Pitcher*	510
T-9	Present State of the ESS Tantalum-Target *B. Guttek*	518
T-10	Neutronics Studies for the ESS Source *D.J. Picton, T.D. Beynon, T.A. Broome*	522
T-11	Nuclear Studies of Different Target Systems for the European Spallation Source (ESS) *D. Filges, R.D. Neef, H. Schaal*	537
T-12	Mercury as a Target Material for Pulsed (Fast) Spallation Neutron Sources *G.S. Bauer*	547
T-13	On the Pressure Wave Problem in Liquid Metal Targets for Pulsed Spallation Neutron Sources *K. Skala, G.S. Bauer*	559
T-14	Thermal Hydraulics of the ESS Liquid Metal Target *B.L. Smith*	577
T-15	Experience With ISOLDE Molten Metal Targets at the CERN-Booster *J. Lettry, R. Catherall, P. Drumm, A. Evensen, O. Jonsson, E. Kugler, J. Obert, J.C. Putaux, J. Sauvage, H. Ravn, M. Toulemonde*	595
T-16	Suitability of Steels as ESS Mercury Target Container Materials *Y. Dai*	604
T-17	Water/Monel Heat Pipes for Cooling of Liquid Metal Targets for SINQ and ESS *M.T.North, J.H. Rosenfeld, D.B. Sarraf, G.S. Bauer, Y. Takeda*	623
T-18	Prospects for Targets and Methane Moderators at ISIS *T.A. Broome*	632
T-19	A Pelletized Solid Methane Moderator for a Short Pulsed Neutron Source *A.T. Lucas, G.S. Bauer, C.D. Sulfredge*	644

T-20 Further Optimization of Coupled Liquid-Hydrogen Moderator for Intense Pulsed Neutron Source 654
Y. Kiyanagi, Y. Ogawa, N. Kosugi, H. Iwasa, M. Furusaka, N. Watanabe

T-21 Recent Progress in Developing High-Efficiency Cryogenic Moderators 659
N. Watanabe, Y. Kiyanagi, M. Furusaka

T-22 High-Efficiency Cryogenic Moderator System for Short Pulse Cold-Neutron Use 666
Y. Kiyanagi, N. Kosugi, Y. Ogawa, H. Iwasa, F. Hiraga, M. Furusaka, N. Watanabe

T-23 Supply System for Cold Neutron Sources for the ESS Proiect 672
K. Stendal

T-24 Handling Devices for the Beam Port- and Cold Moderator Inserts of SINQ 688
W. Wagner, J. Ehrat

T-25 Examination of Disks from the IPNS Depleted Uranium Target 697
R.V. Strain, J.M. Carpenter

T-26 Target and Structural Materials Under Dual Beam Irradiation 707
E. Camus, N. Wanderka, H. Wollenberger

Accelerator Systems and Components 715

A-1 The Los Alamos Long Pulse Spallation Source Driver 717
A.J. Jason

A-2 Moscow Meson Factory Linac for the Pulsed Neutron Source 724
L.V.Kravchuk

A-3 High Current Ion Source Development at Frankfurt 726
K. Volk, H. Klein, A. Lakatos, A. Maaser, M. Weber

A-4 LEBT Design Studies for ESS 732
J. Pozimski, P. Groß, R. Dölling, K. Reidelbach, H. Klein

A-5 Chopping- and Funneling-Studies for ESS at Frankfurt 736
J. Madlung, A. Firjahn-Andersch, A. Schempp

A-6 Recent Development of a Closed Orbit Monitor System in the KEK Booster Synchrotron 740
H. Someya, D. Arakawa, J. Kishiro, I. Yamane

A-7 FFAG Options for Spallation Neutron Sources 745
S. Martin, P.F. Meads, E. Zaplatine, K. Ziegler, R.L. Kustom

A-8 Pulsed Spallation Neutron Source with an Induction Linac and a Fixed-Field Alternating-Gradient Accelerator 750
A.G. Ruggiero, G.S. Bauer, A. Faltens, R.L. Kustom, S.A. Martin, P.F. Meads, E. Zaplatin, K. Ziegler

A-9 A 10-GeV, 5- MW Proton Source for a Pulsed Spallation Source 758
Y. Cho, Y.C.Chae, E. Crosbie, H. Friedsam, K. Harkay, D. Horan, R. Kustom, E. Lessner, W. McDowell, D. McGhee, H. Moe, R. Nielsen, G. Norek, K.J. Peterson, K. Primdahl, Y.L. Qian, K. Thompson, M. White

Project Studies 775

P-1 Feasibility Study for the IPNS Upgrade, A 1MW Pulsed Spallation Neutron Source - Target Stations 777
J.M.Carpenter

P-2 Feasibility Study of a 1- MW Pulsed Spallation Source 789
Y. Cho, Y.C. Chae, E. Crosbie, H. Friedsam, K. Harkay, D. Horan, S. Kim, R. Kustom, E. Lessner, W. McDowell, D. McGhee, F. Mills, H. Moe, R. Nielsen, G. Norek, K.J. Peterson, K. Primdahl, A. Rauchas, K. Symon, K. Thompson, M. White

P-3 A Proposal for a Long Pulse Spallation Source at Los Alamos National Laboratory 798
R. Pynn, D. Weinacht

P-4 BNL Feasibility studies of spallation neutron sources 802
Y.Y. Lee, A.G. Ruggiero, A. Van Steenbergen, W.T. Weng

P-5 Status of Pulsed Spallation Neutron Source Target Work at Brookhaven National Laboratory 808
H. Ludewig, M. Todosow, J. Powell

P-6 Status of the Oak Ridge Spallation Neutron Source (ORSNS) Project 814
B. Appleton

P-7 The European Spallation Source (ESS) Study 819
H. Lengeler

P-8 Status of the AUSTRON-Project 831
M. Schuster, P. Bryant

P-9 Current status of JHP N-arena 836
M. Furusaka, H. Ikeda

P-10 Use of Cold Source and Large Reflector Mirror Guide for Neutron-Antineutron Oscillation Search (Proposal) 843
Yu. Kamyshkov, W. Bugg, H. Cohn, G. Condo, Yu. Efremenko, S. Lamoreaux, R. Lillie, F. Plasil, S. Raman, M. Rennich, K. Shmakov, R. Wilson, G. Young

Our Sponsors 851

Q-1 Cilas 853

Q-2 Descote S.A. 854

Q-3 Helbling Technik AG 855

Q-4 KIWI Systemingenieure und Berater AG 856

Q-5 Linde Kryotechnik 857

Q-6	Loosli Formtech AG	858
Q-7	Noell GmbH	859
Q-8	Pier-Armaturen GmbH	860
Q-9	Prophysik AG	861
Q-10	Schär Engineering AG	862
Q-11	Sulzer Chemtech	863
Q-12	Tensol	864
Q-13	VAT Vakuumventile AG	865
Q-14	Von Roll	866
Q-15	Romabau AG	867
Q-16	Alcatel Kabel AG & Co	868
Q-17	Daimler Benz Aerospace, Dornier	869
Q-18	Alusuisse Road & Rail AG	870
Indices		871
	List of Authors	873
	List of Keywords	877
List of Participants		883
	ICANS-XIII	885
	ESS-PM4	893

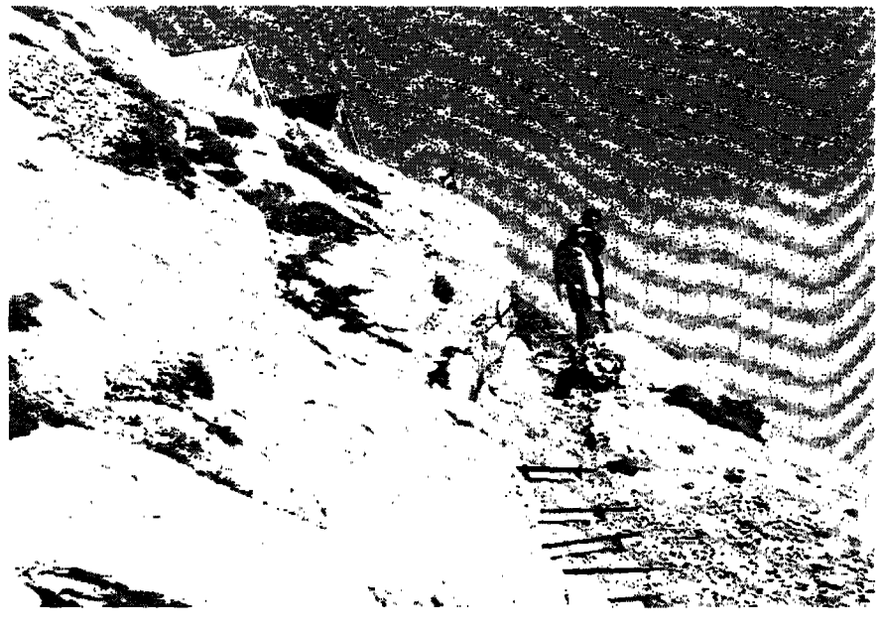

The Summit

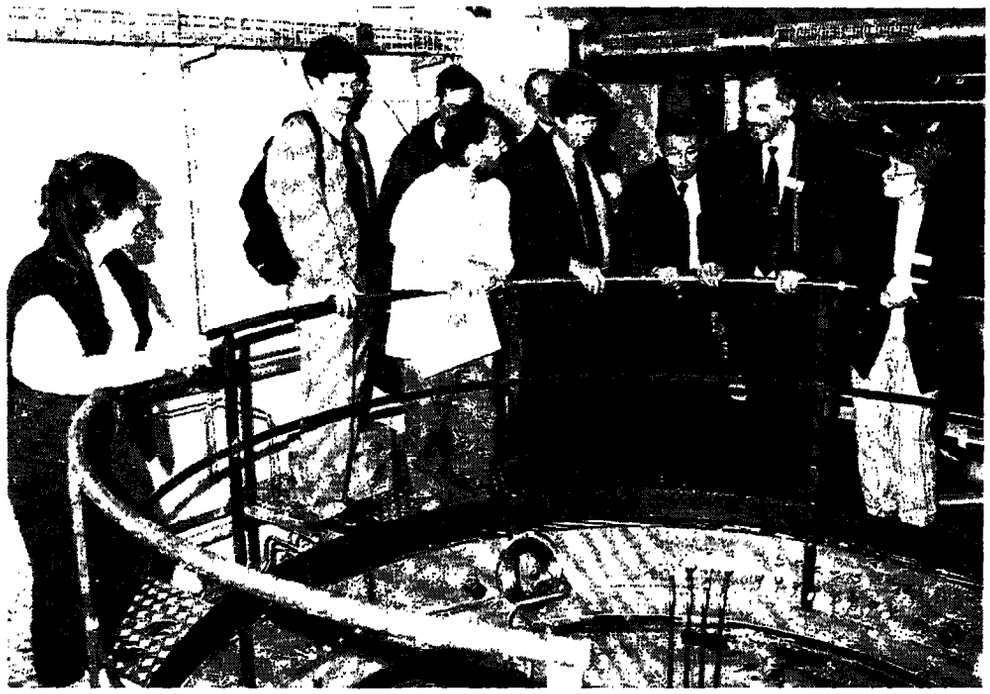

Targets, Moderators and Handling Devices

ICANS-XIII
13th Meeting of the International Collaboration on
Advanced Neutron Sources
October 11-14, 1995
Paul Scherrer Institute, 5232 Villigen PSI, Switzerland

COMPUTATION METHODS FOR NEUTRON, HEAT AND RADIATION DAMAGE PROPERTIES OF PULSED NEUTRON SOURCES

A.V.Dementyev, S.G.Lebedev, O.N.Smirnova, N.M.Sobolevsky, Yu.Ya.Stavissky

Institute for Nuclear Research RAS, Moscow 117312, Russia

ABSTRACT

The results of calculations of neutron yield, heat and nuclei-products distributions for heavy extended targets (natural W, Pb, and depleted U cylindrical targets; D=20 cm, L=60 cm) irradiated with proton beam of energy up to 100 GeV are presented as well as the radiation damage cross sections for thin layers of structure materials. The calculations were made with Monte Carlo method on the base of exclusive high energy hadron transport code SHIELD. The comparison with available experimental data is given. An expediency of elaboration of spallation neutron source based on high-energy accelerator is briefly discussed.[1]

1 .Introduction

Process of neutrons generation in heavy extended target (W, Pb, U) under proton beam irradiation is a background for a number of important trends in nuclear physics and technics. These are, primarily, the pulsed neutron sources, conception of electro-nuclear breeding and connected with it problem of neutron transmutation of the power plant radioactive wastes which became especially actual during last years as well as some more special problems. In fact we are dealing with industrial production of neutrons. At that the questions of a total neutron yield from the target and a neutron energetic cost are very essential and even critical for some conceptions. Parameters of an energy release and nuclei-products distributions over a target volume are very essential also as well as the radiation damage of structure materials ones because of real constraining of beam power and consequently of the neutron yield. For these reasons a series of corresponding experimental and theoretical investigations has been undertaken since the fifties.

However a large-scale measurements with an extended target are very labor consuming and methodical sophisticated. Therefore only a limited number of measurements of total neutron yield from the target were made up to now. Results of early experiments in incident energy range near 1 GeV are presented, for example, in reviews [1]. In recent years the data have been produced in energy range 1 - 8 GeV for lead target [2] and at 70 GeV for tungsten target

[1] Keywords: Target, Neutron yield, Energy deposition, Monte Carlo

[3]. The calorimetric measurements of energy release in targets are presented in a few works only [4,5]. The situation is somewhat better for nuclei-products distributions over a target volume (see e.g. [6,7] and cited therein).

Thus the development of computation methods and computer codes for simulation of beam-target interaction process is necessary condition of a progress in the field under consideration. There are now several modifications of well-known transport code HETC [8] (LAHET-LANL, HERMES-KFA, NMTC-JAERI et al.) which provide mainly the adequate description of spallation-process in the target at proton beam energy up to several GeV. On the other hand presence of theoretical data for much more wide energy range would enable one to discuss some alternative conceptions of nuclear facilities.

Therefore the main objective of this work is systematic computational investigation of the total neutron yield from lead target under irradiation with protons of 0.1 to 100 GeV as well as the computation of energy deposition and nuclide production distributions in heavy targets and comparison with measured data. Question of structure materials radiation damage is briefly considered. The calculations were performed using the universal Monte Carlo hadron transport code SHIELD [9]. It is very close on its power to the HETC code in energy area up to several GeV. At the same time the SHIELD code is applicable for using up to 100 GeV and above.

2. Hadron transport code SHIELD

The SHIELD code is dedicated to the Monte Carlo simulation of hadron cascades in complex macroscopic targets of arbitrary geometric configuration and chemical composition. One can calculate a nucleon, pion, kaon, antinucleon, and muon transfer in energy range up to 100 GeV. The ionization loss of energy for charged particles and straggling are taken into account. At transporting of pions and kaons the main modes of 2- and 3-particles decays are simulated.

The capabilities and quality of a hadron transport code depends substantially on a hadron-nucleus (hA) generator used. hA-generator of the SHIELD code includes known Russian models of nuclear reactions: Dubna version of the intranuclear cascades model detailed in monograph [10]; for more high energies - the hadron-nucleus and nucleus-nucleus generator based on an independent quark-gluon string model [11]; a combined nuclear deexcitation model [12,13] considering the multifragmentation of highly excited nuclei, equilibrium particle emission involving evaporation/fission competition for heavy nuclei and Fermi break-up for light nuclei. The pre-equilibrium emission is taken into account recently. hA-generator of the SHIELD code provides an exclusive description of the nuclear reactions over entire energy range and nuclei-targets mass area.

During a hadron tree generation in target the source of the "evaporated" neutrons is formed as well as the sources of the mesons decay products: γ-rays, e^-/e^+, and neutrinos. Subsequent neutron transport is simulated with the original neutron code LOENT based on 26-group neutron data system BNAB [14]. The electromagnetic (EM) showers are simulated by means of the well-known EGS4 code which is connected to the SHIELD with a special interface.

Each hadron cascade tree is stored without any loss of physical information during its simulation, allowing to divide completely modeling and registrating parts of the code as well as to repeat tree processing and visualize the tree. The SHIELD code's open architecture presumes its modification and improvement.

Some parameters of hadron cascade which are computed with the SHIELD code can be used for further calculations. In particular the individual parameters of residual nuclei in a target (i.e. PKA - primary knocked-out atoms) were used in this work for calculation of the radiation damage cross sections of structure materials.

3. Results of calculations

In our calculations the targets are the cylinders of 20 cm diameter and 60 cm in length from W and Pb of natural isotope composition and from depleted U (0.3% U^{235}). Such dimension guarantees nearly complete absorption of hadron cascade charged component and are the accepted standard for topic in question. Pencil proton beam impinges on center of target along cylinder axis.

Fig.1 shows the yield of neutrons with energies below 10.5 MeV from the whole surface of Pb target in two different manners: while Fig.1a gives the yield in units neutron/proton, Fig.1b demonstrates the specific neutron yield, i.e. the number of escaped neutrons per incident proton and divided by the incident energy (neutron/proton GeV). The specific yield let us to emphasize the energetic optimum of spallation process (curve maximum corresponds to minimal energy cost of one neutron). The value 10.5 MeV is nothing more than upper limit of the 1-st BNAB energy group; the main bulk of the neutron yield is in this low energy region. The experimental data mentioned above are depicted here also. At 70 GeV the experimental neutron yield value [3] is given being recounted from tungsten to lead target according to the relationship $[Y(Pb)/Y(W)]_{exp}=[Y(Pb)/Y(W)]_{theor}$, where theoretical values of yield are obtained using the SHIELD code.

Fig.2 gives fractions of the beam energy expended in W target for

- forming of a source of neutrons with kinetic energies below 10.5 MeV (this fraction includes kinetic and binding energies),
- energy deposition in the target,
- energy leakage from the target during hadron and electromagnetic cascade development

as a percentage of beam energy. In turn the energy deposition is decomposed in its components. Taking the total deposited energy as 100% it is pictured what a fraction was released because of

- direct ionization loss of charged hadrons,
- heating due to EM showers induced by π^0 decays,
- kinetic energy of recoil/product nuclei,
- residual excitation of nuclei-products after particle emission from nucleus is exhausted (this excitation can be removed with γ-transitions only).

As one can see the fraction of the energy pumped from hadron to EM cascades via π^0 -decays exceeds direct ionization loss beginning from incident energies ~10 GeV. The share of residual nuclei in energy deposition is less than several percent in W target at all incident energies. Let us notice that for fissile target a contribution of kinetic energy of nuclei-products (fission fragments) into energy release can become determinative.

Fig.3 demonstrates the distributions of energy deposition along target axis for incident beam energies of 1, 10, and 30 GeV (the curves are result of histograms smoothing). Dotted lines give a variant of computation without simulation of EM showers: it was assumed that EM

energy is deposed locally in π^0-decay point. Evidently last approximation is justified below 1 GeV only while the correct account of energy transfer by electron-photon showers becomes essential for forming of the proper energy deposition profile (including maximum location) as beam energy increases. At 1 GeV the comparison of SHIELD calculations of energy deposition profile with calorimetric measurements [5] for Pb and depleted U targets is presented. One can see a good accordance for both cases. As our calculations have demonstrated the contribution of kinetic energy of fission fragments into complete energy deposition in the target achieves about 70% for this fissile composition.

Fig.4 illustrates the charge distribution of nuclei-products formed during hadron cascade development in Pb target for beam energies of 1, 10, and 30 GeV. The contribution of different nuclear processes is easily observable. The area near Z of the target (Z=~60-83) is determined by deep disintegration (spallation) process. The responsibility for mediate Z area is on both fast fission and multifragmentation of highly excited nuclei processes. The small Z area is determined with the multifragmentation. As would be expected the role of this process increases with incident energy. In Fig.4b the depth distribution of the production rate (nucleus/proton) of radionuclide Pb^{201} is displayed together with measured one from [7] at incident proton energy of 1 GeV just as an example.

The radiation damage cross sections (barn*keV/proton) for structure materials with different Z (Al, Fe, Cu, Mo, W) are presented in Fig.5. Pencil proton beam of 600 MeV impinges normally on a thin material layer. The individual values (A_p,Z_p) for each nucleus-product and its kinetic energy E_0, as these are computed by the SHIELD code, were further used for radiation damage calculations with the RADDAM code [15]. These values (A_p,Z_p,E_0) enable one to calculate the damage energy E_d which, having been convoluted with the residual nucleus production cross section, give us the desired damage cross section. The details of E_d calculation procedure based on the works of J.Lindhard et al (1963) and of M.J.Norgett et al (1975) are described in [15]. The stopping power of the recoil ions in the material was treated in two ways: on the basis of Thomas-Fermi model or using some tabulated empirical data. The contributions into the cross sections were summarized over the whole nuclei-product ensemble. Degree of agreement of different variants between them is clear from the figure. It is difficult to make definite conclusion on the advantage of some variant as the radiation damage cross section defies to a direct measurement and some details of the HETC-calculation are omitted in corresponding articles (see [15] for greater detail).

4. Discussion

Thus the SHIELD code provides the adequate description of varied processes in extended targets at incident energies up to 100 GeV in exclusive (eventual) approach. In other words the code enables one to simulate any individual characteristics (including correlation ones) for each separate event but not just to get the averages on a whole ensemble (e.g. inclusive particle spectra). The SHIELD code is applicable for more high incident energies (up to 0.5 TeV at present time). However we didn't perform some systematic calculations above 100 GeV up to now. Moreover there are no available measured data suitable for comparison in this energy range.

At last let us discuss, using the obtained results, a possibility of designing a neutron source based on a high energy accelerator. As one can see in Fig.1b, the maximal specific neutron yield is observed at incident proton energy near 1.2 GeV. A fall in yield at lower energies is

determined by direct ionization loss of primary protons energy while at more high energies - by energy transfer into electron-photon showers due to generation and decay of neutral pions (see Fig.2). Therefore the optimal energy for generation of neutrons (with respect to the energy cost of one neutron) is approximately 1.2 GeV. However an application of high-current proton beams of such energy is joined with some difficulties at beam forming and injection into a target which are connected, at first, with losses during beam acceleration and transport and, moreover, with radiation damages of materials and high density of energy deposition in target areas near its first wall.

On the other hand although the specific neutron yield decreases with incident proton energy, the total neutron yield is very high in tens GeV region and continues substantially increase (Fig.1a). For example at 70 GeV near 650 neutrons per proton are generated as compared to 24 neutrons at 1 GeV. Therefore one can discuss the possibility of neutron generation by means of 30 - 100 GeV proton beam but at beam intensity on one and a half - two orders below as compared to 1 GeV proton beam. This point of view was for the first time expressed in report [16] as applied to pulsed neutron source on a base of a 30 - 40 GeV energy proton accelerator ("kaon factory"). Decreasing of specific neutron yield by a factor of 2 - 3 in tens GeV region may be compensated by a significant softening of the "first wall" and target cooling problems (as the maximum of energy deposition is shifted inside target and becomes more smooth with incident energy, see Fig.3). Both these factors are very significant in point of realization of neutron generators on a base of the spallation process. It is not improbable that going up more on the incident energy one could generate record neutron fluxes using some existing by the time or building up superhigh energy accelerators [17].

5. References

1. V.S.Barashenkov, *Nucl. Part. Phys.* **9** (1978) 871; R.G.Vassil'kov, V.I.Goldansky, V.V.Orlov, *Uspekhi Fiz. Nauk* **139** (1983) 435
2. R.G.Vasil'kov, V.I.Yurevich, *Neutron Emission from an Extended Lead Target under the Action of Light Ions in GeV Region.* Proc. ICANS-XI, KEK, Japan, October 22-26, 1990, vol. 1, p. 340
3. A.G.Akopyan, N.V.Kolmychkov, A.V.Kuzin, *Atomn. Energ.* **75** (1993) 219
4. W.Fisher, L.Moritz, H.Spitzer, I.Thorson, *Nucl. Sci. Eng.* **93** (1986) 273
5. V.I.Belyakov-Bodin, V.D.Kazaritsky, A.L. Povarov et al., *Nucl. Instr. Meth.* **A295** (1990) 140; *Atomn. Energ.* **70** (1991) 339
6. J.S.Gilmore, G.J.Russell, H.Robinson, R.E.Prael, *Nucl. Sci. Eng.* **99** (1988) 41
7. S.V.Bakhmutkin, A.A.Nosov, A.A.Rimsky-Korsakov, *Atomn. Energ.* **63** (1987) 137
8. T.W.Armstrong, K.C.Chandler.: *Nucl. Sci. Eng.* **49** (1972) 110
9. A.V.Dementyev, N.M.Sobolevsky, *SHIELD - a Monte Carlo Hadron Transport Code.* Proc. of Specialists' Meeting "Intermediate Energy Nuclear Data: Models and Codes", Paris, May 30 - June 1, 1994. NEA OECD, Paris, p. 237; Preprint INR RAS 0874/94, Moscow, 1994
10. V.S.Barashenkov, V.D.Toneev, *Interaction of Particles and Atomic Nuclei of High and Superhigh Energies with Nuclei.* Atomizdat, Moscow, 1972
11. V.D.Toneev, N.S.Amelin, K.K.Gudima, *The Independent Quark-Gluon String Model for Heavy Ion Collisions at Ultrarelativistic Energies.* Preprint GSI-89-52, Darmstadt, 1989; *Yadern. Fiz.* **51** (1990) 1730
12. A.S.Botvina, A.S.Iljinov, I.N.Mishustin, *Nucl. Phys.* **A507** (1990) 649

13. G.D.Adeev, A.S.Botvina, A.S.Iljinov et al., *The Calculation of Mass and Energy Distributions of Fission Residuals in Reactions Induced by Intermediate Energy Particles.* Preprint INR RAS 0816/93, Moscow, 1993
14. L.P.Abagyan, N.O.Bazazyants, M.N.Nikolaev, A.M.Tsibulya, *Neutron Group Constants for Reactors and Shielding Calculations.* Atomizdat, Moscow, 1981
15. S.G.Lebedev, O.N.Smirnova, N.M.Sobolevsky, Yu.Ya.Stavissky, *RADDAM Code for Simulation of Radiation Damage by High Energy Nucleons.* Preprint INR RAS 0896/95, Moscow, 1995
16. Yu.Ya.Stavissky, *Neutron Facilities of Moscow Meson and Kaon Factories.* Proc. ICANS-XI, KEK, Japan, October 22-26, 1990, vol. 1, p. 89
17. Yu.Ya.Stavissky, *Gigantic Pulses of Thermal Neutrons in Target of Superhighenergy Accelerator.* Preprint INR RAS P-215, Moscow, 1981

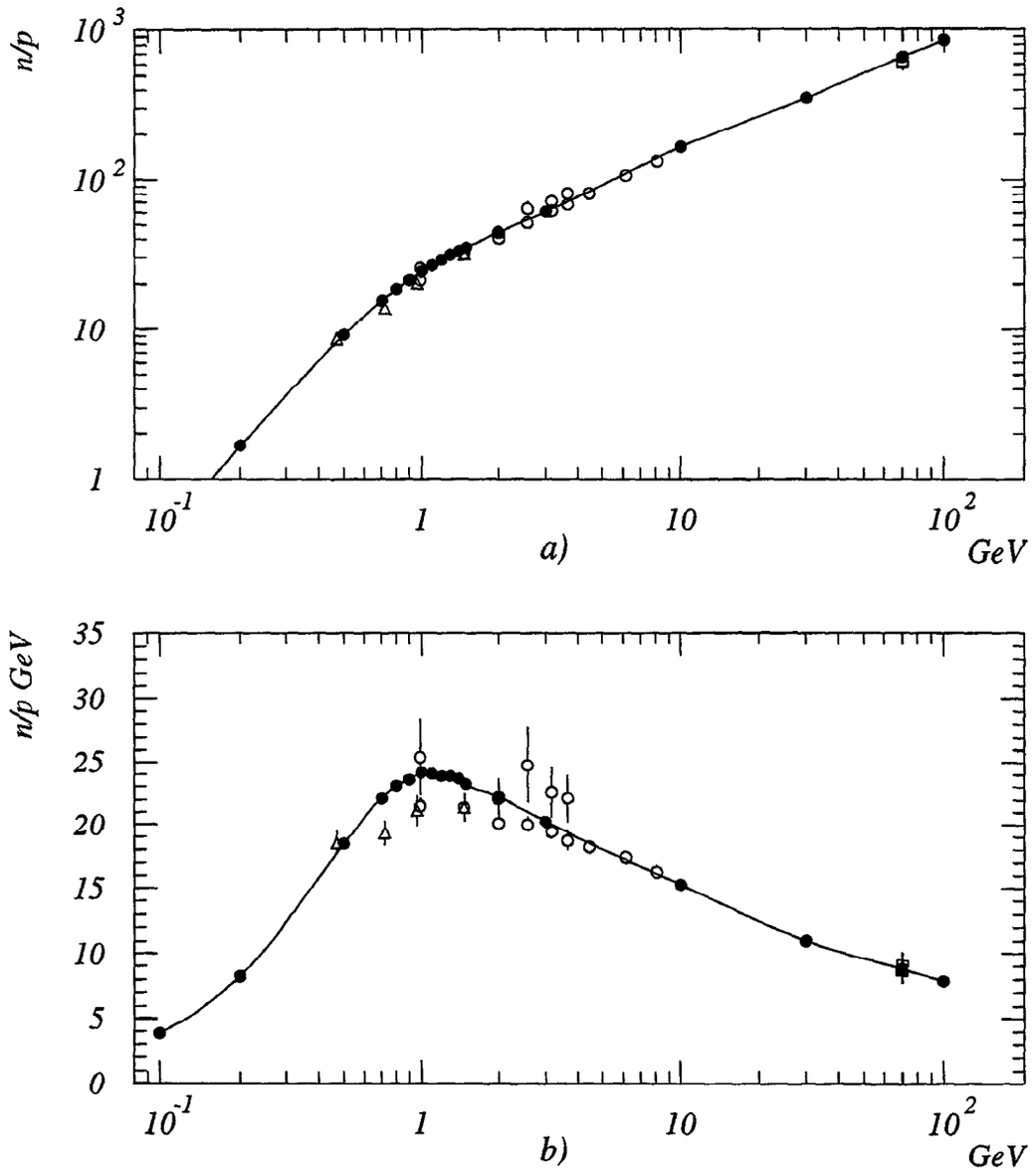

Figure 1: Neutron yield (a) and specific neutron yield (b) from a whole surface of Pb target (E_n <10.5 MeV). Curves approximate the results of SHIELD calculations. Experimental points are taken from works: △ – R.P.Trunnicliffe et al (extracted from [1]); ○ – [2]; □ – [3].

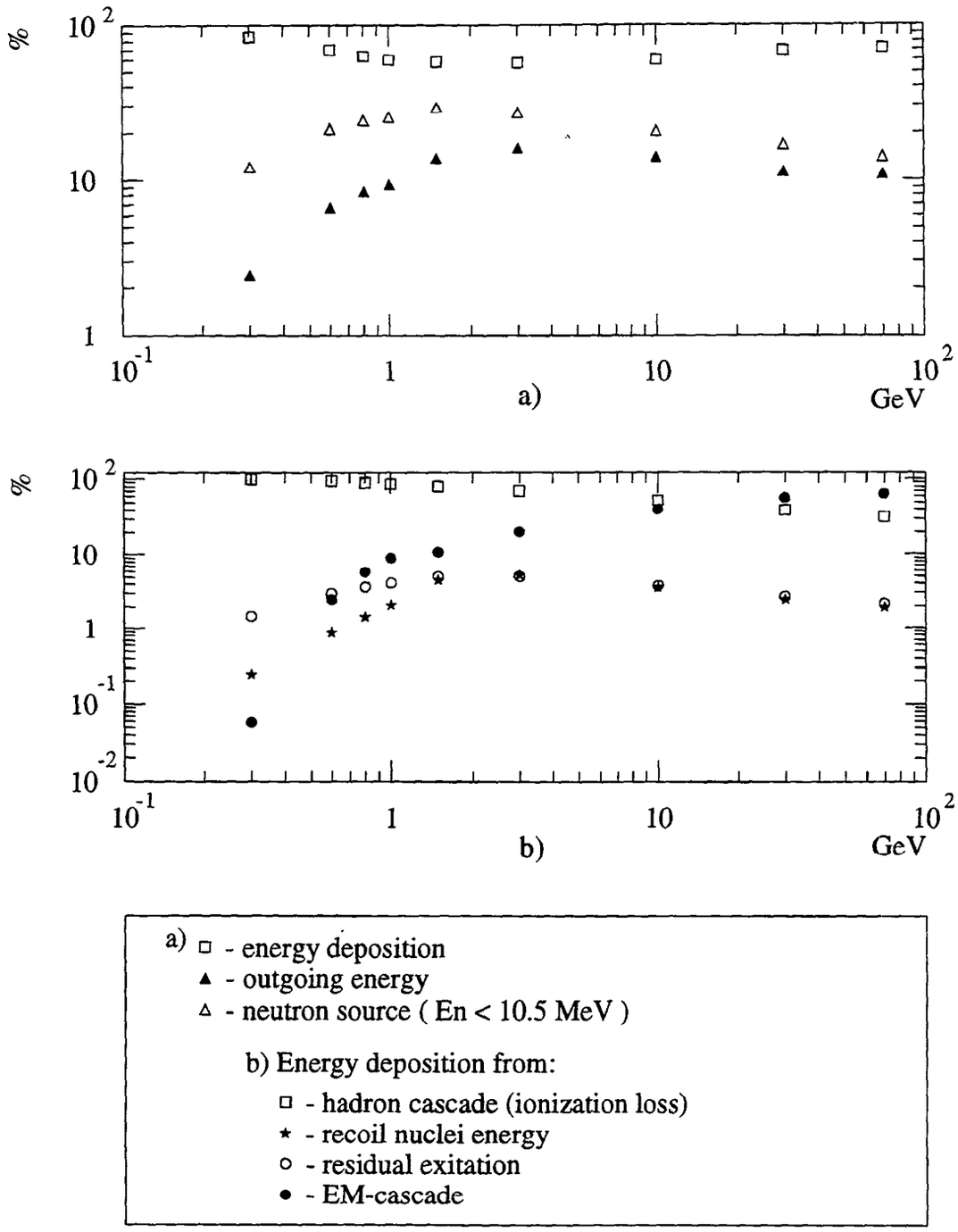

Figure 2: **W target: (a) fraction of proton beam energy (in %) have been spent on neutron source forming, target warming and removed from target (by hadron and electromagnetic cascades); (b) structure of heat release in dependence of primary proton energy (100 % – total energy deposition from both hadron and EM cascades).**

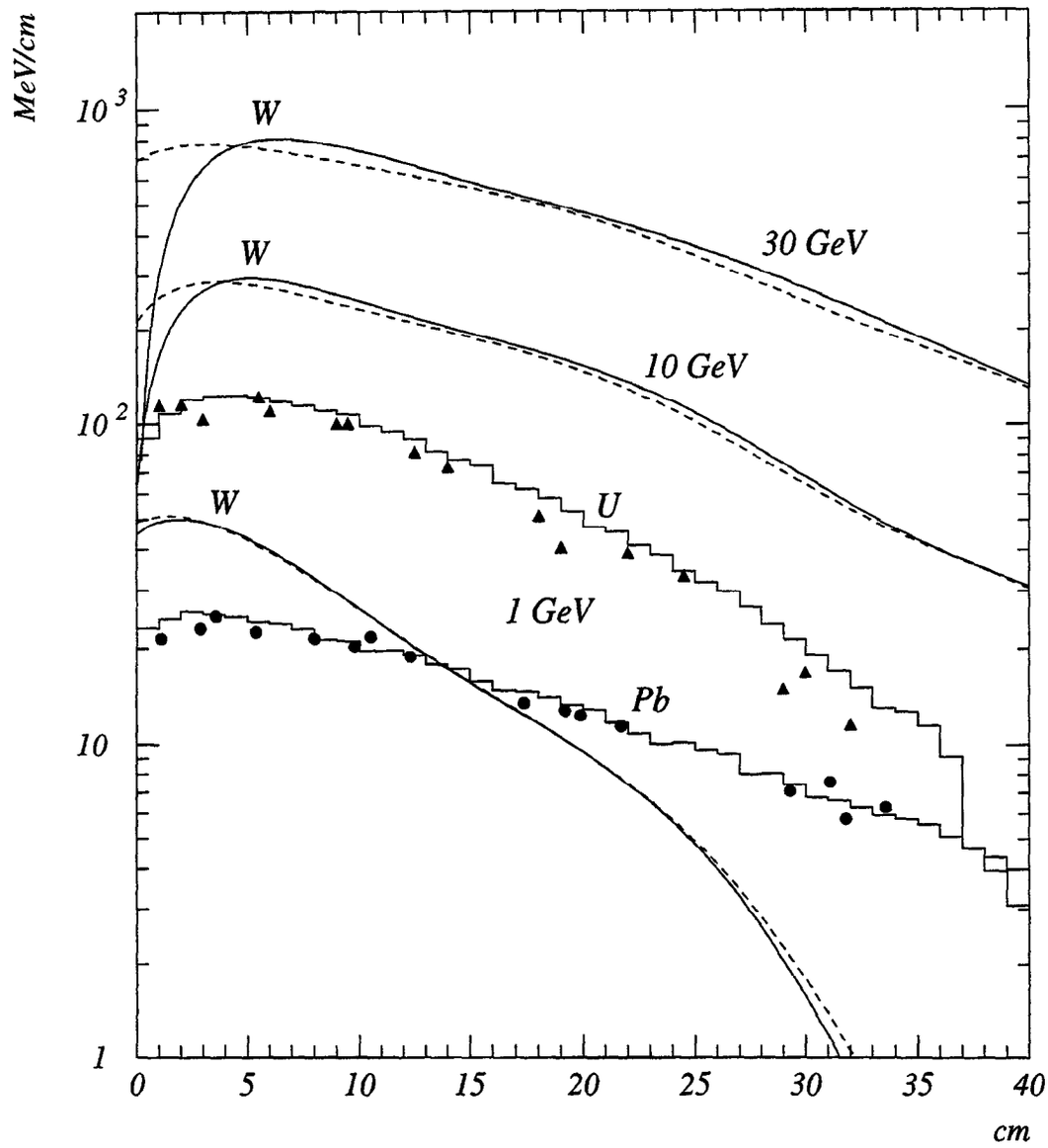

Figure 3: Distribution of energy deposition in Pb, W, and depleted U targets along target axis. Solid line – calculation with consideration of EM showers (EGS4), dashed ones – calculation in assumption of local energy release at point of π^0 decay. Incident proton energy and target material are indicated near curves. Points show the calorimetric mesurements [5].

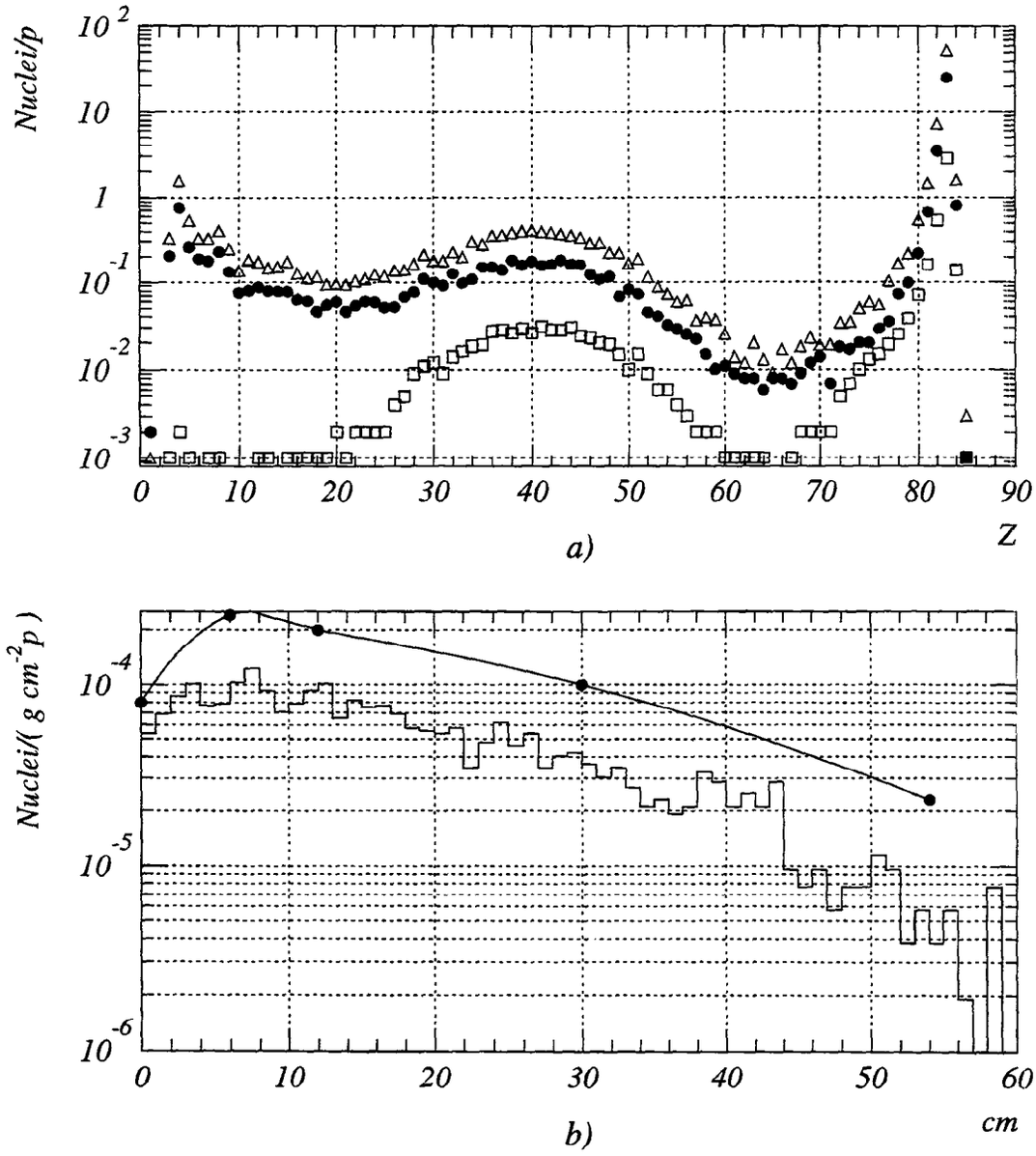

Figure 4: **Nuclei-products charge distribution (a) over a whole Pb target at incident proton energies of: 1 GeV – □, 10 GeV - •, and 30 GeV - Δ. Distribution of product ^{201}Pb along Pb target axis (b) at icident proton energy 1 GeV as compared with measurement [7] - •.**

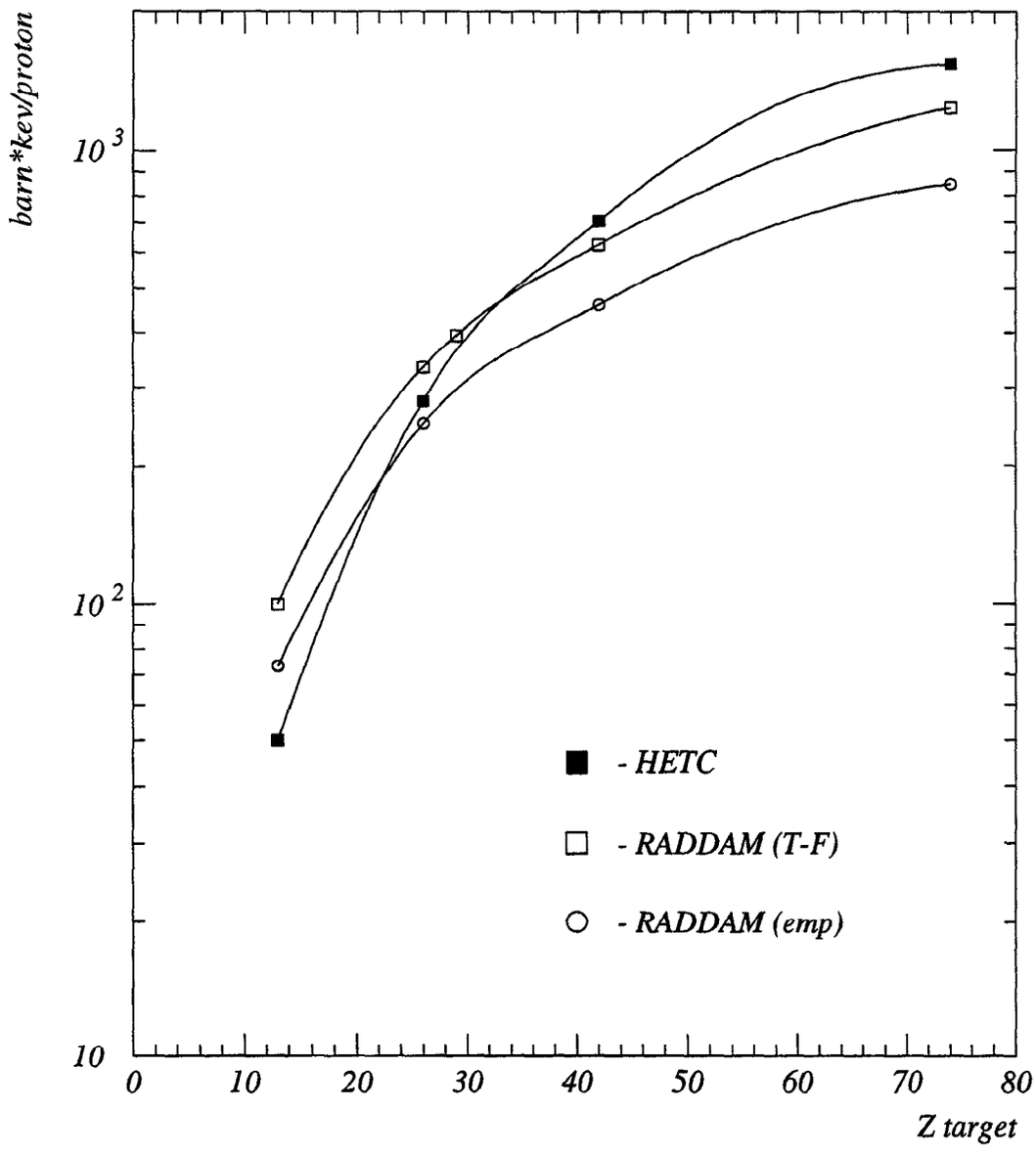

Figure 5: **Radiation damage cross section for thin metallic target of Al, Fe, Cu, Mo, and W under 600 MeV proton irradiation.**

ICANS-XIII
13th Meeting of the International Collaboration on
Advanced Neutron Sources
October 11-14, 1995
Paul Scherrer Institute, 5232 Villigen PSI, Switzerland

Measurements of Spallation Neutrons from a Thick Lead Target Bombarded with 0.5 and 1.5 GeV Protons

Shin-ichiro Meigo*, Hiroshi Takada*, Satoshi Chiba*, Tatsushi Nakamoto**, Kenji Ishibashi**, Naruhiro Matsufuji**, Keisuke Maehata**, Nobuhiro Shigyo**, Yoshihisa Wakuta**, Yukinobu Watanabe† and Masaharu Numajiri††

* Japan Atomic Energy Research Institute, Tokai-mura, Naka-gun, 319-11, Japan
** Department of Nuclear Engineering, Kyushu University, Hakozaki, Fukuoka, 812, Japan
† Energy Conversion Engineering, Kyushu University, Kasuga-koen, Kasuga, 816, Japan
†† National Laboratory for High Energy Physics (KEK), Oho, Tsukuba, 305, Japan

ABSTRACT

Double differential neutron spectra from a thick lead target bombarded with 0.5 and 1.5 GeV protons have been measured with the time-of-flight technique. In order to obtain the neutron spectra without the effect of the flight time fluctuation by neutron scattering in the target, an unfolding technique has also been employed in the low energy region below 3 MeV. The measured data have been compared with the calculated results of NMTC/JAERI-MCNP-4A code system. It has been found that the code system gives about 50 % lower neutron yield than the experimental ones in the energy region between 20 and 80 MeV for both incident energies. The disagreements, however, have been improved well by taking account of the in-medium nucleon-nucleon scattering cross sections in the NMTC/JAERI code.

1. Introduction

With recent progress of the accelerator technology, various utilizations of a high energy and high current proton accelerator are proposed for various purposes such as neutron scattering study and accelerator driven actinide transmutation[1]. For the design of the target and shielding of the accelerator facilities, it is necessary to estimate the reaction rate and the neutron production in a thick medium in the energy region up to several GeV as accurately as possible. Nucleon-Meson Transport Codes such as NMTC/JAERI[2] and LAHET[3] have been widely employed for the neutronics calculation.

It is generally known that the codes can describe the particle productions and the transport in a thick medium. The accuracy of the codes is not completely satisfactory yet. In order to comprehend and improve the accuracy of the code, several studies[4,5] have been performed from both the theoretical and the experimental points of view. A series of measurements of neutron production double differential cross sections were carried out at LANL[6,7,8,9] and KEK[10]. In LANL, the neutron yields in stopping-length targets were also measured with 113 and 256 MeV protons[5,6]. There is only a few data[11,12] on the

Keywords: Neutron spectrum, Time of flight and unfolding technique, NMTC/JAERI, 0.5 and 1.5 GeV

neutron spectra from thick targets bombarded with protons at incident energies higher than 256 MeV.

In this study, the neutron spectra from a thick lead target bombarded with 0.5 and 1.5 GeV protons have been measured at 6 angles between 15° and 150° using the TOF and unfolding techniques. The measured data were compared with calculated results of the NMTC/JAERI-MCNP-4A code system.

2. Experimental Procedure

2.1 *Incident Protons and Target*

The experiment was carried out at the $\pi 2$ beam line of National Laboratory for High Energy Physics (KEK) in a series of double differential neutron production cross section measurements[10]. The illustration of the experimental arrangement is shown in Fig. 1. The incident proton was supplied as the secondary particle generated by an internal target which was placed in the accelerator ring of the 12 GeV proton synchrotron. The intensity of the incident particles was so weak ($<10^5$ particles/macro pulse) that incident protons were counted one by one with beam scintillators. The size of the incident beam was 2.0 cm in the perpendicular plane and 1.6 cm in the horizontal one in FWHM, respectively. The protons were identified from the pions produced at the internal target by the time-of-flight (TOF) technique with a pair of scintillators (Pilot U) which were located at a separation distance of 20 m. Each Pilot U scintillator was connected with two photomultipliers on opposite sides. The beam damp was a carbon block pile of 0.5×0.5 m^2 in the area and 1 m in thickness. The carbon was surrounded by sufficiently thick iron blocks except on the beam-incident surface. The distance from the target to the beam dump was 8.5 m.

The lead target was a rectangular parallelepiped $15 \times 15 \times 20$ cm^3 whose purity was 99.95%. It was thick enough to stop 0.5 GeV protons completely, while it caused the energy loss of 0.26 GeV on average for 1.5 GeV protons.

2.2 *Neutron Detector*

NE213 scintillators having the size of 12.7 cm in diameter and 12.7 cm in thickness were used as neutron detectors. The detectors were placed at angles of 30°, 60°, 90°, 120° and 150° to the beam axis and at a common distance of 1 m from the target. At the angle 15°, the distance was chosen 1.5m so that the higher energy resolution was achieved. In order to reject the events induced by the charged particles (i.e. π, p, d) produced in the lead target, NE102A scintillators of $17 \times 17 \times 1$ cm^3 were used as veto counters. They were placed in front of the NE213 scintillators at a distance of 2 cm.

The pulse height of the neutron detectors was calibrated by standard gamma ray measurements. The gamma ray energies are summarized in Table 1 with the light outputs

Table 1. Light Output at the half height of Compton edge for the source gamma ray

Gamma Ray Source	Energy (MeV)	Light Output (MeVee) [a]
^{137}Cs	0.662	0.493
^{60}Co	1.173, 1.333	1.074 [b]
Am-Be	4.439	4.331

[a] 1 MeVee corresponds to the light output given by 1 MeV electron.

[b] Only one Compton edge is observed, because NE213 has poor resolution to distinguish 2 Compton edges. This light output is calculated with the average energy of 2 gamma rays.

at the half height of Compton edges. The light output was derived from the empirical formula of Dietze[13] and expressed in the unit of electron equivalence. A good linearity between the light output and the measured signal was verified below 4.33 MeVee.

2.3 *Electronic Circuit*

The diagram of the electronic circuit is shown in Fig. 2. When a coincidence of the signals from all beam scintillators took place, a pulse with a time duration of 150 ns was sent to the next coincidence unit. The events arising from incident pions were eliminated with the help of the coincidence pulse of all beam scintillators. The number of incident protons was accumulated by the scaler. A good discrimination for the incident proton against the pion was achieved so that the uncertainty of the counting could be less than 1 %. The TOF spectrum was obtained from the difference of digitized occurrence time between NE213 scintillator and beam scintillators (P01 and P02) pulses.

Anode signals of the photomultipliers connected with NE213 scintillators, were branched out to four pulses. Three pulses and gate signals were supplied to three ADCs that digitized the integrated charge of the pulses during the gate signal independently. The pulse height distribution was obtained from the ADC-3 which collected the total charge of pulse. The other ADC-1,2 digitized the integrated charge of the fast and tail parts of scintillation pulse, in order to reject the events induced by gamma rays employing the two-gate integration method[14]. The conceptual diagram of this method is shown in Fig. 3. All digitized data were taken event by event and stored in the magnetic tape for off-line analyses.

3. Data Analysis

3.1 *TOF Analysis*

Figure 4 shows an example of the TOF spectrum from the target, whose horizontal axis is reversed. A sharp peak due to prompt gamma rays is observed around 3100 channel. The width was typically 1.5 ns in FWHM. After the neutron events were discriminated from the gamma ray ones, the TOF spectrum of the neutrons was obtained as shown in the bottom of Fig. 4. By interposing an iron block of 50 cm in thickness between the target and detector, the room back ground was measured and found to be negligible.

The energy spectrum of the neutron is converted from the net TOF spectrum by the following expression,

$$\frac{d^2n}{dEd\Omega} = \frac{N_n}{N_p\,\varepsilon\,\Delta\Omega\,\Delta E}, \quad E = m_n c^2\left(1\Big/\sqrt{1-L^2\Big/\left(c(t-t_0)+L\right)^2}-1\right) \tag{1}$$

where N_n and N_p are the counts of neutrons and incident protons, respectively, ε the detection efficiency for the neutron, $\Delta\Omega$ the solid angle sustained by the detector to the center of the target, E the neutron energy, t the flight time, m_n the rest mass of the neutron, c the light speed, t_0 the flight time of the prompt gamma ray and L the distance between the centers of target and detector. Here, the distance from the neutron producing point to the detection point is assumed to be L. This assumption was confirmed by a Monte-Carlo calculation which gave the standard deviation of the distance L smaller than 6 %.

The detection efficiencies were calculated for the energy range below 80 MeV with SCINFUL[15] and up to 1.5 GeV with Cecil[16]. The results are shown with the experimental ones in Fig. 5. It is observed that SCINFUL results agree with the experimental data[17,18] much better than Cecil. In the TOF analysis, therefore, the SCINFUL results were used as the detection efficiency below 80 MeV. Above 80 MeV, on the other hand, the

calculated efficiency of Cecil adjusted to connect smoothly with that of SCINFUL at 80 MeV was employed. Two neutron spectra were obtained with two efficiencies using the ^{137}Cs and ^{60}Co biases which were set at the half height of Compton edges for ^{137}Cs and ^{60}Co gamma rays, respectively. The neutron spectra determined with ^{137}Cs bias agreed with those determined with the ^{60}Co bias within the statistical errors. Since the statistical accuracy of the spectra obtained with the ^{137}Cs bias was higher than that of ^{60}Co bias, the results with the ^{137}Cs bias were adopted as the resultant neutron spectra.

3.2 *Unfolding Analysis*

Since the target was thicker than the mean free path for the neutrons with the energy below 200 MeV, most neutrons react with target nuclei more than once in the transport process. The scattered neutron has some delay in the flight time in comparison with the neutron which comes out the target without scattering. The delay makes apparent neutron energy spectrum obtained by the TOF technique softer than the real one. We analyzed the pulse height distribution by the unfolding technique to obtain the neutron spectrum independently. The unfolding analysis employed the code FORIST[19] which used a response matrix calculated with SCINFUL. The neutron spectra in the energy region below 14 MeV were obtained by the unfolding technique, because the pulse height was saturated above 14 MeV.

In Fig. 6, the neutron spectrum at the angle of 30° obtained by the unfolding technique is compared with the one by the TOF technique for 500 MeV proton incidence. In the region below 3 MeV, the difference of the neutron yield was larger than 50 % of that obtained by the TOF technique. This difference is ascribed to the ambiguity of the efficiency around the ^{137}Cs bias used in the TOF technique. Therefore, the neutron spectra derived by the unfolding analysis is more reliable than those obtained by the TOF technique below 3 MeV. The results of unfolding analysis agree with those of TOF quite well between 3 and 14 MeV. This indicates that the time fluctuation by the scattering is negligibly small above 3 MeV. In consequence, the neutron energy spectrum was determined by connecting the result of the TOF technique with that of the unfolding technique at 3 MeV. The error of the unfolding analysis for neutrons below 1.5 MeV was so large that the lowest energy of measured spectra were decided to be 1.6 MeV.

4. Calculation

The calculation was carried out with codes, NMTC/JAERI[2] and MCNP-4A[20]. NMTC/JAERI calculated the nuclear reactions and the particle transport above 20 MeV. MCNP-4A calculated the neutron transport below 15 MeV using a continuous energy cross section library FSXLIB-J3R2[21] processed from the nuclear data file JENDL-3.2[22]. In NMTC/JAERI, the systematics of Pearlstein[23] was implemented to estimate the total, the elastic and non-elastic nucleon-nucleus cross sections in the transport calculation part. The level density parameter derived by Baba[24] was also employed in the statistical decay calculation in NMTC/JAERI.

Additional calculations were also performed by substituting the in-medium nucleon-nucleon cross sections (NNCS) for the free ones in the nuclear reaction calculation part of NMTC/JAERI. In this calculation, were employed the in-medium NNCS parametrized similarly to those by Cugnon[25].

5. Results and Discussion

The present experimental spectra are shown in Figs. 7 and 8. The uncertainty of various quantities is given in Table 2. The uncertainty of the neutron yield was determined from those of the statistical, the neutron detection efficiency and the number of incident protons. The uncertainty of the detection efficiency is estimated at 3.0% for the neutron energy below 20 MeV. With the increase of neutron energy, the uncertainty becomes larger because of the increasing ambiguity the cross section used in the calculation.

The neutron energy resolution is also given in Table 2. It was determined from the uncertainty of the time and the flight path. The time uncertainty is derived from the time resolution of the detector and the fluctuation of the flight time that is spent by an incident proton to move from an incident point to a reaction point. The time resolution of the detector has been determined to be 0.4 ns in the standard deviation by the width of the prompt gamma peak of the thin target measurements[10]. The time fluctuation was approximated to a half value of the transit time of protons in the target which was obtained by Janny[26]. Those are determined 0.6 and 0.4 ns for the 0.5 and 1.5 GeV incident protons, respectively. The uncertainty of the flight path was estimated at 6.0 cm by the Monte-Carlo calculation on condition that the neutrons were produced uniformly in the target and detected uniformly in the detector. Since the correlation between the time fluctuation for incident protons and the flight path is ignored, the real energy resolution will be better than that described here.

Table 2. Uncertainty and energy resolution of neutron spectra expressed in the standard deviation

Neutron Energy (MeV)	Uncertainty (%)				Energy Resolution (%)
	Statistical Error	Detection Efficiency	Number of Incident Proton	Neutron Yield	
3	3 ~ 7	3		4 ~ 7	10 ~ 11
10	5 ~ 10	3		6 ~ 11	10 ~ 11
15	6 ~ 10	3		6 ~ 11	12 ~ 13
20	6 ~ 10	10	1	6 ~ 11	12 ~ 14
50	8 ~ 30	10		13 ~ 32	13 ~ 17
100	7 ~ 46	15		17 ~ 46	16 ~ 22
200	11 ~ 20*	15		19 ~ 25*	20 ~ 32

* For the angle smaller than 90°

Figure 9 shows a comparison between the present data for 1.5 GeV proton bombardment and the measured one at JINR[11]. In the experiment at JINR, a lead target having the size of 20 cm in diameter and 20 cm in length was bombarded with 2.55 GeV protons. It is found that the present neutron energy spectrum is quite similar to those obtained at JINR, although the incident proton energies are different.

The calculated results of the NMTC/JAERI-MCNP-4A code system, which are smeared with the energy resolution, are also shown in Figs. 7 and 8. It is observed that the results calculated with the free NNCS are in good agreement with the experimental ones in the lower energy region below 20 MeV at all angles for both incident energies. The calculated results, however, are about 50 % or more lower than the experimental data between 20 and 80 MeV at all angles. On the other hand, the results calculated with the in-medium NNCS show much better agreement with the experimental ones in this energy region. This improvement is ascribed to the fact that the increase of the high energy nucleon emission

diminishes the excitation energy of a residual nucleus so that the neutron emission from the evaporation process is suppressed. The calculation with the in-medium NNCS successfully reproduces the overall measured neutron spectra in the angular region smaller than 60° for both incident energies although the codes give slightly lower neutron yields below 10 MeV. The underestimation for the backward neutron emission, however, still remains.

In order to investigate the cause of the discrepancy between the calculations and the experiments, the double differential neutron production cross sections were also calculated with the in-medium NNCS for the incident energies of 0.8 and 1.5 GeV, respectively. The results are compared with the experiments[9,10] in Figs. 10 and 11. It is found that the agreement between the calculated and the experimental results for the thick target is as in the same level for that in the thin target. This indicates that the nuclear reaction calculation part should be improved in NMTC/JAERI. Some studies[5,27] showed that the inclusion of the preequilibrium process or the refraction and reflection process improved the backward neutron emission significantly. By the inclusion of those processes, the disagreement of the thick target will be more improved.

6. Conclusion

The neutron spectra from a thick lead target bombarded with 0.5 and 1.5 GeV protons were measured at 6 angles between 15° and 150°. We have obtained the precise neutron spectra in the energy region above 1.6 MeV using the TOF and unfolding techniques with the neutron yield uncertainty of 7 % at 3 MeV and 25 % at 200 MeV. The calculation was also carried out with the NMTC/JAERI-MCNP-4A code system. It was found that results showed fairly good agreement with the experiments, but gave about 50 % lower neutron yield in the energy region between 20 and 80 MeV. The calculation with the in-medium NNCS achieved good agreement with the experiments. The calculation, however, could not reproduce well the backward neutron emission. It is of interest to make systematic experiments with other targets for further investigation of the accuracy of NMTC/JAERI including the in-medium NNCS.

References

[1] For example, T. Takizuka, et al., *Conceptual Design Study of an Accelerator-based Actinide Transmutation Plant with Sodium-cooled Solid Target/Core,* Proc. of OECD/NEA Mtg., Argonne (1993) 398

[2] Y. Nakahara and T. Tsutsui, *A Code System for High Energy Nuclear Reactions and Nucleon-Meson Transport Code, JAERI-M 82-198 (1982)*, [in Japanese]

[3] R. E. Prael and H. Lichtenstein, *Users Guide to LCS: The LAHET Code System,* LA-UR 89-3014 (1989)

[4] *Intermediate Energy Nuclear Data: Models and Code,* Proc. of OECD/NEA Mtg., Paris (1994)

[5] N. Yoshizawa, K. Ishibashi and H. Takada, *J. Nucl. Sci. Technol.* **32** (1995) 601

[6] M. M. Meier, et al., *Nucl. Sci. and Eng.* **102** (1989) 309

[7] M. M. Meier, et al., *ibid.* **104** (1990) 339

[8] S. Stamer, et al., *Phys. Rev.* **C47** (1993) 1647

[9] M. M. Meier, et al., *Rad. Eff.* **96** (1986) 73

[10] K. Ishibashi, et al., *Measurement of Neutron-Production Double-Differential Cross Sections for Incident Protons of 0.8, 1.5 and 3 GeV,* Proc. Int. Conf Nucl. Data for Sci. and Technol., Gatlinburg (1994)

[11] A. D. Kirillov, et al., JINR-P-13-90-193 (1990)
[12] S. Cierjacks, et al., *Phys. Rev.* **C193** (1987) 1976
[13] G. Dietze and H. Klein, *Nucl. Instrum. Meth.* **193** (1982) 529
[14] Z. W. Bell, *ibid.* **188** (1981) 105
[15] J. K. Dickens, *SCINFUL: A Monte Carlo Based Computer Program to Determine a Scintillator Full Energy Response to Neutron Detection for En Between 0.1 and 80 MeV,* ORNL-6436 (1988)
[16] V.V. Verbinski, et al., *The Response of Some Organic Scintillators to Fast Neutrons,* ORNL-P-993 (1965)
[17] S. Meigo, et al., private communication
[18] R. A. Cecil, et al., *Nucl. Instrum. Meth.*, **161** (1979) 439
[19] R. H. Johnson and B. W. Wehring, *The FORIST UNFOLDING CODE,* ORNL/RSIC-40 (1976) 33
[20] J. F. Briesmeister (Ed.), *MCNP A General Monte Carlo N-Particle Transport Code Version 4A*, LA-12625 (1993)
[21] K. Kosako, et al., *A Continuous Energy Cross Section Library for MCNP Based on JENDL-3.2,* JAERI-Data/Code 94-020 (1994)
[22] K. Shibata, et al., *Japanese Evaluated Nuclear Data Library, Version-3 -JENDL-3-,* JAERI-1319 (1990)
[23] S. Pearlstein, *Astrophys. J.* **346** (1989) 1049
[24] H. Baba, *Nucl. Phys.* **A159** (1970) 625
[25] J. Cugnon, T. Mizutani and J. Vandermeulen, *ibid.* **A352** (1981) 505
[26] J. F. Janny, *Atom. Data and Nucl. Data Tables* **27** (1982) 147
[27] H. Takada, submitted to *J. Nucl. Sci. Technol.*

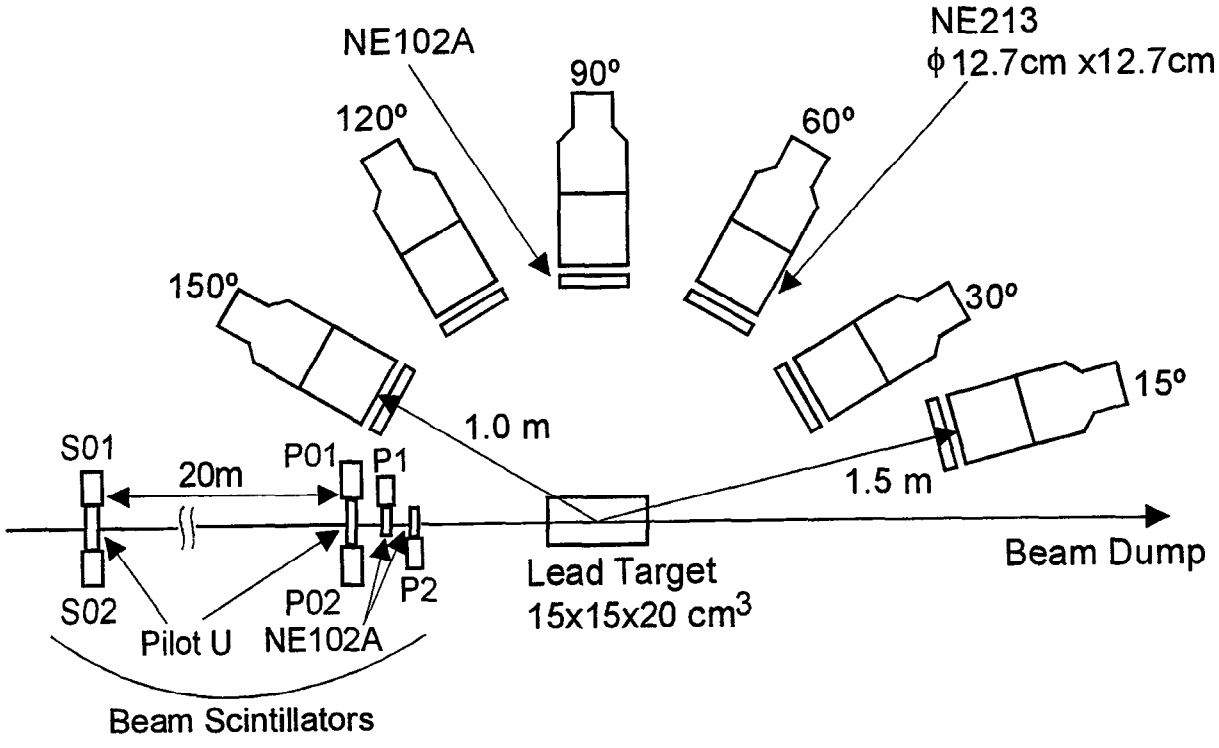

Fig. 1 Illustration of the experimental arrangement

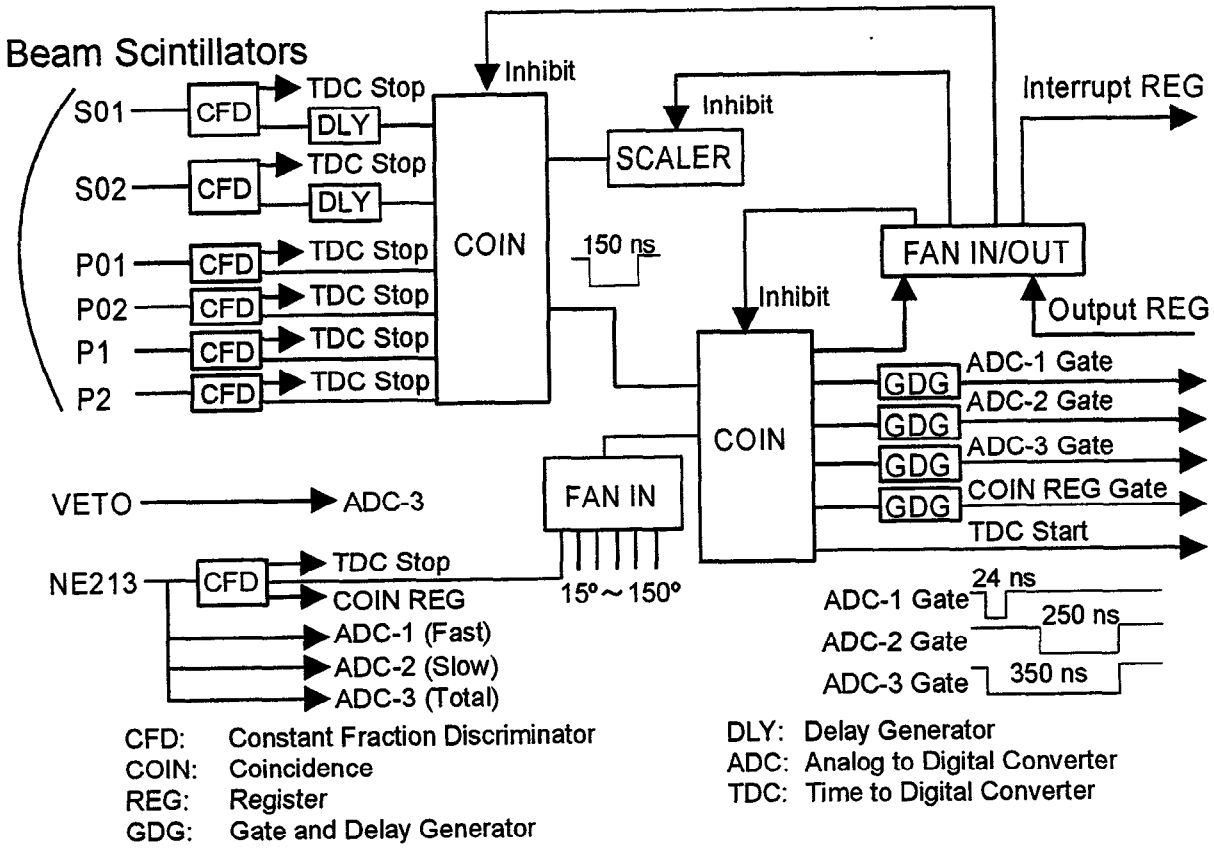

Fig. 2 Diagram of the electronic circuit used in the present experiment

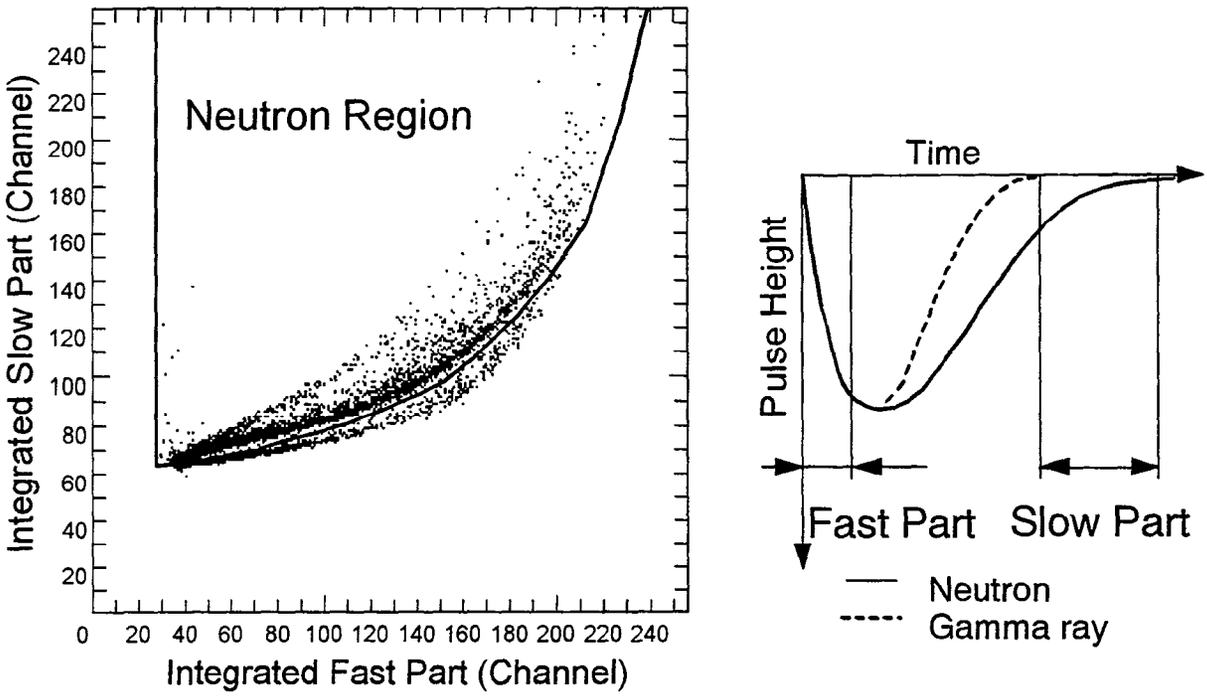

Fig. 3 Conceptual diagram of the two-gate integration method of neutron-gamma discrimination

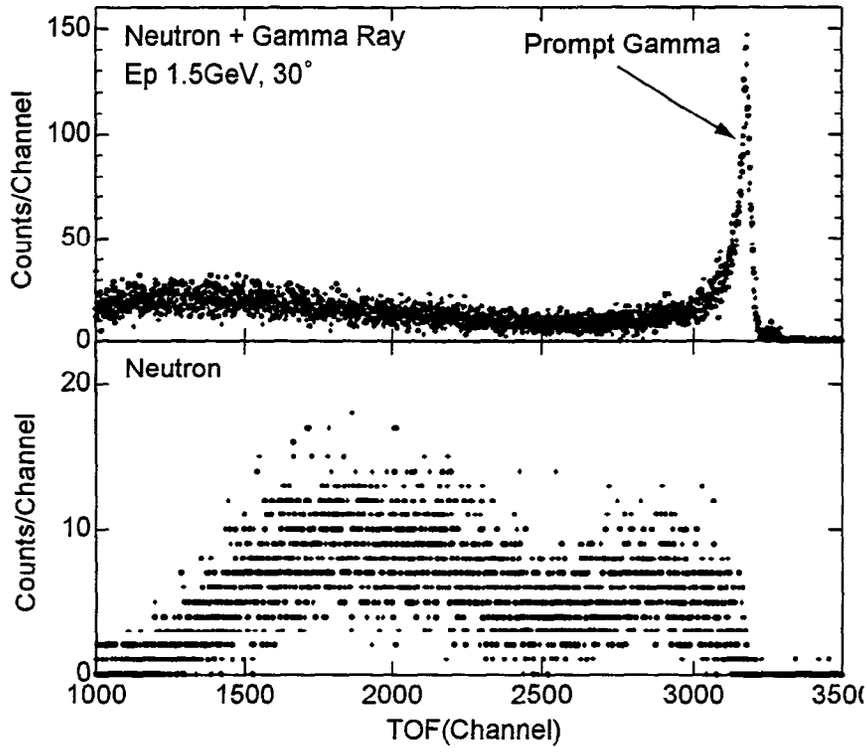

Fig. 4 Time-of-flight (TOF) spectrum measured at 30° bombarded with 1.5 GeV protons (top; for the neutron and the gamma ray, bottom; only for the neutron). Width of the TOF bin is 28 ps/channel.

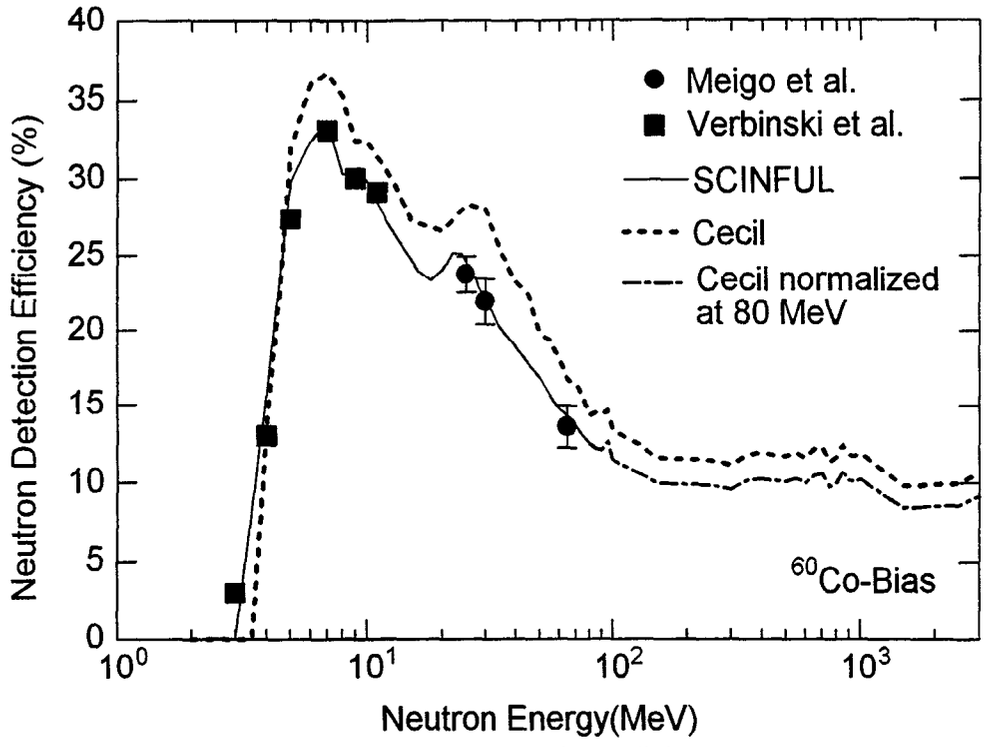

Fig. 5 Calculated and experimental neutron detection efficiency of the NE213 scintillator having the size of 12.7 cm in diameter and 12.7 cm in thickness

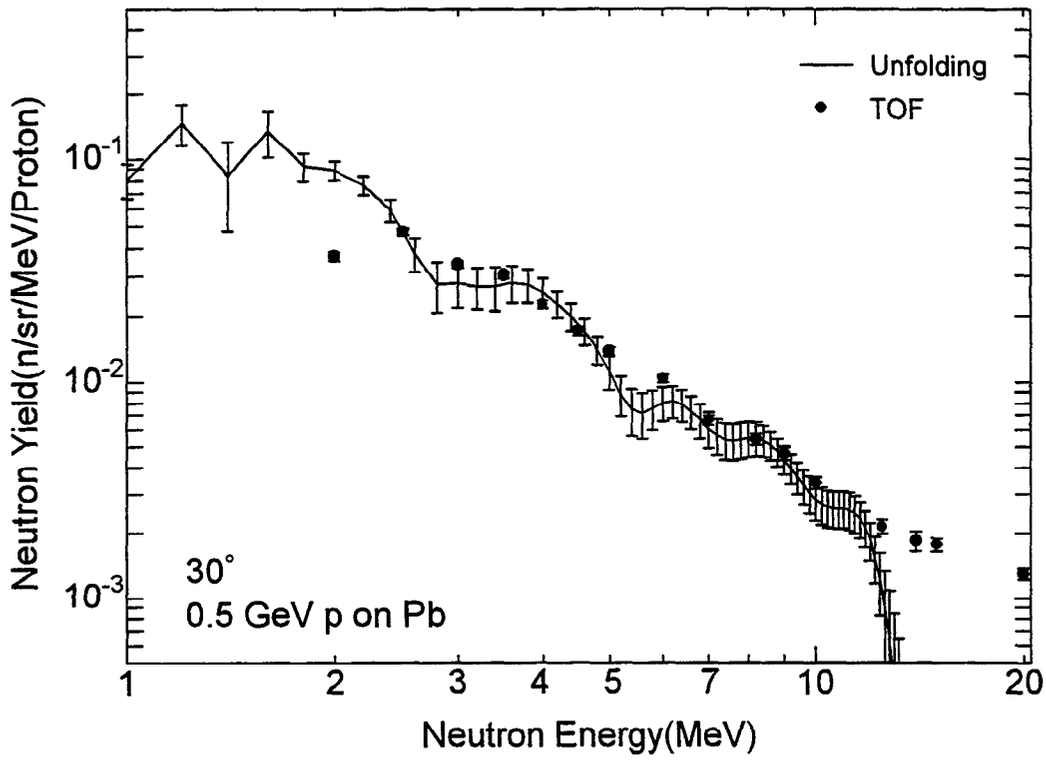

Fig. 6 Comparison of the neutron spectra at 30° obtained by TOF and unfolding methods for 0.5 GeV proton incident on thick lead target

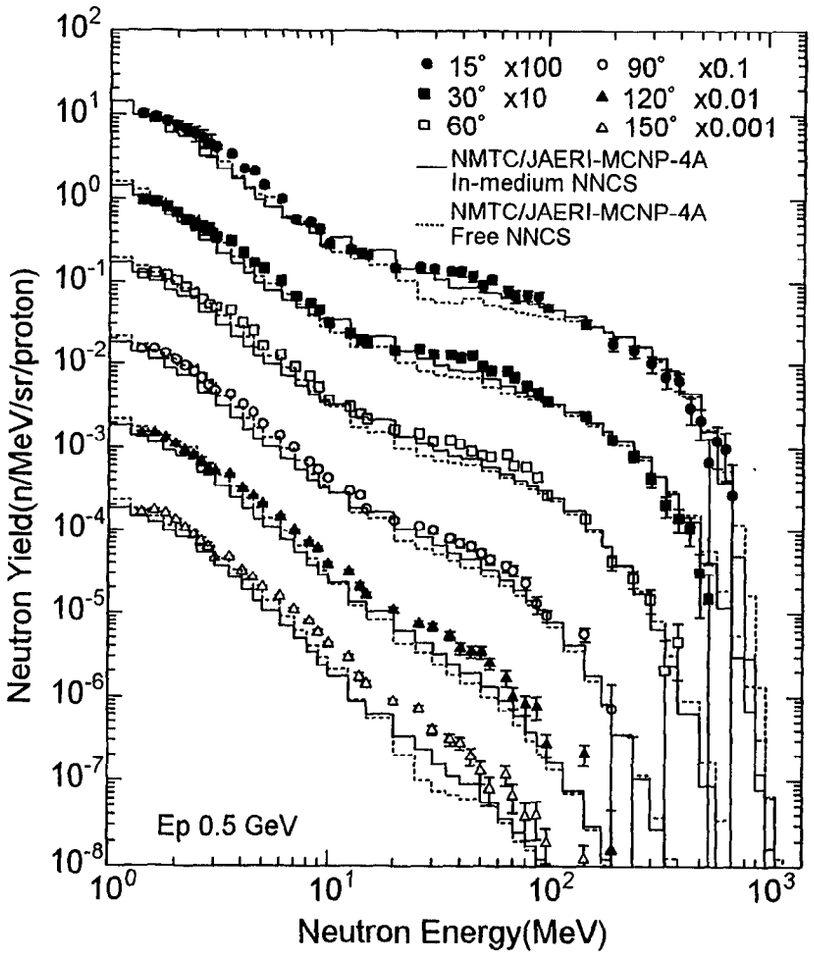

Fig. 7 Experimental and calculated neutron spectra in a lead target bombarded with 0.5 GeV protons. The marks are the experimental data. The dashed and the solid lines indicate the calculated results of the code system with free NNCS and those with in-medium NNCS, respectively.

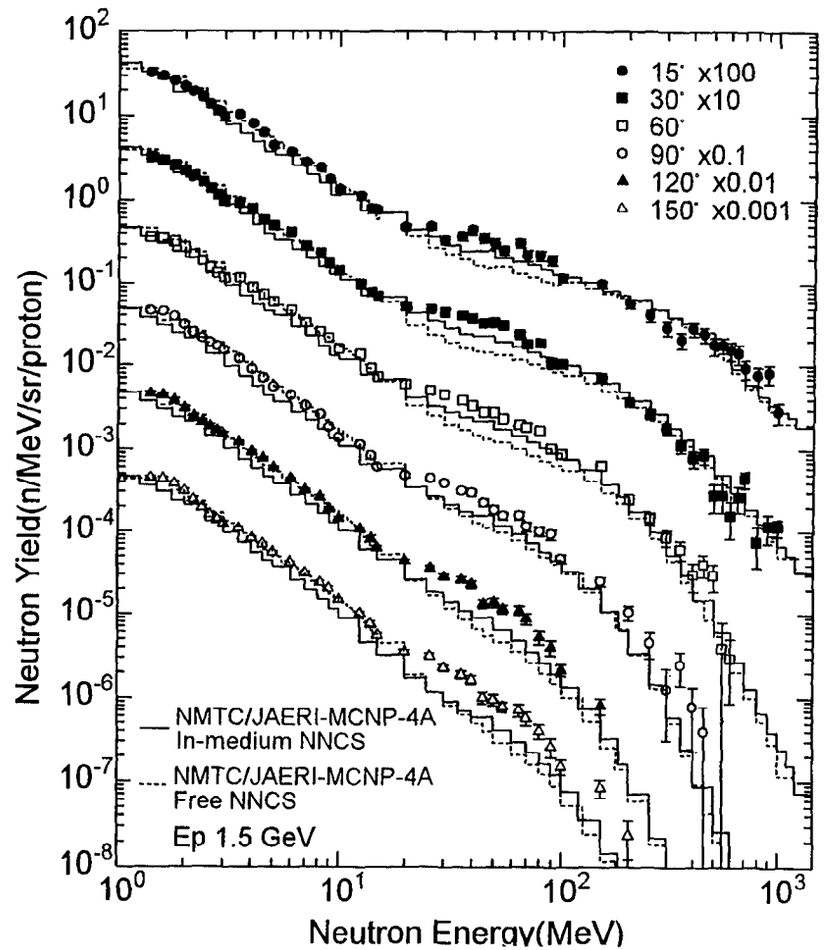

Fig. 8 Same as for Fig. 7, except for proton energy, 1.5 GeV

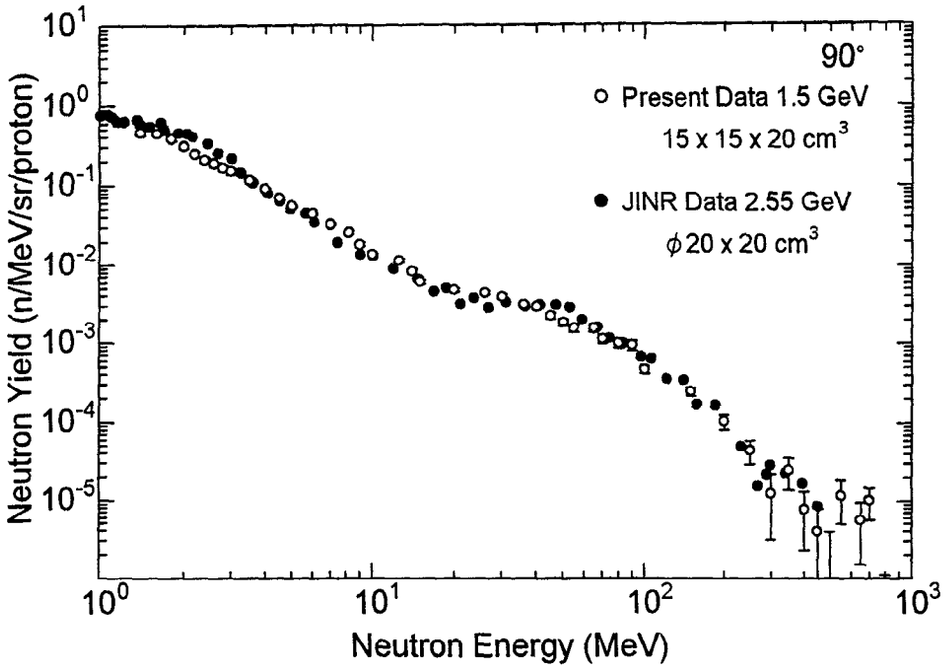

Fig. 9 Comparison of experimental neutron spectrum between the present and the measured one at JINR

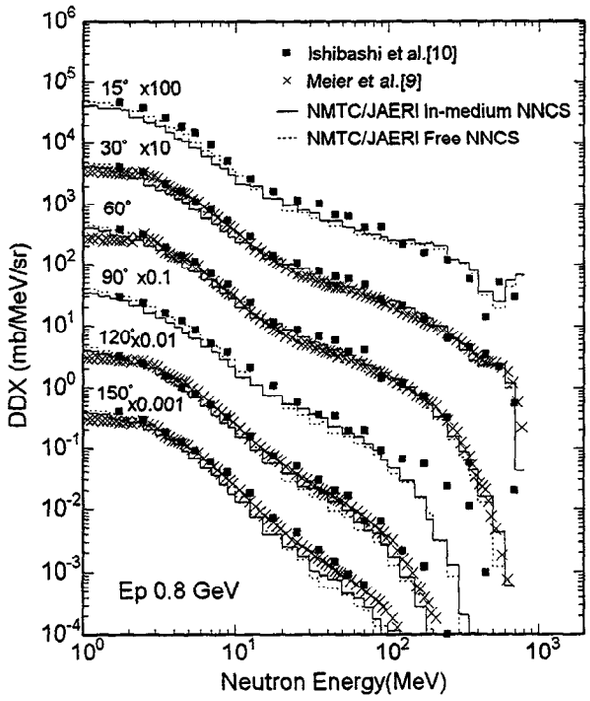

Fig. 10 Double differential neutron production cross sections for 0.8 GeV protons. The solid marks indicate the experimental data[9,10]. The solid and the dash lines show the results of NMTC/JAERI with free NNCS and those with in-medium NNCS, respectively.

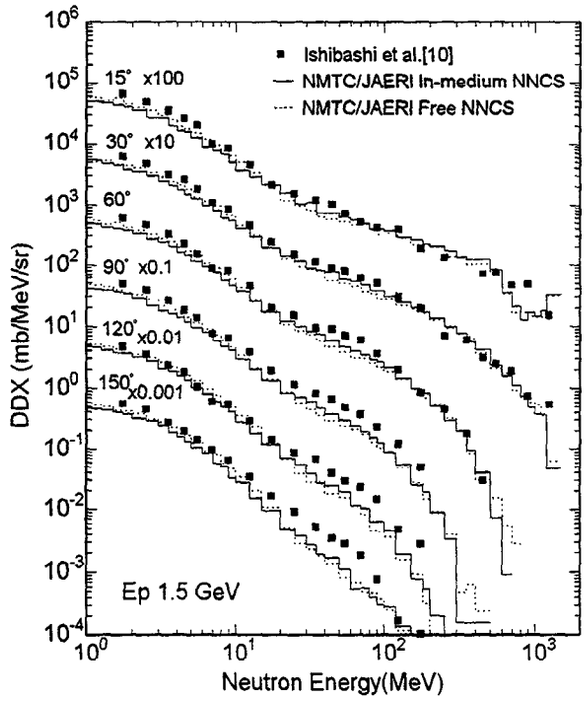

Fig. 11 Same as for Fig.10, except for proton energy 1.5 GeV

ICANS-XIII
13th Meeting of the International Collaboration on
Advanced Neutron Sources
October 11-14, 1995
Paul Scherrer Institut, 5232 Villigen PSI, Switzerland

MULTIPLYING TARGET FOR A HIGH-INTENSITY SPALLATION NEUTRON SOURCE

V.G.Miroshnichenko, S.F.Sidorkin, Y.Y.Stavissky*
V.F.Kolesov**, E.P.Shabalin†, Y.N.Likhachev††

* Institute for Nuclear Research of Russian Academy of Sciences
60th Anniversary of October Ave., 117322 Moscow, Russia
** Russian Federal Nuclear Center, ARSRIEP (Arzamas-16), Russia
† Joint Institute for Nuclear Research, Dubna, Russia
†† State Science Center - Institute of Physical Energy, Obninsk, Russia

ABSTRACT

The possible design of an intensive pulsed neutron source for time-of-flight experiments is considered. Its major characteristics are expected to be: peak and average slow neutron flux density on the moderator surface up to 10^{17} and 10^{14} n/cm^{2}s respectively, neutron pulse duration about 30 μs and pulse repetition rate 25 pps. This level of performance is achieved due to using a multiplying target driven with the proton beam of the Moscow meson factory.

1. Introduction

Wide use of the neutron time-of-flight methods in nuclear and solid-state physics has stimulated development of high-flux research reactors and high-intensity neutron sources based on the pulsed reactors [1] and, more recently, proton accelerators [2,3]. At present, among the facilities actively used in physical experiments we can list the pulsed reactors IBR-30 and IBR-2 (with the average power 30 kW and 2 MW respectively) in Russia [4] as well as neutron sources driven with medium-energy proton beams - LANSCE (LANL, USA), IPNS (ANL, USA), ISIS (RAL, UK) and KENS (KEK, Japan) [2,3].

Several projects of the next-generation pulsed neutron sources are being developed in the US (LANL, ANL, ORNL) and in Europe (ESS - European Spallation Source). Typical design decisions are as follows: pulsed proton accelerator with energy up to 2.5 GeV and beam power up to 5 MW, targets made of Ta or W, light water and liquid hydrogen moderators.

Keywords: Fissile target, Thermal shock, Liquid metal coolant

At INR RAS, the construction of the intense pulsed neutron source IN-06 is near completion now. It has the water-cooled target made of natural uranium silicide [5] and is driven with the 600 MeV proton beam of the linac of the Moscow meson factory transformed by the compressor ring into a sequence of 0.4 μs proton pulses [6].

Fast subcritical assemblies with the multiplication factor about 20 ($K_{eff} < 0.95$) are of certain interest as the targets for pulsed neutron sources. A multiplying target with limited multiplication substantially reduces required proton pulse intensity, while preserving a short enough (1-2 μs) neutron pulse and relatively low inter-pulse background. The desire to keep the latter value as low as possible makes Pu^{239} and U^{233} having low delayed neutron fraction more attractive.

At present, the INR in collaboration with IPE (Obninsk), JINR (Dubna), ARSRIEP (Arzamas), Bochvar's Institute of Inorganic Materials and EDBMB (Nizhny Novgorod) is developing the design of the high-intensity pulsed neutron source RIN-10 with the peak and average slow neutron flux density about 10^{17} and 10^{14} n/cm^{2}s.

To achieve this goal we suppose to upgrade the existing proton accelerator of the Moscow meson factory and employ a fissile target with the multiplication of ~20.

2. Proton accelerator

As a first step to achieve the desired level of neutron source performance it is supposed to upgrade the accelerator: to rise proton energy from 600 to 700 MeV by adding one more section to its main part and to increase duration of the beam macro pulse to 350 μs against the present 100 μs, leaving the pulse current at the design level (50 mA). At present, experiments are conducted with the pulse current up to 20 mA and proton energy up to 420 MeV (the final section of the accelerator's main part is not used due to lack of clystrons).

3. Storage ring

To transform the time structure of the proton beam without affecting its average intensity it is supposed to use a storage ring with the charge-exchange injection and single-turn ejection that is constructed now for the pulsed neutron source IN-06 [6]. After injecting one macro pulse of beam current, accumulated protons are ejected onto the neutron target. Evaluations made show that it is possible to store and eject ~10^{14} protons per pulse at the repetition rate up to 50 pps [7]. That is quite adequate for our purpose, so no upgrading is required.

4. Multiplying target RIN-10

As a neutron-producing target, the fast subcritical assembly with uranium nitride fuel and liquid gallium coolant, having $K_{eff} < 0.95$, is used.

As a prototype for the multiplying target, we have chosen the fast research reactor BR-5 successfully operating at the Institute of Physical Energy (Obninsk) since 1958, in the startup and physical research of which one of the authors participated [8]. This reactor can

use either oxide, carbide or nitride fuel, it has the sodium core cooling and large air-cooled Ni reflector.

The most important difference between the reactor BR-5 and the target of RIN-10 is that the latter should operate in the pulsed mode. The possibility of creating a target of this kind depends mainly on the long-term fatigue strength of fuel element cladding under thermal shocks caused by repetitive power pulses. Other differences are less significant.

Using the nitride fuel with high thermal conductivity allows us to keep the fuel temperature under 1000 K, reducing diffusion of fission products out of crystalline lattice. This feature as well as using U instead of Pu^{239} and low-temperature gallium coolant should be treated as advantages from the standpoint of ensuring environmental safety.

Liquid gallium, which has the melting point 302 K and boiling point 2250 K, does not interact with water and oxygen and is low-aggressive to stainless steel at low temperatures, allows us to choose relatively simple and, as a consequence, reliable design of the coolant circuit. It is supposed that the first loop will contain gallium with forced circulation by electromagnetic pumps; the second loop - demineralised water transferring heat to air.

Neutron capture in Ga^{71} results in production of Ga^{72} having half-life period 14.12 hr and emitting hard γ-radiation (2.2 MeV). No isotopes with longer half-life are produced in interactions of fission neutrons with Ga. But the spallation process induced by primary protons results in production of Ga^{67} with half-life of 77.9 hr and relatively soft γ-radiation (< 388 keV). This isotope is the most unpleasant for service systems, so to minimize the volume of Ga under proton irradiation a special inner tungsten target with low gallium volume fraction is used. Other, non-gallium, radioactive nuclides can be removed by selective absorption in the cooling system.

The above-mentioned considerations led us to the following target design (Fig. 1).

The proton beam is injected through an inclined ion guide into the inner tungsten target consisting of tightly packed metal tungsten rods cooled with gallium flow. Injecting protons through the target corner reduces possibility of coolant loss in case of window failure due to radiation damage or burning by the collapsed beam. At the same time, it enables fuel reloading without disassemblying the beam transport system. The beam window is cooled by gallium.

The target core consists of hexagonal fuel element assemblies. Fuel elements are in the form of tubes made of cold-deformed stainless steel (4C-68XD of 316 steel class) with 6 mm diameter and 0.3 mm thick wall. Tubes are filled with U or Pu nitride with density 11.5 g/cm^3 packed under vibration. The lower tip of the fuel element is short, while the upper part of the tube contains Ni with 1 mm diameter and 200 mm long gas volume. The target core dimensions are ∅300×300 mm, fuel element are distantiated with wire. Coolant flows through both halves of the core in turn. Average heating of coolant at velocity 3 m/s is about 70 K.

The target and moderators are surrounded with the large (∅1300×1300 mm^3) air-cooled Ni reflector. It has several tangential horizontal and vertical channels 150 mm in diameter used for replacement and maintenance of moderators and neutron guides. Lower movable part of

reflector serves as a safety and reactivity control. The target core is decoupled from the reflector and moderators with a boron-containing layer.

Moderators assemblies are inserted into the reflector through vertical channels. It is supposed that two light-water and two liquid-hydrogen moderators will be installed. Each moderator is provided with 6 tangential neutron guides, so, in total, the neutron source will have 24 neutron beams.

The major characteristics of the neutron source for three possible fuel compositions are given in Table 1.

Table 1. Target characteristics for various fuel compositions.

Fissile isotope	U^{233}	U^{235}	Pu^{239}
Fuel density, g/cm^3	11.5	13.5	11.5
Prompt neutron lifetime, ns	70	57	65
Average slow neutron flux density (25 pps), n/cm^{2}s	$7.6 \cdot 10^{13}$	$7.3 \cdot 10^{13}$	$8.1 \cdot 10^{13}$
Peak slow neutron flux density, n/cm^{2}s	$8.6 \cdot 10^{16}$	$8.5 \cdot 10^{16}$	$8.8 \cdot 10^{16}$
Coolant volume fraction, %	52	33	55
Fuel temperature rise per pulse, °C	32	20	30
Thermal power, MW	8.8	9.1	7.6

Neutronic characteristics of the target have been evaluated using the Monte Carlo neutron transport code NeuMC with the total yield, spatial and energy distribution of primary neutrons calculated with the SHIELD code [9].

As it was mentioned above, the possibility to create this target is determined by fatigue strength of fuel element cladding under thermal shock conditions. Unfortunately, up to now there is no experimental information about fuel element behaviour under short (~1 μs) power pulses. Evaluations of few- and many-cycle fatigue made under assumption that the fuel element undergoes about 10 oscillations per power pulse give for 5 mm diameter fuel elements clad with 4C-68XD steel the values of permissible number of power pulses and average lifetime presented in Table 2. Rather steep dependence of lifetime upon the temperature rise per pulse demands for detailed calculation of fatigue strength of fuel elements as well as for an experimental investigation of their behaviour.

Table 2. Fuel element lifetime.

Temp. rise per pulse, °C	Permissible number of pulses	Lifetime, yr
30	$3 \cdot 10^{10}$	25.4
40	$2.5 \cdot 10^{8}$	0.13
50	$5 \cdot 10^{6}$	0.002

The major characteristics of the RIN-10 target in comparison with other pulsed neutron sources are given in Table 3.

Table 3. Comparative performance of the RIN-10 neutron source.

Neutron source	IN-0.6	RIN-10	ESS
Proton energy, GeV	0.6	0.7	1.3
Beam current, mA	0.2	0.4	3.8
Repetition rate, pps	50	25	50
Neutron generation rate, n/s	$1.7 \cdot 10^{16}$	$5 \cdot 10^{17}$	$6 \cdot 10^{17}$
Average slow neutron flux density, n/cm^{2}s	$2.0 \cdot 10^{12}$	$8 \cdot 10^{13}$	$6.3 \cdot 10^{13}$
Peak slow neutron flux density, n/cm^{2}s	$1.2 \cdot 10^{15}$	$8.6 \cdot 10^{16}$	$4.2 \cdot 10^{16}$
Thermal power, MW	0.12	7.6 - 9.2	6.3

5. Acknowledgements

Authors are grateful to V.V.Abramov, A.V.Dementiev, M.I.Grachev, V.V.Khodakovsky, P.L.Kirillov, L.V.Kravchuk, S.G.Lebedev, V.A.Matveev, V.V.Orlov, B.D.Ragozkin, N.M.Sobolevsky, N.K.Zharkih for helpful discussions and practical help.

6. References

[1] I.I.Bondarenko, Y.Y.Stavissky, *Atomic Energy*, vol. 7, No. 15, p.417 (Moscow, 1959, in Russian).
[2] *Proc. of ICANS XI* (KEK, Tsukuba, 1990).
[3] *Proc. of ICANS XII* (RAL, Abington, UK, 1993).
[4] E.P.Shabalin, *Proc. of ICANS XI* (KEK, Tsukuba, 1990).

[5] A.V.Dementiev, V.G.Miroshnichenko et al., *Proc. of ICANS XII* (RAL, Abington, UK, 1993).
[6] S.K.Esin, A.P.Fedotov et al., *Proc. of ICANS XI* (KEK, Tsukuba, 1990).
[7] M.I.Grachev et al., this Meeting.
[8] A.I.Leipunsky et al., "Physical characteristics of the fast reactor BR-5", *Conf. on Nuclear Reactor Physics*, (Vienna, 1961).
[9] A.V.Dementiev, N.M.Sobolevsky, "SHIELD - a Monte Carlo Hadron Transport Code," *Int. Meeting on Intermediate Energy Nuclear Data* (Paris, May 31 - June 2, 1994, NEA OECD).

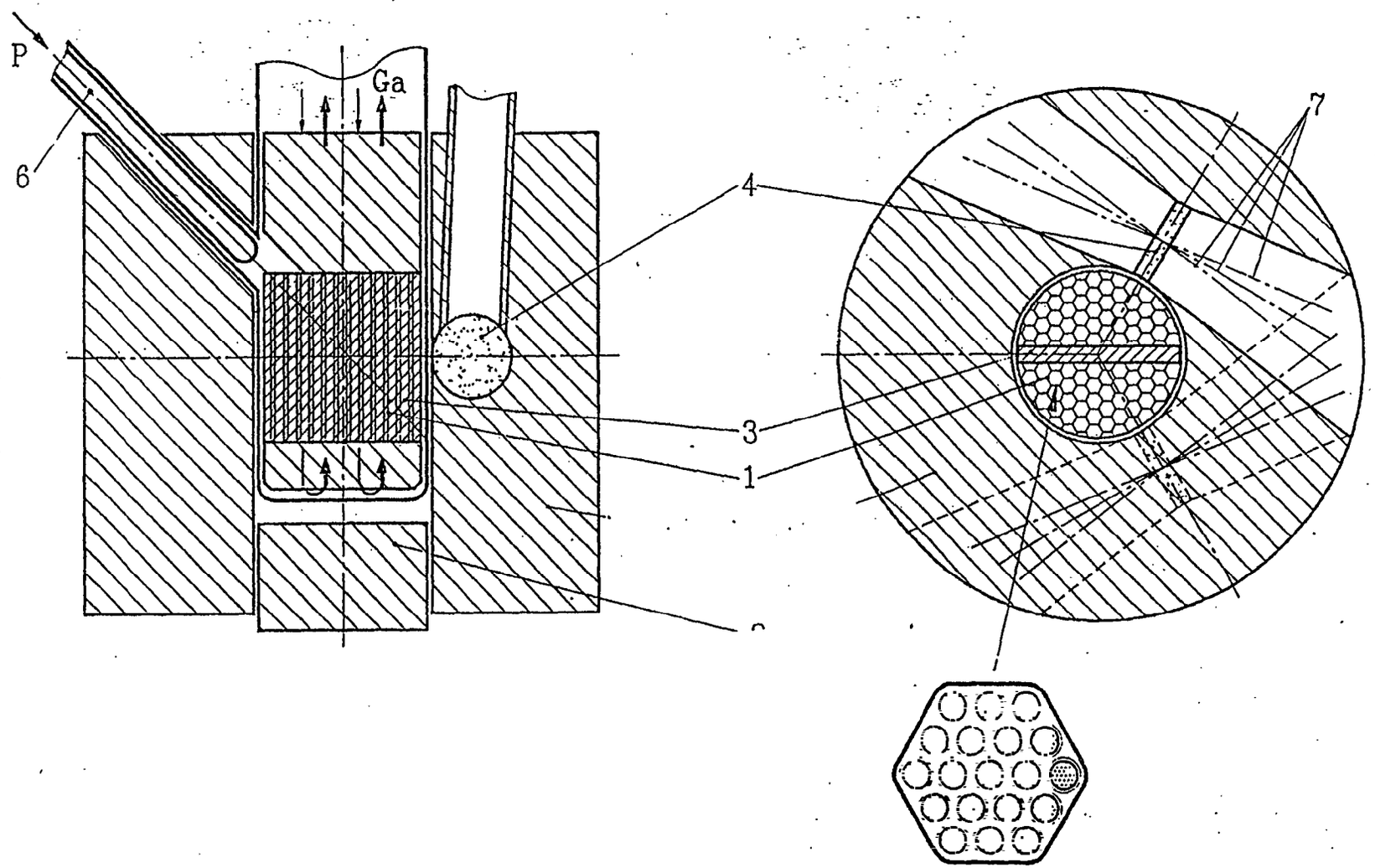

Figure 1. The layout of the RIN-10 neutron source.

ICANS-XIII
13th Meeting of the International Collaboration on
Advanced Neutron Sources
October 11-14, 1995
Paul Scherrer Institute, 5232 Villigen PSI, Switzerland

TUNGSTEN AND URANIUM TARGETS FOR THE MOSCOW MESON FACTORY

A.V.Dementyev, V.G.Miroshnichenko, S.F.Sidorkin*), N.M.Sobolevsky, Yu.Ya.Stavissky
Institute for Nuclear Research of Russian Academy of Sciences,
60th October Anniversary prospect, 7a, 117312 Moscow, Russia.

I.I.Konovalov, A.A.Maslov
Bochvar Institute of Inorganic Materials,
Rogov street, 5, 123060 Moscow, Russia.

I.T.Tretyakov, V.I.Trushkin
Research and Development Institute of Power Engineering
Head Post-office, box 788, 101000 Moscow, Russia.

A.D.Rogov
Frank Laboratory of Neutron Physics, Joint Institute for
Nuclear Research, 141980 Dubna, Moscow region, Russia.

*** - corresponding auther, E-mail: sidorkin@inr.msk.su**

ABSTRACT

This paper describes the concept of uranium targets of Moscow meson factory, reasons for choosing the geometry and material (U_3Si) of target as well as the shape of fuel elements. Results of neutronic computations, data on corrosion rates of design materials and measures for providing their compatibility are presented. The advantages of the chosen fuel composition as compared with others, design details and possible alternatives are discussed.

1. Introduction

The pulse neutron source based on the high-current proton linac (proton energy 600 MeV, average current 0.5-1.0 mA, pulse width 100-200 μs and repetition rate up to 100 Hz) and proton storage ring (pulse width 0.32 μs, average current up to 0.4 mA, repetition rate 100 Hz) /1/ that is under construction at INR RAS will allow one to develop a wide range of research on condensed matter and nuclear physics with thermal and epithermal neutrons.

Keywords: Target,Uranium,Tungsten,Corrosion

The neutron source consists of the following principal parts (see Fig.1):
- water cooled vessel containing target, moderator, reflector and top steel shielding with coolant pipes inside;
- gas vessel with vacuum bend reducing scattered neutron backgrounds at the lower moderator and joining the target and ion guide vacuum system;
- remote-controlled vacuum seal which provides disassembly of the whole neutron source;
- proton beam monitoring system.

The scheme allows us to use vessels with different targets and moderators (including cryogenic ones) and to replace all equipment in the central part, as well as to modify the source. A set of Ti-coated tungsten plates or tight lattice of natural uranium rods in stainless steel cans placed in Al-alloy vessel and cooled with light water are planned to be used as neutron targets /2-4/.

Additionally, we will be able, in future, to use enriched uranium targets with multiplication up to 10 without significant changes of the the existing target design / 5, 6/. Using the multiplying target will allow us:
- to increase by several times the intensity of the pulse neutron source at repetition rates from 10 to 50 Hz, which is the most suitable range for time-of-flight experiments;
- to decrease the beam current usage down to 5-50% of the total accelerator intensity, thus allowing more experimental programs to be executed concurrently;
- to use a relatively low proton current in the storage ring (< 0.5 mA); this will make easier the achievement of required operational parameters and will increase its stability;
to provide a high performance neutron source at the initial stage of accelerator operation, before the design parameters are achieved.

However, multiplying targets have high background caused by delayed neutrons. In order to decrease this background, it is necessary to use fissile isotopes with low fraction of delayed neutrons.

To use highly enriched uranium fuel in the multiplying target instead of natural uranium, it is necessary to decouple it from moderators in order to prevent the neutron pulse broadening and overheating of outer fuel elements by thermal neutrons. We are going to make the identical design for both natural and enriched uranium targets to provide for full-scale testing of all elements of the multiplying target during the natural uranium target operation.

It should be noted that the current design does not enable us to alter transverse core dimensions without replacing the whole central part of the source including the gas tank, the top shielding, and the target vessel. Moreover, altering the core height is limited by the design of neutron channels in shielding within the range of 6-12 cm (Fig.1) /2-4/. Therefore, to unify dimensions of the target vessel and reduce expences, the transverse dimensions of the core could not exceed the earlier adopted diameter of 32.8 cm. The required gain factor could be achieved by changing the height of the target core and upper and lower moderators. If the core height exceeds the vertical distance between neutron guides, which are 20 cm in diameter, additional collimators are needed to prevent direct leakage of the fast neutrons from the core to the

experimental samples. The part of the neutron source shown in Fig.2 includes the core, the lower and upper moderators, and the Be-reflector surrounding the upper moderator /5,6/.

The target design is close to the classical wing arrangement. Thus, if a powerful proton beam is used, it allows us:
- to minimize in a most easy and rational way the inevitably negative influence of several layers of material between the target and moderators, the inlet and outlet collectors, fuel element lattice, etc.;
- to provide reliable cooling of the proton beam window;
- to ensure nuclear safety of multiplying target and to use highly enriched uranium only in minimal quantity.

Other possible layouts (e.g. split target and flux-trap type moderators /7/) require more complex design. In particular, it would be necessary to provide cooling of three proton windows, to have several collectors, etc. In the case of a very high power target, the advantages predicted by simple physical models /8,9/ may completely vanish, as we have experienced with the reproduction factor when going from a simple fast neutron critical assembly without coolant and construction materials to a real breeder.

2. Tungsten and uranium elements

The tungsten target contains 25 plates made of W of high purity (99.95 wt.%) having dimensions of 5x7x160, 5x57x220, 10x57x160 and 10x57x220 mm. The design provides a 0.7 mm gap between the plates for coolant flow. The tungsten plates have a titanium corrosion resistant coating 10 μm thick. Without protection the rate of tungsten corrosion under operating temperature conditions may as great as 50 microns per year /10/.

The uranium target consists of cylindrical fuel elements with intermetallic substoichiometric composition in the form of U_3Si in stainless steel cans of 8 mm diameter and 0.3 mm wall thickness. The fuel element design was chosen for the following reasons. In case of a multiplying target, due to the high price of highly enriched uranium, it is important to provide that the lifetime of the target be at least 3-5 years, corresponding to fuel burnup 1-2 at.%. Moreover, during operation, the target will experience regular and irregilar thermal shocks. These negative phenomena are almost eliminated if the fuel is arranged in the target in the form of cylindrical rods /11,12/.

The triangular packing of the fuel rods, 8-9 mm diameter with a gap between them about 0.4 mm, makes possible single-phase water cooling of the target at a water pressure $(1.5\text{-}2.0)\times10^5$ Pa and flow rate of 3.5-4.5 m/s. In this case the volume fraction of the coolant does not exceed 20%, moreover it provides acceptable physical characteristics of the neutron source and allows removal of the heat power up to 2.0-2.5 MW at proton pulse repetition rates up to 50 pps /13-15/.

The choice of a high density uranium alloy for fuel core was made taking into account the properties, manufacturing technology and existing experience with their operation under

conditions similar to those of neutron target. The characteristics of two types of alloys are shown in Table 1: (1) alloys based on stable phases of the type of U_3Si /16/ and (2) alloys based on metastable solid solutions of the type of U-Mo and U-Nb-Zr /17,18/, both showing satisfactory resistance to corrosion in water up to 200°C. The maximum operating temperature of U-Mo and U-Nb-Zr alloys depends on the thermal stability of their corrosion resistant metastable γ-phases. After several hours at 350°C the beginning of γ-phase disintegration with the appearance on grain boundaries of an α-phase subject to corrosion was detected. This results in the loss of the desired fuel core mechanical properties and an increase of the corrosion rate by 10-100 times, up to unacceptable values 0.2-1.0 mg/cm^2hr. In several cases catastrophic destruction of U-Mo samples after 10-30 days of exposure in water was observed. Some aspects of corrosion failure were discussed in /19/.

Table 1. Characteristics of alloys

Alloy (fractions expressed as weight percents)	U-3.8% Si[1]	U-2.9% Si[1]	U-6% Mo	U-9% Mo	U-5%Nb-5%Zr
Density, g/cm^3	15.1	16.1	18.3	18.1	16.1
Uranium content, g/cm^3	14.5	15.8	17.1	16.5	15.1
Max allowable temperature, °C	550[2]	550[2]	350	350	400
Corrosion rate in water, mg/cm^2hr:					
at 100°C	0.01	0.02	0.01	0.01	0.01
at 200°C	0.11	0.07	0.03	0.01	0.04
at 200-350°C (after annealing at 350°C)	0.5	0.5	1-2	0.5-1	>5
Thermal conductivity at 200°C, W/m·K	19	21	23	21	22

[1] **Contains 0.2-0.4 % of elements stabilizing properties of U_3Si.**

[2] **Recommended temperature, tested up to 680°C.**

Under conditions of frequent changes of the operation regime, shut-downs, uneven heating (thermal shocks ~10·15°C in the case of multiplying targets) it is impossible to provide reliable thermal contact between the can and fuel rod based on U-9% Mo. Experience with U-Mo alloys in breeder blankets with burnup ≤1% shows that the thermal contact is not always achieved even in the case of rare changes of operating conditions and shut-downs. In Fig.3, for targets based on ^{238}U, ^{235}U and ^{233}U, the expected temperature in the centre of the most thermally stressed fuel rods made of U-9% Mo and ^{233}U-2.9% Si alloys is shown as a function of multiplication coefficient at different values of the thermal gap betwen fuel and can, and different pulse repetition rates. For U-9% Mo alloy, the technological gap between the fuel rod and can is varied from 0.025 to 0.05 mm. Due to amorphization (discussed below) U-2.9% Si alloys provides full thermal contact between the fuel and can (δ=0). Plotted on the same graph

is the curve of the stability of the γ-phase of metastable alloys. As it follows from Fig.3, for the proton beam of the Moscow meson facility, U-9% Mo alloy can be used for the targets with low multiplication coefficients ~3-5 at pulse repetition rates ~25-50 pps, respectively. At larger multiplication coefficients, the temperature of both central and peripheral fuel elements exceeds the temperature of γ-phase stability.

For fuel based on uranium silicides, the temperature of the outer layers of fuel elements is about 130°-140°C even at multiplication coefficients 8 - 10. In Figure 3 the dotted line represents the temperature of the most thermally stressed fuel rod in the core based on ^{233}U-2.9% Si. For ^{235}U-2.9% Si the temperature is obviously lower beause of the larger core volume. Therefore, the operating temperatures and corresponding rates of corrosion for U-9% Mo and U-2.9% Si differ substantially. They are indicated by dashes in Table 1.

During reactor experiments with nonhermetical silicide fuel elements it was established that under temperatures less than 200°C the control system did not detected uranium in coolant.

Thus under real operating conditions in multiplying targets we cannot be sure of γ-phase stability and corrosion safety of the target. Moreover, we have not enough experience with U-Mo and U-Nb-Zr fuel elements operation in water coolant, but some experiments indicate that these alloys under irradiation become rigid and deform the fuel element can. In case of non-uniform operating conditions, such as we have for the fuel core in the target, we must expect strong deformation and bending of the fuel elements.

Swelling of uranium alloys under irradiation at temperatures less than 350-400°C is caused by accumulation of fission products in the crystaline lattice with the rate of 2-3 vol.% per 1 at.% of burnup. For fuel elements made of U_3Si the diameter increase of fuel element will be 0.1-0.3 mm at a burnup of about 2 at.% (Fig.4). For comparison, on the same figure, the swelling of U-9 wt.% Mo alloy is presented. For both cases the swelling is shown not accounting for the restriction factor of the can. Radiation amorphization of uranium silicide at temperatures below 210°C and burnup more than 10^{-4}at.% is a useful phenomenon /20/, since it provides:
- increased corrosion resistance of fuel;
- full thermal contact between core and can after several hours of operation; according to experimental investigation, this contact was not broken under non-stable temperature conditions;
- decreased negative influence on fuel element lifetime due to non-uniform core swelling and deformation under thermal shocks.

As we have established, uranium silicide in the amorphous state exhibits radiation creep comparable to that of the crystaline state under temperatures a little lower than the melting point. According to our calculations there will be an outer layer of fuel in the amorphous state under the full range of operating conditions of the target. This outer amorphous layer, as we expect, will prevent the core from cracking, unlike the case of U-Mo and U-Zr-Nb alloys.

In the most powerful operation conditions, that is the case of a multiplying target made of 98% $^{233}U_3Si$, the local maximum heating per pulse will be ~15°C. In order to decrease the additional influence of thermal shocks the fuel core is split into three parts (Fig.2) /11/. The cores made of substoichiometric silicide U - 2.9 wt.% Si are canned in stainless steel without a barrier sublayer, since at temperature less than 500°C and exposure for one year, the interaction layer does not exceed 10 microns.

Current technology enables us to manufacture not only fuel elements from natural uranium, but also from highly enriched uranium. Prototypes of fuel elements were tested under reactor conditions with water cooling for 3.5 years to a burnup of 3 at.%. The maximum local power density of the silicide core ranged up to 660 W/cm^3. This power density for a multiplying target at a design beam current of 0.5 mA will be achieved at a frequency of 25-30 Hz. Increasing the repetition rate up to 50 Hz will raise the power by two times and fuel core temperatures will be close to their operating limit. Thus the parameters of target operation demand careful investigation.

Experience in developing, testing and using the uranium silicide as a high-density fuel for light-water reactors is an additional reason for choosing it.

Besides the silicide, other high density amorphyzing compounds of U_6M - type, where M is Ni, Co, Fe, Mn and their combinations were investigated. But their corrosion resistance in water under temperatures about 200°C was insufficient. Taking this into account as well as the level of investigation of uranium silicide, that material was finally chosen as a fuel for target elements.

3. Core, moderators, reflector

The arrangement of fuel elements in the target lattice and their separation is provided by stainless steel wire 0.4 mm in diameter. Thermal - hydraulic calculations of the compact fuel element lattice was carried out on the basis of experimental data summarized in /13,14/.

In order to compensate for thermal expansion and the swelling of fuel elements in the transverse direction and to prevent vibration due to coolant flow, springy elements embracing the core from three sides are used. The most suitable materials for springy elements is Zr-Mo alloy since it retains elasticity under reactor conditions and has good compatibility with other target materials.

The inlet and outlet channels of the core coolant system must provide uniform coolant flow with the minimum volume of water in order to avoid lengthening of fission neutron lifetime. Therefore collectors are made in the form of vertical narrow channels made of material well-absorbing thermal and epithermal neutrons (item 4, Fig.2). The most suitable materials from the point of view of their nuclear properties, manufacturing technology and compatibility with other materials of core are Hf, Zr- Hf (up to 10 wt.% of Hf) and Ti-Gd (up to 36 wt.% of Gd) alloys. Profiled plates of these alloys are placed on the top of the core partially covering the

collectors.

The presence of different metals and alloys in the core required extensive studies of their compatibility and water coolant chemistry. Corrosion rates of metals under different conditions including neutron flux are shown in Fig.5. For additional corrosion protection the inner side of the aluminium vessel is coated with Ti. Investigations of Al and W samples coated with titanium under reactor conditions have shown that Ti-coating in water at about 80°C was compatible with other materials of the core. No modifications of Ti coating were observed after a period of time comparable with that expected for target operation /10/.

Before entering the core and after leaving it the coolant contacts the Be-reflector surrounding the upper moderator.

The outer vessel surface in the vicinity of the core (operating in vacuum or in the air), the moderators (except the radiating areas), and the reflector are coated with Gd, which acts, in particular, as a decoupler shortening the neutron pulse. In addition, this layer together with other construction materials of flow channels and the core ensures nuclear safety in case of accidental flooding of the gas vessel.

The upper moderator has a radiating area of 12×12 cm^2 and is 5.5 cm thick. A replaceable H-type insert from Ti-Gd alloy splits the moderator into two parts, e.g. 2.0 and 3.5 cm thick, which enables the optimization of moderator properties for certain experiments. The side surface of this insert serves as a decoupler separating the moderator and reflector. For replacement of the insert there is a removable Be-plug in the upper part of the reflector. Of course, the replacement of the insert is only possible on the stopped facility during maintenance periods, since it requires removing the shield and coolant piping. The lower moderator has dimensions of 20×20×3 cm and has been optimized for producing epithermal and intermediate energy neutrons.

4. Neutronics: calculations and optimization

Using rod-shaped fuel elements instead of plates decreases the number of spallation neutrons per incident proton, as the fuel volume fraction is less. The computed conversion coefficient K_n (number of fission and evaporated neutrons per incident proton) and multiplication factor K_m as a function of the core height for U-2.9% Si and U-9% Mo alloys are shown in Fig.6. The K_n coefficients for both a tungsten target and a monolithic natural uranium block of equal size are also shown for comparison.

Using natural uranium rod fuel elements made of U_3Si or U-Mo alloys, the number of generated neutrons increases in 1.4 - 1.5 times in comparison with a tungsten target. The same theoretical value for a monolithic natural uranium block with the density of 19.1 g/cm^3 is 2.0-2.1. The known maximum value of 1.7 was achieved in KENS-1 target consisting of four monolithic low-alloy uranium blocks with a small amount of construction materials /21/.

In all other cases, going to a more powerful proton beam and to arrangements of target fuel elements in the form of plates, this value does not exceed 1.5 /22-24/. Therefore, due to its low efficiency, the natural uranium target is considered only as an intermediate step towards the target with multiplication factor of 2-10. The upper value of the multiplication factor is limited by the delayed neutron background between two pulses, by nuclear safety requirements for subcritical assemblies without control and safety system /25/ and, finally, by the capacity of the cooling system (2.5 MW). Its lower limit is determined by the desire to construct a facility with neutron yield per incident proton more than that for a uranium block target.

It is very important for a pulsed neutron source to achieve the maximum density of fast neutron leakage to moderators. In that case the neutron flux density on the moderator surface also reaches the maximum /26, 27/. The total neutron output from the target and minimum cross section for thermal neutron absorption are important for stationary and quasi-stationary thermal neutron source with heavy water moderators /4,28/. The neutron output in the transverse direction as a function of core height is also shown in Fig.6. One can see that the neutron flux density reaches its maximum at the target height of 5-6 cm. Moreover, this approach enables us to perform optimization calculations in a more rational way, since we can separate optimizations of the target and moderators, using for that purpose experimental and computed data /29-31/ and codes /32-34/.

For a multiplying target based on ^{233}U, a multiplication factor of 6-8 is also achieved for a height of the target core of 6-7 cm. From that point of view, the target based on ^{233}U is more efficient than one of ^{235}U, where this multiplication factor can be achieved at a core height of 11-12 cm /Fig.6/. In the latter case the target is less efficient as the side flux of neutrons leaking away does not contribute to the total thermal neutron flux in moderators.

However, when a multiplying target is used, increasing its height leads not only to increasing K_m and K_n, it also degrades the form factor (due to higher leakage through side surface of the target and longer distance between the target center and moderators) and broadens the fast neutron pulse (the width of the slow neutron pulse is usually determined by the moderator). The competition of these factors determines the optimal multiplication factor /27,35/. Its dependence on the neutron energy E used for TOF experiments and on the average lifetime of prompt fission neutrons in the target core is shown in Fig.7. For calculations it was assumed that the proton beam from a proton storage ring has a pulse width 0.32 μs /1/, pulse duration of moderated neutrons was estimated by equation $\tau_m = 2/\dot{I}E$ (μs). The function FOM = j/θ^2 was used as an objective, where j - density of fast neutrons leakage on the face of the target, and θ - pulse duration of neutrons with the energy E_n in the moderator. It is evident that the optimal value of multiplication is higher for experiments with neutrons of lower energy, and for targets with shorter prompt neutron lifetime.

For a ^{238}U target we have one more option: depending on the relative priority of experiments, we can vary the vertical position of the proton beam and, as a consequence, vary the neutron

fluxes in upper and lower moderators.

Calculations at high energies (20-600 MeV) were made with the SHIELD/CG code, which has been developed from the SHIELD code /36/. Some results were duplicated with the MARS-12 code /37/. Both codes were tested by experimental data /38-40/. Results are shown in Fig.8. One can see that the accuracy of calculation of the spallation process in the energy range up to 600 MeV is better than 10%. In the range of 0.0023 eV to 10.5 MeV the modified version of the MCU code /32,33/, MCNP /34/, and a specially developed Monte Carlo code were used. Test calculations of the fast spectrum critical assemblies /29,30/ and of a moderated pulsed fast reactor /31/ have shown the accuracy of 5% and 10% in criticality and prompt neutron lifetime respectively.

The calculated characteristics of pulsed sources based on W, ^{238}U, 90% ^{235}U and 98.1% U^{233} with a pulse frequency of the beam from the proton storage ring of 25 Hz and for K_m ~6 are given in Table 2.

Table 2. Characteristics of targets for 125 μA, 600 MeV proton beam.

Fuel	W	U^{238}	U^{235}	U^{233}
Average power, kW	78	110	720	600
Background power, kW	0	1	4.6	1.9
Thermal neutron pulse width, μs[1]	35/24	35/24	35/24	35/24
Multiplication	1	1.14	5.7	5.7
Average thermal neutron flux density, n/cm^2s:				
3.5 cm	$0.9 \cdot 10^{12}$	$1.3 \cdot 10^{12}$	$4.1 \cdot 10^{12}$	$5.0 \cdot 10^{12}$
2.0 cm	$0.5 \cdot 10^{12}$	$0.8 \cdot 10^{12}$	$2.4 \cdot 10^{12}$	$2.9 \cdot 10^{12}$
Peak thermal neutron flux density, n/cm^2s:				
3.5 cm	$1.0 \cdot 10^{15}$	$1.5 \cdot 10^{15}$	$4.7 \cdot 10^{15}$	$5.7 \cdot 10^{16}$
2.0 cm	$0.8 \cdot 10^{14}$	$1.3 \cdot 10^{15}$	$4.0 \cdot 10^{15}$	$4.8 \cdot 10^{16}$
Repetition rate, pps	25	25	25	25

[1] **For 3.5 and 2.0 cm sections of water moderator.**

5. Some alternative variants of target cooling

In the course of target development the possibility of using liquid metal coolants is considered. Alkaline metals were not considered because of their flammability.

It was assumed that the Pb-Bi and Ga-coolants enable us /15,41/:
-to increase the neutron output and the linear density of the primary neutron source;
-to extend the range of high-density uranium fuels (UMo, UN, UC), that are compatible with

coolant;
-in powerful targets to avoid coolant boiling and improve the hydraulic stability of parallel channel cooling.
-to avoid the effect of irradiation decomposition of water coolant.

Calculations showed that despite the increase in the fraction of heavy metals in the cases of Pb-Bi or Ga-coolants there is no significant gain in the neutron production density along the beam direction and the total number of primary neutrons per proton. This is the result of additional ionization losses of the proton energy and the decreasing number of non-elastic reactions on uranium per proton. Since uranium nuclei have much higher neutron output as compared to Pb, the decrease of flux and energy of hadrons will result in the degradation of the neutron output, which will not be compensated by heavy coolant.

The total neutron output from the target of 70 mm height with a composition corresponding to the hexagonal lattice of fuel elements 5-13 mm in diameter, with can thickness of 0.3 mm and with 0.4 mm gap, and for natural uranium U-9% Mo alloy is shown in Fig.9. For comparison, this figure shows the neutron output from the target with nitride fuel (UN, ρ = 13.5 g/cm^3) and Gallium cooling. UN is a fuel of increased density and is the most suitable choice in view of its compatibility with liquid-metal coolant (Pb, Pb-Bi, Ga). Calculations were made with the SHIELD code. One can see, that in the interesting range of element concentration in the core, the increasing is about 0.5-0.7 n/p. This difference was even smaller when estimations were made by the method of nucleon flux decomposition into non-elastic interaction integrals /42/ using the data of /43/.

But even this small addition for the multiplying target with metal coolant is eliminated because of the harder neutron spectrum, requiring larger target height for the same multiplication factor and, correspondingly, a larger fraction of neutrons leaking away. The factors mentioned above reduce the density of neutron leakage towards the moderators. Besides the absense of significant gain in neutron output, using liquid metals as coolant raises many technology problems and, as a consequence, leads to a more complicated and expensive design of the target and supporting systems, particularly for Pb-Bi alloys.

Contrary to our expectations, using liquid-metal coolants does not extend the choice of high-density fissile materials compatible with these coolants, since experience with these materials has been obtained, mainly, in sodium-cooled reactors, while high-density fuels have not ever been tested with heavy coolants even in trial operation /44,45/.

As we mentioned above, the problem of ensuring single-phase coolant flow and hydraulic stability becomes significant for powerful multiplying targets. The physical characteristics of such a target which consists of a dense fuel element lattice with highly enriched uranium and water coolant allow us to maintain stable single-phase coolant flow due to high sensitivity to hydrogen content. The experience gained in developing the booster based on the plutonium oxide /46/ and other calculations indicate an abrupt decrease of multiplication factor and target power if any decrease of water concentration occurs due to boiling in either one channel or the whole target (ΔK_{eff} = - (18-20)% for the total coolant loss). This is one of the factors that

ensure nuclear safety, some aspects of which were discussed in /47/. Considering nuclear safety in all its aspects is not an intention of this article.

However, these questions include:
- conditions of fuel element loading;
- the biggest possible fuel cassette size;
- using liquid control additions ($Gd(NO_3)_3$, NaB_5O_8, H_3BO_3) to prevent the local change of spectrum and reactivity rise in case of partial replacement of some fuel elements with water or accidental increase of the coolant fraction.

Table 3. Comparison of characteristic for multiplying water and liquid metal targets

Fuel	**90% ^{235}UN**	**90% $^{235}U_3Si$**
Coolant	**Ga**	**H_2O**
Reflector	**Ni*)**	**Be**)**
Multiplication	**7.1**	**5.7**
Yield, n/p	**11**	**12.5**
Core height, cm	**12.2**	**9.0**
Average power, kW	**850**	**720**
Repetition rate, pps	**25**	**25**
Average thermal neutron flux density, n/cm^{2}s (3.5 cm - moderator)	**$5.8 \cdot 10^{12}$**	**$4.1 \cdot 10^{12}$**
Peak thermal neutron flux density, n/cm^{2}s	**$5.6 \cdot 10^{15}$**	**$4.7 \cdot 10^{15}$**

*** 40 cm Ni - reflector arround all target**
**** Be - reflector around upper moderator**

Stability of hydravlic and increase of target safety may be obtained in case of liquid metal coolant. Computed target parameters with nitride fuel-UN and Ga-coolant are shown in Table 3. Dimensions of target cross sections, fuel elements lattice parameters and ampule diameter are the same, as for silicide fuel with water coolant. In contrast to silicide target, where Be-reflector is sited only in the topof target, in liquid metal target the Ni-reflector (40 cm in thickness) surrounds all target. This is necessary to increase reflector capability, compensate lower density of uranium nitride and to reduce target dimensions.

6. Conclusion

A multiplying target with a gain factor of 10 cannot serve as a proton beam trap unlike the cases of tungsten and natural uranium targets because, at full proton beam power, the average

target heat power will be ~7 MW, that is three times greater than it was assumed.

Fuel elements on the basis of U_3Si with natural uranium, tungsten plates, vessel, shields, berillium moderators and some other elements of the core have already been manufactured.

Choice of core materials, investigation of compatibility and corrosion behaviour have been fulfilled.

The protective covering and assembly of the core are now in process.

For non-traditional usage of neutron source the possibility of rare pulsed booster creation for nuclear laser charging and irradiation of extended objects was investigated. It was shown that in central channel along the distance of more than 1.0 m it is possible to create almost uniform fast neutrons pulsed flux with dencity more than 10^{21} n/cm^{2}s having spectrum similar to that of fission and on outer surfaces more than 10^{20} n/cm^{2}s /48/.

7.Aknoledgements

We thank I.S.Golovnin, V.V.Titova (VNIINM) for useful discussion of uranium alloys properties, R.G.Vasilkov (Moscow Radio-Technical Inst.) for consultations on neutron output in integral experiments, A.V.Kuzin (INR RAS) for comparison of computed data on the basis of MARS-12 code with experimental results, Prof. I.Thorson (Canada, TRIUMF) for discussion of pulsed and quasi stationary target optimization, Prof. J.Carpenter (IPNS) for discussion of uranium and tungsten target efficiencies, V.S.Smirnov (RDIPE) for discussion of neutronic properties of tight lattices of water or liquid metal cooled fuel elements. The authors would like to express their gratitude to Dr. Tim Broom (RAL) for reading the manuscript and for valuable remarks.

8.References

1. S.K.Esin et al., INR linear accelerator and the compressor ring project for the neutron spallation sources. Proceedings of 11th Meeting of the International Collaboration on Advanced Neutron Sources (ICANS-11), V.1 p.194, KEK, Japan, 1990.
2. Yu.M.Bulkin et al., Neutron source complex on the base of proton beams of the Moscow Meson Factory. Proc. Conf. on neutron scattering in the 'nineties, Julich, IAEA (1985) pp.369-376.
3. Yu.Ya.Stavissky, Neutron facilities of Moscow meson and kaon factories. ICANS-11, V.1, p.87.
4. M.I.Grachev at al., Pulsed and quasistationary neutron sources based on proton beams of Moscow meson facility. ICANS-11, V.1, p.454.
5. V.G.Miroshnichenko, S.F.Sidorkin, Yu.Ya.Stavissky, International Seminar on Intermediate Energy Physics, Nov.27-30 (1989) Moscow, USSR.
6. V.G.Miroshnichenko, S.F.Sidorkin, Yu.Ya.Stavissky, Multiplication neutron targets based on the proton beam of Moscow Meson Facility. ICANS-11, V.1, pp. 579.
7. G.J.Russell at al., The LANSCE target system. ICANS-9, pp. 177-205. Villigen, September 22-26, 1986.
8. Y.Kiyanagi, N.Watanabe, Some Neutronic Studies on Flux-Trap Type Moderator. ICANS-11, V.1,

pp. 408-415.
9. Y.Kiyanagi, N.Watanabe, M.Nakajima, Nucl. Instr. and Meth. A 343 (1994) 550-557.
10. I.I.Konovalov, A.A.Maslov, Choice of Materials and Corrosion-resistant Irradiation-stable Coating Technology. Internal report (1990) in Russian.
11. V.P.Lomidze et al., Joint Inst. Nucl. Res. Preprint 3-11550, Dubna. (1978) in Russian.
12. E.P.Shabalin, Fast Pulsed and Burst Reactors, Atomizdat, Moscow (1976); Translated from W.E.Jones, Pergamon Press, 6242 Kronbergaunus, Pferdestrasse 1, Germany.
13. A.V.Zhukov, A.B.Muzhanov, P.A.Ushakov, Phys.-Energetics Inst. Preprint 1203, Obninsk (1981) in Russion.
14. P.L.Kirilov, Yu.S.Yuryev, V.P.Bobkov, Handbook on Thermal-hydraulic Calculations (Nuclear Reactors, Heat Exchangers, Steam Generators). Energe-atomizdat, Moscow (1984).
15. V.I.Subbotin et al., Hydrodynamics and Heat Transport in Atomic Power Plants. Atomizdat, Moscow (1975), in Russian.
16. Yu.Ya.Petrov, S.N.Bashlykov, A.V.Morozov, Uranium Silicides as Nuclear Fuel. Energe-atomizdat, Moscow (1984), in Russian.
17. V.S.Chirkin, Thermal properties of nuclear technics materials. Atomizdat, Moscow (1968), in Russian.
18. V.V.Gherasimov, A.S.Monakhov, Materials of Nuclear Technics. Atomizdut, Moscow (1973), in Russian.
19. J.M.Carpenter, Report on the International Workshop, PSI Villigen, Switzerland Feb. 10-14, 1992.
20. L.D.Panteleev, I.I.Konovalov, V.B.Mallygin et al., Influence of irradiation on structure and dimensional changes of U Si compound. Proc.of Intern. Conf. on Radiation Adaptive Metallurgy, USSR, Alushta, May 22-25 (1990) V.4, pp.98-104, in Russian.
21. N.Watanabe et al. Depleted Uranium Target System. KENS Report-6, p.11, 1985/86.
22. A.E.Knox, J.M.Carpenter et al., Progress on the IPNS Enriched Uranium Booster Target. ICANS-9, 1986, p.557.
23. A.Carne, T.A.Broome, J.R.Hogston and M.Holding, The ISIS target. Advanced Neutron Sourses 1988, IOP Conference Series No 97, p.79.
24. J.M.Carpenter, Private Communication.
25. Nuclear safety regualations for subcritical systems 01-75, in Russian.
26. S.F.Sidorkin, Inst. Nucl. Res. Preprint P-0545, (1987), in Russian.
27. S.F.Sidorkin, Inst. Nucl. Res. Preprint P-0576, (1988), in Russian
28. F.Atchison, Neutronic Considerations in the Design of Targets for SINQ. Technology of Targets and Moderators for Medium to High Power Spallation Neutron Sources. Reports of the International Workshop PSI Villigen, Switzerland Feb.10-14, 1992.
29. S.N.Ishmaev, I.P.Sadikov, A.A.Chernyshev, Kurchatov Atomic Energy Inst. Preprint 2019 (1970), in Russian.
30. G.E.Hansen, H.C.Paxton, Reevaluated Critical Specifications of Some Los-Alamos fast-neutron systems. LA-4208.
31. T.Asaoka, N.Watanabe, An optimization Study of Peak Thermal Neutron Flux in Moderators of Advanced Repetitive Pulse Reactors. Proc. U.S.-Japan Seminar on Fast Pulsed Reactor. 1976.
32. G.F.Liman, L.V.Mayorov, M.S.Yudkevich, Question of atomic science and technology. Ser: Physics and technology of nuclear reactors, V.7, pp.27-31 (1985), in Russian.
33. A.D.Rogov, Joint Inst. Nucl. Res. Preprint P11-82-710, Dubna (1982), in Russian.
34. MCNP - A general Monte Carlo Code for Neutron and Photon transport, Version 3A. LANL, LA-7396 M, Rev.2 (1986).
35. W.Kley, Nucl. Inst. and Methods. V.200(1982) p.175.

36.N.M.Sobolevsky, Joint Inst. Nucl. Res. Preprint B-2-5458, Dubna (1970), in Russian.
37.N.V.Mokhov, The MARS code system: Inclusive simulation of hadronic and electromagnetic cascades and muon transport. Preprint FN-509, FNAL, Batavia.
38.R.G.Vassilkov, Free neutron production with hydrogen ion accelerators for nuclear fuel cycle needs, Muon Catalyzed Fusion 7 (1992).
39.R.G.Vassilkov, V.I.Yurevich, Neutron emission from an extended lead target under the action of ligt ions in the GeV region. ICANS-11, V.1, p.340.
40.J.S.Fraser et al., Phys. Can. 21(2), p.17, 1966.
41.S.P.Yatsenko, Gallium, Interaction with metals. Nauka, Moscow (1974), in Russian.
42.S.F.Sidorkin, Inst. Nucl. Res. Preprint, P-0445, Moscow (1986), in Russian.
43.B.S.Sychev, A.Ya.Serov, B.V.Manko, Radio-Technical Ins. Preprint AS USSR N 799 (1979), in Russian.
44.V.V.Orlov et al., Unconventional Concepts of NPPs with Inherent Safety, Atomic Energy, V.72, I.4,(1992) pp.317-328, in Russian.
45.E.O.Adamov et al., Research Development Inst. Power Eng. Communication, Moscow (1990), in Russian.
46.N.V.Kolmychkov et al., Proc. 2th All Union Seminar on Program of Experimental Researches on the Moscow Meson Facility, Moscow (1981) p.271, in Russian.
47.Pulsed Neutron Source, Internal report of RDIPE, 1981, in Russian.
48.S.F.Sidorkin, V.I.Dergzhiev, S.I.Yakovlenko, Nucl. Inst. and Methods. A306 (1991), pp.240-246.

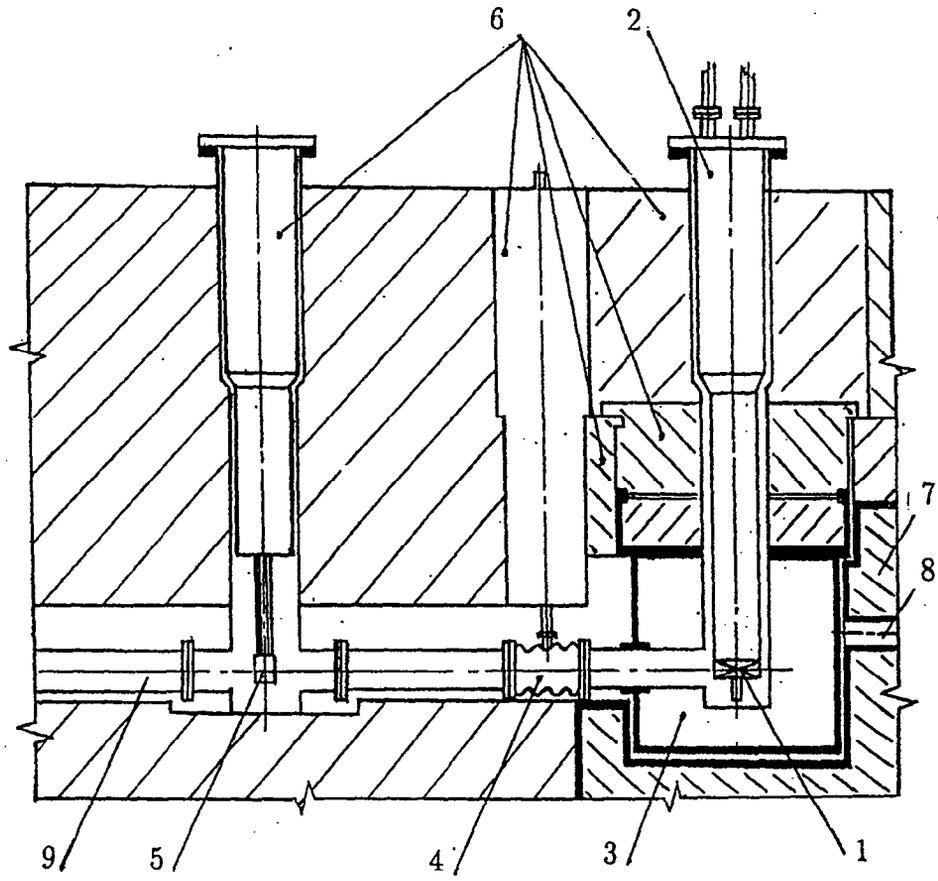

Fig.1. Pulsed neutron source layout: 1 - core; 2 - target.vessel with steel shielding plugs; 3 - gas tank; 4 - remote controlled vacuum seal; 5 - proton beam monitoring system; 6 - shielding plugs; 7 - thermal shielding; 8 - neutron guides in biological shielding; 9 - proton guide.

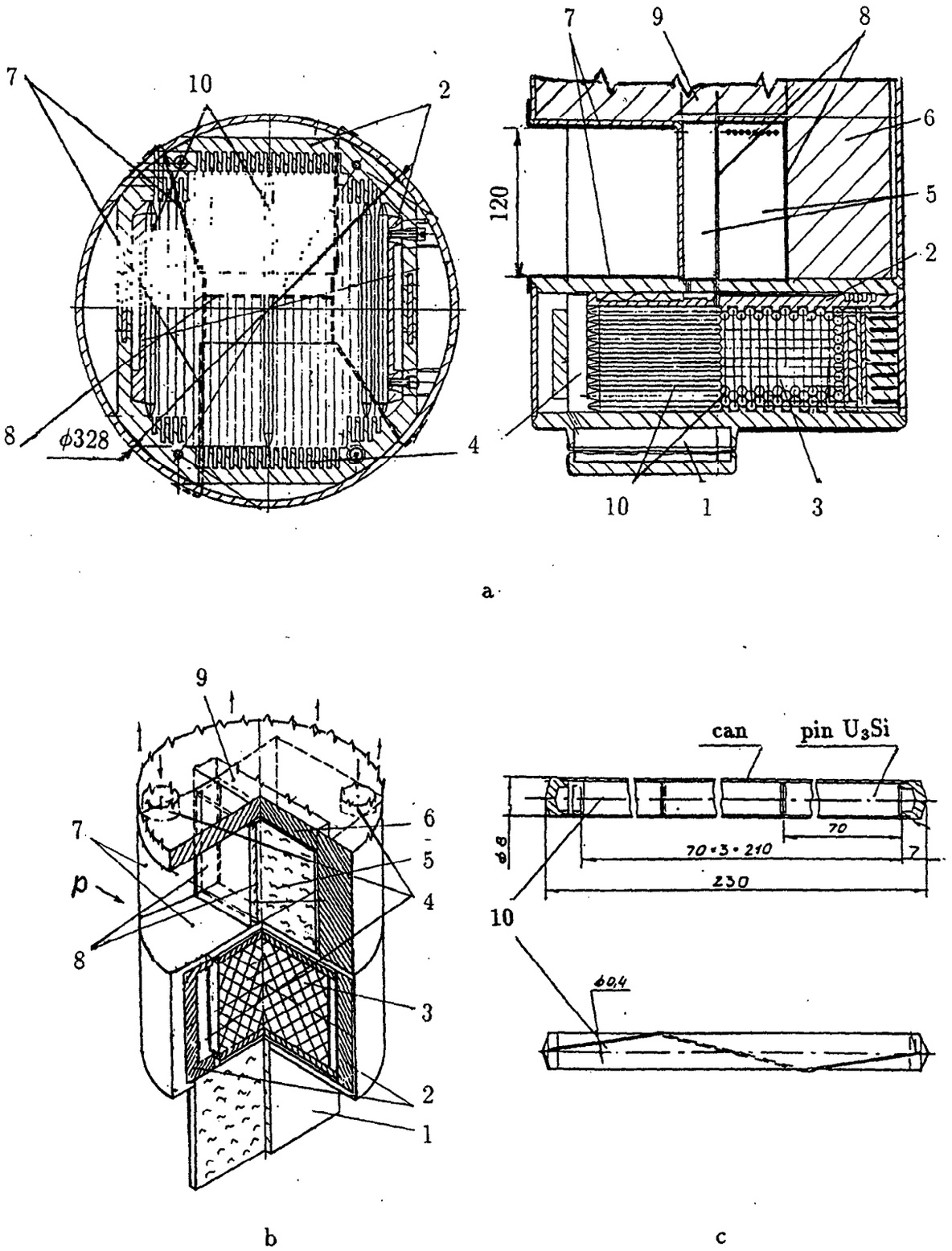

Fig.2. Central part of the pulsed neutron source: 1 - lower moderator; 2 - Ti-Gd decoupler; 3 - core; 4 - coolant inlet and outlet; 5 - upper moderator; 6 - Be-reflector; 7 - Gd - decoupler; 8 - Ti-Gd - insertion; 9 - Be-plug; 10 - fuel element.

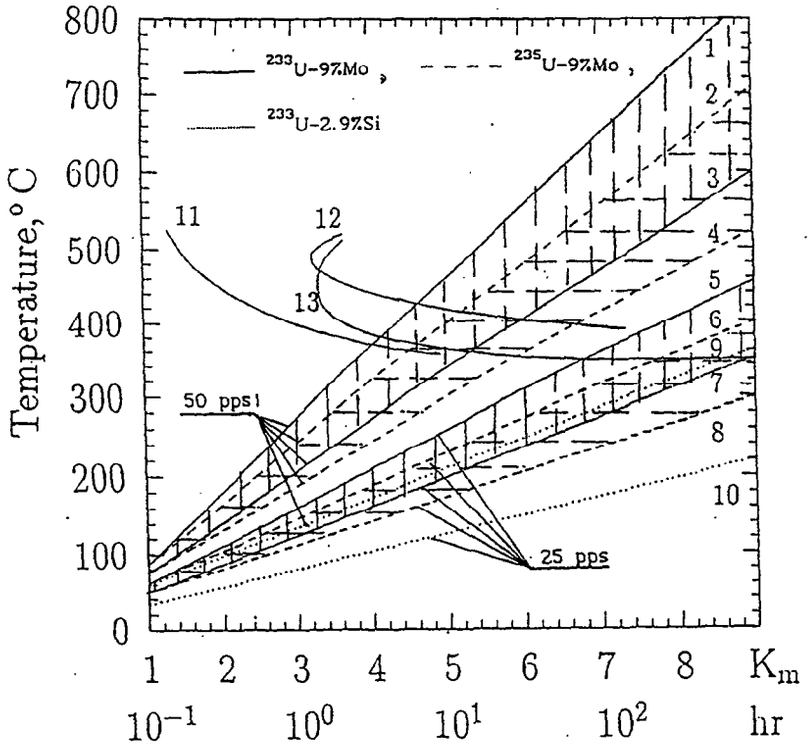

Fig.3. Expected temperatures in the center of the most thermal-stressed fuel element with the core from U-9 wt.% Mo and U - 2.9 wt.% Si alloys vs. the multiplication coefficient - K_m, pulse frequency and gap between core and can (for 1,2,5,6 δ = 0.05 mm; 3,4,7,8 δ = 0.025 mm; 9,10 δ = 0.), the curves represent the time-temperature gamma-phase stability boundaries for the same metastable alloys: 11 - U-Nb-Zr, 12 - U-9% Mo, 13 - U-6% Mo.

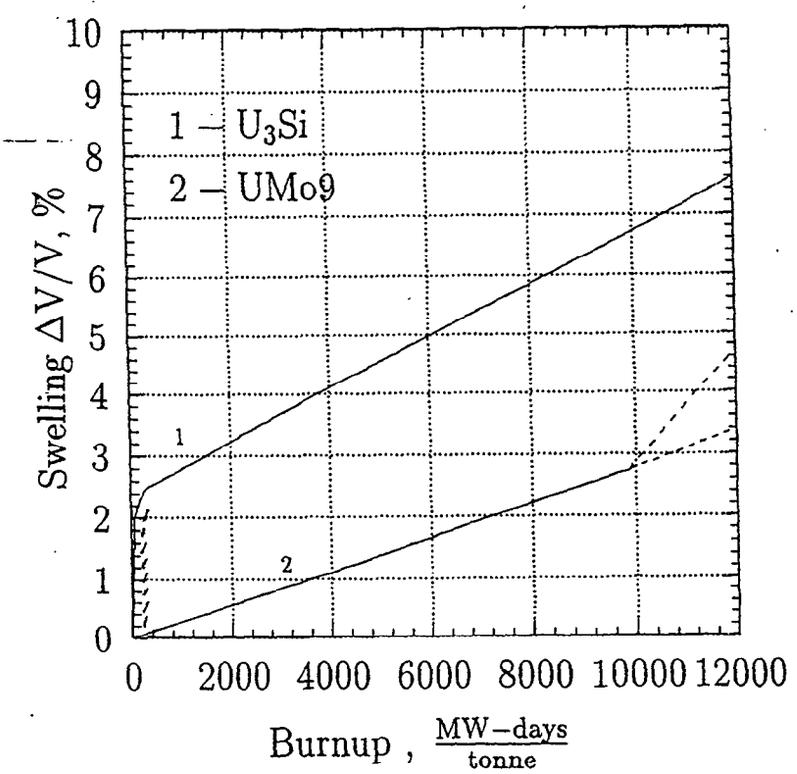

Fig.4. Swelling of core materials. The area of core cracking is shown by the dashed line (1 at % ~ 10000 MW·day/tonne); the area of amorphization is hatched.

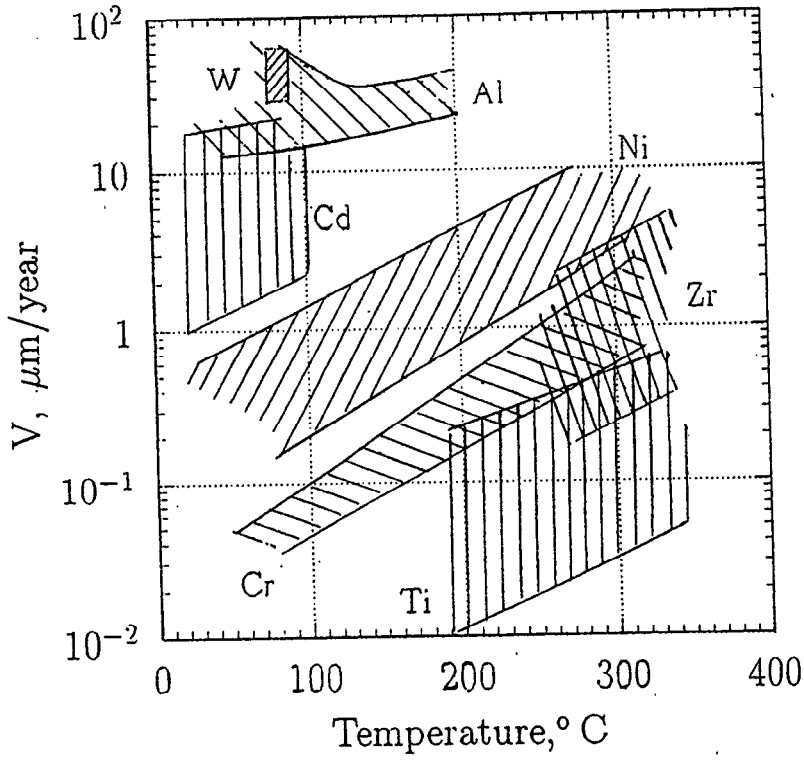

Fig.5. Corrosion rates of materials in distilled water at various temperatures.

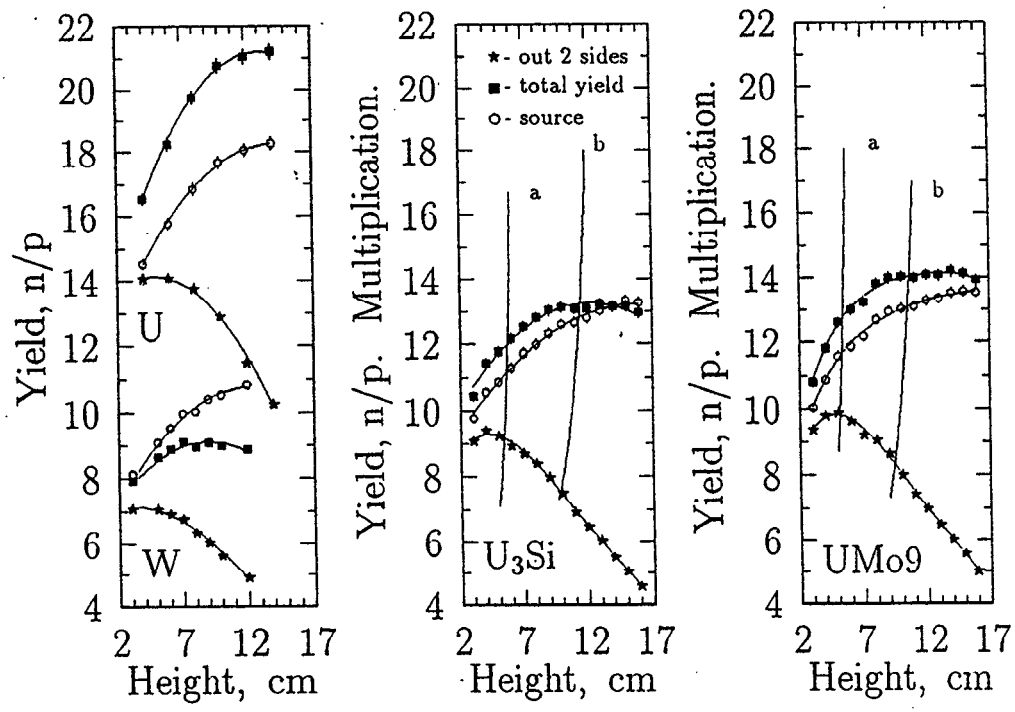

Fig.6. Computed spallation neutron yield per 600 MeV incident proton for W-target and U-2.9% Si and U-9% Mo natural uranium alloys target, and the multiplication factor (a - U^{233}, b - 90% U^{235}) for targets of various height (scale is the same). Neutron leakage from upper and lower surfaces is shown separately.

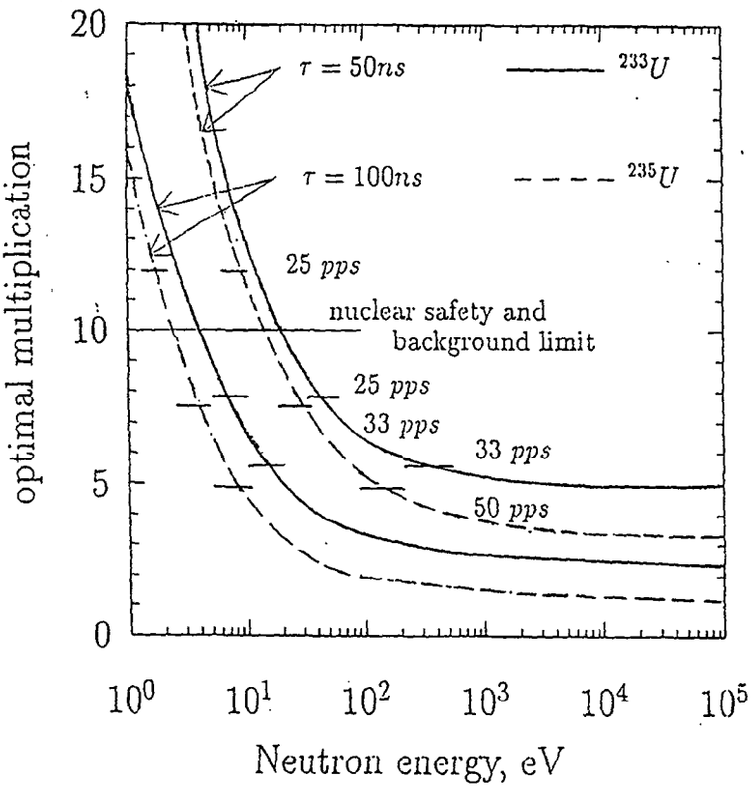

Fig.7. Dependence of optimal multiplication factor on the energy of the neutrons used in TOF experiments with the storage ring for various values of the prompt neutron lifetime. The optimal multiplication factor for the repetition rates of 25 pps, 33 pps, 50 pps are shown by horizon lines.

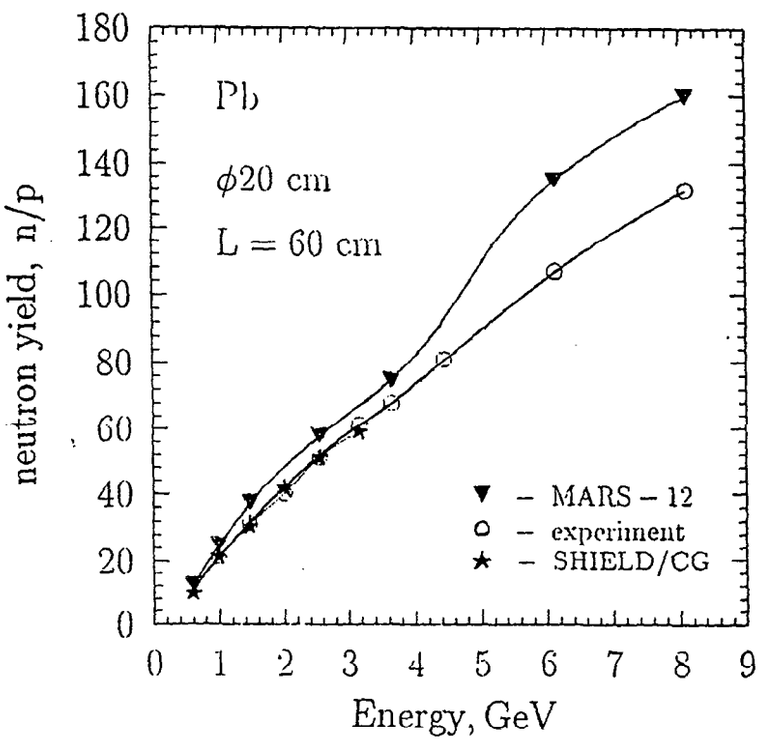

Fig.8. Comparison of experimental and computed data by SHIELD and MARS-12 codes of neutron output from lead cylinder surface.

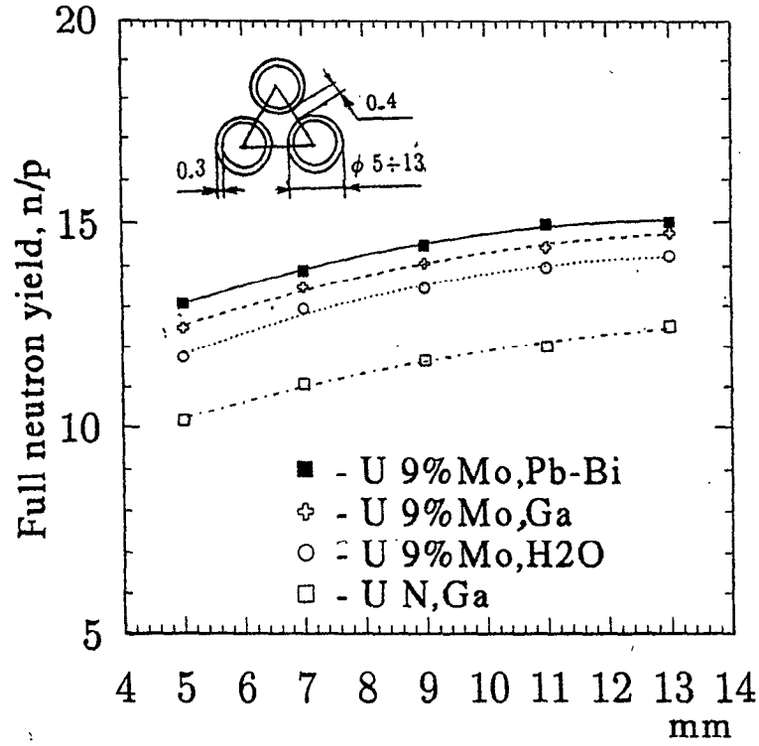

Fig.9. Influence of coolant type and rod fuel element diameter upon spallation neutron yield per 600 MeV incident proton for a target with dimensions of 7.0×19.88×21.1 cm. Core composition corresponds to a hexagonal lattice of fuel elements with U-9% Mo cores from natural uranium with 0.3 mm thick cans and coolant gap - 0.4 mm. For comparison the neutron yield for a target with the UN - core and Ga - coolant is shown separately.

ICANS-XIII
13th Meeting of the International Collaboration on
Advanced Neutron Sources
October 11-14, 1995
Paul Scherrer Institut, 5232 Villigen PSI, Switzerland

The AUSTRON-Target: The Neutron Flux of Decoupled and Poisoned Moderators

G. Muhrer, W. Ninaus, and E. Schachinger

Institute for Theoretical Physics, Technische Universität Graz, Petersgasse 16, A-8010 Graz, Austria

ABSTRACT

This paper discusses in some detail the time resolution of the thermal neutron flux pulse generated by decoupled, poisoned, ambient temperature water moderators in a flat target configured spallation source. The influence of the reflector material on the time resolution of the neutron pulse is also investigated.

1. Introduction

The AUSTRON spallation source concept[1,2] consists of two different target configurations, namely a cylindrical-split target and a flat-target of rectangular cross-section. In both cases, the target material consists of tungsten with 5% rhenium, the cooling is edge cooling only using alternatively normal or heavy water as coolant. The reflector consists of densely packed cylindrical beryllium rods which are cooled by heavy water. So far only coupled moderators have been investigated.

It was one of the interesting results of the calculations presented in the AUSTRON feasibility study[1] that the flat target develops a rather broad peak of intensive neutron flux which can be utilised to couple favourably a number of moderators to the target. It was possible to show that a coupled wing moderator placed at the position of the flat-target's maximum neutron flux density develops on its surface a thermal neutron flux density which is almost identical to the one of a coupled void-moderator in a split-target configuration.

Therefore, this study concentrates on the flat-target concept and studies the physics of decoupled, poisoned, ambient temperature water moderators. The effect of different reflector materials and compositions on the neutron flux at the beam line entry is also investigated. The calculations were performed with the Monte Carlo simulation computer codes known as HERMES in their KFA-Jülich version. We use the EPR-library[3] for most of the calculations. This library has only one thermal group (0 - 0.414 eV) and therefore does not take care of upscatter processes within the thermal energy region. Such processes could effect the physics of the thermal neutrons and thus change the time resolution of the neutron pulse produced by the

Keywords: Spallation Source, AUSTRON Project, Moderators, Neutron Pulse

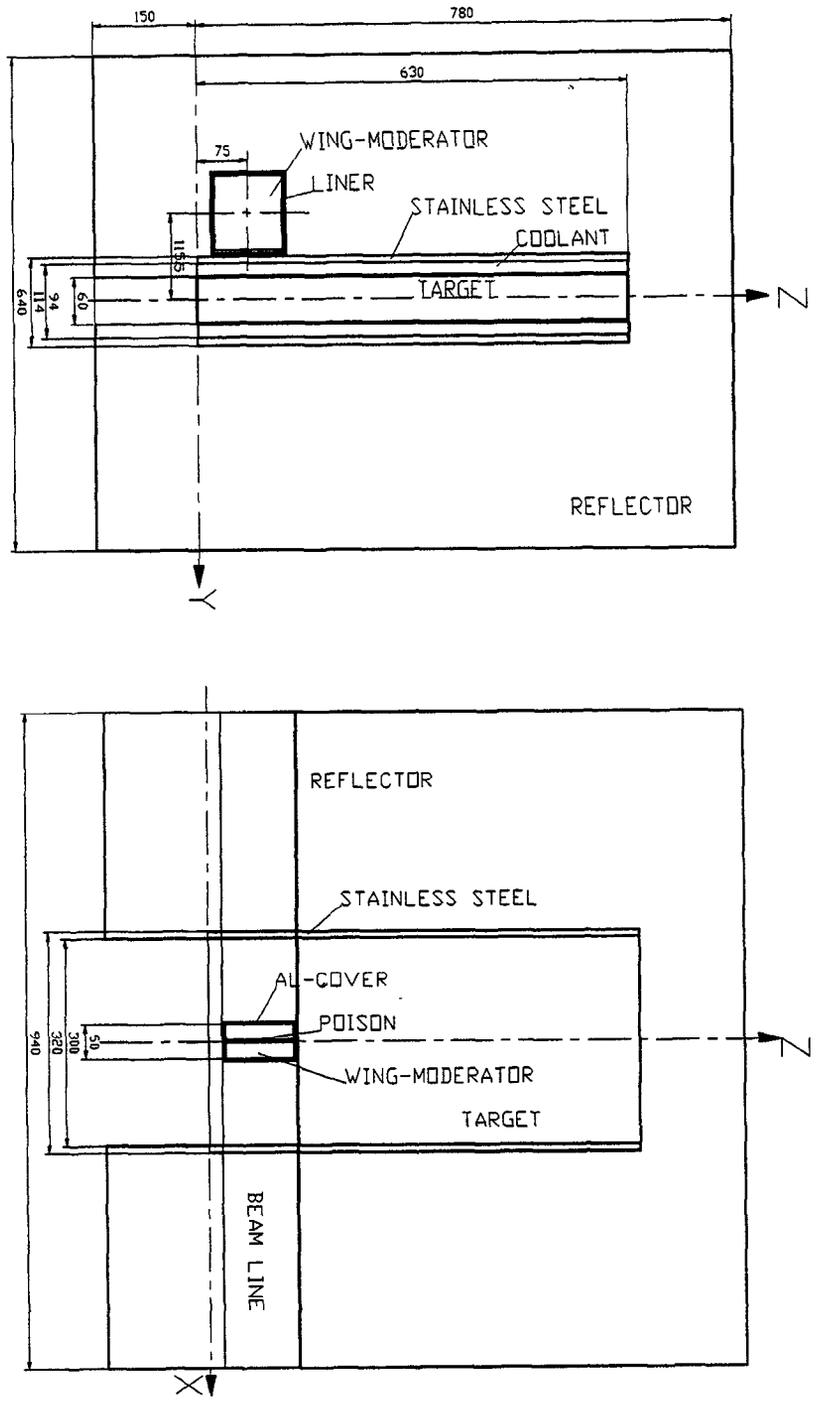

Figure 1. The AUSTRON flat-target configuration. Dimensions are in centimetres.

moderator. This cross-section library has the further disadvantage that it contains only cross-sections for normal and heavy water at 800 K. Our calculations have therefore been supplemented by a number of calculations using a 53 group cross-section library (named Spallation-library) with 16 thermal groups. This library was supplied to us by courtesy of KFA-Jülich. This library has the advantage that the normal and heavy water cross-sections are given for 300 K but so are the cross-sections for all the other materials. This means that we have the wrong temperature especially for the target material.

Thus the results discussed here are meant to give a qualitative picture of the physics involved and can only be used with caution for quantitative statements.

2. Configuration

The configuration of the target complex is shown in Fig. 1. The target itself consists of a tungsten 5% rhenium rod of rectangular cross-section of the dimensions 30x6x63 cm^3 in the (x,y,z)-directions. The top and bottom (x,z)-face of this rod is edge cooled adding about 1.7 cm of a heavy water - target material admixture (75% heavy water, 25% target material) to the structure. Another 1 cm is added by a stainless steel casing. The side (y,z)-faces are not cooled. This complex is symmetrically surrounded by a reflector body of the dimensions 940x640x930 cm^3 in the (x,y,z)-directions. The reflector consists of 90% beryllium, or a combination of beryllium with an outer nickel shell, or graphite and 10% heavy water which is used as coolant.

The target is hit by a proton beam of 1.6 GeV with a pulse frequency of 25 Hz and an average beam current of 128 μA. The (x,y)-cross-section of the proton beam is assumed to be of ellipsoidal shape and the intensity distribution is assumed to be of Gaussian type with a σ_x^2 of 20 and a σ_y^2 of 1.2 cm^2.

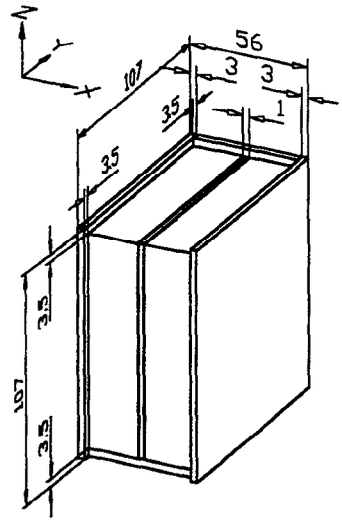

Figure 2. The moderator with the top-(x,y)-face and the front-(x,z)-face removed. All dimensions are in millimetre.

The moderator (see Fig. 2) is placed on top of the steel case (y = 5.5 cm) and is centred around the z-position (= 7.5 cm off the target's front face, Fig. 1) of the maximum in the neutron flux density. The moderating liquid, normal water of ambient temperature, is contained in an aluminium can of 5x10x10 cm^3 volume in the (x,y,z)-directions. The aluminium wall is 3 mm thick and a 0.5 mm thick sheet of ^{10}BC is used as decoupler on the (x,y)- and (x,z)-faces of the can. An additional strip of ^{10}BC is used as poison. This strip is smeared out to a thickness of 1 mm and 50% ^{10}BC for better numerics. The neutron flux leaving the (y,z)-face of the moderator in direction of the positive x-axis is called the *forward-scatter* flux while the one leaving in direction of the negative x-axis is called *back-scatter* flux.

The moderator is connected to a beam line opening in the reflector which is of a 11x11 cm^2 cross-section. This beam-line is built of an aluminium tube of 3 mm wall thickness and a liner of 0.5 mm thickness consisting of ^{10}BC can be added. (For an easier set-up of the geometry data used in the calculations the ^{10}BC was smeared out over the wall, now 3.5 mm thick.) The neutron flux at the end of this beam line (on the outer surface of the reflector) is also monitored throughout our calculations.

3. Results

The calculations concentrated mainly on the time resolution of the thermal neutron flux pulse as it appears on the moderator surface facing the beam line and on the time resolution of the thermal neutron pulse as it appears at the end of the beam line. Fig. 3 compares the time resolution of the average thermal neutron flux density for a moderator which is centred around the *z*-axis. We compare a coupled, a decoupled, a decoupled and poisoned, and, finally, a decoupled, poisoned moderator with a liner in the beam line. The results show, firstly a moderate decrease in the peak flux density for each modification applied to the moderator. With each additional feature added to the moderator the pulse also becomes shorter. The pulse is most efficiently shortened by decoupling the moderator, adding poison and the liner results in an additional reduction of the pulse length. It is also interesting to note that the liner is very effective in reducing the final tail of the pulse while it has almost no influence on the starting ramp. The pulse half-width varies between about 30 μs for the coupled moderator and about 10 μs for the decoupled, poisoned moderator with a liner in the beam-line.

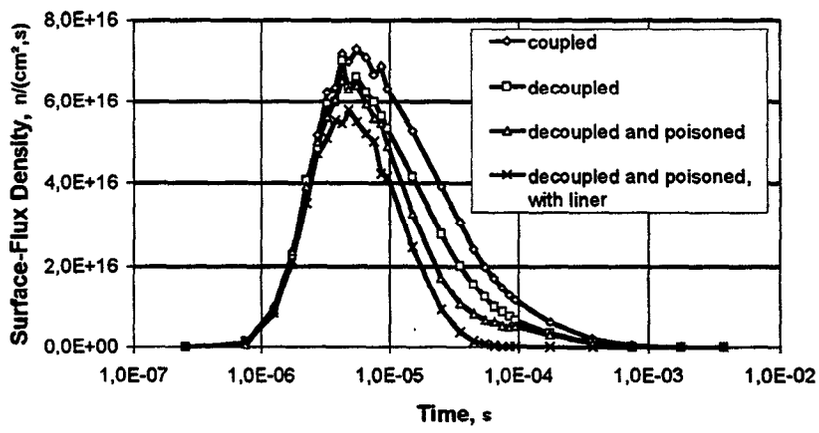

Figure 3. Time resolution of the average thermal neutron flux density on the moderator surface facing the beam-line for various moderator configurations. The moderator is centred around the *z*-axis which results in almost identical results for the forward- as well as the back-scatter mode.

Figs. 4a,b compare the forward- and back-scatter mode of a decoupled and poisoned moderator (with no liner in the beam line) which is moved off its centre position around the z-axis. While the thermal neutron flux barely changes in back-scatter mode, we experience a significant decrease of this flux in forward-scatter mode. Thus if the moderators are to operated in an off-centre configuration the back-scatter mode is to be preferred.

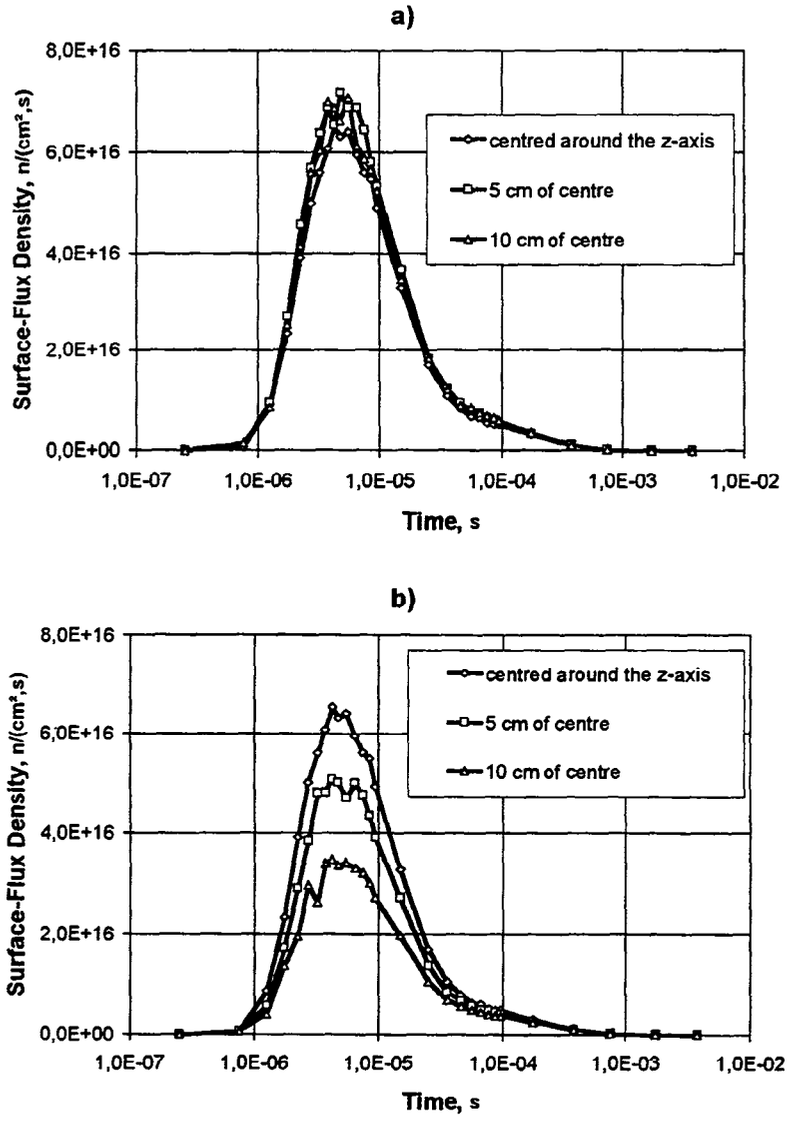

Figure 4: Time resolution of the average thermal neutron flux density on the surface of a decoupled and poisoned, ambient temperature water moderator for various x-positions of the moderator. There is no liner in the beamline. a) Back-scatter mode, b) forward-scatter mode.

Monitoring the neutron pulse at the end of the beam line on the outer surface of the reflector revealed virtually no change at all for the pure beryllium or pure graphite reflectors. A very interesting result can be reported for the beryllium reflector with an outer nickel shell the thickness of which has been varied between 0 and 10 cm. The corresponding results are presented in Fig. 5. They show that an outer nickel shell up to a thickness of about 7.5 cm has

almost no influence on the maximum neutron flux density. This maximum density starts to decrease for nickel shells thicker that 7.5 cm. On the other hand, adding the outer nickel shell results in important improvements in the time structure of the neutron pulse: a 10 cm thick outer nickel shell decreases the initial ramp of the neutron pulse by at least two orders of magnitude and decreases substantially the final tail of the neutron pulse. Thus an outer nickel shell is very favourable for the production of neutron pulses with a clearly defined initial ramp.

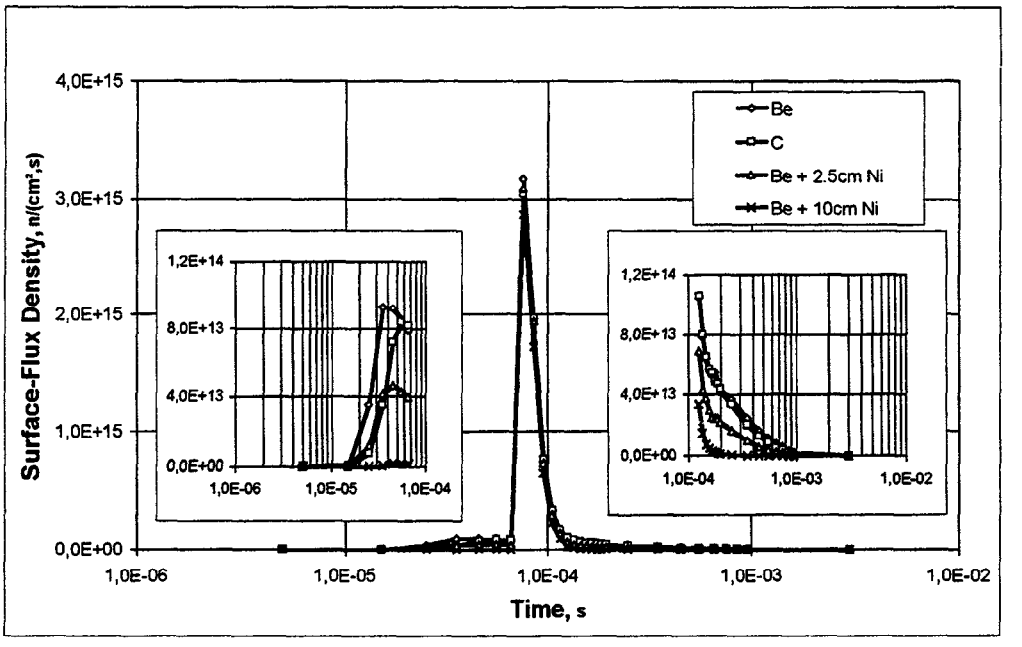

Figure 5: Time resolution of the average thermal neutron flux at the end of the beam line (outer surface of the reflector. The two inserts show the initial ramp of the neutron flux pulse and its final tail, respectively.

All the above results were found using the EPR cross-section library. Additional calculations using the Spallation-library with 16 thermal groups tried to establish the influence of upscatter processes within the thermal energy region on the time resolution of the neutron pulse, for the price of having the wrong temperature for the target material. The results are inconclusive: they do show a slight broadening of the neutron pulse at the moderator surface and also a moderate decrease in the peak value for the flux density. But this could also be due to the wrong temperatures in all the other materials. More calculations are certainly necessary if one wants to clearly separate the temperature effects from the effects caused by upscattering processes within the thermal energy region. Nevertheless, the general trends outlined so far stay unchanged.

4. Conclusions

We studied, using numerical simulation, the time resolution of the neutron pulse produced by decoupled and poisoned, ambient temperature water moderators in a flat-target configuration. We found that decoupling and adding a liner to the beam line through the reflector had the

most influence on the time structure of the neutron pulse. Both reduce the half-width of the pulse and the liner reduces in addition quite substantially the final tail of the pulse. Poisoning results in an additional shortening of the neutron pulse.

Changing the reflector material from beryllium to graphite was found to have no effect on the time resolution of the neutron pulse. Replacing some of the reflector material by an outer nickel shell resulted in a remarkable improvement of the time structure of the pulse by suppressing the initial ramp of the pulse. It also results in an improved tail of the pulse and thus supplements the effect of the liner.

Arranging several moderators which are operated in back-scatter mode around the maximum neutron flux density on the surface of the target-coolant-casing block of our flat-target configuration will result in an over all better performance than a split-target configuration with one void and several wing moderators. Keeping the costs in mind, a graphite reflector seems to be preferable over a beryllium reflector and an outer nickel shell will result in a greatly improved time structure of the thermal neutron pulse.

5. Acknowledgements

The authors are greatly indebted to the ongoing support by KFA-Jülich and in particular by Doz. Dr. D. Filges. The authors also appreciate financial support by the AUSTRON Planungsbüro, Vienna, and, last but not least, by the Verein zur Förderung der Strahlenforschung, Graz.

6. Literature

[1] G. Kahr et al., in *AUSTRON Feasibility Study,* ed. P. Bryant, M. Regler, and M. Schuster (AUSTRON Planungsbüro, Vienna, 1994).

[2] M. Schuster et al., *Physica B* **213&214** (1995) 851.

[3] EPR Neutron Cross-Section Library, DLC-37, *RSIC Data Library Collection* (RSIC Center, Oak Ridge, 1978).

ICANS-XIII
12th Meeting of the International Collaboration on
Advanced Neutron Sources
October 11-14, 1995
Paul Scherrer Institut,5232 Villigen PSI, Switzerland

RADIOACTIVE HALOGEN YIELDS FROM THE TUNGSTEN TARGET IRRADIATED BY HIGH-ENERGY PROTONS

S.V.Ignatjev , D.V.Pankratov , and E.I.Yefimov
Institute of Physics and Power Engineering,
Bondarenko Sq. 1, 249020 Obninsk, Kaluga Region, Russia
Phone: +7(08439) 98703,98452; Fax: +7(095) 2302326, 8833112, E-mail: root@ippe.rssi.ru

ABSTRACT

In this work we present the calculation's results for radioactive halogen's formation rates and yields from the spallation and fission reactions of solid tungsten target irradiated by protons with E_p = 800 MeV and with the target current I_p= 16 mA. The influence of the secondary neutrons on accumulation these nuclides is not analyzed.

1. Introduction

A considerable amount of the radioactive nuclides are accumulated in the target due to influence of the primary-order accelerator's protons and the second neutrons arisen from the target and outside blanket as well. For the proton energy $E_p \approx 1$ GeV the tungsten target will contain the most radioactive isotopes with $Z \leq 75$ as a result of spallation and fission reactions. To forecast the composition of that radioactivity and it's dynamics is rather complicated problem. From the radiation damage effects point of view it is very important to analyze the radioactive volatile gaseous nuclides, which are able comparatively easy penetrate to the coolant, ion guide and atmosphere and thus form a gas-aerosol radioactivity and contaminate the environment. On the basis of nuclear reactor experience among these volatile compounds first of all one can find so-called RPG - radioactive precious (noble) gases (argon, krypton, xenon) and tritium, bromine, iodine, fluorine, chlorine, cesium and strontium isotopes as well. With the exception of the RPG, these isotopes are very chemically-active and able to form different kinds of chemical compounds. Hence, taking into account their chemical formations from the solid and liquid targets, the evaluation of the volatile compound's yields is a high priority and difficult problem.

On one hand, our analyses have shown that the chemical radioactive halogens (bromine, iodine, fluorine, chlorine) can form different compounds with tungsten and it would seem that this process must prevent their release from the target. However, it was rather unexpectedly to find that volatility of the tungsten's halogenides is high. So, taking into account the radiological dangerous such halogens as radioactive iodine this problem was considered in the first approach.

Keywords: Yields, Radioactive Halogens, Target, Tungsten, High-Energy Protons

2. The evaluation of accumulation of the radioactive halogens from the tungsten target under proton action.

The considered nucleuses with Z= 9, 17, 35 and 53 are mainly formed as result of fission process in tungsten target irradiated by high-energy protons. In a thick target the yield of a given nucleus per one bombarding proton can be evaluated under the formula:

$$Y_i = \rho \int_0^{E_p} \left[\sigma_i(E') \Big/ \frac{dE}{dx}(E') \right] dE' \quad , \qquad (1.1)$$

where

$\sigma_i(E')$ - reaction cross-section, which forms the i-th nucleus, depending on energy, sm^2;

$\rho = 6.32 \times 10^{22}$ sm^3 - the concentration of target nucleuses;

$\frac{dE'}{dx}(E')$ - linear density of the ionizing losses of the proton energy, MeV / sm.

In the assumption, that $\sigma_i(E')$ does not depends on energy and is equal to the $\sigma_i(E_p)$ formula (1.1) maybe written as follows:

$$Y_i = \rho \sigma_i(E_p) R \ , \qquad (1.2)$$

where

R= 30 sm - the proton path in the target.

The specific activity of the i-th nuclide a_i from the target volume (V=SR, where S - the cross-section area of the proton beam with the current I), irradiated by protons is equal:

$$a_i = \frac{6.24 \times 10^{18} I \times Y_i \left(1 - e^{-\lambda_i T_{obl}}\right)}{V} =$$

$$= 6.24 \times 10^{18} \rho \sigma_i(E_p) \frac{I}{S} \left(1 - e^{-\lambda_i T_{obl}}\right) \quad , Bq/sm^2 \qquad (1.3)$$

where

λ_i - decay constant of the i-th nuclide, s^{-1} ;

T_{obl} - the time of the target irradiation, 1 year .

The correct evaluations of cross-sections $\sigma_i(E_p)$ or the formations of the i-th nuclides are the main difficulties here. The semiempirical Tsao-Silberberg algorithm for calculation of cross-section for the formation of the nucleus with given (A, Z) was used in the case, when proton or neutron of considered energy E_p interacts with nucleus (A_0 , Z_0) of the target. The appropriate computer program SILBER was realized as PC-code. The formations of the radioactive halogens with a half-lives more than a few hours were considered. The list of that halogens; their half-lives $T_{1/2}$ and decay constants λ_i ; the values of the cross-sections σ evaluated; the specific activities a_i, calculated for the proton beam diameter equal 10 sm (S=78.5 sm); and the values of an equilibrium activity in the ion guide A^u (see paragraph 3) as well are presented in Table 1.

Table 1. The formation's cross-sections, specific activities in the target and equilibrium activities in the ion guide for some radioactive halogens

Nuclide	$T_{1/2}$	λ, c^{-1}	σ, mBn	a_i, Bq/sm^3	A^u, Ci
I-123	13.2 h. [1)]	1.45 -05 [2)]	0.04	3.2 +09	86
I-124	4.18 d.	1.9 -06	0.0196	1.6 +09	43
I-125	60.14 d.	1.3 -07	0.0148	1.0 +09	27
I-126	13.02 d.	0.2 -07	0.0075	6.0 +08	16
I-131	8.04 d.	1.0 -06	0.0011	8.8 +07	2.4
I-133	20.8 h.	9.2 -06	0.00055	4.4 +07	1.2
I-135	6.6 h.	2.9 -05	0.00028	2.2 +07	0.6
Br-77	57.04 h.	3.3 -06	0.095	7.6 +09	200
Br-82	35.3 h.	5.4 -06	0.0025	2.0 +08	54
Cl-36	$3.01*10^5$ y.	7.2 -13	0.085	1.54 +05	0.004

[1)] h.- hours: d- days; y.-years; [2)] should be read as $1.45 * 10^{-05}$

3. Evaluation of the radioactive halogen yield's rate from tungsten target into ion guide. The electronic configuration of halogen atoms brings their ability to attach easily the electrons and, thus, determines their high ability to react with design substances. This ability depends on an aggregate conditions, the pulverization degree, temperature, properties of the formed compounds and other conditions the reaction goes under. For example, such fine-fractionated metals as aluminium Al, antimony Sb, and a copper Cu are inflamed in the atmosphere of bromine vapour. Such active metal, as sodium does not interact with liquid bromine, that depends on tight surface metal film of NaBr. Without water the majority of metals does not interact with iodine and bromine [2]. As is pointed in [3] tungsten does not react with iodine and bromine vapour, to all appearance, due to very small stability of the appropriate

halogen compounds. Based on the data from [4] it appears that bromine and iodine interact with the majority of metals and the result of this interaction is the formations of the bromides and iodides. However, the tungsten and I_2 interact with those metals at T=1073°K. As for fluorine and chlorine tungsten reacts with the first even at 20 °C and with the second one only at 573 °K . In the last case the WCl_6 is formed.

The identified compounds WBr_2, WBr_5, WBr_6, WI_2, WI_4, WCl_5, WCl_6 and other are considered in [5]. All of them are the sufficiently volatile ones. However, it should be noted, that the above view on reactive properties of the halogens is valid only for their macroscopic concentrations. Being interacted with tungsten target the halogens are formed in a very small amount, their mole fractions are $\sim 10^{-8} \div 10^{-11}$. Therefore it is possible to expect that the halogen's formation will be mainly due to low-atomic compounds, for example, such compounds as WBr_2, WI_2 and other one, when the formation rate is considerably higher, than in the reactions with macro-concentrations. The analysis of a temperature data [6], [7] shows, that the pressure of the halogen's saturated vapour very strongly depends on the temperature. Some characteristics of the halogens and their compounds , including the values for pressure saturated vapour are presented in Table 2 under the corresponding temperatures.

Table 2. Some characteristics of the halogens and their compounds with tungsten

Substance	The boiling or the sublimation temperature(^{0}C) for pressure saturated vapour in mm Mercury column					The melting point temperature, ^{0}C	The dissociation temperature, ^{0}C
	0.1 mm	1 mm	10 mm	100 mm	760 mm		
F_2	-226.6(S)	-221.0(S)	-213.7	-202.6	-188.1	-219.6	
Cl_2	-133.3(S)	-118.2(S)	-101.5(S)	-71.9	-34.1	-101.3	
Br_2	-71 (S)	-51 (S)	-26 (S)	8.6	57.9	-7.3	
I_2	12.1 (S)	39.4 (S)	73.2 (S)	115.8	182.8	113.7	
WBr_2							400
WBr_5	120	169	227	300	383	276	
WBr_6							
WI_2							
WI_4							dissociated
WF_6	-89.4 (S)	-71.7 (S)	-49.2 (S)	-21.1(S)	17.7	-0.5	
WCl_2							
WCl_4							dissociated
WCl_5		114 (S)	160 (S)	217 (S)	286	230	
WCl_6	117.4 (S)	153.7(S)	197.6 (S)	255.7 (S)	336.4	284	

(S) - means, that substance is in solid state.

In a general case the maximum evaporation rate of substance in vacuum can be described by a Lengmur equation [8] :

$$G_u = 4.38*10^{-3} P_s \sqrt{\frac{M}{T}} \qquad (2.1)$$

where

P_s - the substance's suturated vapour pressure, Pa;

M - the molecular mass, kg / kilomole;

G_u - the evaporation rate, kg / m^2 s;

T - the solution temperature , ° K.

Taking into account the Raul law for an ideal solution of substance considered (in our case for the tungsten halogens solutions) the formula (2.1) maybe transformed to another expression (2.2):

$$G_u = 4.38\times10^{-3} P_s m \sqrt{\frac{M}{T}} \qquad (2.2)$$

where

m - the mole fraction of the dissolved substance.

For the substance, which is evaporated in the form of the molecules or the single atoms of radioactive samples the expression (2.2) can be immediately written as follows:

$$Q_{ij} = \frac{4.38 \times N_A P_s^j m_j x_{ij} \lambda_i}{\sqrt{M_j T}} \qquad 2.3)$$

where,

N_A - the Avogadro constant, N_A= 6,023 * 10^{23};

x_{ij} - the number of atoms of i-th radioactive isotope from the j-th compound;

λ_i - the decay constant for the i-th radioactive isotopes, s^{-1};

Q_{ij} - the radioactivity quantity of the i-th isotope for j-th compound, evaporated into vacuum from the target's surface unit during time unit, Bq/m^2 s.

Otherwise

$$Q_{ij} = \frac{6.86\times10^{13} P_s^j m_j x_{ij} \lambda_i}{\sqrt{M_j T}} \qquad (2.4)$$

where,

Q_{ij} is expressed in the units of Ci/m^2 s.

Using the expression (2.4) and the data from Table 1 on activity of the Br-82, that is for a_{82}^{Br} = 2.0*10^8 Bq / sm^3, and at target temperature t=200° C (4 73 ° K) the rate of the evaporation from the target's butt-end into ion guide of the Br-82 as a component of the molecule of WBr_5 was calculated for beam diameter d=100 mm. It was assumed, that the target is not separated from ion guide by a membrane, i.e. it is in vacuum. It was assumed also, that all bromine atoms of the WBr_5 are indeed the radioactive isotopes of Br-82 ($T_{1/2}$ = 35.3 hours). The pressure of saturated vapour for WBr_5 at 200 °C was ~ 5 * 10^2 Pa. In these conditions the evaporation rate of the Br-82 was equal ~ 2.1 * 10^{-1} Ci/m^2 s, that corresponds to equilibrium activity of the Br-82 on the ion guide surfaces due to condensed phase of the WBr_5, and $A_{82}^{u} = 300Ci$.

Really, the activity changes released into ion guide is described by the equation:

$$\frac{dA_i^u}{dt} = SQ_{ij} - \lambda_i A_i^u \qquad (2.5)$$

For the equilibrium case $\frac{dA_i^u}{dt} = 0$ è $A_i = \frac{SQ_{ij}}{\lambda_i}$ (2.6)

Thus, our evaluation shows, that the evaporation rate of the WBr_5 at 200 °C is so high, that one can observe the non-conformity of the calculational results on equilibrium activity of the Br-82 on the target itself and on the surface of ion guide. Obviously, the total activity of the Br-82 on the ion guide walls should be less than total equilibrium activity of the Br-82 in a target $A_{82}^{M} = \int_V a_m dV$.

This fact permits to propose the assumption that at the target temperatures higher than 150 - 200° C the halogen's evaporation rate, including radioactive halogens, maybe equal to their formation's rate in tungsten target due to spallation and fission reactions under action of the proton beam in some effective volume of the target. We have also supposed that the halogens diffusion time through the evaporation's surface is much less than their half-lives. From the physical point of view and taking into account the proton energy loss per unit of the target length, , $\frac{\partial E_p}{\partial x}$, that effective target volume is found to be equal ~ 1 / 3 of the target volume V_R, which is correspondent to the proton path R with initial energy E_{Po}. In our evaluations the effective target volume is accepted equal V_{eff} ~ 103 sm^3. Hence, the equilibrium radioactivity of the i-th halogen will be:

$$A_i^u = a_i V_{eff} \qquad (2.7)$$

In case for the Br-82 it's A^{u}_{82} under accepted preconditions will be equal only 5.4 Cm instead of 30 Ci. The calculated values of the other radioactive halogens are presented in Table 1.

One can see, that the total halogen's equilibrium activity in the ion guide reaches 430 Ci. If to assume, that the main part of this activity is deposited on the length ~ 5 m of the ion guide by a diameter ~ 15 sm, than the total surface contamination of this part will be equal ~180 Ci /m^3.

It is necessary to note, that in case the target is separated from the ion guide by a partition and places into the atmosphere of a inert gas (or even air), the halogen evaporation's rate will be reduced approximately in 10^3 times

The similar effect was observed in the earliest works [9], [10], [11] ,[12] in the experiments on lead, lithium, lead-bismuth and polonium evaporation in the vacuum and in atmosphere of the inert gas (argon, helium) as well, conducted at temperatures ~ 250-800° C.

4.Conclusion

1. On the basis of nuclear reactor safety experience the analyses of volatile radionuclide's composition has been carried out. Such nuclides can be formed with proton impact and comparatively easy released from a solid tungsten target.
2. This analyses revealed that halogen containing radiological hazardous iodine and forming high volatile compounds with tungsten are important.
3. On the basis of Silberberg-Tsao systematic the cross-sections of the main long-lived radioactive halogens formation and their build-up were calculated after one year of the target operation. These halogens are produced mainly under target niclei fission by protons.
4. The model was developed for halogens from a tungsten target. It was demonstrated that volatility of both chemically pure halogens and their compounds with tungsten into vacuum determined by saturated vapour pressure is so high that its release rate under temperature 150-200 ° C can be assumed to be equal to the formation rate.
5. At proton energy of 800 MeV, current of 16 mA and the ion guide without diaphragm (window) the equilibrium activity of halogens in the guide reaches 400 Ci. This can result in the surface activity of the guide final part with the length of about 5 m to be equal to 100-200 Ci/m^2, that is rather sufficient value.
6. The data obtained indicate the fact that even in case of a solid target the proton beam insertion without "window" on the guide can results in its contamination with volatile radionuclides and aggravation of radiation safety issues.
7. If there is a gaseous medium with atmospheric pressure in the inner volume of target, the amount of volatile nuclides in this volume will be about 1,000 times less than that into vacuum.
8. Calculations performed are approximate and need further correction. But they clearly demonstrate the fact that the problem of volatile radionuclides release from solid target should be considered closely. In the connection with this arrangement and performance of relevant experiments to be carried out at one of accelerators now on operation seems to be quite reasonable.

5. References

1. R.Silbergberg, C.H.Tsao. The Astrophysical Journal. Suppl. Ser. N 220(1), 25, 315-333 and N 220(II), 25, 335-368.
2. В.И.Ксензенко, Д.С.Стаскневич. Химия и технология брома, йода и их соединений. Москва, издательство "Химия", 1979 г.

3. Справочник металлурга по цветным металлам, т.I, Москва, Металлургиздат, 1953 г.
4. Физико-химические свойства элементов. Справочник. Наукова думка, Киев, 1965 г.
5. Справочник химика, т.II. Основные свойства неорганических и органических соединений. Издательство "Химия", Ленинград, 1971 г.
6. Справочник химика, т.I. Общие сведения. Строение вещества. Свойства важнейших веществ. Лабораторная техника. Издательство "Химия", Ленинград, 1971 г.
7. Физические величины. Справочник. Энергоатомиздат, Москва, 1991 г.
8. Л.Н.Розанов. Вакуумная техника. Москва, "Высшая школа", 1982 г.
9. H.Fenerstein, J.Oschinski and S.Horn. Behaviour of Po-210 in molten Pb-17Li. Journal of Nuclear Materials 191-194 (1992) 288-291. North-Holland.
10. H.Fenerstein, H.Grabner, J.Oschinski, S.Horn and S.Bender. Evaporation of Lead and Lithium from molten Pb-17Li.- Transport of aerosols. Fusion Engineering and design 17 (1991) 203-207.
11. R.B.Tupper, B.Minushkin, F.E.Peters, Z.L.Kardos. Polonium Hazards associated with Lead-Bismuth used as a Reactor Coolant. International Conference on Fast Reactors and Related Fuel Cycles. October 28- November 1, 1991, Kyoto, Japan. Proceeding, vol IV.
12. F. Atchison. The neutronic performance of solid-target alternatives for SINQ. Proceedings of the Eleventh Meeting of the International Collaboration on Advanced Neutron Sources ICANS-XI. KEG, Tsukuba, Japan, October 22-26,1990. P.P. 319-334.

ICANS-XIII
13th Meeting of the International Collaboration on
Advanced Neutron Sources
October 11-14, 1995
Paul Scherrer Institut, 5232 Villigen PSI, Switzerland

COUPLED MODERATOR NEUTRONICS

Gary J. Russell, Eric J. Pitcher, and Phillip D. Ferguson

Manual Lujan, Jr. Neutron Scattering Center
MLNSC, MS H805
Los Alamos National Laboratory
Los Alamos, NM 87545

ABSTRACT

Optimizing the neutronic performance of a coupled-moderator system for a Long-Pulse Spallation Source is a new and challenging area for the spallation target-system designer. For optimal performance of a neutron source, it is essential to have good communication with instrument scientists to obtain proper design criteria and continued interaction with mechanical, thermal-hydraulic, and materials engineers to attain a practical design. A good comprehension of the basics of coupled-moderator neutronics will aid in the proper design of a target system for a Long-Pulse Spallation Source.

1. Introduction.

Target stations are vital components of a spallation-neutron source, and target-station design plays a major role in determining the overall (neutronic and operational) performance of the facility. Many traditional notions will have to be rethought and several new concepts put forward to meet the challenge of designing a target station for the next generation spallation neutron source (5 MW of proton beam power); it is believed a target station designed for 1 MW can employ existing technology. The particulars of a target station depend on whether it is designed for a Short-Pulse Spallation Source (SPSS) or a Long-Pulse Spallation Source (LPSS).

Keywords: Target, Moderator, Reflector, Target System

In the context of this paper, the term *target station* refers to an ensemble of components needed to produce/extract neutrons for various areas of research. The major components of a target station are the *target system*, the *shield*, and the *ancillary systems*. In this paper, we will focus our discussion on the neutronic performance of the *target system*. We define the *target system* as the subset of components (targets, moderators, poisons, decouplers, liners, and reflectors) in the target station that contribute directly to the production of useful neutrons. The target system used at the Manual Lujan, Jr. Neutron Scattering Center (MLNSC) is illustrated in Fig. 1 [1].

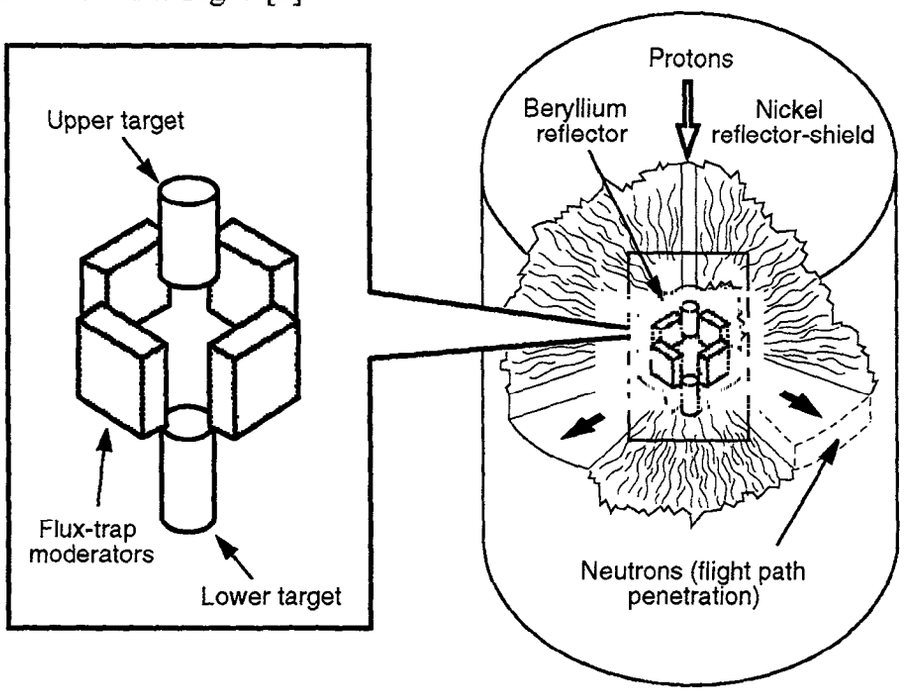

Figure 1. Illustration of the target system used at the MLNSC. The target system consists of a split target of tungsten, four flux-trap moderators of water and liquid hydrogen, an inner moderating reflector of beryllium, and an outer fast neutron reflector and high-energy neutron shield of nickel. The target system forms a right circular cylinder of about 1-m diameter and 1-m high.

We focus here primarily on coupled-moderator neutronics, where the proton pulse width and the choice of target, moderator, and reflector materials and geometry dominate the neutronic performance of moderators. This is in contrast to decoupled-moderator neutronics where the proton pulse width is kept deliberately short compared to the slowing down and thermalization times in moderators and reflectors. For decoupled systems, the intensity and pulse widths of neutrons from a moderator are controlled by the use of poisons, decouplers, and liners in addition to the choice of target, moderator, and reflector materials and geometry. The MLNSC target system in Fig. 1 is a decoupled target system because it employs poisons, decouplers, and liners, and is, therefore, a SPSS. Before we discuss coupled moderator neutronics, we will review the neutronic issues in going from decoupled moderators to coupled moderators, i.e., decoupled to coupled target systems.

2 From an SPSS to an LPSS

2.1 *Decoupled to Coupled Target Systems*

For most users of a pulsed spallation-neutron source, useful neutrons can be defined as those headed in the right direction with appropriate energy at the right time. Unfortunately, spallation neutrons produced directly in the target rarely have the desired characteristics. We must, therefore, add the necessary systems and devices to the bare neutron production target in order to tailor the neutron pulse so that its characteristics are as close as possible to the users' requirements. As mentioned above, a complete target system consists not only of target(s) for the production of neutrons, but also of moderators, reflectors, and, in the case of an SPSS, poisons, decouplers, liners.

In addition to the choice of material, temperature, geometry (*e.g.*, wing versus flux-trap moderators), and the presence or absence of a reflector, moderator neutronic performance is also strongly tied to the presence or absence of poisons, decouplers, and liners. The choice of materials and thicknesses for these target system components is a crucial part of moderator design.

2.1.1 *Poisons, Decouplers, and Liners.* The function of poisons, decouplers and liners is to tailor the temporal and energy characteristics of the neutron pulses emitted by the moderator. Fig. 2 shows the arrangement of poisons, decouplers and liners in the split-target, flux-trap moderator geometry of Fig. 1. Moderator poisons can be either spread homogeneously throughout a moderator, or introduced heterogeneously (as a discrete region) into the moderator [2]. In this paper, we confine our discussion to the use of heterogeneous poisons. For thermal neutrons, the poison neutronically defines that part of the moderator "viewed" by an experiment. Decouplers surround a moderator and both geometrically and neutronically isolate it from the reflector. Liners geometrically and neutronically isolate the moderator "viewed surface" from the reflector. We deliberately define decouplers and liners separately because they can be different materials with distinct thicknesses, as in the MLNSC target system design [3]. The goal of short-pulse moderator design is to get as much useful neutron intensity from a moderator as possible with little or no attendant degradation in the neutron pulse width.

The energy range over which poisons, decouplers, and liners "neutronically" operate is not distinct and depends on the thickness and material used. For example, gadolinium and cadmium have "characteristic" cutoff energies (roughly 0.1-0.2 eV and 0.5-0.6 eV, respectively) above which they are not as neutronically effective, whereas, a "1/v" absorber like boron has a cutoff energy that is not as distinct. For boron, one usually refers to a "1/e" cutoff energy for a given boron atom density and thickness and is usually chosen to be "1/e" in the few eV range [3].

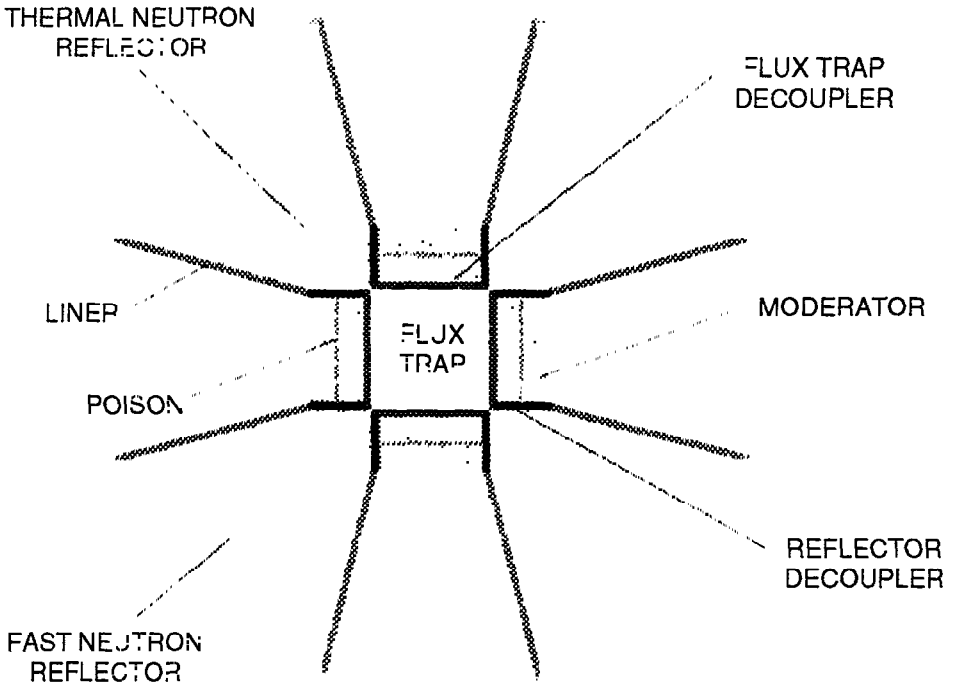

Figure 2. Arrangement of poisons, decouplers, and liners in a flux-trap moderator geometry. Poisons are typically oriented parallel to and positioned some distance (≈1 to 3 cm) behind the moderator viewed surfaces. The flux-trap decouplers neutronically insulate moderators from one another whereas the reflector decouplers neutronically isolate moderators from the adjoining reflector material. Liners neutronically insulate the reflector from the moderator viewed-surface.

2.1.2. *Decoupled Moderators.* If we employ decouplers and liners in conjunction with a moderator surrounded by a reflector, we refer to those moderators as "decoupled" moderators, and the target system as a SPSS. The choice of material and thickness of material for decouplers and liners is important in optimizing the neutronic performance of the next-generation SPSS. Adequately cooling the decouplers and liners for the next generation SPSS will be a design challenge.

2.1.3 *Coupled Moderators.* If decouplers and liners are not used when a moderator is surrounded by a reflector, we call the moderators "coupled." Coupled moderators can be significantly more intense than decoupled ones. However, the neutron pulse width from a coupled moderator is much larger than that from a decoupled one [4]. We illustrate this neutronic gain in Fig. 3 for liquid H_2 (ortho/para 50/50) moderators. For these liquid hydrogen moderators, a totally coupled moderator provides about 6.7 times greater neutron pulse intensity (for $E < 5$ meV) than a decoupled moderator. This is precisely the reason to consider an LPSS over an SPSS. However, as indicated by the standard deviation, the neutron pulses are "broader" in time from a coupled moderator compared to a decoupled one.

Figure 4 depicts the energy-dependent gain in neutron intensity and time distributions for a coupled liquid H_2 (ortho/para 50/50) moderator compared to a decoupled one.

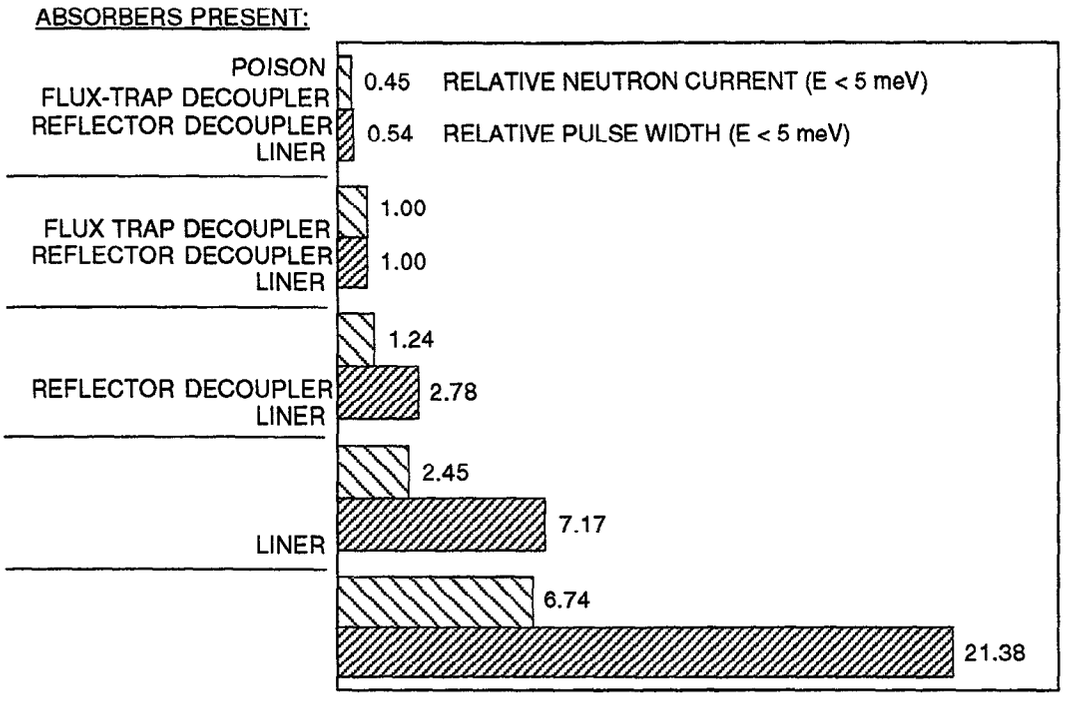

Figure 3. Effect of poisons, decouplers and liners on neutron pulse intensity and pulse width for liquid H_2 (ortho/para 50/50 v%) moderators. The labels on the left side of the bar graph indicate what items are present for the corresponding bars. The neutron pulse width is defined as the standard deviation of the time at which neutrons leak from the moderator viewed surfaces. The 22.5-cm-long, D_2O-cooled W rod-target is singly split and the four 5x13x13-cm^3 moderators are in flux-trap geometry. The poison is 0.00508-cm-thick Gd, and the decouplers and liners are 0.0813-cm-thick) Cd. The reflector is D_2O-cooled Be (D_2O/Be 15/85 v%). The proton beam energy is 800 MeV.

In Fig. 5, we show the decoupled data of Fig. 4 integrated over time; this is *the time-dependent neutron leakage gain*. The results show that the neutron gain depends on the time over which the neutrons can be utilized in an experiment. The maximum gain is the factor of about 6.7 (as $t \rightarrow \infty$).

The coupled-moderator gain will also depend on the type of reflector employed, i.e., whether or not the reflector is a "fast" or "moderating" reflector. We will now discuss the various types of reflectors we can use in a target system.

3. Reflectors

Reflectors enhance the efficiency of useful neutron production by returning neutrons that would have otherwise escaped from the target system to the moderator zones where there is another chance to change them to useful neutrons. The reflector is absolutely essential for this purpose; otherwise, the requisite intensities of useful neutrons would not be adequate [5]. However, reflectors also alter the time structure of neutron pulses from a moderator.

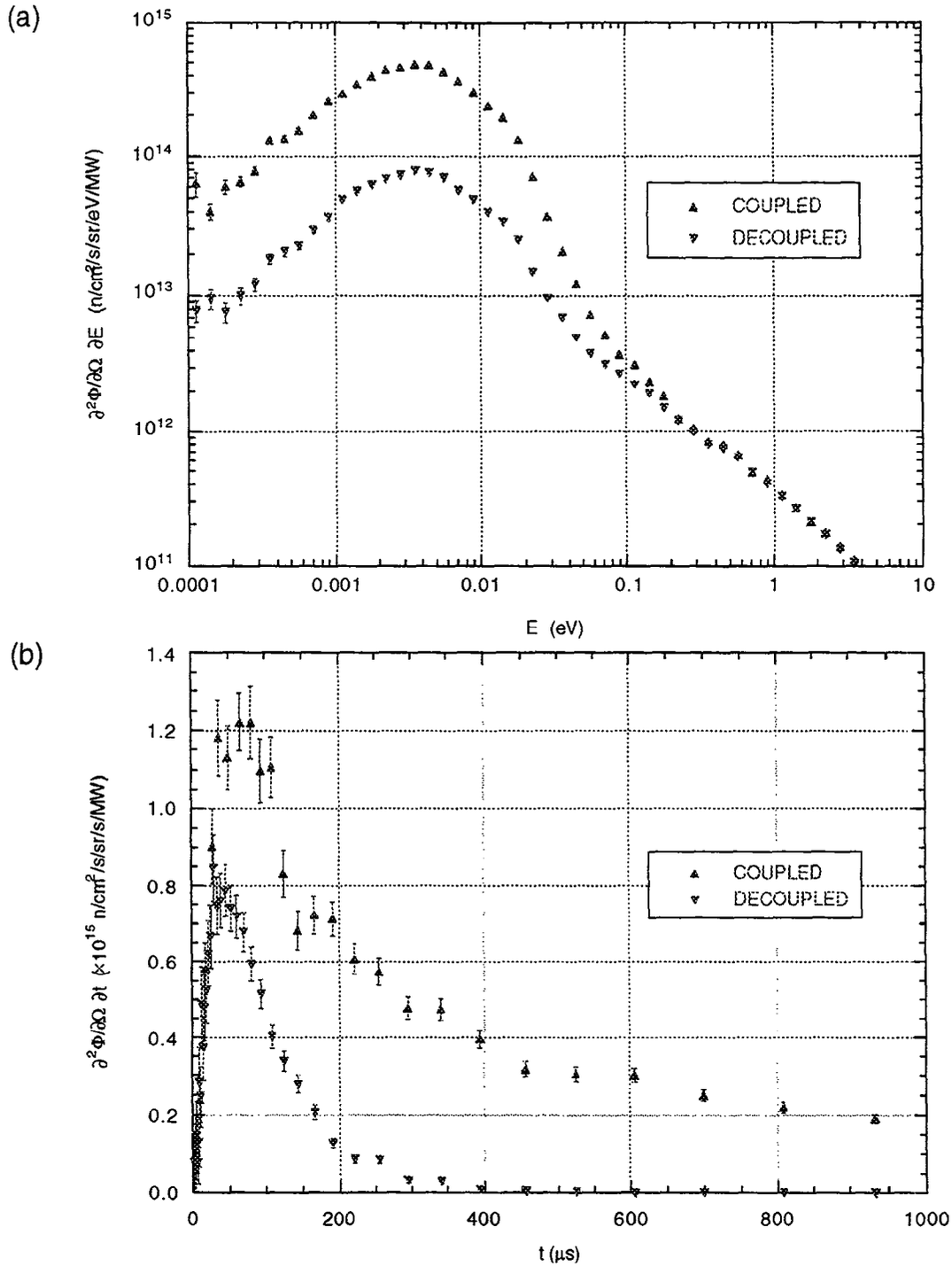

Figure 4. Flux spectrum (a) and time distributions (b) for coupled and decoupled liquid H_2 (ortho/para 50/50) moderator showing the energy-dependent and time-dependent differences, respectively, of leakage neutrons. The moderators are unpoisoned.

3.1. *One-Component Reflectors.* Beryllium has been the classic reflector material for pulsed spallation sources [1, 6-8], and heavy water for quasi-continuous spallation sources [9]. These are examples of one-component reflectors. However, it is useful to combine reflector material types into a composite reflector, and to investigate multiple uses of the components of a composite reflector.

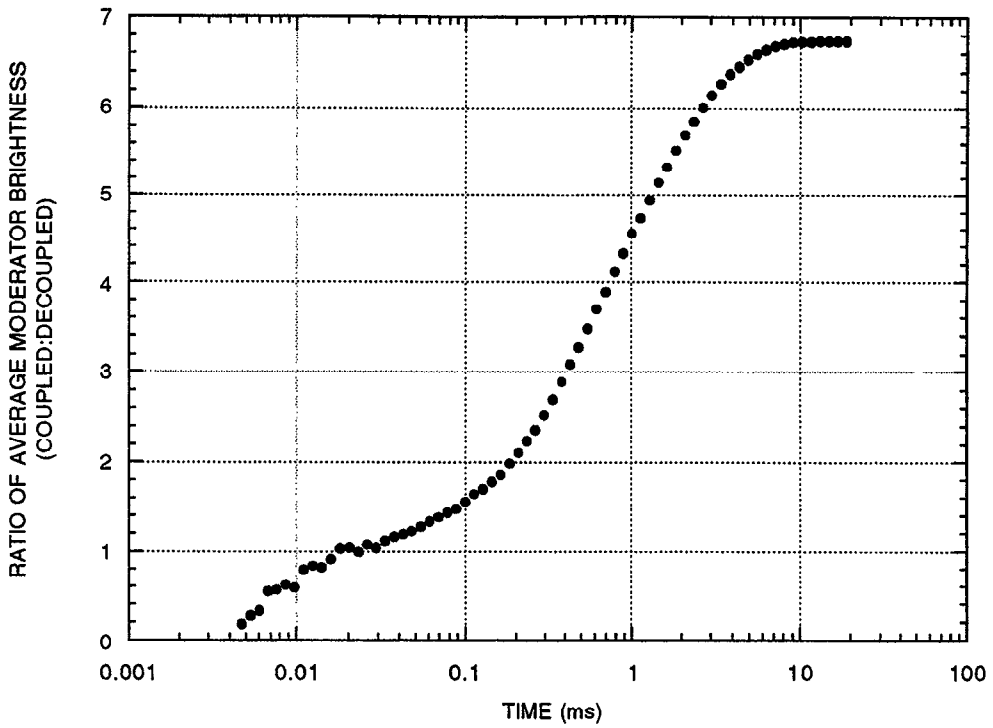

Figure 5. The time-dependent coupled/decoupled gain for unpoisoned liquid H_2 (ortho/para 50/50) flux-trap moderators with an infinite D_2O-cooled Be reflector..

3.2. *Composite (Multiple-Component) Reflectors.* In 1985, we introduced and implemented the notion of a composite reflector at the MLNSC [1]. We designed the MLNSC composite reflector to perform three distinct functions: 1) as a thermalizing and thermal neutron reflector, 2) as a fast neutron reflector, and 3) as the beginning of the high-energy neutron shield. In addition to these three functions, a composite reflector of the proper material can be looked at (from the point-of-view of neutron production) as an extension of the target, i.e., to enhance spallation neutron production and to provide additional (n,xn) neutrons. Also, in the case of the LPSS, the outer portion of a composite reflector can be used to tailor the time distribution of neutrons leaking from a moderator. Thus, a composite reflector can have several distinct neutronic functions. We will now discuss the purposes of the various components of a composite reflector.

3.2.1 *Inner Reflector.* The inner portion of a composite reflector should be a moderating/reflecting zone surrounding the moderators and performing two primary functions: 1) to moderate (thermalize) fast neutrons and redirect them back into the moderators, and 2) to reflect back into the moderators thermalized neutrons escaping from the moderators into non-useful directions. The inner reflector should have two other secondary qualities: 1) the ability to transmit neutrons from the intermediate "fast neutron" reflector back into the moderators (this requires low neutron absorption characteristics for the inner reflector material); and 2) the ability to make (n,xn) neutrons, i.e., to act as a neutron source. Materials studied to date for inner reflectors include H_2O, D_2O, C, and Be.

3.2.2 *Intermediate Reflector.* We use an intermediate reflector zone to return fast neutrons back into the inner reflector, to produce spallation and (n,xn) neutrons, and to act as a high-energy neutron shield. This material should have low or moderate neutron absorption properties. The materials studied to date include Ni, W, and Pb. Figure 1 shows the two-component composite (Be/Ni) reflector used at the MLNSC.

3.2.3 *Outer Reflector.* In our LPSS studies, we are considering an outer "fast neutron" reflector region to return fast neutrons back into the intermediate reflector zone, to produce spallation and (n,xn) neutrons, to help remove "tails" on neutron pulses in an LPSS application, and to act as a high-energy neutron shield. The materials we will be looking at are Ni and W.

4. LPSS Design Issues

There are several key issues that affect the overall neutronic performance of an LPSS. Among the most important concepts are: a) *neutron intensity vs. brightness* - this determines the moderator size; b) *temporal brightness* - this establishes the "peak" neutron intensity in time; c) *number of neutron beam lines* - this affects the absolute overall neutronic performance of the target system; d) *liquid H_2 compared with liquid D_2* - influences how "cold" one can make the neutron leakage spectrum from a moderator; e) *ortho/para- hydrogen fraction* - this affects the neutronic performance of a liquid H_2 moderator; f) *premoderator materials/thickness* - enhances the neutronic performance of a moderator and reduces the energy deposited in the moderator per se; and g) *reflector materials/size* - enhances both the neutronic performance and pulse characteristics of a moderator. We will now discuss a few of these issues in detail.

4.1 *Neutron Intensity vs. Brightness*

In addition to target-moderator-reflector materials and geometry, the total number of neutrons leaking from a moderator surface (the moderator intensity) depends on the overall size of the moderator. Generally, the larger the moderator, the higher the neutron intensity.

Average Brightness - We define the average brightness of a moderator to be the total neutron leaking from a moderator surface divided by the area of the moderator viewed-surface. Figure 6 shows neutron intensity and average brightness for wing moderators [10]. When the moderators are made larger to gain intensity, reflector material is removed, and the target system becomes less efficient (in terms of useful neutrons per incident proton). In general, average moderator brightness decreases with increasing moderator size. Therefore, a criteria for high average moderator brightness requires small moderators, whereas, a criteria for high moderator intensity behooves large moderators. Clearly, a compromise must be struck, and we need objective criteria from instrument designers on the importance issue of *average moderator brightness vs. intensity.*

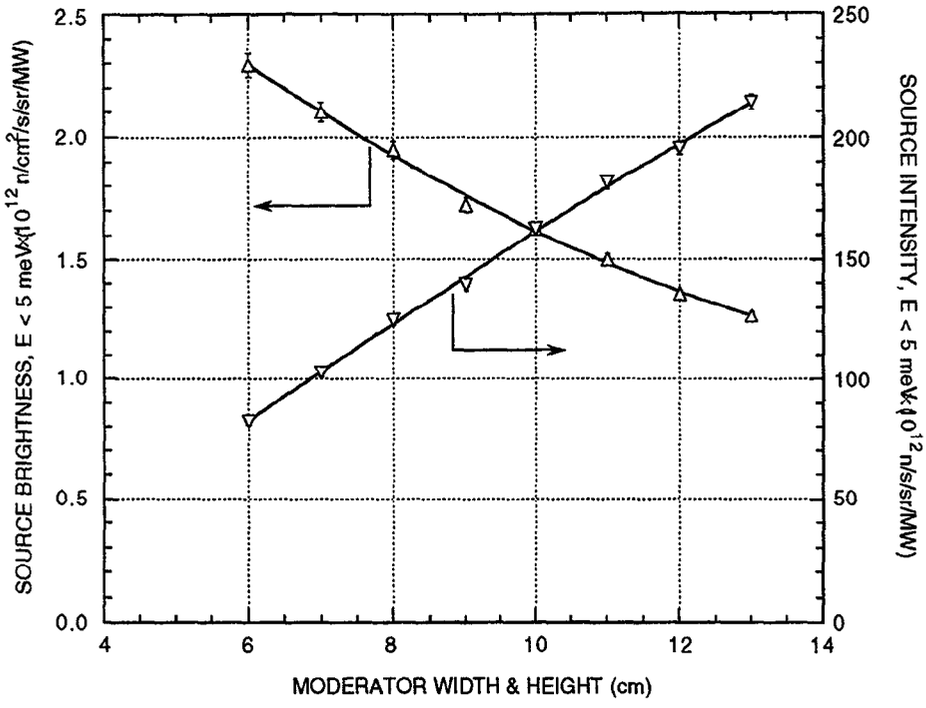

Figure 6. Average moderator brightness and moderator intensity vs. moderator size for wing moderators of liquid H_2 (ortho/para 50/50).

Specific Brightness - For a given moderator size, we define the *"specific moderator brightness"* to be the brightness over a smaller "field-of-view", i.e., over a smaller area of the moderator surface. Figure 7 shows specific brightness vs. field-of-view for both decoupled and coupled liquid H_2 flux-trap moderators. Because of "edge effects" (changes in the spatial distribution of leakage neutrons), the specific moderator brightness of a decoupled moderator is more sensitive to moderator field-of-view than is a coupled moderator.. There also appears to be spectral effects for a liquid H_2 moderator, i.e., the neutrons seem to be colder at smaller specific brightnesses [11].

4.2 *Temporal Brightness*

The *"temporal brightness"* (the peak time-dependent neutron brightness) is an important consideration in both SPSS and LPSS target system design. The temporal brightness can be altered with reflector type and by employing a composite reflector which we discussed above. We have calculated temporal brightness for liquid H_2 moderators coupled to D_2O and Be reflectors as well as for composite reflectors of Be/Ni, Be/W, and Be/Pb. The results are shown in Fig. 8 for an inner reflector size of 60 cm diam by 60 cm high. For the materials studied, D_2O exhibits the worst temporal brightness and a long-time tail. The Be/W composite reflector has slightly better temporal brightness than D_2O/Pb. Because of the moderate neutron absorption in W, the long-time tail for the Be/W composite reflector is better than the D_2O/Pb combination. The temporal brightness is further improved in going to a Be/Ni reflector with shorter long-time tails. An all Be reflector gives a high temporal

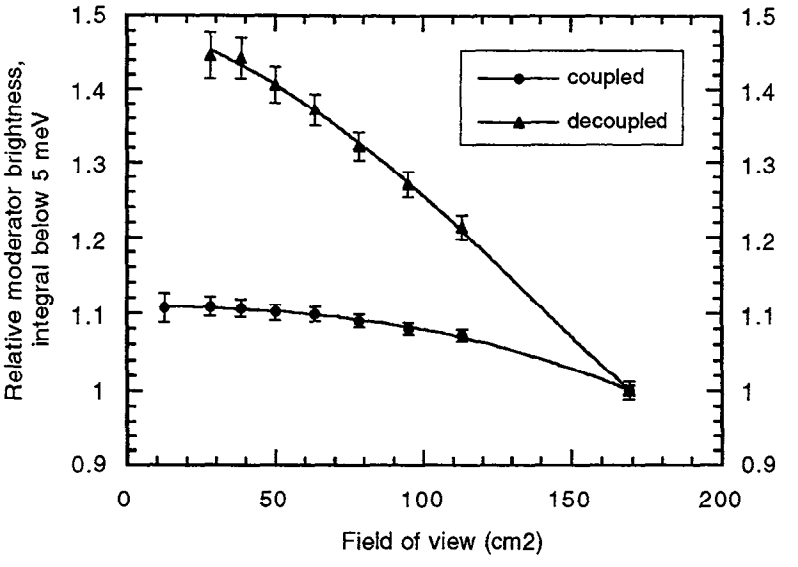

Figure 7. Specific Brightness versus moderator field-of-view for decoupled and coupled liquid H_2 (ortho/para 50/50) flux-trap moderators. The moderators were 5x13x13 cm^3.

brightness, but has a long-time tail. The temporal brightness is the best for the Be/Pb composite reflector; the long-time decay constant is better than that for an all Be reflector but still needs improvement. We are studying ways of keeping the temporal brightness high and decreasing the long-time tails by composite reflectors of Be/Pb/Ni and Be/Pb/W.

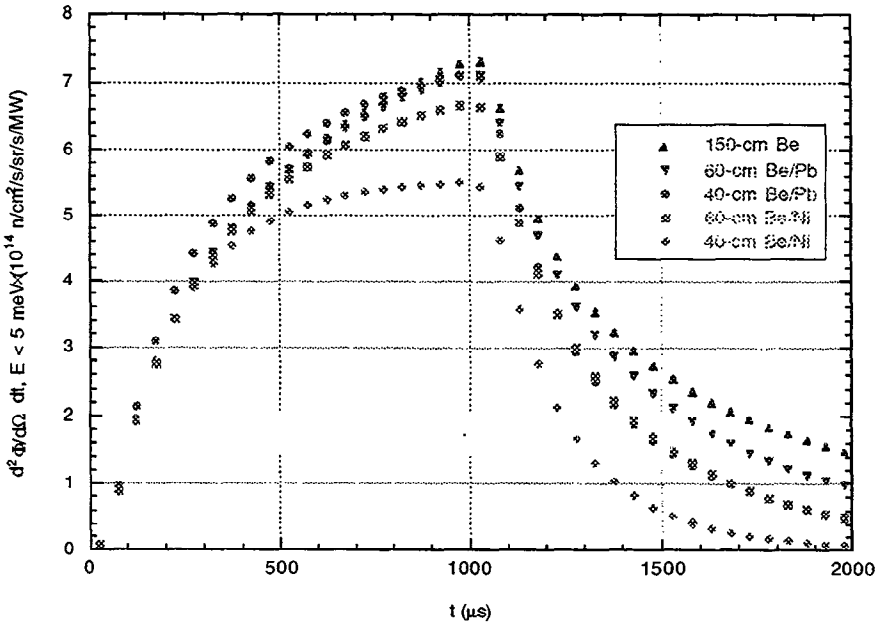

Figure 8. Temporal average moderator brightness from a liquid H_2 (ortho/para 50/50) flux-trap moderator for various reflector types.

4.3 *Liquid H_2 compared with Liquid D_2*

We have calculated the neutron flux inside spheres of liquid H_2 and liquid D_2 surrounded by a Be reflector to understand basic moderator characteristics. We placed an isotropic point source of 1-keV neutrons at the center of two concentric spheres of moderator/reflector (see Fig. 9), and calculated the neutron flux inside the moderator region. The results of the calculations are shown in Figs. 10 and 11.

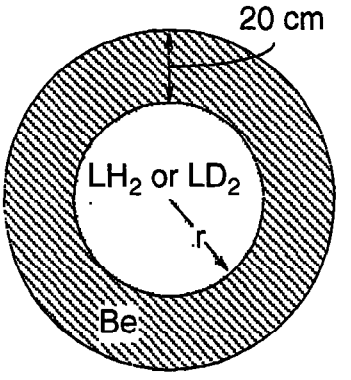

Figure 9. Geometry used to calculate neutron fluxes inside cold moderators of liquid H_2 and D_2 with ortho/para fractions of 50./50. An isotropic source of 1-keV neutrons was placed at the center of the moderator-reflector and the radius of the moderator was varied.

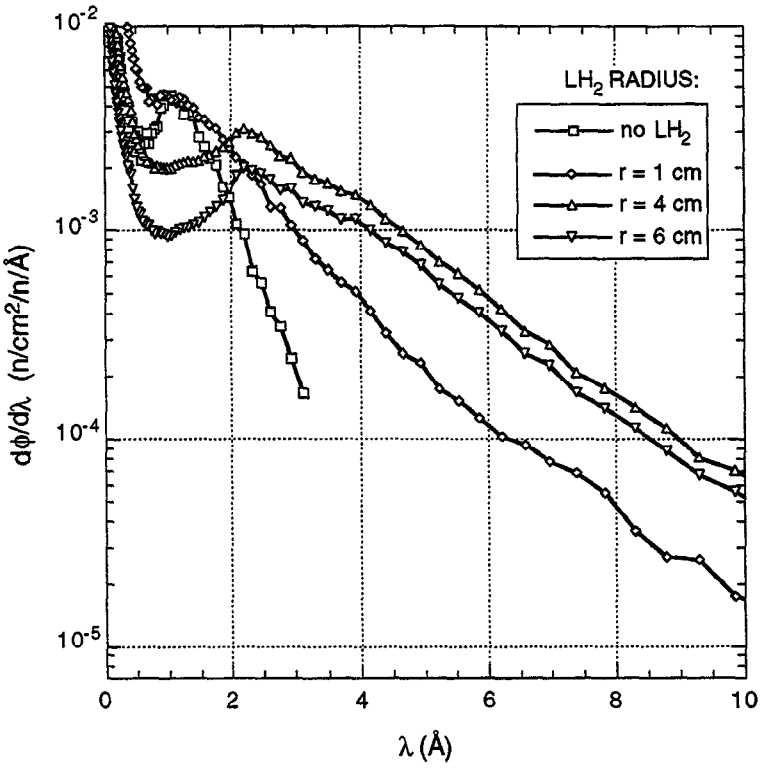

Figure 10. Neutron flux inside liquid H_2 moderator (ortho/para 50/50).

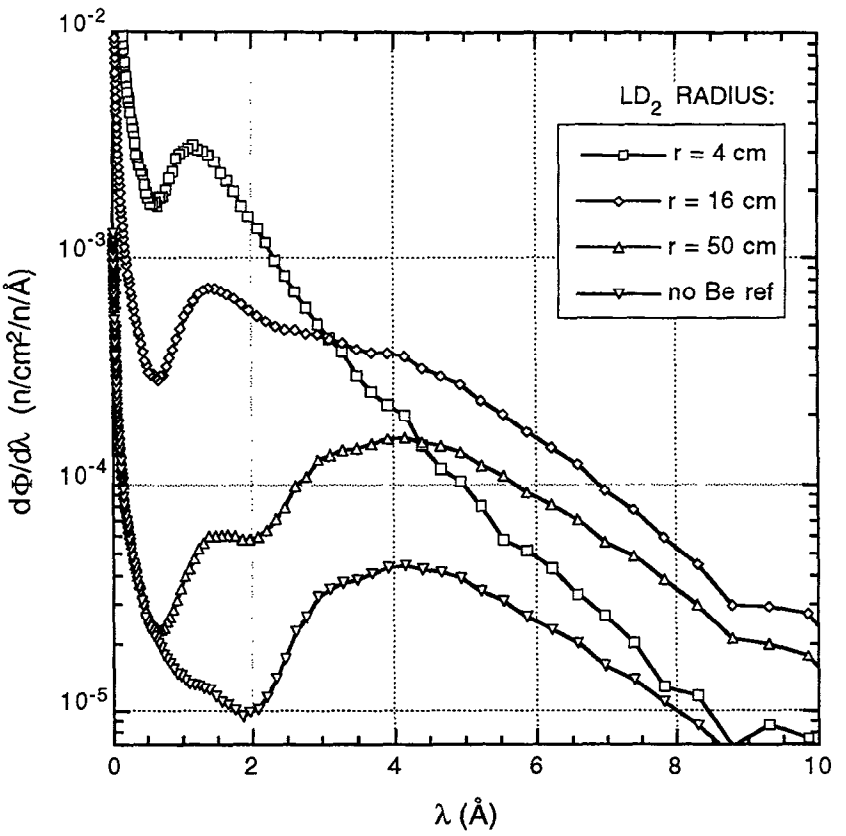

Figure 11. Neutron flux inside liquid D_2 moderator (ortho/para 50/50).

In Figure 10 we see a source of albedo neutrons from the beryllium when there is no hydrogen moderator. When the hydrogen moderator is present we see an increase in the epithermal neutrons and the beginning of the thermalization process. For these calculations, the neutron flux peaks at a radius of about 4 cm. In Figure 11, we see the effects of the beryllium reflector and a peaking in the neutron flux around 4 angstroms. The liquid H_2 doesn't show this peak presumably because of the increased absorption in H_2 compared to D_2. Thus, liquid H_2 produces the brightest cold source, but liquid D_2 produces a much larger volume of *"colder"* neutrons.

4.4 Ortho/Para-Hydrogen Fraction.

We have looked at the effect of ortho/para fraction on average moderator brightness as a function of moderator thickness and ortho/para fraction for coupled liquid H_2 moderators. The results are shown in Fig. 12. The average moderator brightness is largest for the 100% para-H_2 moderator which reaches a maximum around 10 cm. All the moderators with orth/para combinations show a "peaking" in the average brightness as a function of moderator thickness. This peaking occurs around moderator thicknesses of 5-6 cm. This study shows that it is important to know the ortho/para fraction for a liquid H_2 moderator in either a SPSS or a LPSS. Also, the pulse widths of neutrons leaking from a thick liquid H_2 moderators must be understood.

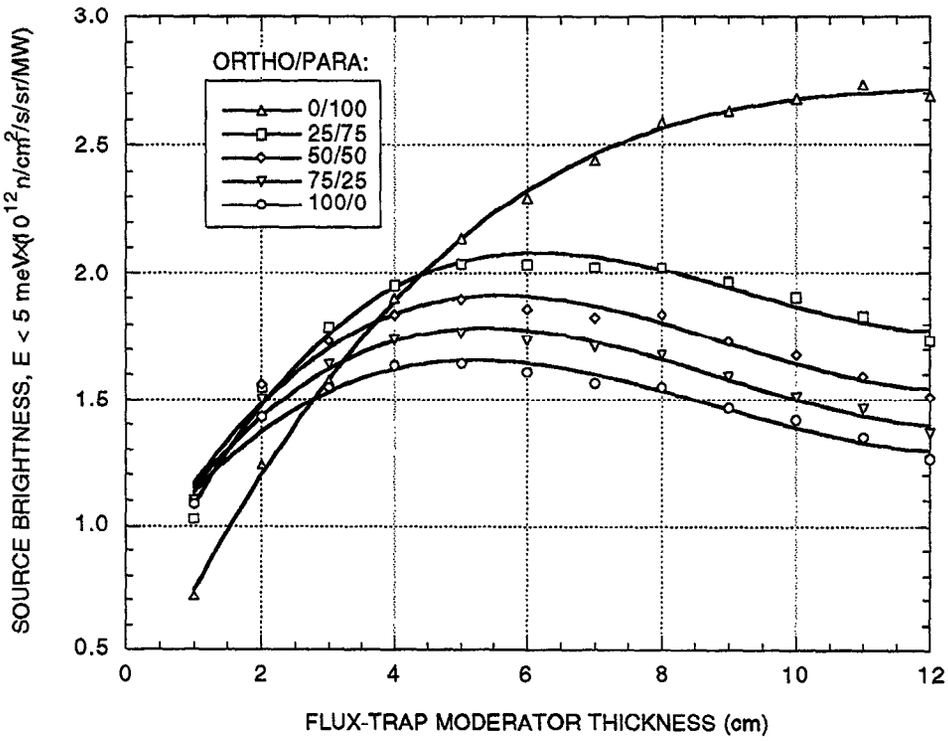

Figure 12. Average neutron source brightness from a 13x13 cm^2 liquid H_2 flux-trap moderator as a function of ortho/para concentration and moderator thickness. The target was D_2O-cooled W and the reflector D_20-Cooled Be (D_2O/Be 15/85).

Figure 13 shows the average moderator brightness of a liquid H_2 flux-trap moderator for several composite reflectors. The overall size of all the reflectors used in this work is 150 cm diam by 150 cm high. The average moderator brightness with a D_2O reflector is about 70% of that with a Be reflector. An "infinite" Be reflector is about 125x125 cm. For inner reflector sizes up to about 20 cm, the average moderator brightness for a D_2O/Pb composite reflector is the same as that of a Be/Pb composite reflector. For inner reflector sizes between about 20 and 125 cm, the average moderator brightness with a Be/Pb composite reflector is better than that of a D2O/Pb composite reflector.

Also, The average moderator brightness with an all Pb reflector is better than with an all Ni reflector and remains so up to an inner reflector size of about 125 cm. However, the neutron pulses from a moderator are shorter for a Be/Ni composite reflector compared to a Be/Pb composite reflector (see Fig. 8).

5. Conclusions

Optimizing the neutronic performance of a coupled-moderator system for a Long-Pulse Spallation Source is a new and challenging area for the spallation target-system designer. For optimal performance of a neutron source, it is essential to have good communication with instrument scientists to obtain proper design criteria, and continued interaction with

mechanical, thermal-hydraulic, and materials engineers to attain a practical design. A good comprehension of the basics of coupled-moderator neutronics will aid in the proper design of a target system for a Long-Pulse Spallation Source.

Many traditional notions will have to be rethought and several new concepts put forward to meet the challenge of designing the target system for a next generation (5-MW) spallation neutron source. However, it is possible to design a high-performance target system for a 1-MW spallation source using existing technology.

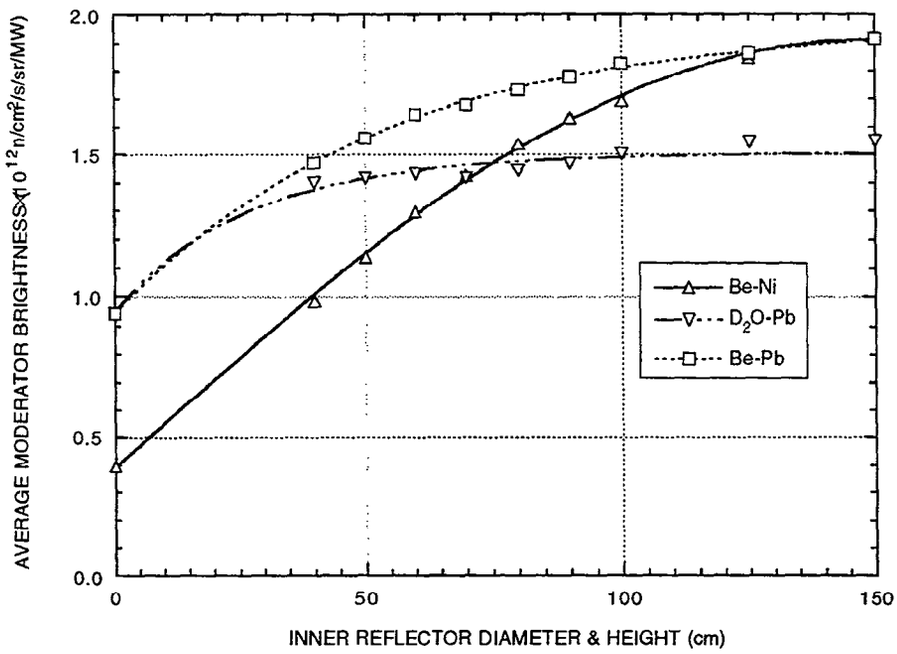

Figure 13. Average moderator brightness as a function of the inner reflector size and composition. The liquid H_2 (ortho/para 50/50) flux-trap moderators were 5x13x13 cm^3. The target was D_2O-cooled W rods.

6. Acknowledgments

We wish to acknowledge valuable discussions with Roger Pynn and Rex Hjelm. This work was supported by the U.S. Department of Energy, BES-DMZ, under Contract No. W-7405-Eng-36.

7. References

[1] G. J. Russell, C. D. Bowman, E. R. Whitaker, H. Robinson, and M. M. Meier, "LANSCE High-Power (200 μA) Target-Moderator-Reflector-Shield," in ICANS-VIII: Proceedings of the Eighth Meeting of the International Collaboration on Advanced Neutron Sources, Rutherford-Appleton Laboratory report RAL-85-110 (November 1985), pp. 272-293.

[2] G. Fluharty, F. B. Simpson, G. J. Russell, and J. H. Menzel, "Moderator Studies for a Repetitively Pulsed Test Facility (RPTF)," *Nuclear Science and Engineering,* **35**, 45-69 (1969).

[3] G. J. Russell, J. S. Gilmore, H. Robinson, G. L. Legate, A. Bridge, R. J. Sanchez, R. J. Brewton, R. Woods, and H. G. Hughes, III, "LANSCE Target System Performance," in *Advanced Neutron Sources 1988: Proceedings of the Tenth Meeting of the International Collaboration on Advanced Neutron Sources (ICANS-X)*, Dianne Hyer, Ed. (IOP Publishing Ltd., Bristol, England), Vol. 97, pp. 483-496.

[4] G. J. Russell, "LANSCE Upgrade Cold Sources," in "Proceedings of the International Workshop on Cold Neutron Sources," Los Alamos National Laboratory report LA-12146-C (August 1991), pp. 471-489.

[5] G. J. Russell, H. Robinson, G. L. Legate, R. Woods, E. R. Whitaker, A. Bridge, K. J. Hughes, and R. D. Neef, "The LANSCE Target System," in *ICANS-IX: Proceedings of the Ninth Meeting of the International Collaboration on Advanced Neutron Sources*, F. Atchison and W. Fischer, Eds., Swiss Institute for Nuclear Research report ISBN 3-907998-01-4 (April 1987), pp. 177-244.

[6] N. Watanabe, S. Ikeda, and Y. Ishikawa, "KENS Target Station, " in *ICANS-IV: Proceedings of the Fourth Meeting of the International Collaboration on Advanced Neutron Sources*, Y. Ishikawa, N. Watanabe, Y. Endoh, N. Niimura, and J. Newsam, Eds., National Laboratory for High Energy Physics report KENS-II (March 1981), pp. 181-199.

[7] A. Carne, "Review of the SNS Target Station," in *ICANS-IV: Proceedings of the Fourth Meeting of the International Collaboration on Advanced Neutron Sources*, Y. Ishikawa, N. Watanabe, Y. Endoh, N. Niimura, and J. Newsam, Eds., National Laboratory for High Energy Physics report KENS-II (March 1981), pp. 136-153.

[8] J. M. Carpenter, C. W. Potts, and G. H. Lander, "Intense Pulsed Neutron Source (IPNS) at Argonne National Laboratory (ANL): A Status Report as of June 1982," in *ICANS-VI: Proceedings of the Sixth Meeting of the International Collaboration on Advanced Neutron Sources*, Argonne National Laboratory report ANL-82-80 (January 1983), pp. 77-101

[9] W. E. Fischer, "Status Report of SINQ: A Continuous Spallation Neutron Source," in *Advanced Neutron Sources 1988: Proceedings of the Tenth Meeting of the International Collaboration on Advanced Neutron Sources (ICANS-X)*, Dianne Hyer, Ed. (IOP Publishing Ltd., Bristol, England), Vol. 97, pp. 67-78.

[10] E. J. Pitcher, G. J. Russell, P. A. Seeger, and P. D. Ferguson, "Performance of Long-Pulse Source Reference Target-Moderator-Reflector Configurations," these proceedings.

[11] P. D. Ferguson, private communication.

ICANS-XIII
13th Meeting of the International Collaboration on
Advanced Neutron Sources
October 11-14, 1995
Paul Scherrer Institut, 5232 Villigen PSI, Switzerland

REFERENCE MODERATOR CALCULATED PERFORMANCE FOR THE LANSCE UPGRADE PROJECT

Phillip D. Ferguson, Gary J. Russell, and Eric J. Pitcher

Manuel Lujan, Jr. Neutron Scattering Center, Los Alamos National Laboratory, USA

ABSTRACT

We have calculated the performance of five moderators of interest to the LANSCE upgrade project. Coupled and decoupled light water and liquid hydrogen moderators in flux-trap geometry surrounded by a neutronically infinite heavy-water cooled beryllium reflector have been studied. Time and energy spectra, as well as semi-empirical fits to the data, are presented. The data has been made available to aid the instrument design and moderator selection process.

1. Introduction

The Manuel Lujan, Jr. Neutron Scattering Center (LANSCE) is currently in the process of an upgrade project. The technical objectives of the project are: 1) improved beam availability to LANSCE, 2) less than 10% downtime from intervals greater than 8 hours, 3) improved capability for routine and sustained operation of LANSCE, 4) personnel access to the LANSCE experimental room #1 (ER-1) with the Proton Storage Ring (PSR) beam on to the LANSCE target, 5) reduced beam delivery operating costs, and 6) reduced radiation exposure [1]. During the upgrade project, the existing target/moderator/reflector/shield system will be replaced and provisions will be made for two additional moderators serving four new flight paths upstream of the upper target. The new moderator types are as of yet undetermined.

The purpose of this work is to present the general moderator performance curves that are being used to determine the LANSCE upgrade project moderator suite. Although the moderator optimization process has not been completed for the LANSCE upgrade project, the moderators presented here do reflect some level of optimization. As such, the results presented here will give reasonable insight into the expected performance of each moderator type. It should be noted that reflector size has a significant impact on the intensity and time distributions from a coupled moderator. For this set of calculations, a neutronically infinite beryllium reflector has been used, resulting in the maximum intensities and broadest pulse shapes from coupled moderators.

Keywords: Moderator, Water, Liquid hydrogen, LANSCE

2. Model Description

The LANSCE Upgrade project Monte Carlo model consists of a singly split tungsten rod target with four identical moderators in flux-trap geometry. A schematic of the model is shown in Fig. 1. A typical poison material is Gd. Depending on the decoupling energy required, Gd, Cd, and ^{10}B or natural B are used as decoupler and liner materials, with Gd decoupling at the lowest energy and B at the highest energy. The Monte Carlo model contains the decouplers, liners, poisons, etc., each of which have a major impact on the neutron time and energy distributions. However, some of the engineering detail, such as the proton beam entry window and the stainless steel reflector canister, are neglected. A more detailed Monte Carlo model will be constructed as the moderator optimization continues, but the current level of model detail provides adequate insight into general moderator performance issues.

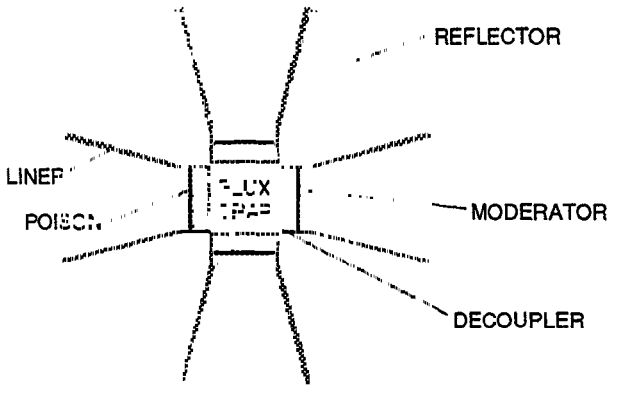

Fig. 1. Schematic of the physics model detailing the locations of the moderators, decouplers, liners, poisons, and reflector.

LAHET Code System (LCS) [2] calculations have been completed for five cases in flux-trap geometry: a) four decoupled high-intensity water moderators, b) four decoupled high-resolution water moderators, c) four coupled water moderators, d) four decoupled liquid hydrogen moderators, and e) four coupled liquid hydrogen moderators. Each water moderator is 3.5 cm thick, and each liquid hydrogen moderator is a 5 cm thick 50/50 mix of ortho-hydrogen and para-hydrogen. Details for each moderator configuration are given in Table 1. For this series of calculations, the reflector was a homogeneous mixture consisting of 85% Be and 15% D_2O by volume. The reflector radius was 75 cm and the height was 150 cm, which approximates an infinite Be reflector.

Table 1. Moderator configurations for the LANSCE 1.5 physics model calculations

	premoderator	moderator	poison	decoupler	liner
high-intensity H_2O	1 cm H_2O	2.5 cm H_2O	0.00508 cm Gd	0.08128 cm Cd	0.08128 cm Cd
high-resolution H_2O	2 cm H_2O	1.5 cm H_2O	0.00508 cm Gd	0.035 cm ^{10}B	0.035 cm ^{10}B
coupled H_2O	none	3.5 cm H_2O	none	none	none
decoupled liquid hydrogen	none	5 cm LH_2	none	0.00508 cm Gd	0.00508 cm Gd
coupled liquid hydrogen	none	5 cm LH_2	none	none	none

3. Energy spectra

Energy spectra for the water and liquid hydrogen moderators are shown in Figs. 2 and 3 respectively. The spectra for the three water moderators were fit using the semi-empirical functional form [3]:

$$E\varphi(E) = E\varphi_{th}(E) + \Delta(E)\varphi_{epi}(E) \tag{1}$$

$$E\varphi_{th}(E) = J\left(\frac{E}{E_T}\right)^2 e^{-\left(\frac{E}{E_T}\right)} \tag{2}$$

$$E\varphi_{epi}(E) = \varphi_{1ev}\left(\frac{E}{1\,eV}\right)^{\alpha} \tag{3}$$

$$\Delta(E) = \frac{1}{1+e^{\left(\frac{a}{\sqrt{E}}-b\right)}} \tag{4}$$

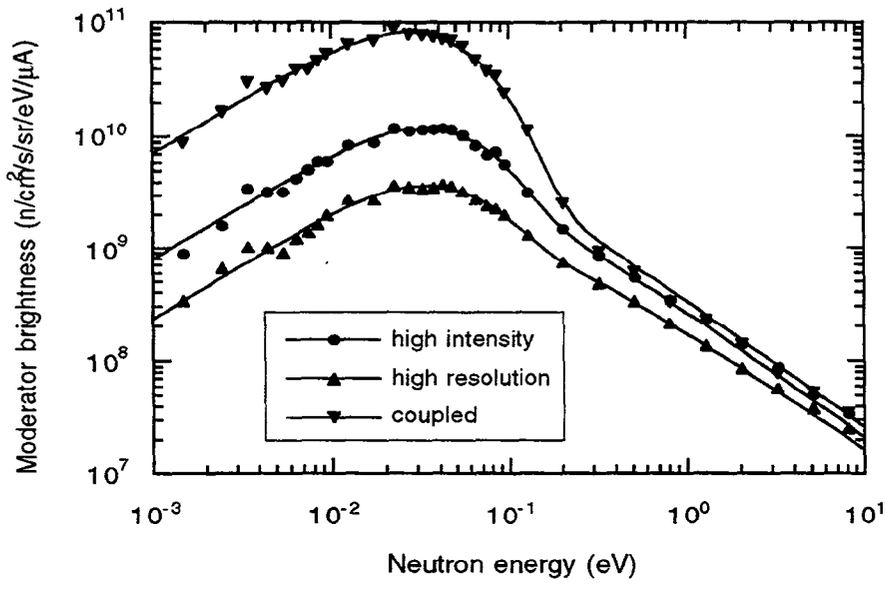

Fig. 2. Average moderator brightness as a function of neutron energy for three water moderators.

Parameters for the water moderator energy spectra fits are presented in Table 2. For an ideal infinite moderator (i.e. no absorption), the slope of the brightness per unit energy near 1 eV is expected to be 1/E [4]. In Fig. 2, the slope is negative for the water moderators due the fact that the moderators are finite and absorbing over the energy range shown. However, the slope is less negative for the high resolution moderator due to the 1/v absorption of the ^{10}B decoupler which preferentially allows more high energy neutrons into the moderator.

Table 2. Fitting parameters for the water moderators

Moderator	J (10^8 n/cm^2/s/sr/μA)	E_T (meV)	$\varphi_{1\,eV}$ (10^8 n/cm^2/s/sr/μA)	α	a (eV$^{0.5}$)	b
High-intensity	7.3	30	3.2	-0.12	0.7	2.2
High-resolution	1.9	28	2.3	-0.05	0.6	1.7
Coupled	53	27	3.2	-0.11	0.7	4.5

The decoupled and coupled liquid hydrogen energy spectra were fit using the semi-empirical functional form [5]:

$$\varphi(E) = \varphi_{th}(E) + \theta_{cut}(E)\varphi_{epi}(E) \tag{5}$$

$$\varphi_{th}(E) = J\frac{E}{E_T^2}e^{-\left(\frac{E}{E_T}\right)} \tag{6}$$

$$\theta_{cut}(E) = 1 - e^{-x}\left(1 + x + 0.5x^2\right)$$
$$x = \begin{cases} 0 & E < E_{cut} \\ \beta(E - E_{cut}) & E \geq E_{cut} \end{cases} \tag{7}$$

$$\varphi_{epi}(E) = \rho(E)\frac{\varphi_{1\,ev}}{E}\left(\frac{E}{1\,eV}\right)^{\alpha}$$

$$\rho(E) = 1 + \delta e^{-y}\left(1 + y + 0.5y^2\right) \tag{8}$$
$$y = \begin{cases} 0 & E < E_\rho \\ \gamma\left(E - E_\rho\right) & E \geq E_\rho \end{cases}$$

Parameters for the liquid hydrogen moderator energy spectra fits are presented in Table 3. The J integral accurately predicts the difference in the Maxwellian peaks, while φ_{1eV} and α reflect the similarity in the two curves above 0.1 eV. The J integral will be lower for a decoupled moderator which uses Cd for a liner material.

Table 3. Fitting parameters for the LH_2 moderator

moderator	J (10^9 n/cm^2/s/sr/μA)	E_T (meV)	φ_{1eV} (10^8 n/cm^2/s/sr/μA)	α	β (eV^{-1})	E_{cut} (meV)	δ	γ (eV^{-1})	E_ρ (meV)
decoupled	0.6	3.1	2.5	0.08	396	2.6	1.3	203	9.8
coupled	2.9	3.6	2.6	0.04	236	0.7	1.6	173	17

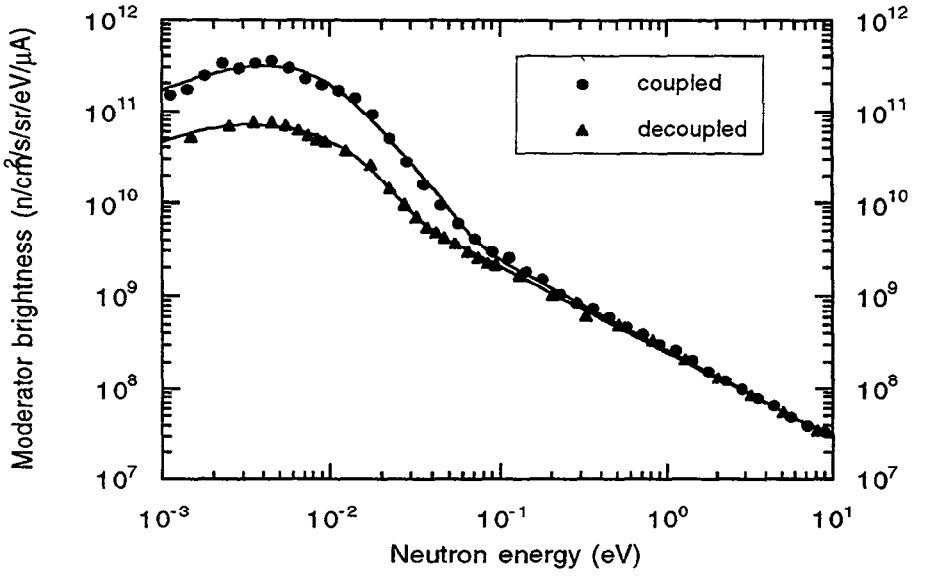

Fig. 3. Average moderator brightness as a function of neutron energy for two liquid hydrogen moderators (50/50 ortho/para mixture).

4. Time spectra

Integral time spectra (10 meV < E < 100 meV) for the three water moderators are presented in Figs. 4 - 6. The units on the time distribution plots are arbitrary because a solid angle of 2 steradians was tallied over to reduce the statistical error associated with each data point. The large solid angle over which the tally was performed does not allow the time-dependent brightness to scale exactly with the steady-state results. However, time constants have been demonstrated to be relatively constant as a function of the solid angle for solid angles up to 4 steradians. Although the units are arbitrary, comparisons can be made between moderators for a fixed energy interval (i.e. the water moderator pulse shapes can be compared directly, as can the LH_2 moderator pulse shapes).

In addition to the data points, which can be used to get an estimate of the full width at half maximum, the exponentially decaying tail of each pulse has been fit and the decay constant is given. From Figs. 2, 4, and 5, the high intensity water moderator results in almost a factor of 4 more intensity than the high resolution water moderator. However, the price for the increase in intensity is approximately a factor of 2 longer decay constant on the pulse tail and an increased full width at half maximum.

The coupled water moderator exhibits much longer decay constants than either of the decoupled water moderators. Several exponentials can be used to fit the tail of the coupled moderator. In Fig. 6, two exponentials have been used as an example. If the data were continued out to longers times, another exponential with a longer time constant would be required to more accurately fit the data.

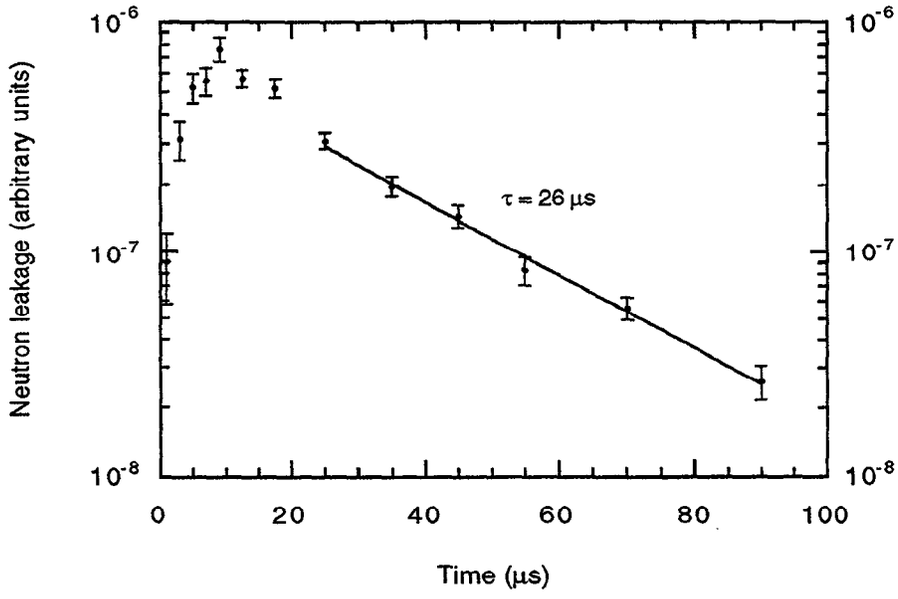

Fig. 4. Time distribution (10 meV ≤ E ≤ 100 meV) from a decoupled high-intensity water moderator for an instantaneous proton pulse.

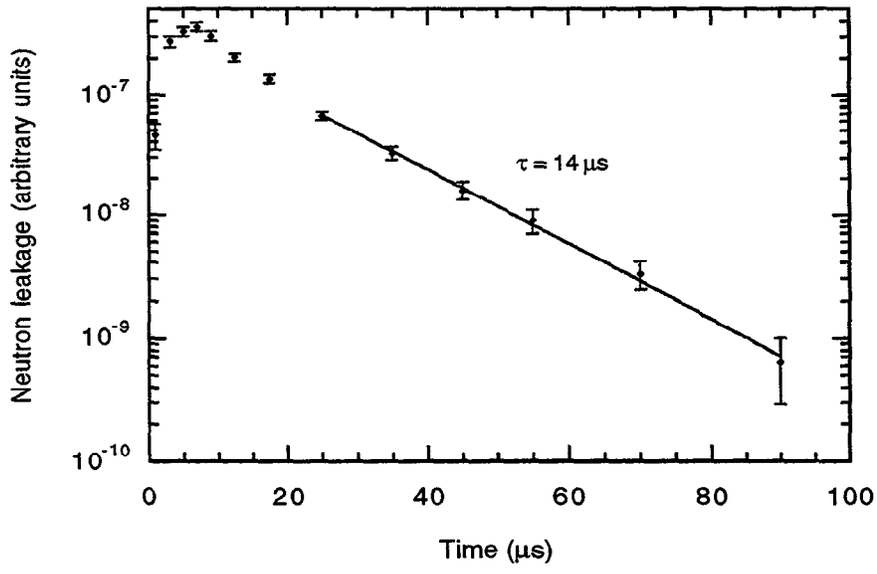

Fig. 5. Time distribution (10 meV ≤ E ≤ 100 meV) from a decoupled high-resolution water moderator for an instantaneous proton pulse.

Time distributions for the liquid hydrogen moderators are shown in Figs. 7 and 8. As expected, the decoupled LH_2 exhibits a time constant much shorter than the coupled LH_2 moderator. The decoupled system is also adequately fit using a single exponential, while several exponentials could be used to fit the coupled system, resulting in different decay constants than those presented here.

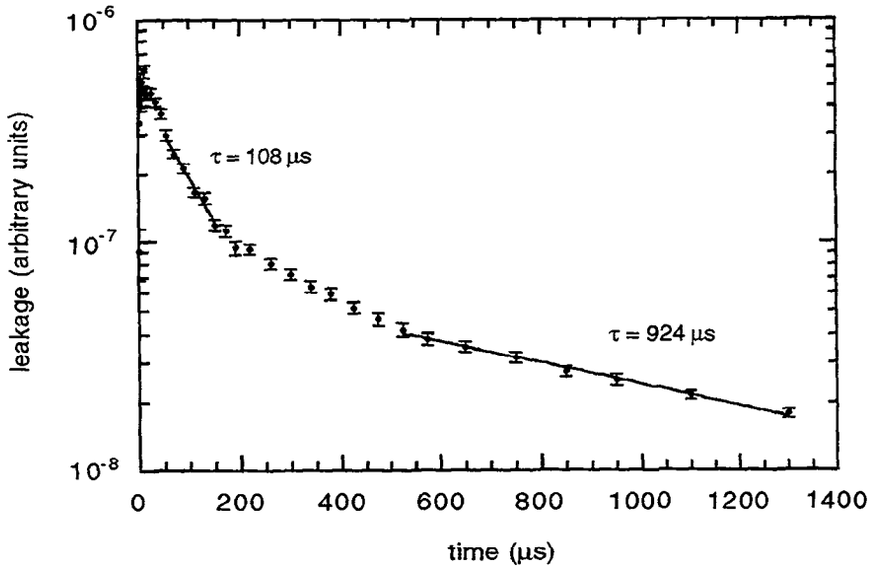

Fig. 6. Time distribution (10 meV ≤ E ≤ 100 meV) from a coupled water moderator for an instantaneous proton pulse.

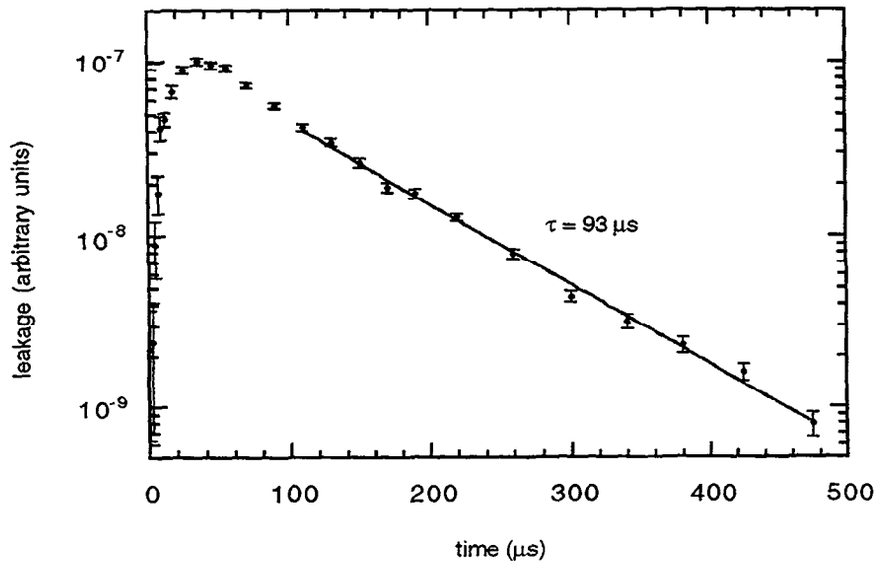

Fig. 7. Time distribution (E ≤ 10 meV) from a decoupled liquid hydrogen moderator for an instantaneous proton pulse.

5. Conclusions

Time and energy spectra have been presented for several moderators of interest to the LANSCE Upgrade project. Semi-empirical data fits for the energy spectra have been completed to aid instrument modeling efforts. This data is intended to support the initial selection of a moderator suite for the LANSCE Upgrade project.

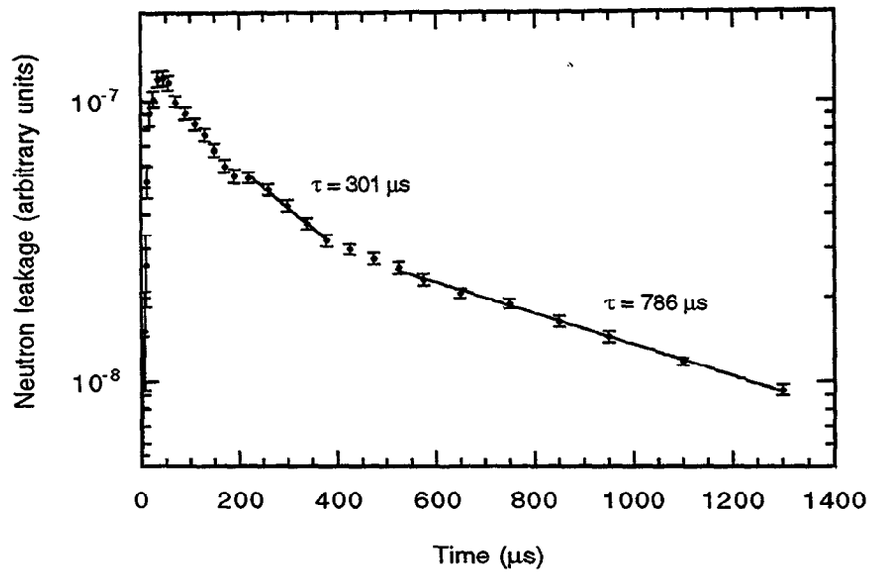

Fig. 8. Time distribution (E ≤ 10 meV) from a coupled liquid hydrogen moderator for an instantaneous proton pulse.

6. Acknowledgments

We wish to acknowledge valuable input from Guy Baker, Torben Brun, and Nathan Bultman. This work was supported by the U.S. Department of Energy under contract No. W-7405-Eng-36.

7. References

[1] Macek, Robert J., A Proposal for LANSCE Performance Improvements, Phase II, submitted to the Secretary of the Army, Proposal R-1339-95 (May 3, 1995).

[2] Prael, Richard E. and Henry Lichtenstein, Users Guide to the LCS: The LAHET Code System, Los Alamos National Laboratory Report LA-UR-89-3014 (September 1989).

[3] Carpenter, J. M., et al, Measurement and Fitting of Spectrum and Pulse Shapes of a Liquid Methane Moderator at IPNS, NIM **A234**, 542 (1985).

[4] Duderstadt, James J. and Louis J. Hamilton, Nuclear Reactor Analysis, John Wiley & Sons, NY (1976).

[5] Brun, T. O., et al., LAHET Code System/CINDER'90 Validation Calculations and Comparison with Experimental Data, in Proceedings of the Twelfth Meeting of the International Collaboration on Advanced Neutron Sources (ICANS-XII), T-26 (1993).

ICANS-XIII
13th Meeting of the International Collaboration on
Advanced Neutron Sources
October 11-14, 1995
Paul Scherrer Institut, 5232 Villigen PSI, Switzerland

PRESENT STATE OF THE ESS TANTALUM TARGET

Bernd Guttek

Zentralabteilung Technologie, Forschungszentrum Jülich GmbH

1. Introduction

The *Reference Design* of an ESS 5 MW target was presented in the figure 4.5 of the ESS outline report published in September 1995. This non-split target for horizontal injection has been composed of a stack of 55 target plates of tantalum hit by the proton beam with a circular footprint of 100 mm diameter. On both sides of the Ta-plates are stacks of Ni-plates integrated as reflector into the target container to result in a ratio of 3:1 between target width and height.

A decision made by the ESS Target Working Group in July 1995 gave way to the prefered development of a Mercury Target for the ESS which will come out in the *Final Conceptional Design*. The first designs of this ESS Mercury Target were presented by Dr. G.Bauer at the ICANS XIII. Nevertheless, the development of an ESS target of solid material is going on, serving as an *Option*. As the *Reference Design* has been fixed, the modifications made on it will lead to the ESS Tantalum Target.

2. Present geometry

A main goal in the design of an optional ESS Tantalum Target is to adapt the dimensions to those of the ESS Mercury Target. Doing so, the dimensions of the reflector and the configuration of moderators and their positions in the reflector are the same for both target concepts; this forms a good base for comparison. The reflector-moderator-assembly consists of a reflector with the dimensions 600 mm x 600 mm x 800 mm (x,y,z) and the reference moderator configuration (see ESS outline report). The reflector allows target dimensions with a cross section of 185 mm height (x) and 335 mm width (y) inserted. The length (z) of a target may be up to 700 mm.

The width of the container of the *Reference Design Target* is 600 mm (width of the Ta-stack: 120 mm, width of each Ni-stack: 140 mm, width of each water channel: 100 mm). As neutronic calculations done by Dr. D.Filges and Dr. R.D.Neef showed that the absence of the Ni-reflector inside of the target container hardly decreases the total neutron flux, the width of the target container has been decreased from 600 mm to 335 mm by taking the Ni-stacks out.

Furthermore, a second cooling system has been designed to allow the cooling of the decay heat of the target in case of failure of the main cooling system under 'beam off'-condition.

Keywords: ESS, target, tantalum, water cooling, helium cooling

Figure 1 shows the present geometry of the ESS Tantalum Target. In z-direction, the height of the target increases from 150 mm to 170 mm meanwhile the width increases from 240 mm to 330 mm. The beam window is part of the target container.

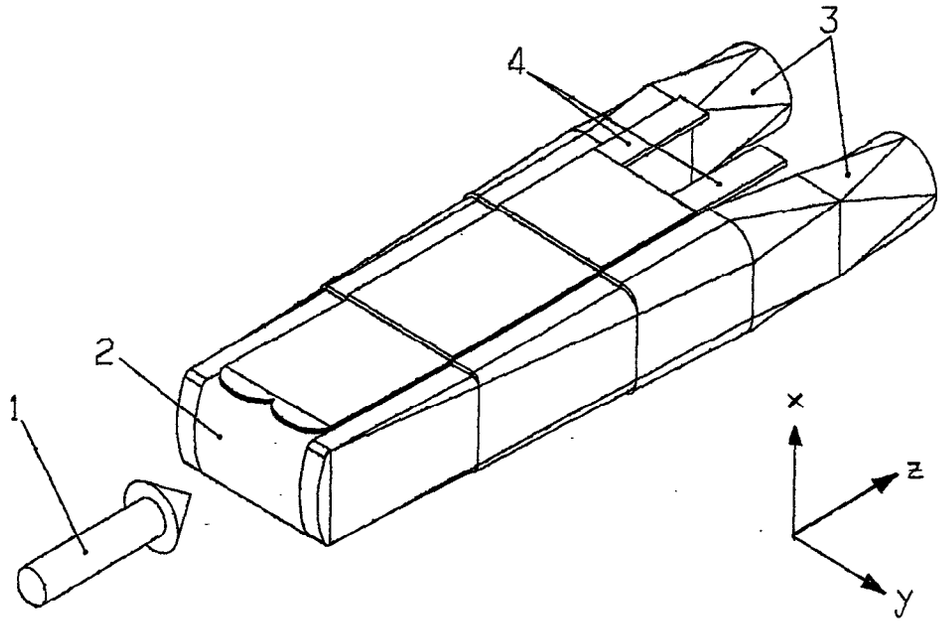

Figure 1 ESS Tantalum Target. 1: proton beam, 2: beam entrance window, 3: coolant in- and outlet of the main cooling, 4: coolant in- and outlet of the second cooling

The internal geometry of the ESS Tantalum Target (see figure 2) is mainly defined by the stack of 55 slightly 1D-bent rectangular target plates of tantalum with an increasing plate thickness from 2.6 mm to 30 mm. The front dimensions of the plates increase with z from 130 mm x 150 mm (x,y) to 150 mm x 170 mm. The cooling gaps have a minimum height of 0.7 mm where the plates contact each other. The average spacial part of cooling medium in the target is 8%.

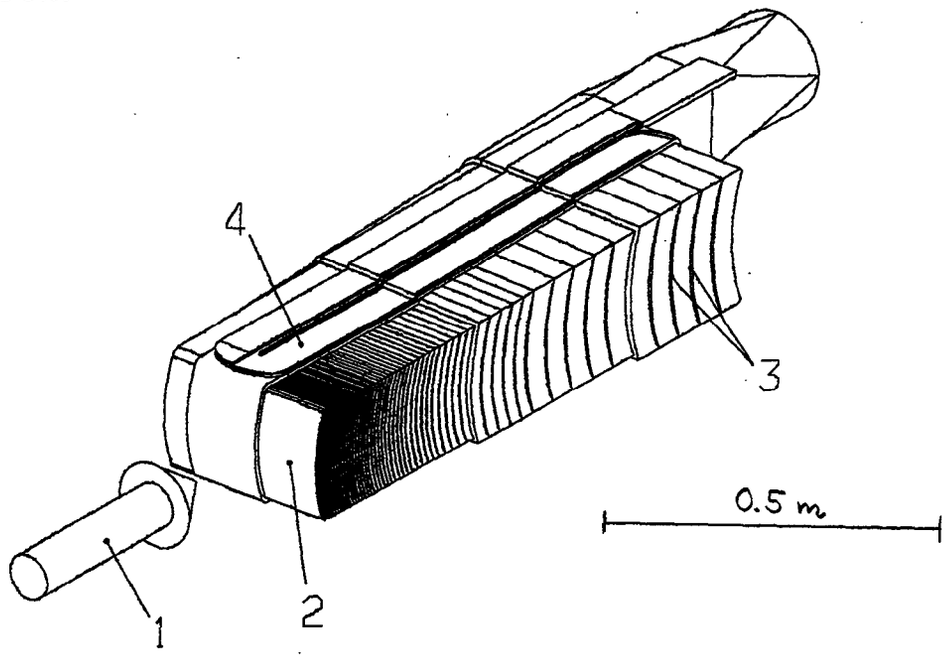

Figure 2 ESS Tantalum Target (cut away view). 1: proton beam, 2: stack of target plates, 3: gaps for main coolant flow, 4: channels for second coolant flow

3. Cooling of the target

The main cooling circuit has to have a performance of 3 MW which is 60% of the proton beam power. An estimation of the performance for the second cooling circuit is 250 kW in operation and 100 kW if the beam is 'off'. Investigations have been done so far only for the main cooling circuit. As cooling media water and helium have been studied.

3.1 Water cooling

On 5 MW beam power, the time averaged maximal volumetric heat deposition in the tantalum is 3100 W/cm^3. The plate thicknesses are chosen to give a heat flow of 375 W/cm^2 in the centre of each plate surface (see figure 3). Sufficient cooling of the target is guaranteed with a water mass flow of 80 kg/s leading to a heat transfer coefficient of about 3.5 W/cm^{2}K, a maximum plate surface temperatures of 180°C and a plate centre temperatures of 250°C. The relatively low surface temperature is chosen so that low pressure water can be used with no problems from boiling. The average water velocity of 7.5 m/s in the cooling gaps causes a pressure drop of nearly 0.1 MPa in the target. On average the water temperature increases about 20 K while passing through the gaps.

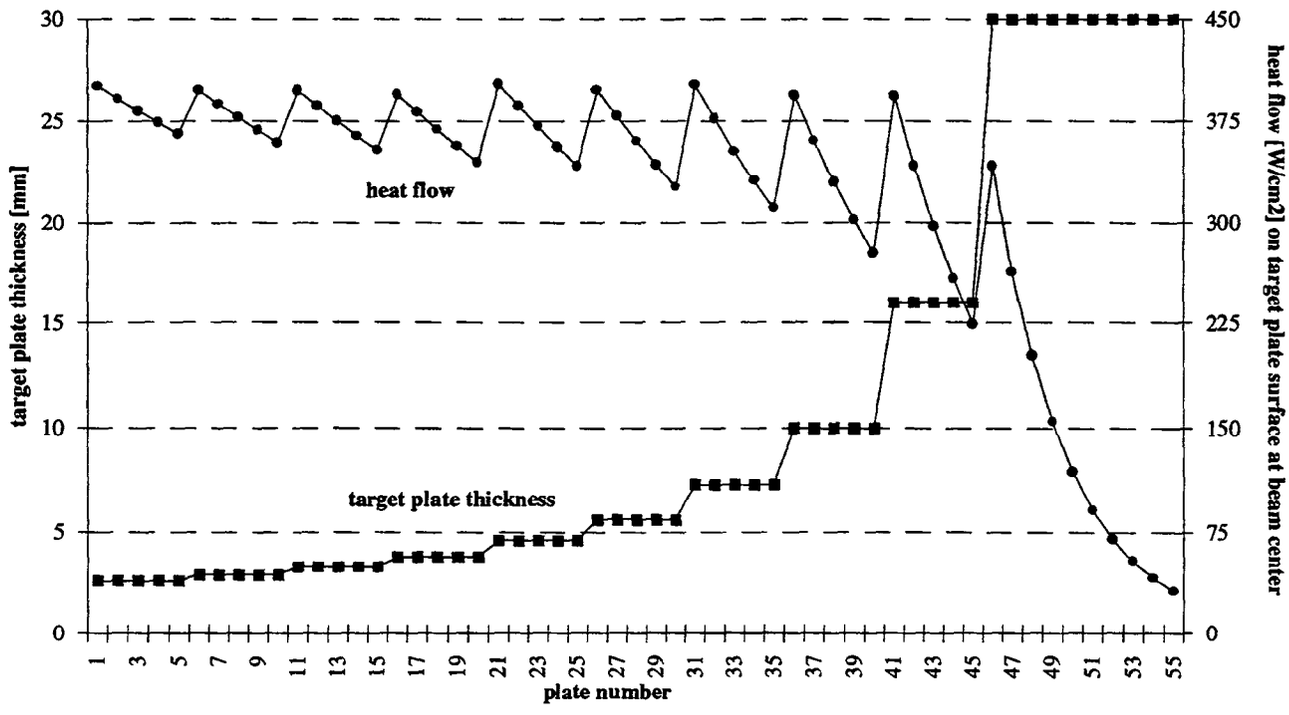

Figure 3 Target plate thicknesses and heat flow on the target plate surfaces at the beam center

3.2 Helium Cooling

As the water content in the target leads to the not wanted effect of premoderation in the target, helium cooling was investigated. The main question under the restrictions of an operation pressure below 10 bar and an helium velocity in the cooling gaps below the speed of sound is:

'What is the upper beam power limit for helium cooling?'

The thickness of the first target plates was decreased to 2 mm to give a heat flow of 300 W/cm^2 in the centre of each plate surface. While the average velocity of the helium is 360 m/s in the gaps the average heat transfer coefficients are 0.4 W/cm^{2}K under a He-pressure of 5 bar and 0.7 W/cm^{2}K under 10 bar. The figure 4 shows a viewgraph of the maximum helium and plate center surface temperature as a function of the proton beam power.

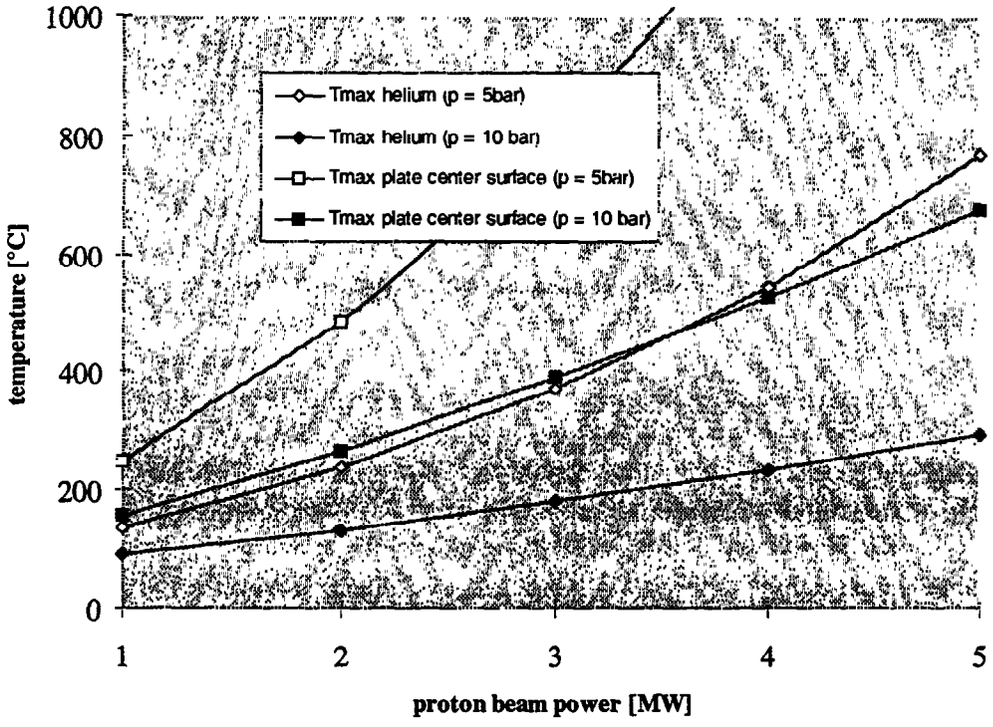

Figure 4 Maximum temperatures of the plate surface and the helium as function of the proton beam power

Conclusion: If the same plate temperatures would be accepted as in case of water cooling, the beam power should be ≤ 1 MW if the He-pressure is 5 bar and ≤ 2 MW if the He-pressure is 10 bar.

4. Mechanical stress in the target plates

So far, calculations have been made on the basis of an averaged, constant heat input and water cooling giving as results maximal stresses of about 50 MPa in the thinnest and 210 MPa in the thickest target plate. These values might be effectively reduced by slitting the plates. Pure unirridiated tantalum might stand 150 MPa at the operating temperatures; its characteristics could be strongly improved by choosing Ta-alloys.

ICANS-XIII
13th Meeting of the International Collaboration on
Advanced Neutron Sources
October 11-14, 1995
Paul Scherrer Institut, 5232 Villigen PSI, Switzerland

NEUTRONICS STUDIES FOR THE ESS SOURCE

D.J. Picton, T.D. Beynon and T.A. Broome

School of Physics and Space Research, The University of Birmingham,
Birmingham B15 2TT, England

ABSTRACT

This paper presents the results of calculations on two alternative target designs for the ESS pulsed spallation source. A conventional target based on the current ISIS design is compared with a split target incorporating both wing and flux trap moderators.

The results presented here focus on three issues, all of which are of general interest in the field of target-moderator systems. Firstly, the moderator performance is compared for the conventional and split target. For the purposes of the ESS study, the split target was found to offer no major advantage over a conventional target. Secondly, the variation of moderator performance with target diameter was examined. The results demonstrate that a flux trap moderator is significantly less sensitive to target diameter than wing moderators; thus a split target would be advantageous if a very large target diameter was found to be necessary. Thirdly, the performance of liquid para-hydrogen as a substitute for liquid methane (which would probably suffer unacceptable radiation damage on the ESS source) is evaluated. The results indicate that a suitably poisoned liquid H_2 moderator could be an acceptable substitute for a similar poisoned liquid CH_4 moderator.

1. Introduction.

This paper considers a fundamental issue in the design of a target for a pulsed neutron source. The calculations were performed primarily for the ESS study, but the results and conclusions are relevant to the design of any powerful spallation source.

A conventional spallation target consists of a single unit containing a high volume fraction of a heavy material, e.g. uranium or tantalum. For the purpose of maximizing neutron current, the best arrangement of moderators would be the 'slab' geometry (i.e. an arrangement similar to Fig. 2 without the target gap). However, this concept is normally rejected on the grounds that the beam lines view the target directly; it is widely believed that the resulting γ and fast neutron backgrounds would be unacceptable. The geometry which is used in practice is the 'wing' geometry (see Fig. 3). This reduces the backgrounds by many orders of magnitude, at the cost of a reduction in moderator performance by about a factor of two.

Keywords: ESS, Spallation, Moderators, Target

An alternative design involves a split target divided into two or more sections. It is then possible to arrange moderators in a 'flux trap' geometry as in Fig. 2. Some of the advantages of slab geometry are then available, without the excessive backgrounds.

A second issue which this paper examines is the optimization of a cold moderator to be used in place of a poisoned liquid methane moderator as employed on ISIS and other current sources. Although the neutronic properties of liquid CH_4 are excellent, its susceptibility to radiation damage probably precludes its use on intense sources such as the ESS; liquid hydrogen, which is essentially immune to radiation damage, would be the best alternative.

2. Details of target and beam geometry

2.1 Conventional Target

The model used for the conventional target is an approximate representation of the ESS tantalum target [1, 2]. For the purposes of our calculations the existing ISIS target-moderator-reflector geometry was used, with the proton energy increased to 1.334 GeV in accordance with the agreed value for the ESS study [3].

A horizontal section through the geometry is shown in Fig. 1. This shows the target, whose diameter is 10cm, and length 33.5cm, measured from the front of the first plate to the rear of the last. The target is flanked by 'cooling wings' represented by a homogenized mixture of stainless steel and heavy water, and a reflector represented by a homogenized mixture of beryllium and heavy water (80% Be, 20% D_2O by volume).

Apart from the energy, the parameters of the proton beam were based on measured values for the ISIS target. A Gaussian profile was specified with σ=1.5cm and a cutoff radius of 3σ, giving a beam diameter of 9cm.

2.2 Split Target

For reasons of simplicity we proposed a two-component target incorporating both wing and flux trap moderators [4].

Figure 2 shows a horizontal section through the target-moderator-reflector configuration, the overall dimensions of which are an $80 \times 80 \times 80$ cm^3 cube. The lengths of the front and rear sections are 15cm and 20cm respectively, and the 'void' between the two target sections is 10cm. (Most of this space is a void; however, it contains two stainless steel windows, at the rear of the front target section and *vice versa*.) Details of the materials used in the calculation (as numbered in Fig. 2 is listed in Table 1.

Four calculations were performed with target diameters D_T of 10cm, 12cm, 14cm and 16cm. In each case a parabolic beam profile was used with a beam diameter D_B given by $D_B = D_T - 4$cm. A proton beam energy of 1.334 GeV was again specified.

For purposes of comparison the 10cm target was also run with the same beam profile as the conventional target: a 9cm diameter, a Gaussian profile and a 3σ cutoff.

3. Moderator design

3.1 Conventional Target

A horizontal section through the upper moderators, all of which are in 'wing' geometry, is shown in Fig. 3. The lower moderators, which comprise an 'upstream' liquid methane moderator and a

Table 1: List of material numbers as used in the calculations for the split target geometry. Note: percentage compositions are by volume.

Material No.	Description
0	Void
3	Light water
5	Be (70%) + D_2O (30%) (homogenized reflector/coolant)
6	Gadolinium (moderator poison)
7	Cadmium (decoupler for H_2 flux trap moderator)
11	Liquid para-hydrogen
14	Boral (decouplers and liners)
16	Stainless steel (50%) + D_2O (50%) (target pressure vessel and coolant, homogenized)
18	Tantalum (80%) + D_2O (20%) (target material and coolant, homogenized)

'downstream' liquid H_2 moderator, have a similar configuration below the target. Calculations were also performed for three alternative configurations in which the methane moderator was replaced by a liquid para-hydrogen moderator of thickness 6cm, 8cm or 10cm. Only the geometry of the moderator and its aluminium containers was varied; the boral and stainless steel decouplers and liners remained the same in all cases.

The parameters of the four moderators, and the three alternative liquid hydrogen moderators, are summarized in Table 2.

3.2 Split Target

The two pairs of moderators each consisted of a water moderator and a liquid hydrogen moderator (assumed to be pure para-hydrogen). The transverse dimensions of the moderators were $12 \times 12\text{cm}^2$ for the flux trap moderators, and $10 \times 10\text{cm}^2$ for the 'wing' moderators. Further information about the parameters of the moderators is given in table 3.

The arrangement of the flux trap moderators and their associated beam ports is shown in Fig. 2. There was one wing moderator of thickness 5cm with decoupler and poison above the front target module and below it there was a 10cm thick wing moderator with no decoupler or poison.

In all cases the upper and lower boundaries of the beam ports were specified as parallel, horizontal surfaces. However, the vertical surfaces were made to diverge at an angle of 15° relative to a direction normal to the target axis.

4. Computational details

The calculations were performed using the LCS suite of codes [5]. The code LAHET was used for the high energy calculation (> 20MeV), and the neutron transport calculation was continued down to thermal energies using the code HMCNP4A, a version of MCNP modified to interface

Table 2: Moderator parameters for the conventional target. (Dimensions in cm. except where stated. Decouplers are equidistant from the two moderator faces unless otherwise stated.)

Moderator	**Dimensions (cm^3)**	**Decoupler**	**Poison**
H_2O (upstream) (300K)	12.5 × 12.0 × 4.5	6.5mm Boral	2 × .025mm Gd (each 1.05cm from nearest face.)
H_2O (downstream) (300K)	12.5 × 12.0 × 4.5	6.5mm Boral	.05mm Gd
CH_4 (upstream) (90K)	11.5 × 12.0 × 4.4	6.5mm Boral	.05mm Gd
Para-H_2(downstream) (20K)	12 × 11 × 7.6	1mm Cd	None
20K para-H_2 used in place of CH_4:			
6cm thickness	11.5 × 12.0 × 6	6.5mm Boral	.05mm Gd
8cm thickness	11.5 × 12.0 × 8	6.5mm Boral	.05mm Gd
10cm thickness	11.5 × 12.0 × 10	6.5mm Boral	.05mm Gd

Table 3: Moderator parameters for the split target.

Material	**Dimensions (cm^3)**	**Decoupler**	**Poison**
H_2O (wing)	10 × 10 × 5	6mm boral	.05mm Gd
H_2 (wing)	10 × 10 × 10	None	None
H_2O (flux trap)	12 × 12 × 5	6mm boral	.05mm Gd
H_2 (flux trap)	12 × 12 × 10	1mm Cd	.05mm Gd

with other LCS codes.

The moderator performance in this paper was characterized by an estimate of the outgoing neutron current at 1eV in a direction normal to the moderator surface. This quantity was derived from the surface current J_{calc} in the energy range 1eV to 1.47eV and in an angular bin defined by

$$0.75 < \cos\theta \leq 1.0$$

where θ represents the direction of the neutron relative to a normal to the moderator surface.

In general the outgoing current $J(\theta)$ from a moderator conforms to the approximate relationship

$$J(\theta) = J(0)\cos^2\theta \tag{1}$$

On the basis of equation (1) it can be shown that the relationship between $J(0)$ and J_{calc} is approximately

$$J_0 = 1.30 J_{calc}$$

Equation (1) can also be used to estimate the reduction in moderator performance when it is viewed at a significant angle to the normal. For example, if an instrument sees the moderator surface at an angle $\theta = 20°$ this will reduce the detected neutron intensity by a factor of $\cos^2 20° = 0.883$.

5. Results and conclusions

5.1 Conventional target

The results of the calculation of 1eV leakages (in a direction orthogonal to the surface of the moderator) are shown in Table 4. An interesting aspect of these results is the relatively small difference between the performance of 'upstream' and 'downstream' moderators. On the current ISIS target, with a proton beam energy of 800 MeV (as compared with 1.334 GeV for these calculations), the performance of the downstream moderators is worse than that of the upstream moderators by about a factor of two. It should be noted that our result is dependent on the placement of the moderators relative to the position of peak neutron 'brightness' from the target. In the ISIS target (proton energy 800 MeV) the front moderators coincide with the peak. The higher proton energy in our calculations shifts the peak further down the target so that it lies between the front and rear moderators, equalizing their performance. However, the positioning of moderators on the current ESS tantalum target (as modelled in [1]) is similar to ISIS; the front moderators are placed at the peak in neutron production, and the rear moderators again give a performance which is worse by about a factor of two.

Figs. 4 and 5 show the calculated leakage spectra below 1 eV for the methane moderator and the three replacement hydrogen moderators. The spectra were tallied in equal-lethargy energy groups, with six groups per decade.

The results indicate that a disadvantage of the hydrogen moderator would be a relatively poor performance in the energy range 20 to 100 meV; in the worst energy group the leakage from hydrogen is lower from methane by about a factor of two.

Table 4: Calculated 1eV fluxes from the conventional target. The quantity $J(0)_{1eV}$ represents the neutron current at 1eV per Sr per eV per cm^2 per second. The beam power of 1MW represents a proton current of 750μA or 4.68×10^{15} protons per second.

Moderator	$J(0)_{1eV}$
H_2O (upstream)	$2.77 \times 10^{11} \pm 2.3\%$
H_2O (downstream)	$2.33 \times 10^{11} \pm 3.5\%$
CH_4 (upstream)	$2.42 \times 10^{11} \pm 0.8\%$
H_2 (downstream)	$2.78 \times 10^{11} \pm 3.3\%$
Replacement H_2 upstream moderators:	
6cm	$2.24 \times 10^{11} \pm 1.3\%$
8cm	$2.33 \times 10^{11} \pm 1.3\%$
10cm	$2.50 \times 10^{11} \pm 1.2\%$

Figs. 6 to 8 show examples of the calculated thermal time distributions for the methane and hydrogen moderators. The upper energy limit (indicated by a vertical dotted line in Figs. 4 and 5) was 46.5 eV for liquid methane or 21.5 eV for liquid hydrogen.

Table 5 shows calculated pulse width parameters for the four alternative moderators. Here the quantity Δt_n represents the full width of the pulse at $n\%$ of its peak height [6]. Thus Δt_{50} represents the full width at half maximum (FWHM); the other Δt_n values indicate how rapidly the leakage intensity decays at later times.

The results indicate that an 8cm thick hydrogen moderator would produce a similar thermal time distribution to the 4.4cm methane moderator. The choice of an optimum thickness for the hydrogen moderator would be a compromise between the requirements of high neutron leakage and short time distributions. On the basis of these results, a thickness of about 8cm would be a reasonable choice. However, further optimization of a hydrogen moderator would probably be possible, e.g. by the use of a somewhat thicker moderator with two decoupler foils.

The anomalous thermal spectrum seen for the hydrogen moderator, with its strange peak at about 4 meV, is in conflict with measured spectra whose shape conforms more closely to a Maxwellian. It is believed that this result arises from the use of pure para-hydrogen in the model. A small proportion of ortho-hydrogen is probably be present in practice, and would significantly increase the total cross section at low energies.

Fig. 9 presents the results of a preliminary calculation to investigate the effect of a small proportion of ortho-hydrogen in the moderator. The spectrum from an 8cm liquid hydrogen moderator with with 5% ortho-, 95% para-hydrogen is compared with the spectrum previously calculated for a pure para-hydrogen moderator. The presence of the ortho-hydrogen changes the thermal spectrum significantly, removing the anomalous peak.

Table 5: Calculated pulse width parameters (in μs) for alternative poisoned methane and hydrogen moderators.

Moderator	Δt_{50}	Δt_{30}	Δt_{10}	Δt_3	Δt_1
Methane (4.4cm)	26	43	79	126	175
Hydrogen (6cm)	24	34	57	93	146
Hydrogen (8cm)	30	43	71	121	180
Hydrogen (10cm)	37	52	91	145	211

Table 6: Results of moderator performance calculations. The quantity $J(0)_{1\text{eV}}$ represents the neutron current at 1eV per Sr per eV per cm^2 per second. The beam power of 1MW represents a proton current of 750μA or 4.68 $\times$ 10^{15} protons per second.

Target dia. D_T(cm)	10	10	12	14	16
Beam dia. D_B(cm)	9	6	8	10	12
Beam Profile	Gaussian (3σ cutoff)	Parabolic	Parabolic	Parabolic	Parabolic
Moderator	$J(0)_{1\text{eV}}(\times 10^{11})$				
H_2O (flux trap)	2.09 $\pm$ 1.8%	2.16 $\pm$ 1.8%	2.10 $\pm$ 1.8%	1.91 $\pm$ 1.8%	1.80 $\pm$ 2.0%
H_2 (flux trap)	2.38 $\pm$ 1.9%	2.46 $\pm$ 2.0%	2.26 $\pm$ 2.0%	2.25 $\pm$ 2.0%	2.02 $\pm$ 2.1%
H_2O (wing)	2.28 $\pm$ 1.5%	2.36 $\pm$ 1.4%	2.10 $\pm$ 1.5%	1.89 $\pm$ 1.6%	1.72 $\pm$ 1.6%
H_2 (wing, no poison/decoupler)	3.20 $\pm$ 1.4%	3.19 $\pm$ 1.3%	2.90 $\pm$ 1.4%	2.59 $\pm$ 1.4%	2.31 $\pm$ 1.6%

5.2 Split target

The results of the calculation for $J(0)_{1\text{eV}}$ are given in Table 6. The results for the cases with a parabolic beam profile are presented in Figs. 10 and 11, in the form of plots of $J(0)_{1\text{eV}}$ vs. target diameter D_T. Figs. 10 and 11 show the results for flux trap and wing moderators, respectively.

The following conclusions can be drawn from the results:

1. The results in Table 6 indicate that the moderator performance is insensitive to the precise choice of beam profile. Here the change in $J(0)_{1\text{eV}}$ when the Gaussian profile is used in place of the parabolic profile is not statistically significant.

2. An optimum moderator configuration should probably match the performance of moderators in different locations. The chosen target-moderator configuration achieves this: the 'wing' moderators placed above and below the front section of the target give a similar performance to the

corresponding flux trap moderators.

3. A comparison of the plots in Fig. 10 and Fig. 11 reveals an interesting result: the performance of flux trap moderators is much less sensitive to target diameter than the performance of wing moderators.

4. A direct comparison between the two targets is possible for the two water moderators on the 10cm targets.

A comparison of the 'upstream' (front) water moderators on the two targets favours the conventional design. (See Tables 4 and 6. This moderator gives $J(0)_{1eV} = 2.77 \times 10^{11}$ neutrons cm^{-2} eV^{-1} Sr^{-1} on the conventional target, compared with 2.28×10^{11} on the comparable split target (about 80% of the performance on the conventional target.) In the case of the 'downstream' water moderator the results are more similar: 2.33×10^{11} for the conventional target and 2.09 $\times 10^{11}$ for the split target (about 90% of the performance on the conventional target.) Some caution must be exercised in interpreting this result, because no attempt has been made to arrive at a fully optimized configuration for the split target. However, it appears that the split target, as modelled for this paper, offers no advantage over a conventional target. This conclusion might be modified if the target diameter had to be increased substantially above 10cm. As indicated by Figs. Fig. 10 and Fig. 11, the consequent reduction in moderator performance would be significantly less for flux trap moderators than for wing moderators.

6. Acknowledgements

L.L. Daemen (Los Alamos National Laboratory) is acknowledged for the provision of geometry and materials specifications for the ISIS target.

7. References

[1] D. Filges, "Nuclear studies of different target systems for the European Spallation Source" and B. Guttek, "Actual state of the ESS tantalum target station." Papers presented at ICANS-XIII, October 11-14 1995, Villigen, Switzerland.

[2] I.S.K. Gardner, H. Lengeler and G.H. Rees, "Outline design of the European spallation neutron source." ESS Report no. ESS 95-30-M, September 1995.

[3] D.J. Picton, T.D. Beynon and T.A. Broome, "Performance of a liquid hydrogen moderator on the 1MW reference target." Paper presented at the Third General ESS Meeting, Baden, 22-25 March 1993.

[4] D.J. Picton, T.D. Beynon and T.A. Broome, "Moderator performance for the split target option for the 1MW Target station." Paper presented at the Third General ESS Meeting, Baden, 22-25 March 1993.

[5] R.E. Prael and H. Lichtenstein, "User Guide to LCS: the LAHET Code System," Radiation Transport Group, Los Alamos Laboratory. LANL Report no. LA-UR-89-3014 (1989)

[6] D.J. Picton, D.K. Ross and A.D. Taylor, "Optimization Studies for a Moderator on a Pulsed Neutron Source", *J. Phys. D* **15**(1982), 2369-2400.

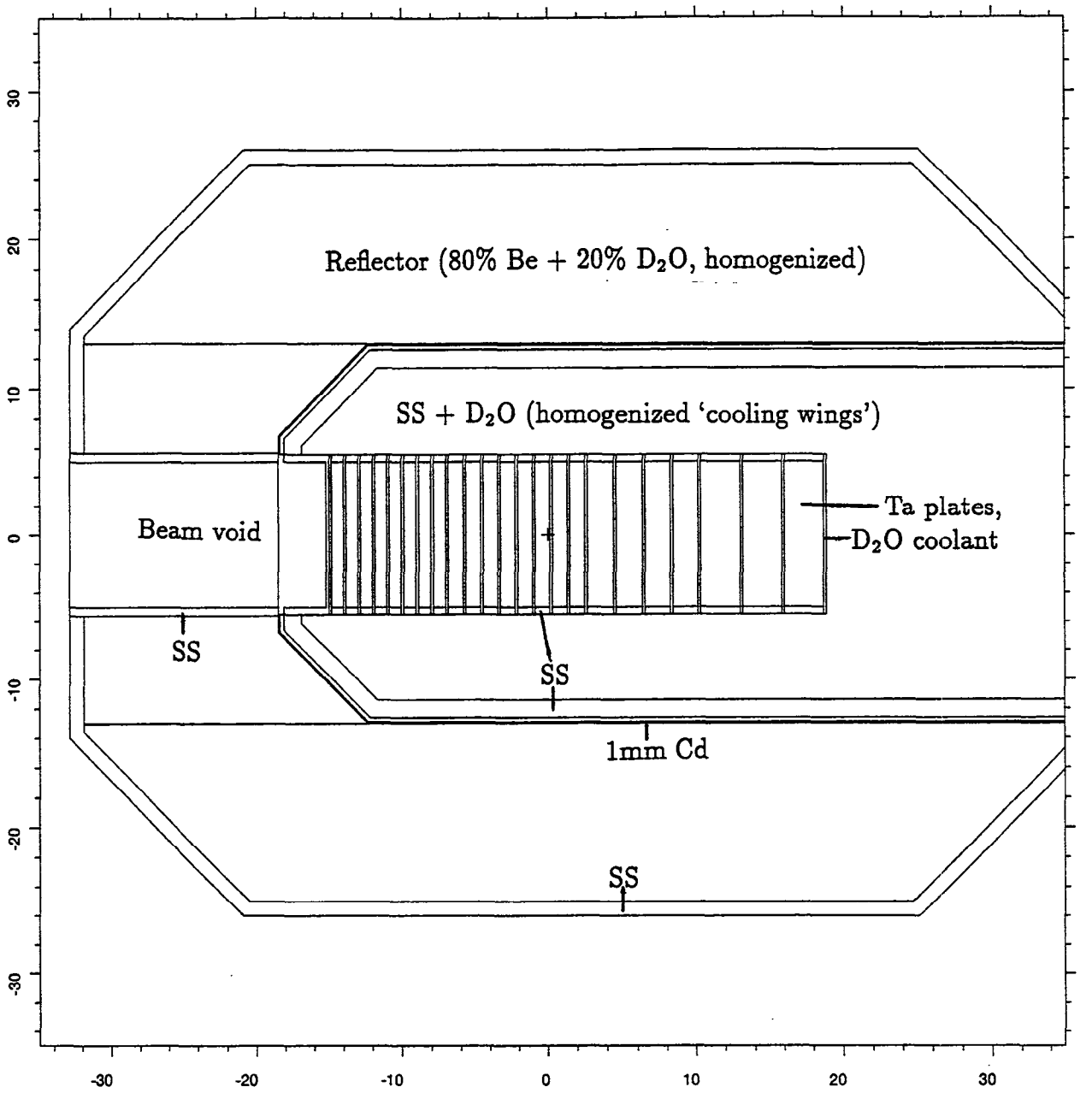

Fig. 1. Horizontal section through the conventional target showing the major components of the target-reflector assembly.

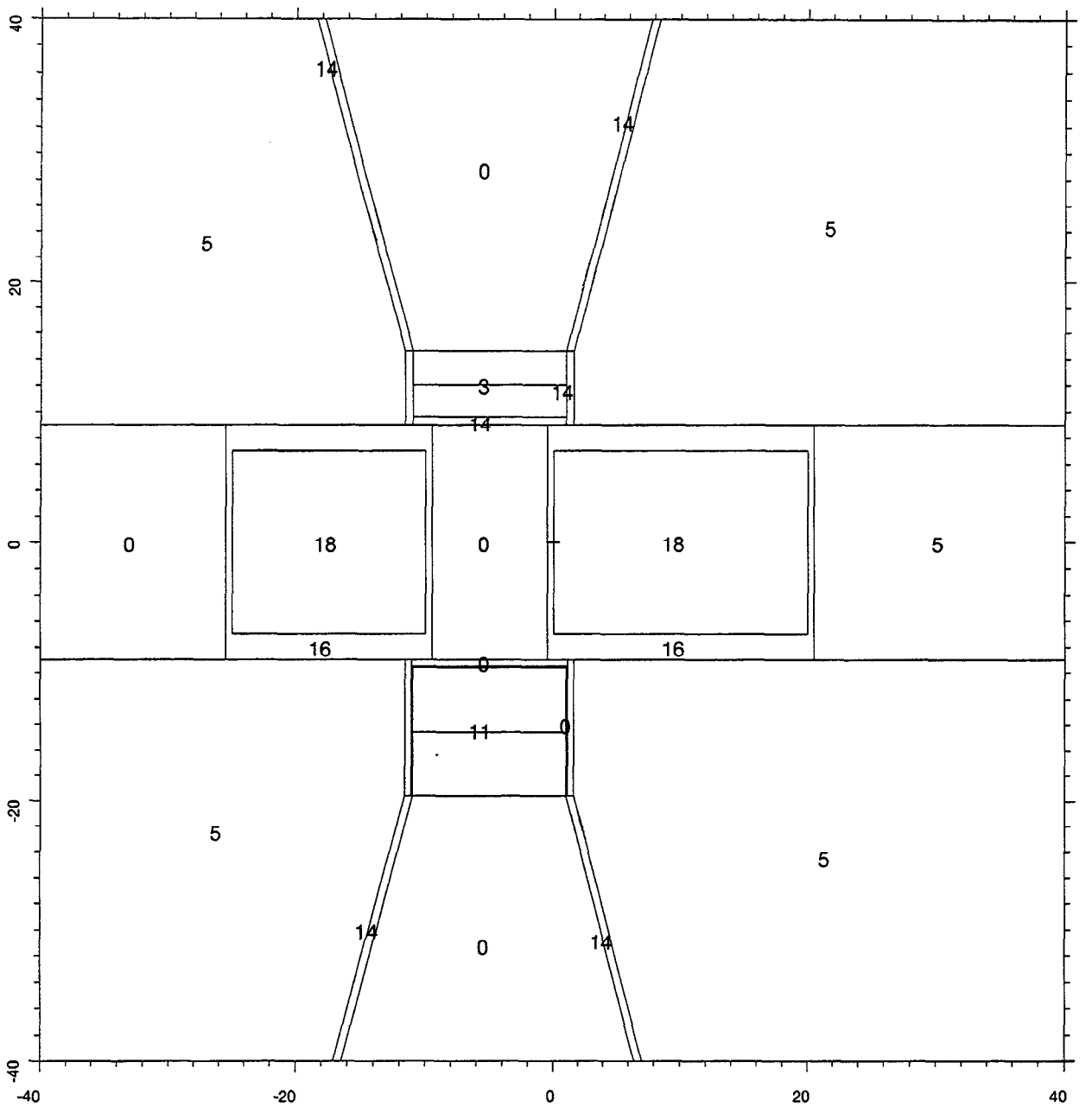

Fig. 2. Horizontal section through the split target geometry showing the front (left) and rear (right) target sections and the two flux trap moderators. The material numbers are listed in Table 1.

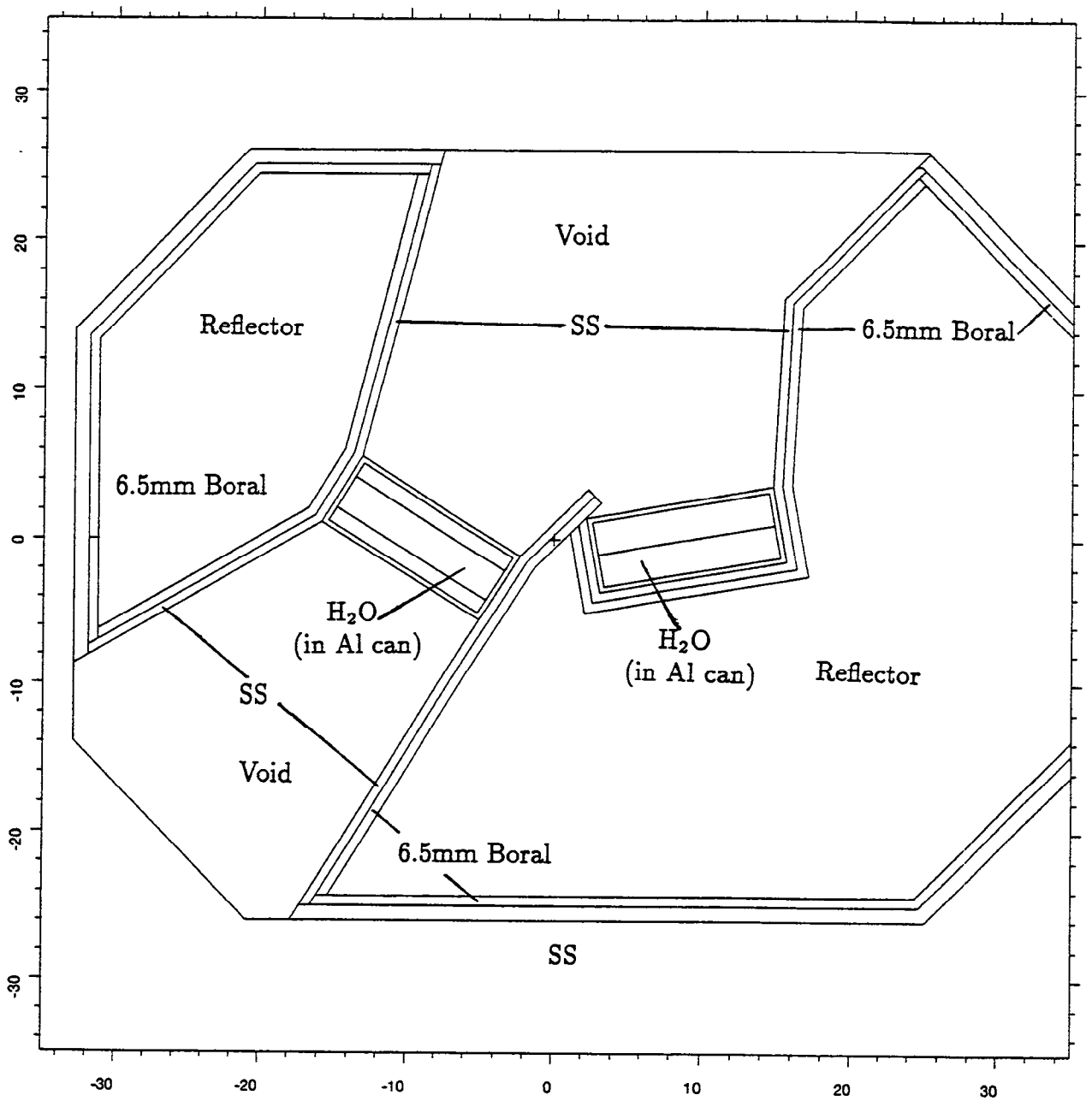

Fig. 3. Horizontal section through the upper (ambient temperature) moderators on the conventional target.

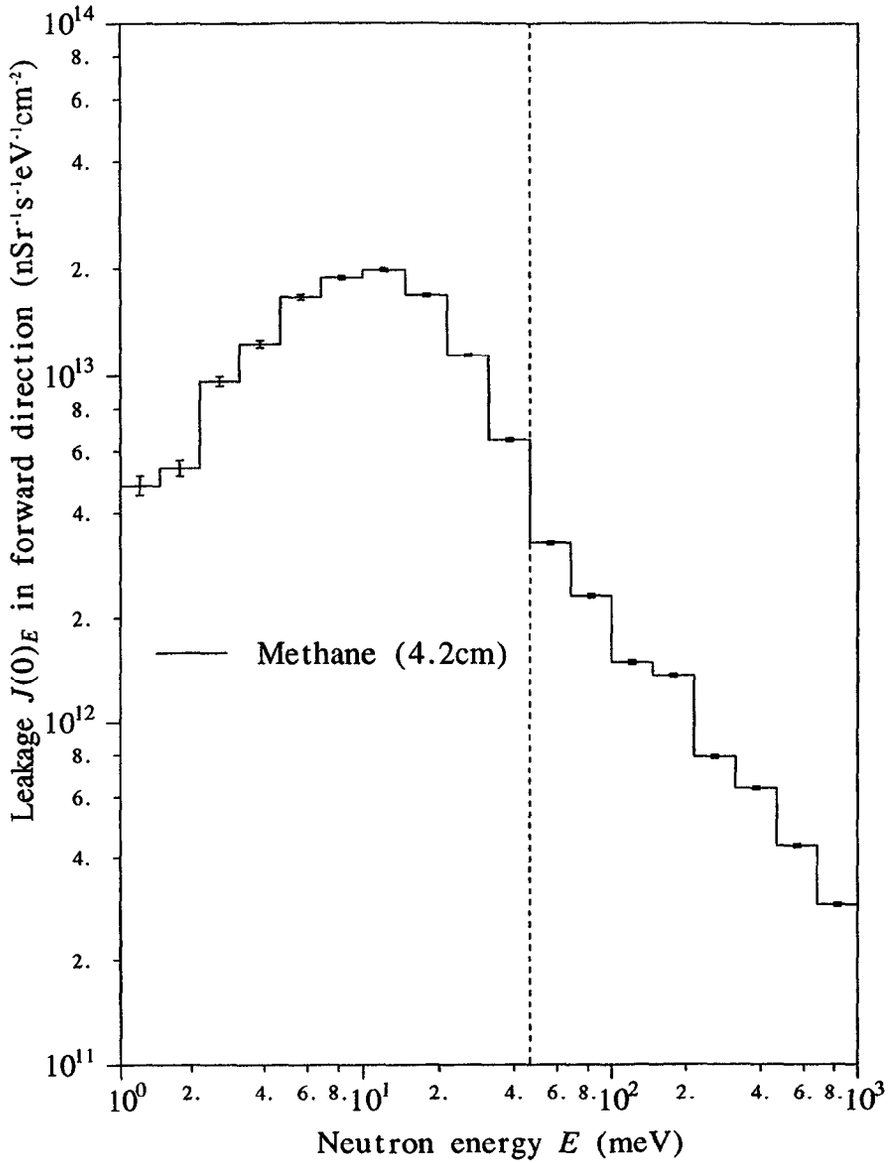

Fig. 4. Calculated leakage spectrum below 1eV from the 'upstream' methane moderator on the conventional target. The horizontal dashed line indicates the upper energy limit used for the calculation of thermal time distributions.

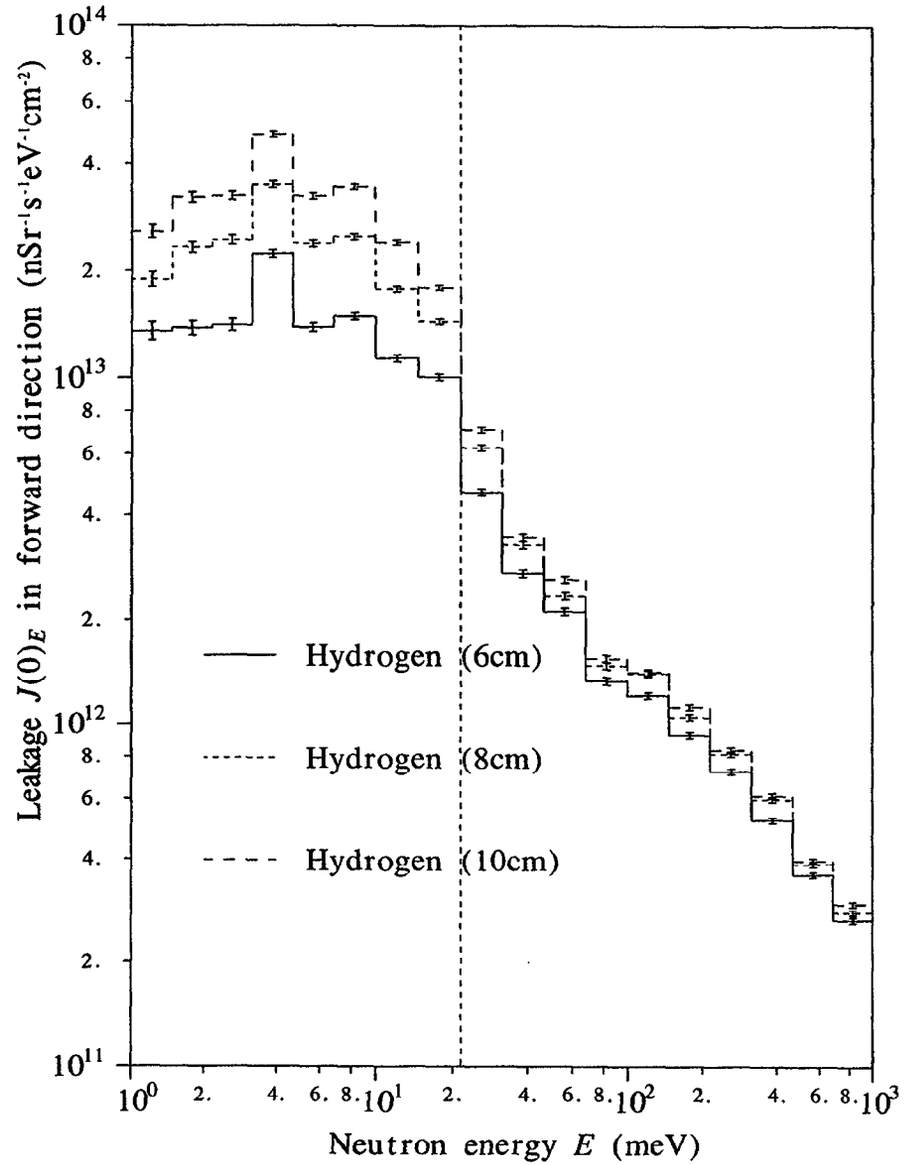

Fig. 5. Calculated leakage spectra from liquid hydrogen moderators used in place of the upstream methane moderator on the conventional target. The horizontal dashed line indicates the upper energy limit used for the calculation of thermal time distributions.

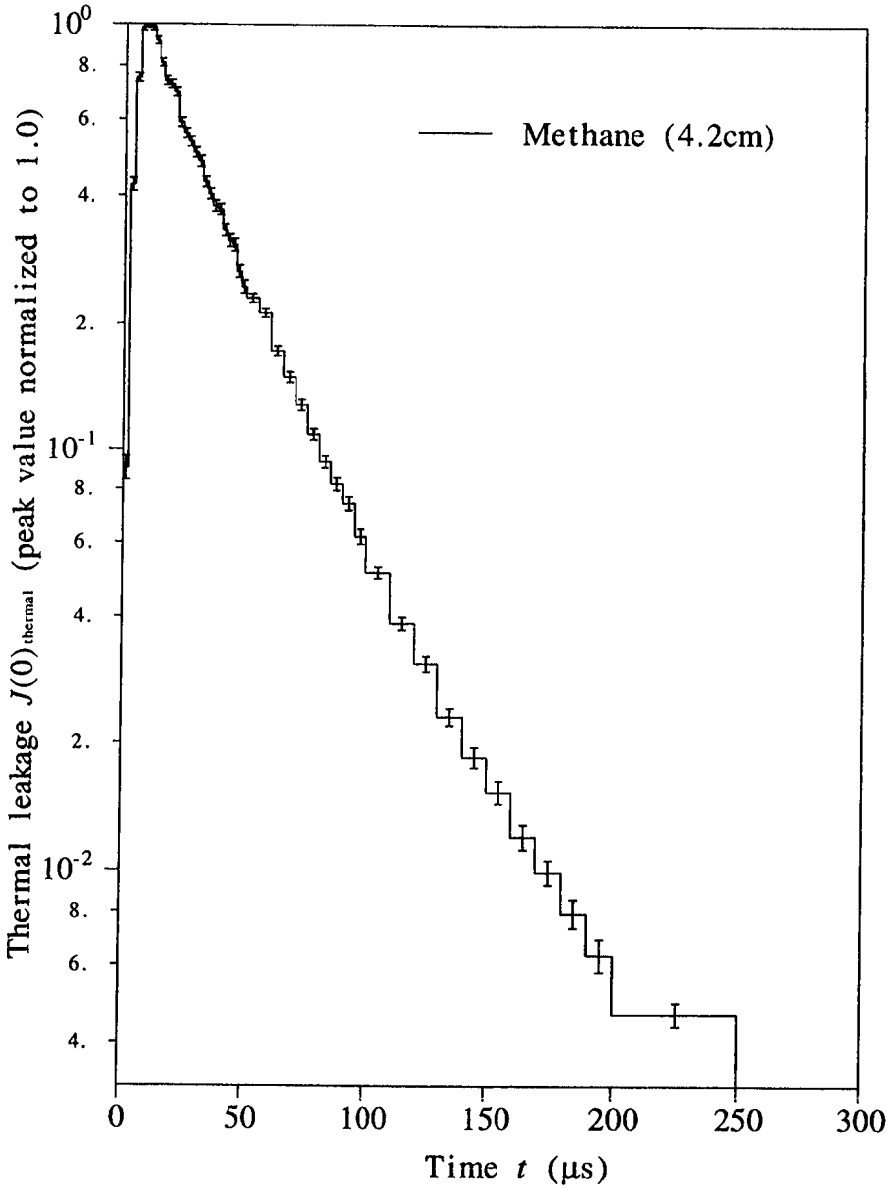

Fig. 6. Calculated thermal time distribution for the methane moderator on the conventional target.

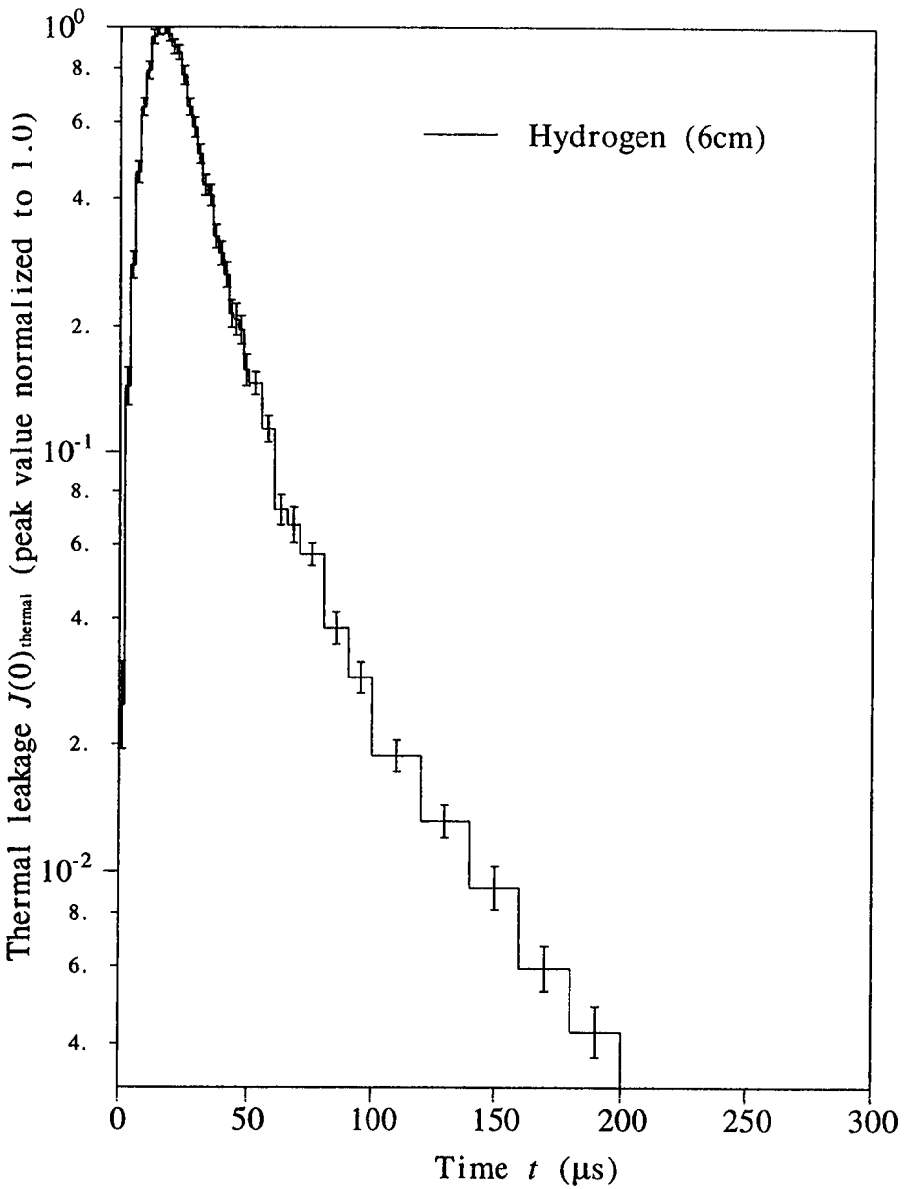

Fig. 7. Calculated thermal time distribution for the 6cm hydrogen moderator used in place of the methane moderator on the conventional target.

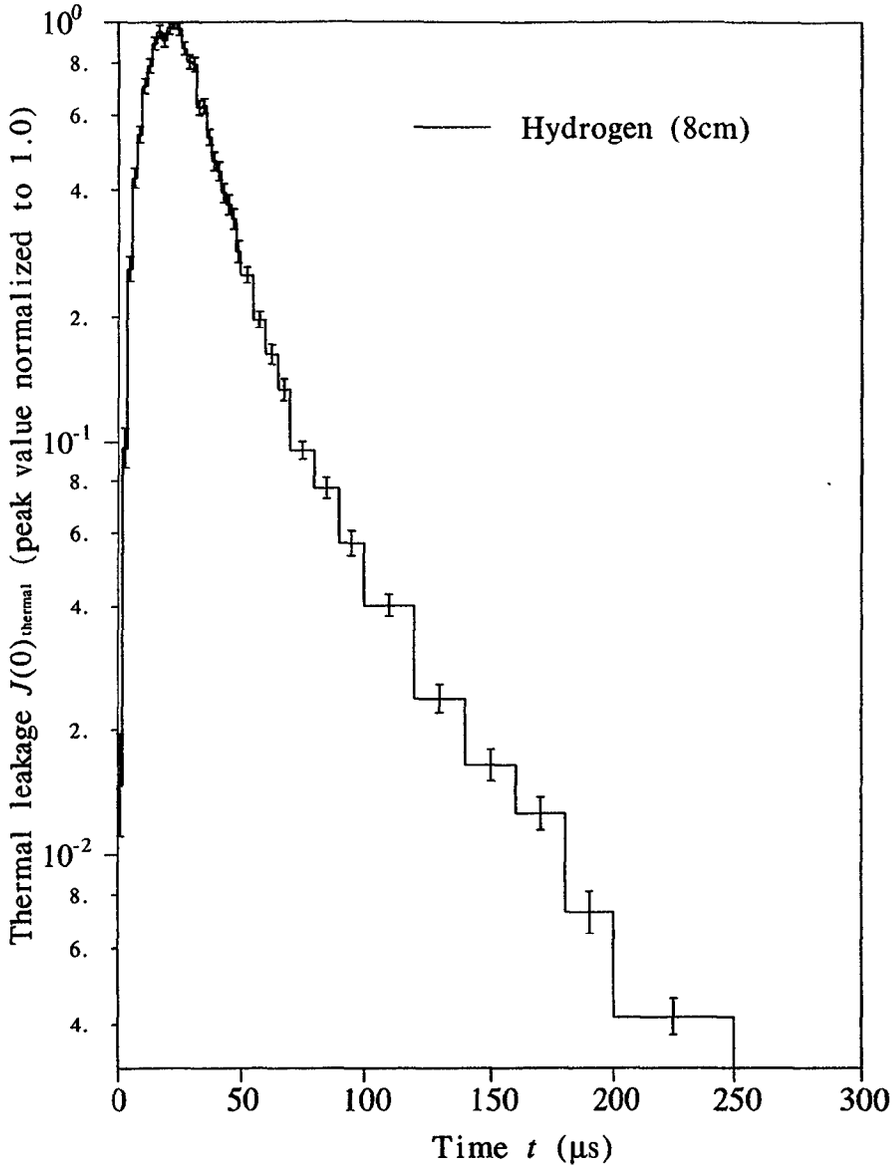

Fig. 8. Calculated thermal time distribution for the 8cm hydrogen moderator used in place of the methane moderator on the conventional target.

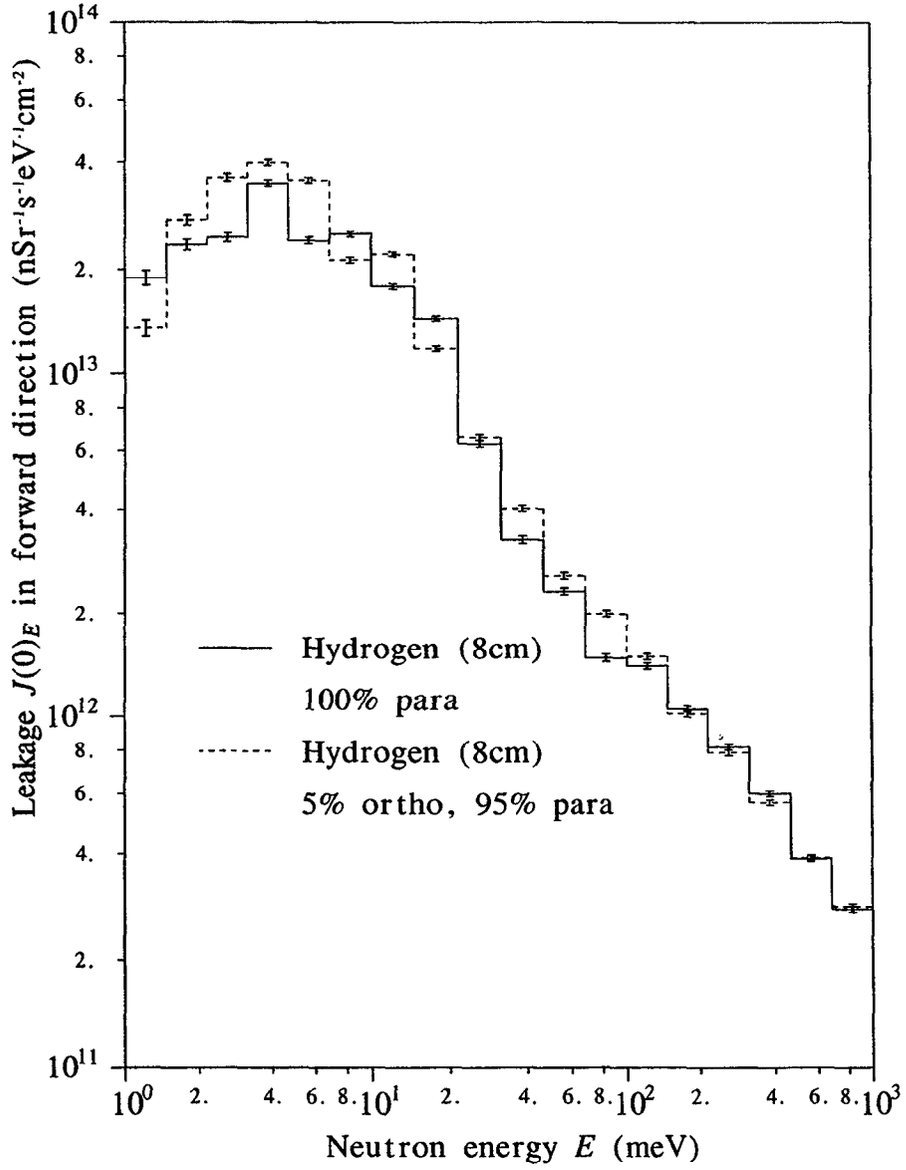

Fig. 9. Comparison of calculated neutron spectra from pure para-hydrogen (8cm) and 5% ortho-, 95% para-hydrogen (8cm).

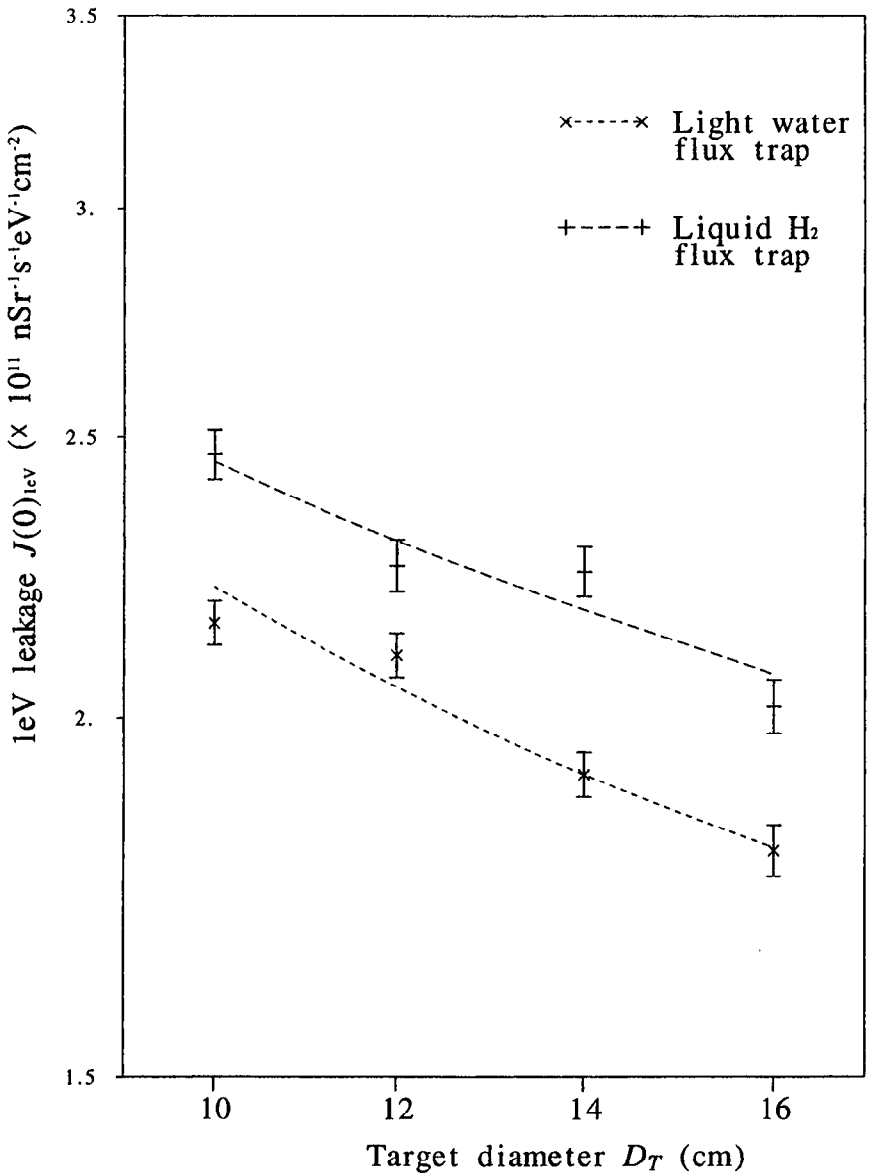

Fig. 10. Performance of the flux trap moderators on the split target (characterized by the 1eV leakage) as a function of target radius.

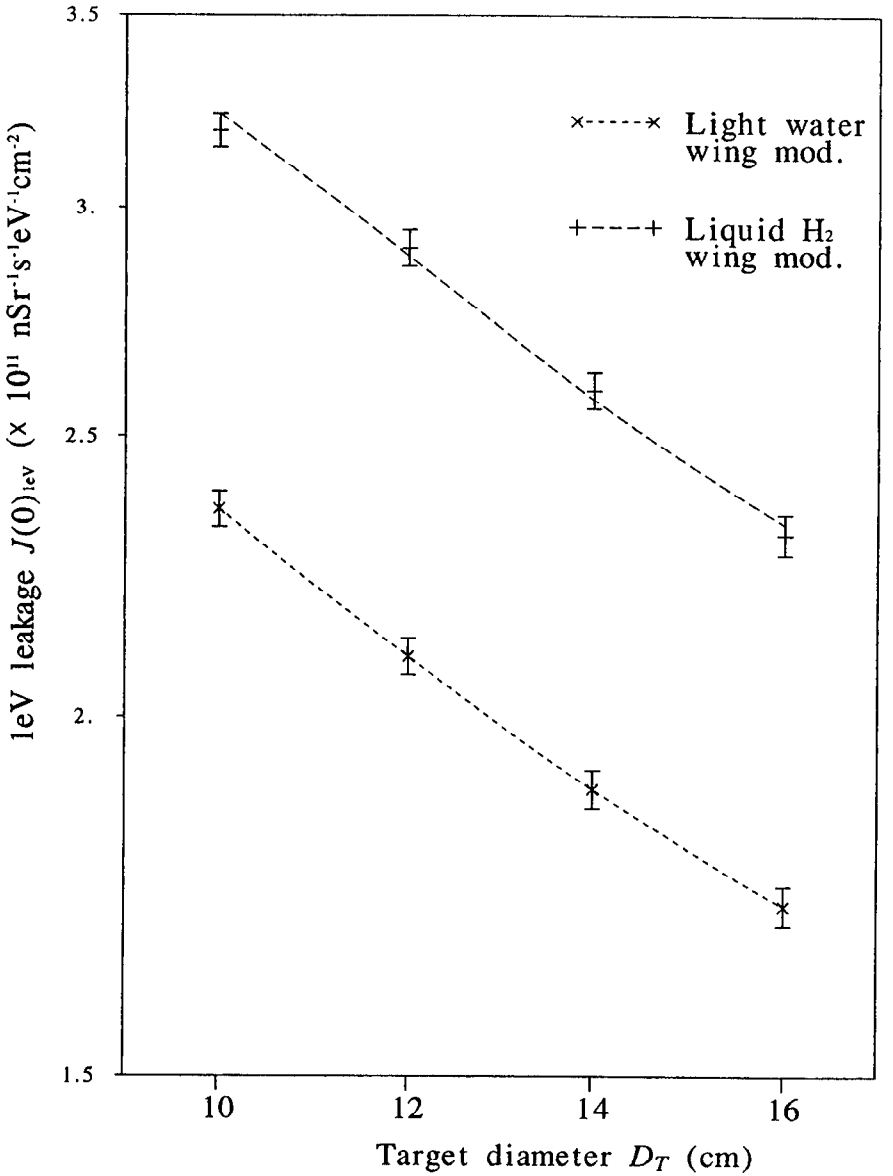

Fig. 11. Performance of the wing moderators on the split target (characterized by the 1eV leakage) as a function of target radius.

ICANS-XIII
13th Meeting of the International Collaboration on
Advanced Neutron Sources
October 11-14, 1995
Paul Scherrer Institut, 5232 Villigen PSI, Switzerland

NUCLEAR STUDIES OF DIFFERENT TARGET SYSTEMS FOR THE EUROPEAN SPALLATION SOURCE (ESS)

D. Filges, R.D. Neef and H. Schaal
Forschungszentrum Jülich GmbH, Institut für Kernphysik, D-52425 Jülich, Germany

ABSTRACT

This paper summerizes nuclear simulation calculations to study various target concepts for the „European Spallation Source (ESS)" concerning a proton beam power of 5MW.For different target systems as rotating wheel targets,stationary targets and liquid metal targets results of beam energy - and target material investigations,induced radioactivity and afterheat production as well as usuable neutron fluxes are discussed.

1. Introduction

The simulation calculations were done using the HERMES code system [1] .This theoretical study here is directed towards assessing physics feasibility of discussed ESS target station concepts.The aim is to show the feasibility of the anticipated nuclear parameters,which will be necessary for the evaluation of the final design.

2. Beam Energy Studies

One of the first questions to us was which is the optimum proton beam energy in respect to a high thermal neutron flux in the moderators, to a long lifetime of target windows and target material, and in respect of necessary cooling power. From the experience of running spallation sources it was clear that proton beam energy should be in the energy range from 800 MeV up to 3000 MeV. In the beginning of the project we calculated a double wheel target (Fig. 1) and a double split target (Fig. 2) with three moderator positions with first moderator in front of the target, second moderator in flux trap position between target one and two, and third moderator behind second target. In Fig. 3 we can see a linear decrease of thermal neutron flux of the upstream moderator with increasing proton energy from 800 MeV up to 3000 MeV. The proton beam energy dependent thermal neutron flux in the intermediate moderator, decreases less with proton energy at a higher flux level. In contrary to neutron flux dependence

Keywords: Spallation, Simulation, ESS-Targets

in moderators above the thermal neutron flux in the downstream moderator increases with increasing proton beam energy. Around 1500 MeV proton beam energy fluxes of up- and downstream moderators have similar values. Therefore, from neutron flux calculations there is no strong tendency to a special proton beam energy and either energy should be good.

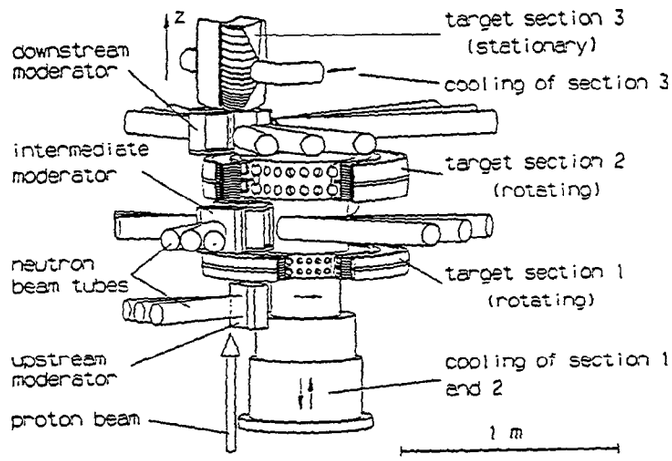

Fig. 1: Rotating double split target for vertical proton beam injection (rotation frequency 1 Hz)

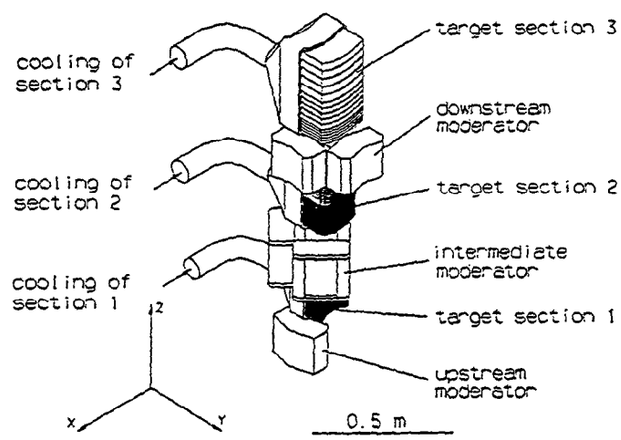

Fig. 2: Stationary double split target for vertical proton beam injection

Figure 4 shows the proton energy dependent power deposition in the first part of the split target and in the whole target. Between 800 MeV and 1600 MeV there is a strong decrease of power deposition which is much less versus higher proton energies. From this figure the proton beam for a target should not be far below 1500 MeV.

We investigated the power deposition in the target plates in an area of radius 1cm around the proton beam axis. Figure 5 shows a power deposition of 11 kW/cm**3 in the first two target plates. This power deposition is reduced by a factor of two by increasing the proton beam energy from 800 MeV to 1600 MeV. A further doubling of the proton energy gives less reductions than factor two for the power deposition.

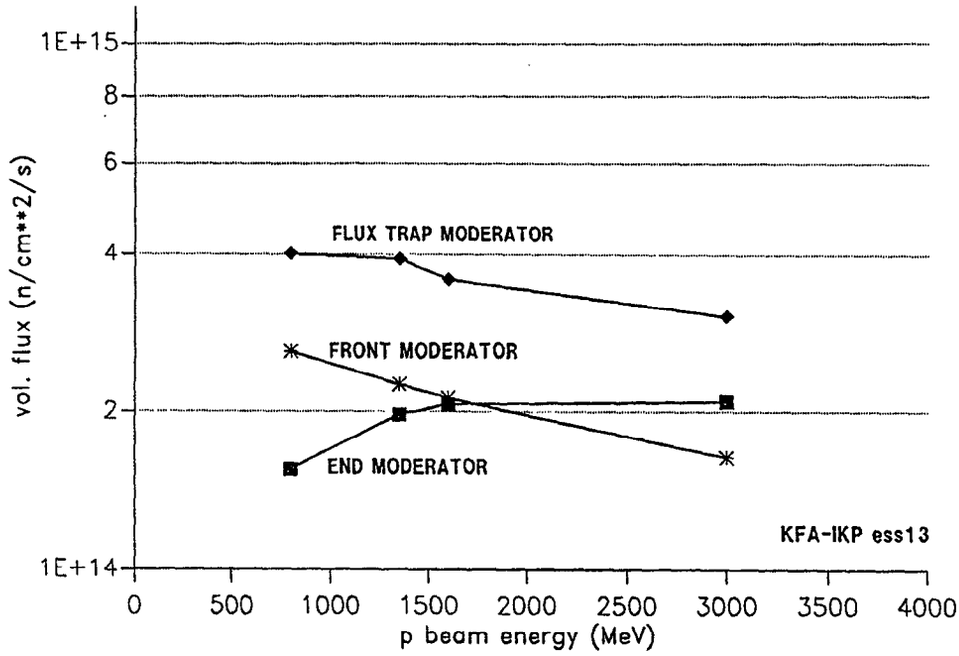

Fig. 3: Thermal neutron fluxes in moderators as a function of incident proton energy

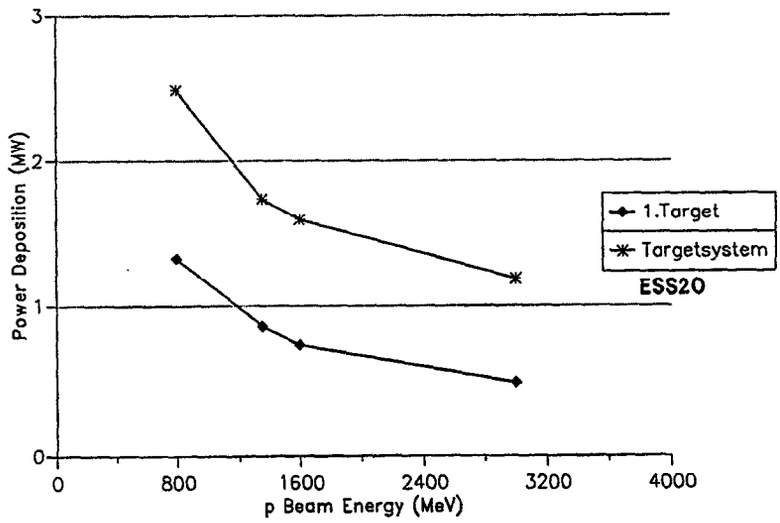

Fig. 4: Energy deposition in target systems as a function of incident proton energy

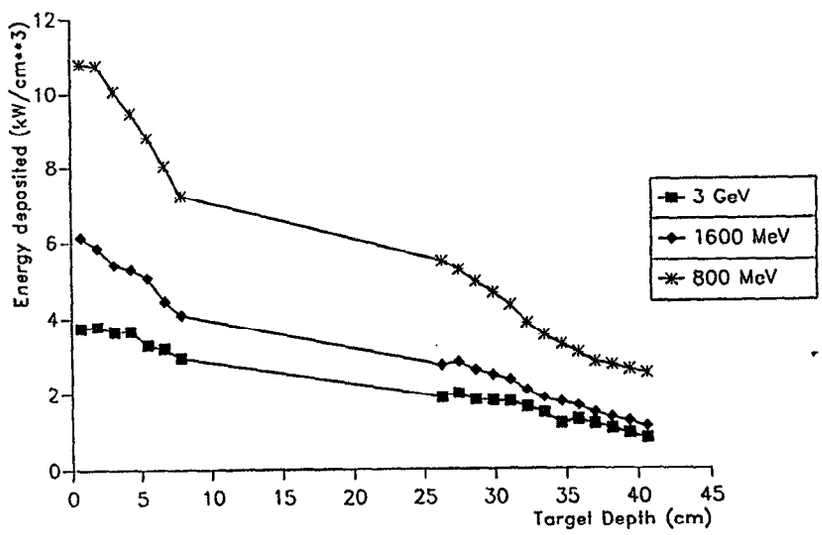

Fig. 5: Energy deposition in target plates in an area of radius 1cm around beam axis

Each proton pulse of a 5 MW at 50 Hz machine contains an energy of 100 kJ which is introduced into the target. This produces a space dependent temperature jump in the target material. In Fig.6 the temperature jump is plotted for the first W-Target plate as functions of proton beam diameter in an area of radius r = 1 cm for three proton energies. We see for a gaussian shaped circular proton beam (σ = 2.5) truncated at diameter 10 cm a temperature jump of 40 K, 25 K, and 15 K for 800 MeV, 1600 MeV, and 3000 MeV, respectively.

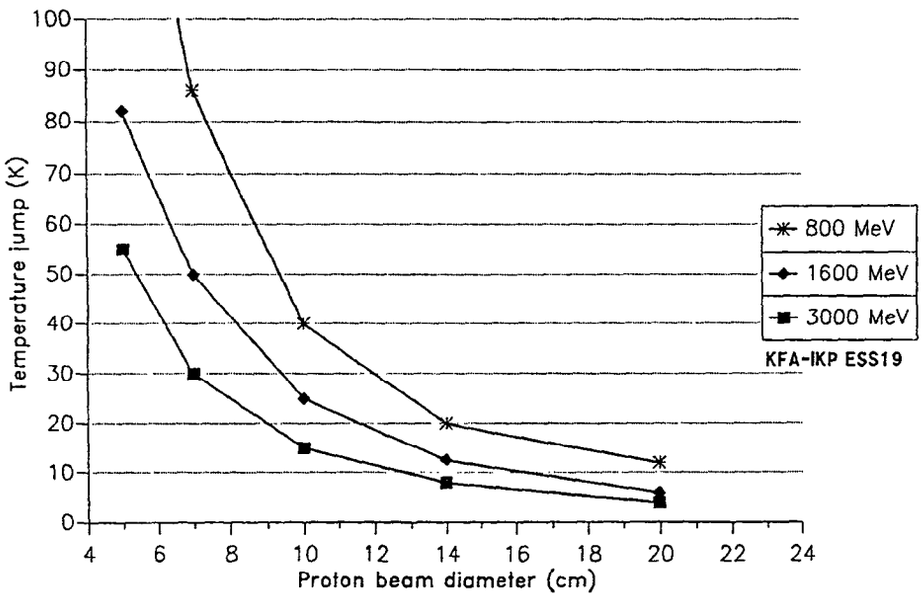

Fig. 6: Temperature jump in tungsten target as a function of proton beam diameter for different beam energies around beam axis

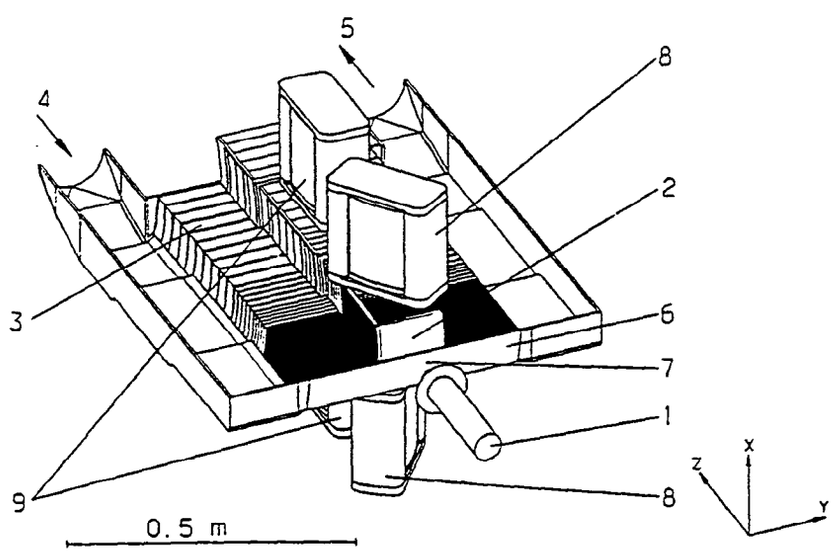

Fig. 7: Reference 5 MW ESS target with moderators
(1: proton beam,2: target plates,3: wing reflctor plates,4: coolant inlet,5: coolant outlet,6: target vessel,7: beam window,8: cold moderator,9: room temperature moderator)

The double wheel split target Fig. 1 and the stationary split target (Fig. 2) from neutronical point of view do not differ much from one another. The rotating target has the advantage that irradiation damages and heat loads of beam window and target plates are considerably lower by a factor of 50 and this means a longer lifetime by a factor of 50. The advantage of the stationary target is the lower fabrication cost. As reference target a non-split stationary target as depicted in Fig. 7 was chosen(see details in Ref. [2].
(ESS reference proton beam energy is 1.334 GeV)

3. ESS Reference Energy Studies

The reference 5 MW target (see Fig. 7) is horizontal, non-split and cooled by H_2O. It consists of three stacks of slightly 1D-bent rectangular plates. The centre stack, made of tantalum as reference material, acts as the target, the two other stacks on its left and right side integrated in the target are part of the reflector and are manufactured of nickel. All stacks are cooled by the same water stream in y-direction. The described target plate configuration has the front (x-y-plane) dimension of 120 x 400 mm^2 which increases to 160 x 400 mm^2 to allow for the scattering of the proton beam. The length (z-direction) of solid target material is 580 mm and, due to the cooling gaps between the plates, the overall length of the target is 690 mm. The rest of the nickel reflector, not shown in Fig. 7, encloses the target inside the volume of 900 x 800 x 1050 mm^3 (x,y,z).The ESS proton beam energy was choosen to 1.334 GeV.

To achieve the same heat flow on the surface of each target plate their thicknesses are increased in bundles of five plates from 2.6 mm up to 30 mm. The total number of plates in each stack is 55. Because of the thickness variation the water content in the cooling gaps decreases from 22% in the first cooling gap down to 8% in the last .The average water content in the target is 10%. The beam window is part of the target container and will be 2D-curved.

To simulate the transport of hadrons and to estimate particle fluxes, energy deposition and induced radioactivity the HERMES code system [1] has been used. First neutron flux estimations for the 5 MW target have been performed under the condition that all four moderators were H_2O-moderators at room temperature. For these calculations the target material was tungsten to compare the results with of the SNQ study [3]. A detailed 3D-geometry configuration of the target has been considered. In Table 1 neutron yields per proton for the reference target with tungsten as target material are compared to various target systems of the SNQ study [3].

Targets and moderators which have been studied in the SNQ project have been compared for their average thermal neutron flux with a similar fast moderator at the ESS target. The average ESS thermal neutron flux differs by less than 5% from that of the corresponding SNQ value, for a 5 MW beam power.

Table 1: n/p values for various targets

target	n/p 1100 MeV	n/p 1334 MeV
SNQ: U_{dep}-H_2O-Al	33.1	40.2
SNQ: Pb-H_2O-Al	21.5	26.0
SNQ: W-H_2O-Al	23.4	28.4
SNQ: W_{solid}	25.6	31.1
ESS: W*	-	31.5

Table 2: Comparison of thermal neutron fluxes in fast moderators of the SNQ and ESS for 5 MW proton beam power

target	$\Phi_{thermal}$ [n/(cm^2·proton)]	$\Phi_{thermal}$ [n/(cm^2·s)]
SNQ: U_{dep}-H_2O-Al	$2.6 \cdot 10^{-2}$	$7.5 \cdot 10^{-14}$
SNQ: Pb-H_2O-Al	$1.6 \cdot 10^{-2}$	$4.5 \cdot 10^{14}$
SNQ: W-H_2O-Al	$1.8 \cdot 10^{-2}$	$5.1 \cdot 10^{14}$
SNQ: W_{solid}	$2.0 \cdot 10^{-2}$	$5.6 \cdot 10^{14}$
ESS: W*	$2.1 \cdot 10^{-2}$	$4.9 \cdot 10^{14}$

One should take into account that the flux values of Table 2 depend on the chosen target-moderator-reflector geometry and should be taken as first approximations of the expected neutron flux.

4. Target Material Studies of Tantalum,Tungsten and Mercury Targets

4.1 Usuable Neutron Fluxes

Based on the above discussed scoping calculations we compared the nuclear properties of three target material candidates, namely tantalum, tungsten, and mercury using the target geometry given in Fig. 7. For optimal positioning of the moderators it is important to know the distribution of the neutron flux density along the surface of the target. In Fig. 8 for bare reference targets (Ta- and W- with water cooling; and Hg-filled,-only with mercury-) we show the surface leakage current distributions of neutrons below energies of 20 MeV as a function of target depth. The tantalum target delivers the lowest neutron current. In the maximum of the neutron current distribution W and Hg target give same values but downstreams the Hg target produces higher currents.

Figure 9 shows for lead-reflected target systems that the tantalum target delivers the lowest neutron current. A tungsten target gives a neutron current which is about 20% higher in the maximum. The highest neutron currents at the target surface are produced by the mercury target and are more than 30% higher compared to the tantalum target. Especially along the target surface the current gradient in case of Hg is lower than in case of the W target. This

means that the downstream moderators receive an even higher percentage of neutrons in case of mercury.

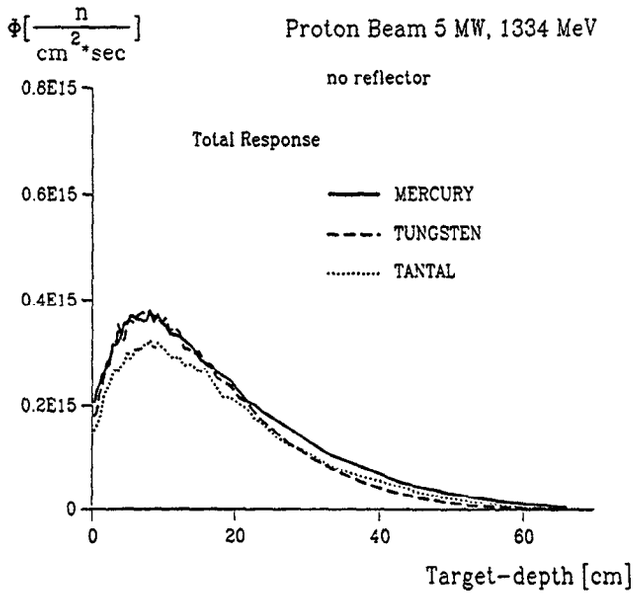

Fig. 8: Leakage distributions for neutrons below 20MeV of bare reference targets

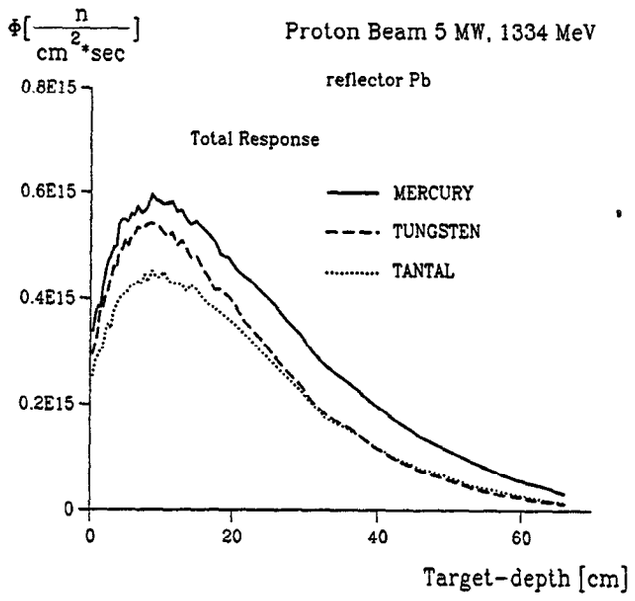

Fig. 9: Leakage distributions for neutrons below 20MeV of reflected reference targets

The following table (Tab. 3) shows a comparison of possible fast and thermal neutron fluxes averaged about the moderator volume.

Table 3: Fast and thermal neutron fluxes of Ta, W, and Hg targets

Target	Φ_{fast} [n/(cm^2 · s · 5 MW)]		$\Phi_{thermal}$ [n/(cm^2 · s · 5 MW)]	
	upstream Moderator	downstream Moderator	upstream Moderator	downstream Moderator
Tantalum	$7.25 \cdot 10^{13}$	$2.30 \cdot 10^{13}$	$3.19 \cdot 10^{14}$	$1.52 \cdot 10^{14}$
Tungsten	$6.42 \cdot 10^{13}$	$2.14 \cdot 10^{13}$	$3.52 \cdot 10^{14}$	$1.67 \cdot 10^{14}$
Mercury	$8.21 \cdot 10^{13}$	$3.52 \cdot 10^{13}$	$3.91 \cdot 10^{14}$	$2.29 \cdot 10^{14}$

4.2 Induced Radioactivity and Afterheat Production

The procedure to calculate the radioactivity and afterheat in the different materials Ta, W, and Hg proposed as ESS target materials consists of using the HERMES system[1] to calculate the nuclide production rates caused by the spallation process and to generate the neutron source and then using MORSE[1] with the recently released cross section library MATXS11[4] to calculate the production rates caused by neutrons with energies below 15 MeV. All nuclide production rates are handed over to the nuclide generation and depletion code ORIHET[5], which calculates radioactivity and thermal power for different beam and decay times.

All calculations described here were performed for ESS beam energy 1.334 GeV and 5 MW proton beam power, i.e. for 3.748 mA beam current. The geometry used for the Monte Carlo calculations is described above. Because the reason of the study is the comparison of the different target materials Ta, W and Hg, we restrict ourselves to calculate the values of the target zones only, assuming that the activity and afterheat of the surrounding reflectors, moderators, and cooling systems are nearly the same for the different target materials. The nuclide generation and depletion was calculated for a full power beam time of 1 year and after shut down of the beam for decay times reaching from 1 day to 100 years. The results are given separately for those caused by spallation and those caused by neutrons with energies below 15 MeV.

The most interesting time with respect to problems of cooling and handling of the target is the time when the beam is shut down. The amount of radioactivity and thermal power for the three different targets is compared in Table 4. It can be seen that the activity and thermal power caused by spallation are nearly the same for all three targets, but the amounts caused by the low energy neutrons are quite different. Therefore the total amount of activity and afterheat is largest in the tantalum target, followed by the tungsten target. Here the mercury target shows the lowest values.

Table 4: Comparison of radioactivity and thermal power at shut down time for different targets for 5 MW proton beam power and 1 year full power operation

	Tantalum	Tungsten	Mercury
Radioactivity [Tbq]			
-total power	$4.55 \cdot 10^5$	$1.63 \cdot 10^5$	$1.10 \cdot 10^5$
-caused by spallation	$6.94 \cdot 10^4$	$7.73 \cdot 10^4$	$7.28 \cdot 10^4$
-caused by neutrons below 15 MeV	$3.85 \cdot 10^5$	$8.75 \cdot 10^4$	$3.67 \cdot 10^4$
Thermal power [kW]			
-total.power	56.9	15.40	9.21
-caused by spallation	8.94	8.75	7.21
-caused by neutrons below 15MeV	48.0	6.60	2.00

Next question is about the long term radioactivity and afterheat production with respect to storage and waste management. The time behaviour of the three targets is shown in Figs. 10 and 11. In Table 5 we give the total values for the time 100 years after shut down. It should be mentioned that the radioactivity and afterheat caused by the low energy neutrons have no importance for the long term behaviour of all targets. Therefore the total amounts given in Table 5 are caused by the spallation products only.

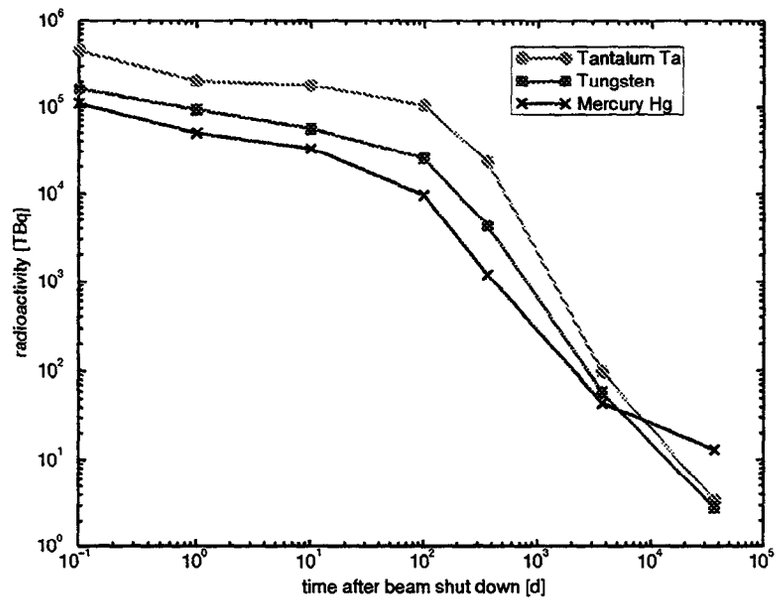

Fig. 10: Time behaviour of radioactivity in Tbq in Ta-, W-, and Hg- targets after 1 year full power operation

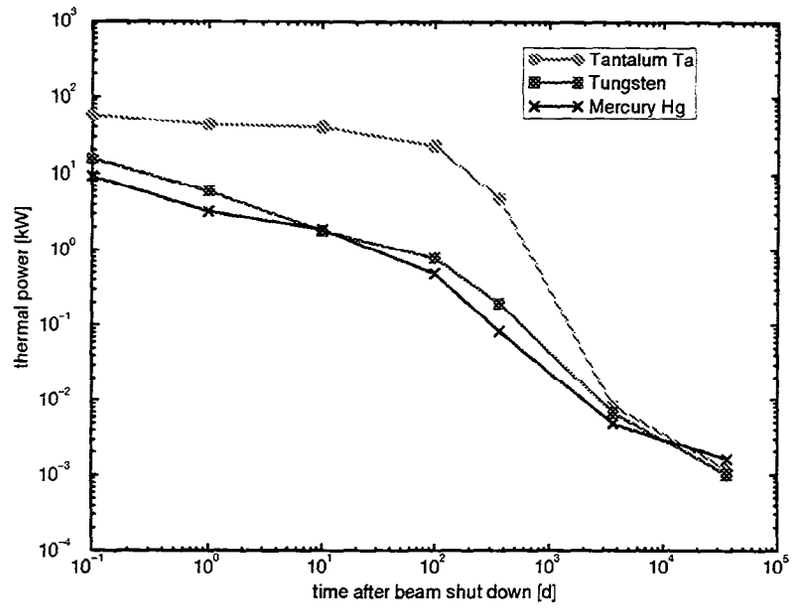

Fig. 11: Time behaviour of thermal power in kW in Ta-, W-, and Hg- targets after 1 year full power operation

Table 5: Comparison of total radioactivity and total thermal power after 100 years decay time for different targets for 5 MW proton beam power and 1 year full power operation

	Tantal	Tungsten	Mercury
Total Radioactivity [TBq]	3.40	2.83	13.00
Total Thermal Power [kW]	$1.16 \cdot 10^{-3}$	$9.94 \cdot 10^{-4}$	$1.58 \cdot 10^{-3}$

It should be mentioned that the nuclide data base of the code ORIHET is incomplete. We found that the nuclide production rate, which is generated by HETC and not treated by ORIHET, is less than 10 percent of the total production rate. The nuclides caused by low energy neutrons were entirely treated by ORIHET. Therefore the results of activity and thermal power caused by spallation should be increased by about 10 percent.

5. References

[1] P.Cloth et al.,*HERMES,A Monte Carlo program system for beam materials interaction studies*, Report Jül-2203,May 1988

[2] I.S.K.Gardner,H.Lengler,G.H.Rees,(Editors), *Outline Design of the European Spallation Neutron Source*, Report ESS 95-30-M,September 1995

[3] SNQ-Project *Proposal for a Spallation Neutron Source*, KFA-Jülich, Dec. 1991

[4] R.E.MacFarlane MATXS 11, RSIC Data Library Collection, Report DLC-177, 1994

[5] J.Bell, ORIGEN, *The ORNL Isotope Generation and Depletion Code*, ORNL-Report 118680, 1973

ICANS-XIII
13th Meeting of the International Collaboration on
Advanced Neutron Sources
October 11-14, 1995
Paul Scherrer Institut, 5232 Villigen PSI, Switzerland

MERCURY AS A TARGET MATERIAL FOR PULSED (FAST) SPALLATION NEUTRON SOURCES SYSTEMS

Günter S. Bauer

Paul Scherrer Institut, CH-5232 Villigen PSI, Switzerland

ABSTRACT

For spallation neutron systems which are not adversely affected by the high thermal absorption cross section, mercury seems to be a good target a material because it is liquid at ambient temperatures, shows good compatibility with low nickel content steels, has a high neutron yield, is easy to purify and has no truly long lived isotopes. Its performance in an engineered target for pulsed spallation sources is expected to be superior to that of its solid competitiors Ta and W and equivalent to that of Pb or Pb-Bi but at much less overall technical effort.

1. Introduction

Using a flowing, molten, heavy metal as target material has been considered at least as an option for all medium-to-high-power spallation neutron sources studied in the past [1], [2], [3], [4] The obvious advantages are

- a high heat removal capacity by convective flow of the heated material as a whole
- a high average density of the target material in the beam interaction zone, giving a high source brightness
- no moderation of the primary neutron spectrum inside the target, reducing the likelihood of resonant absorption and resulting in a high reflector flux and good neutronic moderator coupling
- no water present in the proton beam interaction zone, reducing radiolysis and radioactivity in the cooling water circuit substantially
- no structural radiation damage in the target material, making regular replacement necessary only for the part of the target shell exposed to high particle flux

Keywords: Mercury, Liquid Metal, Vapour Pressure, Solubility

- the content of hazardous volatile species in the target material that could be released in an accident scenario is low because they will escape from the target continuously and be safely removed on line.

Desirable properties of a material to be used as liquid target for a spallation neutron source are:

- a high atomic number to give good neutron yield
- a high density to give high source brightness
- a low melting point to make choices for structural materials and operation easier
- a low corrosive activity (solubility of elements of the container material) to avoid problems with mass transport from hot to cooler parts of the system
- chemical inertness to minimize formation of possibly abrasive compounds that would be transported in the system
- a low neutron resonance integral to minimize absorption of neutrons before they get thermalized
- a high scattering cross section for fast and epithermal neutrons to improve reflector action of the target
- a low thermal neutron absorption cross section, at least if the target is to feed a neutron source which builds up a high thermal flux through a long life time of the neutrons in the reflector.

Table 1 gives an overview of the candidate material and their properties.

Table 1: Liquid Metal Target Candidate Materials and their Relevant Properties in Comparison

Property	Pb	Bi	LME	LBE	Hg
Composition	elemental	elemental	97.5%Pb +2.5%Mg	45% Pb +55%Bi	elemental
Atomic Number Z	82	83			80
Atomic Mass A (g/mole)	207.2	209			200.6
Density (g/cm^3) solid (20°C)	11.35	9.75			
liquid	10.7	10.07	10.6	10.5	13.55
Coefficient of thermal expansion (K^{-1})	$2.91 \cdot 10^{-5}$	$1.75 \cdot 10^{-5}$			$6.1 \cdot 10^{-5}$
Contraction on solidification (%)	3.32	-3.35	≈0	≈3.6	
Melting point (°C)	327.5	271.3	250	125	-38.87
Boiling point at 1 atm. (°C)	1740	1560			356.58
Specific heat capacity (J/g/K)	0.14	0.15	0.15	0.15	0.12
Thermal neutron absorption (barn)	0.17	$3.4 \cdot 10^{-2}$	0.17	0.11	389
Corrosivity	moderate	highest	moderate	high	low
Chemical activity	moderate	highest	moderate	high	low

Since all neutron sources that considered liquid metal targets so far were conceived with a large and non-absorbing reflector to produce a high time average thermal neutron flux, mercury was excluded as a potential candidate because of its high thermal neutron absorption cross section. If, however, thermal neutron absorption is not a primary concern - or is even a desirable property to ensure proper functioning of the system, as in short pulse spallation sources, pulse shape optimized intermediate pulse length sources or fast neutron systems involving fissionable material, mercury certainly deserves special attention.

2. Neutronic properties of mercury

In order to get a full picture of the neutronic performance of a spallation target, it is necessary to perform Monte Carlo calculations, but certain general aspects can also be derived from rules-of-thumb and other known facts. As noted before, mercury, in its natural isotopic composition, has a high thermal neutron absorption cross section, which is mainly due to the isotope of mass number 199, which accounts for 367 of the total of 389 barn (Table 2). Another 13 barn are due to the isotope of mass number 200. While one might expect the isotopes with high neutron absorption cross section to "burn" in a high thermal neutron flux, this will not play a significant role in a liquid metal spallation target, because only a small fraction of the roughly 1 m^3 of mercury in the circuit will be exposed to the neutrons at any moment.

Table 2: Thermal neutron properties of Hg and its stable isotopes

Thermal neutron absorption cross section			389 barn
Resonance integral			75 barn
Scattering cross section		bound	26.3 barn
		epith.	15 barn
Neutron mean free path:			
		scattering	0.93 cm
		thermal neutron absorption	0.06 cm
Stable Isotopes			
Mass	Abundance (a/o)	Therm. neutr. absorption @ 2200 m/s	
196	0.15	3080 barn	
198	10.1	1.9 barn	
199	17	2162 barn	
200	23.3	60 barn	
201	13.2	8 barn	
202	29.6	4.9 barn	
204	6.7	0.4 barn	
all	100	389 barn	

On the other hand, the high thermal neutron absorption is not necessarily an undesirable property in a pulsed spallation neutron source: In order to keep thermal and cold neutron pulses short, the moderators are normally surrounded by a material which is transparent for epithermal and fast neutrons and highly absorbing for slow neutrons, in order to prevent slow neutrons from returning to the moderator after rattling around in the reflector for some time. Such a material is boron. The problem with boron at high neutron flux is that it emits an α-

particle of short range and therefore heats up substantially, requiring intensive cooling. In Fig. 1 the thermal neutron absorption cross sections of boron and mercury are compared to one another. Up to about 200 meV the cross section of Hg is less than a factor of 2 lower. The mean free path of thermal neutrons in Hg is about 0.06 cm, compared to 0.04 in B_4C and 0.025 cm in BN. Other boron-containing materials such as Boral have a much longer mean free path. It is also important to note that the ratio of the mean free paths for absorption and for scattering is 0.065, which shows that mercury is indeed a good "decoupler" for thermal neutrons. The absorption cross section vanishes at about 10 eV. In order to achieve a short pulse throughout the range of interest for an ambient temperature moderator, decoupling becomes important below about 0.4 eV. It is obvious that mercury should serve well in the whole regime, whereas boron tends to reduce also the intensity of higher energy neutrons, which could still be accepted as return flux from the "reflector".

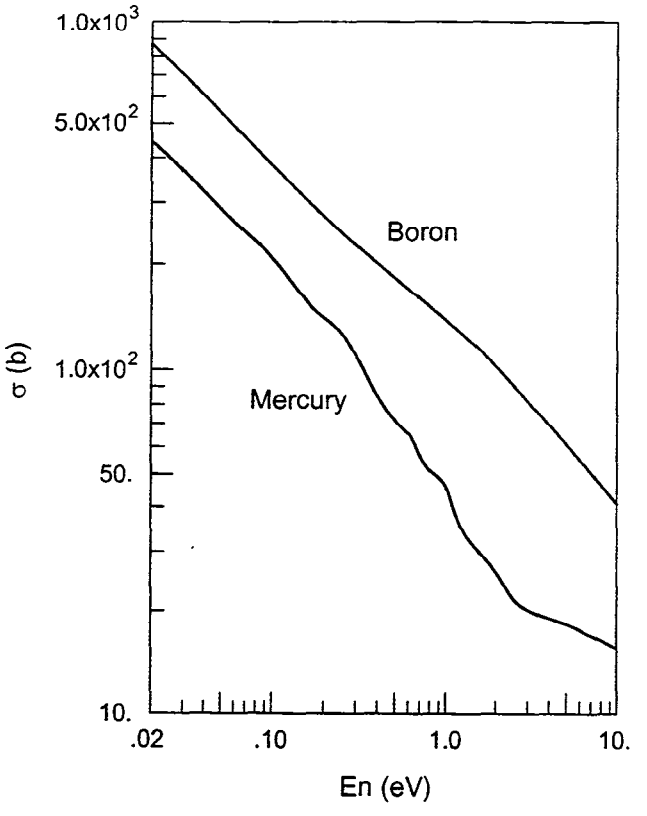

Figure 1: Thermal neutron total cross section of mercury and boron

In Table 3 a few data for the high energy regime are given. The range of 1.35 GeV protons, the neutron yield and the mean free path between inelastic collisions were calculated by the relations given by Carpenter [10]. It can be seen that almost no slowing-down of fast neutrons takes place in a Hg-target because the mean free path between elastic collisions is about 2.5 cm in the keV-MeV range and 1800 collisions would be required for complete thermalization. We may therefore expect the leakage spectrum from a mercury target to be harder than that from a H_2O- or even D_2O-cooled Ta or W-target, where the volume fraction of coolant would have to be of the order of 30 ÷ 50 % at ESS-power densities of up to 3 kW/cm^3.

Table 3: Some high energy neutron data for mercury

Range of 1.35 GeV protons	70 cm
Approx. mean free path between inelastic collisions	15 cm
Approx. neutron yield at 1.35 GeV from spallation (20 cm diam. target)	27 n/p
Slowing down properties for neutrons:	
Log. enegy decrement per collision	0.01
Nr of collisions 2 MeV -> 25 meV	1832

This may have some effect on n-2n or n-3n processes in some reflector materials. Or, conversely, reflector materials containing elements with high n-2n, n-3n cross section and low threshold energies should be particularly desirable.

Table 4: Radioactive isotopes of mercury and their half lives

Radioactive isotopes	mass	T 1/2	Comments
from n-capture (ß-active)			
	203	46.59 d	
	205	5.2 min	
	(206)	8.15 min	Unlikely to be
	(207)	2.9 min	produced
from spallation			
	197	64.1 h	Where two decay modes
	195	40 h	exist, the longer half life
	194	**367 a**	is given
	193	17.65 h	
	192	5 h	
	191	3.18 h	
	190	42.8 m	
	189	8.7 min	
	188	8.8 min	
	187	2.4 min	
	186	1.4 min	
Hg<186 have half lives less than some alpha-activity		1 min	

Listed in Table 4 are the radioactive isotopes of Hg, together with their half lives. Radioactive isotopes can be generated by neutron capture or in the spallation process. With one exception, all radioactive isotopes decay with half lives less than 50 hours, most of them significantly less. While this may not be very significant for handling and maintenance work during the service time of the target material, it may well be significant when it comes to final disposal. Since Hg is relatively easy to purify by chemo-physical means, all the non-Hg radioactive spallation products can be separated off and disposed of separately. The remaining mercury will be of very low specific activity and have negligible surface dose after a year or so, because only Hg-194 will be left as β^+-emitter. It is of particular significance to the general risk perception, that there is no polonium production, in particular no ^{210}Po (α-emitter with

half life of 138.4 days) to be expected in a mercury target. Some α-active isotopes of Hg, Au, Pt etc. may be generated during target operation, but they all have half lives well below 1 minute.

3. Physical and chemical properties of mercury

Since, obviously, from a neutronic point of view, mercury is a very promising candidate for fast neutron spallation systems, the next question is about its physical and chemical properties.

Listed in Table 5 are the relevant physical properties for the design and operation of a mercury spallation target. The most important feature, of course, is the fact that Hg is liquid at room temperature, thus avoiding the need for auxiliary heating to keep the metal molten even if the source is not in operation. This is important for two reasons: a) it takes a long time to safely melt a large mass of the order of 10 tons in a complicated target circuit with pumps, heat exchangers, diagnostics equipment etc. and b) for all other candidates listed in Table 1, there is either a large volume change at the solid-liquid phase transition, or a long term expansion after solidification (case of Pb-Bi). In both cases the risk of undesirable mechanical load on circuit components exists (enclosure in the case of expansion, internal structures in the case of contraction) and would require complicated heating systems and process protocols for solidification and melting in order to avoid damage.

A potential problem could arise from the high vapour pressure of mercury, shown in Fig. 2. Certain materials considerations may require operating temperatures of a few hundred degrees [11], which will require a system pressure of several bars, in particular if mechanical pumps are to be used and cavitation effects must be avoided. On the other hand care must be taken to avoid local overheating to more than about 500 °C, if the system pressure is to be kept at 10 bars or below[1].

Hg is known to have a very high surface tension and to form tiny droplets when spilled. This might require special care when the liquid metal circuit must be emptied for repair or maintenance purposes. On the other hand the surface tension seems to depend strongly on the degree of purity of the mercury. Also, opportunities exist to provide cooling for parts of the circuit near the most likely positions which have to be opened (e.g. the target shell) to less than -40°C and thus solidify any Hg-residues for the period when the circuit is open. The high thermal expansion coefficient of Hg will require a sufficiently large ullage tank to accommodate the volume change upon heating to operating temperature. It also has the effect of generating a large (hindered) expansion during each power pulse of the beam in a pulsed system. Fortunately, Hg also has a relatively high compressibility, which helps to keep the

---

[1] Note: The high vapour pressure in principle opens up the interesting opportunity to design an isothermal target cirucit with heat removal based on evaporation of the target material. Mercury has been widely used in this mode in diffusion pumps in the past. This would, in view of the rather high latent heat of vaporisation (almost 300 J/g) not only mean that only a small amount of the Hg is in circulation (10 kg or 0.8 litres per second would have to be evaporated for a 5 MW beam depositing 3 MW in the target), it would also minimize thermal and static mechanical stress on the target and make removal of gaseous products straight forward. In view of the uncertainties related to the pulsed nature of the power deposition in ESS, this is not considered, for the time being. It would, however, be an interesting option for a large cw fast neutron system, where otherwise very large mass flows of liquid metals are necessary to remove the heat. In such systems direct use of the Hg-vapour for energy conversion could be an option. Hg-gas turbines have already been built and operated sucessfully.

pressure level that builds up in the liquid in the same regime as for other target materials such as lead. The problem of pressure waves and their effect on the container material is common to all liquid metal targets in pulsed operation [5] and has been discussed elsewhere [6].

Table 5: Physical properties of mercury

Atomic number		80	
Atomic weight		200.61	
Density	°C	g/cm^3	
	20	13.55	
	100	13.35	
	200	13.12	
	300	12.88	
	350	12.76	
Coefficient of thermal expansion	(0-100°C)	61 E^{-6}	K^{-1}
Melting point		-38.87	°C
Boiling point (1 atm)		357	°C
Critical temperature		1477	°C
Vapour pressure (298-630 K),mm Hg log p = -3308/T+10,373-0,8 log T			
	mm Hg	°C	
	1	126.2	
	10	184	
	40	228.8	
	100	261.7	
	400	323	
Latent heat of fusion		11.72	J/g
Latent heat of vaporisation		291.82	J/g
Specific heat	°C	J/g/°C	
	0	0.1396	
	100	0.1373	
	200	0.1359	
	300	0.1354	
	450	0.1363	
Thermal conductivity	°C	J/cm/sec/°C	
	0	0.0821	
	60	0.0967	
	120	0.1093	
	160	0.1168	
	220	0.1269	
Surface tension	°C	N/cm	
	20	0.00465	
	100	0.00456	
	200	0.00436	
	300	0.00405	
	350	0.00395	

Table 5 cont.

Viscosity	°C	centipoise	
	20	1.554	
	100	1.24	
	200	1.032	
	300	0.95	
	350	0.914	
Compressibility		$3{,}6 \cdot 10^{-11}$	m^2/N
Electrical resistivity	°C	microhm*cm	
	50	98.4	
	100	103.2	
	200	114.2	
	300	127.5	
	350	135.5	
Coefficient of resistivity (0-100°C)		$0{,}9 \cdot 10^{-3}$	K^{-1}

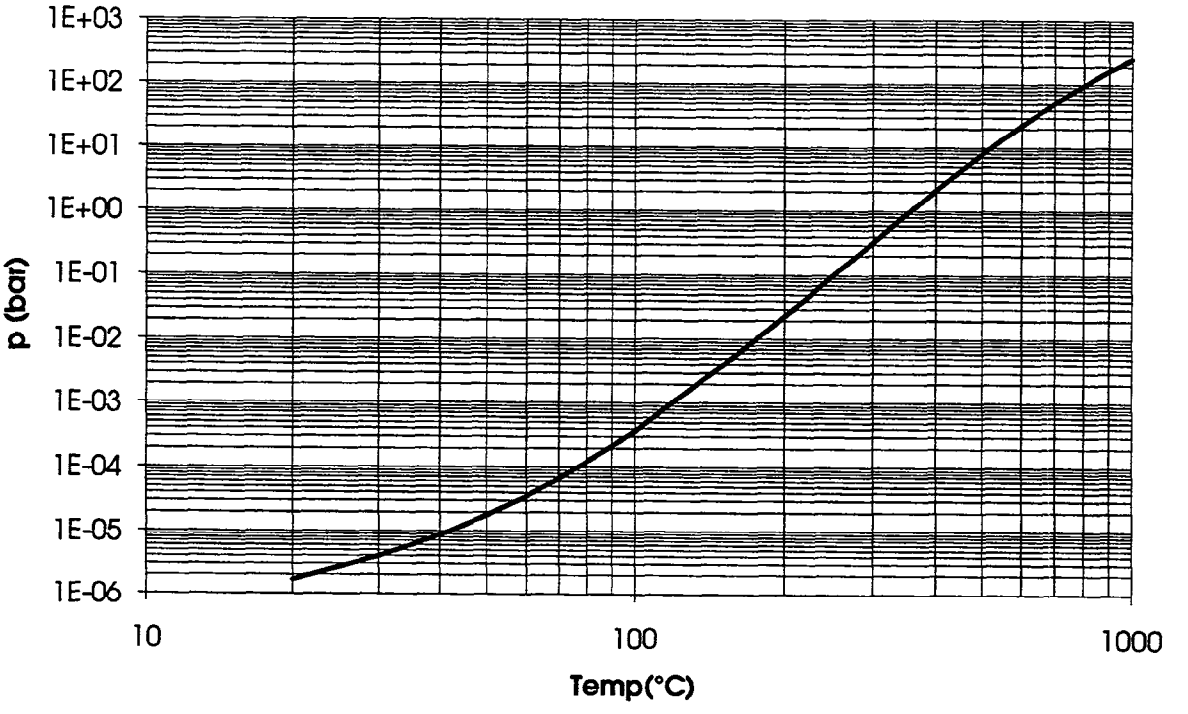

Figure 2: Vapour pressure of mercury

The high vapour pressure of Hg has yet another consequence: While Hg, as a spallation product, would evaporate from any other candidate liquid metal target circuit (based on Pb and/or Bi), all non-gaseous elements are expected to remain in the mercury. This can be seen from Fig. 3, where the calculated partial molar enthalpies of evaporation are given and compared to those at infinite dilution in a Hg-bath [7]. Obviously, there is no element with a lower enthalpy of evaporation than Hg itself.

Another question of interest is the chemical behaviour of the spallation products generated in the mercury. Some intermetallic or metal-non metal compounds can be quite abrasive and produce damage when swept across the target window at high velocity. Also, it is important to know whether such compounds or the pure elements would remain in solution or segregate to certain regions of the circuit (e.g. the heat exchanger). As a first step towards an assessment of these problems, the enthalpies of formation of intermetallic compounds with Hg were examined [8]. Some results are shown in Fig. 4. Negative values of ΔH_f show a

tendency to form amalgams, whereas elements for which ΔH_f is positive will segregate out if their limit of solubility is exceeded. Prominent examples of the latter group are the heavy 3d-metals Mo and Ta and the elements of the iron group (i.e. the main constituents of steels).

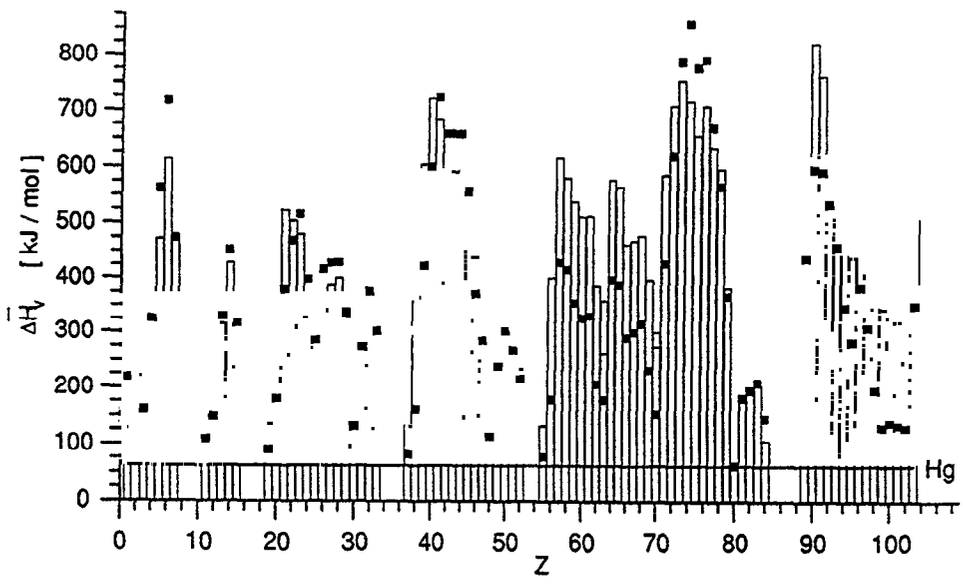

Figure 3: Calculated molar enthalpies of vaporization of the pure elements (black dots) and in infinite dilution in mercury (open bars).

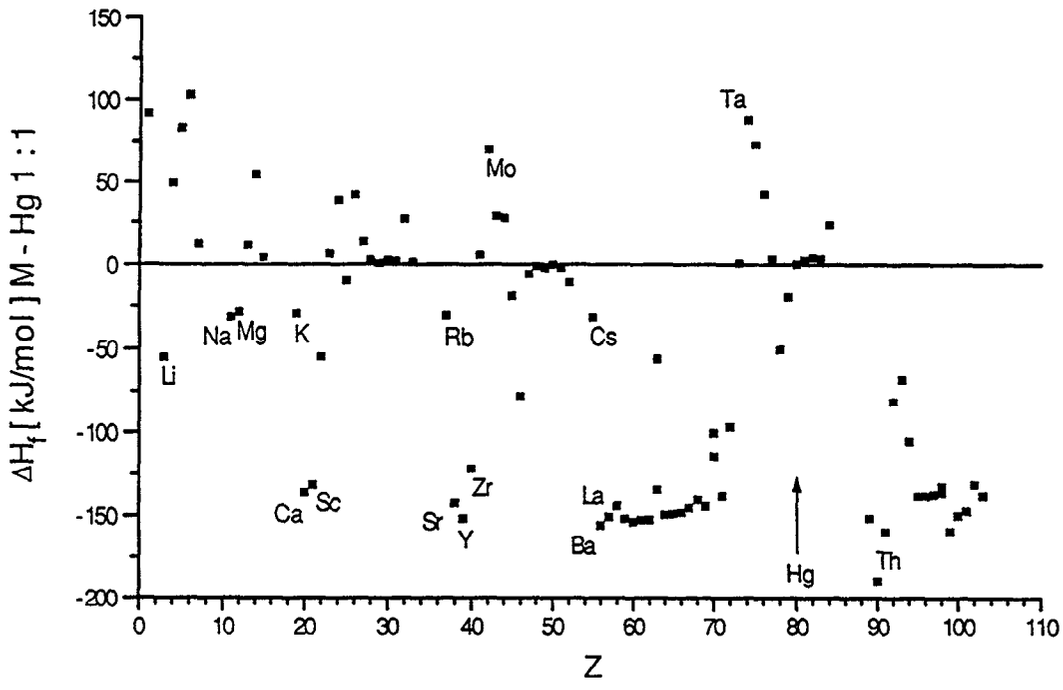

Figure 4: Enthalpy of formation of intermetallic compounds M-Hg

The solubility of non-amalgamating elements in Hg, in particular those which are components of the container material, is important because liquid metal corrosion very often results from dissolution of parts of the container material at the hot parts of the system and segregation at the cooler parts (this is one of the reasons, why too large temperature differences in the

system should be avoided). For the most important elements, Fe, Cr, V, Ni and Ti, experimental data have been compiled [8] and are shown in Fig. 5. As a general feature, solubilities in Hg are about 2 orders of magnitude lower than in Bi (and about 1 order of magnitude lower than in Pb). As in other liquid metals, Ni has the highest solubility of the ones shown. While perhaps not a problem for reasons of corrosion in Hg, Ni should be avoided in the container material also because of its He-production under slow neutron irradiation. Low nickel content or nickel-free steels are therefore the preferred container material for liquid mercury spallation targets for the time being, but other favourable options may exist and further research is needed also in this respect.

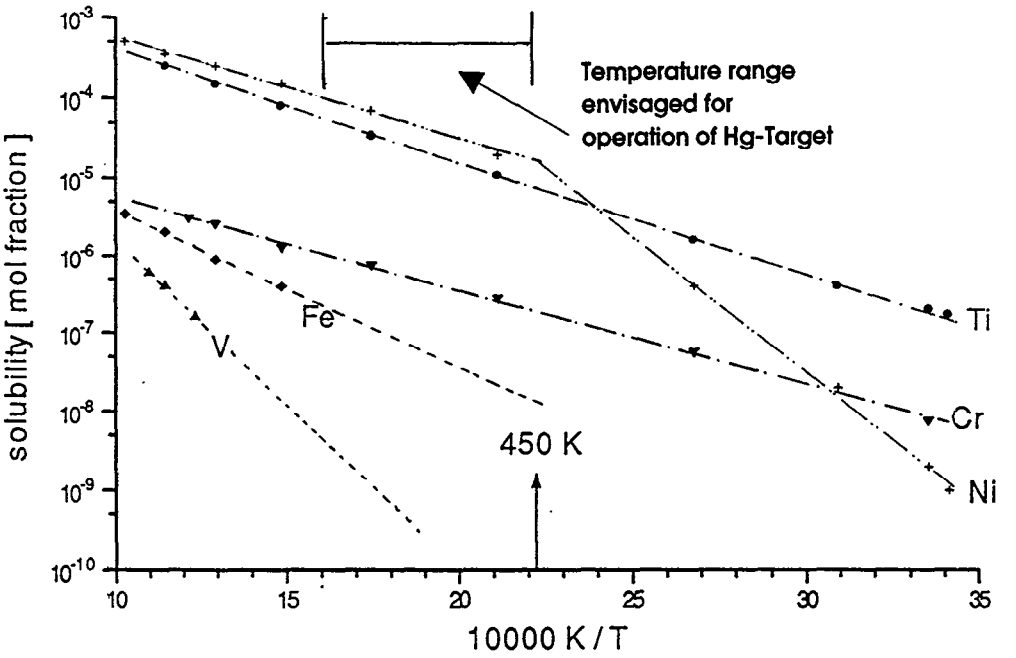

Figure 5: Solubility of metals Ti, V, Cr. Fe, Ni in Hg (exp. data); lines are guides to the eye only.

It has also been pointed out [9] that attack of low carbon steels by mercury can be inhibited by small additions of Ti and Zr (at a level of about 1 to 10 ppm) due to the formation of insoluble titanium or zirconium carbide-nitride films on the surface of the steel. Furthermore, addition of about 50 ppm of Mg has been recommended to (a) improve the wetting properties of the mercury by removing the oxide layer on the steels and thus improve heat transfer and (b) prevent the inhibitors from being removed from the Hg by oxidation.

Finally, it should be noted that mercury does not react with water, an important feature if a leak springs between the mercury circuit and a possible secondary water cooling loop. On the contrary, water is used in the purification process to obtain high purity mercury. Since, as mentioned before, purification of mercury may be desirable not only during operation of a mercury target, but, in particular, also at the end of its service life, we briefly quote the procedure used [9]: To purify mercury it is first treated in a stoneware crock with diluted nitric acid (1 part and in 4 parts water) accompanied by vigorously bubbling air up through the mercury. This is followed by thorough washing with water to remove the residual acid. The noble metals are then removed by destillation (evaporation) of the mercury under reduced pressure at 250 °C. Impurities not left behind in the destillation process will float on the mercury after a period of standing and are removed by filtering through Pyrex glass wool. The purity of the mercury obtained in this way is between 99.99998 and 99.99999 %.

4. Conclusions

Although the present assessment is far from complete, a large number of details need still to be looked at and several technical problems must still be solved, mercury seems to be a promising candidate target material, avoiding many of the problems associated with water cooled solid targets and relaxing the technical efforts and risk potential particular to other heavy liquid metal options, especially those containing bismuth. Presently no basic problems can be seen that would impede the implementation and safe operation of a target system based on liquid mercury. By developing such a system, the route might be opened up to spallation neutron sources well beyond the 5 MW level of the current European Spallation Source (ESS) project, for which a mercury target has now been adopted as the first priority concept. Also accelerator-based fast neutron systems for nuclear power might profit from the use of mercury as spallation target material.

5. Acknowledgment

Mercury was suggested for consideration as a target material for pulsed spallation sources during a workshop held at PSI in 1992 in the group chaired by B. Sigg. Subsequently, many discussions with my colleagues at PSI and elsewhere helped to clearify the picture and lead to the final publication of this article. The work was performed with support from the Swiss Bundesamt für Bildung und Wissenschaft (BBW) under contract Nr. 94.0134 in the frame of a contribution to the ESS-project study funded in part through the EU-Human Capital and Mobility program, Contract Nr. CHRX-CT94-0503.

6. References

[1] G.A. Bartholomew and P.R. Tunnicliffe (eds), "The AECL-Study for an Intense Neutron Generator"; *rep. AECL*-2600 (1966)

[2] G.S. Bauer, H. Sebening, J.-E. Vetter, and H. Willax (eds.) "Realisierungsstudie zur Spallations-Neutronenquelle" report Jül-Spez-113 and KfK 3175 *Kernforschungsanlage Jülich und Kernforschungszentrum Karlsruhe* (1981)

[3] G.S. Bauer, "SINQ- Status Report Oct. 1990" *Proc. ICANS-XI*, Tsukuba, 1990 KEK-report 90-25 (1991) p.41-60

[4] Y. Takeda and W.E. Fischer, "Thermofluid dynamics of liquid metal target of SINQ" *Proc. ICANS-XI*, Tsukuba, 1990 KEK-report 90-25 (1991) pp. 492-507

[5] J. Lettry, R. Catherall, P. Drumm, A. Evensen, O. Jonsson, E. Kugler, J. Obert, J.C. Putaux, H. Ravn, M. Toulemonde" Experience with ISOLDE Molten Metal Targets at the CERN PS-Booster" *Proc. ICANS-XIII, Paul Scherrer Insitut*, PSI-Proceedings 95-02 (1995)

[6] K. Skala and G.S. Bauer "On the Pressure Wave Problem in Liquid Metal Targets" *Proc. ICANS-XIII, Paul Scherrer Insitut*, PSI-Proceedings 95-02 (1995)

[7] B. Eichler and R. Dressler "Verflüchtigung von Kernreaktionsprodukten aus geschmolzenen Metalltargets" *PSI-Bericht* 95-33, Feb 1995

[8] B. Eichler and R. Dressler "Zum Verhalten von Spallations-Spalt- und Korrosionsprodukten in einem flüssigen Quecksilbertarget" in: ESS-Liquid Metal Taget Studies / 2nd Status Report; Report ESS-95-??-T (1995)

[9] A.H. Fleitman and J.R. Weeks "Mercury as a Nuclear Coolant", *Nuclear Engineering and Design,* 16, (1971), 266-278

[10] J.M. Carpenter, "Pulsed Spallation Neutron Sources for Slow Neutron Scattering"; *Nucl. Inst. Meth.* 145 (1977) 91-113 North Holland, Amsterdam

[11] Y. Dai, "Suitability of Steels as ESS Mercury Target Container Materials" *Proc. ICANS-XIII, Paul Scherrer Insitut,* PSI-Proceedings 95-02 (1995)

ICANS-XIII
13th Meeting of the International Collaboration on
Advanced Neutron Sources
October 11-14, 1995
Paul Scherrer Institut, 5232 Villigen PSI, Switzerland

ON THE PRESSURE WAVE PROBLEM IN LIQUID METAL TARGETS FOR PULSED SPALLATION NEUTRON SOURCES

Karel Skala, Günter S. Bauer

Paul Scherrer Institut, 5232 Villigen PSI, Switzerland

ABSTRACT

A liquid metal target for a pulsed spallation neutron source was modelled on the computer to investigate the effect of the high instantaneous power deposition (60 kJ in 1 μs) on the pressure in the liquid and the resulting stress on the container. It was found that for the short pulse duration the resulting stress would be likely to exceed the allowable design stress for steels of the HT-9 type with low nickel content. Adding a small volume fraction of gas bubbles might be a way to suppress almost completely the generation of pressure waves.

1. Introduction

Using a molten heavy metal as target material for spallation neutron sources has so far been considered mainly for continuous sources like ING [1] and SINQ [2]. The obvious advantages are

- a high heat removal capacity by the moving target material
- the absence of cooling water and its related problems of radiolysis and corrosion in the target region
- no structural radiation damage in the target material
- high heavy metal density in the interaction region (no dilution by cooling channels)
- volatile or potentially volatile spallation products can be removed "on line"
- a low specific afterheat due to a large target mass, which, together with the fact that the liquid can be drained into a dump tank, makes forced cooling during exchange operations not necessary.

In view of these attractive features and of the risk of damage in solid targts in pulsed spallation sources of high power level like the 5 MW for the European Spallation Source

Keywords: Liquid target, Pressure waves, Mercury, Stress

Project (ESS) [4], the question was investigated whether a liquid target could be used also in this case. One of the main differences between a pulsed and a continuous spallation neutron source is the very high instantaneous power (100 kJ per pulse for ESS) injected into the material during very short times at high repetition rate, (1 μs at 50 Hz). About 60% of the beam energy are deposited in the target which under these conditions, cannot be accommodated by thermal expansion during the pulse and will give rise to pressure waves that can result in substantial stress loads on the container wall. Although the material for the container wall can - within limits - be chosen for high mechanical stability, it is of prime importance to keep the load in a safe regime for long time operation even under the effect of radiation damage. In the present paper we report on preliminary calculations to examine these problems.

2. The physics model

Under the assumption that the target material will be either Pb, Pb-Bi eutectic or Hg in the liquid state we exclude the effect of phase transitions and related latent heat effects. All deposited energy will therefore be converted into heat, leading to thermal expansion. In view of the short duration of the energy pulse, this expansion is strongly hindered by the surrounding material and a force will be excerted that causes a pressure wave to travel through the material. Since this means acceleration and motion of material, it will have an immediate feedback effect on the pressure which must be taken into account through a coupling loop. Fig. 1 shows the conceptual basis of the calculations:

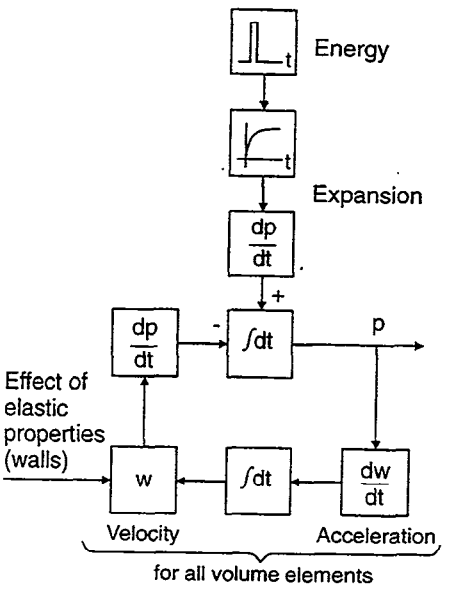

Figure 1: Simplified scheme of the calculational procedure to examine pressure waves in a liquid metal target. Accelerations and displacements are only allowed to occur to the extent permitted by the elastic properties of the system. Otherwiese they are treated as "virtual" and used to calculate the change in local pressure.

The pulse-like deposition of a large amount of energy in any volume element of the target is short enough, so that no change in volume is possible (isochoric case). It gives rise to a subsequent (hindered) expansion of the material whose time constant can be varied. The result is an increase of pressure as a function of time. This pressure is the cause of acceleration of the surrounding material, whose velocity is again obtained via an integration over time. The motion of this material will reduce the local pressure, giving rise to feedback

between the volume elemtens in the target. The pressure wave will thus travel through the material, mediated by the finite compressibility. It will pass through the non-heated zones of the target and reach the wall where it causes mechanical stress. Due to the elastic properties of the wall it will be reflected back into the material, giving rise to superposition. In a solid this might occasionally result in negative pressures (tensile stress) in the material. In the liquid we assume voiding to occour and hence we limit the minimum pressure to a small negative value or to zero (optional). At present we do not account for the latent heat of vaporization required to fill the void with metal vapour, nor do we account for any short term underswing of the pressure due to cohesive forces in the liquid, delaying the void formation. Both effects could be incorporated into the model for at a later stage if considered important and if sufficient information is available. Neglecting them keeps us on the safe side in terms of stress on the walls.

3. The geometrical model

The geometrical model is three dimensional but at present only elliptical target cross sections have been implemented (including, of course, the circular cross section as a special case). The target is taken long enough for its downstream end (parallel to the proton beam) not to affect the pressure during the time intervals considered (a few hundred μs). For the upstream end (beam entry point) one of three options can be selected

- an open surface
- a rigid flat cover
- an elastically flexible domed cover

In the case of an open surface, target material is allowed to leave the surface under the effect of the following forces

- pressure inside the liquid
- gravity
- inertia
- internal friction caused by viscosity.

The liquid volume, as well as the surrounding walls are subdivided into triply indexed elements limited by surfaces in the following way (Fig. 2).

- planes perpendicular to the beam axis (index I)
- cylinders concentric to the beam axis (index K)
- planes containing the beam axis (index L)

The volume elements can be defined as belonging to the liquid or as representing solid material. In the latter case tensile forces and shear stress are allowed to occur.

4. The mathematical model

All dynamical processes are described by algebraic relations and differential equations. The latter ones are solved by numerical integration. The pressure resulting in a medium is given by the general relation

$$dp = \left(\frac{\partial p}{\partial V}\right)_T dV + \left(\frac{\partial p}{\partial T}\right)_V dT \qquad (1)$$

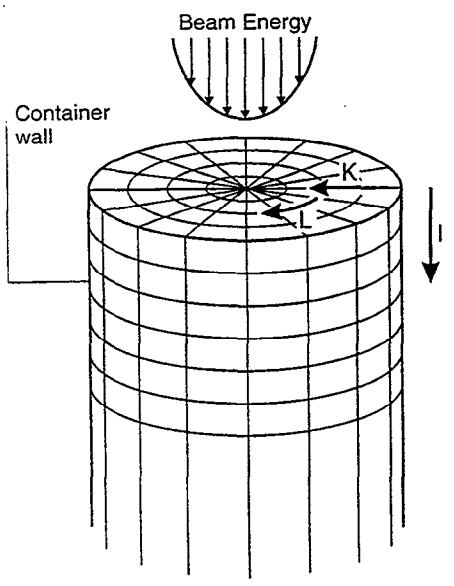

Figure 2: Scheme for the subdivision of the target volume into elements by surfaces and assignment of the indices I, K, L.

During the very short energy pulses no volume change can occur and hence only the second term in equation (1) is important (isochoric case). Following the energy deposition the resulting pressure will spread adiabatically in the medium and the first term in eqn. (1) becomes dominant because in liquid and solid media the adiabatic compression occurs practically without any change in energy, since c_p and c_v, the specific heat capacities at constant pressure and at constant volume are almost equal. The temperature rise caused by depositing an amount of energy E_d in a volume of mass m is then given by

$$\Delta T = \frac{E_d}{m \cdot c_v} \tag{2}$$

In our practical calculations the small change in temperature during the adiabatic expansion is in fact taken into account as shown in the appendix A1. where a derivation of the formulae used is given.

The result is a pressure increase Δp given by

$$\Delta p = \frac{c_p}{c_v} \cdot K \cdot \frac{\Delta V}{V_0} = \tilde{K} \cdot \frac{\Delta V}{V_0} \tag{3}$$

where K is the isothermal modulus of volume elasticity,

$$K = V_0 \left(\frac{\partial p}{\partial V} \right)_T \tag{3a}$$

and $\tilde{K}$ shall be called the "adiabatic modulus of volume elasticity". Using this quantity accounts for the change in temperature during adiabatic expansion. This allows us to drop the condition of short pulses and use our system of equations also for longer pulses (e.g. a 500 µs pulse of a long pulse souce).

The force excerted on any given volume element is the result of three components

- the difference in pressure on both sides
- friction caused by viscosity
- gravity.

The net force on any volume elemtent causes acceleration of the material which, through integration over time, finally yields a theoretical net displacement of the material. For each volume element the velocities and net displacements are calculated for the six faces of the element (Fig. 3). This allows to calculate a ficticious ("virtual") change in volume

$$\Delta V = \sum_{i=1}^{6} S_i \cdot B_i \tag{4}$$

with S being the area of the surface under consideration and B the displacement. We call the volume change "virtual" because it does not occur in reality but is the cause of a change in pressure as shown in Fig. 1.

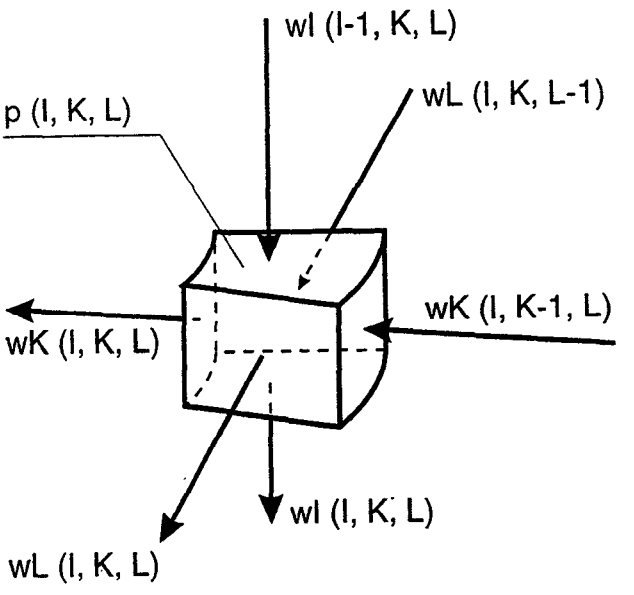

Figure 3: Velocities and displacements contributing to the "virtual" change in volume of a target element.

In this way the spreading of the pressure is followed through the target material as a function of time until it reaches the container wall. Due to the tensile strength of the wall, the pressure gives rise to stress in the wall material which is the sum of the direct pressure load on the surface element under consideration and the influence of the neighbouring elements, where the pressure wave may arrive at a different time. The toal stress is therefore a combination of pure tensile and stress (Fig. 4). The bending stress is calculated in analogy to the case of a beam with two fixed ends under lateral displacement.

The options mentioned for the beam entry face are treated in the following way:

- for the free surface the pressure above the liquid is set to zero and the equations of motion are used without restrictions

- for the rigid flat cover no displacements, velocities or accelerations are allowed at the boundary surface, i.e. the boundary surface acts as a "mirror".

- the domed flexible cover is treated in analogy to the elastic cylinder wall accounting for the double curvature in this case.

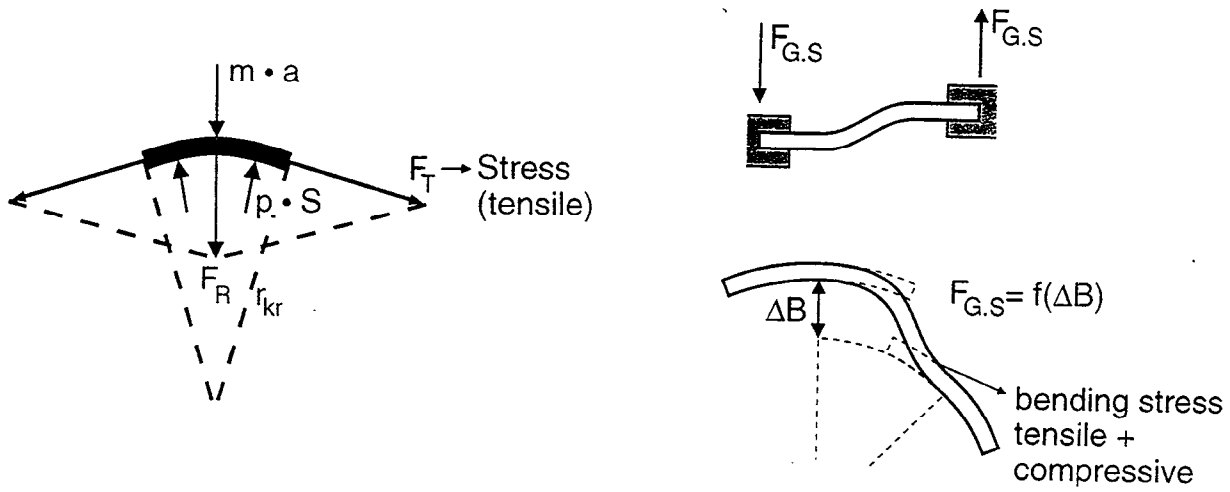

Figure 4: Modelling of different stress contributions in the target container wall.

5. The effect of the elastic modulus of the liquid

According to eqn. (3) the pressure rise in the liquid is directly proportional to its elastic modulus K_e, resp. $\tilde{K}_e$. Accounting for the fact that gases are orders of magnitude more compressible than solids or liquids, we assume that a small amount of gas bubbles can be continuously added to the region where the interaction between the target material and the proton beam takes place.

Any change in volume of the mixture ΔV_m will then be the sum of the change in volume of the gas ΔV_g and of the liquid ΔV_l:

$$\Delta V_m = \Delta V_g + \Delta V_l \tag{5}$$

According to eqn. (3) the second term is given by

$$\Delta V_l = -\frac{V_{l,0}}{K} \cdot \Delta p \tag{6}$$

In order to determine the first term of eqn. (5), we need to know whether the compression is isothermal or adiabatic. This depends on the rate of heat exchange between the metal and the gas, which should be high due to the smallness of the bubbles and their large surface. On the other hand the compression is very fast which would favour the adiabatic case. The general case is a polytropic compression

$$p \cdot V_g^n = p_0 \cdot V_{g,0}^n \quad with \quad 1 \le n \le \kappa \tag{7}$$

where n=1 holds for the isothermal and n = κ holds for the adiabatic case.

Calling the volume fraction of gas bubbles ε with

$$\varepsilon = \frac{V_{g,0}}{\left(V_g + V_l\right)_0} \tag{8}$$

it is easy to show (see appendix A2) that the modulus of elasticity for the mixture is given by

$$K_m = \left\{ \frac{1}{K_l} + \frac{1}{n} \cdot p_0^{\frac{1}{n}} \cdot \varepsilon \cdot p^{-\frac{n+1}{n}} \right\}^{-1} \tag{9}$$

For the case of mercury ($K_l = 2.77 \cdot 10^{10} \frac{N}{m^2}$) this quantity is shown in Fig. 5a and b as a function of pressure for various values of ε and for n=1 and n=1.63 (isothermal and adiabatic compression respectively). It is obvious that in the adiabatic case K and, as a consequence of the feedback also p, are much smaller than in the isothermal case, but the effect at moderate pressure levels is enormous even for very small values of ε, of the order of a few percent. We can therefore anticipate that, due to the high compressibility of the gas bubbles, there will be almost no overall pressure increase in the liquid as long as the total volume of the gas bubbles is sufficient to absorb the total volume increase in the liquid at moderate pressure increase in the gas.

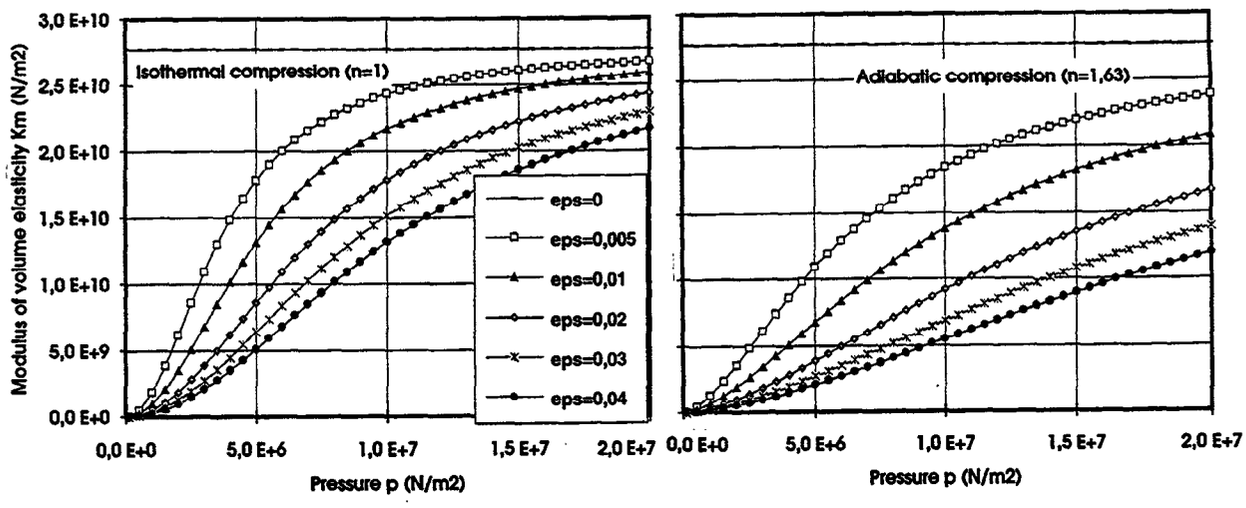

Figure 5: Dependence of the modulus of volume compressibility K_m of a mixtrue of liquid and gas on the pressure for different volume fractions of gas, ε. (a) iothermal case (b) adiabatic case.

For very small volume fractions of ε, on the other hand there may exist a positive feedback in pressure development because, while energy is initially stored in the compression of the bubbles, K_m increases rapidly towards the value of K_l and the pressure wave will spread as in the bubble-free case. However, as soon as the pressure starts dropping the energy stored in the bubbles will be released, causing the pressure to drop more slowly and eventually to give rise to interference maxima which may exceed the values obtained in the bubble-free case. Of course, these effects are strongly geometry dependent, too, and detailed calculations are needed for each sitation. As a general rule it may be stated however that, if gas bubbles are used to suppress the pressure waves, a volume concentration slightly above the "critical" one is much safer than one below. More details are given in the following chapter.

6. Some examples of results obtained so far

Our main interest in the current context are the stress levels induced in the container walls as a function of the various parameters and the target geometry. For the time being, the following effects are completely neglected

- static or quasi-static stress caused by temperature gradients in the walls
- static stress caused by hydraulic pressure
- stress caused by flow reversal at the beam entry window
- etc.

For the energy deposition in the liquid we assumed that about 60% of the beam energy are deposited in the target material, i.e. 3 MW time average or P_p = 60 kJ per pulse for the ESS case. The spatial distribution is taken as essentially exponential along the beam axis and as parabolic in radial direction with a base width of $2r_s$=10 cm. For each volume element the heating during the pulse is then given by

$$P(r,z) = c_{it} \cdot V_e \left(1 - \exp\left(-\frac{z - z_a}{\lambda_a}\right)\right) \cdot \left(\exp(-\Sigma \cdot z)\right) \cdot \left(1 - \left(\frac{r}{r_s}\right)^2\right) \tag{10}$$

where V_e is the volume of the element under consideration, λ_a is a buildup length taken as 6.5 cm, z_a is an extrapolation length (1.77 cm), Σ is the macroscopic cross section of mercury for 1.3 GeV protons (0.07 cm^{-1}) and c_{it} is a quantity determined by iteration under the condition that the sum over all volume elements must give the value P_p. The numbers chosen are based on a compilation generated for the German SNQ project [3]. Fig. 6 shows the axial dependence of the power deposition integrated over the beam diameter.

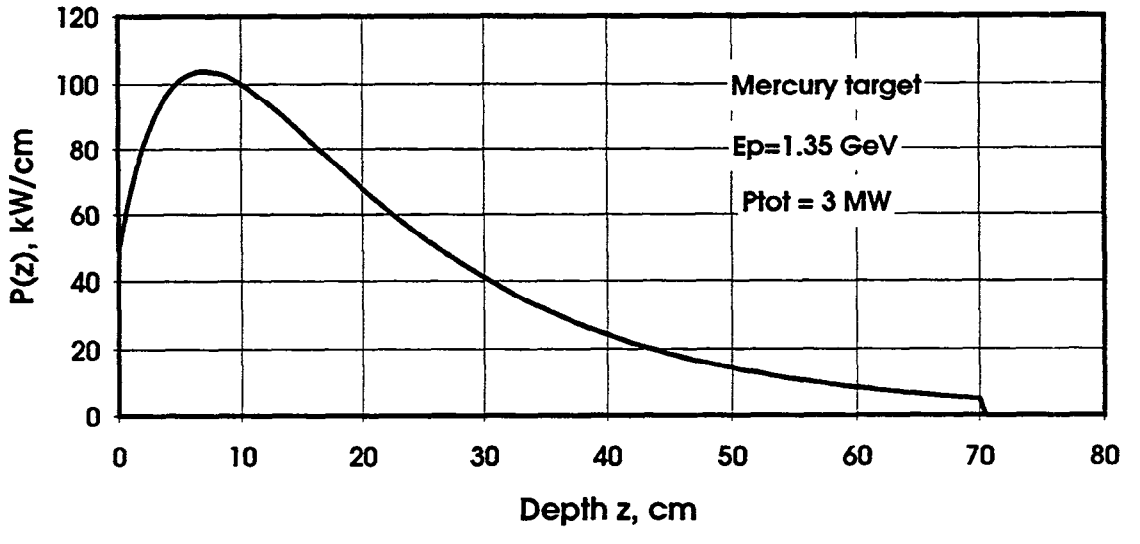

Figure 6: Axial dependence of the power deposition (integral over the beam diameter) used as input for the heating calculations.

The aspect ratio and area of the ellipse representing the target cross section can be varied to examine the effect of travelling times of the pressure waves from their origin to the walls.

Immediate effects are, of course, obtained at the target head where heating occurs directly behind the walls. For all other positions along the container wall the stresses are rather complicated functions of position and time due to the osciallatory behaviour of the system.

In Fig. 7 we show the stress as a function of time obtained for an elliptic target cross section with an area of 707 cm^2 and with an aspect ratio of 3:2 at the points A and B (plane of maximum stress) for the situation of the target with a rigid cover. Clearly one can see the effects of travelling time and of local curvature of the wall:

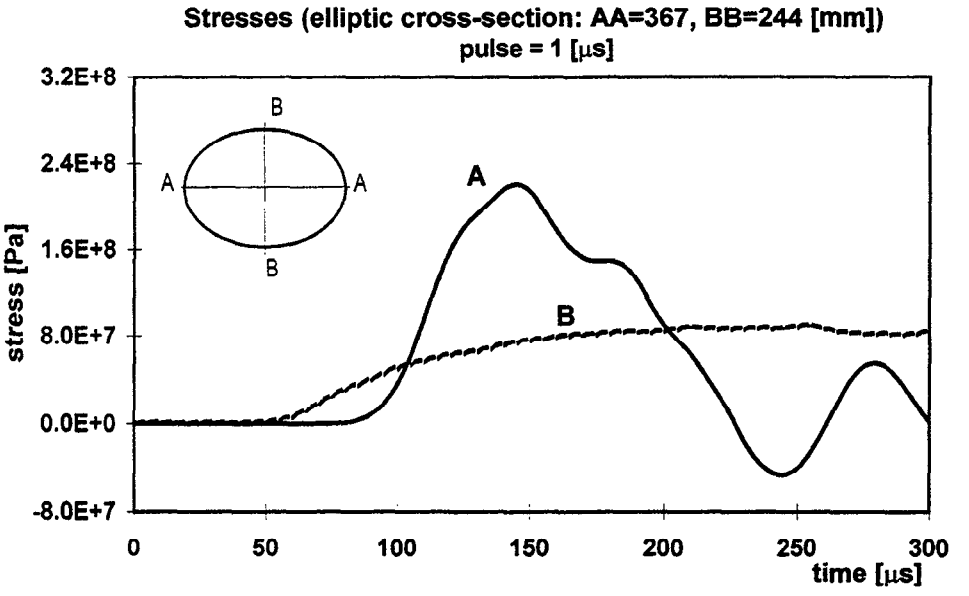

Figure 7: Calculated stress as a function of time for the two positions A and B at the level of maximum stress along the cylinder walls of 8 mm thickness for a 1 μs long power pulse of 60 kJ total engery.

While the pressure wave reaches point B (b=122 mm) about 50 μs after the pulse, the pressure rise is rather moderate due to the softness of the wall at this position (large radius of curvature). The farer point A is reached after 80 μs but the stresses rises much more rapid due to the stronger curvature of the wall at this position. The maximum stress is reached after about 150 μs at a level of 145 MPa. Some oscillatory behaviour is clearly seen in both cases. The maximum level reached is close to the recommended design stress for HT-9-type steels (Fig. 8). Also, it must be noted that this is only the dynamic contribution from the pressure waves in the target and a wall of 8 mm thickness was assumed. This is probably too thick to be cooled. Hence a reduction of the pressure wave contribution is highly desireable.

As an illustrative example we show in Fig. 9 the same geometry but for the case of a 250 μs long proton pulse of the same total energy content. While the curves are topologically similar to those of Fig. 7, the stress level reached is only 10% of the former, mainly dominated by the height of the rising edge of the pulse. This shows that for a long pulse neutron source stress waves in the target should not be a problem.

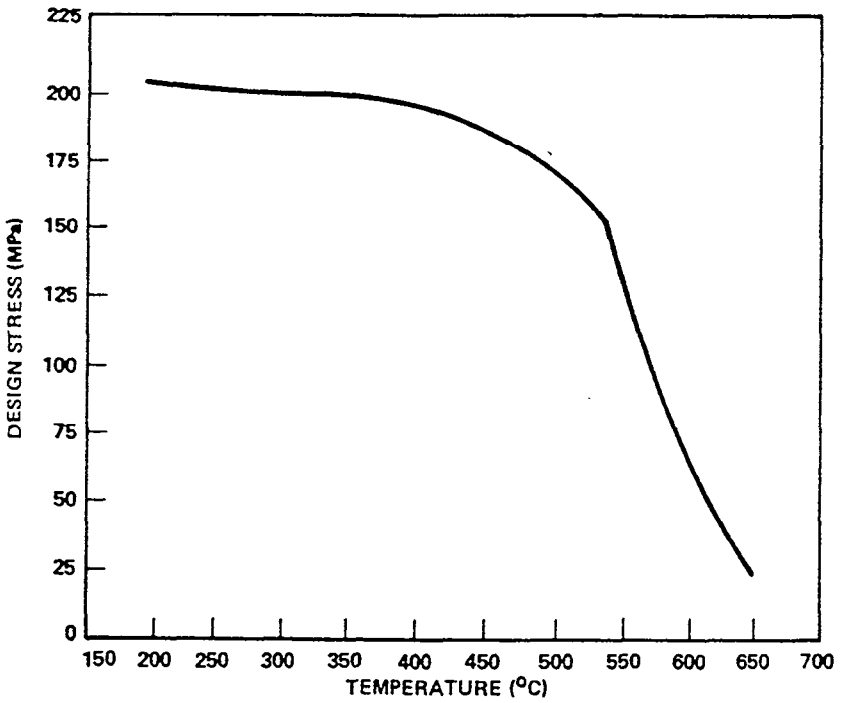

Figure 8: Allowable design stress in HT-9-type steel as a function of temperature (after [5]).

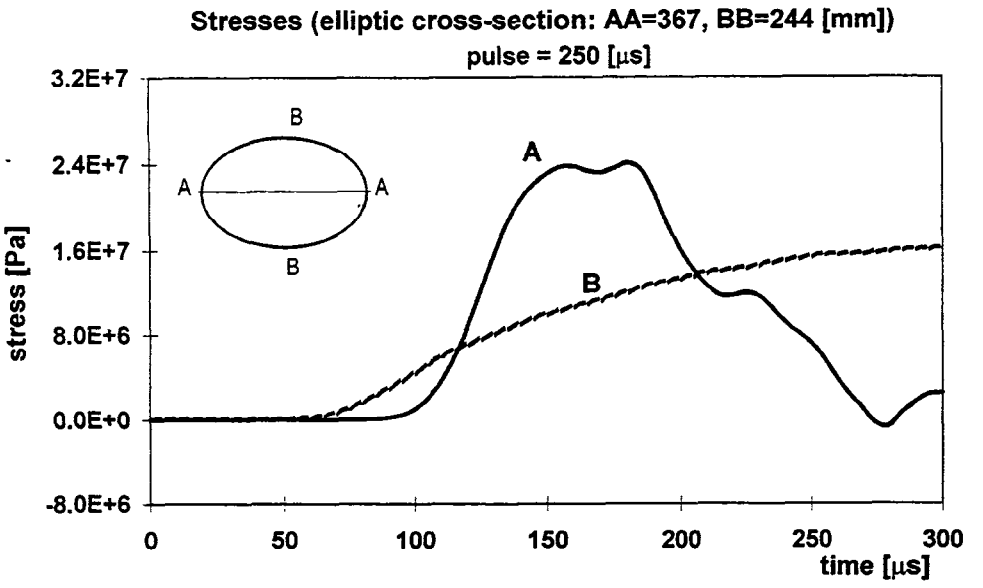

Figure 9: Calculated stress as a function of time for the same situation as Fig. 8, but with an assumed pulse duration of 250 μs.

For the case of a circular target cross section, somewhat higher maximum stress levels are obtained but the difference is not large. Similarly, allowing a free surface or using a domed cover at the point of beam entry has a noticeable but not really significant effect on the maximum stress along the wall.

For the case of the open surface, liquid is found to be expelled through the surface Figs. 10a and b give the velocity profile and the surface contour of the liquid at 300 μs after the beam

hits the target. The maximum velocity obtained can be seen to be of the order of 10 m/s. The profile ressembles very closely to that observed for underwater explosions!

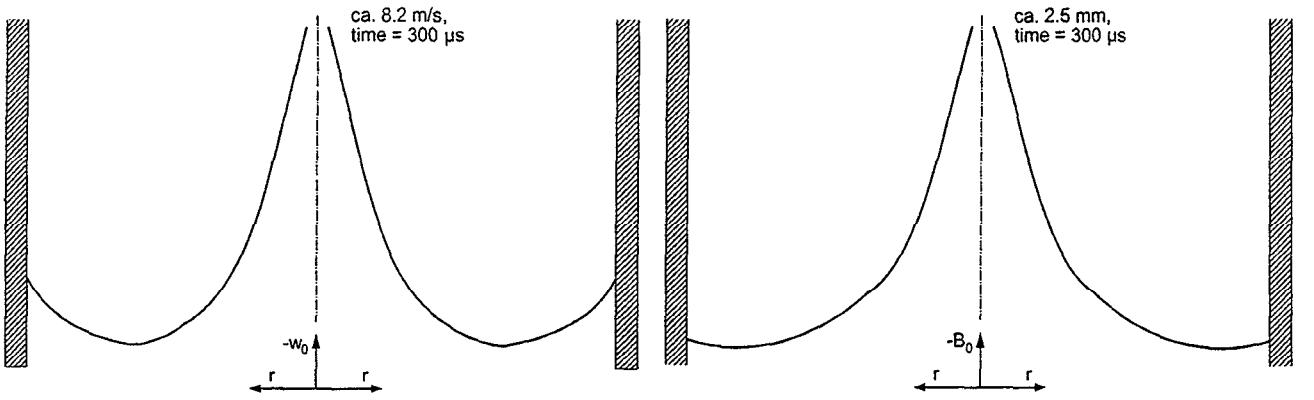

Figure 10: Calculated expulsion of the liquid through the open surface of beam entry for a 1 µs pulse of 60 kJ. (a) Velocity profile at 300 µs after the pulse (b) Surface contour at 300 µs after the pulse.

For the case of an elastic dome-shaped cover the stress distribution along a line running from the apex of the cover down the dome and along the cylindrical wall is shown in Fig. 11 for two different times after the pulse. It can be seen that there results a rather complicated vibrational behaviour which is caused by the elastic properties of the system on the one hand and the different travel times of the pressure waves to the various points along this line on the other. The geometry used here was a cylindrical cross section and a wall thickness reduced to 6 cm which explaines the somewhat higher peak at 150 µs compared to Fig. 8.

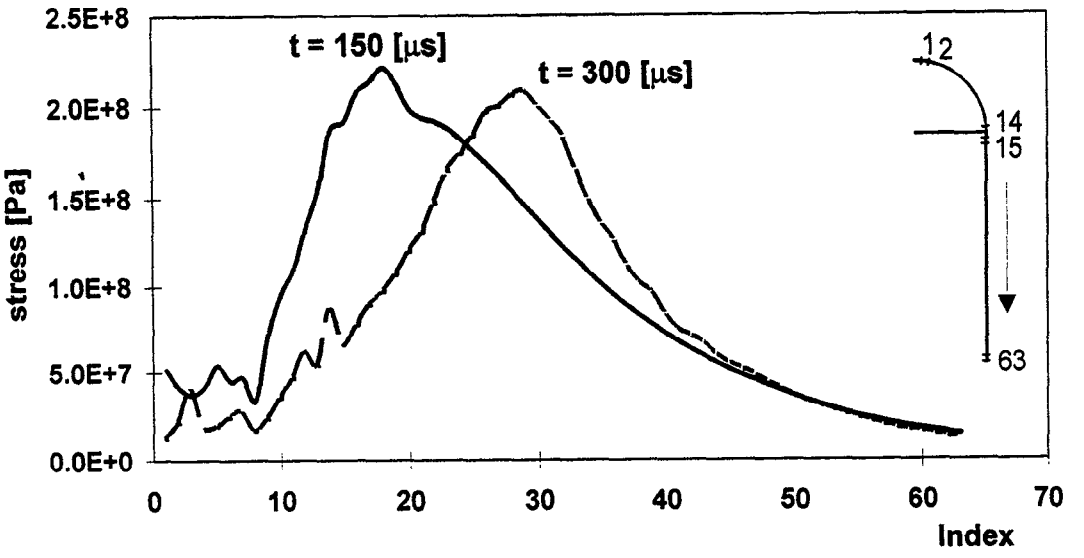

Figure 11: Calculated stress distribution along a line running from the apex of the dome-shaped beam entry window along the dome and down the cylindrical wall (6 mm thick), shown for two different times after the pulse.

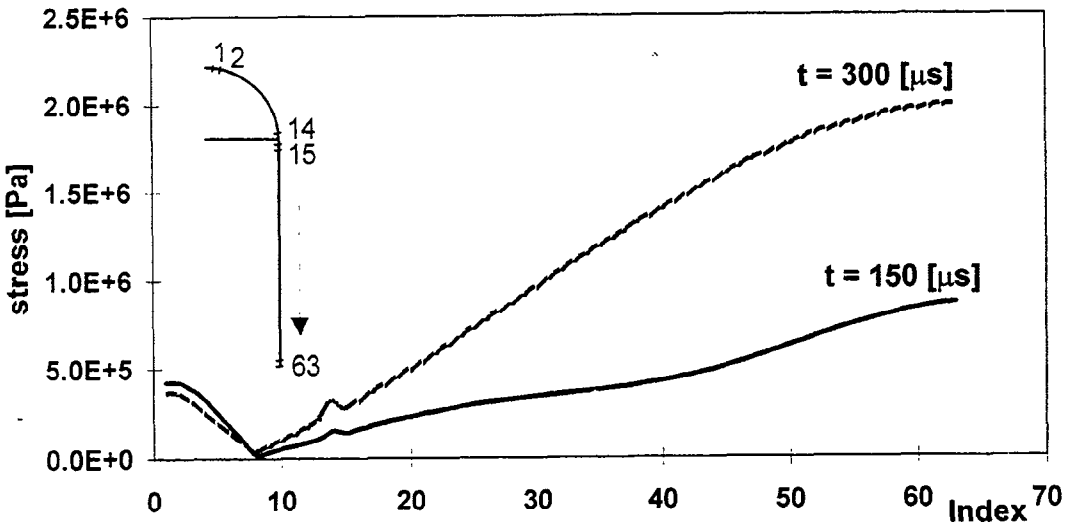

Figure 12: Calculated stress distribution for the same situation as Fig. 11, but with a volume concentration of 3% He in the liquid.

The most significant effect is found after adding a small volume fraction of bubbles to the liquid. Fig. 12 shows the same situation as Fig. 11, but this time 3% of the volume were assumed to be gas bubbles. The maximum stress on the wall has decreased by two orders of magnitude, to an almost insignificant level. It is also obvious that the system reacts much softer with the stress rising during a much longer time after the pulse. As discussed before, this effect depends rather critically on a minimum fraction of bubbles. In the regime where the volume of the bubbles is not enough to accommodate the full expansion of the liquid we find some puzzling effects which we still need to investigate in more detail.

7. Conclusions

While our results are still of preliminary nature in particular as far as absolute numbers are concerned, the program system we have developed clearly allows us to judge the effect of parameter variations such as the pulse duration and the beam geometry in the system. In particular the opportunity of injecting gas bubbles in the beam interaction region might, if a technical solution can be found, provide a means to supress nearly totally the effect of pressure waves. This will make the heat deposition in the window itself, which has so far been neglected completely in our calculations, the main source of stress. From our results we are confident that a liquid metal should be a viable solution not only for continuous sources but also for pulsed sources in the beam power regime of several MW.

8. Acknowledgement

This work has profited from many discussions with various collegues, in particular B. Smith and Y. Takeda. We would also like to thank L. Ni for help with the calculations and producing the figures. The work was carried out in the frame of a grant obtained from the Bundesamt für Bildung und Wissenschaft (BBW-contract Nr. 94.0134) in the context of the Human Capital and Mobility Program of the EU, contract Nr. CHRX-CT94-0503.

9. References

[1] G.A. Bartholomew and P.R. Tunnicliffe (eds.) "The AECL-Study for an Intense Neutron Generator", *Rep. AECL-2600.* (1966)

[2] G.S. Bauer, "SINQ-Status Report Oct. 1990" in *Proc. ICANS-XI,* Tsukuba, KEK-report 90-25 (1991) p. 41-60

[3] G.S. Bauer, H. Sebening, J.-E. Vetter and H. Willax (eds.) "Realisierungsstudie zur Spallations-Neutronenquelle" *Report Jül-Spez-113* and *KfK 3175* Kernforschungsanlage Jülich und Kernforschungszentrum Karlsruhe (1981)

[4] H. Lengeler and J.L. Finney "The European Spallation source", *Europhysics News,* 25, (1994) p.37 - 38

[5] J.D. Gordon, J.K. Garner, N.M. Ghoniem, J. F. Farmer "Ferritic Steel Applications in the MARS High Temperature Blanket" *Proc. Topical Conference on Ferritic Alloys for Use in Nuclear Energy Technologies*, Met. Soc. AIME (1984) pp. 157 - 167

Appendix

A1 Computing the pressure in the liquid metal

General

The pressure being a function of volume V and temperatur T, we have for any differential change:

$$dp = \left(\frac{\partial p}{\partial V}\right)_T dV + \left(\frac{\partial p}{\partial T}\right)_V dT \tag{A1.1}$$

The modulus of isothermal volume compressibility K is defined as

$$K = \left(\frac{\partial p}{\frac{\partial V}{V_0}}\right)_T = V_0 \cdot \left(\frac{\partial p}{\partial V}\right)_T \tag{A1.2}$$

and the coefficient of volume expansion α_v is

$$\alpha_V = \left(\frac{\frac{\partial V}{V_0}}{\partial T}\right)_p = \frac{1}{V_0} \cdot \left(\frac{\partial V}{\partial T}\right)_p \tag{A1.3}$$

If the interval of heating of the liquid volume is very short, the material will not be able to accomodate the resulting change in volume, i.e. we are dealing with the case of isochoric heating (heating at constant volume). After the pulse there is no further heat input and since thermal conduction effects are much slower that the velocity of sound we may safely assume an adiabatic expansion.

Isochoric case:

The change in temperature due to the depostition of an energy ΔQ into a volume element of mass m is

$$\Delta T = \frac{\Delta Q}{m \cdot c_v} \tag{A1.4}$$

with c_v being the specific heat capacity at constant volumes (J/kg K).

Using dV = 0 in eqn. (A1.1) and eqns. (A1.2) and (A1.3) we have

$$\Delta p = \left(\frac{\partial p}{\partial T}\right)_V \cdot \Delta T = \left(\frac{\partial p}{\partial V}\right)_T \cdot \left(\frac{\partial V}{\partial T}\right)_p \cdot \Delta T = K \cdot \alpha_v \cdot \frac{\Delta Q}{m \cdot c_v} \tag{A1.5}$$

Adiabatic case:

Although, in the adiabatic case, the change in pressure is mainly dominated by the first term on the right hand side of eqn. (A1.1), the minor change in temperature is accounted for in our calculations in order to remain as general as possible.

We rewrite eqn. A1.1:

$$dp = \left(\frac{\partial p}{\frac{\partial V}{V_0}}\right)_T \frac{dV}{V_0} + \left(\frac{\partial p}{\partial T}\right)_V dT \tag{A1.1a}$$

Using the condition for adiabatic expansion (dQ=0) we have

$$dQ = dU + pdV = Cv \cdot dT + pdV = 0 \tag{A1.6}$$

$$\text{with } C_V = m \cdot c_V = \left(\frac{\partial U}{\partial T}\right)_V \tag{A1.7}$$

$$\text{or } p = -C_V \cdot \frac{dT}{dV} \tag{A1.6a}$$

Using

$$C_p = C_V + p \cdot \left(\frac{\partial V}{\partial T}\right)_p \tag{A1.8}$$

and inserting (A1.6a) we obtain

$$C_p - C_V = -C_V \cdot \frac{dT}{dV} \cdot \left(\frac{\partial V}{\partial T}\right)_p$$

which we can rewrite as

$$dT = \frac{\frac{c_p}{c_V} - 1}{\left(\frac{\frac{\partial V}{V_0}}{\partial T}\right)_p} \cdot \frac{dV}{V_0} = \frac{\frac{c_p}{c_V} - 1}{\alpha_V} \cdot \frac{dV}{V_0} \tag{A1.9}$$

Inserting (A1.9) into (A1.1a) and using (A1.2) we obtain

$$dp = K \cdot \frac{dV}{V_0} - \frac{\frac{c_p}{c_V} - 1}{\alpha_v} \cdot \left(\frac{\partial p}{\partial T}\right)_V \cdot \frac{dV}{V_0} = K\left(1 - \frac{\frac{c_p}{c_V} - 1}{K \cdot \alpha_v} \cdot \frac{\partial p}{\partial T}\right)_V \cdot \frac{dV}{V_0} \tag{A1.10}$$

which, with the help of eqns. (A1.2) and (A1.3) can be rewritten to yield

$$dp = K \cdot \frac{c_p}{c_V} \cdot \frac{dV}{V_0} \tag{A1.10a}$$

$$\text{or, } \Delta p = K \cdot \frac{c_p}{c_V} \cdot \frac{\Delta V}{V_0} = \tilde{K} \cdot \frac{\Delta V}{V_0} \tag{A1.10b}$$

The quantity $\tilde{K}$ is called the adiabatic modulus of volume elasticity. Its use makes (A1.10b) formally equal to the first term of (A1.1a) but including the effect of the second term. c_v can be calculated from c_p, which is usually known, by using eqns. (A1.8) and eqn. (A1.3):

$$c_p = c_V + p \cdot \frac{\alpha_V}{\rho}$$

with ρ being the density of the material.

ΔV in eqn. (A1.10b) is obtained as a result of all mass displacements into and out of the grid volume considered and is treated as a "virtual" expansion because it is used to compute the resulting change in pressure.

General case of "slow" heating

In order to be able to treat also the more general case, where some expansion can take place during the power deposition period ("long pulse source") we finally consider the non-isochoric case.

Describing the process as a combination of isochoric heating and subsequent adiabatic compression, we can use

$$dT = \left(\frac{\partial T}{\partial V}\right) dV = \left(\frac{\partial T}{\frac{\partial V}{V_0}}\right) \cdot \frac{dV}{V_0} \tag{A1.11}$$

and eqn. (A1.3) to justify the relation

$$dT = \frac{1}{\alpha_V} \cdot \frac{dV}{V_0} \quad \text{or} \quad \Delta T = \frac{1}{\alpha_V} \cdot \frac{\Delta V}{V_0} \tag{A1.12}$$

which, together with $\Delta Q = C_v \Delta T + p\Delta V$ (eqn. A1.6) yields, for the thermal contribution to the change in volume:

$$\Delta V_{th} = \frac{\Delta Q}{\frac{c_V}{\alpha_V} \cdot \rho + p} \tag{A1.13}$$

The first term in the denominator is of the order od 10^{10} N/m^2 for the case of liquid metals and hence at least 1000 times greater than any value of p to be considered. Neglecting p and using eqn. (A1.3), eqn. (A1.13) can be transformed to yield eqn. (A1.4), which shows that the general case is physically not much different from the isochoric case but the amount of energy is deposited over much longer time periods which, at any point in time, makes ΔQ and the resulting pressure much smaller.

A2 The modulus of volume elasticity for a liquid gas-mixture

Assuming we have a mixture of a liquid matrix of volume V_l with finely distributed gas bubbles of volume V_g we write:

$V_m = V_l + V_g$ (A2.1a), $dV_m = dV_l \cdot dV_g$ (A2.1b)

From the definition V of the modulus of volume elasticity K for the liquid we have

$$dV_l = -\frac{V_{l,0}}{K} \cdot dp \tag{A2.2}$$

In order to determine the second term on the right hand side of eqn. (A2.1b) one needs to know whether the compression of the gas is adiabatic (due to the short time involved) or isothermal (due to the fact that the bubbles are very small and their surface is large). The general formula

$$p \cdot V_g^n = p_0 \cdot V_{g,0}^n \tag{A2.3}$$

holds for the general case of a polytropic compression with

$$1 \leq n \leq \kappa \tag{A2.4}$$

($n = 1$ for purely isothermal and $n = \kappa$ for purely adiabatic compression).

From (A2.3) we have

$$V_g = p_0^{1/n} \cdot V_{g,0} \cdot p^{-1/n} \tag{A2.5}$$

and

$$dV_g = -\frac{1}{n} \cdot p_0^{1/n} \cdot V_{g,0} \cdot p^{-(n+1)/n} dp \tag{A2.6}$$

Inserting (A2.2) and A2.6) into (A2.1b) we obtain

$$dV_m = -V_{l,0}\left[\frac{1}{K} + \frac{1}{n} \cdot p_0^{1/n} \cdot \frac{V_{g,0}}{V_{l,0}} \cdot p^{-(n+1)/n}\right] dp \tag{A2.7}$$

which we formally rewrite as

$dV_m = -V_{l,0} \cdot \frac{1}{K_m} dp$ in analogy to (A2.2). Defining the volume ratio

$$\varepsilon = \frac{V_{g,0}}{V_{m,0}} = \frac{V_{g,0}}{V_{l,0} + V_{g,0}} \tag{A2.8}$$

and taking into account that we are only interested in cases where $V_{g,0} << V_{l,0}$ (up to a few percent), we can set

$$K_m = \left(\frac{1}{K_l} + \frac{1}{n} \cdot p_0^{1/n} \cdot \varepsilon \cdot p^{-(n+1)/n} \right)^{-1} \tag{A2.9}$$

The magnitude of K_e is of the order of 10^{10} N/m^2 and hence K_m is stronlgy affected by ε. Since we don't know exactly what value of n to use, we remain on the safe side (less reduction of K_m relative to K_l, if we use the case of isothermal compression (n=1), although for very short pulses adiabatic compression of the gas bubbles seems more likely.

For He-gas we have $\kappa = 1.63$ and hence

$$1 \leq n \leq 1.63 \tag{A2.10a}$$

$$2 \geq n+1/n \geq 1.61 \tag{A2.10b}$$

EUROPEAN SPALLATION SOURCE
General ESS Meeting
October 16-19, 1995
Weinfelden, CH

Thermal Hydraulics of the ESS Liquid Metal Target

B. L. Smith
Thermal-Hydraulics Laboratory
Paul Scherrer Institute
Würenlingen and Villigen
Switzerland

Abstract

A two-dimensional, CFD[1] study has been initiated to examine the thermal hydraulic processes occurring in one design of the ESS liquid metal target. A progress report on this activity is presented in this article.

Introduction

One conceptual design for the ESS target [1] consists of a horizontal cylinder containing a liquid metal – mercury is considered in the present study – which circulates by forced convection and carries away the waste heat generated by the spallation reactions (Fig. 1). The protons enter the target via a beam window from the left, which must withstand the thermal, mechanical and radiation loads to which it is subjected. For a beam power of 5MW, it is estimated that about 3.3MW of waste heat is deposited in the target material and associated structures. The aim of the present study is to confirm, by detailed thermal-hydraulics calculations, that a convective flow of the liquid metal target material can effectively remove the waste heat and avoid any threat to the structural integrity of the target and its components due to overheating.

The target design adopted for the present study is shown in Fig. 2. The cylinder cross-section is elliptical and the beam window consists of an ellipsoidal dome of thickness 3mm, but tapering to 1.5mm at the centre. An internal flow guide directs cold liquid towards the window from below with a flow contraction near its exit to accelerate the flow over the window and promote efficient wall/fluid heat transfer. One idea to prevent the creation of a stagnant flow region on the outflow side is to make the flow guide perforated [2].

In this initial study, a two-dimensional model is employed which represents a vertical slice along the centre-line of the target. Conservative estimates are made concerning the beam heating power in order that the 2-D model represents a "worst-case" situation.

Numerical Model

Calculations are presented using two multi-purpose, transient fluid dynamics and heat transfer codes, ASTEC and CFDS-FLOW3D, both marketed by AEA Technology, based at Harwell [3,4]. The codes have been developed over many years and are used extensively in Europe and North America for the simulation of practical flow problems and as bases for the development of advanced physical models and computational techniques. A custom-built, interactive, grid-generator program (SOPHIA) is provided as part of the software package, together with a post-processor (JASPER) for the graphical display of results. The pre- and post-processors are fully compatible for the two codes, ensuring that the same mesh structure is maintained for the parallel ASTEC and FLOW3D simulations, and that a meaningful comparison of results can be made.

A 2-D finite-element-type mesh was created to model the target consisting of 6700 meshes, body-fitted to the target geometry, Fig. 3. The front and back faces are defined as symmetry planes and the model is made two elements thick to suppress motion in the third dimension. Note there are mesh concentrations towards the structure boundaries, particularly over the window surface, in order to resolve the expected temperature and

[1] Computational Fluid Dynamics

velocity gradients in the boundary layers adjacent to non-slip (heated) walls. For the last three calculations in the series the structure material of the cylindrical confinement (hull) is also represented. Five elements are used through the thickness to resolve the temperature gradient to the outside surfaces, which are treated as adiabatic boundaries. Note the thinning of the material towards the centre of the window.

The first calculations in the series examine the fluid flow characteristics of the system with the beam turned off; later simulations include heating effects. All calculations reported here are performed for a nominal inlet mass flow rate of 220 kg/s, equivalent to a mean inlet velocity of 1.6 m/s and an inlet Reynolds number close to 3.5×10^5. The high Reynolds number k-ϵ turbulence model with standard coefficients is used throughout. The flow outlet is assumed to be a constant pressure boundary.

Beam Heating

For the target design under consideration, the beam footprint is elliptical with a normalized, transverse power distribution

$$P(x,y) = \frac{2}{\pi x_o y_o}\left(1 - \frac{x^2}{x_o^2} - \frac{y^2}{y_o^2}\right),$$

with x_o(=3cm) and y_o(=10cm) the semi-minor and semi-major axes of the ellipse, respectively (Fig. 2). For the 2D simulation we use

$$P(x,y) = \frac{2}{\pi x_o y_o}\left(1 - \frac{x^2}{x_o^2}\right),$$

maintaining the parabolic distribution in the vertical x-direction, but uniform horizontally. In essence, we are analysing a thin vertical slice through the centre of the target and, since the beam heating is there a maximum, this represents a 'worst-case' scenario. Including the axial variation, the complete power density distribution in the mercury is given by:

$$P(x,y,z) = 6334\left(1 - \frac{x^2}{x_o^2}\right)\exp(-z/L_A)\left[1 - 0.7632\exp(-z/L_B)\right] \quad W/cm^3,$$

in which L_A=14.5cm is the attenuation length and L_B=6.55cm the build-up length. The power deposition in the window material is taken as

$$P(x,y) = 1000\left(1 - \frac{x^2}{x_o^2}\right) \quad W/cm^3.$$

A simple heat balance calculation

$$\dot{Q} = \dot{m}c_p\bar{\Delta T} \tag{1}$$

for the given inlet mass flow rate, $\dot{m}$=220 kg/s, and specific heat, c_p=138 J/kgK, would result in an average temperature increase $\bar{\Delta T}$=184°.

Results

A number of calculations have been performed in a step-by-step process of increasing complexity and flow guide perforation ratios. Results for the cases considered are summarised in Table 1, with more explanation below.

Case A

This is the base case of the series. A target length of 200 mm was chosen (to minimise computer run time) and an impervious flow guide was assumed. The computed flow field is given in Fig. 4 and shows that, as would be expected, a large recirculation region has been formed behind the flow guide, on the outlet side. In fact, the region extends to the outlet, where some inflow is seen, indicating that the length of the model is inadequate for this simulation. The decrease in pressure associated with the venturi contraction at the end of the flow guide is not recovered on the expansion side and a residual pressure drop Δp = 0.026 bar remains between the inlet and outlet channels. Thus, if the flow guide were perforated, the pressure drop

Case No.	Target Length (mm)	Flow Guide Porosity	Recirculation Zone Length (mm)	Mass Flow over Window (%)
A	200	0.0	430	100
B	550	0.0	430	100
C	550	0.15 (z <550)	–	2
D	550	0.06 (z <550)	–	5
E	550	0.06 (z <50)	440	41
F	550	0.06 (z <300)	–	12
G	Case F above with hull structure			
H	Case F above with hull structure and heat			
I	Case E above with hull structure and heat			

Table 1: Cases Considered

would enable bleeding of the inlet flow through the flow guide wall, as proposed to suppress the formation of the recirculation region.

Case B

This is the same as the Case A above except that the target length has been extended to 550 mm to capture the entire recirculation zone. Velocity vectors and negative axial velocity contours are given in Fig. 5 for this case and show that the recirculation extends to a distance 430 mm from the window. Otherwise, the flow is similar to Case A. Hereafter, all calculations refer to this extended model, whether or not the recirculation region exists.

Case C

For this calculation the flow guide is made porous along its entire length with a uniform perforation ratio γ=0.15. The pressure drop through the pores of the plate is assumed to be of the form

$$\Delta p = \frac{1}{2}\rho\zeta u^2,$$

in which u is the superficial velocity; that is, $u = \gamma u_d$, with u_d the actual velocity through the perforations. The value of the friction coefficient, ζ=94, is derived from tables of hydraulic resistances [5].

There is now no recirculation region (Fig. 6), demonstrating that the concept of a bleed flow through the flow guide wall has achieved the desired result and improved flow efficiency. One sees that most of the pressure loss in flow guide channel occurs before the contraction. In fact, the mass flow over the window is reduced to 2% of the inlet flow, and is surely insufficient to maintain adequate window cooling. Clearly, better optimisation of the design is necessary.

Case D

For this variant the perforation ratio is reduced to γ=0.06, again assumed uniform along the entire length of the flow guide, and the friction coefficient increased to ζ=590 [5]. The calculation reveals that, despite the increased flow resistance through the flow guide wall, the mass flow discharge to the window increases only marginally to 5% of the inlet flow. Otherwise, the flow field is qualitatively similar to Case C. Evidently, there is too much flow leakage at the upper end of the flow guide which does not contribute to the elimination

of the recirculation zone and is then unavailable for target cooling.

Case E

Here, only the curved end of the flow guide is perforated, with a perforation ratio γ=0.06, and the remainder is considered impervious. With this arrangement, though the flow discharge to the window region is now 41% of the total flow, the recirculation on the downstream side has reappeared and is much the same length (440mm) as before. Clearly, some intermediate configuration must be sought.

Case F

For this calculation the flow guide is perforated over about half its length (z <300mm) with γ=0.6, as before, and solid thereafter. With this combination, the recirculation zone has again disappeared but the discharge flow to the window is reduced to 12% of the total flow which may not be sufficient to maintain effective window cooling.

Interestingly, some of the flow which permeates the end of the flow guide is swept over the window rather than towards the outlet (Fig. 7). This fluid, whilst in transit, is subjected to beam heating and therefore brings extra heat to the window area and forms a stratified mixing layer with the cooler fluid coming from below, via the flow guide. The combined effects could be undesirable and, anyway, rather complex.

Case G

This is a repeat of Case F above, except that the structural elements of the hull are included for the first time. The case is included in the series solely as a consistency check on the mesh development and no further elaboration is necessary.

Case H

We now examine heat transfer effects by turning on the beam power. As noted earlier, the mean temperature increase across the target has been calculated as 184°, based on simple heat balance considerations. The temperature contours in Fig. 8a show local heating considerably in excess of this value. The temperatures are given in Kelvin in the Figure, with an inlet temperature 293.15K (20°C). The peak temperature increase in the target material is 1272° and, in fact, the mean temperature increase from inlet to outlet is 382°. The increase over the theoretical value occurs because the perforations in the flow guide allow some of the coolant to by-pass the heated region, thereby reducing the effective mass flow rate in Eqn. (1).

Temperatures along the axis of the target are given in Fig. 8b, together with those on the upper and lower surfaces of the cylinder. The sharp decrease of about 72° around z=0 is the temperature drop from the outside to the inside of the beam window (thickness 1.5 mm). This should not pose any thermal stress problems for the window material and shows that the constriction at the throat of the flow guide, and the accompanying flow acceleration, maintains adequate window cooling. However, due to the essentially stagnant flow conditions in the body of the target, the overall temperatures are very high and the upper cylinder wall is clearly overheating.

Case I

In this variation, which is a repeat of Case E above but including heating effects, we examine the consequences of increasing the mass flow to the window even though, in the isothermal case, this induced a recirculation zone on the downstream side of the flow guide. Shaded temperature contours for this case are shown in Fig. 9a. Qualitatively, the results are similar to Case H above with peak temperatures in the bulk flow region where the beam heating is greatest, and local overheating on the upper cylinder wall. The peak temperature increase in the target material is 947°, which is 325° lower than for Case H. The mean temperature increase from inlet to outlet, 377°, is little changed, however.

Temperatures along the axis of the target and the upper and lower surfaces are displayed in Fig. 9b. Temperature peaks are generally 200° lower than the Case H and the temperature drop across the window is 71°, little changed from before. In broad terms, it may be stated that, in the present model, the increased mass flow to the window region has more than compensated for the reappearance of the recirculation zone.

Conclusions

First steps have been undertaken in the construction of a computer model to examine the thermal hydraulic behaviour of one design of the ESS liquid metal target. The principle of using a perforated flow guide to discourage the formation of a recirculating flow on the downstream side of the window has been confirmed by means of fluid dynamic computations, for a number of perforation ratios.

Further calculations have been performed which have included beam heating effects. The flow constriction at the throat of the flow guide channel induces a fast streaming of the fluid across the target window from the lower to the upper side. It is shown that this arrangement leads to adequate window cooling, even if only 12% of the inlet mass flow is available for this purpose. However, the stagnation region on the downstream side of the flow guide remains, where the beam heating of the liquid metal itself is a maximum. This leads to extreme temperatures near the axis of the target and overheating of the upper surface. Perforations in the guide tube sufficient to eliminate the recirculation zone allow too much of the flow to by-pass the heated region of the target and the net effect is to exacerbate the overheating problem.

Admittedly, the calculations are two-dimensional and conservative. In particular, natural circulation currents in the transverse plane will go some way to alleviating the high temperatures on the axis of the target. Three-dimensional calculations would need to be performed to quantify this effect, and perhaps parameter studies would then need to be undertaken to determine an optimum design. However, there remains a fundamental defect in the present design in that maximum beam heating occurs in the region of minimum flow, and this will always lead to local overheating. The present study indicates that it would be prudent to pursue alternative liquid metal target designs and try to combine the cross-flow window cooling arrangement with a forced convection flow down the centre of the target to deal with the bulk-heating effect. This idea will be pursued in future CFD studies.

References

1. Gardner, I. S. K., Lengeler, H. & Rees, G. H. *Outline Design of the European Spallation Neutron Source*, ESS 95-30-M, Sept. 1995.

2. Bauer, G. PSI Internal Memorandum, 31 July 1995.

3. ASTEC Release 4.2 User Manual, AEA Technology, Harwell, UK (Aug. 1992).

4. CFDS-FLOW3D Release 3.3 User Manual, AEA Technology, Harwell, UK (June 1994).

5. Idel'Chik, J. E. *Handbook of Hydraulic Resistance: Coefficients of Local Resistance and Friction*, AEC-tr-6630 (1966).

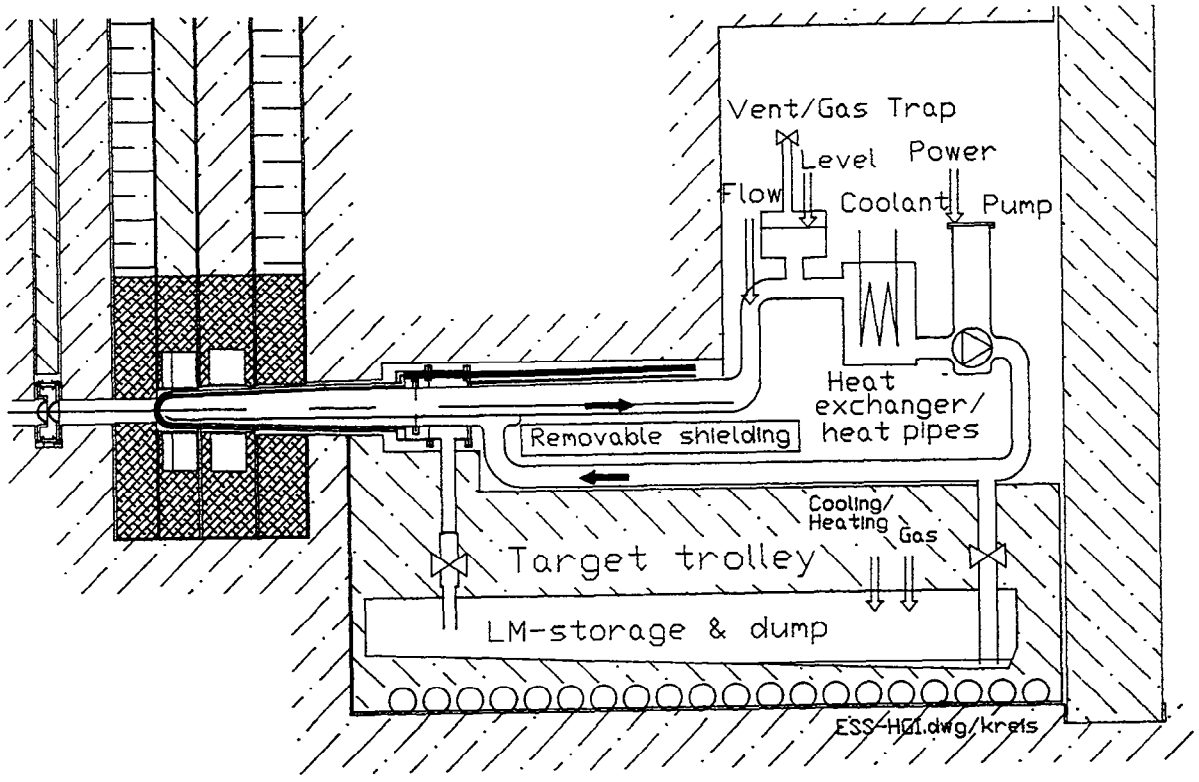

Figure 1: Schematic of ESS Liquid Metal Target Components

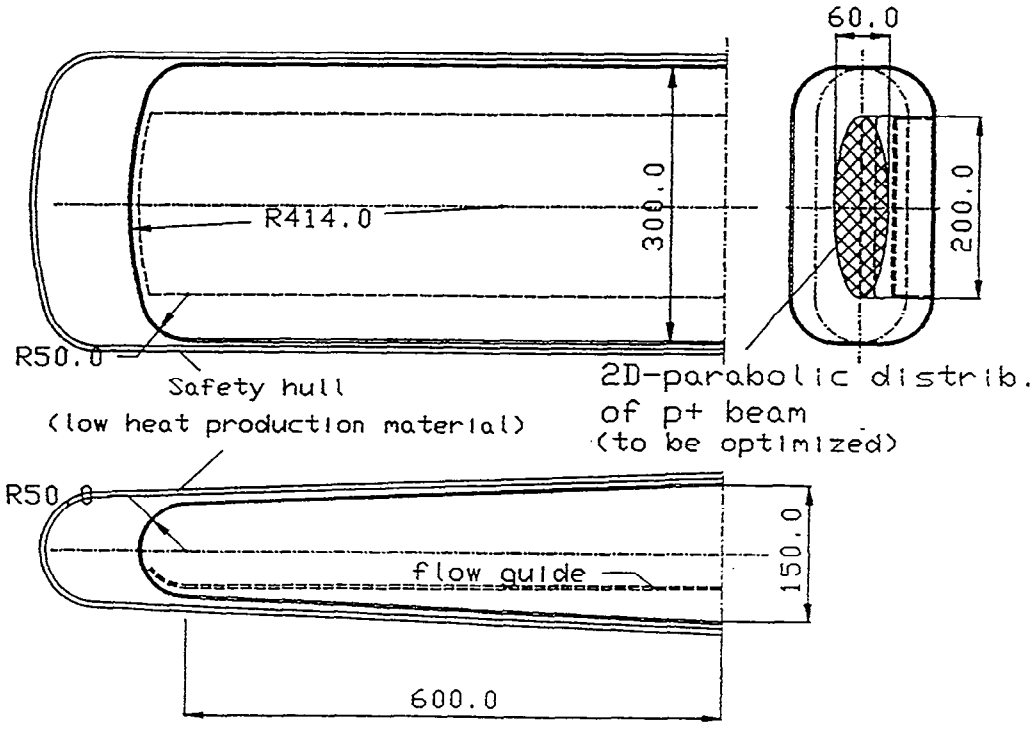

Figure 2: Proposed Target Geometry

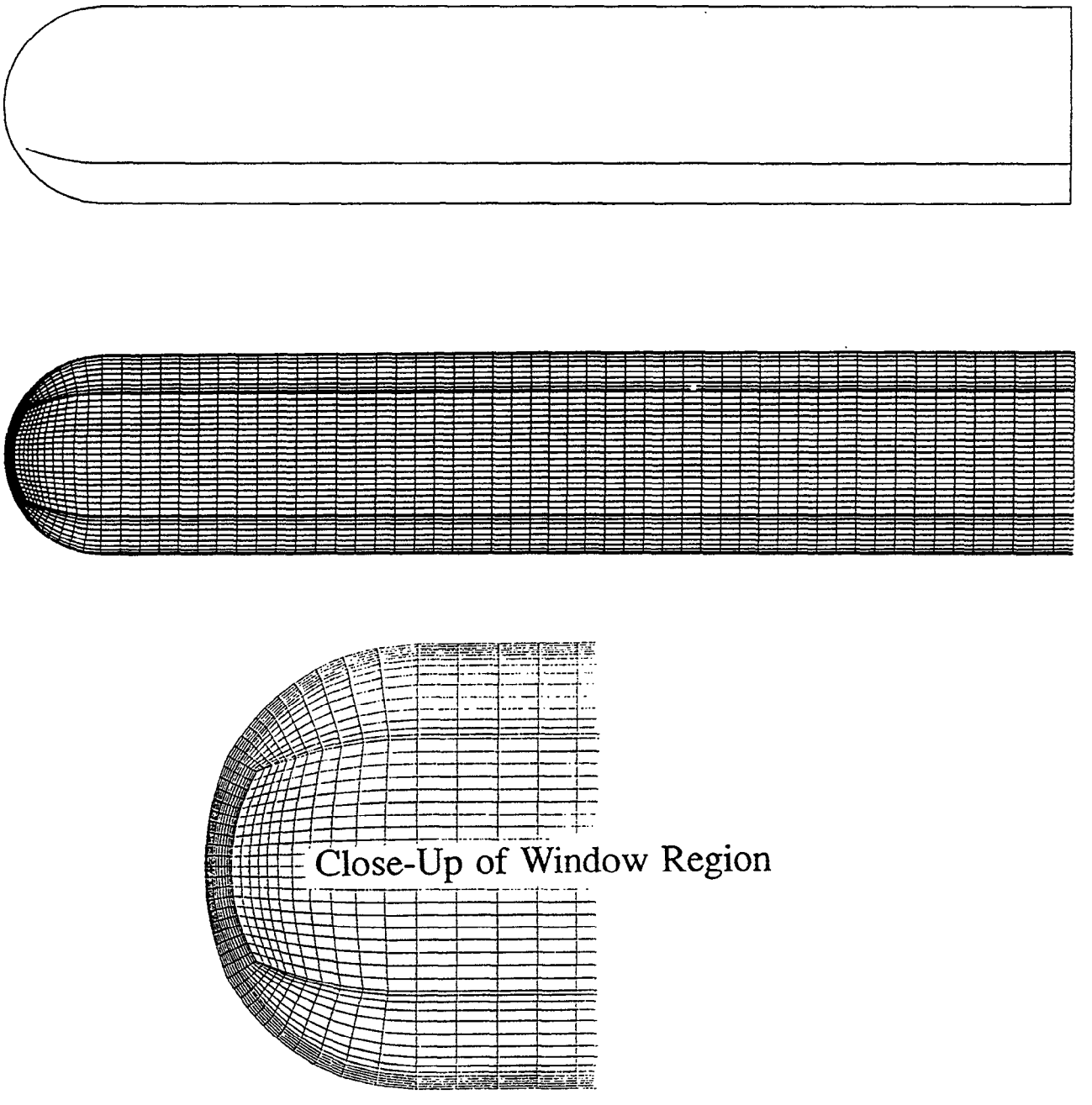

Figure 3: Mesh Geometry

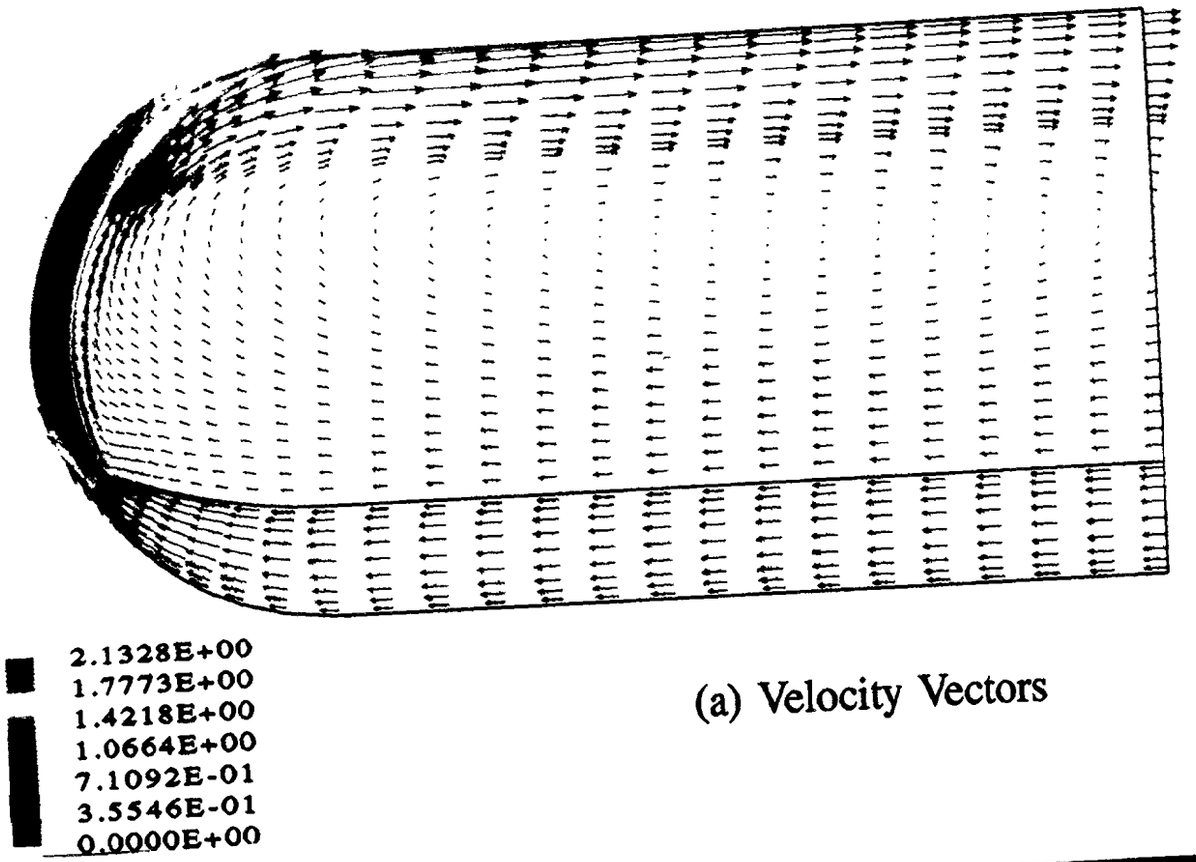

(a) Velocity Vectors

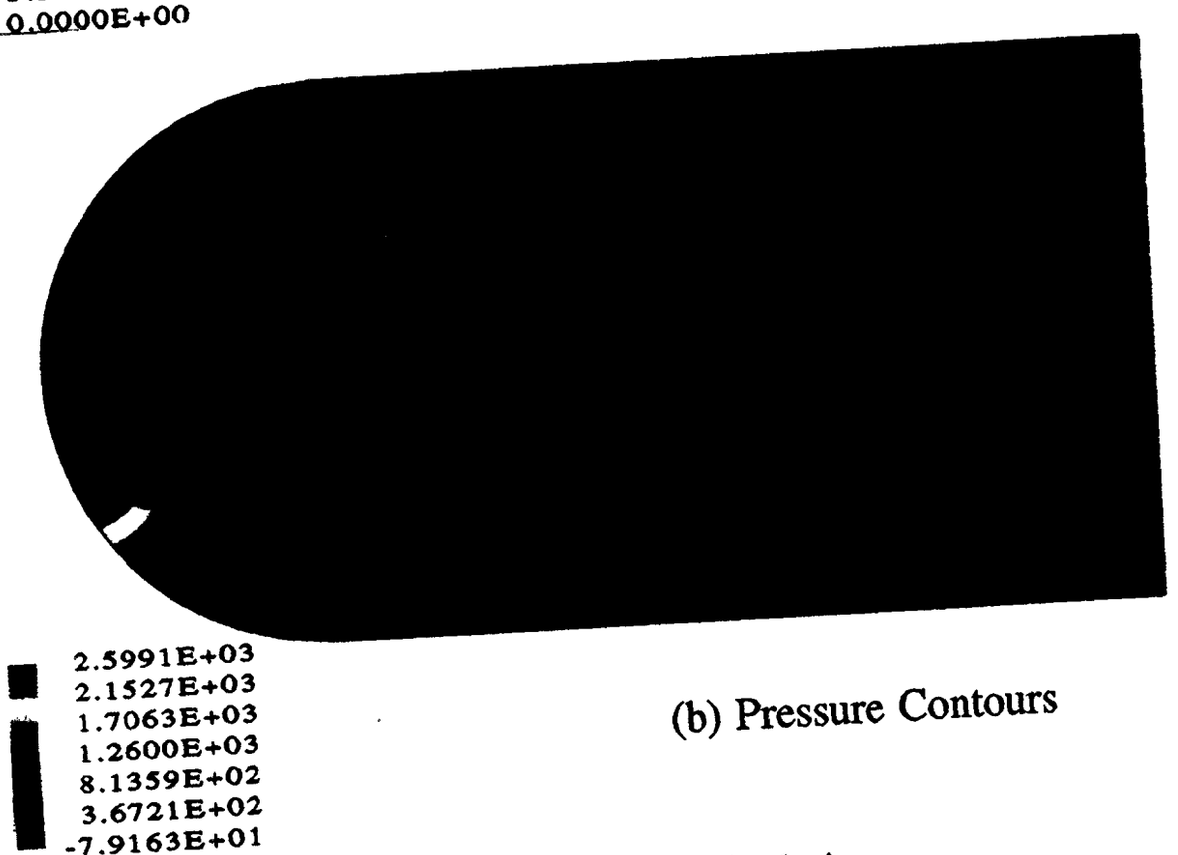

(b) Pressure Contours

Figure 4: Case A Calculation

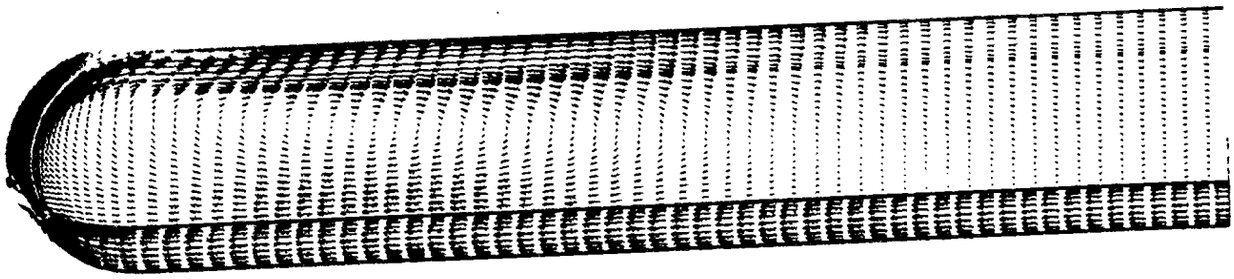

(a) Velocity Vectors

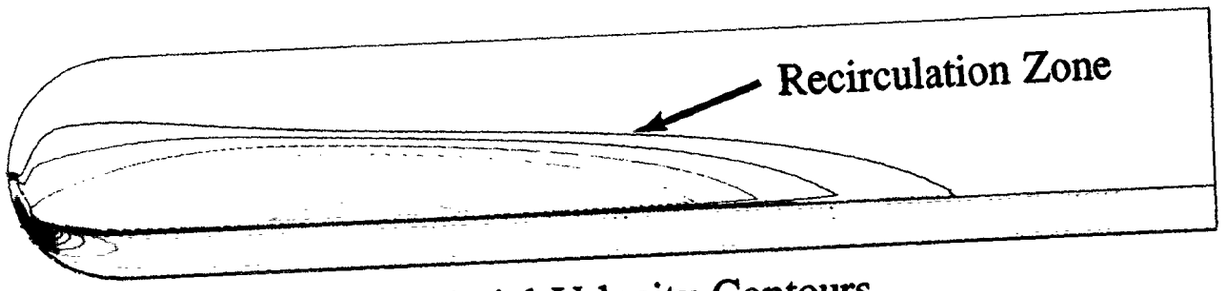

(b) Axial Velocity Contours

Figure 5: Case B Calculation

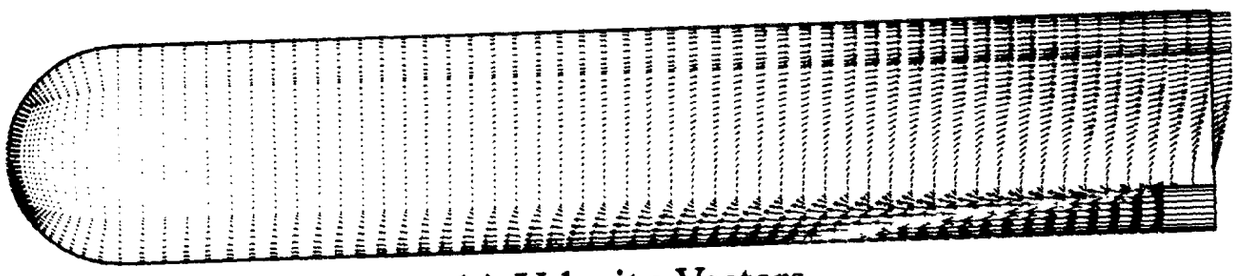

(a) Velocity Vectors

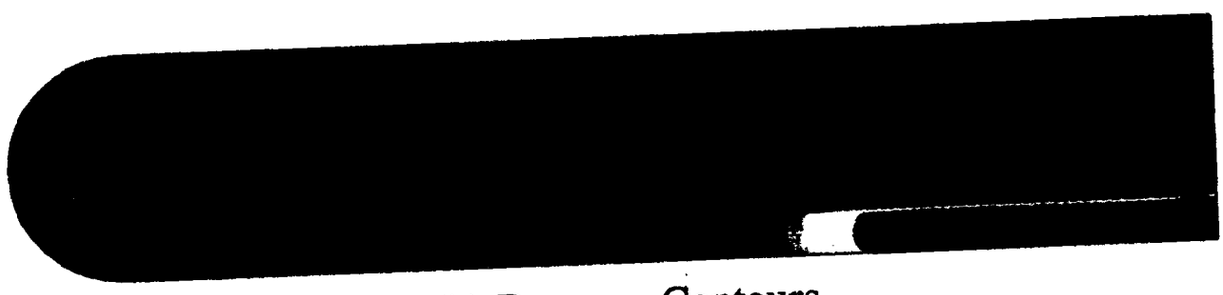

(b) Pressure Contours

Figure 6: Case C Calculation

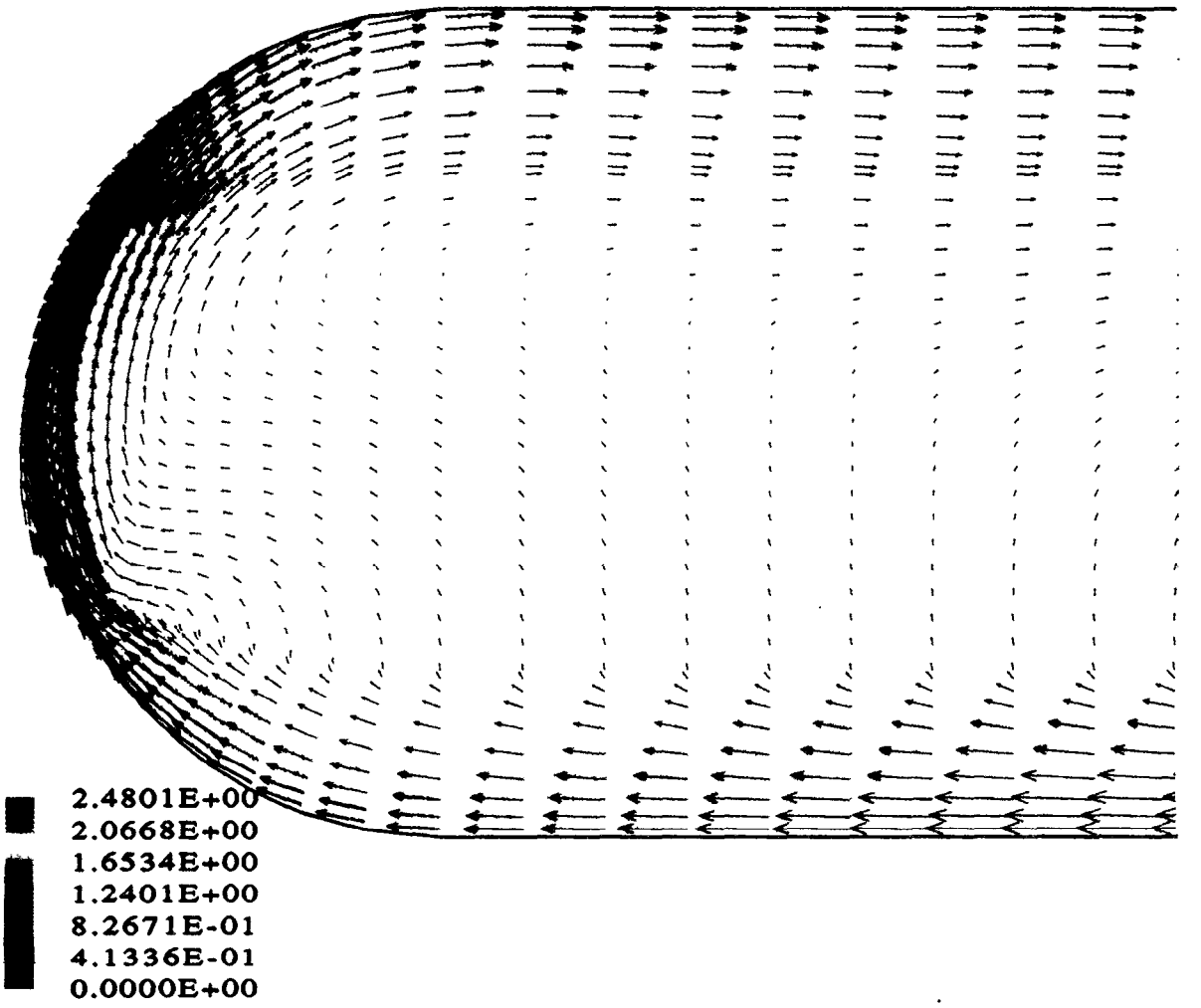

Figure 7: Case F Calculation
Details of the Flow in the Window Region

1.5651E+03
1.3531E+03
1.1411E+03
9.2910E+02
7.1712E+02
5.0513E+02
2.9315E+02

(a) Temperature Contours

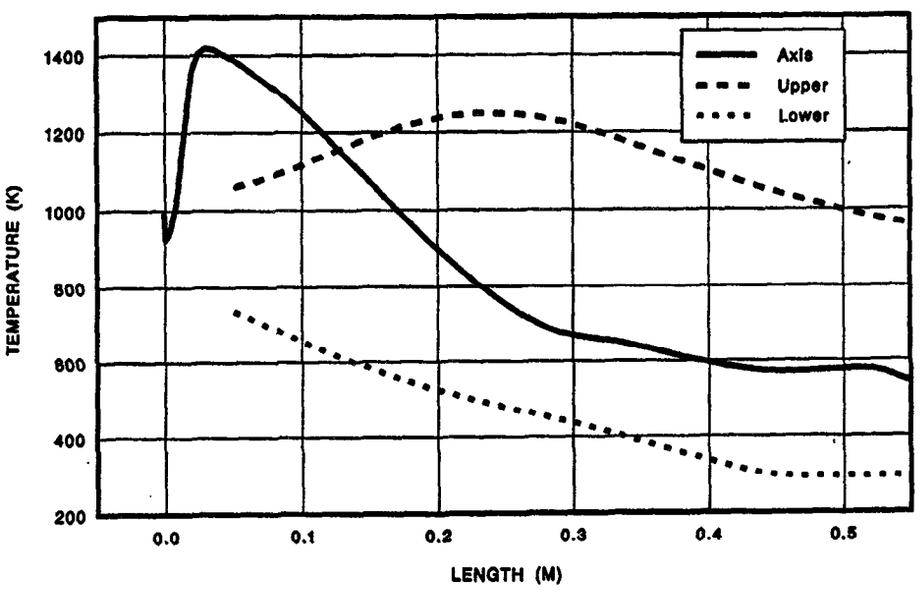

(b) Axial Temperature Distributions

Figure 8: Case H Calculation

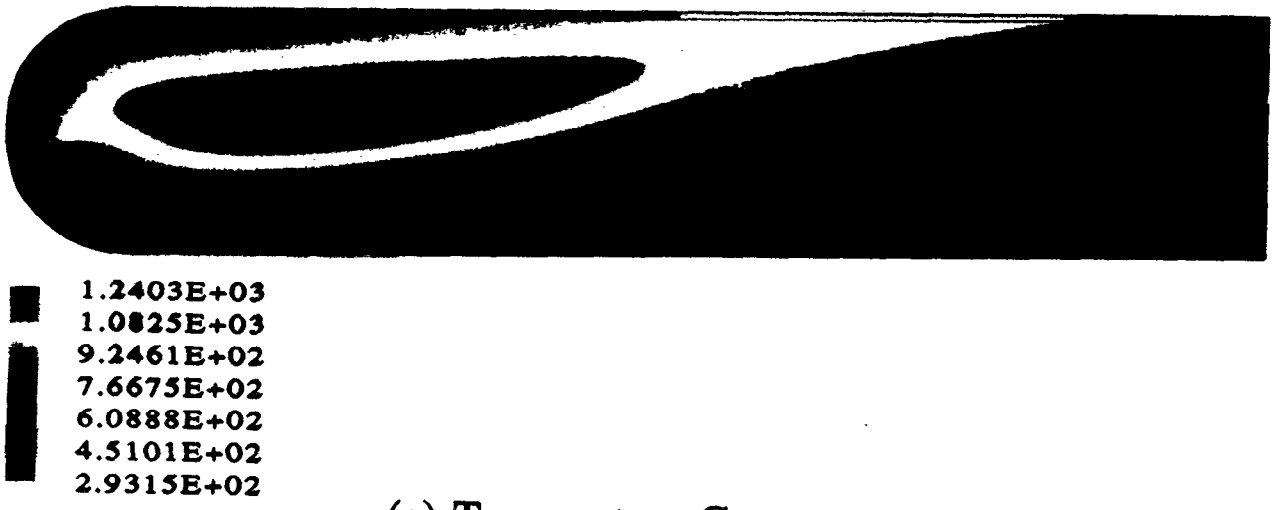

(a) Temperature Contours

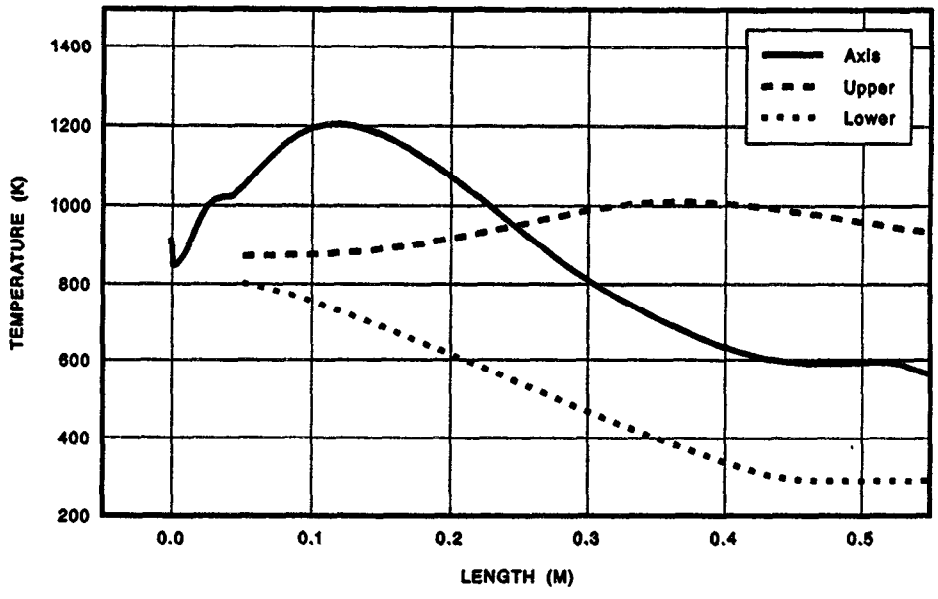

(b) Axial Temperature Distributions

Figure 9: Case I Calculation

ICANS-XIII
13th Meeting of the International Collaboration
on Advanced Neutron Sources
October 11-14, 1995
Paul Scherrer Institut, 5232 Villigen PSI, Switzerland

EXPERIENCE WITH ISOLDE MOLTEN METAL TARGETS AT THE CERN PS-BOOSTER

J. Lettry[1], R. Catherall[1], P. Drumm[1], A. Evensen[1], O. Jonsson[1], E. Kugler[1], J. Obert[2], J.C. Putaux[2], J. Sauvage[2], H. Ravn[1], M. Toulemonde[3]
and the ISOLDE Collaboration

[1] CERN, CH-1211 Geneva 23, Switzerland.
[2] IPN, F-91486 Orsay, France.
[3] CIRIL, F-14040 Caen, France.

ABSTRACT

By moving the ISOLDE mass separators from the 600 MeV Synchrocyclotron (SC) to the 1 GeV PS-Booster Synchrotron [1] the instantaneous energy density of the proton beam went up by 3 orders of magnitude. Sixteen molten metal targets and ion-source units have been used under pulsed proton beam conditions at ISOLDE between 1991 and 1995 and the development of the SC-units to match these requirements is described. Sets of baffles have been designed. Installed in the transfer lines which link the targets and the ion-sources they prevent splashes of the molten metals to flow into the ion sources. The liquid metal containment has been modified so that the electron-beam welds are no longer in contact with the melt. A pyrocarbon disk inserted behind the proton beam entry window reduced its corrosion. Reduction of the energy density of the proton beam obtained by spatial defocusing and time staggered extraction allowed to reduce the shock effect of the pulsed proton beam.

1. Introduction

At ISOLDE [2], radioisotopes are produced by spallation, fragmentation or fission reactions of the target material induced by 1 GeV protons. Typical target materials are refractory metal foils (Ta, Ti, Nb), carbides (Si, U, Th), oxides (Ca, Mg) and molten metals (La, Pb, Sn). They are contained in a 20 cm long, 2 cm diameter Ta-tube of 0.5 mm wall thickness. These containers are heated up to nominal temperature which range from 600 to 2200°C by a DC-current of typically 500 to 1000A. The radionuclides diffuse out of the target material and effuse into the ion-source where they are ionized onto a hot surface, in a plasma or by a resonant laser beam [3,4]. After acceleration to 60kV and mass-separation these radioactive ion-beams are distributed to 15 experimental areas. Under the new pulsed beam conditions at the PS-Booster (3

Keywords : Liquid metal, Target, Shock-waves, CERN-ISOLDE

10^{13} protons/pulse, beam impact area : 3×4.5 mm^2, pulse width 2.4 μs and repetition rate 0.8 to 0.4 Hz) a number of breakdowns were observed when molten metals were used as targets such as flow of the target melt into the ion source, broken welds and corroded proton beam windows. Effects which were not observed during operation at the SC proton beam (1.5 10^{11} protons/pulse of a width of 30 μs and a repetition rate of 100-300 Hz).

2. Design of molten metal targets

Under a pulsed proton beam, the target container and material are submitted to pulsed thermal stress (typically 10^6 cycles), dilatation waves and corrosion. The observation of target units dismantled in a hot-cell showed that none of the above mentioned effects can be neglected. In this section, the computable parameters such as temperature, thermal stress and vapor pressure and the chosen technical issues to the observed damages are presented.

2.1 Temperature pulse and vapor pressure

The energy deposition from the proton beam has been calculated using the Monte-Carlo programs GEANT and FLUKA [5]. The temperature increase and its time evolution was computed by solving the cylindrical symmetric heat equation. The temperature increase at the center of a Ta-disk after one pulse of 3 10^{13} protons reach 600°C. Its time evolution is shown in figure 1. The vapor pressure was calculated and is shown in figure 2 for the hottest spot of the target material for three representative cases : Proton beam turned off, after a nominal proton pulse and for a defocused proton pulse.

2.2 Thermal stress and tensile strength

The thermal stress in a Ta-disk resulting from a nominal proton pulse is 70 Mpa. It is comparable with the expected tensile strength of Tantalum at 1400°C. Indeed, the observations made on metal foil targets showed that the Ta-containers and metal foil target materials which have been used at temperatures up to 80% of their melting points were strongly deformed.

2.3 Baffles

Cross sections of molten metal containers used at the SC are shown in figure 3. The ion-source of a molten Lanthanum target is located 5 mm above the surface of the melt and was found to be filled up with Lanthanum after very few proton pulses. A special unit was then constructed and showed that a contact was established synchronous with the proton pulses, between the melt and Ta-electrodes which hang between 3 and 10 mm above the surface. This was the first evidence of a proton-beam induced movement in an ISOLDE liquid metal target. Baffles were designed and tested which protected the ion source from the splashes (figure 4). Three successive flat baffles installed under 30 degrees in a 50 mm vertical chimney were sufficient to prevent the liquid Lanthanum splashes generated by the proton pulses ($3x10^{13}$ protons within 2.4 μs) to reach the ion source. A temperature controlled helix was inserted in a 60 mm vertical chimney on the Lead target and tested up to 2/3 of the maximum proton pulse intensity. The temperature controlled helix acts as a condensation loop of the Lead vapors which allows working at a higher melt temperature. Finally a set of

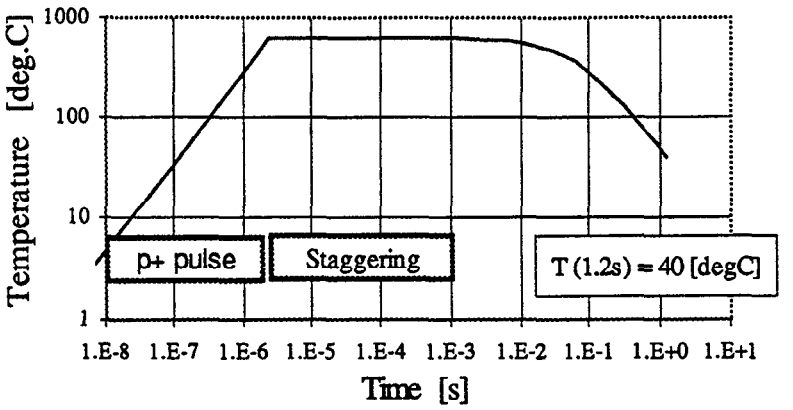

Figure 1. Temperature evolution at the center of a Tantalum disk hit by a 1 GeV proton pulse from the PS-Booster (3 10^{13} protons, beam impact area FWHM : 3×4.5 mm, pulse length 2.4 μs). The time spread of a staggered pulse (≤500 μs between rings) is shown. After a cooling time of 1.2 s the temperature in the center of the disk has increased by 40°C .

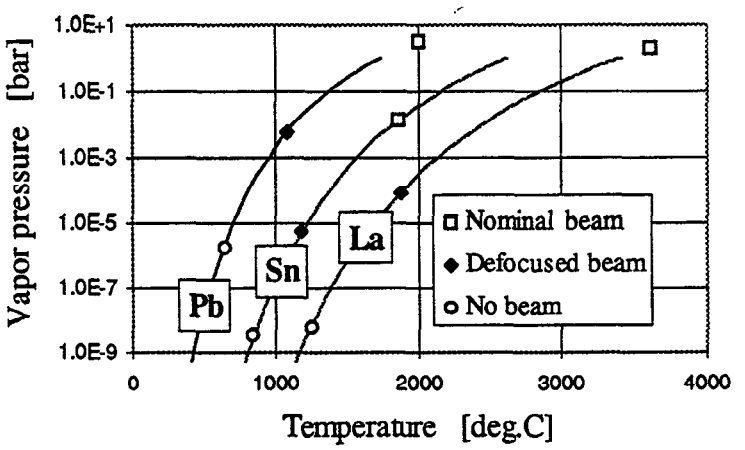

Figure 2. Temperature dependence of the vapor pressure for Lanthanum, Lead and Tin. The Vapor pressure at the typical temperature of the melt (O), the maximum temperature after a nominal proton pulse(□) and the maximum temperature after a defocused proton pulse (◆) are indicated.

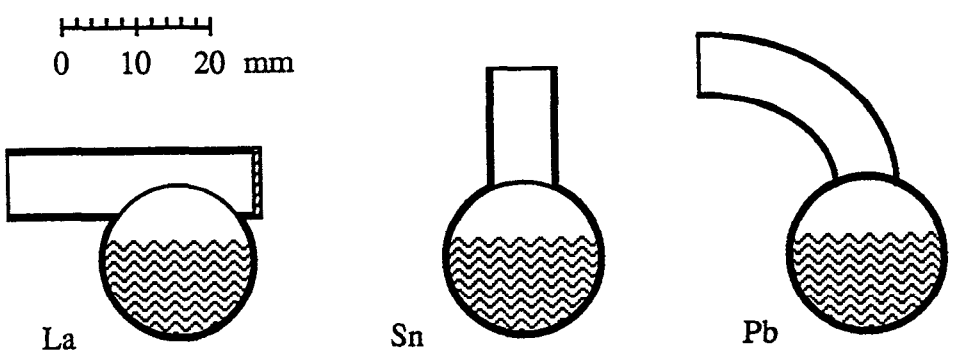

Figure 3. Section of the molten Lanthanum, Tin and Lead target containers successfully used with the SC proton beam. The first part of the transfer lines linking the target to the ion sources are shown.

three temperature controlled Tantalum cones inserted in a 60 mm vertical chimney were successfully tested up to maximum proton beam intensity with a liquid Tin target.

2.4 *Container*

The strength of the pressure wave in the liquid metal was sufficient to break the welds of the thermocouple pockets which were hanging from the top of the container into the melt and the welds of a stainless steel container. The thermocouple were therefore moved outside the containers. The simulation of the target temperature at equilibrium showed that all liquid metal targets are heated by the conduction (and then convection) of the heat generated by the ohmic losses in the current feed welded on both ends of the container tube. Therefore, an improvement of the mechanical strength of the container was obtained by doubling the wall thickness of the Ta-tube (from 5/10 to 1 mm). In addition, the uniformity of the temperature was increased by placing Ta-heat screens around the container.

2.5 *p^+-beam window and welds*

A metallographic investigation of the tungsten-innert-gas (TIG) welds of Ta containers showed that the grain size is much larger than the material thickness thus explaining the large grain boundary leaks observed on the Ta-container of a molten Lanthanum target. Electron beam welds have a much smaller recrystallisation region and the grain size obtained is small compared to the size of the weld. The proton beam window is now cold crimped into the Ta-tube of the container and then electron-beam welded. The recrystallized part is separated from the melt by 10 mm of cold crimped tube (figure 5).

In a test set-up, a liquid Lead target kept at 700 °C was equipped with an temperature controlled Iron helix. A pyrocarbon disk (thickness 4 mm) was inserted behind the proton-beam window in order to prevent the Lead to corrode the Tantalum. The energy deposition of the proton beam on the window was simulated with a 1 kV electron beam. After 4 days, the window was analyzed by electron beam microscopy which showed a 1 mm deep cavity in the container material at the warmest spot of the container which was not covered by the pyrocarbon disk. Ta-Fe alloy in form of grains and layers were found in the colder regions and on the container surface. It could be concluded that, a pyrocarbon layer is a good protection for the proton beam window, and that helix and container must be made out of the same material.

3. Wave threshold

The environment of the targets used for the production of radioactive ion beam is : High temperature (needed for a rapid diffusion through the bulk material), high voltage, and high radiation rates [6] (average dose per target unit : 1 MGy at 10 cm) which excludes investigations during ion-beam production at least with standard target units. A well known feature of the liquid metal targets is their rather slow release time constants (typically ≥30 s) [7,8] and section 4. This time constant is much larger than the time between two proton pulses (which averages to 2.4 seconds) therefore the intensity fluctuation of an ion beam (half life ≥ 30 s) should be below 6% as observed for Mercury and Cesium isotopes obtained at the SC from molten metal targets of Pb and La respectively. In fact, for low proton beam intensities at the PS-Booster the ion-

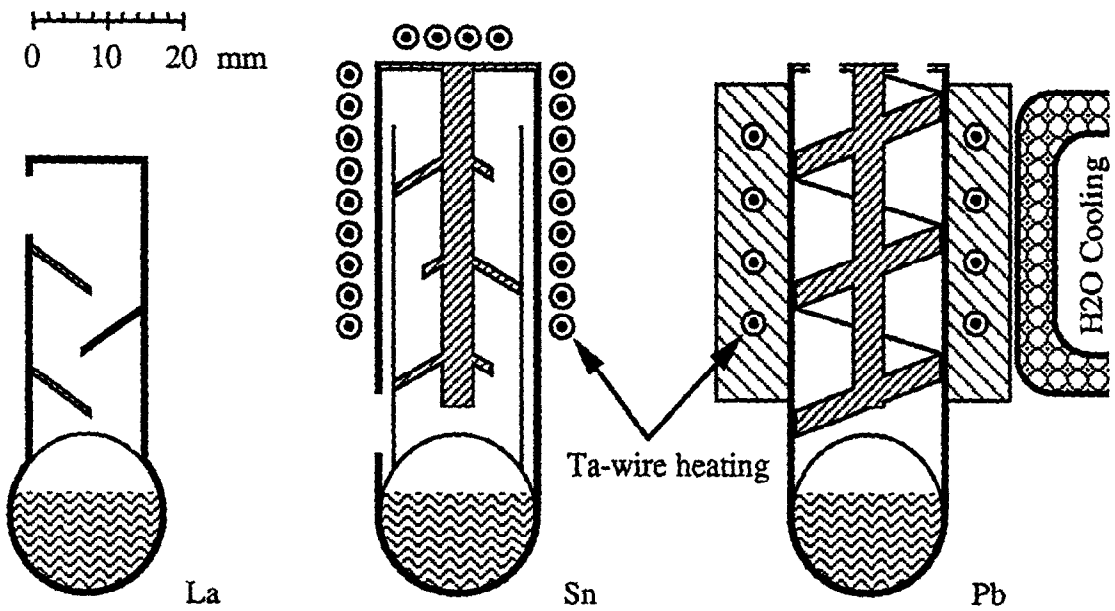

Figure 4. Section of the molten Lanthanum, Lead and Tin target containers designed for operations with a pulsed proton beam. The baffle systems which prevents splashes from liquid metal to reach the ion-source are shown. The chimney of the Tin target can be heated up to 1000°C with a Ta-wire (insulated by Al_2O_3 tube sections). The temperature control (water cooling and regulated Ta-wire heating of the Copper block surrounding the vertical chimney) of the Lead target is designed to operate between 350 and 550 °C.

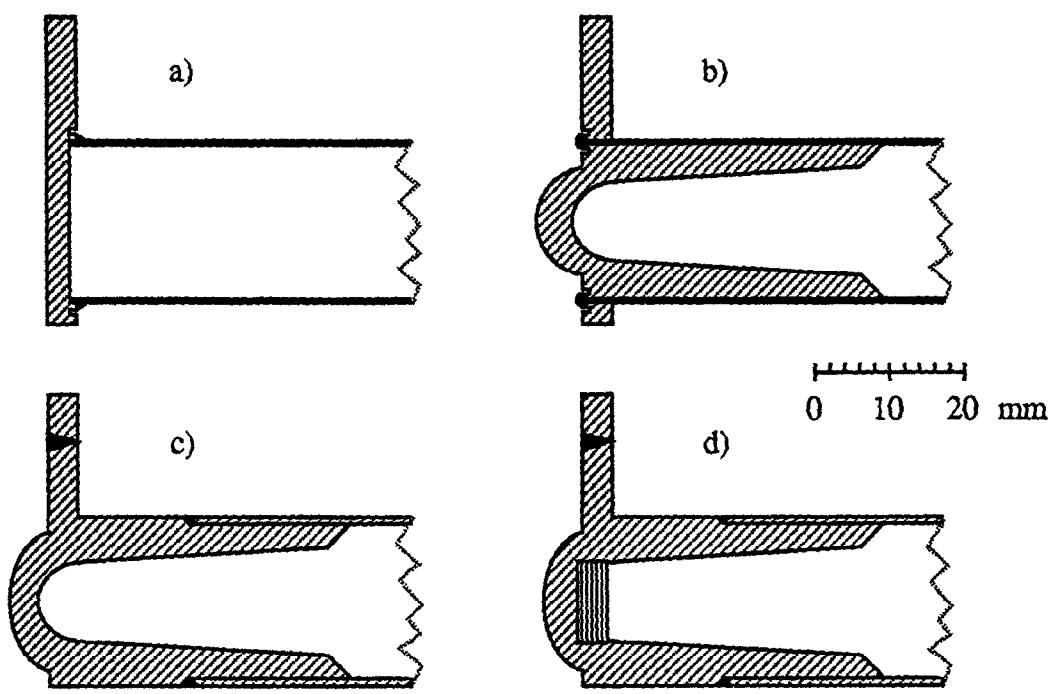

Figure 5. Proton beam windows of the liquid metal containers. a) standard window with TIG-welds and 5/10 mm tube. b) Protected TIG-weld. c) Electron beam weld protected from a direct contact with the melt by a -2/100 tight fit. d) Protected e-beam welds, in addition a 4 mm pyrocarbon disk is tightly fitted under vacuum inside of the proton beam window.

beam intensity is almost constant but large fluctuations of the ion-beam intensities were observed above a given proton pulse intensity. This change in the release mode did coincide with the proton intensity at which contact between the melt and the electrodes has been observed during the "wave test" described in section 2.3. Therefore, a so called "wave threshold", was defined and the smooth or fluctuating behavior of the ion beam intensity is used to monitor the state of the liquid metal. Figure 7 shows a set of successive beam intensity measurements, where smooth behavior is observed below and strongly fluctuating behavior above the threshold.

3.1 Defocalisation test

The energy deposition of the pulsed proton beam heats up the target material and the proton beam window. The target containers which are already at high temperature are therefore submitted to particular high thermal stress. Since the temperature increase is proportional to the energy density, the most natural way to reduce the temperature is to increase the proton beam size. The effect of a two fold increased beam size was investigated by monitoring the ion-beam intensity. We could observe that the wave threshold is 10% higher for a doubled proton beam size (spot size FWHM : 7×11 mm^2) and that the losses in radioactive ion production remains marginal.

4. Hg-release from a molten Pb target

The radioisotope concentration in a molten metal follows an exponential law. At the SC, the time needed to release half of the Mercury isotopes (release time constant) from a molten lead target was typically 120 s [7]. At the PS-Booster a release time constant of 5 s was measured. This short time constant cannot be explained by its temperature dependence (a temperature above three thousand degree would be needed). The faster release is most probably linked to the violent shaking of the liquid metal after a proton pulse and should improve the production of short lived isotopes.

5. Staggered beam test and Cs-release from a molten La target

The PS-Booster consists of four synchrotrons (Rings) each containing five proton bunches (fifth harmonic). The four rings are extracted at time intervals of 0.6 μs. A "standard" proton pulse from the PS-Booster consists of twenty proton bunches delivered in four groups within 2.4 μs. The speed of sound in liquid metal is typically of the order of 10^4 m/s, therefore the time criteria for the existence of a "shock wave" in a molten metal target is met since the relaxation time for a typical ISOLDE target is of the order of 5 to 10 μs. It is therefore of interest to investigate the effects of a time-staggered extraction of the four acceleration rings on the targets and on the release of radioisotopes. The staggering is obtained by increasing the extraction time intervals between rings.

5.1 Proton beam and experimental set-up

In the staggered extraction mode, only three out of the four rings can be used and the time between two rings can be stretched from its original setting of 0.6 μs up

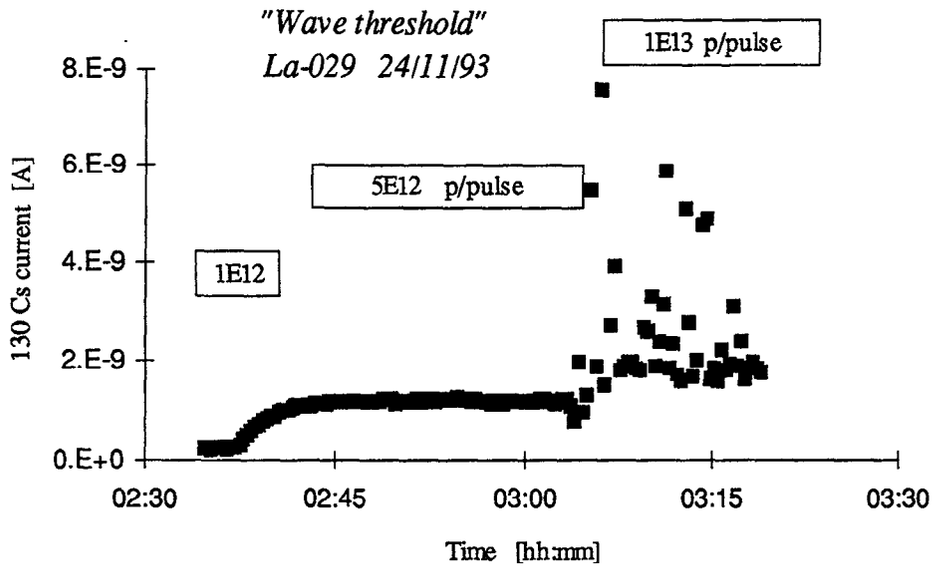

Figure 6. ^{128}Cs ion-beam intensity recorded with successive Faraday cup measurements for different proton pulse intensities. Seven proton pulses were delivered onto the target within the 14.4s PS supercycle. At a proton pulse intensity of 10^{12} and 5×10^{12} protons per pulse the release is smooth, but for a proton pulse intensity of 10^{13} proton/pulse the onset of strong fluctuations of the ion beam intensity are observed.

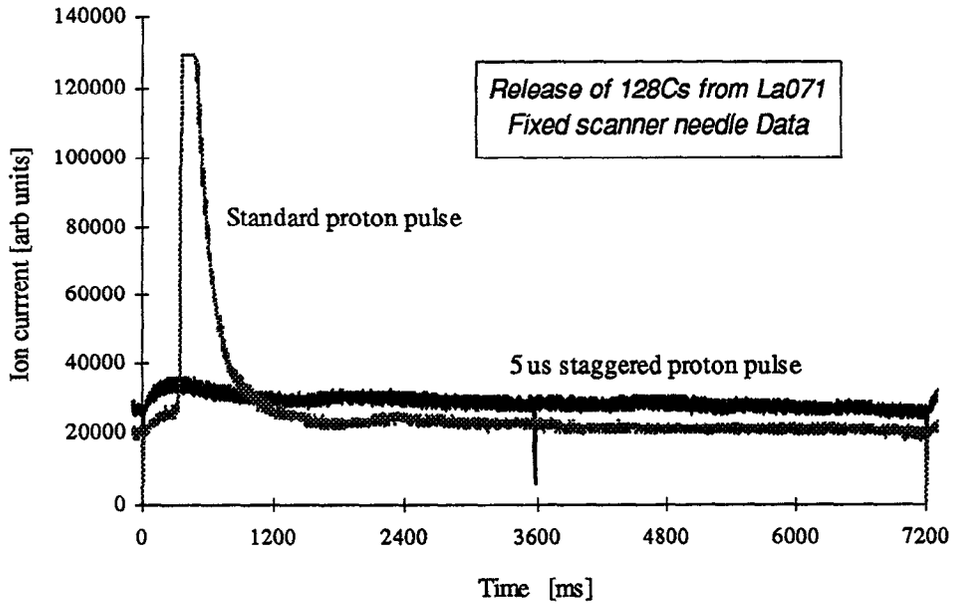

Figure 7. ^{128}Cs ion-beam release from a Liquid Lanthanum target for staggered (5μs between rings) and standard (pulse width of 2.4 μs) PS-Booster proton pulses (1.5 10^{13} protons, FWHM : 7×11 mm). This *"Fixed Scanner Needle"* measurement is an on-line collection of the charge of the ion-beam on a metallic needle, amplification of the signal and readout via a storage oscilloscope.

to 500 μs. Two tests have been performed with a liquid Lanthanum target equipped with a temperature controlled transfer line and a baffle arrangement. During the test, proton pulses were delivered onto the target every 7.2 s.

5.2 *Production yield*

For a fixed staggering time of 500 μs the proton pulse intensity was increased from 7.5 10^{12} to 2.3 10^{13} proton/pulse. The $^{128}Cs^{+}$ beam intensity has been determined after collection of the ion-beam on an aluminized tape and measurement of its β-decay count rate (Tape Station) and by direct measurement of the charge current of the ion-beam (Faraday Cup or Scanner Needle intercepting the ion beam). The ratio of the ^{128}Cs atoms to the proton pulse intensity was found to be almost constant over the full range. A ≤8 % reduction was observed at maximum beam intensity.

5.3 *Influence of the staggering time on the release curve*

At a fixed proton pulse intensity of 1.5 10^{13} proton/pulse the staggering time was reduced from 500 to 5 μs and finally brought to the standard settings of 0.6 μs between two rings. The $^{128}Cs^{+}$ beam intensity as function of time (Release shape) was recorded with tape station and scanner needle measurements. Within the precision of these measurements, all release shapes for staggering time higher or equal to 5 μs are identical. Their release time constant do correspond to the SC value [8]. For standard proton beam, the ion beam intensity shows a different behavior. Large ion-beam peaks are recorded on top of the smooth release shape which is observed with staggered proton beam. These peaks show an ion beam intensity 5 to 10 times higher than the smooth part and a FWHM of 0.3 to 0.5 s as shown in figure 8. The rise time (10 to 90%) of these peaks is typically 20 ms. The distribution of the times between the proton pulse and the start of the peak is not constant, half of them do appear 0.3 ±0.2 s after the proton impact but the remaining are "randomly" distributed. In addition, no "closed transfer line" effect could be observed which would have explained the fluctuations by accumulation of the radioactive vapors during temporary obstruction of the transfer line (by splashes) followed by a sudden release. At the end of the test, the proton beam was switched off while recording the intensity of the radioactive ion beam for 150 s. The time constant of the "beam-off" release of the Cesium from Lanthanum was 32.1 s and is in perfect agreement with the SC measurements for a melt temperature of 1250 °C.

6. Conclusion

The liquid Lanthanum and Lead target are delivering ion-beams to the user community with a proton pulse intensity of typically 10^{13} proton/pulse. The containers, ion-sources and proton beam windows are still operational after $2x10^{18}$ protons.

It was shown that for a staggering time greater than the typical relaxation time of 5 μs and for proton pulse intensities up to 2.2 10^{13} proton/pulse the production yield of radioisotopes is not depending on the pulse intensity, and their release time is identical to what was measured with ISOLDE targets at the SC.

Acknowledgments

This development work was made possible thanks to the following contributions :

Prototypes and calibration :	H. Barbero, J.C. Fabris, M. Gasparini, R. Stoeckli
PS-Booster :	G. Cyvogt, M. Lindroos, K.Schindl, E. Wildner
Shock waves :	G. Bauer, K. Skala, F. Takeda
Metallurgy :	J.C. Dalin, J. Haffner, S. Sgobba
Electronics :	G.J. Focker
Hot Cell :	J.C. Bertrand

7. References

[1] Move of ISOLDE - Implications for the PS BOOSTER, CERN PS/HI 89-7 ISOLDE at the PS BOOSTER, CERN PS/92-46 (PA)

[2] ISOLDE PS Booster Facility at CERN : Experiments with slow radioactive beams, Nucl. Phys. News, Vol 3, No 2, 1993.

[3] S. Sundell, H. L. Ravn, Ion-sources with combined cathode and transfer line heating, Nucl. Instrum. Meth. phys. Res., B 70 (1992), 160-164.

[4] V. I. Mishin et. al., Chemically selective laser ion-source for the CERN-ISOLDE on-line mass separator facility, Nucl. Instrum. Meth. phys. Res., B 73 (1993) 550-560.

[5] P.A. Aarnio, A. Fasso', A. Ferrari, J.-H. Moering, J. Ranft, P.R. Sala, G.R. Stevenson, J.M. Zazula, Proc MC93 Int. Conf. on Monte-Carlo Simulation in High-Energy and Nuclear Physics, Tallahassee, Florida, 22-26 February (1993), World Scientific, p. 88 and p. 227 (1994).

[6] A.H. Sullivan, Radiation safety at ISOLDE, CERN/TIS/RP/93-13

[7] E. Hagebo, *et. al.*, The ISOLDE isotope separator on-line facility at CERN VIII "Performence of the ISOLDE target system" CERN 70-3, 1970, 94-107.

[8] H.L. Ravn, S. Sundell and S. Westgaard, New molten metal targets for ISOLDE, 8th Int. EMIS conf. on low energy ion accelerators and mass-separators. Ed. by G. Andersson and G. Holmen, Chalmers TH, Gothenburg, 1973, 432-444.

ESS-PM4
4th Plenary Meeting of the European Spallation Source
October 16-19, 1995
Weinfelden, Switzerland

Suitability of Steels as ESS Mercury Target Container Materials

Y. Dai

Paul Scherrer Institut, 5232 Villigen PSI, Switzerland

ABSTRACT

A liquid mercury (Hg) target concept has been selected as the first priority development target for the European Spallation Source (ESS). The stability of the Hg target container is one of the most important issues, as under high intensity 1.35 GeV proton irradiation the beam window will be subject to very intensive radiation damage and high thermomechanical loads. In the present report, the material selection for the container will be considered, discussing mostly the data-base accumulated by the fusion program. Two candidate materials, solution annealed 316 type austenitic stainless steel (SA 316) and Sandvik HT-9 martensitic steel, are of primary interest.

1. Introduction

The target-group of the ESS has decided to study a liquid Hg target as the first priority target concept of the ESS target. One of the key issues of this target is the material of the container of the liquid Hg target, as the beam window will receive a very intense irradiation from both 1.35 GeV protons and spallation neutrons: the maximum proton beam density is about 100 $\mu A/cm^2$ for a 10 cm diameter beam of 5 MW [1], the corresponding displacement damage rate is about 0.15 displacement per atom (dpa) per day in steels, and the damage produced by neutrons is at a comparable rate [2], i.e. in total about 0.3 dpa per day. At the same time transmutation elements in particular helium and hydrogen but also other impurities will be produced at high rates. For example in iron about 300, 1450 and 330 appm/dpa of He, H and impurities, respectively, will be generated (calculated by using HETC code). Both radiation damage and transmutations will degrade the mechanical properties of the materials severely. In addition, the corrosion of mercury, which may be enhanced by irradiation, will shorten the lifetime of the container.

The beam window will be subject not only to an intensive radiation load but also to a high thermomechanical load which is due to: 1) the temperature gradient between inside and outside surfaces can be as high as about 90°C for a 2 mm thick wall [1], which produces a static thermal stress at a level about 50 to 100 MPa; 2) pulsed protons can generate stress from

Keywords: Mercury target, Structural materials, Radiation effects

pressure waves with an amplitude of several tens of MPa [3]; and 3) the deflection of the Hg flow at the window may produce ~50 MPa pressure. Therefore, the material of the liquid mercury target container (LMTC) should be able to support the mechanical loads, have a good radiation damage resistance and resist mercury corrosion.

At present, data on the property changes of materials under high energy proton irradiation is still very limited, especially for dose >1 dpa. However, a large database on materials for nuclear applications, particularly for future fusion reactors has been achieved in the last two decades by using fission neutron irradiation. These results can be a good reference, although there are large differences between high energy proton irradiation and fission neutron irradiation.

In the fusion program, both austenitic stainless steels and martensitic/ferritic (MF) steels are favoured as reference materials for the first wall and blanket of future fusion reactors. SA 316 is considered the most feasible one. The main disadvantage of austenitic stainless steels is the high void swelling rate at temperatures above ~400°C. The MF steels, on the other hand, present a ductile-brittle transition temperature (DBTT) which usually is increased substantially by irradiation [4]. In this paper, our interest will be focused on the behaviours of SA 316 and MF steel Sandvik HT-9 at low irradiation temperatures (≤~500°C, the optimised maximum design temperature of LMTC), as representative examples of both classes of steel, although SA 316 seems to be too soft to support the mechanical load on the beam window. Other possible classes materials for this application, such as vanadium and titanium alloys will not be discussed in this paper.

2. Microstructures and properties of unirradiated SA 316 and HT-9

2.1. Compositions and microstructure

Compositions of AISI 316 and HT-9 are given in Table 1 which includes also some other steels whose properties will be mentioned in the present paper.

In the solution annealed condition (~1050°C for ~2 h), SA 316 has a very low dislocation density, $< 10^{12}$ m^{-2}, and is precipitate free.

Table 1. Chemical compositions of steels discussed in the present paper (wt %)

Type	Steel	Fe	Ni	Cr	C	Mo	Mn	Nb	Ti	Si	Other
Austenitic	AISI 316	bal	13.7	17.3	0.05	2.26	1.64	-	-	0.56	
	AISI 304	bal	9.35	18.5	0.07	0.02	1.55	-	-	0.48	
	DIN 1.4970	bal	15.2	14.9	0.10	1.24	1.75	-	0.48	0.40	
	PCA	bal	16.6	14.3	0.05	1.95	1.83	-	0.31	0.52	0.05Al
Ferritic	HT-9	bal	0.50	12.0	0.02	1.00	0.50	-	-	0.40	0.5W, 0.33V
	9Cr-1MoVNb	bal	0.09	8.61	0.08	0.90	0.37	0.07	-	0.11	0.21V
	MANET-I	bal	0.92	10.8	0.14	0.77	0.7	0.16	-	0.37	0.2V
	EM10	bal	0.18	8.76	0.10	1.05	0.48	-	-	0.37	0.024N

Like other MF steels with 9-12Cr, HT-9 is usually used in a normalized (austenitizing for 5 min to 1 h at ~1040 - 1080°C, then quenching or air cooling) and tempered (at ~750 - 780°C for 1 to 2.5 h, then quenching or air cooling) condition. The heat-treatment produces a martensitic lath structure with carbide precipitates ($M_{23}C_6$ + MC) at grain boundaries and a partially recovered dislocation network [5,6].

2.2. Tensile properties

Unirradiated SA 316 is relatively soft. As indicated by the data in Table 2, the yield stress (YS) of SA 316 decreases continuously from about 300 MPa to about 160 MPa as temperature increases from room temperature to 430°C, although the ultimate tensile strength (UTS) remains ~ 500 MPa. However SA 316 has an excellent ductility. The uniform elongation is above 30%. Cold-working increases the yield stress of austenitic steels to high levels, however, at the expense of their ductility.

Compared to SA 316, HT-9 is stronger; both YS and UTS are much higher. With increasing temperature, the YS and UTS of HT-9 decrease slightly up to ~ 450°C, then very fast above 500°C. The uniform elongation (UE) and total elongation (TE) of HT-9 are, however, much lower than those of SA 316. The UE and TE of HT-9 first decrease with increasing temperature to a minimum at ~350°C, then increase with temperature.

Table 2 Tensile properties of SA 316 and HT-9 as a function of temperature

SA 316 [7]*					HT-9 [8]				
Temp. (°C)	YS (MPa)	UTS (MPa)	UE (%)	TE (%)	Temp. (°C)	YS (MPa)	UTS (MPa)	UE (%)	TE (%)
27	305	610	48	62	25	607	759	9.7	11.9
77	250	550	41	53	232	547	678	6.1	8.2
227	203	500	31	41	400	504	598	5.1	8.1
327	190	490	31	40	450	508	610	5.7	8.4
426	162	490	34	42	500	484	561	7.8	11.4
577	150	430	31	39	550	418	459	6.7	18.6

* Original data are of SA 316LN which should be not very different to those of SA 316.

2.3 Thermal stress resistance

Thermal stress resistance is an important parameter for the LMTC materials, as very high thermal stresses may be produced by pulsed high energy protons. The thermal stress resistance of materials is a function of thermal conductivity κ, thermal expansion coefficient α, Poisson's ratio ν, Young's Modulus μ and yield stress σ_y, and can be quantified by the relation [9]

$$M = \frac{2\sigma_y \kappa (1-\nu)}{\mu\alpha} \qquad (1)$$

HT-9 has a higher thermal conductivity than SA 316 (~24 W $m^{-1}K^{-1}$ to 16.2 W $m^{-1}K^{-1}$ at 100°C) and a lower thermal expansion coefficient (~11 μm $m^{-1}K^{-1}$ to 15.9 μm $m^{-1}K^{-1}$ at 100°C). These, together with the higher yield stress, result in a much superior thermal stress resistance for HT-9; the parameter M is 8.5 W m^{-1} for unirradiated HT-9 and 1.3 W m^{-1} for unirradiated SA 316 [9].

3. Radiation induced property changes

Data reviewed in this report are mostly from irradiations in both fast and mixed-spectrum reactors. The difference between these two types reactor irradiation is that in mixed-spectrum neutron irradiation, helium is produced in steels containing Ni by a two-step reaction with thermal neutrons:

$$^{58}Ni + n \rightarrow {}^{59}Ni + \gamma \quad \text{and} \quad {}^{59}Ni + n \rightarrow {}^{56}Ni + {}^{4}He \qquad (2)$$

In a fast reactor, with a lower thermal neutron flux, the helium production rate (< 1appm He/dpa in SA 316) is much lower than that in a mixed-spectrum neutron case (~10 -30 appm He/dpa) for Ni containing alloys.

Apart the neutron irradiation results, those of ion irradiation and implantation will also be reviewed.

3.1. SA 316

SA 316 is considered to be the most feasible structural material for the first wall and blanket of a fusion reactor because of the large database available from fission reactor applications and the extended manufacturing experience [4]. In addition to 316 type steels, a number of other Fe-Cr-Ni austenitic stainless steel compositions such as 304 type, PCA (Prime Candidate Alloy) and DIN 1.4970 (see Table 1 for the compositions) have been also investigated intensively in both SA and CW (cold worked) conditions. The results on these steels have been reviewed by a number of authors, e.g. [4,10-14] and will be sometimes shown as a comparison.

3.1.1. Microstructure and swelling

The irradiation induced microstructure in solution annealed austenitic stainless steels is strongly temperature dependent.

Limited data at low temperatures (< ~300°C) and low doses (≤0.5 dpa) shows that the main feature is the formation of small dislocation loops of interstitial type [15,16]. The average size of the loops is 1-2 nm and is almost independent of dose. The loop density was found to be as high as 2×10^{24} m^{-3} at 0.03 dpa for an irradiation performed at 90°C and to decrease by a factor ~10 after a 290°C irradiation [16]. The loop density was measured to be 2.9×10^{23} m^{-3} in the specimens irradiated to 0.5 dpa at 120°C [15], These data suggest that the density of loops saturates or even decreases at higher doses.

At 300°C and above, the small loops disappear. Instead, large (< 10 nm in diameter) Frank loops were observed [17,18]. Studies of both SA and CW 316 irradiated to 34 and 57 dpa in HFIR show that the Frank loop concentration increases slightly with temperature from 300 to 400°C, then decreases as the temperature increases to 500°C. The average size, however, increases continuously with temperature from ~10 nm at 300°C to ~21 nm at 500°C.

In SA 316 ,below 400°C, there are essentially no irradiation induced precipitates formed up to 20 dpa and very few small precipitates were observed at higher doses. At 400-500°C, M_6C and γ'-Ni_3Si phases were observed in HFIR irradiated specimens [19], and $M_{23}C_6$, M_6C, γ'-Ni_3Si, G and phosphides were observed in EBR-II irradiated specimens [19,20].

Small cavities were observed in SA 304L specimens at temperatures and doses as low as 120°C and 0.5 dpa (35 appm He) though in very low concentrations, ~1.5×10^{22} m^{-3} [15]. At 300-500°C, cavities are usually observed abundantly at high doses. With increasing temperature, the size of cavities increases and the density decreases [17,18].

Void swelling of austenitic stainless steels usually has a incubation period at lower doses, followed by a linear dose dependence (steady state swelling) with a rate up to 1% per dpa. The length of the incubation depends strongly on composition, heat treatment, temperature etc.. For SA 316, below 300°C, there is no or very low swelling [4,18,21]. At ~ 400°C, in the SA 316 irradiated at HFIR, swelling was still very low (< 1%) up to 57 dpa and 4300 appm He [18,21], but it can be also as high as 4% at ~ 35 dpa for other SA 316 steels [22]. This could be attributed to differences in the compositions.

3.1.2. Tensile properties and fracture toughness

At temperatures below 400°C the small dislocation loops and dislocation networks formed during irradiation result in a substantial increase of the yield strength. The yield strength is proportional to the square root of the dose at low doses and saturates at high doses. The saturation is dependent on the temperature but independent of the initial condition (annealed, cold worked or weld) of the steels and of the irradiation neutron source, when they are compared on the basis of dpa [10,12]. At 300°C the yield strength saturates at about 800 to 900 MPa at a dose of ~10 dpa. In the case of saturation, the yield stress reaches about the same level as the ultimate stress, i.e. σ_u/σ_y is equal to ~1 and no work hardening is present in the tensile curve.

The change in ductility due to irradiation at low temperatures is still uncertain due to the few data available, especially at around 100°C. Generally, in the temperature range from 200 to 400°C, at doses between 10 and 30 dpa, the UE of the steels decreases to less than 1%, followed by some recovery at higher doses. The UE is usually greater than 1% at a temperature between 400 and 600°C and greater than 5% at 50°C. Although the UE is very low at temperatures between 200 and 400°C, the TE is maintained above 5% for the steels irradiated up to 44 dpa / 3500 appm He in HFIR and other reactors [7,10,11, 23-26], see Fig. 1. This indicates that the steels still have a substantial capacity for plastic deformation.

Helium and hydrogen effects on tensile properties were also studied by post-implantation tests at 200°C in SA 316L base material and at 200 and 400°C in its welds, with helium and hydrogen concentration up to 375 and 2750 appm, respectively [27]. The results show that the effect of helium implantation is more pronounced than that of hydrogen implantation. At 200°C hardening and reduction of ductility occurred. At 400°C most hydrogen implantation induced changes are recovered. Ductile failure were observed in all cases.

The hardening and the loss of ductility result a significant decrease in the fracture toughness (resistance to crack initiation) and even more severely in the tearing modulus (resistance to crack propagation). For SA steels and their welds, the fracture toughness, K_{1C}, decreases from ~300 MPa $m^{1/2}$ at unirradiated condition to about 50 to 100 MPa $m^{1/2}$ at the saturation dose level (< ~10 dpa) and the tearing modulus decreases from ~300 to as low as 10 to 20 at the same time [28-30].

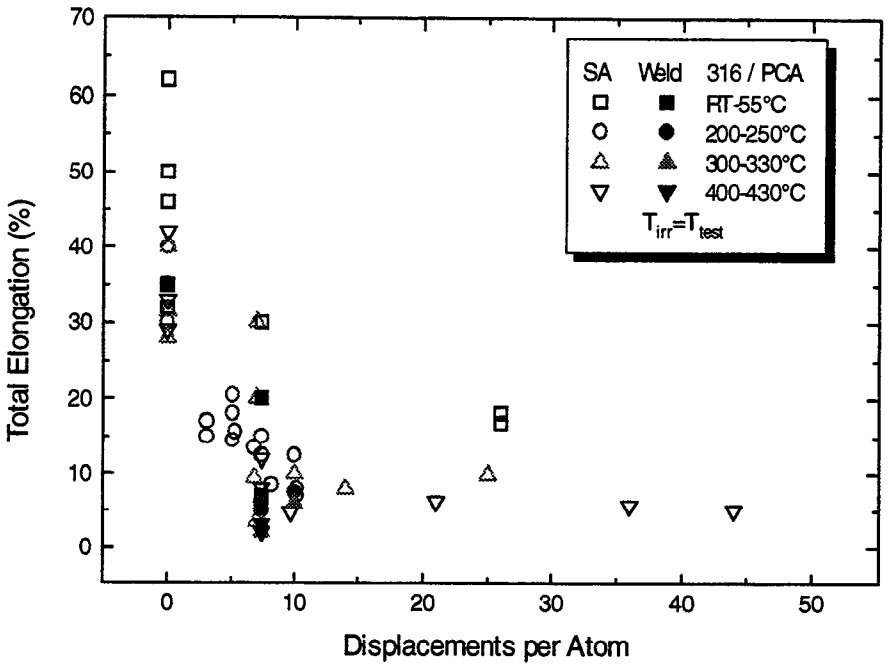

Fig. 1 Total elongation of SA 316 / PCA and their welds as a function of irradiation dose. Data are quoted from [7,10,11,23-26].

3.1.3. Creep and rupture

The effects of irradiation damage can produce very large changes in dimensions in austenitic steels and their welds by means of void swelling and irradiation creep.

As mentioned above, as the LMTC window will be subjected to a high mechanical load, irradiation creep is an important consideration.

Limited data published in 1970s on solution annealed 316 type steels showed that the creep rate of SA steels was similar to or even lower than that of CW (~20%) ones [31-33]. This is supported by recent results demonstrating that at 400°C, there is essentially no difference in the creep rates of 10, 20 and 30% cold worked titanium modified 316 (D9) stainless steels [34]. Fig. 2 shows the results from [32,33] given as stress-normalised creep strain versus irradiation dose. The difference between two data bands may arise from the different compositions of the steels as well as from the different dose rates in the two irradiation sources. Creep rate was found to have either a linear dependence on dose rate [4,35] or to be proportional to the square-root of dose rate [4,31,36].

The irradiation creep rate of the stainless steels has a weak dependence on temperature in the range 200 to 600°C [4,10,31] but it has been found to increase substantially at 600°C for 316 and PCA irradiated in the ORR spectral tailoring experiment [10,37].

Only one set of data [38] showed that the higher He/dpa ratio in ORR increased the creep rate of 25% CW PCA as compared to an irradiation in FFTF. The increase is expected to be due mostly to the lower displacement rate in ORR [4]. The very limited data at relatively low helium concentration (≤ 200 appm) is insufficient to understand at this point the effects of helium on irradiation creep.

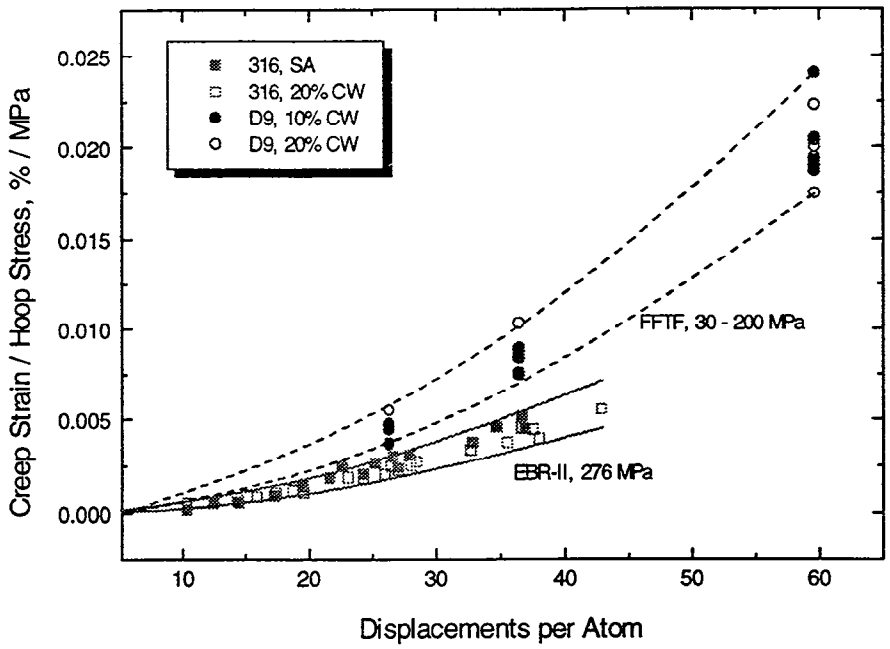

Fig. 2 Stress-normalised creep strains as a function of dose for 316 and D9 stainless steels (pressurized tubes) irradiated in EBR-II [32] and FFTF [34] at 400°C.

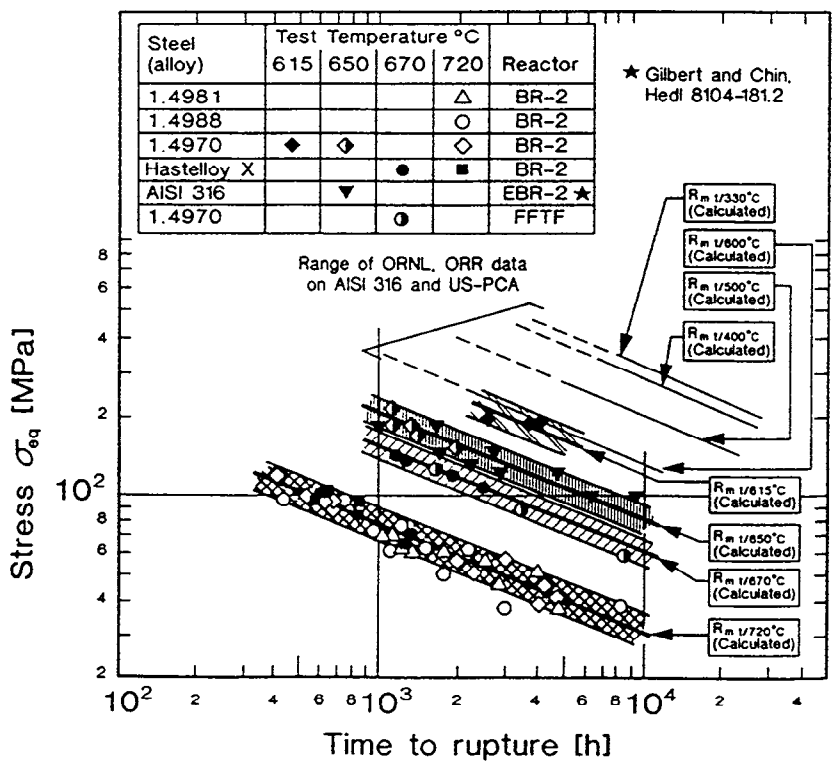

Fig. 3 Creep rupture life vs. stress of austenitic alloys irradiated in fast and mixed-spectrum reactors. (After [10])

At high temperatures (> 500°C), the loss of ductility and the reduction of creep rupture life are usually attributed to the growth and coalescence of helium bubbles on grain boundaries, namely helium embrittlement [10,39,40]. However, at 400°C and below there are no indications of helium embrittlement up to a concentration of 3500 appm [41].

Creep rupture life of a number of austenitic stainless steels was investigated in a temperature range from 575 to 720°C by performing in-pile experiments in reactors BR-2, EBR-II and FFTF [10,42,43]. The results of [43] are given in Fig. 3. The rupture lifetime obtained by [42] has a similar slope with stress but about half of value of that in Fig. 3. These results show that creep rupture life is affected by stress (at ~-5/2 power) and temperature, and is insensitive to factors such as the type of the austenitic alloy, heat treatments, the dose rate and the He to dpa ratio. The extrapolation of the results to low temperatures is demonstrated also in the figure.

3.1.4. Fatigue

Radiation and helium effects on fatigue life of austenitic steels [44-51] and their welds [52] have been investigated in a number of cases by performing post-irradiation or post-implantation tests, where the highest dose and helium concentration are 50 dpa and 4110 appm, respectively [48]. At 550°C and below, fatigue life shows no severe (less than a factor of 2) degradation in most cases [45-47, 49-51], although observations showed a reduction in fatigue life of CW steels by a factor of 3 to 10 at 430°C with low strain rate of 4×10^{-3} s^{-1} [45, 48]. The general trend is that the degradation decreases with decreasing temperature and increasing frequency or strain rate. Transition from large degradation and intergranular fracture at low cycle to no or little degradation and transgranular fracture at high cycles was observed [47,51].

3.2. Martensitic/ferritic (MF) steels

The high resistance to swelling and helium embrittlement of MF steels enables them to be widely used in nuclear applications and has made them the tentative candidate materials for the first wall and blanket in fusion reactors. A number of different type steels have been tested. Our interest is basically focused on HT-9 which is mainly used in the US. Some results on other MF steels with 9-12Cr, e.g. MANET (DIN 1.4914), 9Cr-1MoVNb and EM10 are also given below. The compositions of HT-9 and some other MF steels are given in Table 1.

3.2.1. Microstructures and swelling

Irradiation effects on the microstructure and swelling of MF steels are reported to be dependent on composition, irradiation temperature, irradiation source, dose, and also heat-treatment. The following general features are observed after irradiation at temperatures between 300 to 600°C:

- Irradiation produced dislocation loop density decreases with increasing temperature, but loop size remains constant. Above ~500°C, loops are unstable and the dislocation density remains constant or decreases with irradiation [8,53,54]
- Irradiation induced precipitation of G, α', M_6C and chi-phases were observed after irradiations at temperatures below ~550°C. The $M_{23}C_6$ phase showed no change during irradiation [6, 53-55].
- Helium bubbles were observed in the MF steels irradiated with mixed-spectrum neutrons at 300 to 600°C [56]. Voids, however, were mainly observed at 400 to 500°C [54,56,57]. Void swelling has maximum values in the range of 400 to 450°C [6,54-57].
- HT-9 shows an extremely high swelling resistance [6,54,55] with a swelling rate as low as 0.012%/dpa under fast neutron irradiation up to 208 dpa [58] and mixed-spectrum neutron irradiation up to 37 dpa and ~87 appm He [54] at 400°C.

3.2.2. Tensile properties

Irradiation induced hardening in MF steels is temperature dependent. The YS of HT-9 irradiated in FFTF rises sharply with decreasing temperature from about 420°C down to about 360°C (inlet temperature of FFTF). At 450°C and above, there was essentially no change or even a decrease in YS [4,59]. This phenomenon has been widely observed in MF steels [60,61]. The trend at low temperature seems to extend at least down to 300°C [62]. It is not clear how the strength evolves with irradiation temperature from 300°C down to 25°C as the increase of YS is similar at 300°C and 25°C at a similar dose. The hardening saturates at <10 dpa in HT-9 irradiated in HFIR and EBR-II [60,63] but at a much lower dose (about 1 dpa) in MANET I irradiated in HFR-Petten at 253°C [64].

The effects of irradiation on the ductility of MF steels is less pronounced than in the case of austenitic stainless steels, but the ductility of unirradiated MF steels is already much lower than that of austenitic stainless steels. In Fig. 4, data is also included for unirradiated steels after ageing (e.g. 5000 h at the irradiation temperature), showing essentially no difference with the unaged steels. From the limited data it can be seen that at 450 and 500°C the ductility is influenced little by irradiation. At 400°C and below the ductility decreases but the TE is generally above 3%, except for those irradiations at room temperature to 5-10 dpa, which show the largest reduction in ductility.

The data described above is for materials irradiated by neutrons. However, there are also some limited results from high energy proton irradiation. Following irradiation with 800 MeV protons in the Los Alamos Meson Physics Facility (LAMPF) to ~1.5 dpa at 400°C, HT-9 showed a slight hardening and no significant change in ductility [65]. However, for MANET-I irradiated with 590 MeV protons in the PIREX facility in Paul Scherrer Institut to 0.4 and 0.7 dpa at 170 and 420°C and tested at 20 and 350°C, the results show substantial hardening and reduction of ductility [66].

Helium effects on the tensile properties of MF steels were investigated in Ni-doped HT-9 and 9Cr-1MoVNb irradiated in HFIR at 50°C to doses 5 - 24 dpa [63]. It showed that both the increase itself and rate of increase of yield strength with fluence increased with helium concentration, i.e. largest in the highest helium containing 2%Ni-doped materials, followed by 1%Ni-doped materials and normal materials. Whether the change is due to helium effects is not yet clear because: 1) The yield strength of unirradiated Ni-doped HT-9 and 9Cr-1MoVNb increased with Ni content. This means that Ni itself modifies the mechanical properties; 2) The absolute values of the increase of yield strength are almost independent of the amount of helium; 3) At 400°C and above the difference disappears [62]; and 4) Helium effects were not observed in MANET-I up to 500 appm He [67] and DIN 1.4914 with 100 appm He [68], but observed in 9Cr-1MoVNb and 9Cr-2W [69].

A review of the results produced by European laboratories with accelerator based injected He [67], concluded that in the lower temperature region (≤ ~400°C), no He effects on the mechanical properties had been detected.

3.2.3. Impact properties and DBTT

The irradiation effects of most concern in MF steels are reduction of fracture toughness, tearing modulus and increase of DBTT after irradiation.

For HT-9 irradiated with doses up to 180 dpa, the fracture toughness is little influenced in general, and the reduction of tearing modulus depends on irradiation temperature T_{irr}, as shown in Fig. 5. When T_{irr} is in between 380 - 420°C, the tearing modulus reduces to 70 - 40. When $T_{irr} \geq 450$°C, there is no reduction [59,71,72]. Results of irradiation at 360°C (Fig. 5) and 250°C [73] show larger reduction of tearing modulus when tested at 200 - 250°C, dropping to zero at room temperature. However, for irradiations at 50°C [74] and 90°C [73], the situation becomes better, as the tearing modulus is above 25.

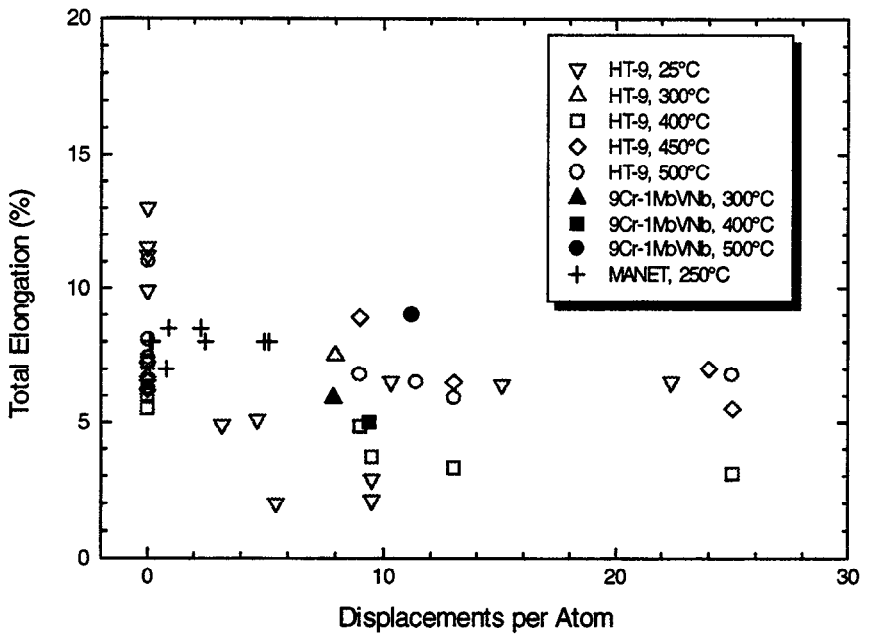

Fig. 4. Irradiation effects on the total elongation of HT-9, 9Cr-1MoVNb and MANET-I at different temperatures. Data are from [60,62-64,70]

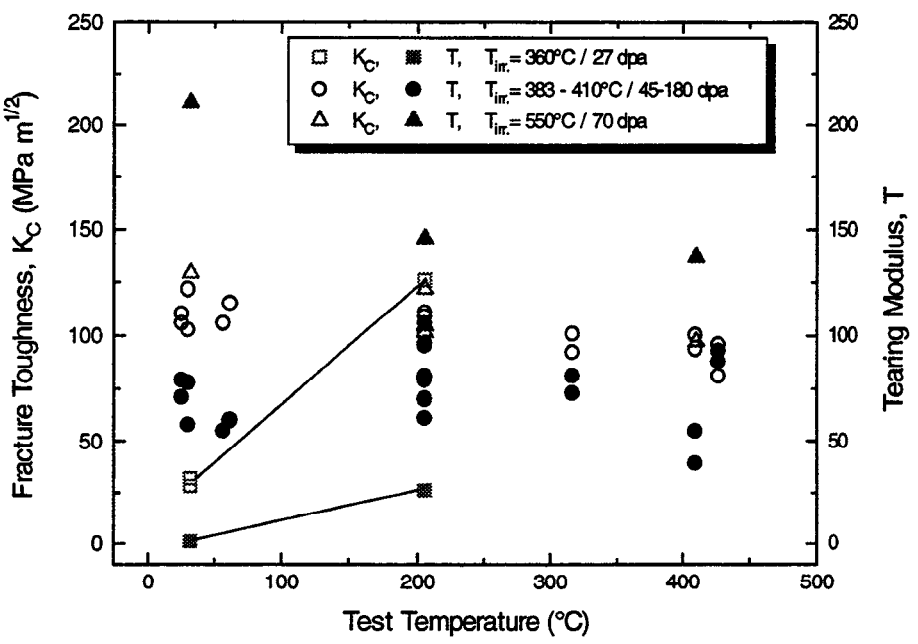

Fig. 5. Irradiation effects on fracture toughness and tearing modulus of HT-9. Data are from [59,71,72].

Increase of yield strength and loss of toughness in irradiated MF steels are accompanied by an increase (shift) of DBTT and a decrease of upper shelf energy (USE). The DBTT of unirradiated HT-9 is dependent somewhat on the heat treatment and specimen size, and varies normally between -10 to -60°C [75,76]. The shift of DBTT is found to be dependent on the irradiation temperature. As shown in Fig. 6, the shift of DBTT has a maximum at irradiation temperatures between ~150°-350°C; decreases rapidly between ~350° to 450°C and changes little above 450°C.

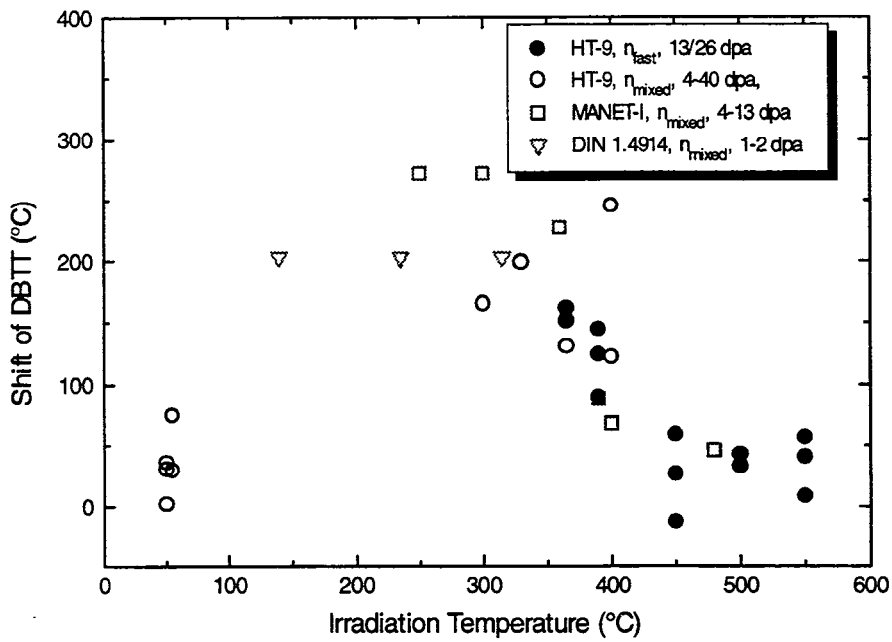

Fig. 6. Variation of DBTT with temperature for HT-9, MANET-I and DIN 1.4914 irradiated with fast neutrons (in FFTF and EBR-II) and mixed-spectrum neutrons (in HFIR, ORR and HFR). Data are from [75-81].

The change of DBTT depends also on the irradiation source. The increase in DBTT of HT-9 irradiated with fast neutrons saturates to ~140°C, but in mixed-spectrum neutron irradiation cases it goes up to 245°C [77]. The reason is suspected to be the higher helium content produced by mixed-spectrum neutrons. The situation is not clear, though, since at the same irradiation conditions, 9Cr-1MoVNb in which less helium has been produced, shows an even larger difference in the DBTT shifts.

3.2.4. Creep and fatigue

Irradiation creep of HT-9 has been investigated during fast neutron irradiation to a dose as high as 208 dpa at 400°C [82]. Fig. 7 shows the dose and stress dependencies of the stress-normalized creep strain rate at the midwall of HT-9 pressurized tubes. The stress enhanced swelling is ignored. The increase of normalized creep rate with stress indicates a non-linear stress dependence. Below 450°C thermal creep is less pronounced than irradiation creep. There are still no results on helium effects on low temperature irradiation creep.

Fatigue results on MF steels are limited to low cycle or low strain rate (the order of $10^{-3}s^{-1}$) cases. Two tests were conducted at room temperature on HT-9 irradiated in HFIR to 10 and 15 dpa with 34 and 53 appm He. The results show that the number of cycles to failure N_f is

greater in one case (10 dpa / 34 appm He)) and 3 times lower in the other (15 dpa / 53 appm He) as compared to the unirradiated steel [83]. However, another two tests show greater N_f of 9Cr-1MoVNb with 2.5 and 3.3 dpa (2 and 4 appm He) than that of unirradiated material. For MANET a number of tests were performed at low doses (≤1.6 dpa) and with helium up to 400 appm using dual beam (30 MeV protons and 104 MeV α-particle) irradiation[84,85] and 590 MeV proton irradiation [66,86,87]. Both post-irradiation [66,84-86] and in-beam [85-87] tests were conducted. Stress softening (stress decreasing with cycle number) was observed in all unirradiated, post-irradiated and in-beam isothermal fatigue tests under a strain-control mode. In-beam results show a reduction of less than a factor of 2 in N_f in the temperature range 300-420°C, which is less than the reduction of N_f in post-irradiation cases, a factor of ~1.5 to 15. At 250°C and below, the N_f of in-beam tests decreases by a factor of more than 2 [87]. Helium effects on N_f have been investigated by performing dual-beam tests with He/dpa ratios of 10 and 170 appm/dpa and show no significant difference at 450°C [84]. Helium effects at low temperatures (<400°C) have not yet been studied.

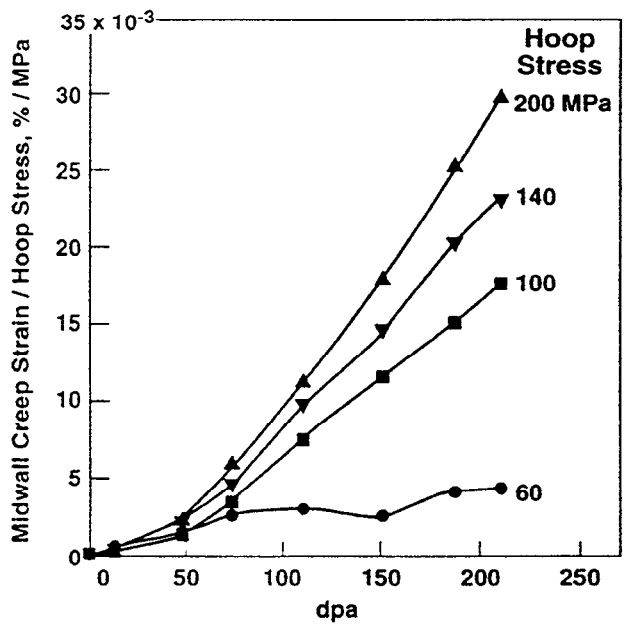

Fig. 7 Stress-normalized creep strains as a function dose for HT-9 (pressurized tubes) irradiated in FFTF at 400°C, after [82].

3.2.5. Hydrogen effects

Hydrogen embrittlement is a well known problem in MF steels. For example, it was found that fatigue lifetime of MANET-II (DIN 1.4914) was much shorter when tests were performed in hydrogen than in both vacuum and air at room temperature [88]. Another example is that charged hydrogen can significantly reduce ductility of both neutron irradiated and unirradiated 9Cr-2W martensitic steel at room temperature [89]. Hydrogen effects introduced by irradiation has been investigated in MANET-I after irradiation with 30 MeV protons between 80 and 500°C. 500 appm implanted H produced about 10 - 15% increase in yield strength and a slight reduction in ductility at 80 and 120°C showed but no effects at higher temperatures. The authors considered that the effects at 80 and 120°C might not be due to hydrogen but to 0.02 dpa damage produced during irradiation [90]. This view is reinforced by the second example

above where it was found that hydrogen effects almost disappeared after 20 min of ageing at room temperature [89].

4. Liquid mercury corrosion

Liquid mercury corrosion of materials has been investigated in numerous cases [91-94]. Liquid Hg corrosion is the consequence of a slight solubility of materials in Hg, which depends on temperature. The variation of solubility of different chemical elements is given in detail in [95]. It shows that W, Ta, Mo, V, Fe, Si and C have good corrosion resistance, Be, Co, Cr, Ti and Zr have fair resistance, and Al, Cu, Mg, Mn, Nb, Ni, etc. have poor resistance to Hg corrosion [91,95].

The resistance of a given alloy is primarily a function of base metal resistance and amount of base metal present in the alloy. The influence of alloying additions depends on the resistance and quantity of each alloying element, and the nature of the alloying action, such as formation of new phases, solid solutions, intermetallics etc. For iron-base alloys, the corrosion was found to be dependent on total Ni, Cr and Mn content. Fig. 8 shows weight-losses of a number of iron-base alloys in slowly flowing Hg at 482°C (900°F) for 30 days [92]. It is clear that MF steels with generally less than 15% Ni+Cr+Mn additions have much better resistance than austenitic alloys with usually more than 30% of Ni+Cr+Mn additions. The typical Hg corrosion rate at 482°C for MF steels is less than 100 μm/yr and for austenitic alloys is about 500 to 1000 μm/yr [96].

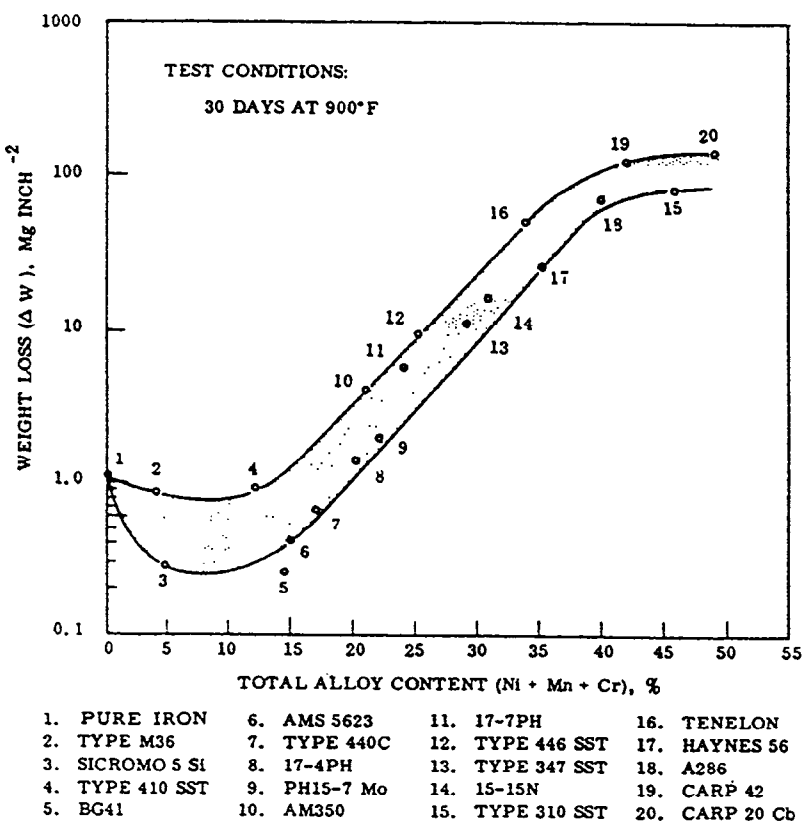

Fig. 8 Effect of Ni, Cr and Mn content on mercury corrosion of iron-base alloys, after [92].

The temperature dependence of mercury corrosion rate of materials can be expressed by an Arrhenius equation [92,95]:

$$\frac{d\ln\gamma}{dT} = \frac{E}{RT^2} \qquad (3)$$

where γ is the corrosion rate, E is the activation energy in corrosion process, T is the absolute temperature, and R is the gas constant. For iron-base alloys, E is about 5400 cal/mole at low temperatures (<~700°F or 370°C) and about 38000 cal/mole at high temperatures [91]. At low temperatures, therefore, the corrosion rate is much less sensitive to temperature as compared to at high temperatures, where the corrosion rate changes by a factor 5 for a temperature change of about 100°C [92].

5. Discussion and conclusion

Comparing the above results from SA 316 and HT-9 at relatively low temperatures, it can be seen that HT-9 has certainly superior properties in terms of strength, thermal conductivity, thermal expansion, mercury corrosion resistance, void swelling and irradiation creep resistance. HT-9 has also less degradation in impact properties when the irradiation temperature is above 380°C. Although after irradiation the ductility of HT-9 is lower than that of SA 316, it is generally above 3% at doses up to 25 dpa and temperatures between 300 and 500°C (is not known between 25 and 300°C). Helium effects are not clear, particularly in the MF steels. Furthermore, the radiation effects on high cycle fatigue lifetime of HT-9 are not known. The main disadvantage of HT-9 is that the DBTT increases substantially in low temperature irradiations. In addition, it seems that hydrogen has greater effects in HT-9.

The stress level and operation temperature at the LMTC will determine which class steel will be applied. Based on above discussion and the maximum allowable design stress of HT-9 and annealed 316 [97,98], given as Fig. 9, it can be discussed in the following terms: For HT-9, the best application temperature range is from ~380 to 450°C where it has high strength and low degradation by irradiation. It should also be applicable in a wider temperature range from ~300 to 500°C. Outside this range, it may have severe embrittlement problem below 300°C and large thermal creep above 500°C. SA 316 is applicable up to ~350°C. At temperatures above 350°C, it may have large swelling. SA 316 is likely a better choice than HT-9 below 300°C when the stress is lower than its design stress level. Therefore application ranges of SA 316 and HT-9 can be given schematically as in Fig. 9. The upper margins added to original design stress levels are by considering that first, the design stress levels are much lower than the corresponding YS levels (see Table 2), especially for HT-9; and second, the materials will be rapidly hardened during the intensive irradiation. However, it is difficult to give definite values of the margins as radiation creep will be enhanced at higher stress levels.

It should be also noted that, as the existing results are limited, Fig. 9 is not a definitive conclusion. For example, two HT-9 windows have been irradiated in LAMPF to fluences about 3×10^{21} p/cm^2 (~9 dpa / 1700 appm He) at temperature <~180°C and show no visible degradation [99,100]. However, detailed examinations have yet to be carried out. Due to the same reason, the lifetime of the LMTC cannot be predicted at this point. A number of unknown issues and uncertainties which need to be investigated urgently are:

I). Helium effects on the overall mechanical properties are still not well understood. In steels, 1.35 GeV protons produce helium at a rate similar to that in iron, i.e. as high as

~300 appm He/dpa. This rate is much higher than in the fast neutron case, generally < 1 appm He/dpa, and in the mixed-spectrum neutron case, < 80 appm He/dpa, which depends strongly on both the Ni content of the steels and the precise neutron spectrum. For HT-9 which contains ~0.5% Ni, it is < 5 appm He/dpa in both types of neutron spectra. Therefore, if helium has an effect it will be more pronounced under high energy proton irradiations.

II). For HT-9, the shift of DBTT and the change of tensile and impact properties in the irradiation temperature range between 25 - 300°C are not known. Furthermore, the irradiation effects on fatigue lifetime are not clear either.

III). High energy protons can produce hydrogen at a very high rate, ~1400 appm H / dpa in iron for 1.35 GeV protons. In the case of HT-9, this may cause severe embrittlement, as has been shown by fatigue tests performed in hydrogen (see §3.2.5.). Since in post-irradiation tests most hydrogen may have escaped from the specimens, the results of post-irradiation tests may not reflect the real hydrogen effect.

IV). The mercury corrosion results reviewed in this paper are for the materials in a slow mercury flow. Corrosion may increase in a fast (several m/s) flow, especially at the beam window where the flow will be deflected. Irradiation may still enhance corrosion. These effects as well as stress corrosion cracking have not yet been investigated.

V). The details of the distribution of stress and temperature at the beam window and other parts of the container are under calculation.

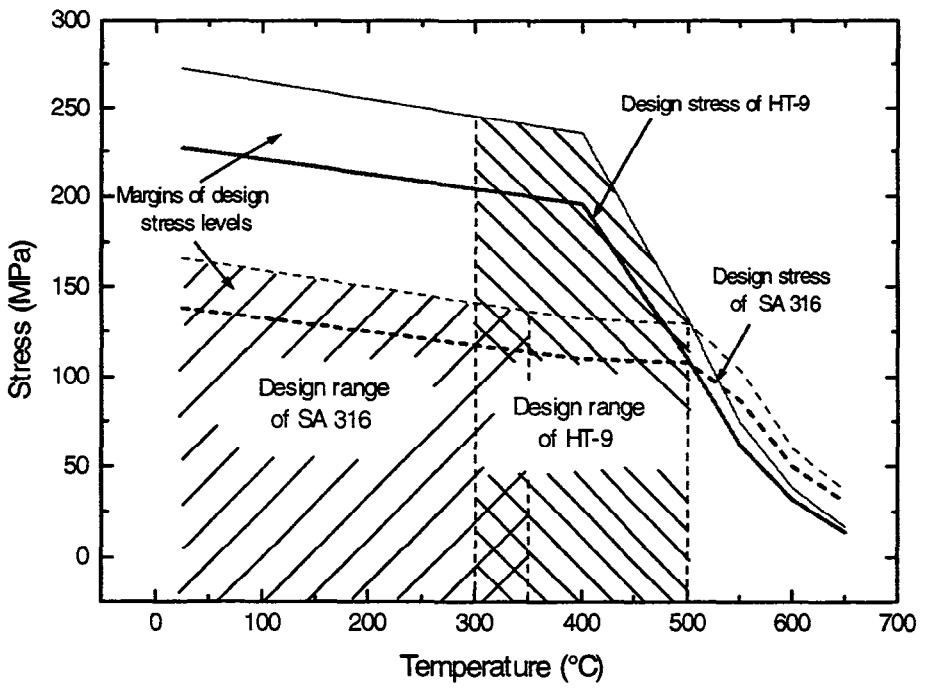

Fig. 9 Sketch showing design stress and temperature range for SA 316 and HT-9. The design stresses are quoted from design concepts of fusion reactor first wall and blanket structures [97,98].

Acknowledgements

The author is grateful to M. Victoria (PIREX-CRPP, PSI Villigen), W.F. Sommer (LAMPF, Los Alamos), H. Ullmaier (KFA, Jülich), F. Carsughi (KFA, Jülich) and G. Bauer (PSI Villigen) for their very useful discussion and careful reading the manuscript.

References:

[1] G. Bauer, **ESS 95-20-T**, 1995.
[2] H. Ullmaier and F. Carsughi, *Nucl. Instruments and Methods in Phys. Reseach*, **B 101** (1995) 406. or **ESS 95-17-T**, 1995.
[3] K. Skala and G. Bauer, this proceedings.
[4] F.A. Garner, in *Materials Science and Technology*, ed. R.W. Cahn, P. Haasen and E.J. Kramer, (VCH, Weinheim, 1994), vol. 10A, p. 419.
[5] J.M. Vitek and R.L. Klueh, in *Proc. Topical Conf. on Ferritic Alloys for Use in Nuclear Technologies*, (AIME, Warrendale, PA, 1984), p.551.
[6] P. Dubuisson, D. Gilbon and J.L. Séran, *J. Nucl. Mater.* **205** (1993) 178.
[7] M.G. Horsten and M.I. de Vries, *J. Nucl. Mater.* **212-215** (1994) 514.
[8] W.L. Bell, T. Lauritzen and S. Vaidyanathan, in *Proc. Topical Conf. on Ferritic Alloys for Use in Nuclear Technologies*, (AIME, Warrendale, PA, 1984), p. 113.
[9] S.N. Rosewasser, P.Miller, J.A. Dalessandro, J.M. Rawls, W.E. Toffolo and W. Chen, *J. Nucl. Mater.* **85&86** (1979) 177.
[10] M.L. Grossbeck, K. Ehrlich and C. Wassilew, *J. Nucl. Mater.* **174** (1990) 264.
[11] A. Kohyama, M.L. Grossbeck and G. Piatti, *J. Nucl. Mater.* **191-194** (1992) 37.
[12] G.R. Odette and G.E. Lucas, *J. Nucl. Mater.* **179-181** (1991) 572.
[13] G.R. Odette and G.E. Lucas, *J. Nucl. Mater.* **191-194** (1992) 50.
[14] J.C. Van Duysen, P. Todeschini and G. Zacharie, in *Effects of Radiation on Materials: 16th Inter. Sym.* (ASTM STP 1175, 1993), p. 747.
[15] S.J. Zinkle and R.L. Sindelar, *J. Nucl. Mater.* **155-157** (1988) 1196.
[16] N. Yoshida, *J. Nucl. Mater.* **174** (1990) 220.
[17] P.J. Maziasz, *J. Nucl. Mater.* **205** (1993) 118.
[18] S. Hamada, M. Suzuki, P.J. Maziasz, A. Hishinuma and M.P. Tanaka, in *Effects of Radiation on Materials: 14th Inter. Sym.* (ASTM STP 1046, 1989), p. 172.
[19] D.F. Pedraza and P.J. Maziasz, in *Radiation-Induced Changes in Microstructure: 13th Inter. Sym.*, (ASTM STP 955, 1987), p. 161.
[20] W.J.S. Yang, in *Radiation-Induced Changes in Microstructure: 13th Inter. Sym.*, (ASTM STP 955, 1987), p. 628.
[21] P.J. Maziasz, *J. Nucl. Mater.* **200** (1993) 90.
[22] J.L. Boutard, *J. Nucl. Mater.* **179-181** (1991) 1179.
[23] S. Jitsukawa, M.L. Grossbeck and A. Hishinuma, *J. Nucl. Mater.* **191-194** (1992) 790.
[24] J.D. Elen and P. Fenici, *J. Nucl. Mater.* **191-194** (1992) 766.
[25] F.W. Wiffen and P.J. Maziasz, *J. Nucl. Mater.* **103&104** (1981)
[26] S. Jitsukawa, P.J Maziasz, T. Ishiyama, L.T. Gibson and A. Hishinuma, *J. Nucl. Mater.* **191-194** (1992) 771.
[27] H. Schroeder and W. Liu, *J. Nucl. Mater.*, **191-194** (1992) 776.
[28] J.E. Pawel, D.J. Alexander, M.L. Grossbeck, A.W. Longest, A.F. Rowcliffe, G.E. Lucas, S. Jitsukawa, A. Hishinuma and K.Shiba, *J. Nucl. Mater.* **212-215** (1994) 442.
[29] G.E. Lucas and D.S. Gelles, *J. Nucl. Mater.* **155-157** (1988) 164.
[30] G.E. Lucas, *J. Nucl. Mater.* **206** (1993) 287.

[31] D. Mosedale, D.R. Harries, J.A. Hudson, G.W. Lewthwaite and R.J. McElroy, in *Proc. of Inter. Conf. on Radiation Effects in Breeder Reactor Structural Materials*, (AIME, New York, 1977), p.209.
[32] L.C. Walters, G.L. McVay and G.D. Hudman, in: *Proc. of Inter. Conf. on Radiation Effects in Breeder Reactor Structural Materials*, (AIME, New York, 1977), p.277.
[33] J.L. Straalsund, in: *Proc. of Inter. Conf. on Radiation Effects in Breeder Reactor Structural Materials*, (AIME, New York, 1977), p.191.
[34] F.A. Garner, M.L. Hamilton, C.R. Eiholzer, M.B. Toloczko and A.S. Kumar, in *Effects of Radiation on Materials: 16th Inter. Sym.*, (ASTM STP 1175, 1993), p. 696.
[35] A.S. Kruglov, M.E. Bul'Kanov, V.N. Bykov and Y.M. Pevchikh, *Atomnaya Energiya*, **48** (1980) 258.
[36] G.W. Lewthwaite and D. Mosedale, *J. Nucl. Mater.* **90** (1980) 205.
[37] M.L. Grossbeck, L.K. Mansur and M.P. Tanaka, in *Effects of Radiation on Materials: 14th Inter. Sym.*, (ASTM STP 1046, 1990), p. 537.
[38] M.L. Grossbeck and J.A. Horak, *J. Nucl. Mater.* **155-157** (1988) 1001.
[39] H. Ullmaier, *Nuclear Fusion*, **24** (1984) 1039.
[40] H. Schroeder, *J. Nucl. Mater.* **155-157** (1988) 1032.
[41] L.K. Mansur and M.L. Grossbeck, *J. Nucl. Mater.* **155-157** (1988) 130.
[42] R.J. Puigh and M.L. Hamilton, in *Effects of Radiation on Materials: 13th Inter. Sym.*, (ASTM STP 956, 1987), p. 22.
[43] C. Wassilew, K. Ehrlich and H.J. Bergmann, in *Effects of Radiation on Materials: 13th Inter. Sym.*, (ASTM STP 956, 1987), p. 30.
[44] M.L. Grossbeck and K.C. Liu, *Nuclear Technology*, **58** (1981) 538.
[45] M.L. Grossbeck and K.C. Liu, *J. Nucl. Mater.* **103&104** (1981) 853.
[46] K. Sonnenberg and H. Ullmaier, *J. Nucl. Mater.* **103&104** (1981) 859.
[47] I.S. Batra, H. Ullmaier and K. Sonnenberg, *J. Nucl. Mater.* **116** (1983) 136.
[48] M.P. Tanaka, S. Hamada, A. Hishinuma and M.L. Grossbeck, K. Sonnenberg, *J. Nucl. Mater.* **155-157** (1988) 957.
[49] W. Vandermeulen, W. Hendrix, V. Massaut and J. Van de Velde, *J. Nucl. Mater.* **155-157** (1988) 953.
[50] B. Van der Schaaf, *J. Nucl. Mater.* **155-157** (1988) 156.
[51] M.I. de Vries, in *Effects of Radiation on Materials: 11th Inter. Sym.*, (ASTM STP 782, 1982), p 665.
[52] A.A. Tavassoli, in *Effects of Radiation on Materials: 15th Inter. Sym.*, (ASTM STP 1125, 1992), p. 1103.
[53] R.L. Klueh, K. Ehrlich and F. Abe, *J. Nucl. Mater.* **191-194** (1992) 116.
[54] E.A. Little and L.P. Stoter, in *Effects of Radiation on Materials: 11th Inter. Sym.*, (ASTM STP 782, 1982), p. 207.
[55] P.J. Maziasz, R.L. Klueh and J.M. Vitek, *J. Nucl. Mater.* **141-143** (1986) 929.
[56] D.S. Gelles and L.E. Thomas, in *Proc. Topical Conf. on Ferritic Alloys for Use in Nuclear Technologies*, (AIME, Warrendale, PA, 1984), p.559.
[57] D. Gilbon, J.L. Séran, R. Cauvin, A. Fissolo, A. Alamo, F. le Naour and V. Lévy, in *Effects of Radiation on Materials: 14th Inter. Sym.*, (ASTM STP 1046, 1989), p. 5.
[58] C.Y. Hsu, D.S. Gelles and T.A. Lechtenberg, in *Radiation-Induced Changes in Microstructure: 13th Inter. Sym.*, (ASTM STP 955, 1987), p. 545.
[59] F.H. Huang, in *Effects of Radiation on Materials: 15th Inter. Sym.*, (ASTM STP 1125, 1992), p. 1267.
[60] R.L. Klueh and J.M. Vitek, *J. Nucl. Mater.* **182** (1991) 230.
[61] J.L. Séran, A. Alamo, A. Maillard, H. Touron, J.C. Brachet, P. Dubuisson and O. Rabouille, *J. Nucl. Mater.* **212-215** (1994) 588.

[62] R.L. Klueh and J.M. Vitek, *J. Nucl. Mater.* **150** (1987) 272.
[63] R.L. Klueh and J.M. Vitek, *J. Nucl. Mater.* **161** (1989) 13.
[64] B. van der Schaaf and M.I. de Vries, *Proc. IEA Workshop on Ferritic-Martensitic Steels*, (Tokyo, 1992), p. 259.
[65] R.D. Brown, M.S. Wechsler and C. Tschalär, in *Effects of Radiation on Material Properties: 13th Inter. Sym.*, (ASTM STP 956, 1987), p. 131.
[66] P. Marmy and M. Victoria, *J. Nucl. Mater.* **191-194** (1992) 862.
[67] M. Victoria, in *Proc. IEA Workshop on Ferritic-Martensitic Steels*, (Tokyo, 1992), p. 366.
[68] H. Schroeder, *Report KFA Jülich*, (Jül-2454, 1994).
[69] A. Hasegawa, N. Yamamoto and H. Shiraishi, *J. Nucl. Mater.* **202** (1993) 266.
[70] R.L. Klueh, J.M. Vitek na M.L. Grossbeck, *J. Nucl. Mater.* **104** (1981) 887.
[71] F.H. Huang and M.L. Hamilton, *J. Nucl. Mater.* **187** (1992) 278.
[72] F.H. Huang, *Engineering Fracture Mechanics*, **43** (1992) 733.
[73] D.J. Alexander, J.E. Pawel, M.L. Grossbeck and A.F. Rowcliffe, *Fusion Materials Semiannual Progress Report*, (DOE/ER-0313/16, ORNL, 1994), p. 173.
[74] F.H. Huang, in *Effects of Radiation on Materials: 14th Inter. Sym.*, (ASTM STP 1046, 1990), p. 459.
[75] R.L. Klueh and D.J. Alexander, in *Effects of Radiation on Materials: 16th Inter. Sym.*, (ASTM STP 1175, 1993), p. 591.
[76] R.L. Klueh and D.J. Alexander, in *Effects of Radiation on Materials: 16th Inter. Sym.*, (ASTM STP 1125, 1992), p. 1256.
[77] C. Wassilew, M. Rieth and B. Dafferner, in *Proc. IEA Workshop on Ferritic-Martensitic Steels*, (Tokyo, 1992), p. 295.
[78] R.L. Klueh, J.M. Vitek, W.R. Corwin and D.J. Alexander, *J. Nucl. Mater.* **155-157** (1988) 973.
[79] W.L. Hu and D.S. Gelles, in *Influence of Radiation on Material Properties: 13th Inter. Sym.*, (ASTM STP 965, 1987), p. 83.
[80] W.L. Hu and D.S. Gelles, in *Effects of Radiation on Materials: 14th Inter. Sym.*, (ASTM STP 1046, 1990), p. 453.
[81] R.L. Klueh and D.J. Alexander, *J. Nucl. Mater.* **212-215** (1994) 736.
[82] M.B. Toloczko, F.A. Garner and C.E. Eiholzer, *J. Nucl. Mater.* **212-215** (1994) 604.
[83] M.L. Grossbeck, L.M. Vitek and K.C. Liu, *J. Nucl. Mater.* **141-143** (1986) 966.
[84] R. Lindau and A. Möslang, *J. Nucl. Mater.* **178-181** (1991) 753.
[85] R. Lindau and A. Möslang, *J. Nucl. Mater.* **212-215** (1994) 599.
[86] P. Marmy, *J. Nucl. Mater.* **212-215** (1994) 594.
[87] P. Marmy, *Plasma Device and Operations,* (1995) in print.
[88] J.I. Shakib, H. Ullmaier, E.A. Little, R.G. Faulkner, W. Schmitz and T.E. Chung, *J. Nucl. Mater.* **212-215** (1994) 579.
[89] A. Kimura, H. Kayano and M. Narui, *J. Nucl. Mater.* **179-181** (1991) 737.
[90] K.K. Bae, K. Ehrlich and A. Möslang, *J. Nucl. Mater.* **191-194** (1992) 905.
[91] J.F. Nejedlik and E.J. Vargo, *Electrochem. Techn.*, **3** (1965) 250.
[92] J.F. Nejedlik and E.J. Vargo, *Corrosion*, **20** (1964) 384.
[93] A.H. Fleitman, A.J. Romano and C.J. Klamut, *J. Electrochem. Soc.*, **110** (1963) 964.
[94] A.H. Fleitman and J.R. Weeks, Nucl. Eng. and Design, 16 (1971) 266.
[95] *Metals in Mercury*, eds. C. Hirayama, Z. Galus and C. Guminski, (Pergamon Press, Oxford, 1986).
[96] Handbook of Stainless Steels, ed. D. Peckner and I. M. Bernstein, (New York, McGraw-Hill, 1977)

[97] S.N. Rosenwasser, P. Miller, J.A. Dalessandro, J.M. Rawls, W.E. Toffolo and W. Chen, in *Proc. Topical Conf. on Ferritic Alloys for Use in Nuclear Technologies*, (AIME, Warrendale, PA, 1984), p. 177.
[98] J. D. Gordon, J.K. Ganer, N.M. Choniem and J.F. Parmer, in *Proc. Topical Conf. on Ferritic Alloys for Use in Nuclear Technologies*, (AIME, Warrendale, PA, 1984), p. 157.
[99] M. Dubs and J. Ulrich, ICANS-XI, (Japan, 1990).
[100] W.F. Sommer, private communication.

ICANS-XIII
13th Meeting of the International Collaboration on
Advanced Neutron Sources
October 11-14, 1995
Paul Scherrer Institut, 5232 Villigen PSI, Switzerland

WATER/MONEL HEAT PIPES FOR COOLING OF LIQUID METAL TARGETS FOR SINQ AND ESS

Mark T. North[1], John H. Rosenfeld[1], David B. Sarraf[1], Günter S. Bauer[2] and Yasushi Takeda[2]

[1] Thermacore, Inc., 780 Eden Rd., Lancaster, PA 17601, USA
[2] Paul Scherrer Institut, CH-5232 Villigen PSI, Switzerland

ABSTRACT

A heat pipe based heat exchanger has been designed for extracting waste thermal energy from the lead-bismuth eutectic (LBE) beam target for the SINQ project at Paul Scherrer Institut (PSI). An array of eight heat pipes is designed to carry a thermal load of 400 kW. The heat pipes feature a double wall evaporator which can reduce the risk of injecting water directly into the liquid metal pool in the case of primary wall failure. The heat pipes can be used without redesign in a larger array in a secondary heat exchanger for mercury target cooling for the European Spallation Source (ESS).

1. Introduction

Both the SINQ project at Paul Scherrer Institut (PSI) and the European Spallation Source (ESS) being developed by the European Union (EU) involve bombarding heavy nuclei by a proton beam to create neutrons. In the SINQ target, the liquid metal (LM) bath is composed of lead-bismuth eutectic (LBE); the ESS target LM bath will be pure mercury. Because of the high heat loading created by the proton beam, cooling of the LM bath is required. Natural convection circulation and cooling of the LM bath will not be adequate at the power levels (~1MW/liter) anticipated for these projects; consequently, some form of active cooling will be required.

Pumped water will be the ultimate sink for the energy dissipated in the LM bath. The high temperature level during operation and the need to avoid cooling of the bath below a certain level during shutdown, however, make direct cooling via a standard design heat exchanger difficult. Preventing the LM temperature from falling below a certain level seems desirable for two reasons: In the case of Pb-Bi-eutectic solidification must be avoided to protect the vessel from stresses resulting from expansion of the material. Secondly, irradiation of the container material causes the ductile-to-brittle transition temperature to rise and therefore the system should be kept above this temperature, in particular in view of sudden load changes due to the variation of the proton beam intensity.

Keywords: Heat Pipe, Liquid Metal, Spallation Target, Cooling

Heat pipe thermosyphons offer a solution to cooling the LM bath without the difficulties associated with circulating water directly in the bath. Heat pipes operate by the evaporation and condensation of a small quantity of working fluid inside a vacuum tight pressure vessel. A diagram showing the operating principles of a heat pipe is shown in Figure 1. The working fluid evaporates and removes heat at one end of the heat pipe, and condenses at the other end of the heat pipe, rejecting heat to the ultimate heat sink, usually at a lower heat flux. Upon condensation, the working fluid is returned to the evaporator by either capillary action, i.e. with a wick, or with the aid of gravity, as in a thermosyphon, or both.

The conductance of a heat pipe can be made variable by introducing a small quantity of noncondensible gas (NCG). Because the NCG does not condense, it does not circulate with the working fluid. Instead the gas collects in the condenser. As the operating temperature of the heat pipe varies, the pressure inside the heat pipe varies; this variation is dictated by the vapor pressure curve of the working fluid. The volume of the NCG will change in response to this change in pressure. When the heat pipe temperature is low the NCG will occupy a large portion of the condenser, reducing the area for the working fluid to condense and lowering the conductance of the heat pipe. At high heat pipe temperatures the volume of the NCG is very small, the condenser area available for condensing working fluid is near its maximum, and the conductance of the heat pipe is high. This feature provides also a convenient way for decay heat removal at a temperature level compatible with the needs mentioned above.

The evaporator can be made double-walled with a gas gap between the walls. This provides two layers of containment between the water working fluid and the liquid metal. If one of the heat pipes does fail, the remaining heat pipes will provide sufficient cooling to allow a safe and controlled shutdown of the target. In the unlikely event that both walls of a single heat pipe fail simultaneously, only a fraction of the roughly 1 kg of water present in the heat pipe would escape into the LM bath instead of several tens of kilograms. Finally, with variable conductance heat pipes, the heat pipe heat exchanger will self regulate how much heat it transfers; this will keep the minimum temperature of the LM bath at a predetermined level, independent of the actual power input.

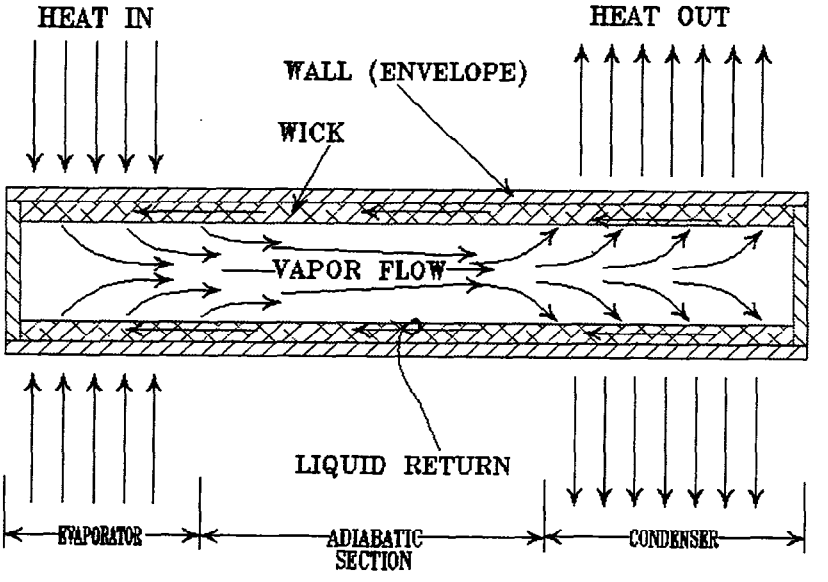

Figure 1: Working Fluid and Heat Flow in the Three Sections of a Generic Heat Pipe

Cross sectional diagrams of the SINQ and ESS targets are shown in Figure 2a and b. In the SINQ LBE bath, an array of vertical water heat pipes would extract heat from the LBE bath and reject it to the cooling water. The heat pipes for this application are constrained to fit in

an annular space with an inner diameter of 15 cm and an outer diameter of 40 cm. Additional design parameters for the SINQ target and the ESS target are shown in Table 1 below.

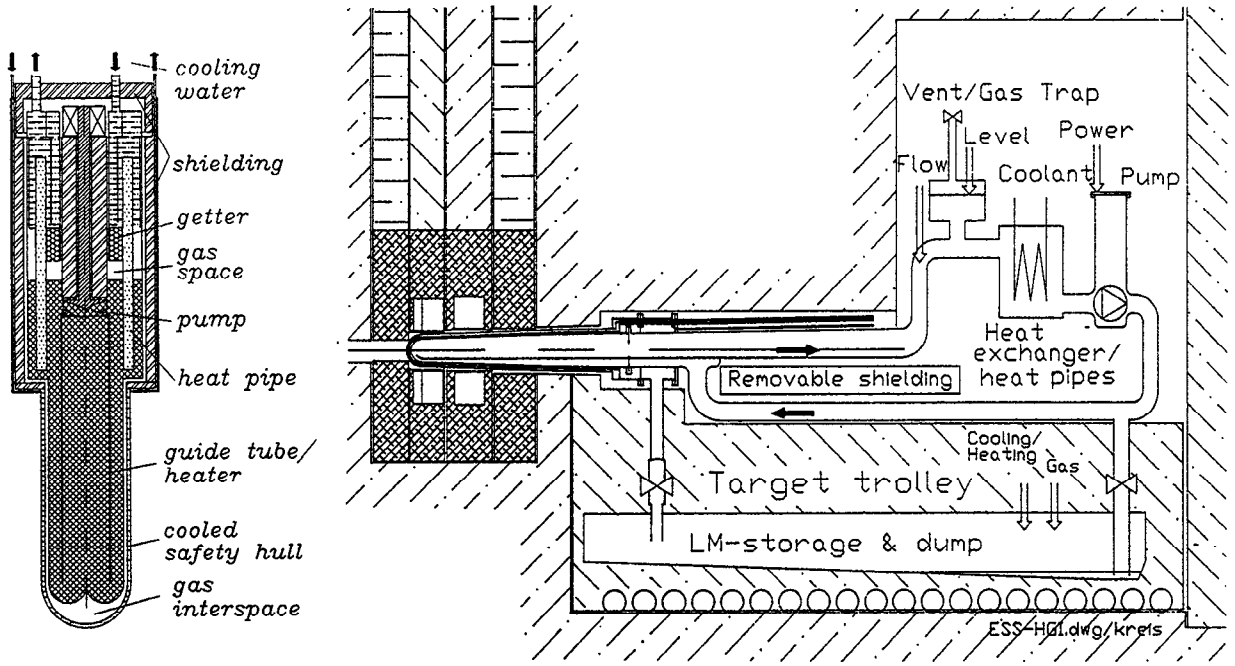

(a) (b)

Figure 2: Schematics of the SINQ and ESS LM-target arrangment

TABLE 1: SINQ AND ESS TARGET COOLER REQUIREMENTS

Requirement	SINQ	ESS
Power Removal (MW)	0.4	3.2
Orientation	Vertical Ring of Heat Pipes	Vertical Array of Heat Pipes
Target Coolant	Lead/Bismuth Eutectic	Mercury
Heat Sink Fluid	Water	Water
Heat Sink Temperature	20-100°C	20-100 °C
Min. LM Target Temperature	170 °C	170 °C
Max. LM Target Temperature	450 °C	450 °C
Evaporator Length	Up to 1.8 m	Same as SINQ
Condenser Length	Up to 1.0 m	Same as SINQ
Operating Life	Minimum of 20,000 hrs	Maximize
Ring Outer Diameter	40 cm	N/A
Ring Inner Diameter	15 cm	N/A

The same heat pipe design can be used for the ESS LM bath; the ESS project will require more heat pipes because of its larger heat load, but there will be no particular geometry constraints because the secondary heat pipe heat exchanger will be separated from the beam target area. Even an inclined mounting position is possible, which would improve the heat transport capability of the individual heat pipes. Using the same heat pipe design, however,

will eliminate the cost of redesigning a heat pipe for the heat exchange system of the ESS project. This paper describes the design of the heat pipes for cooling of the LM bath for the SINQ and ESS projects.

2. Heat Pipe Design

A cross sectional drawing of the heat pipe is shown below in Figure 3. The heat pipe features a double-walled gas gap evaporator as well as a concentric tube annular flow condenser. The outer evaporator wall is to be made of HT-9 martensitic steel, and the inner wall is to be made of Monel K-500.

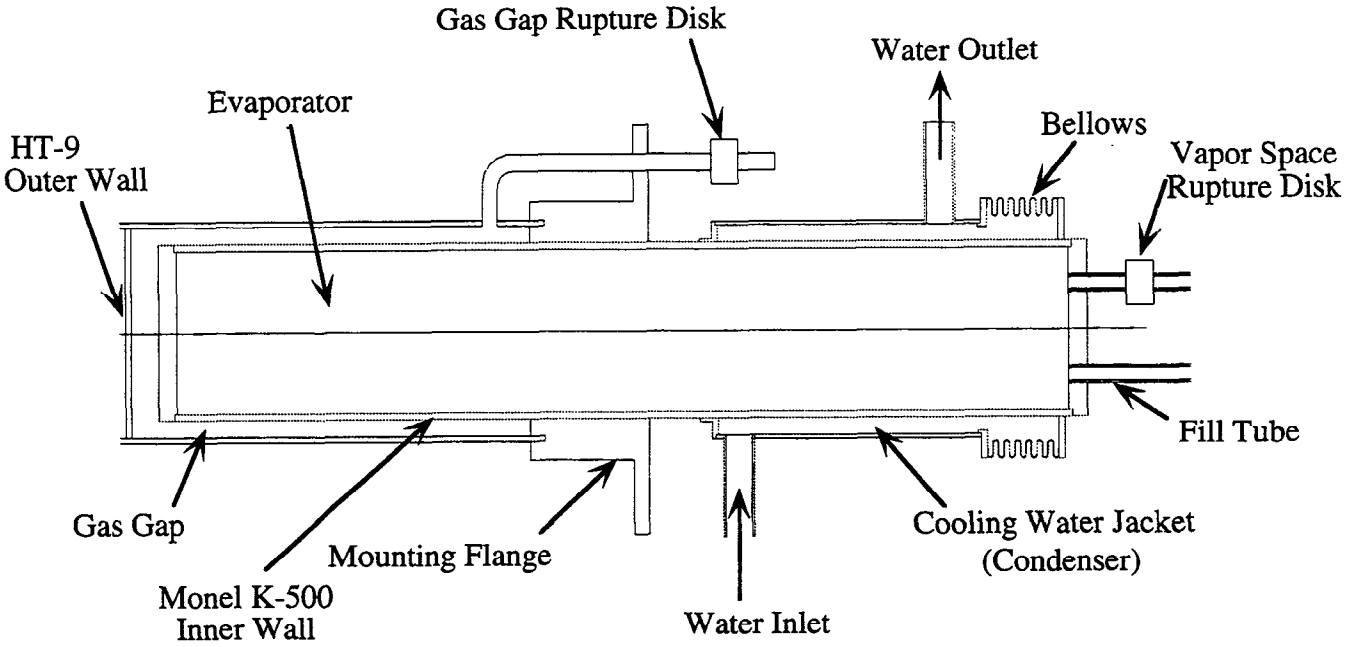

Figure 3: Cross Sectional Drawing of the SINQ-ESS Target Cooler Heat Pipe

A number of analyses were performed during the design of the SINQ-ESS target heat pipe cooler. These included consideration of aspects of the heat pipe design both internal and external to the heat pipe. A description of each of these is given below.

2.1 Heat Pipe External Design

The heat pipe external design included consideration of the heat pipe size and spacing, a bellows for accommodation of differential thermal expansion of the inner and outer condenser walls, and the interface between the heat pipe mounting flange and the wall above the LM bath. Each of these are described in this section.

2.1.1 Heat Pipe Size and Spacing

The heat pipe array in the SINQ target is constrained to fit in an annular space which has an inner diameter of 15 cm and an outer diameter of 40 cm. Heat pipes may be arranged in a number of different ways in this space. The heat pipes must have sufficient space between them to allow the LM to flow between them without excessive pressure drop. Three possible configurations are shown below in Figure 4. The possible configurations span a range between a small number of large diameter heat pipes and a large number of small diameter heat pipes. Each of these was further investigated to determine the optimum for performance and ease and cost of fabrication. Final selection of the heat pipe size and spacing was determined from internal design analyses described below.

2.1.2 Condenser Bellows

To accommodate the differential thermal expansion between the inside and outside walls of the condenser water jacket, a bellows will be placed in the outer wall of the condenser. This will allow the inner wall to expand as the working fluid heats the inner wall while the outer wall stays cool due to the circulating cooling water.

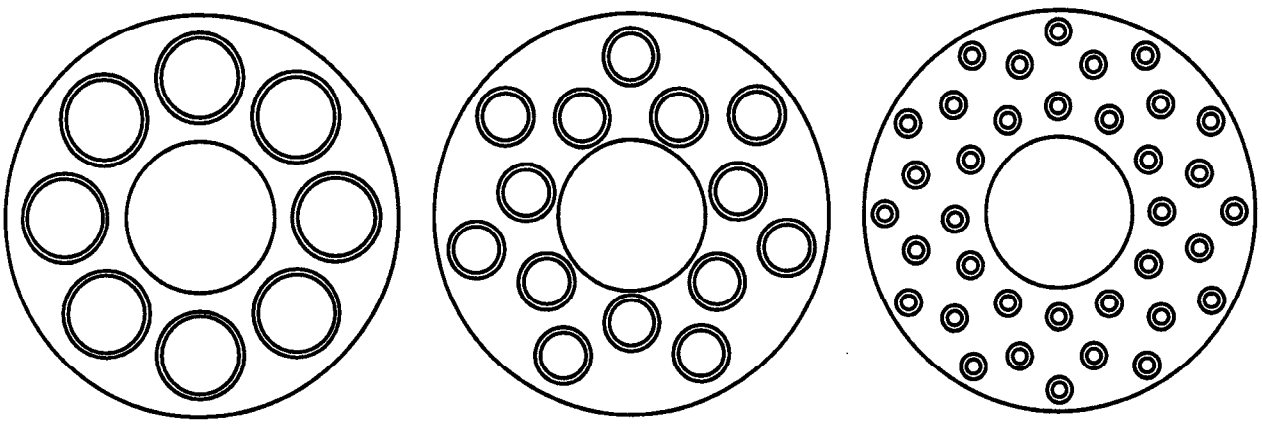

(a) (b) (c)

Figure 4: Alternative heat pipe arrays for the SINQ target in 15cm ID/40cm OD annulus. (a) Eight 8.9cm diameter heat pipes, (b) Fourteen 5.7cm diameter heat pipes, (c) Thirty-six 2.54cm diameter heat pipes.

2.1.3 Interface Design

Each heat pipe will have a flange brazed onto the heat pipe wall between the evaporator and condenser. This plate will in turn be mounted into an interface plate above the LM bath. The gas gap rupture disk will penetrate the flange and be integral with it. This will allow the whole heat pipe and rupture disk assembly to be installed and removed/replaced as a single unit. The interface plate will form the wall between the LM bath and the outside environment. All rupture disks and cooling line connections will be made on the outside side of this plate.

2.2 Heat Pipe Internal Design

The heat pipe internal design included consideration of the appropriate operating limits, the size of the gas gap, the wick design, the appropriate gas charge to achieve the required variable conductance, the sizing of the rupture disks, and materials selection. Each of these are described below.

2.2.1 Flooding Limit

In the SINQ and ESS applications, the heat pipes will operate as thermosyphons, using gravity to return the condensed working fluid to the evaporator. In a thermosyphon, the applicable operating limit is the flooding limit. The flooding limit is reached when the counterflowing vapor entrains liquid flowing down toward the evaporator, returning the liquid to the condenser and preventing the evaporator from being resupplied with working fluid. This limit was correlated by Kutateladze [1] and later improved by Tien and Chung [2], and is given by the following:

$$q_{\max} = \frac{C^2 A_{vapor} h_{fg} [\sigma g(\rho_1 - \rho_v)]^{0.25}}{\left(\frac{1}{\rho_1^{0.25}} + \frac{1}{\rho_{v1}^{0.25}}\right)^2} \quad (1)$$

where C2 = 3.2 for water, nomenclature see ch. 5.

Equation (1) was used to determine the flooding limit for each of the geometries shown in Figure 4. The outer evaporator wall was assumed to be 0.10cm thick and the gas gap between the walls was assumed to be 0.018cm. The thickness of the inner wall was computed to contain the pressure of the supercritical water at 450 °C (40MPa). The results of these calculations is shown in Figure 5 below. In each case, the flooding limit is shown with the required heat transport rate corresponding to the number of heat pipes. These plots show that the design margin (difference between the peak in the flooding limit and the requirement) decreases as the number of heat pipes is increased. In addition, the peak in the flooding limit occurs at the same temperature, suggesting that the optimal operating temperature for the heat pipes is 250 °C. The design margin is the greatest for the array of eight heat pipes. Using the smallest number of heat pipes has the additional benefit of being the lowest in cost to fabricate. However,for the time being, it was felt that this array might not provide sufficient shielding for the SINQ-arrangement, where the source of energetic neutrons is located vertically under the heat pipes. For this reason, the array of fourteen heat pipes was selected as the reference design.

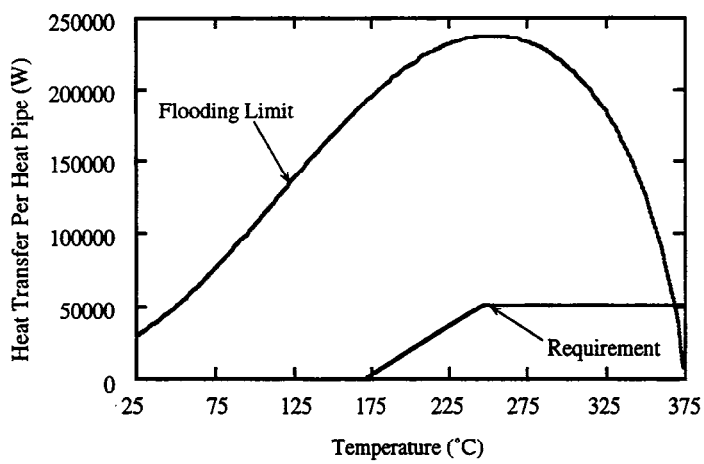

Figure 5a:Flooding Limit for 8 Heat Pipe Array. Max. heat transfer/Requirement = 4.75

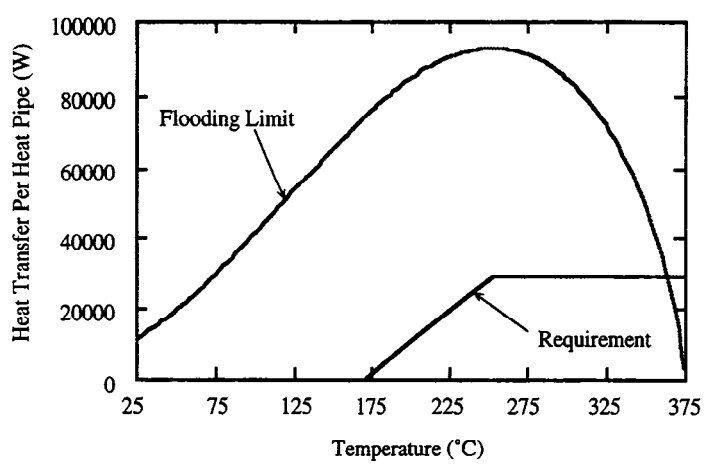

Figure 5b: Flooding Limit for 14 Heat Pipe Array. Max. heat transfer/Requirement = 3.25

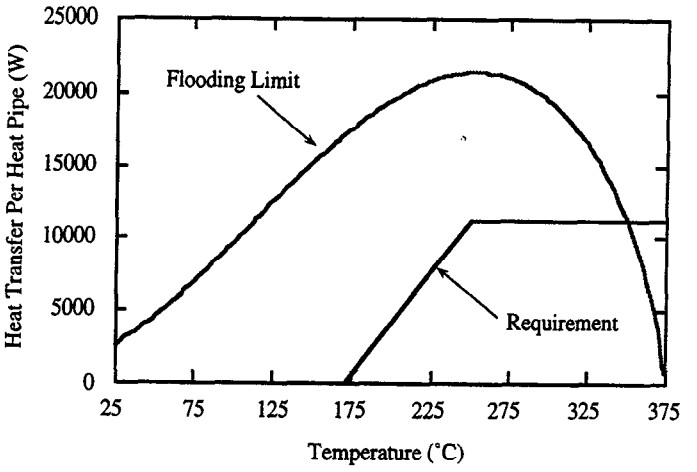

Figure 5c:Flooding Limit for 36 Heat Pipe Array. Max. heat transfer/Requirement = 1.93

2.2.2 Gas Gap

The evaporator of the heat pipe will feature a double wall containment with a gas gap between the two walls. The purpose of the gas gap is fourfold. Primarily, the gas gap provides a material barrier to prevent crack propagation through both the inner and outer walls. If the inner wall fails, high pressure water vapor from the heat pipe will be vented in to the gas gap. This will, in turn, cause the rupture disk to burst, allowing the water vapor to exhaust to a location outside the LM bath. The second purpose of the gas gap is to provide a high thermal resistance heat transfer path between the LM bath and the water heat pipe. The high thermal resistance results in a high temperature difference between the LM bath and the water heat pipe. This makes it possible to cool the 450 °C liquid metal bath with heat pipes which are operating at approximately 250 °C; having the heat pipes well coupled to the hot liquid metal is undesirable because the heat pipe is unable to transport any heat above the critical temperature of the working fluid, which is 374 °C for water. The third purpose of the gap is to reduce thermal stresses in the walls due to a small temperature drop across the walls and a large one across the gap. Finally, the design with a gap enables us to use two different materials for the inner and the outer wall, each selected for optimum compatibility with the medium it is in contact with.

2.2.3 Wick Design

The heat pipe will have two different wicks in the evaporator and condenser. The evaporator will have a felt metal wick. This is the same type of wick previously demonstrated on a water/monel Faraday shield heat pipe [3]. This wick has demonstrated capabilities to operate at high temperature at heat fluxes up to 50W/cm^2 with low ΔT. Having a capillary wick in the evaporator will allow the water inventory inside the heat pipe to be reduced because it will not be necessary to fill the entire evaporator with a pool of working fluid to assure wetting and evaporation from the entire evaporator surface.

Heat transfer in the condenser will be enhanced with a knurled surface. The tops of the knurled surface features will extend through the liquid film, reducing the ΔT between the condenser surface and the saturated vapor and improving condensation heat transfer. The grooves in the knurled surface will help channel the condensate away from the condensation surface and return the liquid to the evaporator wick. In addition to its effectiveness in

reducing the effective film thickness in the condenser, the knurled surface is a low cost option for providing wicking to the condenser surface.

2.2.4 Variable Conductance Heat Pipe Design

In the SINQ application, it is desired to prevent freezing of the LBE on the outside of the evaporator wall. Therefore it is necessary to use a variable conductance heat pipe which will not transport heat when the bath temperature falls below the minimum LM bath temperature (170 °C). Similar considerations also hold for the ESS case, where the temperature of the beam window should not be allowed to be below 180 °C when the beam starts, as mentioned above. The variable conductance feature is achieved by charging the heat pipe, in addition to the appropriate quantity of working fluid, with 0.028g of argon. The argon will not condense or circulate inside the heat pipe. Instead, it will collect in the condenser end of the heat pipe where it will displace working fluid vapor. As the temperature of the LBE bath falls, the vapor pressure of the working fluid will decrease and the volume which the fixed mass of argon occupies will increase. The mass of argon is chosen so that it will completely fill the condenser when the bath temperature falls to 170 °C; this prevents additional heat from escaping from the LBE bath through the heat pipe heat exchanger and the liquid metal bath, as a result of decay heat (~ 5 kW after 1 day), will remain at approximately constant temperature.

2.2.5 Rupture Disk

Each heat pipe will be equipped with two rupture disks for safety reasons. The first rupture disk will be installed in the evaporator gas gap. In the event of a failure of the evaporator inner wall, this rupture disk will allow the water vapor to escape into the space outside of the LM bath. This allows the target to continue operating without contaminating the liquid metal bath with water. A second rupture disk will be attached to the heat pipe vapor space. This will allow the heat pipe working fluid to be vented outside of the liquid metal bath in the event that the heat pipe temperature exceeds the critical temperature of water. This reduces the required thickness of the inner evaporator wall because the internal pressure of the heat pipe will not reach supercritical pressures if loss of coolant causes the heat pipe temperature to exceed the critical temperature of the working fluid. In addition, the heat pipe may then be reused by simply replacing the rupture disk and reprocessing the heat pipe rather than replacing the whole heat pipe due to a wall failure.

2.2.6 Materials Selection

The outer wall of the heat pipe evaporator will be made of HT-9 martensitic steel. This is a low nickel alloy which has been shown in the past to demonstrate resistance to corrosion by the LBE and which retains ductility after exposure to high neutron fluence at elevated temperature [4]. Compatibility with mercury is also known to be good. The inner wall will be made of Monel K-500. This material is chosen for its high strength and compatibility with water in a heat pipe. The outer wall of the condenser water jacket will be made of stainless steel 304. The primary requirements for this material is low cost and easy weldability.

3. Future Work

Two pieces of work are planned before full scale heat pipe heat exchangers are produced. These are material life tests and quarter scale prototype fabrication. Each of these are described below.

3.1 Life Tests

A sub scale life test heat pipe will be fabricated using identical materials and fabrication techniques to determine the compatibility of water and Monel K-500 in the temperature range of interest for the target cooling applications. The test will be run for at least several thousand hours at temperatures between 250 and 300 °C. Although water and Monel K-500 have successfully been demonstrated in a heat pipe in the past [3], the higher temperature range of interest for the present target cooling application indicates that a life test be performed in this temperature range.

3.2 Quarter Scale Prototype

Before a full scale heat exchanger is fabricated, the reference design will be reconsidered in detail. A quarter scale heat exchanger of the final design will be fabricated and tested. This prototype will consist of one quarter of the number of heat pipes required to remove the heat from the SINQ target as described above, each built to full scale and designed to transfer the required amount of heat at operating temperature. The purpose of this is to demonstrate fabrication processes and show that the heat pipes will operate as expected under design power and design temperature conditions.

4. Conclusions

A heat pipe has been designed to remove heat from both the SINQ LBE liquid metal target and the ESS mercury target. The heat pipe is designed to transport up to 50 kW per heat pipe of waste heat energy out of the LM bath. The heat pipe design minimizes fabrication costs and can also be used in both target systems without change.

5. Nomenclature

A	cross sectional area, [m^2]
C	coefficient in equation (1), [-]
g	gravitational acceleration, [m/s^2]
h_{fg}	heat of vaporization, [J/kg·K]
q	heat flow, [W]
ρ_l	liquid density, [kg/m^3]
ρ_v	vapor density, [kg/m^3]
σ	surface tension, [N/m]

6. References

[1] Kutateladze, S.S., "Elements of Hydrodynamics of Gas-Liquid Systems", Fluid Mechanics- Soviet Research, v. 1, pp. 29-50 (1972).

[2] Tien, C.L. and Chung, K.S., "Entrainment Limits in Heat Pipes", AIAA Journal, v. 17, p. 643 (1978).

[3] Rosenfeld, J.H., and Lindemuth, J.E., "Heat Pipe Cooling of Faraday Shields", Final Report for contract DE-F601-90-ER81058, U.S DOE, Germantown, MD, July 9, 1993.

[4] Dai, Y. "Suitability of Steels as the ESS-Mercury Target Container Material" these proceedings

ICANS-XIII
13th Meeting of the International Collaboration on
Advanced Neutron Sources
October 11-14, 1995
Paul Scherrer Institut, 5232 Villigen PSI, Switzerland

PROSPECTS FOR TARGETS AND METHANE MODERATORS AT ISIS

T A Broome

ISIS Facility, Rutherford Appleton Laboratory, CCLRC, Chilton, Didcot, UK

ABSTRACT

This paper reviews the performance of targets and methane moderators at ISIS, the spallation neutron source at the Rutherford Appleton Laboratory. The operational experience is summarised and the plans for the future are outlined.

1. Introduction.

From the inception of the project to build ISIS it was recognised that the choice of depleted uranium for the target and methane as one of the moderators presented a considerable technical challenge. What little was known about the behaviour of these materials in the radiation field of a spallation source indicated that irradiation could cause serious deterioration in their physical properties. The justification for the choice made was the significant gain in neutron fluxes in the beamlines resulting from their use, compared to the alternatives.

Operational experience has confirmed the expected performance. Neutron fluxes from the Uranium target are twice that from the tantalum target, the increased background from neutron emitting nuclides produced in the uranium is, for most experiments, acceptable. The spectrum, intensity and pulse widths of the beams from the methane moderator have been a vital factor in the scientific success of ISIS.

However, the operational experience has shown that, if anything, the original assessment underestimated the effects of irradiation on the materials. This is best illustrated by the lifetimes achieved which is discussed below. A great deal of information has been collected during more than ten years of operation and the research and development programmes currently in progress are aimed at addressing the problems of limited lifetime so there is good reason to be optimistic for the future.

The operational experience is outlined below together with an assessment of the prospects of using uranium targets and methane moderators in the future.

Keywords: ISIS, Targets, Moderators

2. Targets

The design of the target has been reported at previous ICANS meetings [1] so only a brief outline is given here. A schematic diagram is shown in figure 1. The targets are constructed from 9 cm diameter disks held in stainless steel frames. The thickness of the disks varies from 7.7 mm at the front of the target where the proton beam enters to 26.2 mm at the back of the target. Spacers are arranged to give cooling channels 1.75 mm wide between the plates. These frames are welded into a module, fitted with manifolds to direct the water cooling and this assembly then welded into a pressure vessel.

The coolant is D_2O which flows through three main channels, each channel serving up to nine plate cooling gaps. The temperature at the centre of each plate is measured with a thermocouple. The flow and pressure drop of each of the three main cooling channels are measured. A quantity called the 'gap constant', which is flow/(pressure drop)^n is used to monitor the width of the gaps between plates. The index n is calibrated for each target and each of the three cooling channels and typically has a value close to 0.5. In the units used, the gap constant has a value of between 20 and 35 and a reduction by 1 unit means that one plate gap has become seriously blocked. A test rig has confirmed the sensitivity of this method of monitoring the target plate gaps.

The plates themselves are either depleted uranium clad in Zircaloy II or tantalum

2.1 Uranium Targets

To date nine uranium targets have been manufactured and eight installed. The mechanical design has been the same for all as described above.

The lifetimes of both the uranium and tantalum targets are shown in table 1.

Table 1. ISIS Target Performance Summary

Target	Gross Thermal Cycles	Integrated Current mAh	Typical Proton Current μA	Neutron Production mg
U#1	Not measured	92.4	30	75
U#2	40000	53.1	45	52
U#3	10389	174.9	65	163
U#4	4147	138.8	75	128
U#5	5074	295.6	90	273
U#6	2628	126.1	110	116
U#7	1805	107.2	125	99
U#8	Not	Used		
U#9	815	113.2	150	104
Ta#1	73378	1751.6	170	1037
Ta#2 *	21138	618.1	170	366

* Still in use

The lifetime of all the uranium targets has been disappointingly short. To be practical in the context of the ISIS operations a reliable lifetime of at least 400 mAh is required which is equivalent to three user cycles. In all cases the final manifestation of failure is a breach in the cladding releasing a small quantity of fission products into the cooling water. A gamma spectrometer is used to monitor for this.

Targets number 2 and 7 have been dismantled for examination. The results from the examination of target number 2 were reported at ICANS X [2]. The failure of this target was attributed at the time to cladding failure caused by thermal cycling growth of the uranium. Experience with uranium targets at IPNS [3] when combined with that at ISIS no longer supports thermal cycling growth as the primary mechanism for failure.

Temperature monitoring of the plates indicated that the failure in target 7 was associated with a problem in plate 1. The target was dismantled and examined in the Hot Cell facility at AEA Technology, Harwell and the condition of plate 1 is shown in figure 2. There is an obvious bulge in the plate and the cladding had failed. Much of the swelling can be attributed to chemical reaction between the water leaking through the crack in the cladding and the uranium producing a mixture of uranium hydride and oxide which occupies about three times the volume of the uranium. Also outside the immediate region of the central bulge the plate appears wrinkled. This wrinkling is present on all plates from 1 to 19 becoming progressively less pronounced with distance from the proton beam entrance window. The last three plates were not wrinkled. Figure 3 shows the condition of plate 3. With the exception of plate 1 there was no definite evidence of cladding failure although plates 4,7 and 9 had marks which could be interpreted as cracks in the clad.

A jig was constructed to measure the cross section profile of the plates. The aim was to distinguish between distortion with no volume increase and distortion with an associated volume increase. The jig had two direct measuring dial gauges with a resolution of 0.0001 inches. The plate being examined was mounted in the jig and scanned past the dial gauges which measured the profile of the plate on both faces simultaneously. Several plates were measured and a typical scan is shown in figure 4. The results of these measurements showed consistently that a bulge on one side of a plate was always associated with a depression on the other side. No evidence was found for an increase in volume of the plates. It was also clear that some plates had buckled are were no longer flat.

This data was interpreted as evidence for the dominant mechanism leading to failure as being irradiation growth. This is consistent with experience gained from neutron irradiation of uranium in reactors. Growth of individual uranium grains under irradiation is unavoidable but its bulk effects are crucially dependant on the size and orientation of the grains. The Zircaloy is bonded to the uranium using hot isostatic pressing, typically the conditions used are applying pressure to the plate and cladding with argon at 1850 bar pressure at a temperature of 850 C. There is a complex preheating and cooling cycle as part of this process and for the first eight targets manufactured the last part of the cycle was a slow anneal. This results in growth of the uranium grains. Figure 5 shows a micrograph of the uranium structure present in targets 1-8.

The grain size is ~ 1-2 mm. The wrinkling observed on the plates is consistent with growth of clusters of aligned grains of this size.

Development of the heating and cooling cycles used to produce the plates was undertaken to produce a cycle which would result in much smaller and randomly oriented uranium grains. This requires that the last process is a quench of the plate from high temperature. This operation puts substantial stress on the uranium/Zircaloy bond. A temperature cycle was developed which resulted in excellent bond integrity and small random grains as shown in figure 6.

The plates in target number 9 used this production method. The target instrumentation showed the time taken from good condition to failure was very similar to the previous targets [2], the increase in the temperature of plate 1 and the change in the associated gap constant taking about 12 hours. As can be seen in table 1 no increase in lifetime resulted. This implies that irradiation growth is not the dominate mechanism leading to failure as all experimental evidence would suggest that the use of small grains should produce a marked decrease in the bulging and wrinkling of the plates for the same dose.

It is now crucial to the future of uranium targets on ISIS that target number 9 is examined in detail to determine cause of failure. Irradiation in a spallation source has some important differences to that in a reactor and the behaviour of the small grain target was not what was expected on the basis of reactor experience. The main difference is that hydrogen and helium production is much greater in a spallation source than a reactor.

The effect of hydrogen in both Zircaloy and uranium is to form hydrides and thus cause embrittlement. This suggests two possibilities:

1. The embrittled Zircaloy cracked under the temperature stresses and allowed water to come into contact with the hot uranium. The resulting chemical reaction caused the plate to swell and this blocked the cooling channel causing the high temperature.

2. The embrittled uranium cracked under the temperature stresses and caused failure of the cladding. Detailed examination, at Argonne National Laboratory, of an IPNS target showed extensive cracking of the uranium.

Efforts are now underway to define a programme for such a detailed examination.

Finally, two used targets have now been disposed of to BNFL Sellafield. This has required a considerable investment both in a new transport flask and in the remote handling equipment used to load the target into the flask. Both transfers went without difficulty.

2.2 Tantalum Targets

Two tantalum targets have been used so far and the second is the current production target. Neither target has given any significant problems in operation.

The change in cooling characteristics reported previously [4] continued in that the time taken for a target plate to cool after a proton beam trip increased with total proton dose on the target. It is now clear that this is a direct effect of a change in the heat transfer properties of the target plates. The peak target temperature shows an increase with proton dose consistent with the change in cooling time. The peak temperature in target number 1 in its last running period was 320 C which is to be compared to the peak temperature in the second target of 180 C, identical to number 1 except for irradiation, in its first running period.

While for ISIS this effect has no significant effect on operations it is an important consideration when designing new targets. For example, the design of an optimised target for ISIS will have to take into account this change in the ability to remove heat as the total number of incident protons builds up. This will place a limit on the allowable plate thickness which will have to be somewhat thinner than would be the case for an unirradiated target.

The only problem encountered with the tantalum target occurred when it was removed from the target, moderator and reflector assembly. This was done several times in its life either to be replaced by a uranium target or to allow for moderator changes. In storage the target released significant quantities of tritium. The total inventory of tritium in target number 1 has been calculated to be 7 TBq and in storage there has been a steady release of about 500 MBq/day in the form of tritiated water vapour. This is the main source of tritium release from the ISIS target station. It may be affected by the temperature of the target in storage. The storage wells are not cooled and the heat from radioactive decay heat results in a temperature of about 150 C.

The main reason for removing the first tantalum target was to make it available for materials studies as part of the European Spallation Source studies. It is planned to dismantle this target and make detailed examinations of the condition of the tantalum.

2.3 The Future

There are two main options. It is clear that there is a case for redesigning the tantalum target. The current geometry has not been optimised for tantalum and a more efficient design could give and increase in flux of ~15%. The problems of containing the tritium releases from a stored tantalum target will also be addressed. At present there are no plans to change to tungsten.

The future for uranium depends on establishing, unambiguously, the detailed cause of failure. If it turns out that cracking of the uranium leading to cladding failure is the cause then there is no obvious practical solution. The uranium density in the alternative alloys and uranium compounds reduce the gain in neutron flux to the point where the costs of production and disposal of the targets is not longer justified. In this case it is almost certain that no more uranium targets will be produced. Were the cause to be cladding failure then there is a case for seeking an alternative to Zircaloy for cladding the uranium..

3. Methane Moderators

The overall design of the moderator is shown in figure 7. The practical effects of irradiation of methane are production of hydrogen gas and formation of solid deposits in the moderator can. This was described in detail in [5]. It is the production of solid deposits which limits the lifetime of the moderator when the blockage results in insufficient flow to maintain the cooling of the moderator.

3.1 Lifetime

To date six moderators have been used and a summary of their lifetime is shown in table 2. To take account of the factor of two difference in neutron production(and hence dose to the moderator) between uranium and tantalum targets the integrated proton current for tantalum target running has been scaled by 0.5 in this table.

In the original design the liquid methane entered the moderator at the bottom ad left at the top down the central tube. Reversing the flow direction cured an instability in the system caused by the build-up of bubbles of hydrogen gas in the top of the moderator can. However, as can be seen in table 2 this resulted in a substantial decrease in lifetime.

Table 2. The lifetime of the methane moderators at ISIS.

Moderator	Equivalent Integrated Proton Current mAh
#1 single foil	747
#2 single foil	575
#3 double foil reverse flow	198
#4 single foil reverse flow	164
#5 single foil reverse flow modified inlet pipe	142
#6 single foil reverse flow modified inlet pipe	61 * Still in use

(Integrated current is in units of equivalent mAh for 800 MeV protons on a Uranium target)

Moderator 3 was fitted with two poison foils to reduce the pulse width of the neutrons. The reduction in neutron intensity which resulted was unacceptable so the moderator was replaced.

The lifetime of moderator 4 was too low to be practical as the task of changing a moderator takes about 3 weeks. For the ISIS running schedule to be maintained there are only two shutdowns in the year when this can be done. This requires a minimum lifetime of about 400 mAh

The neutronic performance of moderator 4 was acceptable throughout its life. This contrast with moderators 1 and 2 where significant deterioration in neutron fluxes occurred towards the

end of their operation. Moderator 4 was dismantled. Figure 8 shows that the blockage in this moderator was local to the top of the outlet pipe in contrast to moderator 1 where the moderator can was found to be essentially filled with solid [5].

While a development programme, described below, was carried out the methane moderator was replaced by water.

3.2 Development Programme

The development programme concentrated on two main topics, the fluid flow regime in the moderator and the radiation chemistry of methane.

Detailed analysis of the flow in the moderator was carried out using finite element analysis and mock up experiments. It was found that the design for the moderator where methane entered at the bottom the original shape of the outlet pipe resulted in a region of recirculating flow just at the place where the solid deposits were found in the examination of moderator 4. A simple redesign of the pipe orifice removed this as illustrated in figure 9. Moderator number 5 was made with the new pipe design. It operated successfully with no change in pressure drop characteristic of a blockage. It was replaced due to leak in the vacuum insulation can. Moderator number 6 is currently in operation.

A model of the radiation chemistry has been made. Radiative bombardment of methane produces free radicals which react to give higher molecular weight hydrocarbons that form wax at low temperatures. The wax which is insoluble in liquid methane then forms a deposit in the moderator eventually leading to blockage. Irradiation of the wax releases hydrogen and the end product is carbon. The chemical basis of this process is:

$$CH_4 + \text{ENERGY} \rightarrow C^*H_3 + H_*$$

Followed by a reaction where the hydrogen radical reacts by abstracting a further atom from a methyl radical

$$C^*H_3 + H_* \rightarrow {}^*C_*H_2 + H_2$$

The di-radical would then be expected to react preferentially with other di-radicals and build up a chain of repeating methylene units $--(CH_2)_n--$ i.e. the wax.

An examination has been made of the possibilities of reducing the production rate of high mass hydrocarbons and thus hydrogen gas by chemical additives or catalysts. There is a substantial amount of published information on the effects of radiation on methane and on the chemistry of the recombination of free radicals in for example ethane-methane systems. This work has been with room temperature and cold systems. A survey of the literature indicates that the rate of formation of the hydrocarbons which lead to blockage could well be reduced by the addition of chemical agents. This is based on a hydrogen radical being the active species responsible for the formation of the wax. A typical example of this is ethylene ($CH_2=CH_2$) where the hydrogen will react with the double bond rather than a methyl radical. It also appears possible that a catalyst, such as nickel, could be used to cause the hydrogen to recombine with the methyl radicals Both of these processes could reduce concentration of hydrogen radicals in the system and thus limit the production rate of wax.

These ideas will be tested directly in irradiation experiments on methane. The equipment is complete and measurements should start soon.

3.3 Prospects for the Future

Operation of the current design of moderator is satisfactory but requires that the charge of methane is changed by the liquid replacement system [5] every few days. This is due to instability in the circuit caused by the build-up of hydrogen gas in the methane. The hope is that the experiments on the radiochemistry will identify an additive which will both inhibit the production of high mass hydrocarbons with a consequent reduction in hydrogen production. The aim is for a moderator which lasts a full year of ISIS operation.

5. References.

[1] A. Carne.
Review of SNS Target Station.
Proceedings of ICANS IV, p136, KENS, 1980

[2] A. Carne, T. A. Broome, J. R. Hogston and M. Holding.
The ISIS target.
Advanced Neutron Sources 1988, p79, IOP Conference series 97

[3] J. M. Carpenter and A.G. Hins.
Experience with IPNS targets.
Proceedings of ICANS XII, pT1, Vol. 2. RAL 94-025

[4] G. M. Allen, T. A. Broome, M. A. Clark-Gather and C. W. Planner.
Measurement of Cooling Characteristics of the ISIS Tantalum Target.
Proceedings of ICANS XII, pT12, Vol. 2. RAL 94-025

[5] T. A. Broome, J. R. Hogston, M. Holding and W. S. Howells.
The ISIS Methane moderator.
Proceedings of ICANS XII, pT156, Vol. 2. RAL 94-025

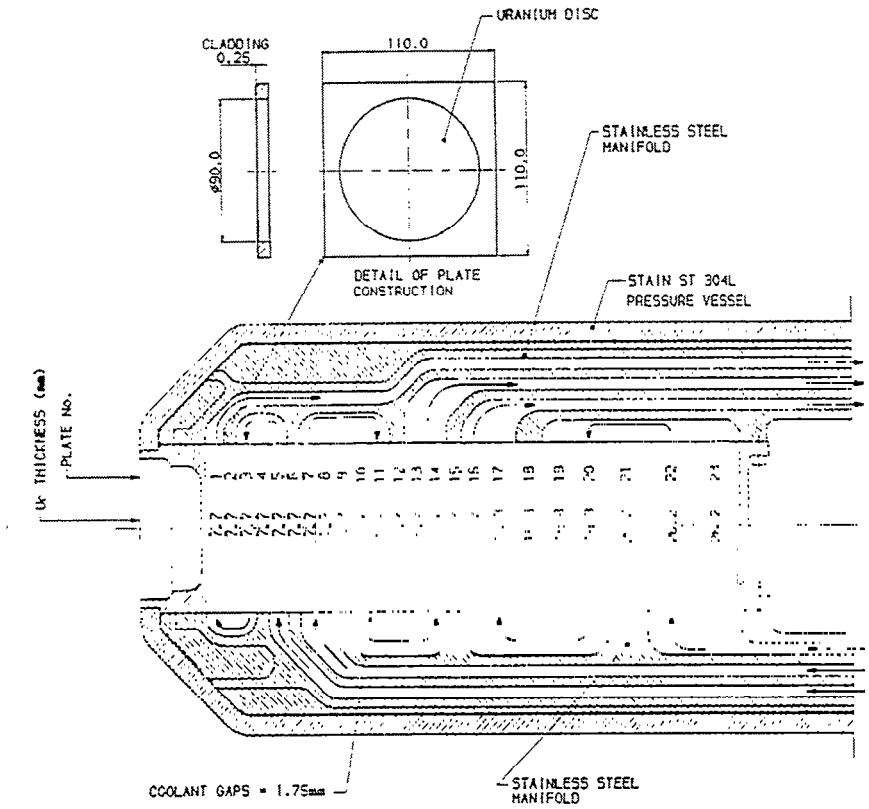

Figure 1. A Schematic layout of the ISIS target.

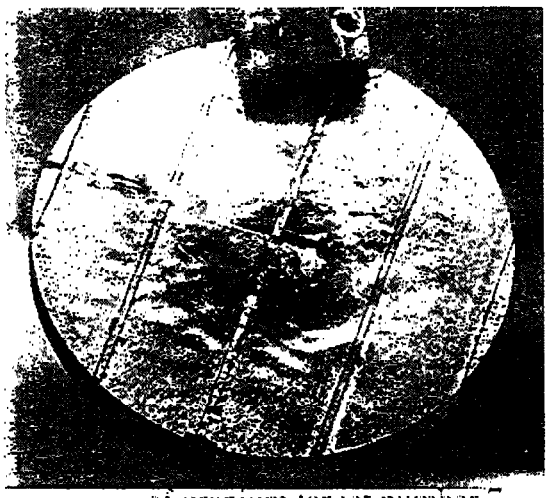

of uranium target number 7

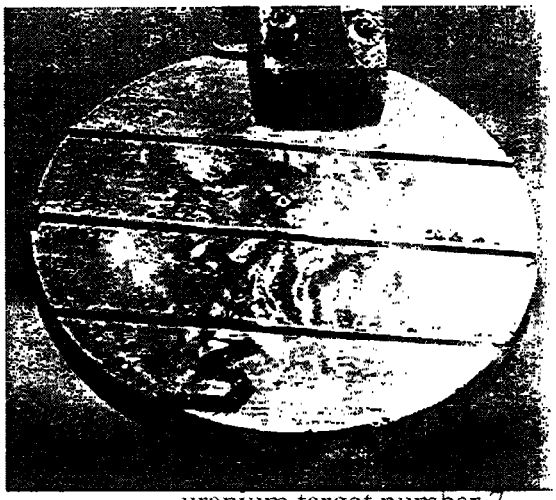

uranium target number 7

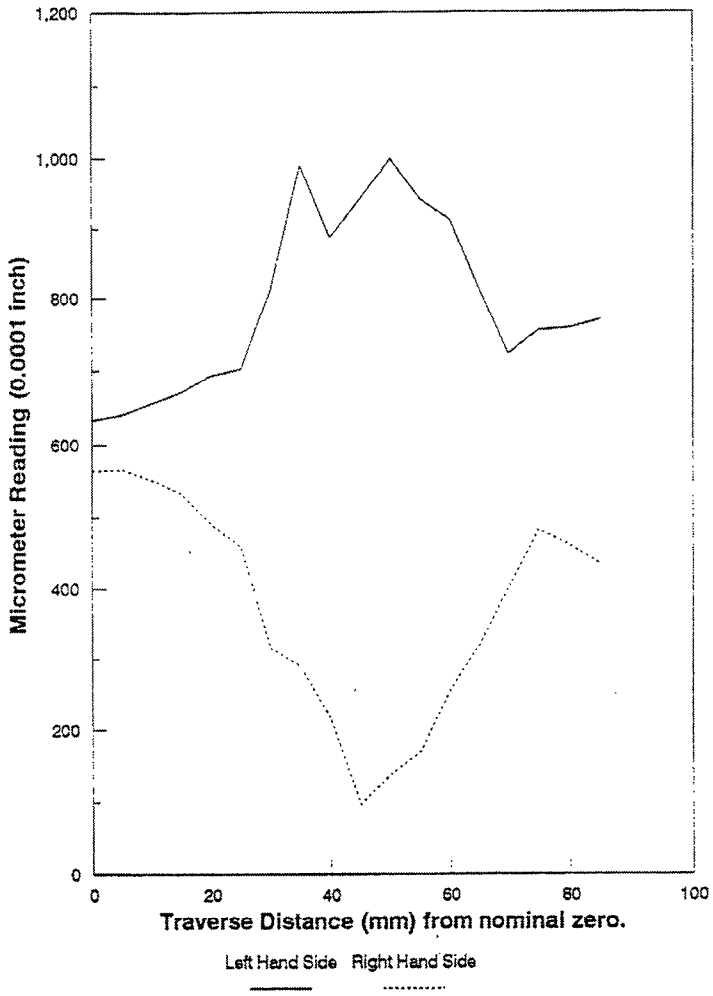

Figure 4. Profile scan of plate number 4, uranium target number 7.

|----------4.4 mm----------|

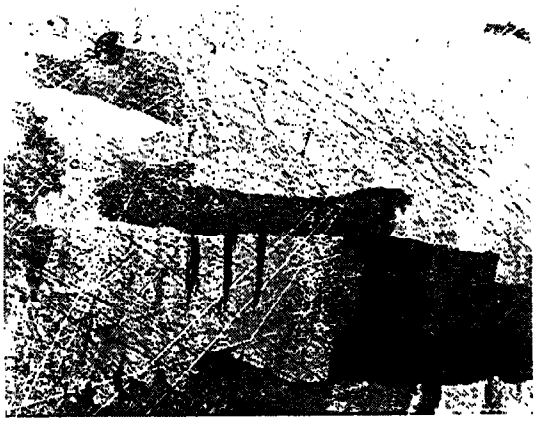

Figure 5. The grain size typical of uranium target numbers 1-8

|----------4.4 mm----------|

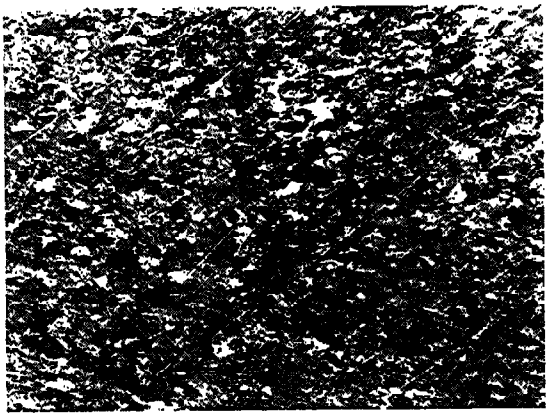

Figure 6. The grain size typical of uranium target number 9

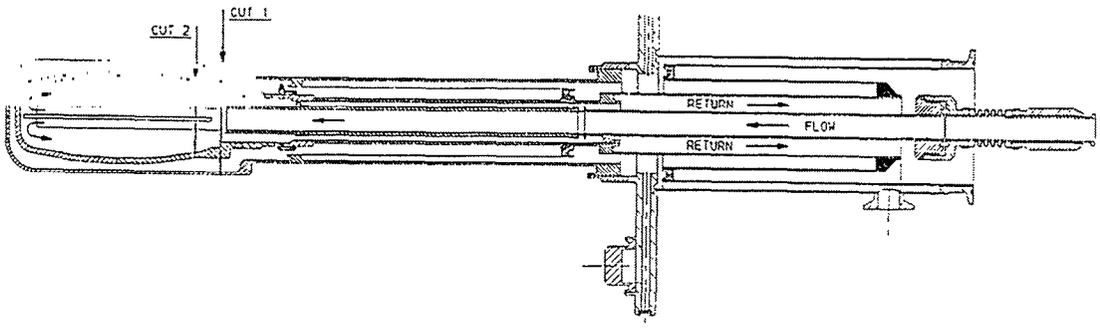

Figure 7. A schematic view of the ISIS methane moderator

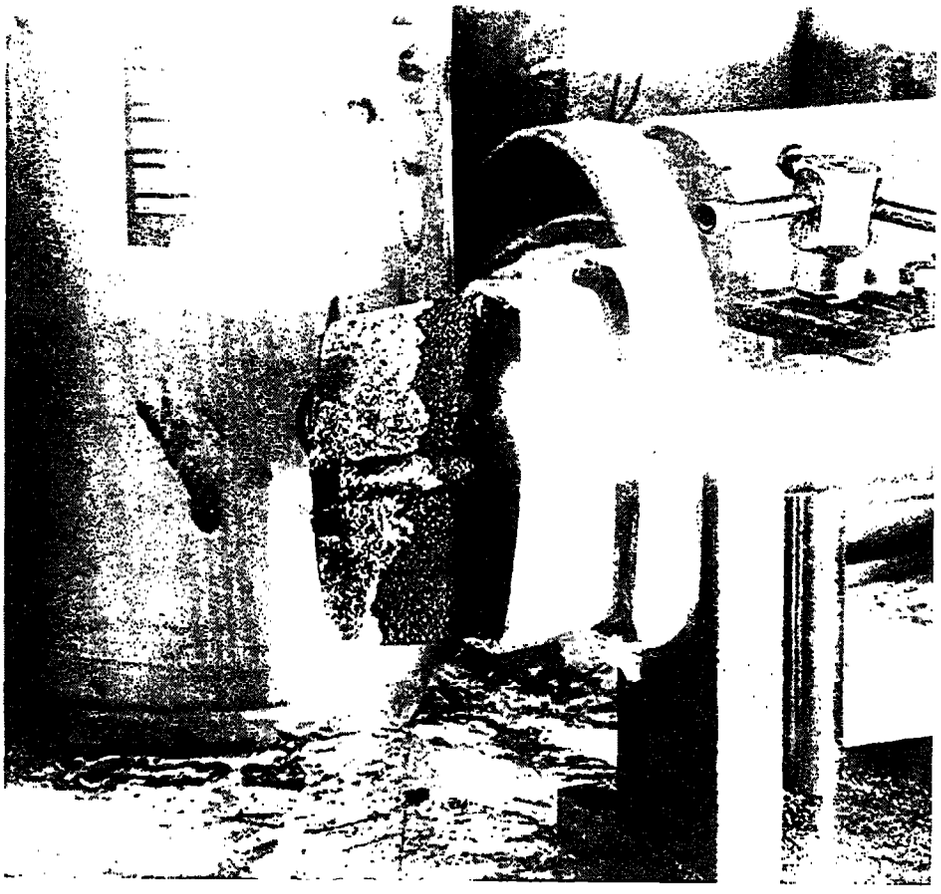

Figure 8. The carbon deposits in methane moderator number 4. Note the build-up at the end of the outlet tube.

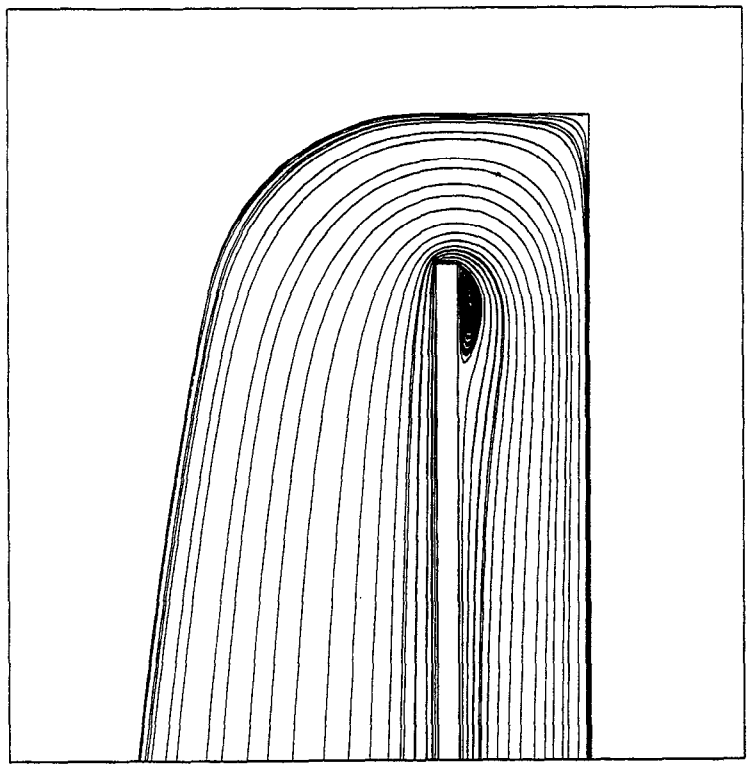

Figure 9a. The flow pattern in the top quarter of the moderator for the original design. Note the recirculation region at the end of the internal tube.

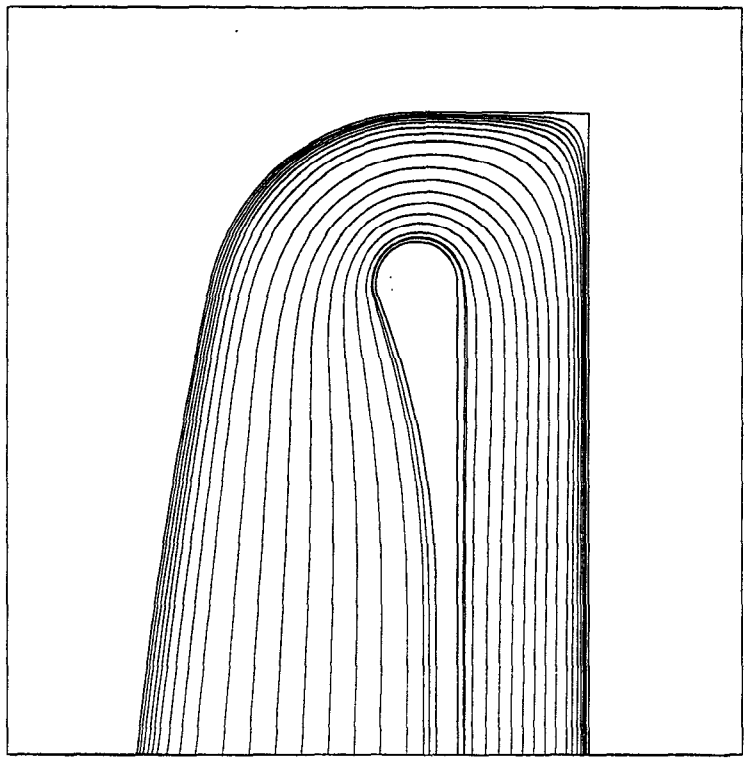

Figure 9b. The flow pattern in the top quarter of the moderator for the modified design with no recirculation region at the end of the internal tube.

ICANS-XIII
13th Meeting of the International Collaboration on
Advanced Neutron Sources
October 11-14, 1995
Paul Scherrer Institut, 5232 Villigen PSI, Switzerland

A PELLETIZED SOLID METHANE MODERATOR FOR A MEDIUM-TO-HIGH POWER NEUTRON SOURCE

A.T. Lucas*, G.S. Bauer†, C.D. Sulfredge*

*Oak Ridge National Laboratory, Oak Ridge, USA
† Paul Scherrer Institut, 5232 Villigen PSI, Switzerland

ABSTRACT

Solid methane has been an elusive neutron moderator medium for some years. Good physics has been done using frozen blocks of methane and innovative ways have been found to compensate for its low thermal conductivity. Annealing techniques have been evolved to release chemical energy by polymerization, but the use of solid methane remains limited to low power applications. This paper describes a possible way of using solid methane for very much higher energy applications. It presents some ideas on how mobile solid methane in the form of pellets might be employed. Initial feasibility calculations are included along with a possible configuration for a practical moderator. Well-developed techniques, like those used in fusion reactor systems have been explored for the production of pellets.

1. Introduction

Methane has long been known as one of the most desirable moderator materials, in particular for pulsed spallation neutron sources. It excells by the following properties (see e.g. ref [1]):

- Methane has a relatively rich spectrum of low energy rotational modes with strong transition lines at 1,2,3 meV and up. As a consequence, neutrons can still lose energy when already very cold and slowing-down occurs to very low energies. This means that the narrow line width of the slowing-down spectrum can extend down below 20 meV and excellent time-of-flight resolution can be obtained.

- Methane has a high density of hydrogen atoms which means that the time between collisions is short and the energy transfer per collision is high. This leads to a very narrow time distribution in the slowing-down regime. The product of neutron velocity v and pulse width Δt_s is of the order of 1 cm, 25% better than for H_2O!

The most desireable temperature to use methane is around 25 K, because this avoids possible complications that might arise from the phase transitions at 14 - 15 and 20 K and provides some margin to cool with liquid hydrogen. This gives an effective moderator temperature of

Keywords: methane, cold moderator, pellets, radiation effects

about 40 K and extends the slowing down regime below 20 meV. Solid methane as a block can, however, be cooled only at very low beam power sources such as KENS (5 kW).

Furthermore, while liquid methane tends to form oily and tar-like polymerization products already under moderate radiation levels [2], solid methane stores $CH_3^{\cdot}$-radicals up to a certain level due to the low mobility of the radicals. However, since polymerization of the radicals is an exothermal process it can be set off at a certain temperature and concentration and then proceed like an avalanche. While potentially dangerous if left uncontrolled, this "burping" can be induced by a gentle temperature increase without causing damage to the container [1], [3]. Depending on the radiation load, this may have to be done rather frequently and may becoem quite impractical at high power sources.

In an attempt to bypass these difficulties, we examine in the present paper the possibility of using solid methane in the form of spheres. This is an extension from a paper presented at ICANS-X [4] with emphasis on avoiding polymerization in the system at points where it could give rise to clogging or hamper the performance of the moderator in some other manner.

Our main goal is thus threefold:

a) devise a system with the highest practical moderator efficiency, i.e. the highest possible hydrogen content in the moderator volume at the lowest possible temperature

b) devise a system where the polymerization products can be safely and continuously removed and which can be operated at spallation sources with several MW of beam power

c) devise a system where "burping" can be allowed to occur spontaneously without affecting the whole moderator or large parts of it at the same time.

2. Function and Operation

Using the solid methane in pellet form enables it to be handled as a semi-fluid. The principle objective described in this paper is to allow the pellets to pass across a moderator under gravity at a rate designed to suit the specific application. As they cross the moderator vessel the pellets are heated volumetrically and they also suffer from radiation damage, releasing hydrogen and leading to stored radicals which, at some point, can polymerize in an exothermal reaction. The required transport rate across the moderator vessel is governed by the dominant of these two factors. In an extreme case, radiation damage could completely transform pellets to a carbon-like consitency [2]. It is unlikely that this would be a serious problem, nor would the melting of a few individual pellets. Both situations are a real possibility since some pellets will almost certainly be irradiated more than others. The development program discussed later includes an investigation into the rate of spontaneous energy release within pellets of different sizes. Together with an understanding of the heat transfer mechanisms involved, this would enable good estimates of the transport rate to be calculated.

3. Pellet Preparation

Frozen pellets made from a variety of materials, including hydrogen, are used routinely in fusion experiments. Although this application does not place particular importance on pellet size and shape, it has been demonstrated that repeatable spheres can be produced using the

same techniques. A development program would be required to optimize a moderator bed which might have a practical packing density of up to 68%.

4. Preliminary Feasibility Calculations

In order to examine some of the possible problems involved in manufacturing methane spheres for use in a pelletized cold source, several preliminary scoping calculations have been carried out. The thermophysical properties for methane at its freezing point of 90.67 K are collected in Table 1 as obtained from the literature [4-6] for use in the analysis.

Table 1: Thermophysical Properties of Methane [4-6]

Freezing point	90.67 K
Liquid density ρ_l	453.0 kg/m^3
Solid density, ρ_s	522.0 kg/m^3
Liquid thermal conductivity, k_l	0.216 W/ m · K
Solid thermal conductivity, k_s	0.26 W/ m · K
Liquid specific heat, $c_{p,l}$	3348.8 J/kg · K
Solid specific heat, $c_{p,s}$	2737.6 J/kg · K
Latent heat of fusion, h_{fs}	58680 J/kg

The first question that needed to be addressed was how large the methane spheres could be before internal heat generation would lead to melting inside the pellets while they were within the moderator vessel. Although some cracking or radiation damage to the solid methane might occur before the center of a sphere reached the melting point, onset of melting serves as a useful thermal limit for preliminary analysis. Since the pellets are assumed to be surrounded by liquid hydrogen during operation, they would enter the moderator vessel at a uniform temperature of 20 K and their outer surfaces would be maintained at approximately 20 K while they were exposed to nuclear heat generation. The problem thus reduces to calculating the transient internal temperature profile of a sphere subjected to uniform heat generation. In addition, pellet temperatures throughout the transient heating process will be bounded by the final steady-state solution. From Incropera and DeWitt [7], the steady-state temperature difference between the center and surface of a sphere is given by

$$T_0 - T_s = \frac{qR^2}{6k_s} \tag{1}$$

where q is the volumetric heat generation and k_s is the solid thermal conductivity. Equation (1) can be used to solve for the pellet radius that corresponds to a particular temperature difference once the heat generation is specified.

Setting the surface temperature T_s = 20 K and using T_0 = 90 K to reflect the maximum permissible center temperature allows one to calculate the largest sized pellet for no melting at steady-state. To provide a representative calculation for this feasibility study, a value of 1 kW/l = 10^6 W/m^3 (corresponding to several MW of beam power in a spallation neutron source) was assumed for the nuclear internal heat generation. Although the source would operate in a pulse mode with a repetition rate of 25 to 50 Hz, steady state conditions are considered an appropriate approximation because, at 50 Hz and 10^6 W/m^3, heating during each pulse is of the order of 0.015 K, which obviously does not constitute a severe deviation

from steady state heating. The estimated maximum radius predicted for the methane spheres under these conditions was R = 10.45 mm. Table 2 shows the pellet radii associated with several other values of T_0 -T_s ranging from 70 K down to 5 K with the same internal heat generation of 10^6 W/m^3. According to these calculations, it is clear that reasonably large methane spheres can be placed inside the moderator vessel with no danger of internal melting, even under steady-state conditions.

Table 2: Preliminary steady-state results for methane pellet heating in the moderator

Radius of methane spheres (mm)	Volumetric heat generation (W/m^3)	Steady-state temp. difference (T_0-T_s) (K)	Approximate time to establish the steady-state profile (s)
10.45	10^6	70*	350
6.84	10^6	30	150
3.95	10^6	10	45
2.79	10^6	5	20

* Maximum allowable temperature difference for no melting at steady state

Another important factor involved in optimizing pellet sizes is the time that would be required to establish the steady-state internal temperature profile in pellets that entered the moderator at a uniform temperature of 20 K. Calculations to answer this question were carried out using HEATING7 [8], a transient finite-difference code developed at Oak Ridge National Laboratory for solving heat conduction problems in up to three spatial dimensions. Results of the HEATING7 analysis are also included in Table 2 for each of the pellet sizes examined. Even for the largest pellet size of R = 10.45mm, only about 350 s are needed for internal temperatures to rise to their steady-state levels. Reducing R to 2.79mm so that T_0 -T_s = 5 K at steady state allows the final temperature profile to be reached in only 20 s. Given the rapid heat-up times reflected in Table 2, the pellets in a finalized design would probably be sized based on internal temperatures for optimum effective neutron temperature. There are, however, several other criteria that enter the final sizing decision such as ease of pellet frabrication, obtainable homogeneity, hydrogen release, heating upon radical recombination and ease of transport to and from the moderator vessel. Some of these are discussed below.

At least two approaches are available for making the pellets: Freezing in liquid nitrogen at 77 K followed by cooling to 20 K in liquid hydrogen, or direct freezing and cooling to 20 K in a liquid hydrogen bath. The first option has the advantage of using cheaper, non-explosive liquid nitrogen for much of the cooling process but would result in a somewhat more complex operating cycle. Several additional HEATING7 calculations were performed to investigate both these possible techniques of pellet formation for the sphere sizes from Table 2. The results are summarized in Table 3 for the liquid nitrogen/liquid hydrogen production cycle and in Table 4 for the cycle using only liquid hydrogen. All these HEATING7 runs started from uniform liquid methane spheres at 95 K and first calculated the time necessary for a one-dimensional freezing front to propagate inward all the way to the center, assuming a high heat transfer coefficient so that the sphere surface temperature T_s was essentially equal to the bath temperature. Once the solidification phase change part of the process was completed, cooling was allowed to continue in liquid nitrogen or liquid hydrogen to produce uniform methane spheres at 20 K. Freezing and cooling times were combined to yield the total pellet production times found in the last column of Table 3 and Table 4.

Table 3. Preliminary results for methane pellet production in liquid N_2 at 77K

Radius of methane spheres (mm)	Freezing time in liquid N_2 (s)	Total freezing & cooling time to 77 K in liquid N_2 (s)	Additional cooling time from 77 to 20 K in liquid H_2 (s)	Total production time (s)
10.45	300	540	450	990
6.84	120	270	210	480
3.95	45	90	70	160
2.79	20	40	35	75

Table 4. Preliminary results for direct methane pellet production in liquid H_2 at 20K

Radius of methane spheres (mm)	Freezing time in liquid H_2 (s)	Additional cooling time from 90 to 20 K (s)	Total production time (s)
10.45	120	360	480
6.84	45	195	240
3.95	15	75	90
2.79	8	32	40

Examination of Tables 3 and 4 shows several interesting features. Because of methane's relatively low heat of fusion, most of the pellet production time is consumed in cooling the frozen spheres from the solidification temperature of 90 K down to the working temperature of 20 K. This is particularly true when the cooling process is accomplished in two stages using both liquid nitrogen and liquid hydrogen. Furthermore, all the production times obtained are short enough to be incorporated into a realistic methane pellet system. Pellets near the smaller end of the size range described by the tables would probably be selected for use in an actual system because they would maximize fluidity for the moderator and keep the pellet internal temperature relatively low. For such pellet sizes, production times of 2-3 minutes are quite sufficient, even when a liquid nitrogen stage is used in the cooling process.

One factor that is not taken into account by HEATING is the increase in density that accompanies the freezing process. If solidification progresses from the outside of each sphere inward, the shrinkage associated with formation of the solid phase might be trapped as an internal void inside the pellet. The final void volume for this case is readily calculated based on the solidification shrinkage fraction, γ, for the material:

$$\gamma = \frac{V_{void}}{V_{total}} = 1 - \frac{\rho_l}{\rho_s} \tag{2}$$

Using the available solid and liquid densities for methane yields a value of γ = 13.2% maximum void inside each pellet fabricated. It remains to be investigated whether this pellet void fraction represents an unavoidable reduction in moderator density or whether ways can be found to "grow" the pellets with a minimum void volume. For uniform-sized spheres, the

theoretical maximum packing density is already $(\pi/6)2^{1/2} = 74.05\%$ before considering the internal void fraction. These limitations on hydrogen atom density in a pelletized moderator compared to solid methane could be improved to some extent by using two different pellet diameters, with smaller pellets fitting into the interstitial spaces between the larger ones is a theoretical possibility. However, the pellet production system would then have to be considerably more complicated. Heat removal by liquid hydrogen flowing between the pelletes will also require some reasonable degree of "porosity" to avoid excessive pressure drops.

5. Radiation effects

The spontaneous recombination of radiation-induced radicals was first observed at the IPNS-moderator at Argonne [1], where it led to destruction of the moderator vessel. Subsequent investigations showed that the likely explanation is as follows:

The methane molecules dissociate into H^+ and CH_3^- under the effect of ionizing radiation. While the H is relatively mobile and most of it can diffuse out of the methane or accummulate in internal voids, diffusion of the CH_3^- is mainly by H^+-exchange with neighboring CH_4-molecules, and therefore slow. In this way a fair concentration of CH_3^- can accumulate before polymerization can occur. The CH_3^--diffusion is strongly temperature dependent and therefore polymerization can be triggered by even a gentle temperature increase. Once triggered, the effect is self-amplifying due to the exothermal nature of the reaction. The destructive effect observed at IPNS is explained by hydrogen still trapped in the methane reaching a high enough pressure during the "burp" to cause the container vessel to rupture. Carpenter [1] and Beljakov et al. [3] have investigated this problem using similar relations for the temperature dependence. The one given by Beljakov et al. reads:

$$Q_R \cdot T_{act} \cdot a \cdot K(T)\, N^2/(\lambda \cdot T^2) \quad = \quad 0.88 \qquad (3)$$

where Q_R is the energy of recombination, T_{act} the activation temperature, K(T) an Arrhenius factor, λ is the thermal conductivity, a represents a linear dimension of the methane slug and N is the concentration of radicals in the methane.

This shows that one would expect "burping" to occur at higher radical concentration for smaller pellets. Also, pellets at different temperatures will behave differently.

In the moderator type considered here one would not expect burping to be a safety problem for the following reasons:

- The moderator vessel will always contain pellets exposed to different radiation levels and at different temperatures, so that simultaneous burping in a large number of pellets is unlikely.
- The pellets can be considered small enough not to accummulate significant amounts of hydrogen in voids, so no pressure increase is expected.
- Even if individual pellets should explode, this would not have a noticeable effect on the container walls.
- The pellets are sufficiently well cooled on their surface to prevent spreading of a temperature increase from one pellet to its neighbours.

It should therefore be possible to operate the moderator without intentionally triggering burping as has become a routine at IPNS. Note that, while at IPNS one "burp" per day is sufficient to release the radicals acummulated, the corresponding irradiation dose would be reached at a 5 MW source within about 2 min! It should also be noted that the performance of the methane as a moderator is expected to deteriorate only after a large number of "burps". According to Beljakov et al. [3], the CH_4-destruction occurs at a rate of roughly $0.2 \cdot 10^{-7}$ mole/J. Using again our assumed energy deposition of 10^6 W/m^3, we find on average rate of CH_4-destruction of $6 \cdot 10^{-8}$ sec^{-1}, or 0.22% per hour. This shows that the residence time of the methane pellets in the moderator vessel is not a problem from this point of view.

Taken as a whole, all the preliminary calculations conducted indicate that a pelletized methane moderator system shows considerable promise. Solid methane has a high enough thermal conductivity that reasonably small pellets are in no danger of melting while in the moderator. In addition, methane's low heat of fusion and relatively high freezing point mean such pellets can be produced quickly and efficiently in either liquid nitrogen or liquid hydrogen. Although a great deal of work remains to be done to optimize such parameters as the pellet sizes, production rates, and moderator residence times, the project definitely appears feasible.

6. Alternative Design Configurations

Fig. 1 shows the scheme postulated in a previous paper [4]. The pellets are produced at the top of the moderator by pulsing liquid methane through nozzles into a flowing hydrogen matrix. The liquid hydrogen is subcooled and mechanically circulated at a flowrate sufficient to prevent boiling under its own internal heat load and a portion of that generated within the pellet bed. A melting zone at the bottom of the moderator is warmed by circulated helium gas. The liquid pool created at the bottom is then removed, cleaned, and re-used or disposed of. The presence of the pool helps to prevent hydrogen from entering the methane system by forming a liquid barrier.

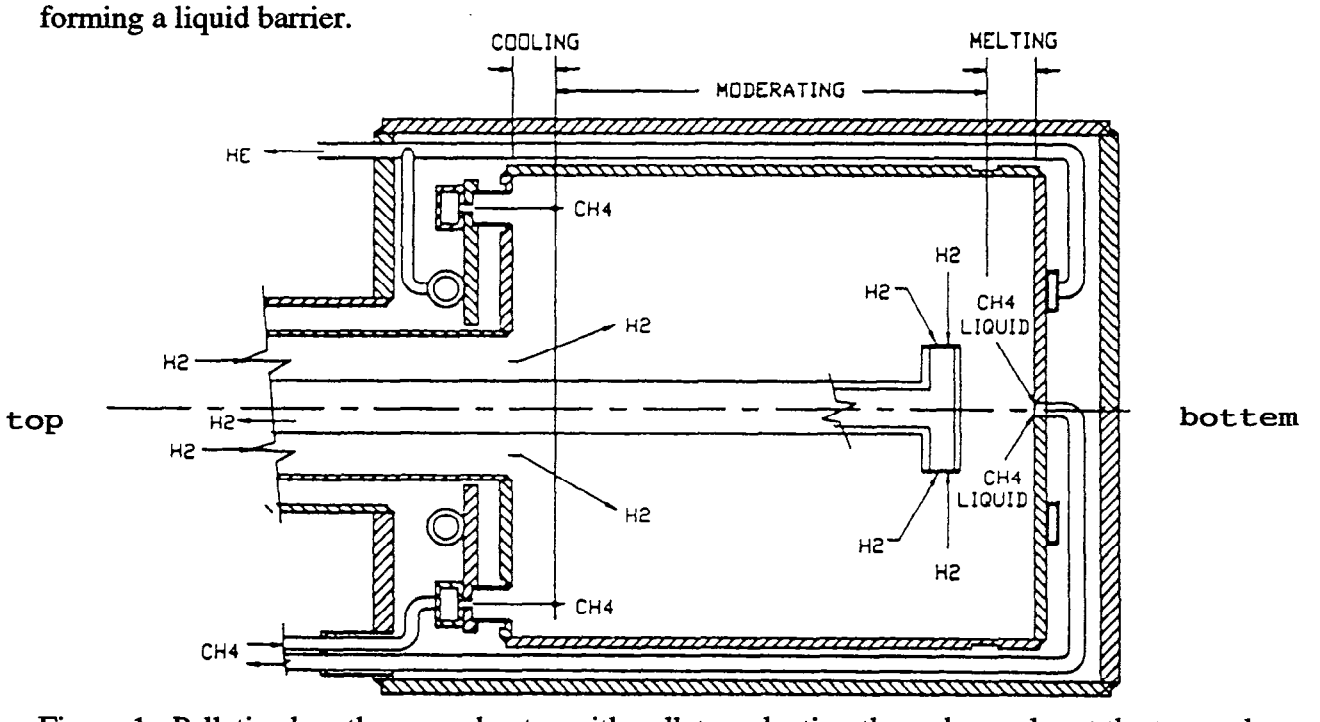

Figure 1: Pelletized methane moderator with pellet production through nozzles at the top and with melting zone at the bottom of the moderator canister as proposed in ref. [4].

The principal advantage of this compact arrangement is its operational simplicity and compactness and the absence of mechanical transport systems. Also, the liquid hydrogen, in addition to acting as a coolant to extend the useful life of the pellets, helps improve the overall moderator flux.

Unfortunately, however, it requires considerable space which would be at the expense of reflector material, placing severe limitations on its application. Furthermore, it would be very difficult to monitor the many complex operational parameters in this highly fluent region and servicing would be extremely difficult, if not impossible, after a short operational period. Melting the spheres at the bottom of the moderator vessel also is likely to free the radicals and encourage polymerization and sticking to the walls.

Fig. 2 represents a slightly more complex system retaining the advantages and avoiding potential problems of the previous one. A liquid hydrogen loop is provided, but the pellet supply and removal operations are relocated to a low radiation area outside the reflector. The pellets are then removed in a solid state by a mechanical system. Removal of the trapped radicals or polymerization products from the spheres by melting is also relocated to an area where negative effects on the circuit can be avoided. This is accomplished by a separation of functions:

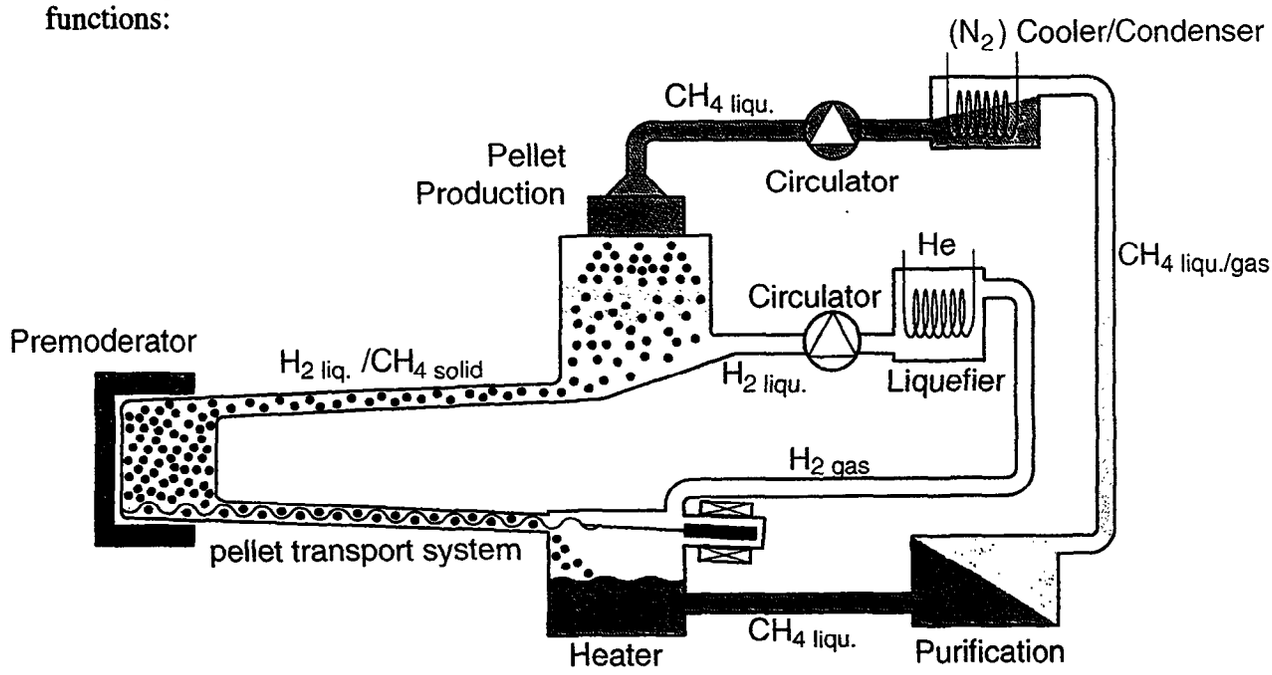

Figure 2: Pelletized methane moderator system with pellet production outside the radiation zone and pellet removal from the moderator canister by mechanical means. Melting of the pellets occurs outside the radiation zone, where also the hydorgen used to cool the pellets is separated. H_2 and CH_4 can be recirculated.

In the moderator vessel the pellets serve to slow the neutrons down, together with the liquid or supercritical hydrogen flowing between them. The heat deposited is removed by the flowing hydrogen. Hydrogen release from the pellets is not a concern because of the liquid hydrogen present. Radicals accummulated in the pellets may give rise to "burping" in individual pellets, but not in the whole system at the same time because

- the radiation load is not the same for all the pellets and
- the tempearture is not the same over the whole volume.

The pellets, together with the radicals and polymerization products trapped in them, are transported to a vessel outside the reflector. The rate of removal is controlled by a mechanical transport system. The methane is melted (polymerization of the radicals will proceed at this stage) and the H_2-gas is separated off by controlling the level of the melt in the vessel. The molten mixture of CH_4 and polymerization products is purified to obtain the remaining CH_4, which can be dumped or recirculated. CH_4 -gas is precooled (liquified) in a condenser and transported to the pellet-generating machine, where it is again immersed in the liquid hydrogen which is refrigerated in a separate circuit. The flow of liquid hydrogen is assumed to transport the pellets back to the moderator.

While this scheme reflects our present way of thinking, it may well be possible that some simplifications can be introduced in the course of a practical development program.

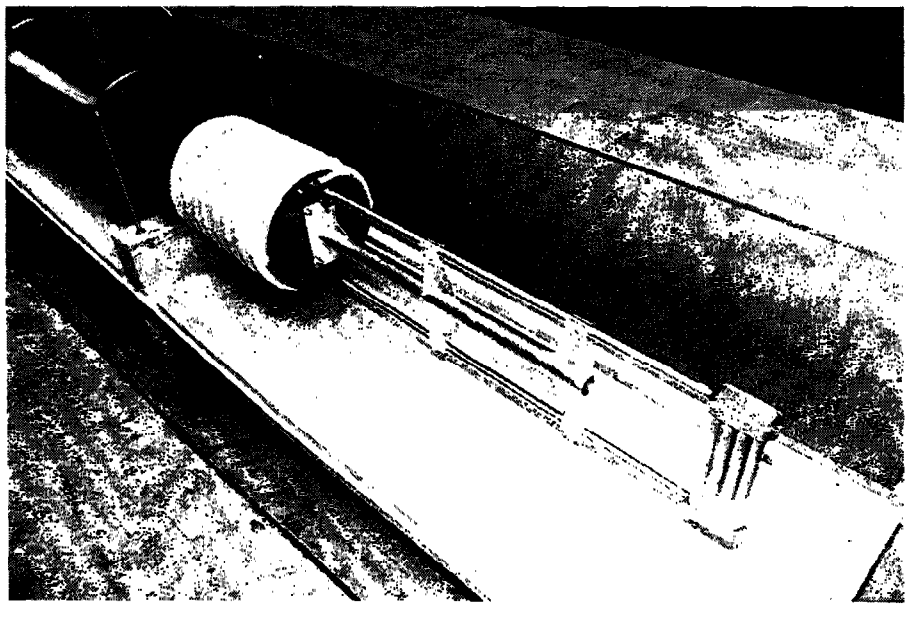

Figure 3: The water scatterer vessel at the PSI spallation neutron source SINQ. This vessel and holder plug can be replaced by a pelletized solid moderator as described.

7. Development Program

A practical working system would require a comprehensive, multidisziplinary R&D program involving computer modeling and analysis to examine the flow and heat transfer problems at various levels of the operation. It would also require a considerable experimentation and testing program together with an all-embracing safety and health physics involvement. It might be that such a work program could best be divided between two or more laboratories, each able to carry out tasks for which they are best qualified. A first-order task breakdown of the program would be as follows:

1) A basic study of the polymerization process using data from existing liquid and solid methane moderators. Possible radiation testing under controlled conditions might be considered. This would give a lead to the development of an optimum pellet size and residence time in the radiation field.

2) In parallel with the first task, a theoretical pellet size could be developed from the point of view of body heating and surface cooling. Practical aspects such as the initial forming and solidification, would have to be considered and an effort made to minimize internal voids.

3) Development of a reliable working system for producing the pellets continuously. In this regard, the very considerable work done by fusion groups might be applied. Pellet size and shape and some form of tolerance in each regard would be required before this task could be sensibly started.

4) Computer modeling of the loop systems would be used to examine the flow characteristics of a postulated configuration. This would include thermal and hydraulic considerations. A practical exercise of physical modeling using a surrogate fluid might be required.

5) Development of a final realistic model which would be designed for a specific operation in an existing facility. Suitable provisions have already been made in the SINQ spallation source now under construction at PSI. The water scatterer which would eventualle be replaced by a pelletized moderator system is shown in Fig. 3.

8. Conclusions

The practical feasibility of a system such as considered in this paper seems reasonable. Given sufficient time and effort, a working system based on these principles could be devised that would expand the capabilities of current cold neutron facilities. In light the of potential gains in neutron source performance with such a system, the development effort outlined above seems more than justified.

9. References

1. J.M. Carpenter, Cold Moderators for Pulsed Neutron Sources, *Proc. Int. Workshop on Cold Neutron Sources*, LANSCE, Los Alamos, Report LA-12146-C pp. 131-154, 1990

2. T.A. Broome, J.R. Hogston, M. Holding and W.S. Howells, The ISIS Methane Moderator *Proceedings ICANS-XII*, Abingdon, Rutherford Appleton Report 94-025 T156-T163, 1994

3. A.A. Beljakov, V.E. Ermilov, V.L. Lohmidze, V.V. Melichov and E.P. Shabalin First Experience of Cold Moderator Operation and Solid Methane Irradiation at the IBR-2 Pulsed Reactor, *Proceedings ICANS-XII*, Abingdon, Rutherford Appleton Report 94-025 T144-T155, 1994

4. K. D. Williamson and A. T. Lucas, A Combined H_2/CH_4 Cold Moderator for a Short Pulsed Neutron Source, *Proceedings of the ICANS X Conference*, Los Alamos, NM, pp. 559-564, 1988

5. T. E. Daubert and R. P. Danner, Data Compilation Tables of Properties of Pure Compounds, *American Institute of Chemical Engineers*, New York, NY, 1985.

6. C. L. Yaws, *Physical Properties: A Guide to the Physical, Thermodynamic, and Transport Property Data of Industrially Important Chemical Compounds*, McGraw-Hill Publishing Co., New York, NY, pp. 88-96, 1977.

7. F. P. Incropera and D. P. DeWitt, *Fundamentals of Heat and Mass Transfer*, 3rd ed., John Wiley, New York, NY, 1990.

8. K. W. Childs, *HEATING7.2 User's Manual*, ORNL/TM-12262, Oak Ridge National Laboratory, Oak Ridge, TN, 1993.

ICANS-XIII
13th Meeting of the International Collaboration on
Advanced Neutron Sources
October 11-14, 1995
Paul Scherrer Institute, 5232 Villigen PSI, Switzerland

FURTHER OPTIMIZATION OF COUPLED LIQUID-HYDROGEN MODERATOR FOR INTENSE PULSED NEUTRON SOURCE

Y. Kiyanagi, Y. Ogawa, N. Kosugi, H. Iwasa, M. Furusaka* and N. Watanabe*

Faculty of Eng., Hokkaido University, Kita-13 Nishi-8, Kita-ku, Sapporo 060, Japan
*National Laboratory for High Energy Physics, Oho 1-1, Tsukuba-shi 305, Japan

ABSTRACT

Optimization studies for increasing cold neutron intensity from a coupled liquid-hydrogen moderator with a premoderator were performed. Optimal thickness of hydrogen moderator was found to be 5 cm. A beryllium (Be) reflector-filter placed in front of the moderator chamber gave almost no intensity enhancement in a cold neutron region. Narrow beam extraction was effective for some instruments which view a small area of the moderator surface. Beam intensity decreased a little by extracting neutron beams from both sides of the moderator in comparison with a single beam extraction.

1. Introduction

A composite moderator (liquid-hydrogen with hydrogenous premoderator) is now well known to be the best candidate for intense pulsed neutron source due to its high efficiency[1]. In order to have more intensity we experimented by making some modifications to this moderator system.

Our previous experiment shows that the cold neutron intensity from the composite moderator which had 2 cm thick liquid-hydrogen was lower than the one which had 5 cm[2]. This suggests that the thickness of 5 cm for the main cryogenic moderator (liquid hydrogen) may not be optimal. Therefore, it is interesting to check thickness dependence of the cold neutron intensity. We measured the cold neutron intensity from moderators with three different thicknesses to examine the thickness dependence.

We thought another approach for increasing intensity would be to examine the effects of a Be reflector-filter in front of the viewed surface of the liquid hydrogen moderator. It was reported that for a bare moderator system this method brought about a gain factor of 1.7-2.2 depending on the Be thickness (2-4 cm)[3]. Therefore, it would also be interesting to study whether this method is also useful for the composite system for increasing intensity. We performed a measurement of the cold neutron intensity from the composite moderator system with a Be reflector-filter.

Spatial distribution of cold neutrons from a coupled composite moderator in wing geometry was found to be have a brightest region near the target. Therefore, this distribution is useful for small angle neutron scattering, reflectometry etc., in which only a small part of the moderator is viewed by those instruments. Thus, the following idea emerges, that is, the cold neutron intensity can be increased to some extent if the remaining part of the moderator is covered by an additional premoderator. We looked into this idea.

Keywords: Pulsed Neutron, Liquid hydrogen, Cold neutron, Intensity

In actual application of this kind of moderator, it may be interesting to know how the neutron intensity decreases if the neutron beams are extracted from both sides of the moderator. We also studied this effect experimentally.

2. Experimental set-up and results

Experimental set-up is essentially the same as the previous one[1]. In the thickness dependence study, composite moderators with 2, 5 and 6.5 cm thick liquid hydrogen were measured. The lateral dimension was 12 cm x 12 cm. A light water premoderator of 2 cm thickness was used. Figure 1 shows measured results. The moderator system is shown in the inset. The cold neutron intensity is almost saturated around 5 cm thick. The present result is a lot more different from the bare and decoupled moderator case[4]. This is due to the nature of the composite moderator: since the neutrons flowing into liquid hydrogen are well moderated by the premoderator, adding more hydrogen does not produce more cold neutrons but in fact decreases them.

In the Be reflector-filter experiment, liquid hydrogen of 5 cm thick was used. As a Be reflector-filter a 1.5 cm thick Be plate (lateral dimension: 10 cm x 10 cm) was attached to the main cryogenic moderator chamber (see Fig.2). Therefore, the temperature of the Be plate was about 20K. Figure 2 shows spectral intensities from this moderator system with and without the Be reflector-filter. There is no additional gain in the cold neutron region by introducing Be. We were not expecting such a result. However, the present result was natural if we consider that this system is already well reflected and the insertion of additional reflecting material simply screens thermal neutrons flowing into liquid hydrogen.

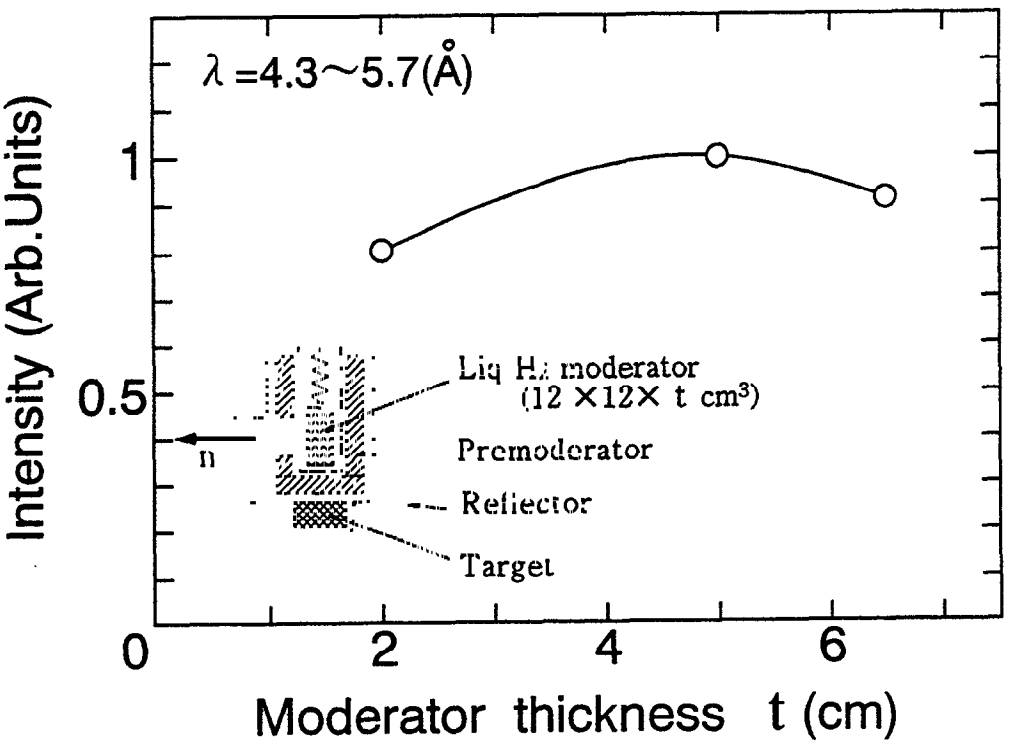

Fig. 1 Cold neutron intensity vs. thickness of liquid-hydrogen moderator. The composite moderator examined is shown in the inset.

The spatial distributions of cold neutrons were measured over the brightest region 0.5-4.0 cm from the moderator bottom, with and without the additional premoderator, by moving a Cd slit with 0.5 cm high and 8 cm wide. The moderator systems studied here are shown in Fig. 3. The results are shown in Fig. 4. The gain with an additional premoderator is about 15%. This situation was almost unchanged by introducing a beam hole on the opposite side.

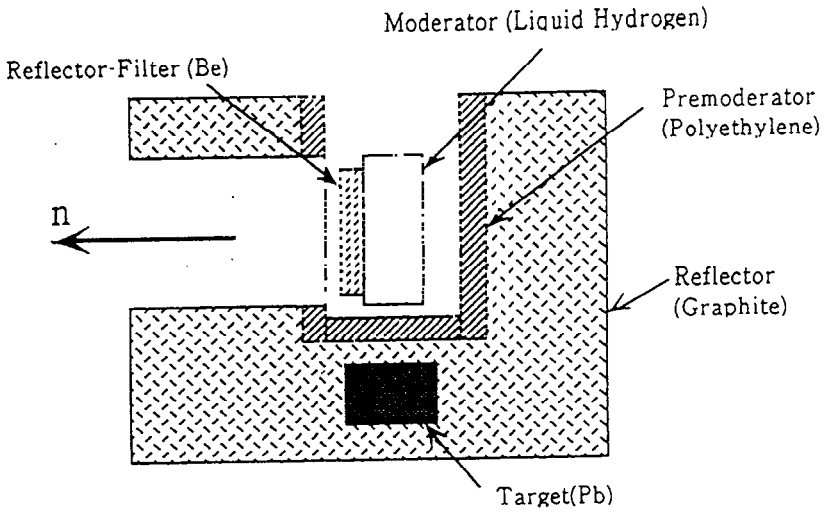

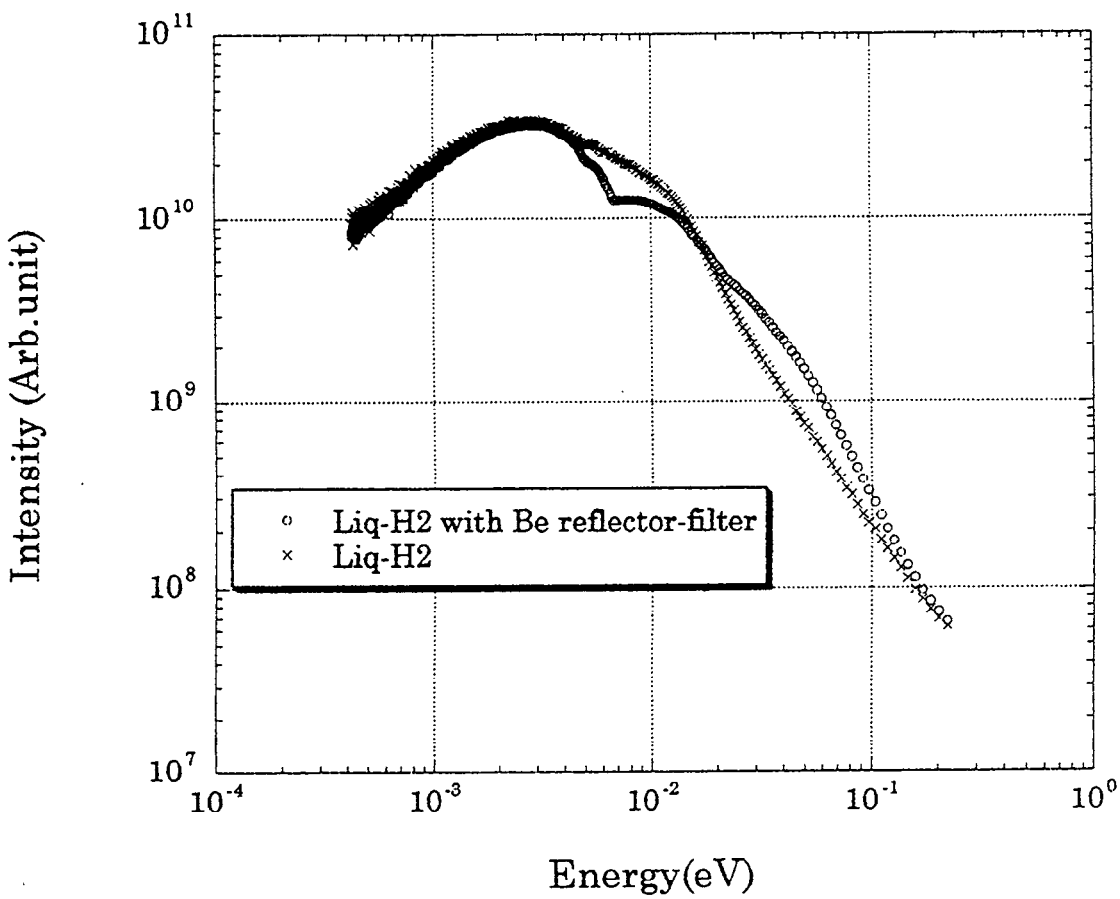

Fig. 2 Energy spectra from a composite liquid-hydrogen moderator and from the same moderator with Be reflector-filter. The moderator system with Be is also shown.

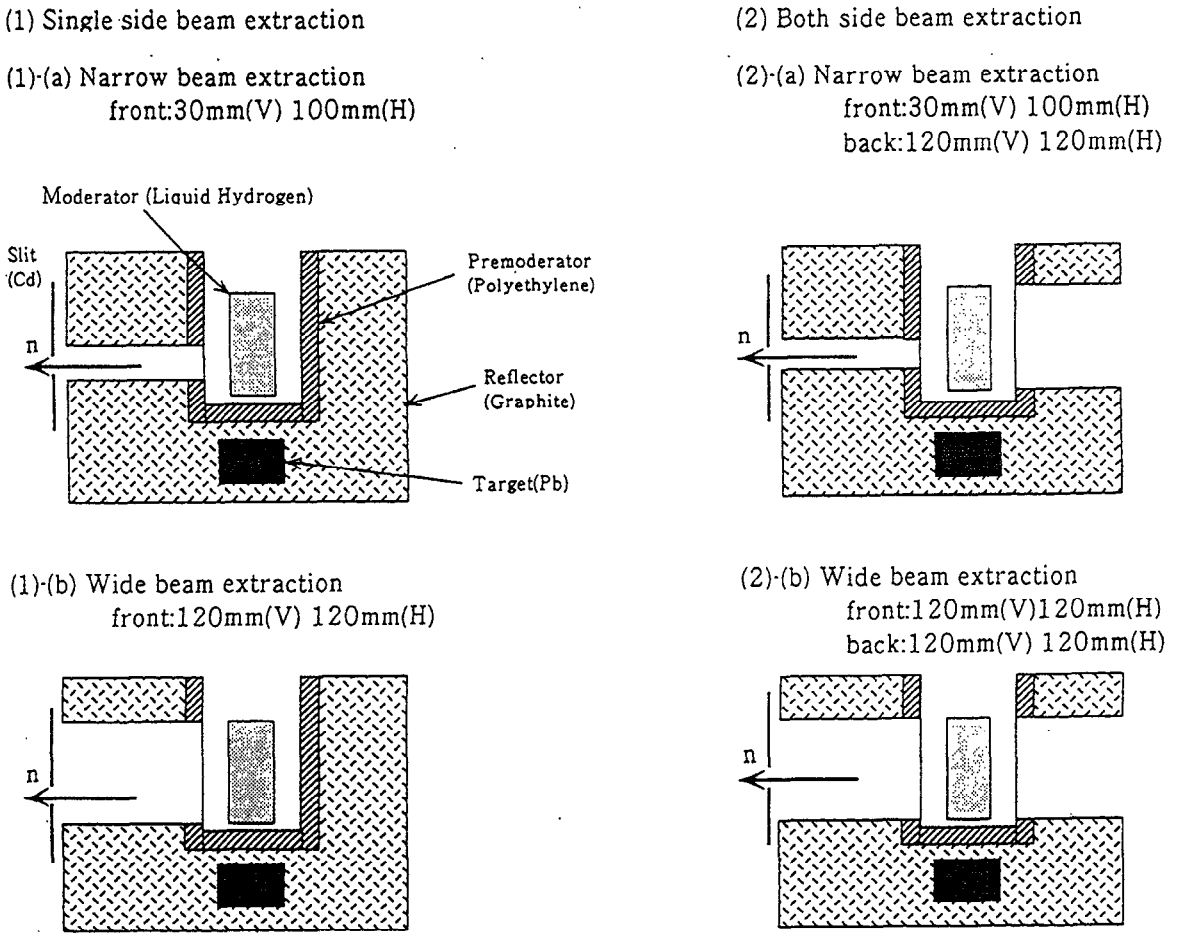

Fig. 3 Moderator systems used for narrow beam extraction experiments. Single and double beam extractions were examined. As a reference a moderator system with a wide beam hole of a size commonly used was also studied.

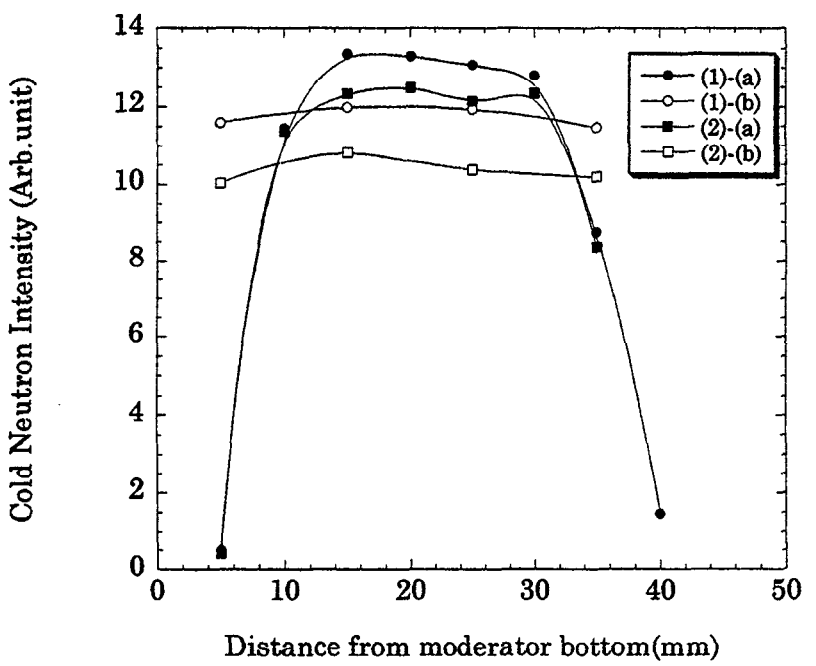

Fig. 4 Spatial distributions of cold neutron intensities along the vertical direction from the bottom of the moderator.

Finally, we measured the decrease of cold neutron intensity by extracting neutrons from the opposite side of moderator (see Fig. 3(2)). If the premoderator of the opposite side in Fig. 3(1)-a is removed and a standard straight beam extraction hole (12 cm x 12 cm) is opened in the reflector (see Fig. 3(2)-a), the intensity decreases by about 6%. This decrease would be acceptable. Next, if the premoderator of the opposite side in Fig. 3(1)-b is removed and the standard beam hole is opened (see Fig. 3(2)-b), the intensity decreases by about 12%.

3. Conclusion

The optimal thickness of hydrogen moderator to obtain the highest cold neutron intensity from a composite moderator system was found to be about 5 cm. A reflector-filter was not effective to increase the cold neutron intensity in this system. Partial enhancement of the cold neutron intensity could be achieved by narrow beam extraction, which is useful for small angle neutron scattering, reflectometry and so on. Beam extraction from both sides of the moderator causes very small reduction in intensity. So, it would be better to use this type of beam extraction than to equip two moderator systems for individual beam extraction.

We are now planing to examine a composite moderator with a grooved hydrogen moderator which extracts cold neutrons from the deep part of the moderator where neutron flux is high.

4. References

[1] Y. Kiyanagi, H. Iwasa and N.Watnabe, Nucl. Instr. Methods A312 (1992)561.
[2] Y. Kiyanagi, S. Satoh, H. Iwasa, F. Hiraga and N. Watanabe, Physica B 213&214(1995)857.
[3] S. N. Ishmaev, I. P. Sadikov and A. A. Chernyshov, Report IAE-2019(1970).
[4] Y. Kiyanagi and F. Hiraga, J. Nucl. Sci. Tech., 28(1991)1128.

ICANS-XIII
13th Meeting of the International Collaboration on
Advanced Neutron Sources
October 11-14, 1995
Paul Scherrer Institute, 5232 Villigen PSI, Switzerland

RECENT PROGRESS IN DEVELOPING HIGH-EFFICIENCY CRYOGENIC MODERATORS

N. Watanabe, Y. Kiyanagi* and M. Furusaka

National Laboratory for High Energy Physics, 1-1 Oho, Tsukuba-shi, Ibaraki 305, Japan
* Department of Nuclear Engineering, Hokkaido University, Sapporo 060, Japan

ABSTRACT

Extensive experimental efforts have been devoted to develop high-efficiency cryogenic moderators for: (1) cold intense, (2) cold sharp, and (3) thermal sharp neutron pulses based on a composite moderator concept. Various ideas to enhance the cold neutron intensity have been examined. New moderators, such as a decoupled composite moderator and a composite moderator with poisoned premoderator, have been proposed and tested in order to realize a narrower cold neutron pulse without sacrificing the peak height. At a longer wavelength region (say >6 Å), the performance of the new moderator is close to that of a decoupled solid methane moderator.

1. Introduction

In a high-power pulsed spallation neutron source, it is rather difficult to expect a higher target efficiency, as in a low-power one; generally, he neutronic efficiency of the target decreases with increasing proton-beam power. Thus, R&D of a high-efficiency moderator system becomes important to increase, or at least to keep up with, the total neutronic efficiency of the existing sources. R&D of the moderator is also important, since moderators are the final devices of a pulsed-neutron source, which determine the quality of experiments.

Extensive efforts have been devoted to develop three kinds of high-efficiency cryogenic moderators for: (1) intense cold neutron pulses for any pulse width; (2) narrower cold neutron pulses with the highest peak height; and (3) narrower thermal neutron pulses, under the condition that solid and liquid methane cannot be used at intense sources. Thus, liquid-hydrogen (L-H_2) becomes only one cryogenic moderator material. Our moderators under development are all based on L-H_2.

2. Development of composite moderators for intense pulses of cold neutrons

For experiments such as small angle neutron scattering (SANS) and critical scattering (reflectometry), the time-integrated intensity of cold neutrons per pulse is, in principal, only

Keywords: Pulsed neutron, Cryogenic moderator

important (independent of repetition rate) within a realistic range of the repetition rate. In this case, the figure-of-merit (FOM) for a pulsed source is written as [1]

$$FOM(\lambda) \propto \int I_1(\lambda, t)\, dt,$$

where $I_1(\lambda, t)$ is the neutron intensity per pulse at wavelength λ and emission time t. A coupled composite moderator of L-H_2 and a hydrogenous premoderator at ambient temperature is best for this purpose among the moderators which we studied. Here, we summarize the results of R&D already achieved on this moderator system and future plans.

2.1 Already achieved or studied

(1) Gain factor

A gain factor of about 6 has been obtained compared to that of a typical decoupled L-H_2 moderator (coupling gain factor 3 $\times$ premoderator gain factor 2). [2]

(2) Premoderator material

Polyethylene, light water (H_2O) and zirconium hydride (ZrH_2) were compared.[3]
Polyethylene gave the highest gain factor. H_2O gave a lower gain factor (about 90% of the polyethylene gain factor). ZrH_2 was the worst.

(3) Function of premoderator

Thermal and epithermal neutron intensities from premoderator boxes (without L-H_2) comprising polyethylene, H_2O and ZrH_2 of various thicknesses were compared. From this comparison it was found that the cold-neutron intensity is almost proportional to the thermal-neutron intensity produced inside the premoderator box. [3]

(4) Realistic premoderator material

Polyethylene cannot be used at an intense source. Thus, H_2O becomes the best premoderator material, although the gain factor is slightly loywer than that of polyethylene.

(5) Gain factor vs. premoderator thickness

From a neutronic point of view, there is an optimal premoderator thickness (beyond which the gain factor starts to decrease) for each material. The optimal thicknesses are about 2 cm for polyethylene and 2-3 cm for H_2O. [2-4]

(6) Choice of premoderator thickness

It is now well known that a premoderator plays an important role not only to enhance the cold neutron intensity from a cryogenic moderator, but also to reduce the energy deposition in it. For the latter purpose, a thicker premoderator is better. Therefore, a compromise is necessary in determining the premoderator thickness.

(7) Coexistence of coupled and decoupled moderators

In the large-scale facilities under planning, two target stations dedicated to low and high repetitions are being considered. Usually, in a low-repetition-target station, both coupled and

decoupled moderators must be installed in one target-moderator-reflector assembly. In this case it is important to know how much the gain factor of a coupled moderator decreases in the presence of decoupled moderators. This problem was studied experimentally.[2] The decrease is about 16%.

(8) Various efforts to increase the intensity

How to increase the cold neutron intensity from a coupled composite moderator system is one of the most important tasks in the R&D of this kind of moderator. Various efforts have been devoted to this purpose. The results are briefly described below :

(a) Grooved premoderator

It is already known that in a wing geometry the premoderator gain factor is most sensitive to the thickness of the bottom premoderator adjacent to the target. We therefore expected that grooving the bottom premoderator might increase the intensity. The additional gain by this procedure was only 3%.[2]

(b) Optimal thickness of L-H_2

Our previous result showed that the cold neutron intensity from a coupled composite moderator with 2 cm thick L-H_2 was considerably lower than that with 5 cm thick L-H_2,[4] suggesting a further intensity gain with a thicker L-H_2. However, the measured result with 6.5 cm thick L-H_2 showed no further gain (the gain factor decreases beyond at 5 cm thick).[5]

(c) Be reflector-filter

A 1.5 cm thick Be reflector-filter cooled down to 20 K was attached in front of the L-H_2, expecting a further gain. The result was pessimistic; no additional gain was found.[5]

(d) Partial enhancement of intensity

For cold-neutron experiments, such as SANS and reflectometry, only a part of the moderator is viewed by instruments. By masking the remaining surface of the moderator by an additional premoderator, a further gain of about 15% has been achieved.[5]

(e) Solid methane with a premoderator

It may be interesting to know whether a coupled composite moderator with solid methane as a main cryogenic moderator can give a higher intensity than that with L-H_2, although solid methane cannot be used at an intense source. The result of direct comparison measurements showed that a composite moderator with solid methane can not surpass a coupled composite with 5 cm thick L-H_2.[4]

2.2 Other ideas for increasing intensity

The following ideas should be examined:

(1) Grooved composite moderator

A coupled composite moderator with a grooved L-H_2 would be interesting to test. A cryogenic moderator chamber (total thickness of 9 cm with 4.5 cm deep grooves, 12 cm wide and 12 cm high) has been arranged for this test.

(2) Overlap composite moderator

In simple decoupled moderators at room-temperature in a flux-trap geometry we were successful to obtain a 40-50% higher intensity than that of a conventional configuration, by overlapping part of the moderator with the target.[6] This idea will also be worth testing in the case of coupled composite moderators.

3. Development of a composite moderator for narrow pulses of cold neutrons

Another important field of a scattering experiments utilizing cold neutrons is high-resolution (μ eV or sub μ eV) spectroscopy. A simple inverted-geometry-type spectrometer is typical for this purpose, since the instrument has high efficiency (for example, LAM-80ET at KENS and IRIS at ISIS), and a very wide energy window compared to the corresponding reactor instruments. In this application the FOM of the cold-neutron source is proportional to the peak height of the neutron pulse $\hat{I}_1(\lambda, t)$ as[1]

$$FOM(\lambda) = \hat{I}_1(\lambda, t) ,$$

provided that the required length of the neutron guide is available between the moderator and the sample. We have proved experimentally that a coupled composite moderator with 5 cm thick L-H_2 can provide about a 2-times higher pulse height than the typical decoupled L-H_2 moderator. However, from a practical point of view, a longer guide tube (say more than 200 m) may not be acceptable. A moderator which can provide a narrower pulse without sacrificing the peak height then becomes more acceptable. From extensive measurements, we found that the pulse width (FWHM) and the long-time tail can be controlled to some extent (as described below).

3.1 Already achieved or studied

(1) Effect of a premoderator and reflector

It was found that the pulse width is mainly determined by the premoderator, while the long-time tail is mainly affected by the deflector.[7],[8]

(2) Decoupled composite moderator

Therefore, by decoupling a composite moderator from a reflector, one can eliminate or improve the long-time tail. On the other hand, by reducing the premoderator thickness, one can squeeze the pulse width (see Fig. 2 in ref.8). For example, a decoupled composite moderator with the 5 cm thick L-H_2 and a 1 cm thick premoderator can reduce the pulse width down to 40% at a cost of the peak intensity about 20% (see Fig. 2 in ref.8). A simple coupled 5 cm thick L-H_2 moderator without a premoderator can bring about a similar improvement in the pulse width without sacrificing the peak height, as shown in Fig. 1. However, the long-time tail from the decoupled composite moderator is largely improved compared to the simple coupled one.

(3) Poisoned premoderator

It is well known that in a decoupled moderator an interleave poison can improve the pulse characteristics (pulse width and long-time tail) at a cost of the time-integrated intensity. It is interesting to examine what would happen with a composite moderator comprising 5 cm thick L-H_2 with a poisoned premoderator. In recent experiments based on this idea, the following results were obtained. A composite moderator with 5 cm thick L-H_2 and a poisoned bottom premoderator (0.5 cm thick H_2O inside the Cd interleave poisoning plate and 1 cm outside for bottom premoderator) gives better pulse characteristics than does a decoupled composite moderator with 5 cm thick L-H_2 and a 1 cm thick H_2O premoderator (a slightly higher peak height, a narrower pulse width and a faster decay time), as shown in Fig.4 in ref.8 .

3.2 Can a composite moderator equal decoupled solid methane ?

As far as the time-integrated intensity is concerned, it has already been proved that a coupled composite moderator with 5 cm thick L-H_2 and a 3 cm thick H_2O premoderator can provide about a 2-times higher cold-neutron intensity than a decoupled 5 cm thick solid-methane moderator. For narrow-pulse use, an important question is whether the decoupled composite moderator described in (3) in the foregoing section can equal solid methane? It is one of the most important targets of our R&D work to seek a new moderator by which a decoupled solid methane moderator can be replaced. At the present stage it can be said that the performance of the composite moderator described in (3) is very close to that of the decoupled solid methane at a longer wavelength region (say above 6 Å), but not yet at a shorter wavelength region(~4 Å).[8]

3.3 Other ideas

The following ideas should be examined.

(1) Use of a non-moderating reflector

The use of a non-moderating reflector (for example, iron) will allow a decoupler to be removed in both simple and composite moderators. This may bring about a better result in intensity without deteriorating the decay time or long-time tail.

(2) Thinner L-H_2

The pulse width of cold neutrons from the decoupled composite moderator described in (3) is close to that from a simple decoupled 5 cm thick L-H_2 moderator. The premoderator of this thickness has
little effect on the pulse width. This result suggests that a composite moderator with a thinner (<5 cm) L-H_2 may bring about a better result.

(3) Removing the side premoderator

In the composite moderator described in (3), we have confirmed that the cold neutron intensity was somehow increased by removing the outside premoderator in the side premoderator.[8] We have not yet measured the pulse characteristics of this moderator, which should be better than those of the former.

4. Moderator for a narrow thermal-neutron pulse

For such experiments as high-resolution powder diffraction and high-resolution spectroscopy using thermal neutrons, narrow thermal-neutron pulses are essentially important; a solid-methane moderator (KENS) or poisoned liquid-methane (L-CH_4) moderator (ISIS) has been used up to now. The use of an L-CH_4 moderator becomes more and more difficult with increasing proton-beam power due to radiation damage. Thus, R&D of a new moderator which can replace a poisoned L-CH_4 moderator becomes important. One idea is a decoupled composite moderator with L-H_2 and ZrH_2 at low temperature (20K). A thin L-H_2 moderator is used in this case with a hydrogenous moderator which can compensate for any shortage of the hydrogen number density of L-H_2, and must be free from radiation damage. ZrH_2 will be a good candidate due to its higher hydrogen number density and higher resistance against radiation damage. In this application ZrH_2 must be cooled down to a low temperature in order to suppress any pulse-width broadening. A preliminary experiment was performed on this kind of moderator.[9] However, the instrumental time-resolution for measuring the pulse shape was not sufficient at a shorter wavelength region (say, below 1.5Å) to judge the pulse width from such moderators. A new time-focusing crystal analyzer having a large solid angle is under preparation. Measurements of various moderators will be performed after the completing the new instrument.

References

[1] N.Watanabe and Y. Kiyanagi : Physica B 180 &181 (1992) 893.

[2] Y.Kiyanagi, N.Watanabe and H.Iwasa : Nucl. Inst. Methods A 312 (1992) 561.

[3] Y.Kiyanagi, N.Watanabe and H.Iwasa : Nucl. Inst. Methods A 343 (1994) 558.

[4] Y.Kiyanagi, S.Satoh, H.Iwasa, F.Hiraga and N.Watanabe : Physica B 213 & 214 (1995)857.

[5] Y.Kiyanagi, Y.Ogawa, N.Kosugi, H.Iwasa, M.Furusaka and N.Watanabe : Further optimization of coupled liquid hydrogen moderator for intense neutron sources, on this proc.

[6] Y.Kiyanagi, N.Watanabe and M.Nakajima : Nucl. Inst. Methods A 343 (1994) 550.

[7] Y.Kiyanagi, J.M.Carpenter, N.Kosugi, H.Iwasa, F.Hiraga and N.Watanabe : Physica B 213 & 214 (1995) 854.

[8] Y.Kiyanagi, N.Kosugi, Y.Ogawa, H.Iwasa, F.Hiraga, M.Furusaka and N.Watanabe : High-efficiency cryogenic moderator system for short pulse use, on this proc.

[9] Y.Kiyanagi, J.M.Carpenter, N.Watanabe, H.Iwasa and M.Nakajima : Proc. ICANS-XII (Abingdon, UK, 24-28 May , 1993) T206.

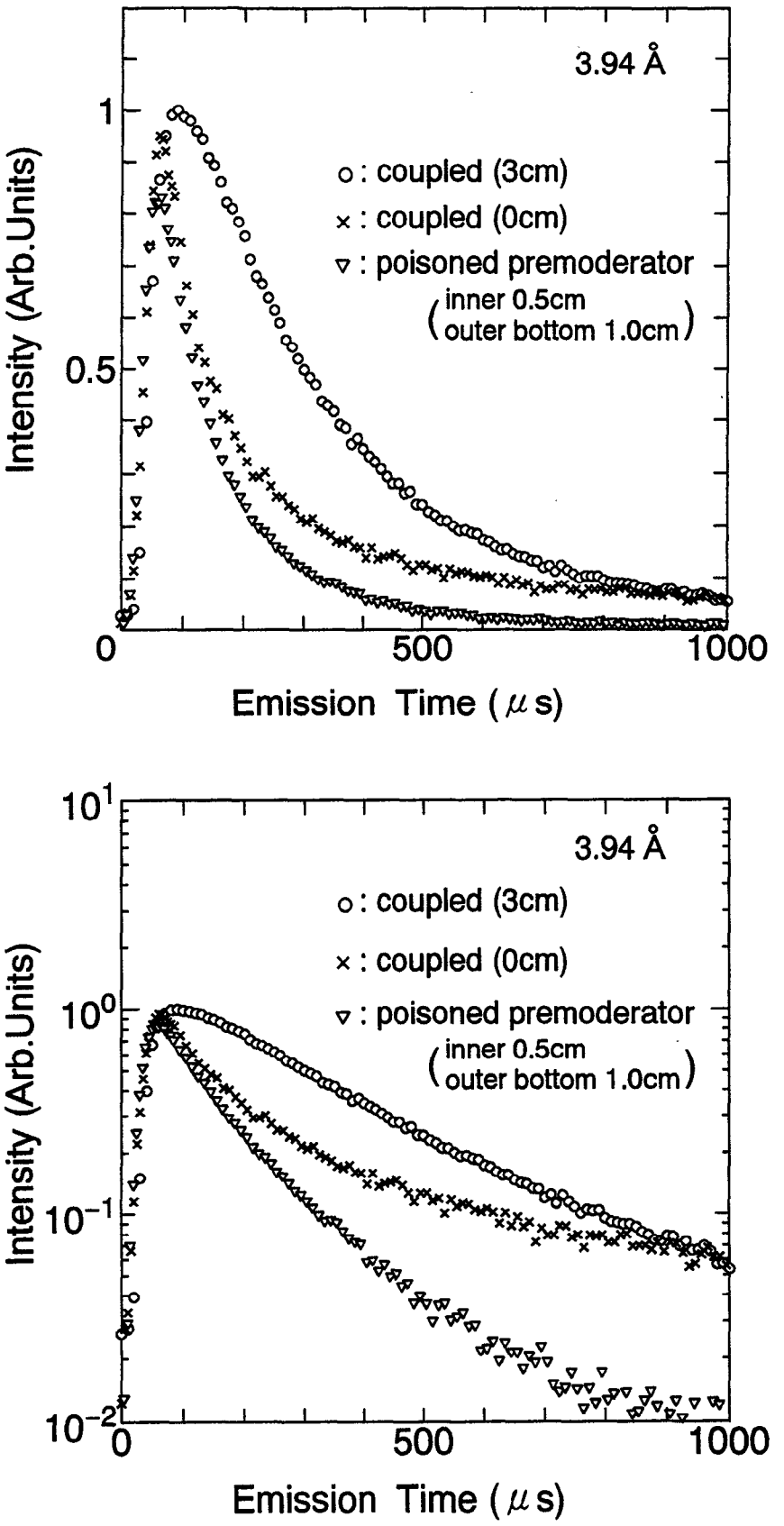

Fig.1 Comparison of cold-neutron pulse shapes (linear and semi log plots) from three moderator systems: a coupled 5 cm thick L-H_2 with 3 cm H_2O premoderator (coupled (3 cm)), the same L-H_2 without premoderator (coupled (0 cm)), and the same L-H_2 with a poisoned premoderator.

ICANS-XIII
13th Meeting of the International Collaboration on
Advanced Neutron Sources
October 11-14, 1995
Paul Scherrer Institute, 5232 Villigen PSI, Switzerland

HIGH-EFFICIENCY CRYOGENIC MODERATOR SYSTEM FOR SHORT PULSE COLD-NEUTRON USE

Y. Kiyanagi, N. Kosugi, Y. Ogawa, H. Iwasa, F. Hiraga, M. Furusaka* and N. Watanabe*

Faculty of Eng., Hokkaido University, Kita-13 Nishi-8 Kita-ku, Sapporo 060, Japan

*National Laboratory for High Energy Physics, Oho 1-1, Tsukuba-shi 305, Japan

ABSTRACT

Two kinds of methods were examined to improve pulse shapes of cold neutrons from a coupled liquid-hydrogen moderator with a premoderator. One is to decouple a premoderator from the reflector and the other is to use a poisoned premoderator. In the former case, the pulse shapes became narrower with a slight decrease of pulse peak height by reducing the premoderator thickness. The pulse shape was further improved by using a poisoned premoderator.

1. Introduction

Broader pulses from a coupled-liquid hydrogen moderator with a premoderator are quite acceptable for the majority of cold neutron experiments such as small angle scattering, reflectometry, etc., because the figure of merit (FOM) of source, in this case, is proportional to the time-integrated intensity of cold neutrons per pulse within a realistic range of repetition rate[1]. On the other hand for high-resolution spectroscopy using an inverted-geometry type spectrometer, the FOM of the source is proportional to the peak height, independent of pulse width and repetition rate, provided that a neutron guide of the required length is available between moderator and sample[1]. However, from a practical point of view, a long guide tube (say more than 200 m) may not be acceptable. A moderator which can provide a narrower pulse without sacrificing the peak height, then becomes preferable. From extensive measurements, we found that the pulse characteristics can be controlled to some extent by decoupling the composite moderator system (liq.H_2+premoderator) from the reflector[2].

We performed further optimization studies on a decoupled composite moderator system by changing premoderator thickness. A poisoned premoderator was also proposed and tested.

2. Experimental

The moderator systems used in the present measurements are shown in Fig. 1. Fig. 1(a) is a composite moderator with a decoupled premoderator and (b) a poisoned premoderator. The measuring system is essentially the same as that used in the previous measurements[3]. The moderator system consists of a liquid-hydrogen moderator (12x12x5 cm^3) surrounded by a light-water premoderator of various thicknesses at ambient temperature coupled or decoupled to a graphite reflector of about 1 m^3. A 0.5 mm thick Cd plate was used for both the decoupler and the interleave poisoning plate. As a pulsed neutron source, the electron linac at Hokkaido University was used with a lead target.

3. Experimental Results

Keywords: Pulsed neutrons, Cold neutrons, Liquid hydrogen, Short pulses

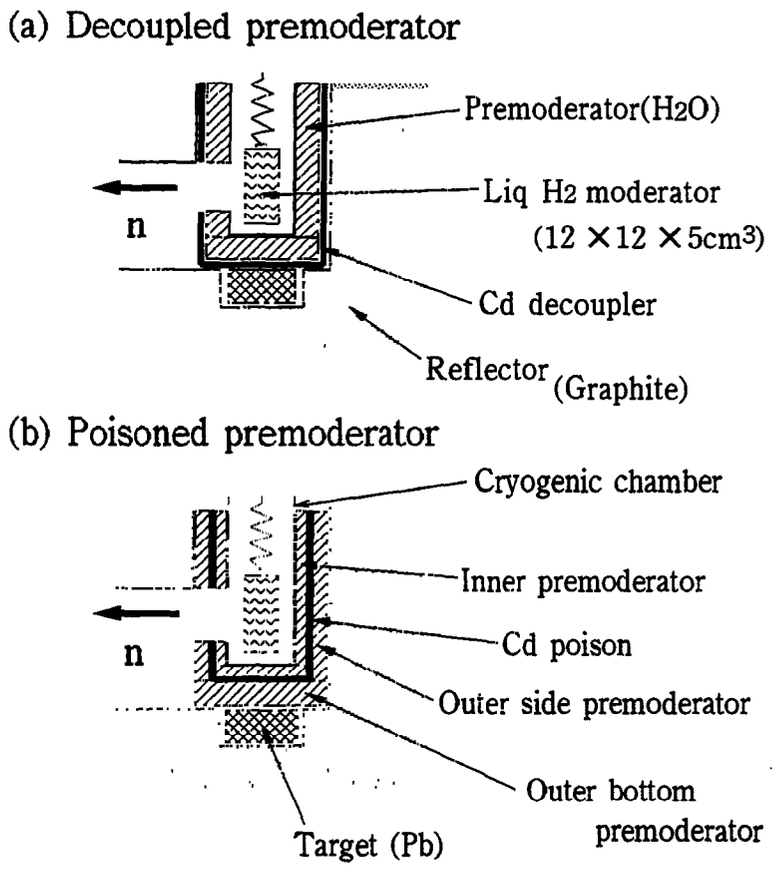

Fig. 1 Composite moderator with a decoupled premoderator (a), and with a poisoned premoderator (b).

Figure 2 compares the pulse shapes of cold neutrons at 3.94 Å and 6.57 Å from the moderator with three premoderator thickness, 1, 2 and 3 cm. The pulse shapes from the eference coupled composite moderator (5 cm thick Liq-H_2 + 3 cm thick H_2O premoderator) are also plotted for comparison. The pulse width in full width at half maximum, FWHM, from the decoupled one is considerably improved with a small sacrifice of the peak intensity. The long time tails are also improved to some extent.

Next, we studied some moderator system with poisoned premoderators (see Fig. 1 (b)). In these measurements, we studied two inner premoderator thicknesses of 0.5 and 1.0 cm, by changing the outer premoderator thickness. By removing the outer side premoderator but leaving the outer bottom premoderator, the intensity was increased by about 5%. This is due to the fact that since the neutrons entering liquid hydrogen from the sides are well moderated, outer side premoderator simply acts as an attenuater, while the outer bottom premoderator is still effective for providing low energy neutrons to liquid hydrogen.

Therefore, we removed the side premoderator and changed the thickness of the outer bottom premoderator. Figure 3 shows integrated intensity of cold neutrons in the range of 4.3-5.7 Å as a function of outer bottom premoderator thickness for two different inside premoderator thicknesses. The intensities increase slightly with increasing outer premoderator thickness (almost unchanged). As a reference the intensity from the moderator with 1 cm inner and 1 cm outer premoderator (namely 1 cm outer side premoderator was attached) is also depicted in the figure as a dot.

We performed pulse shape measurements on the moderator with a 0.5 cm thick inner and 1.0 cm thick outer bottom premoderator. We chose 0.5 cm thick inner premoderator since this will give narrower pulse width than the 1.0 cm one and we placed only the 1.0 cm thick outer

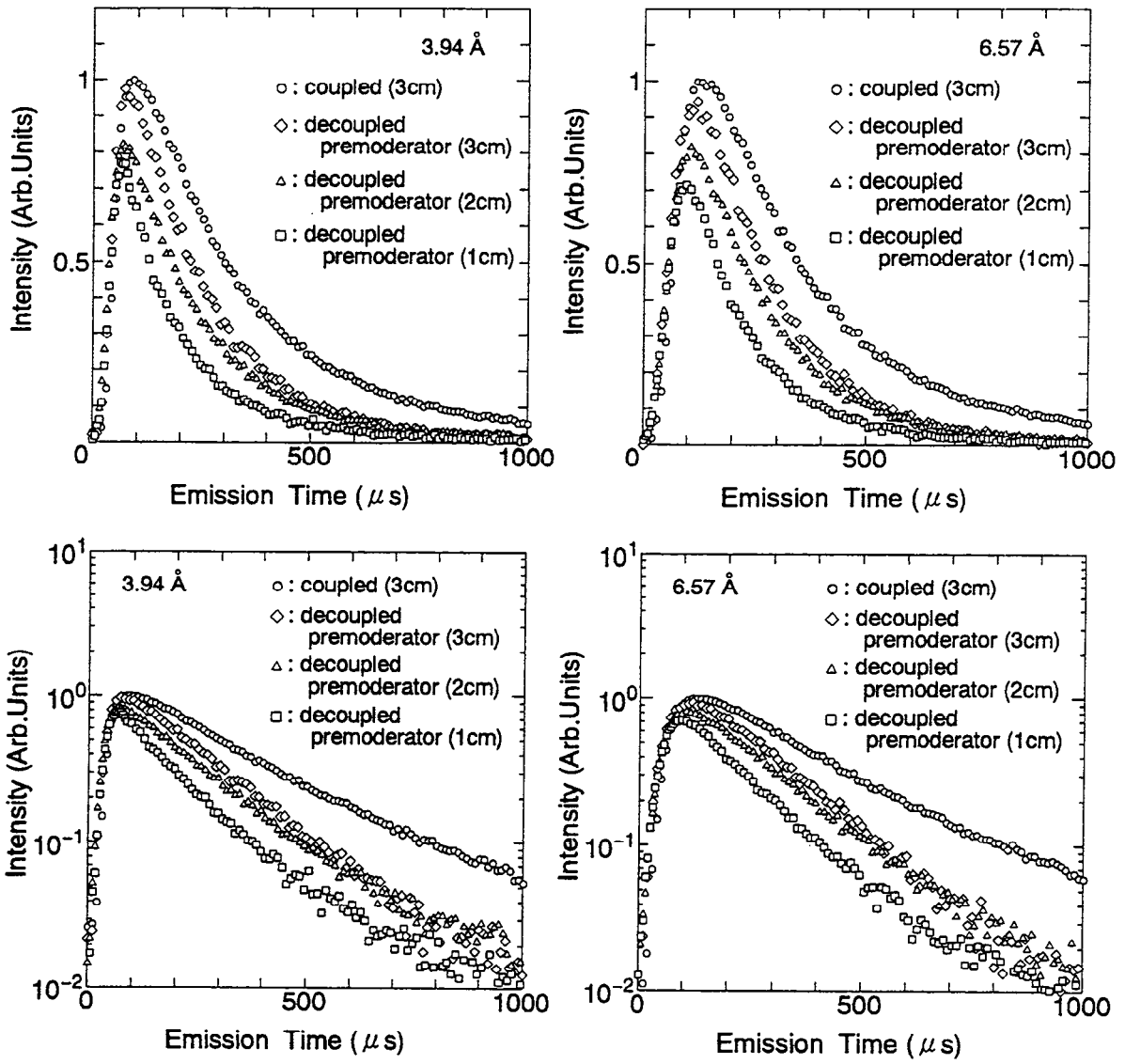

Fig. 2 Comparison of pulse shapes (linear and semi log) from the moderators with different thicknesses of the decoupled premoderator.

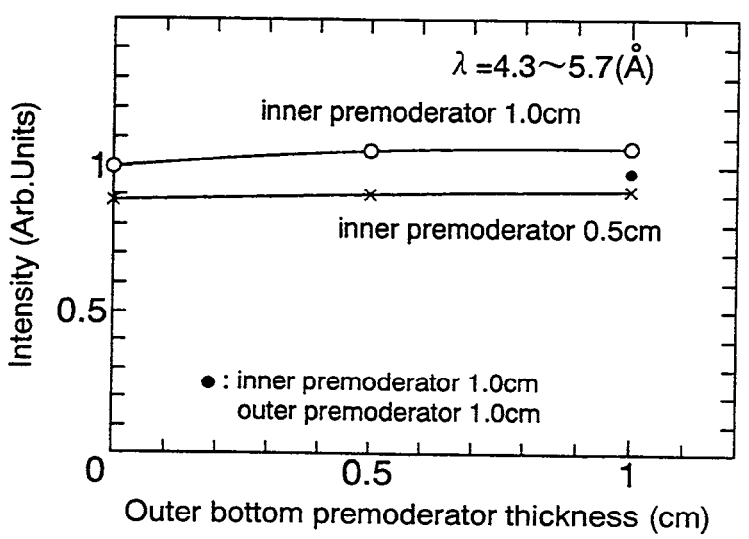

Fig. 3 Effect of thickness of the outer bottom premoderator on the cold neutron intensity.

premoderator at the bottom. This premoderator was confirmed to enhance the intensity to some extent.

Figure 4 shows pulse shapes of cold neutrons from this moderator at two wavelengths 3.94 Å and 6.57 Å compared with the decoupled composite moderator of 1 cm thick premoderator (that is 1 cm inner and 0 cm outer). The pulse width was improved somehow keeping the peak intensity. Long-time tail also improved to some extent compared to the premoderator (1 cm thick) decoupled system.

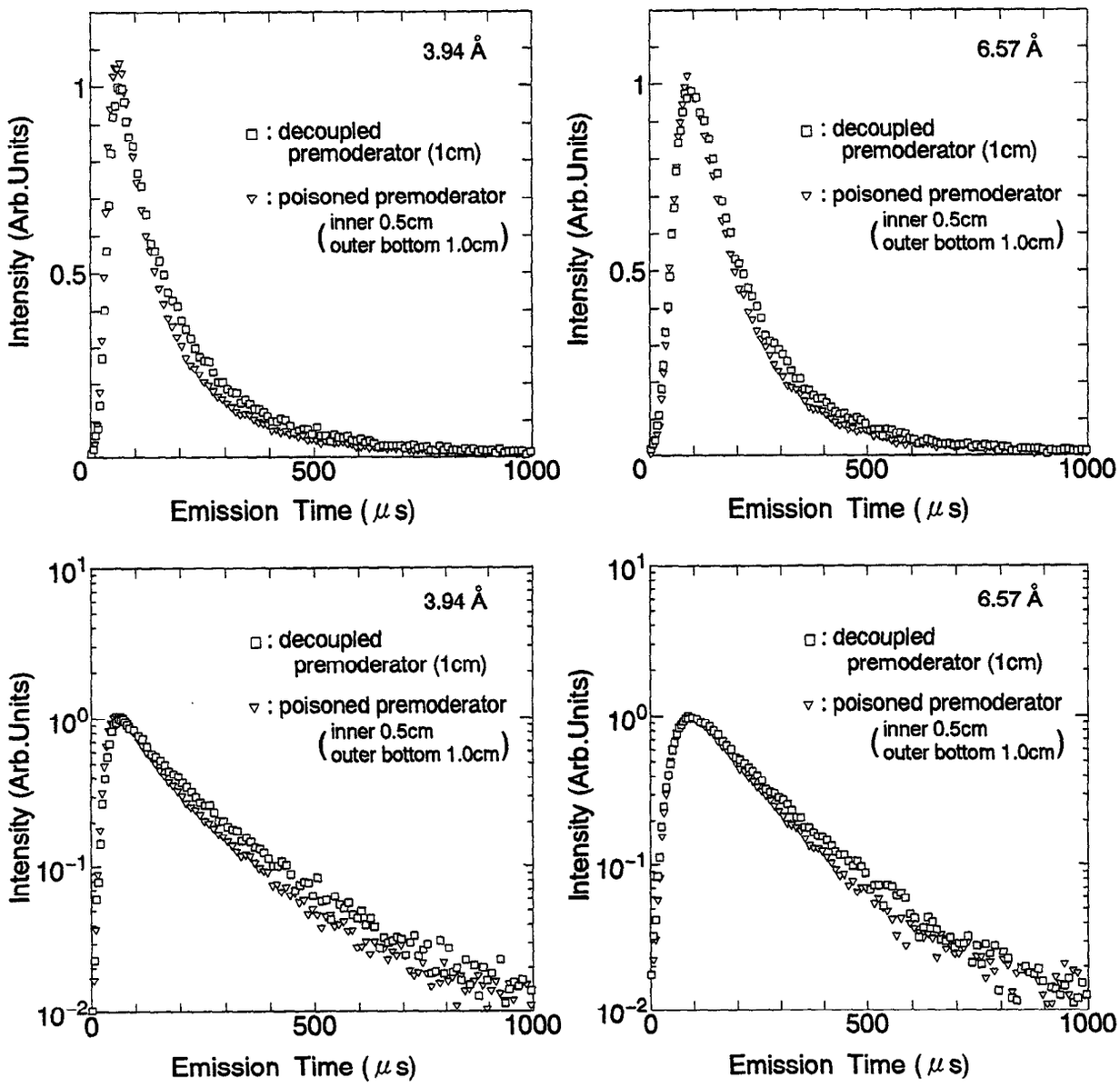

Fig. 4 Comparison of pulse shapes (linear and sem log) from moderators with decoupled premoderator and poisoned premoderators.

Figure 5 compares the pulse shapes from various composite moderators with the 5 cm thick decoupled solid methane (20 K). Pulse shapes from a decoupled liquid hydrogen are also indicated as a reference. At about 4 Å superiority of solid methane moderator is apparent while at the longer wavelength region the composite moderator with a poisoned premoderator gives closer pulse characteristics to the decoupled solid methane moderator.

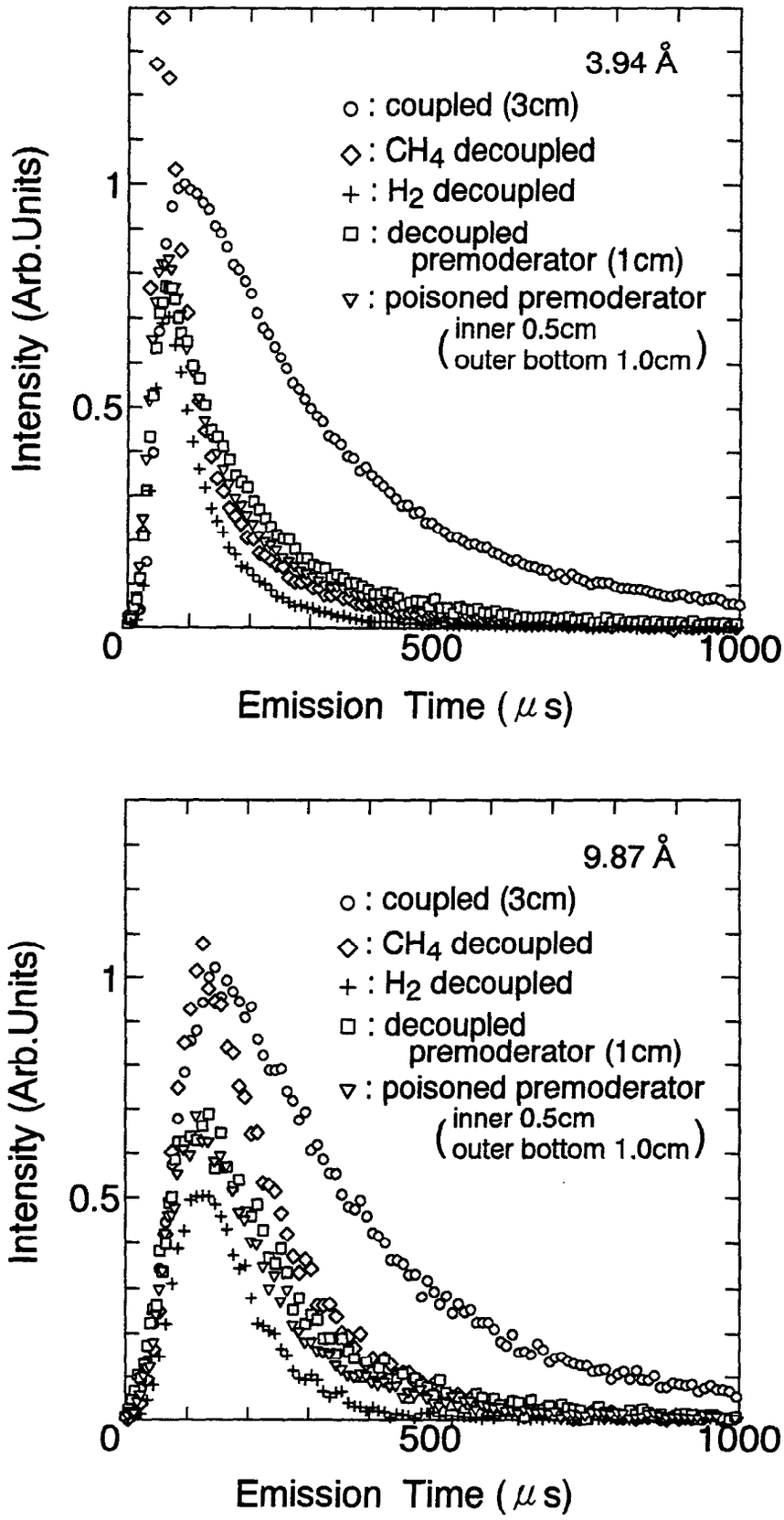

Fig. 5 Comparison of pulse shapes from various types of moderator system.

4. Conclusion

The pulse shapes of cold neutrons were considerably improved by using a poisoned premoderator in comparison with those from a coupled liquid-hydrogen moderator with a premoderator. The pulse characteristics from a liquid-hydrogen moderator with a poisoned premoderator were close to those from a decoupled solid methane moderator at a long wavelength region.

5. References

[1] N. Watanabe and Y. Kiyanagi, Physica B 180&181(1992)893.
[2] Y. Kiyanagi, J. M. Carpenter, N. Kosugi, H. Iwasa, F. Hiraga and N. Watanabe, Physica B 213&214(1995)854.
[3] Y. kiyanagi, H. Iwasa and N. Watnabe, Nucl. Instr. Methods A312(1992)561.

ICANS-XIII
13th Meeting of the International Collaboration on
Advanced Neutron Sources
October 11-14, 1995
Poul Scherrer Institut, 5232 Villigen PSI, Schwitzerland.

Supply System for Cold Neutron Sources for the ESS-Project.

Karsten Stendal.
Risø National Laboratories, Box 49, 4000 Roskilde, Denmark.

ABSTRACT.
This paper describes the cooling plant behind the hydrogen moderators in the ESS-project.

1. Introduction.

Background

In the plans for the European Spallation Source, Cold Neutron Sources are a major part of the project.

This part of the study has its background in three existing cold neutron sources placed at RISØ (DEN), HMI and GKSS (GER). The Risø source, which has been in service since 1975, was designed and manufactured by RISØ staff alone, and the two others were produced by a consortium of Interatom (GER) and RISØ (DEN), and started operating in 1989. The experiences with these three sources are the basis for this study, which later will result in a price estimation for the ESS project and a preliminary design.

2. Safety Philosophy.

Hazard with hydrogen only exist, when oxygen is present too, and it may occur in two ways. Firstly, if some source of ignition is present, the elements combine exothermically to form water. Secondly, if atmospheric air is irradiated at cryogenic temperatures, ozone is formed from oxygen, and nitrogen may form oxides and ozonides which decompose explosively and initiate a hydrogen/oxygen reaction.

The basic principle for safety of a cold neutron source is to preclude any possibility, that air may enter either the hydrogen system or regions of the equipment containing hydrogen, especially at cryogenic temperatures and in fields of high radiation.

By adopting the triple containment philosophy ,se fig.1, the above mentioned basic principles for safety are fulfilled. For the cold neutron source the triple containment philosophy is used for all hydrogen equipment inside the target hall i.e. all hydrogen equipment is contained

---

Keywords:Supply system for Cold Neutron Sources.

within a high-vacuum system, which again is surrounded by a third containment filled with helium. The helium in the "blanket" is always at a small positive pressure, so that a leak in the system can be detected, and no atmospheric air can penetrate. In that way it is ensured, that even in the event of a leak developing in the vacuum casing, no hazard will arise, as air is precluded, and helium will enter into the vacuum system and give a pressure increase indicating the leak.

3. Basis for the study.

In the ESS study there are foreseen two target stations, one at 1 MW and one at 5 MW. The two targets are foreseen equipped with moderators cooled in two different ways: With water at room temperature, or with hydrogen at 25 K. This paper only describes the supply systems for the hydrogen cooled moderators

Specifications:

1MW target: Two moderator chambers cooled with supercritical hydrogen at 25K. Nescessary cooling capacity is 15kw for both chambers.
5MW target: Up to six moderator chambers cooled with supercritical hydrogen at 25K. Nescessary cooling capacity is 15kw for all six chambers.

It is foreseen, that the two targets are equipped with systems independent of each other, but identical as far as possible, giving the best possibilities for sharing spare parts, repairing staff, workshops, subsuppliers etc.

As the layout has been taken from existing reactor installations, also the emergency and safety precautions are as demanded for at reactors. There will be other conditions and wishes, when the neutron sources are coupled to spallation targets, but untill these are described and discussed with relevant authorities, the "reactor conditions" will serve as reference.

4. The supercritical system. (Fig.1)

General description:

In principle the cold neutron source consist of hydrogen filled moderator chambers placed close to the spallation target. The moderator chamber and the hydrogen pipes are surrounded by a vacuum containment. This vacuum is used to insulate the cold parts and act as the second safety barrier for the hydrogen. The vacuum system is surrounded by a helium containment, to form the
third safety barrier for the hydrogen, in the triple containment system.

Hydrogen is used as moderating material and as moderator chamber coolant at a pressure of 15 bar, which is above the critical pressure (se later). The hydrogen is circulated between the moderator chamber and the heat exchanger by means af fans. The minimum moderator temperature is 25K.

As mentioned the system is supercritical, i.e. the hydrogen pressure - 15 bar abs. - is above the critical pressure, which is 13 bar abs. Above this critical pressure hydrogen will always remain in a single phase. As the temperature during operation is expected to be ajustable between 25 and 35K, it may be seen from T-S charts, that the density will vary from 68- to 23 g/l.

The supercritical system offers some advantages over other systems, as no phase change takes place, and as the density of the hydrogen changes with the temperature. The absence of phase change also admits standby cooling of the moderators just by circulating the hydrogen. Furthermore it may be possible to optimize the neutron gain by adjusting the temperature.

5. Cooling plant. (Fig.2)

The cold hydrogen circuit is heated by radiation and by different other kind of heat input. This heat is removed from the hydrogen in a heat exhanger, where the necessary cooling is provided by a flow of cold helium gas from a cryogenic cooling plant.

The heat exhanger is of the counterflow plate and fin type. It is not yet decided whether there will be one common heat exhanger for each target station, or the system will be split up in f.ex. one heat exhanger for each moderator chamber. This is dependant on the accessibility of the system, and the lenght of the various liners, because it is important to keep the liners between heat exhanger and moderators as short as possible,(the triple containment liners) while the helium liners between expansion turbines and the heat exchangers are less critical.(Only vacuum isolated liners), and the liners between compressor and expansion turbines are almost uncritical. The approximate temperatures and pressures in the systems can be seen at figure 2.

The amount of hydrogen passing the heat exhangers will be approx. 700 ccm/sec/kw when cooled from 26 K to 24 K.

The cryogenic cooling plant (the expansion turbine) is connected to the helium compressor (screw compressor) by a doubble helium liner at room temperature. This compressor can be placed in some distance from the target hall. Furthermore there is a buffer in the helium system, and the position of this is also relative free, as it can be placed in open air and the lenght of the connecting pipe is of less importance.

The principle function of the helium cooling plant can be explained from figure 2. He-gas is compressed to maximum 16 bar in the screw compressor, after which it passes a series of oil separators and filters, of which the last one is a charcoal filter. This system is very effective, so effective that the amount of oil in helium after the separators is messured not in parts pr million PPM, but in parts pr billion PPB.

After having passed a series of heat exchangers the gas is expanded in the expansion turbine unit. This unit can be constructed in various ways, dependent on the supplier. It can be with a two step expansion with two turbines in serie, with heat exhangers after each step, or with a one step expansion after a pre-cooler, cooled with liquid nitrogen.

After the expansion unit the helium will be at 2 bar at minimum 18 K and ready to pass the heat exchanger where the hydrogen is cooled. After this the returning helium will act as coolant in the heat exchanger at the inlet to the expansion turbine, and it will be back at the entrance of the compressor at approximately room temperature and 1,8 bar.

The heat exchanger B and the expansion turbine unit are contained in a "cold box", with continiously pumped vacuum and highly thermal insulation. (Se fig.3). The "cold box" is a unit assembled on a skid, which also contains some auxillary systems and instrumentation and control for the cooling plant. Also the pipes to and from the helium/hydrogen heat exhanger are insulated by this vacuum system.

An examble of a expansion turbine with gas bearings is shown in fig.4. This turbine is a small single-stage centripetal turbine, that drives a directly coupled single-stage centrifugal brake compressor. The turbine is equipped with selfacting gas bearings, supplemented by auxillary magnetic bearings for start up. The work (energy), which the turbine extracts from the helium, is transferred into the brake compressor circuit and from here transferred as heat to the cooling water in a helium gas/water heat exchanger. The turbine rotates with approximately 200.000 rpm. The turbine does not require maintenance, and is in many ways comparable to turbochargers, which has become almost standard equipment in many automobiles.

6. Hydrogen circuit. (Fig.5)

Hydrogen at 15 bar is circulated in moderator chambers and heat exchanger by one of the two fans in the circuit. Under normal conditions only one of the two fans is in operation. The other fan is standby and start is initiated by a rise in temperature of the moderator chamber. The hydrogen temperature is measured both at inlet and outlet of heat exhanger and at the moderator chamber.

Hydrogen buffer system.

The purpose of this system is to keep the hydrogen pressure within the operational range during the temperature changes and to provide the system with clean hydrogen.

This system is placed outside the target building. The size of the buffer tank depends upon the total volume of the complete hydrogen system, as the volume should be big enough to avoid formation of liquid hydrogen in the system, which is formed, if the pressure falls below the critical pressure, 12.8 bar, by decreasing temperatures. Furthermore, pressures above 18 bar are avoided, when the system is heated up. The pressure changes during cooling down and operation. The buffer vessel is isolated from the system, by closing two remote operated valves near the vessel, if the pressure falls below 14 bar.

The supply system is based upon the use of high purity hydrogen, i.e. hydrogen with a purity better than 99.99%. Even though there is used high purity hydrogen, it is passed through a cleaning device, before it is fed into the system.

If the system pressure is higher than 18.6 bar, the pressure control system opens a blow of valve, and if that fails, a relief valve opens at a pressure of 19 bar, and the system is vented

to open air through the relief box, outside the target hall.

7. Hydrogen standby cooling circuit. (Fig.5)

This cooling circuit is started by the control system whenever temperature in the system exceeds a certain level, f.ex. when heated by target radiation without the cryo cooling system operating. The signal to start the standby circuit is taken from thermocouples on the moderator chambers, and the circuit is circulated by separate and more powerfull fans placed in the outdoor part of the circuit. These fans will operate in series with the allready operating fan.

8. Vacuum systems. (Fig.5)

All hydrogen containing equipment in the target building will be contained within high vacuum systems. For the cold hydrogen equipment the vacuum is further acting as thermal insulation.
This vacuum containments will be split up in sections as there are different demands upon the various parts. The sections which covers the parts beeing radiated must fulfil the triple containment philosophy, and here it is necessary, that the pumps also are contained in the helium containments. Therefore these section are sealed of after beeing pumped down, and further pumping is performed by iongetter pumps, inside the helium containment. The other vacuum containments are pumped down in usual way with turbomolecular pump sets.

The various vacuum systems are protected against over pressure by exhaust to open air via systems of relief valves and bursting discs.

9. Helium blanket system. (Fig.5)

Where the triple containment principles must be established, the
vacuum containments must be surrounded by a helium blanket. This blanket is also divided in sections following the vacuum systems. The helium is always at a small positive pressure, say 1.3 bar abs., so the helium pressure will decrease if there is a leak in the containment. This decrease gives a warning in a 1-out-of-3 connection at 1.2 bar, and shuts down the cooling plant in a 2-out-of-3 connection at 1.2 bar. The helium containment systems are connected to a common helium supply system.

10. Cooling of vacuum and helium containment casings. (Fig.5)

Heat absorbed in radiated parts of vacuum and helium containments is removed by arrangements of water cooling, with water circulated in closed systems. The water can be pressurerized with helium, if there is need for leak indication, when the water circuit passes vacuum pumped vessels f.ex. the volume around the target.

11. Syphon type moderators. (Fig.6)

In this arrangement, the liquid moderating media is contained in a vessel placed at the lower end of a vertical supply liner. The pressure and temperature in cryo conditions are 3 bar and 25 K.

The supply liner is composed of two concentric pipes, one for the upstreaming gas phase and one for the downfloating liquid phase of the moderator media. The media is evaporated in the moderator chamber and condenced in the heat exhanger at the top of the liner. The circulation goes on without fans or other mechanical equipment but by natural circulation. Therefore the heat exhanger (condensor) must be placed in a position above the moderator chamber, and the supply liner must be arranged in vertical or slanting position without obstacles of any kind.
If the cryo cooling fails, there is no way of establishing an alternative cooling, and therefore the spallation source must shut down if there is any trouble with the moderator.

When not operating at cryo temperature the moderating media will be kept in a metal hydrid store. This store consist of one or more vessels filled with a hydrid transforming alloy. This vessel is cooled (by water) when producing hydrid and heated (by electricity) when the moderating media is released. The hydrid vessels must be carefully constructed in a way giving no possibilities for overheating or water leaks into the metal hydrid.
The chemical binding in the hydrid is perfect in an order bringing the remaining pressure in the system down to 10 Pa.

To prevent pressure over a certain level, it is necessary to incorporate a buffer tank, and a complicated system of remote controlled valves and bursting discs in the system to satisfy the safety precautions, just as is the case with the supercritical neutron source. Buffer tank and hydrid vessels must be covered by protection gasses also for safety reasons.

Arguments for the two types. (Fig.7)

Thermo Syphon.
- Simple circulation with no fans or pumps.
- Low pressure in the moderator system.

Supercritical system:
- No boiling in media
- Forced circulation giving no restrictions for liner geometry.
- Standby cooling.
- Large components can be placed outside the target hall.
- No hydrid store tanks.
- Relative small heat exchangers.

12. Triple containment liners. (Fig.8 and 9)

There are two design arrangements of the triple containment liners which can be compared. One with parallel running forward and return pipes for the hydrogen, and one with concentric

running hydrogen pipes. (see fig.8). Both concepts can be used, but the one with parallel pipes seems to have some advantages, (especial in this project, which will have substantial lenght of this liner systems.)
- Easier and cheaper to fabricate.
- Coupling arrangements between sections are more simple.

In both concepts the hydrogen pipes must be polished on the outside, and the vacuum pipes on the inside - if possible - to minimize heat radiation. The hydrogen pipes can be wrapped in super insulating material in pipe sections not passing highly radiated volumens.

The heat loss is aproximately (for both concepts):
- 7 W/m pipe, and
- 4 W/m with super insulating material on hydrogen pipes.

No organic material can be used in regions with high radiation, and metal seals must be used in all couplings (Aluminium or Indium).

These liners are expensive and complicated to build (see fig.9) and operate, so the total layout must favour as short liners as possible, i.e. joint boxes placed close to the targets.

13. Moderator chambers. (Fig.10 and 11)

The design is determined partly by geometrical considerations and partly by the nuclear heat and the neutron absorption.

The closer the chamber is to a ball-shape, the less material is necessary to contain a certain volumen of hydrogen in the vessel. Also geometrical considerations in relation to the cross section of the beam liners have to be examined. At the moment there are two different suggestions for these chambers.

- A square shaped chamber designed at KFA. (fig.10)
- A super eliptical shaped chamber designed at RISØ. (fig.11)

A third parameter can also be determining these designs, and that is the lifetime of the material in the chambers. The shorter the life, the simpler the design and the easier production and replacement procedures of inpile parts are necessary. A suggestion for a simple in-pile part design is shown at fig.12.

For the 1 MW target there are only foreseen two moderator chambers. This could give the possibility for using the Syphon type hydrogen circuit, as there might be more room on top of the target shielding. This decision has to wait till more specific target designs are available .

14. Power consumption for system.

The power consumption for the complete system at maximum load (25K and 15 kw pr. target) will approximately be:

- Compressor unit	900-1000 kw
- Cryocooling unit(s)	40 kw
- Joint box(es)	5 kw
- Water cooling of in-pile parts	40 kw
- Instrumentation, pumps, etc.	40 kw

All together about 1,1 MW pr target.

Nescessary sypply systems for the operation of the cold neutron sources are:

- Electricity
- Water
- Compressed air
- Nitrogen (option for precooling of expansion turbines)

15. Maintenance.

With reference to existing cold neutron sources, there should be no problems with the ratio between maintenance time and operation time of less than 10%, which is the goal for the project, but during the detail design phase great attention must be paid to the question of accessibility and handling time when repairing or shifting components. Especially at the 5MW target with the 6 moderators it is important, that the chambers can be shifted fast and easy, and that the supply system is split up in sections, able to operate independently of each other, as suggested in fig.13. Thereby it will not be necessary to shut down the complete spallation source plant, just because of problems with one moderator chamber.

16. Final arrangement. (Fig. 13, 14, 15 and 16)

The exact arrangement of the moderators, the supply liners and the cooling systems must wait, till the first drawings of the targets are ready, but a suggestion for placing of the main components is shown at fig.14 and 15. A diagram for a complete cold neutron source is shown at fig.16, including most of the valves and measuring points in the system.

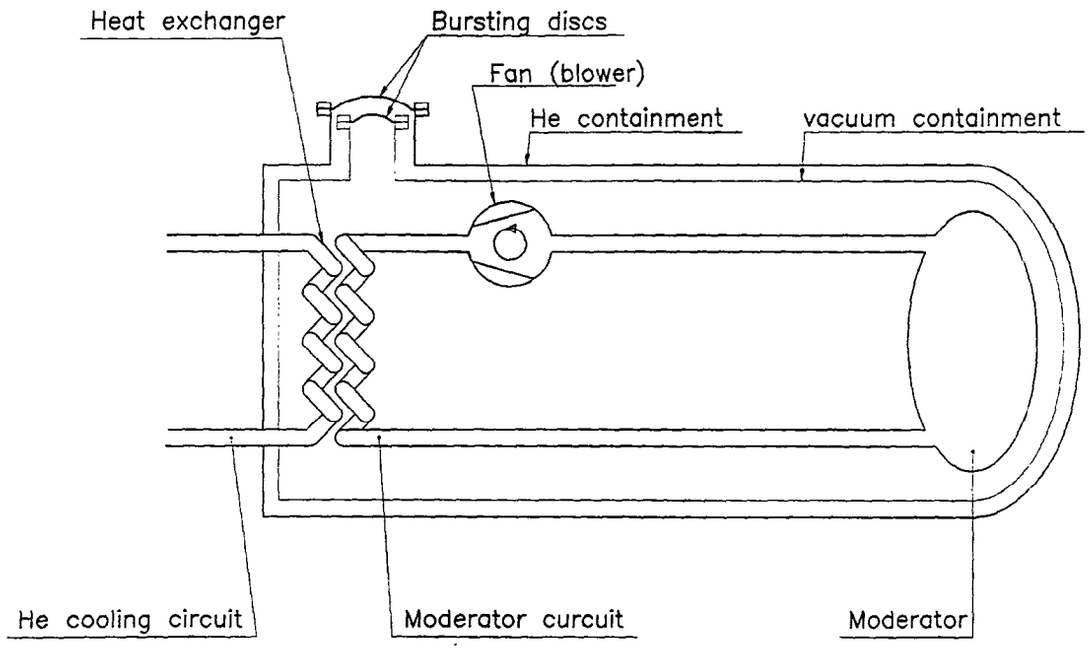

FIG.1

(Kilde1)

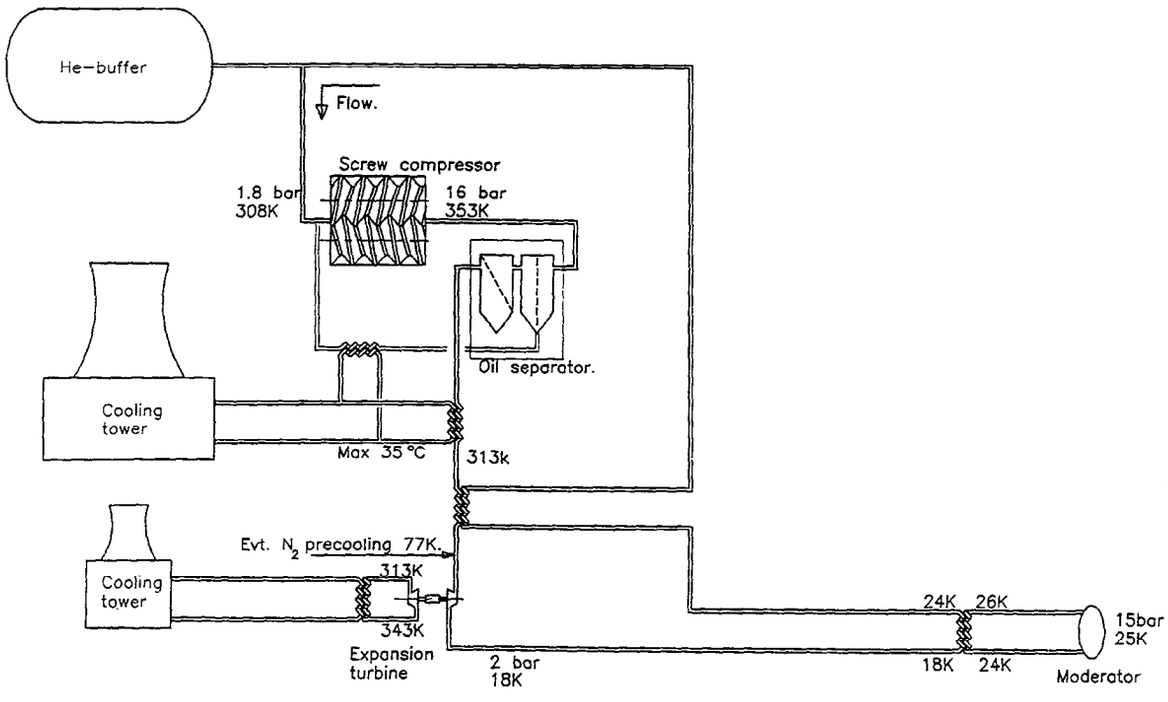

He-circuit

FIG.2

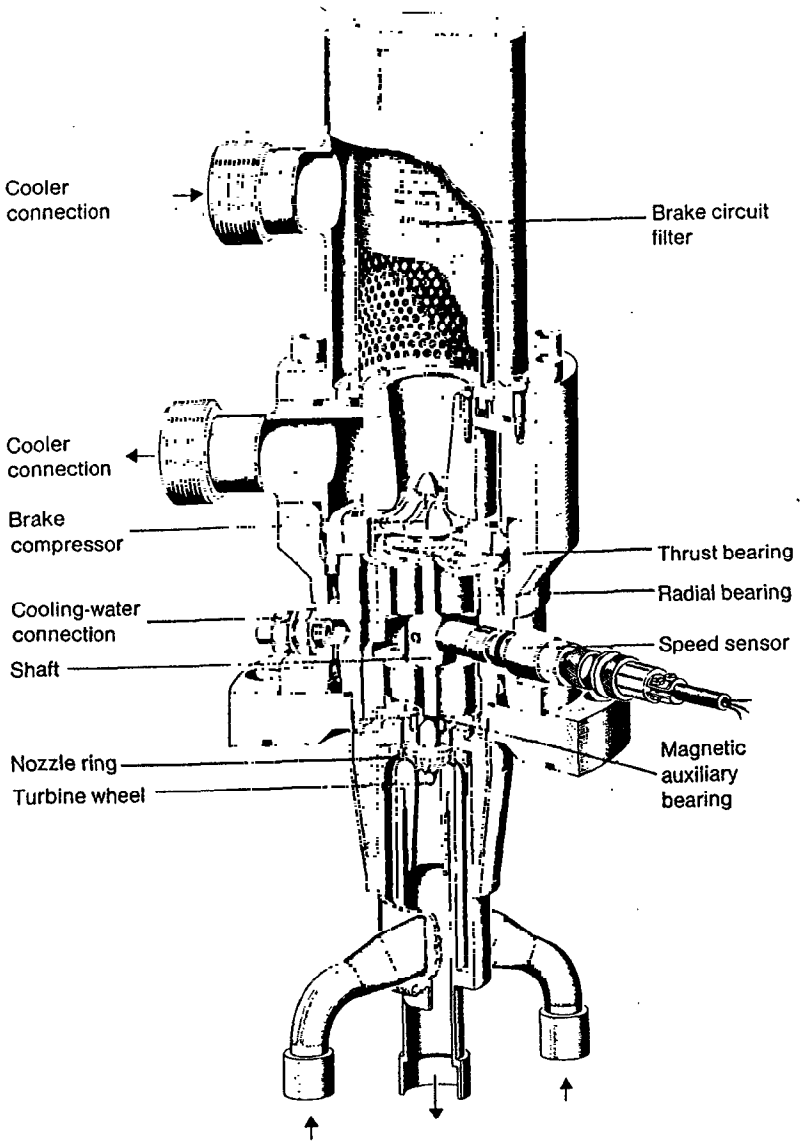

Expansion turbine.
FIG.4

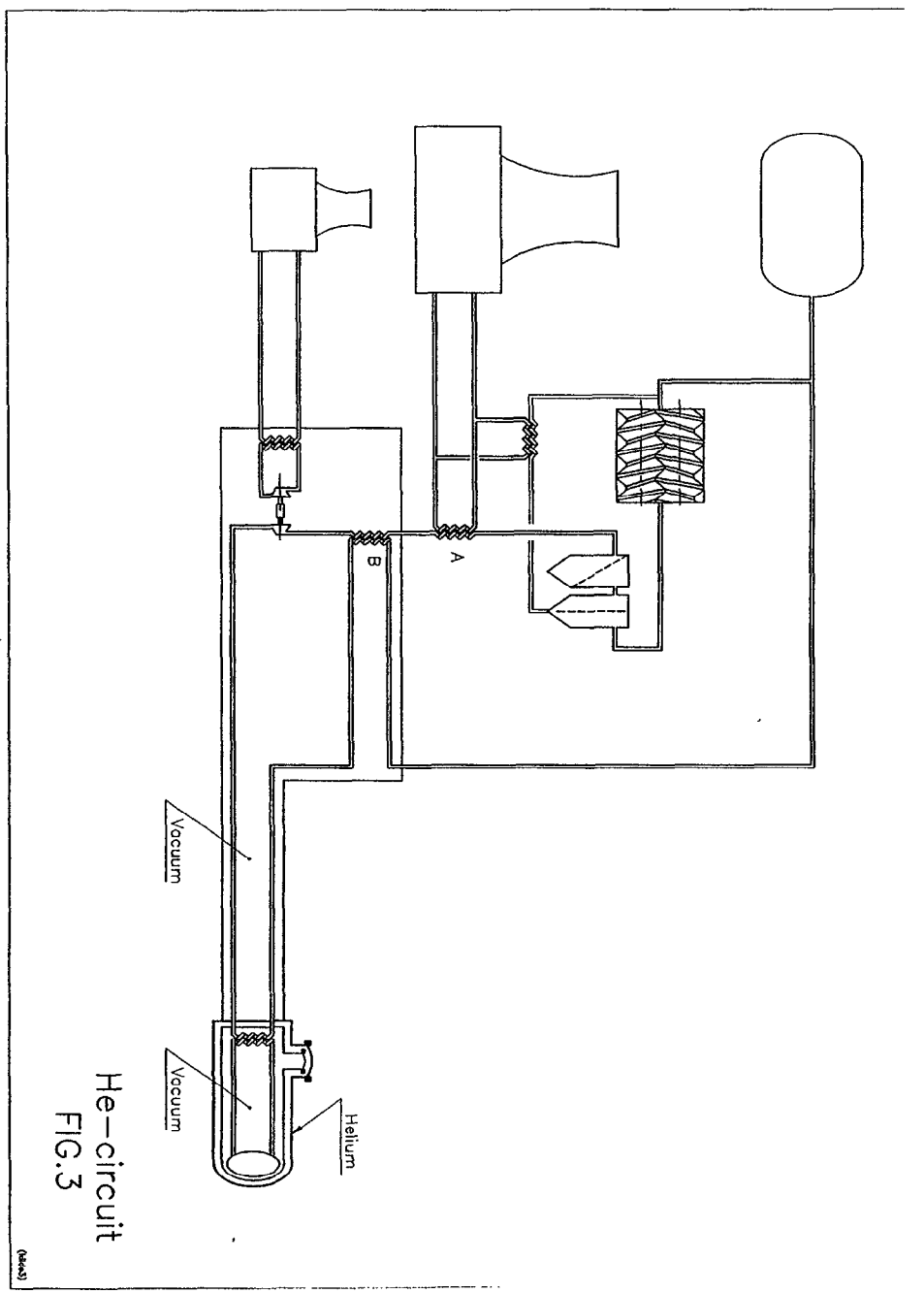

He-circuit
FIG.3

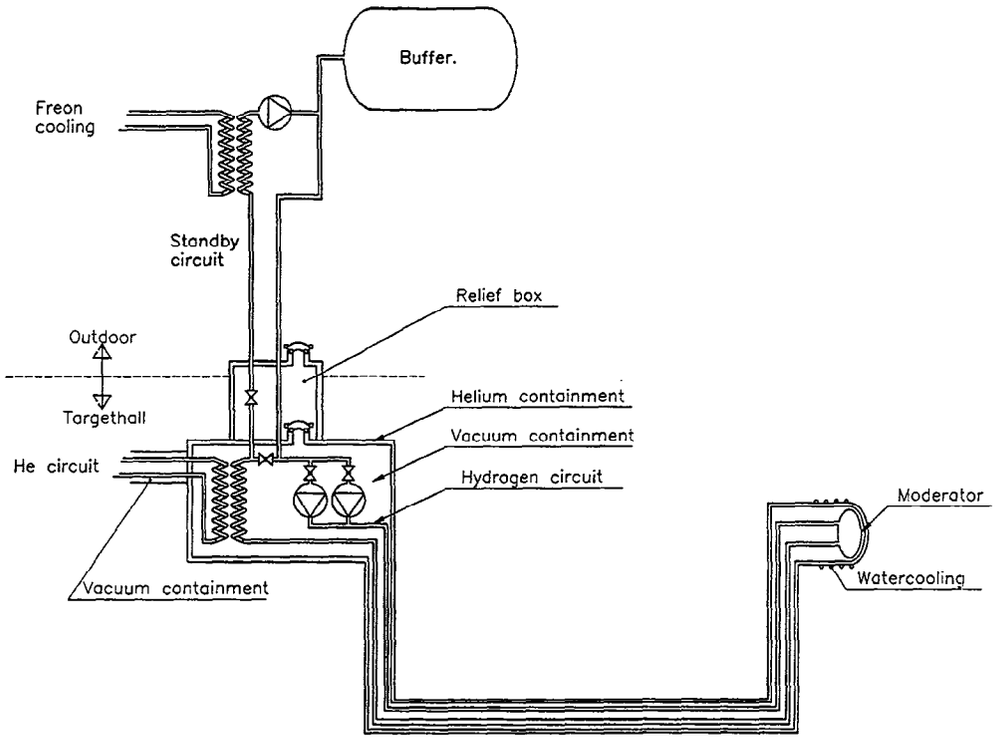

Supercritical source
FIG.5

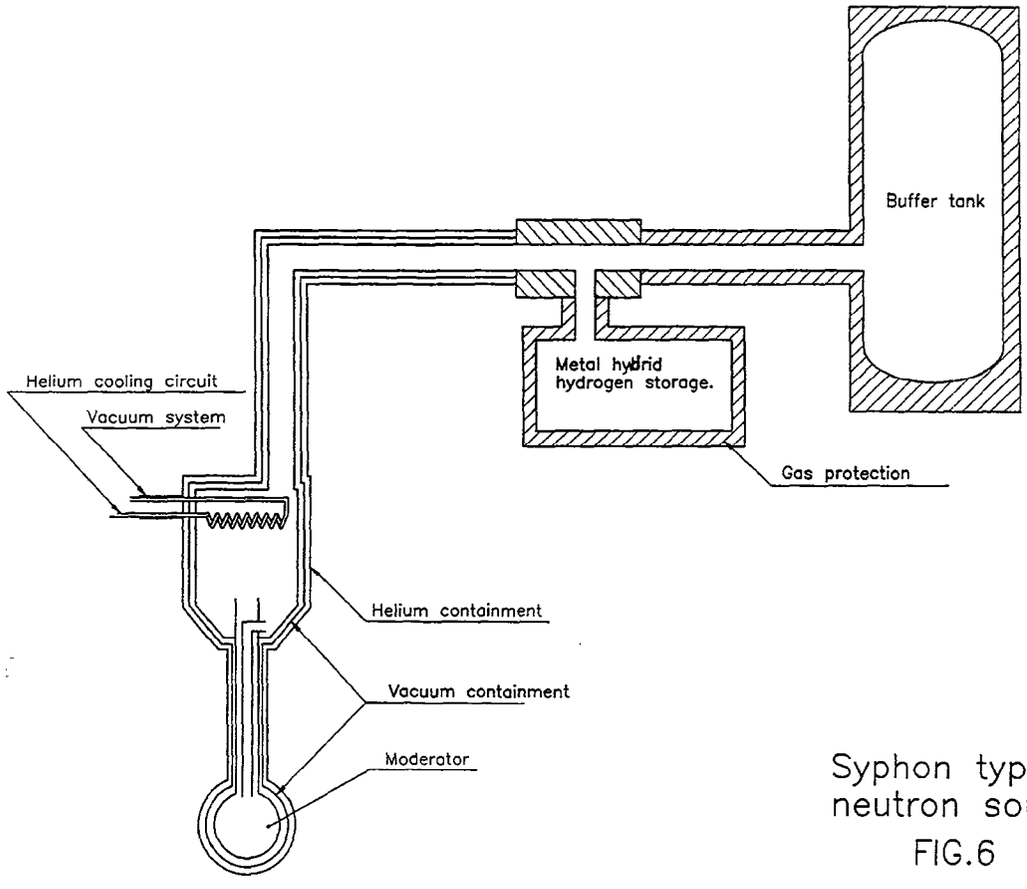

Syphon type neutron source
FIG.6

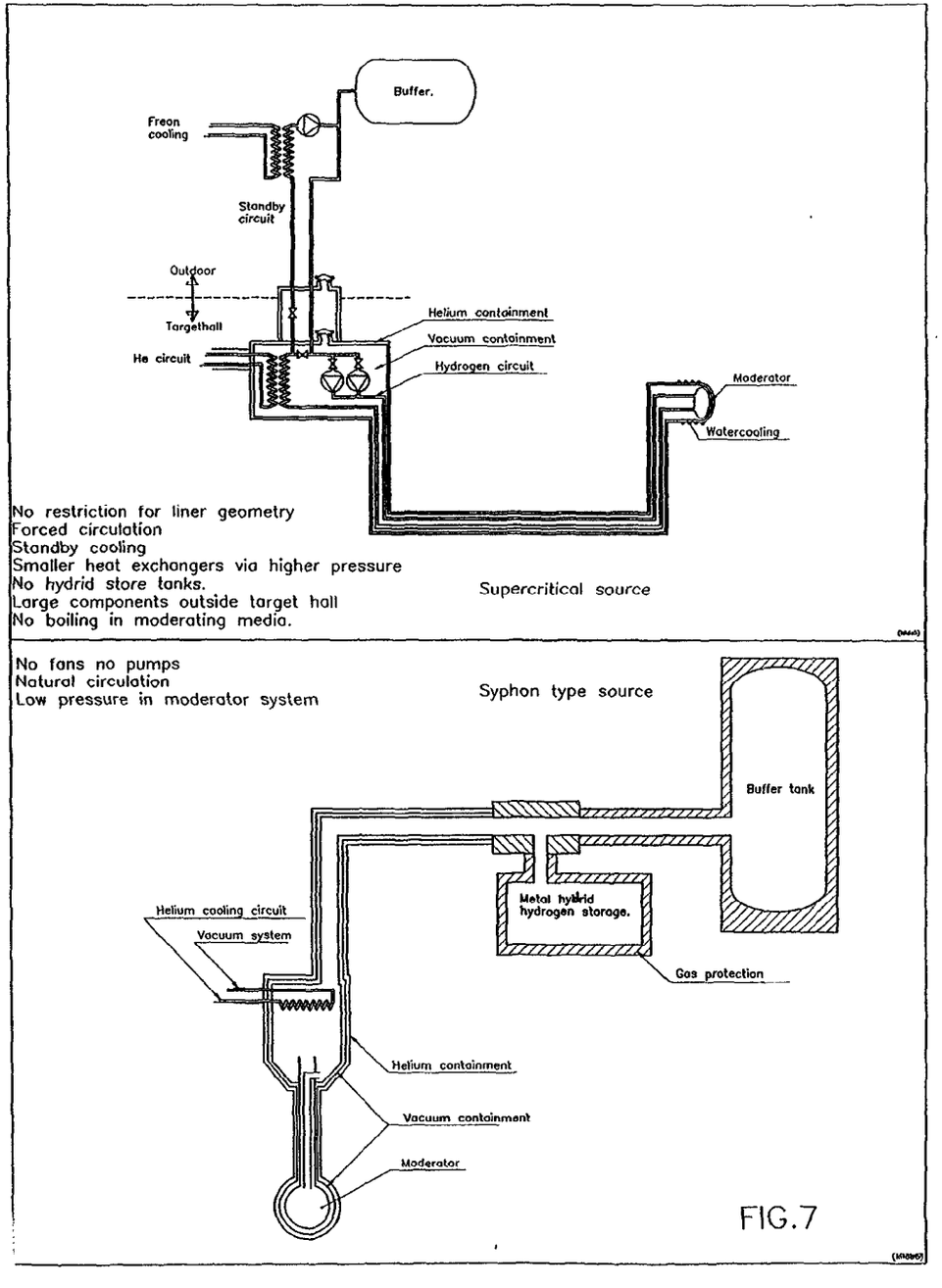

FIG.7

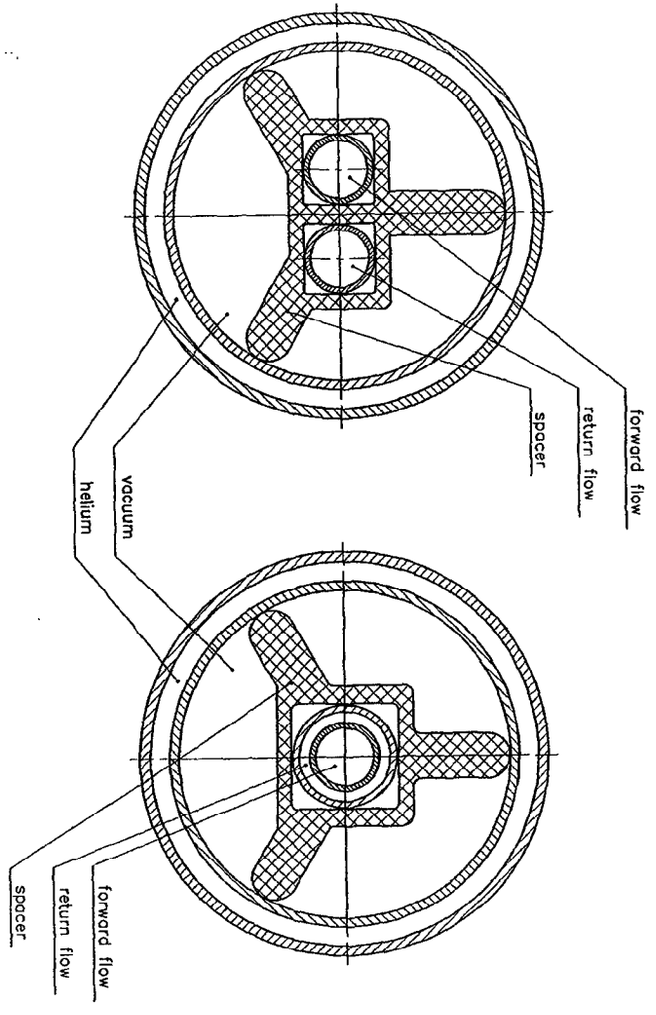

Triple containment liners.

FIG.8

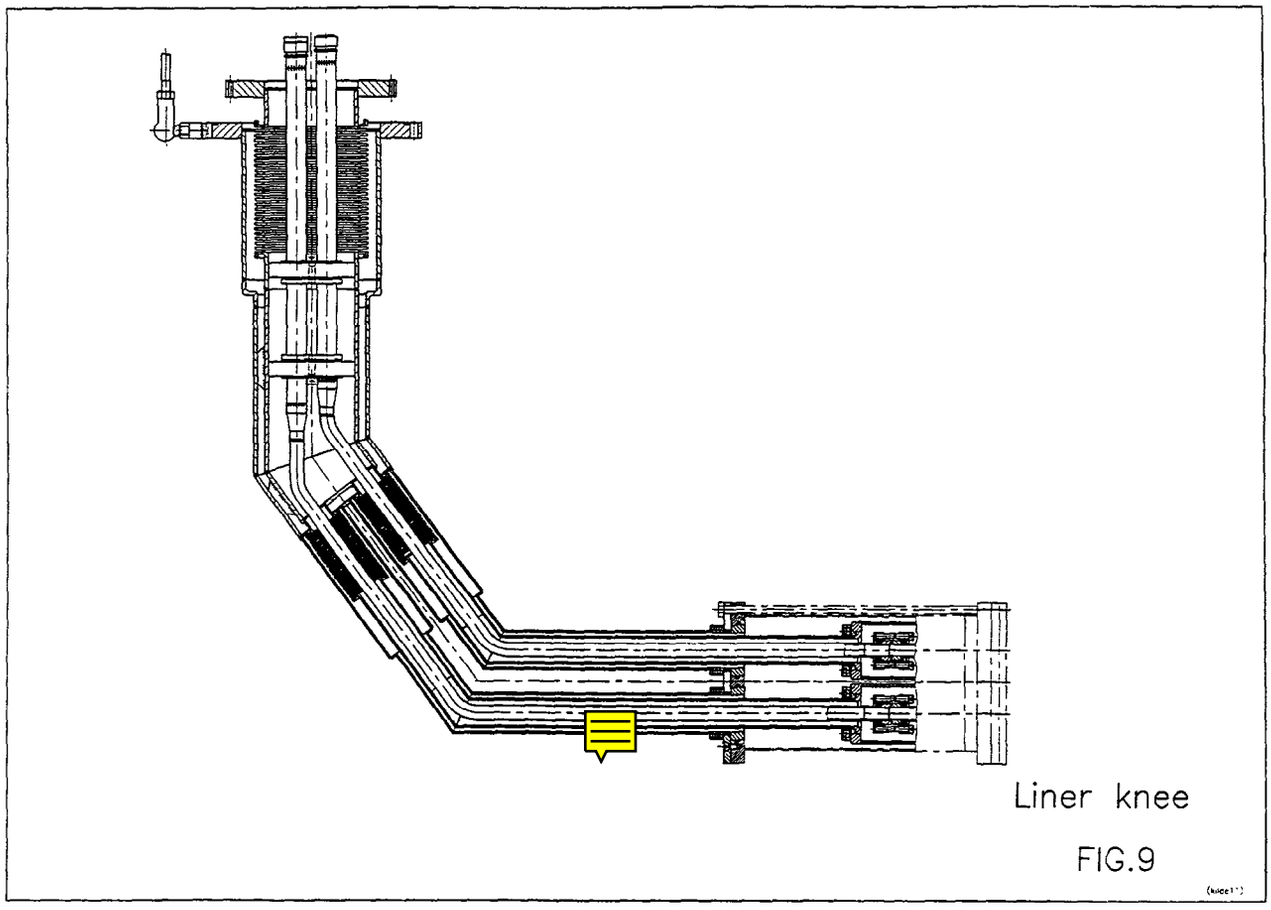

Liner knee

FIG.9

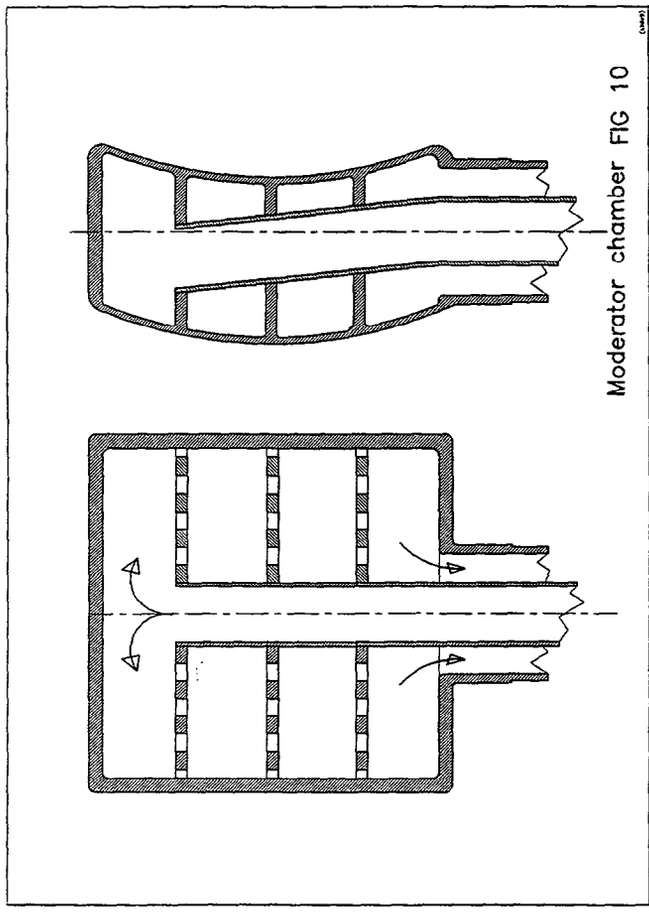

Moderator chamber FIG 10

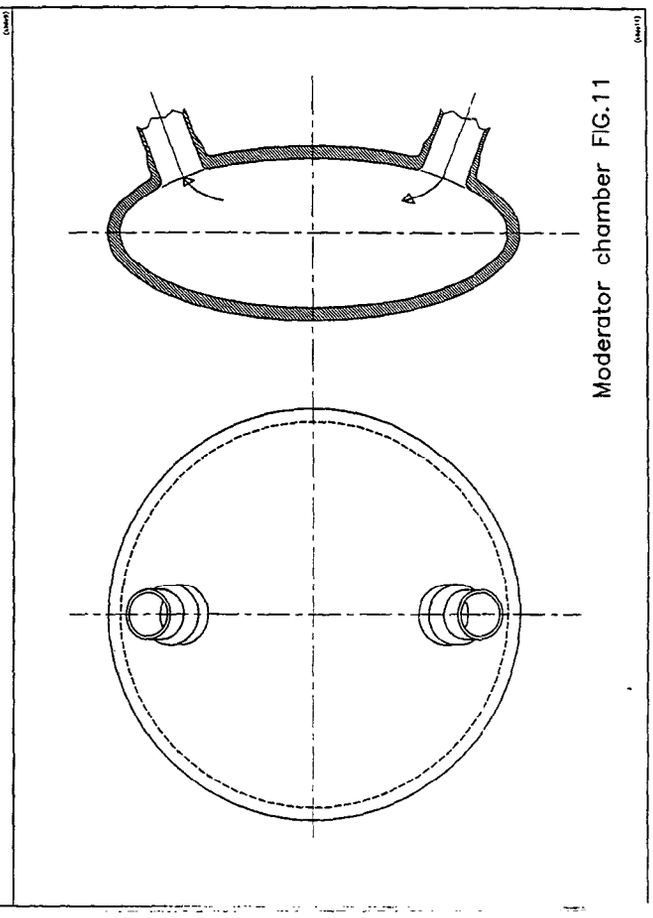

Moderator chamber FIG.11

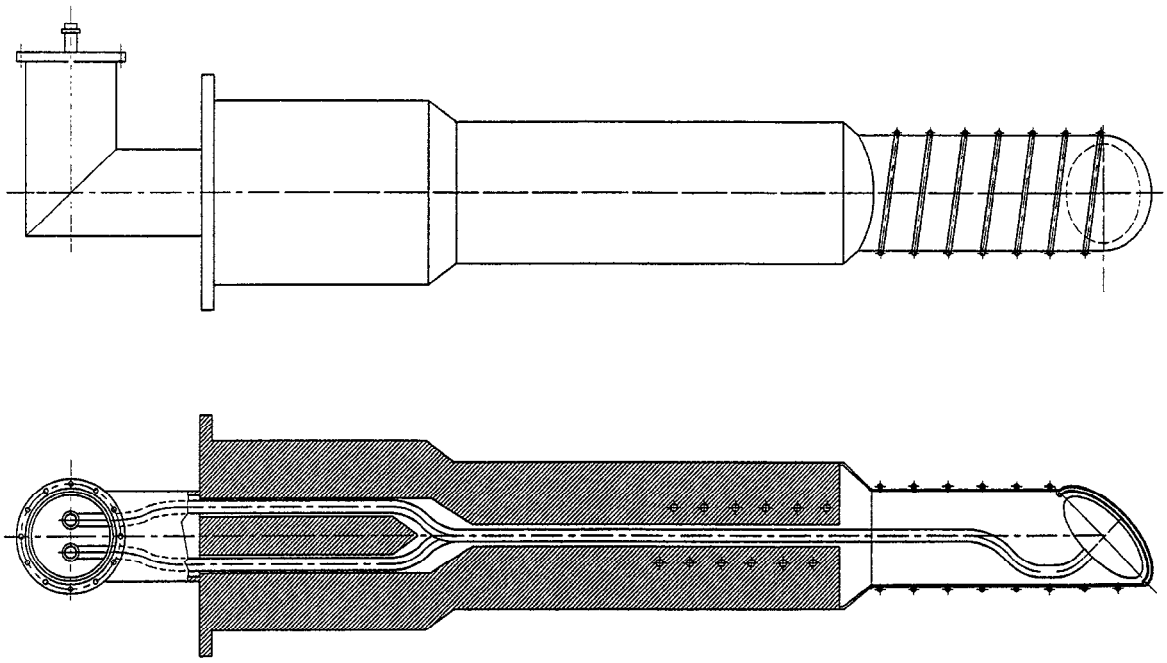

FIG.12

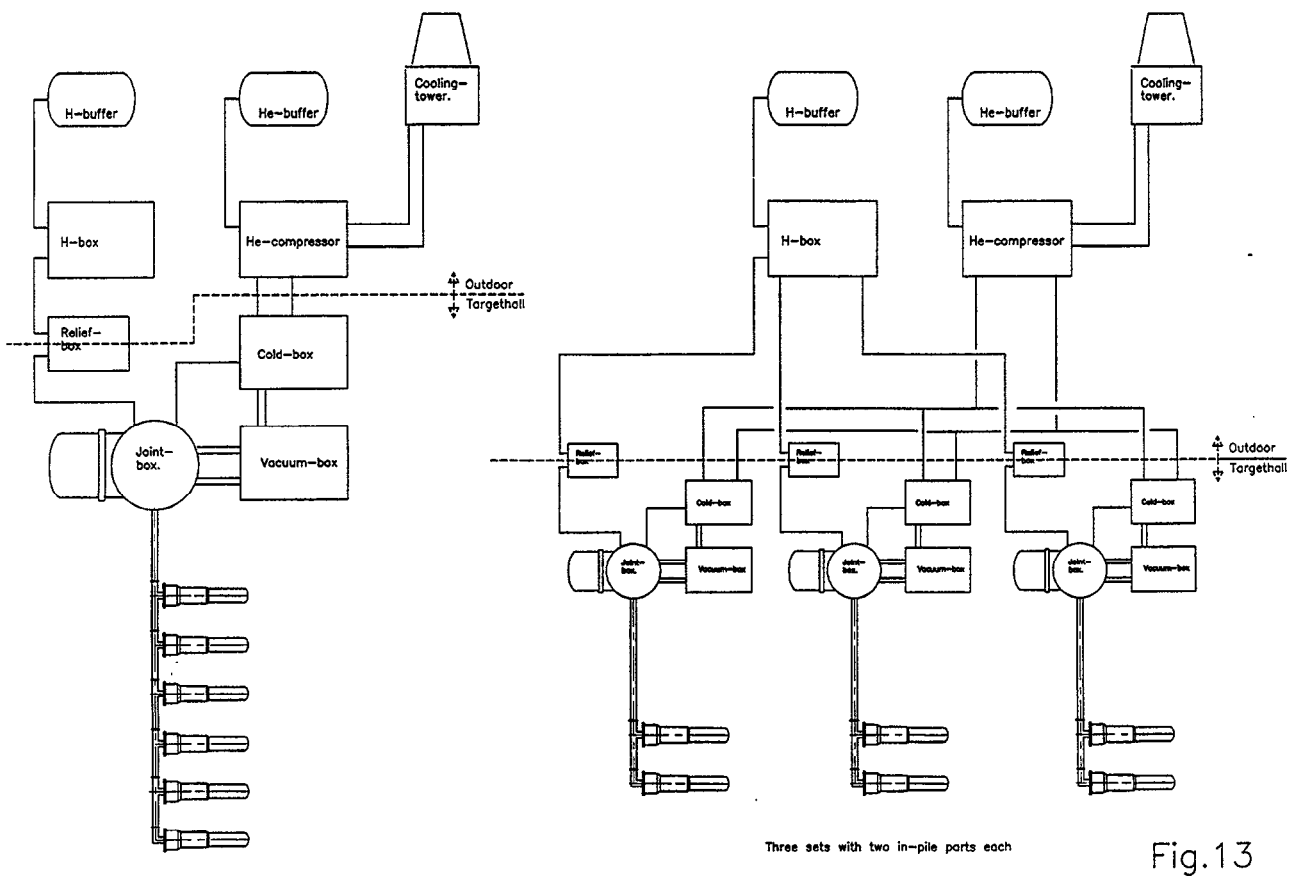

One set with 6 in-pile parts.

Three sets with two in-pile parts each

Fig.13

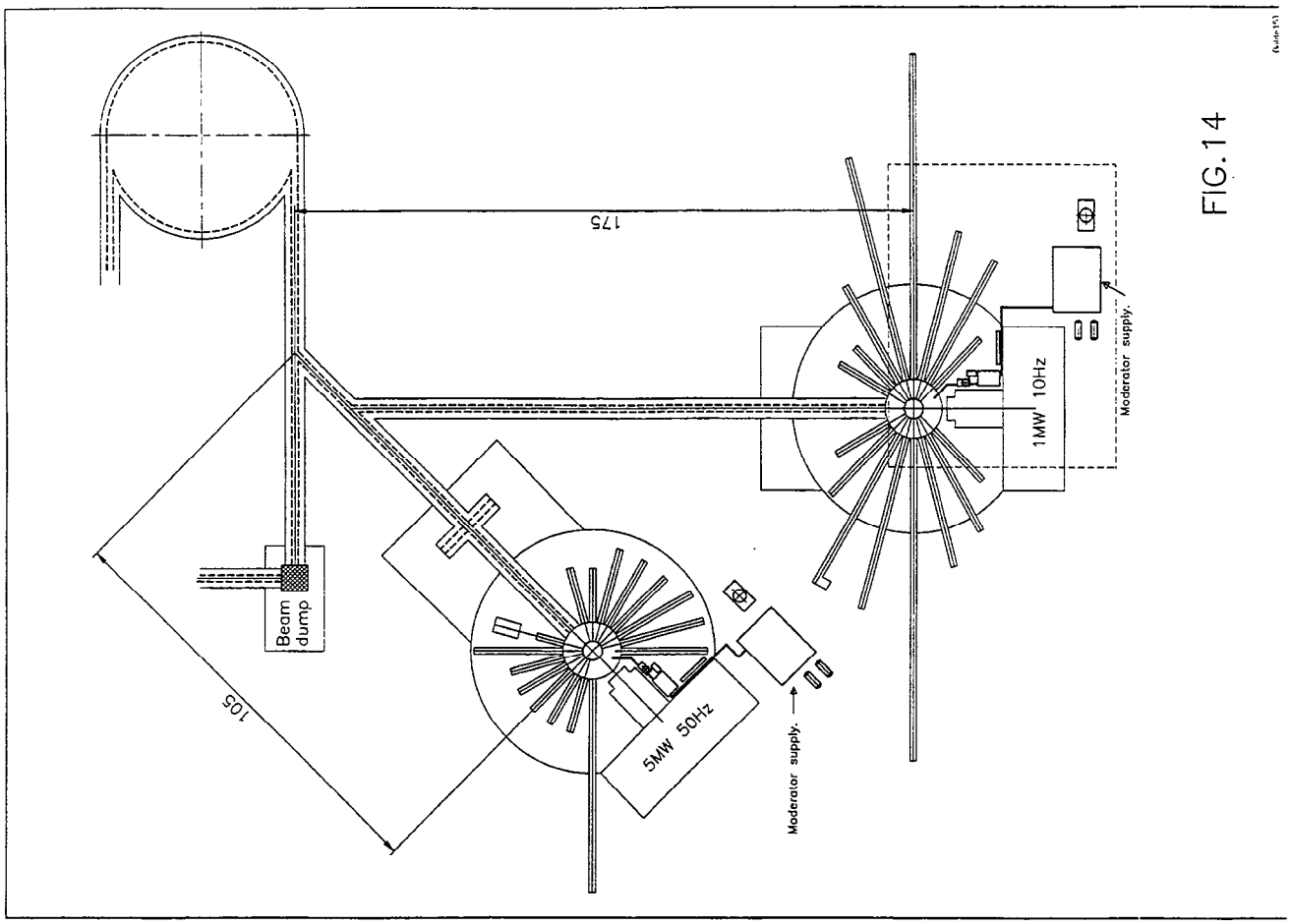
Beam dump
105
175
5MW 50Hz
1MW 10Hz
Moderator supply.
Moderator supply.

FIG.14

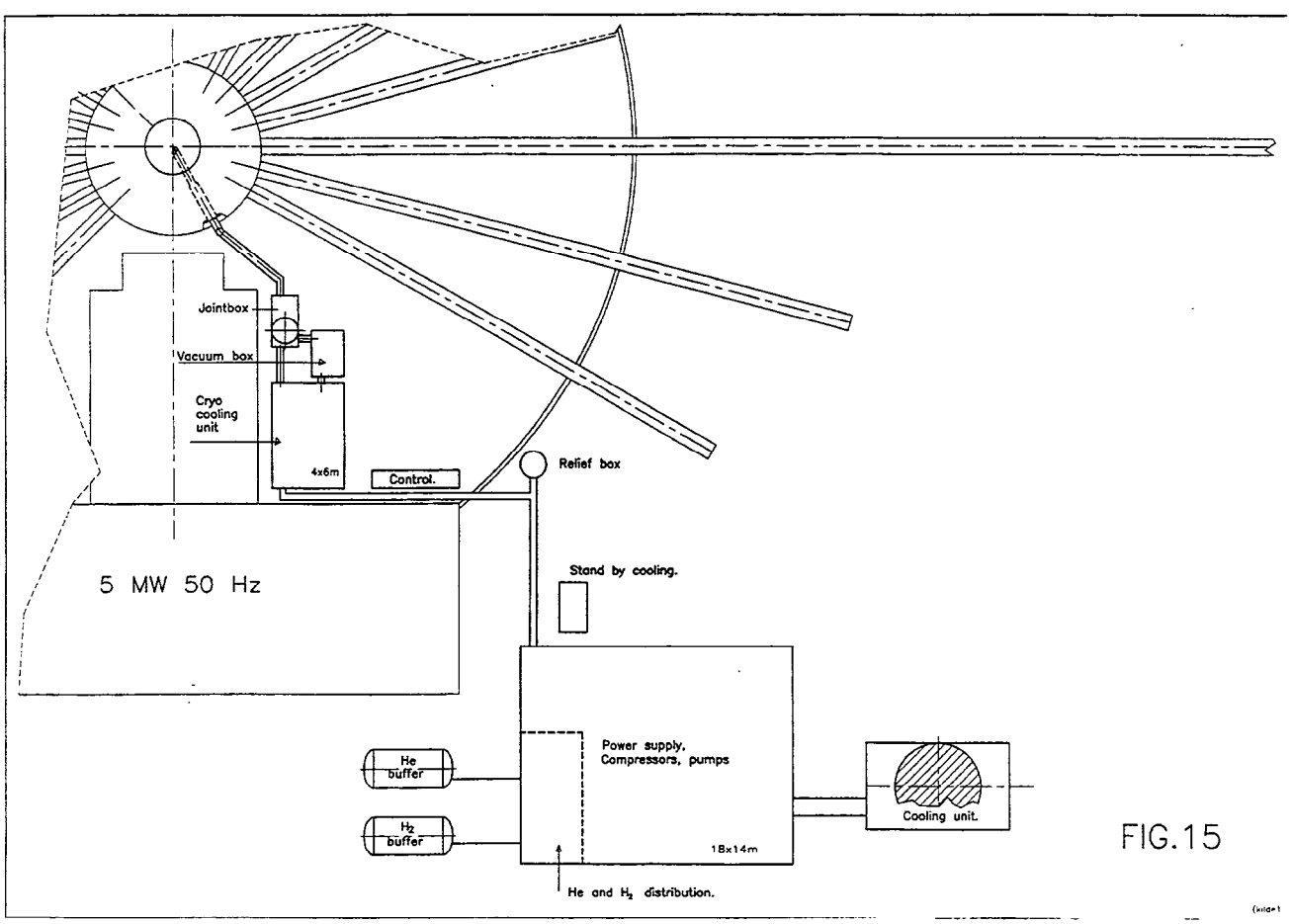
Jointbox
Vacuum box
Cryo cooling unit
4x6m
Control.
Relief box
5 MW 50 Hz
Stand by cooling.
He buffer
H_2 buffer
Power supply, Compressors, pumps
18x14m
Cooling unit.
He and H_2 distribution.

FIG.15

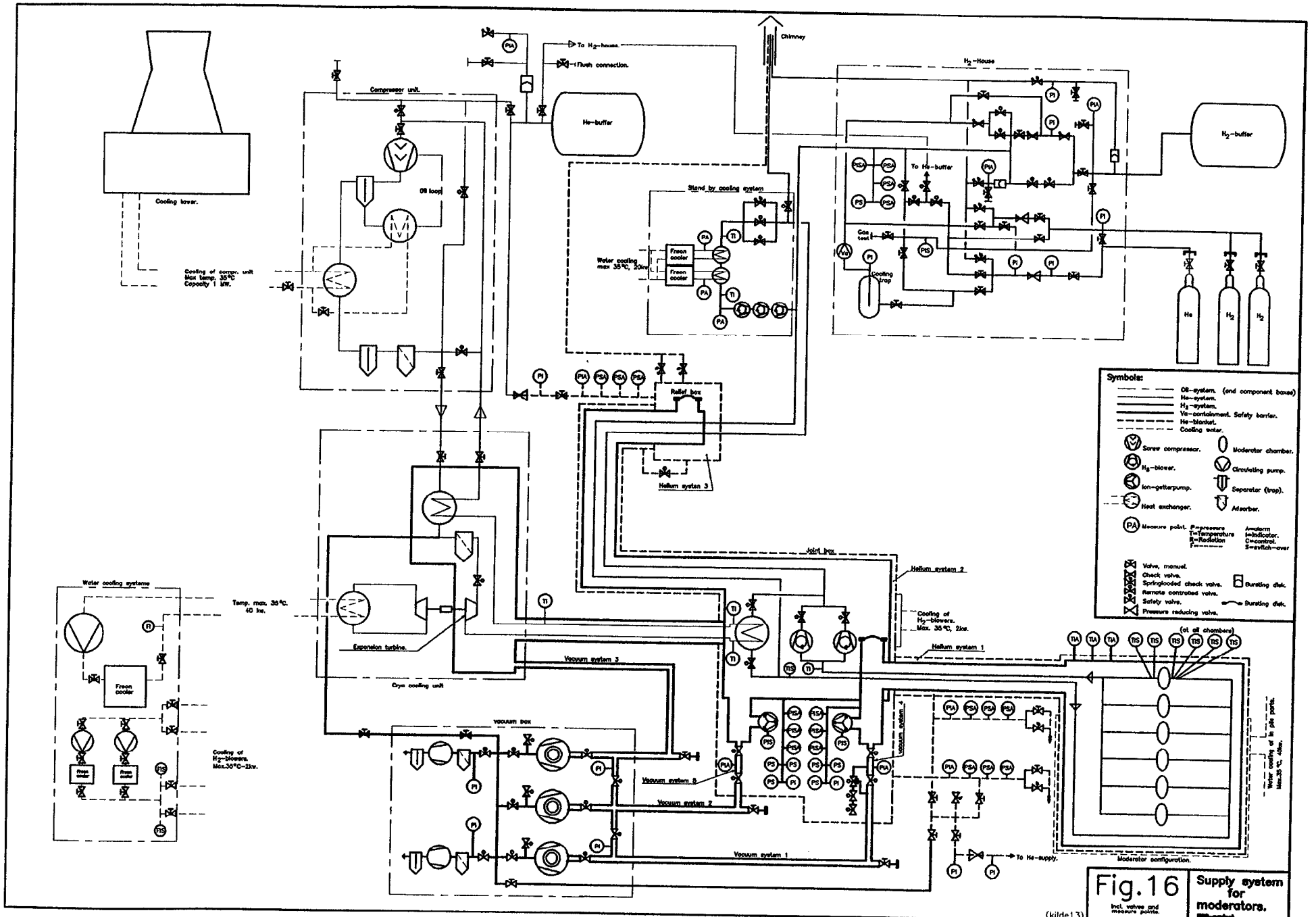

Fig. 16

Incl. valves and measure points.

Supply system for moderators.

SSB-project.

ICANS-XIII
13th Meeting of the International Collaboration on
Advanced Neutron Sources
October 11-14, 1995
Paul Scherrer Institut, 5232 Villigen PSI, Switzerland

HANDLING DEVICES FOR THE BEAM PORT- AND COLD MODERATOR INSERTS OF SINQ

Werner Wagner, Jakob Ehrat

Paul Scherrer Institut, 5232 Villigen PSI, Switzerland

ABSTRACT

A total of eight horizontal casings have been installed around the SINQ target block serving as ports for beam extraction or cold moderator insertion. These casings are filled with their operational units, e.g. beam holes with shutters and collimators, the D_2-cold moderator, neutron guide plug etc. These filling units are generally combined with massive shielding material of a total weight of up to 35 tons for each casing. In order to be able to install those heavy but mechanically quite delicate units, and to remove and replace them after being activated during SINQ-operation, a system of devices has been designed at PSI, which allows the required safe and remote handling.

Meanwhile these handling devices, at PSI known as the "yellow machines", are built and commissioned and were operating successfully for the initial installation of the port inserts. Their design principle combines a flexible, rail-carried support carriage with lifting and tilting units for alignment, motorised trolleys or sledges for the insert handling and shielding covers for handling and transportation of activated elements. A computerized control unit allows easy and reliable operation.

1. Introduction

The SINQ target shielding is constructed as a solid block of steel and conrete with a lateral thickness of about 4.5 m around the moderator vessel. In the horizontal plane around the target this shielding has eight penetrations lined with steel casings [1]. Five of them, each with a twin set of two ports at an angle of 10° relative to one another, are foreseen for beam extraction or the insertion of irradiation devices. One other casing, facing the cold moderator at the inside, accomodates the in-shielding part of the neutron guide system [2]. The two remaining ones allow to insert devices for neutron moderation or scattering; those accomodate the insert holding the D_2 cold moderator [3] and a thermal scatterer, respectively.

The three types of casings have different shapes: the ones for the twin ports are rectangular, divided in the middle by a wedge-shaped shielding wing, and stepped threefold to optimize the shielding performance. The rectangular casing for the neutron guide insert is straight

Keywords: Handling devices, beam port inserts, cold moderator handling, activated inserts

without central division, and has only one shielding step because it leads into the shielded neutron guide bunker. The casings for the moderator and scatterer insert are cylindrical with a circular shielding step each. Due to the given beam tube arrangement in the moderator vessel the casings are located at different heights with their axes between 1350 and 1585 mm above the floor.

All units which fill these casings are combinded with massive shielding material, the single units weighing typically two to five tons, the neutron guide insert even up to 25 tons.

The most delicate parts to be handled are the so-called hot blocks. They carry the window for the inner HeI barrier and must be fixed helium tight to the front end of each casing. With a weight of about 1.5 tons they need cantilever handling and have to be bolted remotely to the front end flange with a helicoflex metal seal. Cantilever handling is also necessary for the vaccum jacket of the D_2-cold moderator system. All other parts rest on wheels or roller bearings and are self-supporting.

For the purpose to ensure appropriate handling of the filling components of the casings, also - and in particular - when the components are activated after SINQ operation, a set of special devices was designed, built and commissioned at PSI. The principal requirements which these handling devices have to fullfill are the followings:

- They must allow a sufficiently precise and stable positioning and alignment in front of the casings.
- They must ensure a remote and safe handling of all devices with the required precision, considering the combination of heavy weight and fragile and delicate functional units, e.g. the thin-walled moderator vessel, cooling pipes, thermocouples etc.
- Appropriate handling must be ensured also when the components are activated after SINQ-operation. Therefore the handling devices must be completed by shielding boxes and shielding gates such that they allow the handling of activated components and also the transport to hot-cell areas for further processing, repair or conditioning for permanent storage.

2. Technical concept

The base for the handling devices is a transportable rail system and a stable support carriage on steel wheels. Except where fixed rails are installed permanently, the transportable rail system is placed on the floor in front of the casing, briding cable channels in the floor and other unevenesses. The carriage is placed on the rails where it can be moved back and forth parallel to the port axis. Several spindle-driven adjustment devices for lifting and tilting allow the adaption in height and the precise alignment of the carriage.

The real handling device, placed on top of the carriage, consists of a solid base plate of steel, 20 cm thick, which gives the required stability and also serves as radiation shielding towards the bottom. It carries the driving and handling units which are either fixed on sledges or move on guide rails on the plate.

In the course of the design procedure it turned out that the requirements for the three types of inserts, i.e. beam ports, neutron guides and cold source, were too different to be served by a single, universal handling device. Therefore, special base plates with specially adapted driving and handling units were built for each of the three types. They are supplemented by a

vertical steel plate of 20 cm thickness at the rear end, combined with a cable feedthrough and a cable fold up drum. These cables connect the driving units to the supply and controll units.

Base plate and rear plate are part of the shielding box. When activated parts must be handled this is completed by further steel plates mounted on the sides and covering the top, and by a shielding gate at the entrance. Further shielding gates are foreseen in front of the open casings to shield against radiation when the inserts have been removed.

3. Realisation and performance

In Figs. 1-5 the function of the handling devices is illustrated for selected situations. Fig. 1 shows the mounting of the (unactivated) hot block in one of the twin-port casings. At the top of the figure, the hot block is shown outside the shielding attached to its handling- and bolting device. The latter is hooked-up to the electric traction engine. Inside the casing, a set of three filler plates are inserted to bridge the shielding steps. At the bottom of the figure, the hot block is shown mounted, with tractor and handling device removed to the outside. Because the mounting axes of the hot block and the beam port axis, i.e. the axis of insertion, do not coincide, a specially curved rail is needed inside the casing, which is part of the upper step filler plate.

Fig. 2 shows the same device, now handling parts of the beam ports insert, the so-called high energy shutters. Furthermore, the device is shown complemented by the shielding units, including the two gates at the entrance. One of them is part of the handling device and the other one covers the partly empty (activated) casing.

Fig. 3 shows the handling device, mounting the vacuum jacket of the D_2-cold moderator system. The handling device is shown complemented by the shielding cover. Further, the vacuum jacket is filled with a shielding plug at its rear end which is necessary to enable the hand-operated bolting of the vacuum jacket to the flansh of the casing when activated inside. After this operation the shielding plug is remotely removed to make room for the moderator insert.

In Fig. 4, the same device is shown mounting of the D_2-cold moderator insert, here without shielding cover. The insert, carrying the moderator vessel at its front end mainly consists of heavy steel shielding. It has roller bearings spread out 45° to the side, which move on rails mounted on a spindel driven sledge on the base plate. This sledge pushes the rails with the insert to the edge of the casing to bridge the gap between base plate and casing edge. Then the insert is rolled in pushed by the traction engine.

Finally, Fig. 5 shows the third version of the handling device, serving for the neutron guide insert. The insert waggon shown in the figure is the heaviest part to be handled, weighting about 25 t. Furthermore, it has to be introduced with the highest precission (angular tolerances of $\leq 10^{-4}$ rad) to ensure the correct alignment of the neutron guides in the insert. The device is designed to allow remote exchange of the neutron guides when they are damaged or their performance has degraded after a certain time of SINQ-operation. This exchange is executed through the open bunker roof, using a crane with a magnetic lifting device. Due to the high activation level expected, all the exchange operation must be remotely controlled. This procedure has successfully been tested with the unactivated guide insert.

4. Conclusions

A user-dedicated neutron facility like SINQ with a potential for further development requires flexible and safe handling of the insert devices of the target shielding block: **Safe** in the sense of nondestructive for the components but also ensuring a minimum radiation exposure of the personell involved in the operation, **flexible** in the sense to be able to respond quickly to changes in the users' demand, and to act quickly if components have suffered any damage during the operation and must be repaired or replaced. The concept of the handling devices provided by PSI is expected to meet these requirements. So far, they worked successfully and reliably during the initial installation, which also was a test for the later handling of the components when activated. The knowledge and experience gathered therewith may also be of more general interest.

5. References

[1] G.S. Bauer, *Proc. of ICANS-XI*, International Collaboration on Advanced Neutron Sources (1990), 41

[2] W. Wagner and J. Duppich, *Proc. of ICANS-XII*, International Collaboration on Advanced Neutron Sources (1993), I-368

[3] H. Spitzer, A. Höchli, G.S. Bauer and W. Wagner, *Proc. of ICANS-XI*, International Collaboration on Advanced Neutron Sources (1990), 430

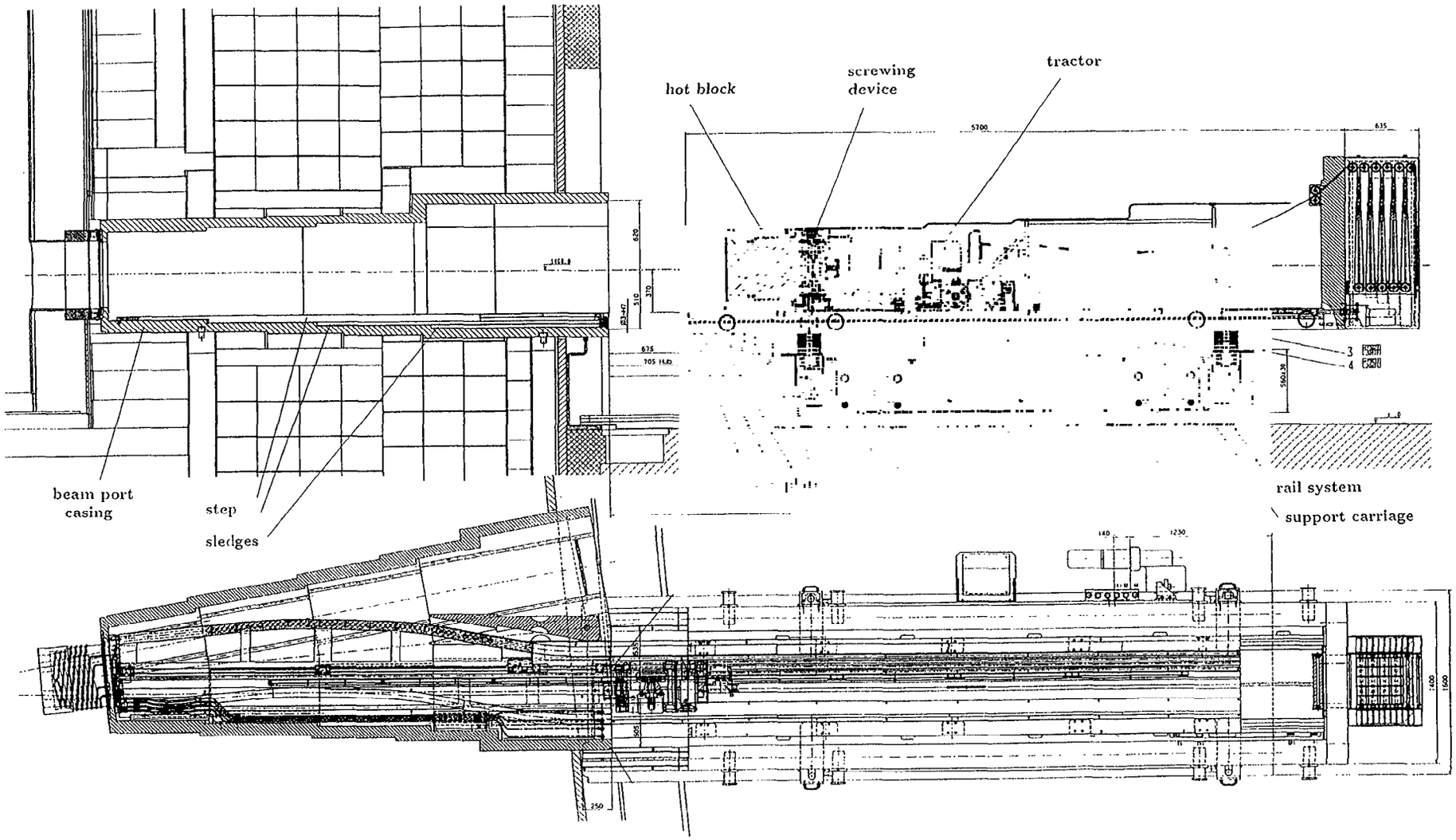

Figure 1: Illustration of the hot block mounting

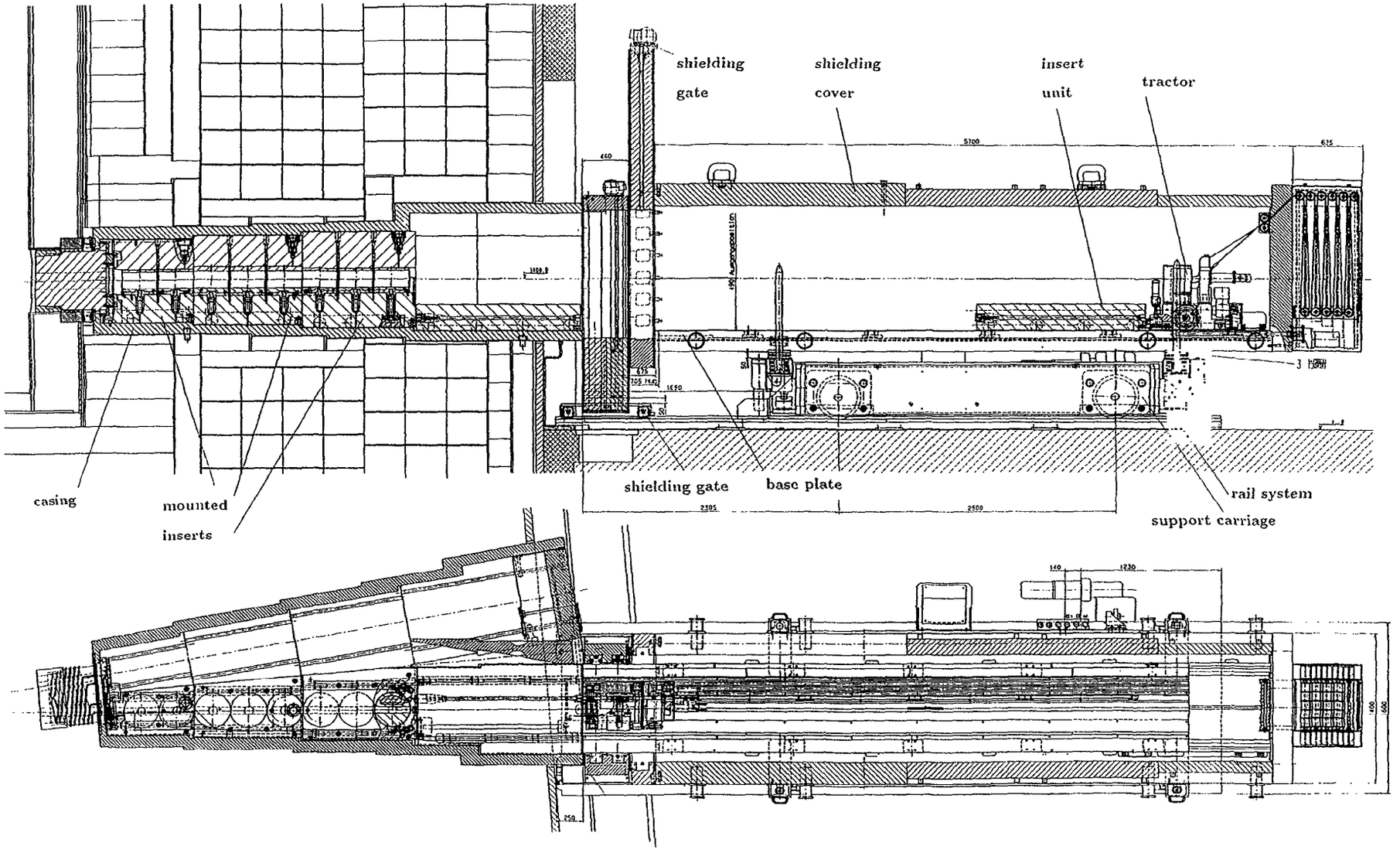

Figure 2: Mounting or exchange of beam port inserts with the shielded handling device

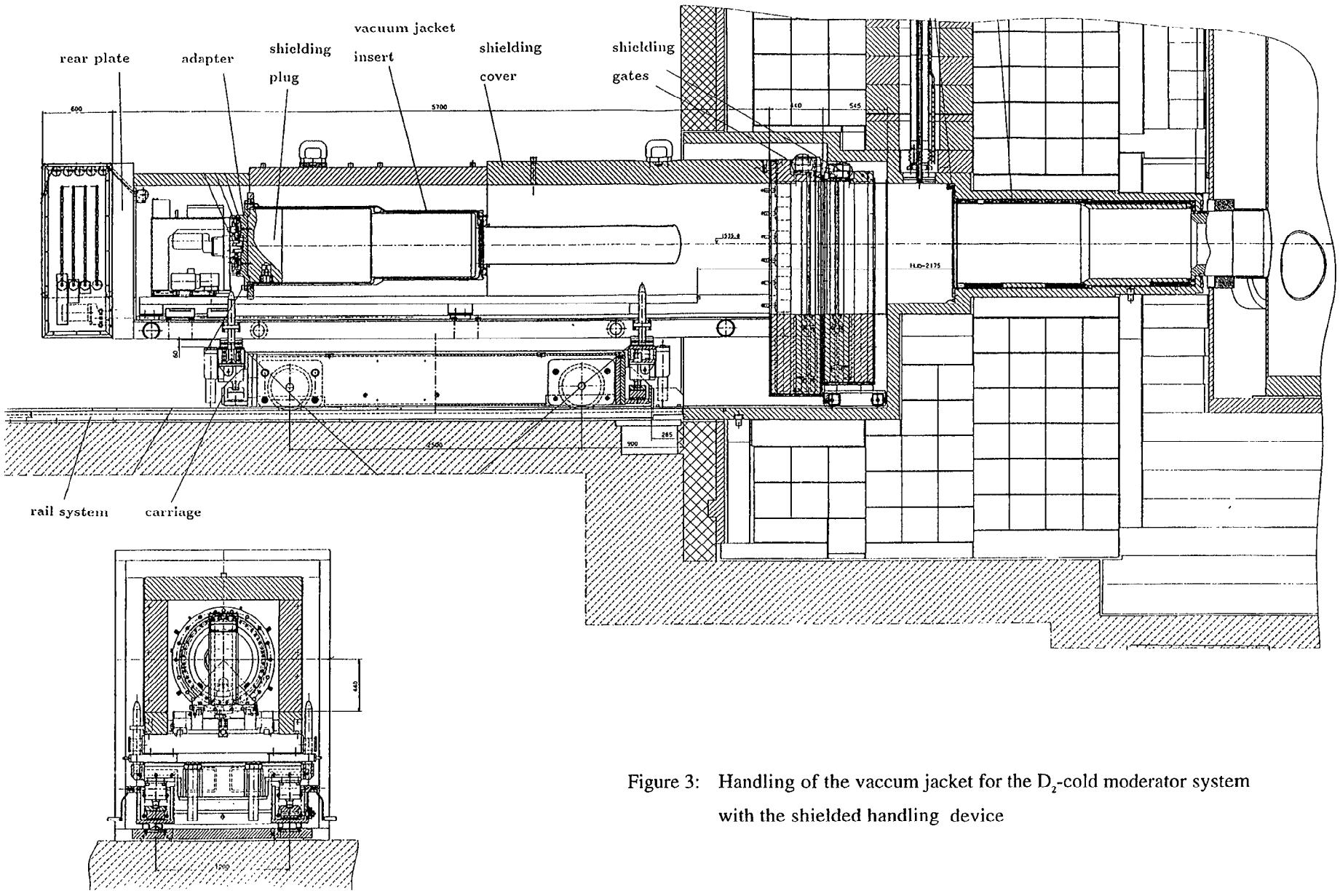

Figure 3: Handling of the vaccum jacket for the D_2-cold moderator system with the shielded handling device

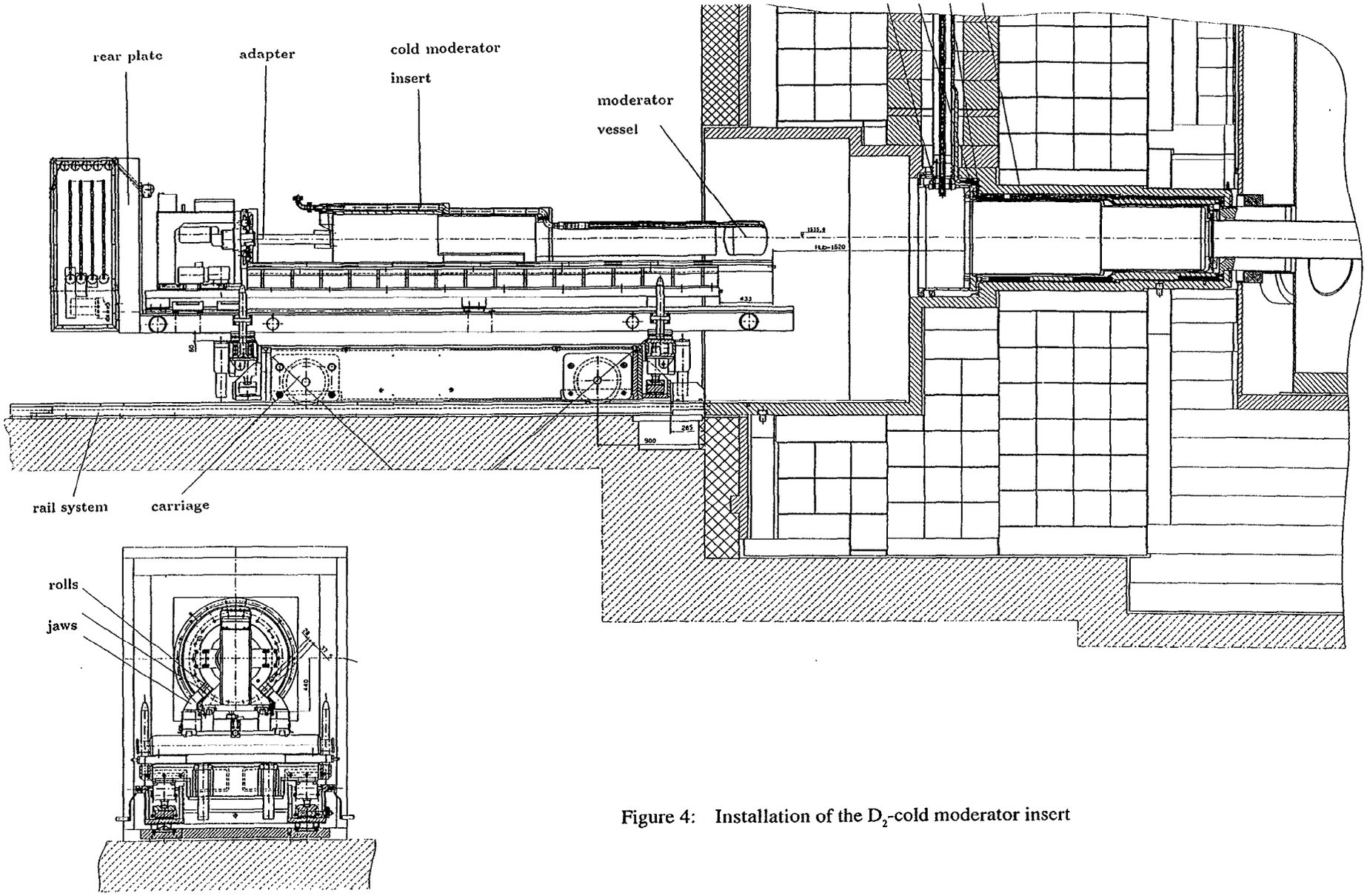

Figure 4: Installation of the D_2-cold moderator insert

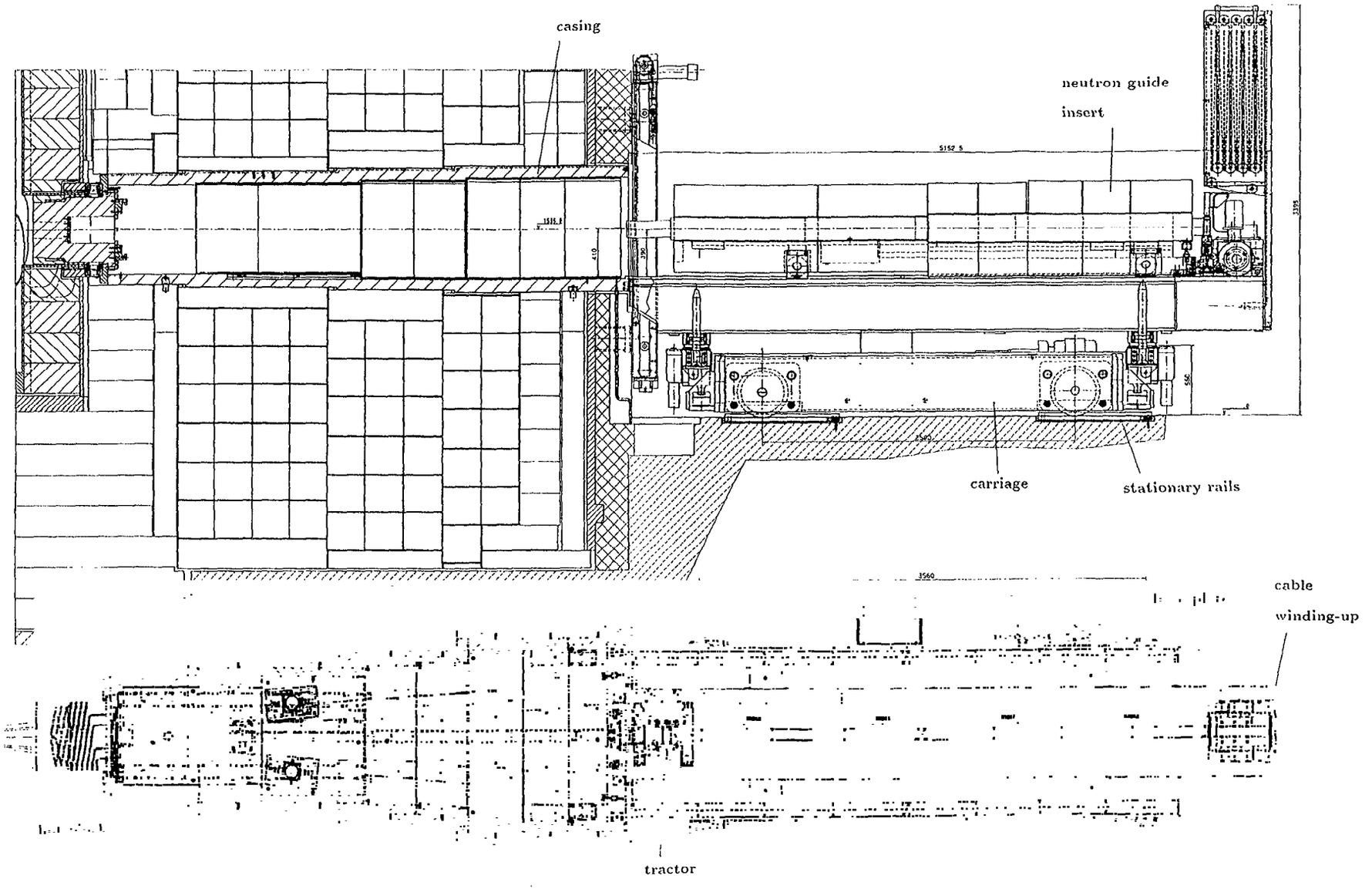

Figure 5: Handling of the waggon carrying the neutron guide inserts.

ICANS-XIII
13th Meeting of the International Collaboration on
Advanced Neutron Sources
October 11-14, 1995
Paul Scherrer Institut, 5232 Villigen PSI, Switzerland

EXAMINATION OF DISKS FROM THE IPNS DEPLETED URANIUM TARGET

Robert V. Strain* and John M. Carpenter†

*Energy and Environmental Science and Technology Division
†Intense Pulsed Neutron Source
Argonne National Laboratory, Argonne, IL 60439, USA

ABSTRACT

This paper describes the results of visual, gamma ray scanning, and destructive metallurgical examination of two disks from the depleted uranium target of the Intense Pulsed Neutron Source.

1. Introduction

This report describes the results of examining the Zircaloy-2 clad depleted uranium disks (with emphasis on the first two) from the Intense Pulse Neutron Source (IPNS) Target. That target operated from August, 1981 to June, 1988 and from September, 1991 to September, 1992 at 450 MeV, pulsing at 30 Hz with a time average proton current of about 15 μA. The target was removed from service when the presence of fission products (^{135}Xe) in the coolant cover gas indicated a failure in the Zircaloy-2 cladding. Altogether, the target had absorbed about 240 mA hours of proton current, and endured between 50,000 and 100,000 thermal cycles. The purpose of the examination was to assess the condition of the disks and determine the cause of the cladding failure.

The IPNS depleted uranium target consisted of eight water-cooled uranium alloy disks, 10 cm in diameter and 2.7 cm thick, clad with Zircaloy-2. The peak centerline temperature during operation was ~225 C in the second disk. The first, third, fifth, and seventh disks contained stainless steel sheathed thermocouples in diffusion bonded Zircaloy-2 wells to measure the temperature near the center of the disk.

The uranium alloy (450 ppm carbon, 250 ppm iron, and 350 ppm silicon) core material is often referred to as Springfield adjusted uranium and has superior performance in the form of reduced swelling (compared to high-purity uranium) in the 400 to 600 C temperature range. The results of the original design study[1] indicated an expected total dimensional change ($\Delta L/L$/year) estimated to be 0.014 most of it resulting from thermal cycling-induced growth (0.006) and thermal expansion (0.005). The design study also indicated that the cladding on the disk subject to the highest stress was predicted to fail after about 500 days of operation as a result of thermal cycling fatigue. Other failure mechanisms that were considered included 1) irradiation induced swelling, 2) failures of the seam weld at the circumference of the each disk, 3) failures in the welds at the thermocouple well, and 4) separation between the uranium alloy and the cladding as a result of inadequate bonding. Such a separation could result in higher than normal temperatures and acceleration of the thermal cycling-induced growth and irradiation swelling, which might lead to early failure of the cladding.

Keywords: Argonne, Uranium, Targets, Metallurgy

2. Non-destructive Examinations

Non-destructive examinations of the eight disks consisted of visual examination (including macro-photography), dimensional measurements (diameter and thickness), and gamma scanning.

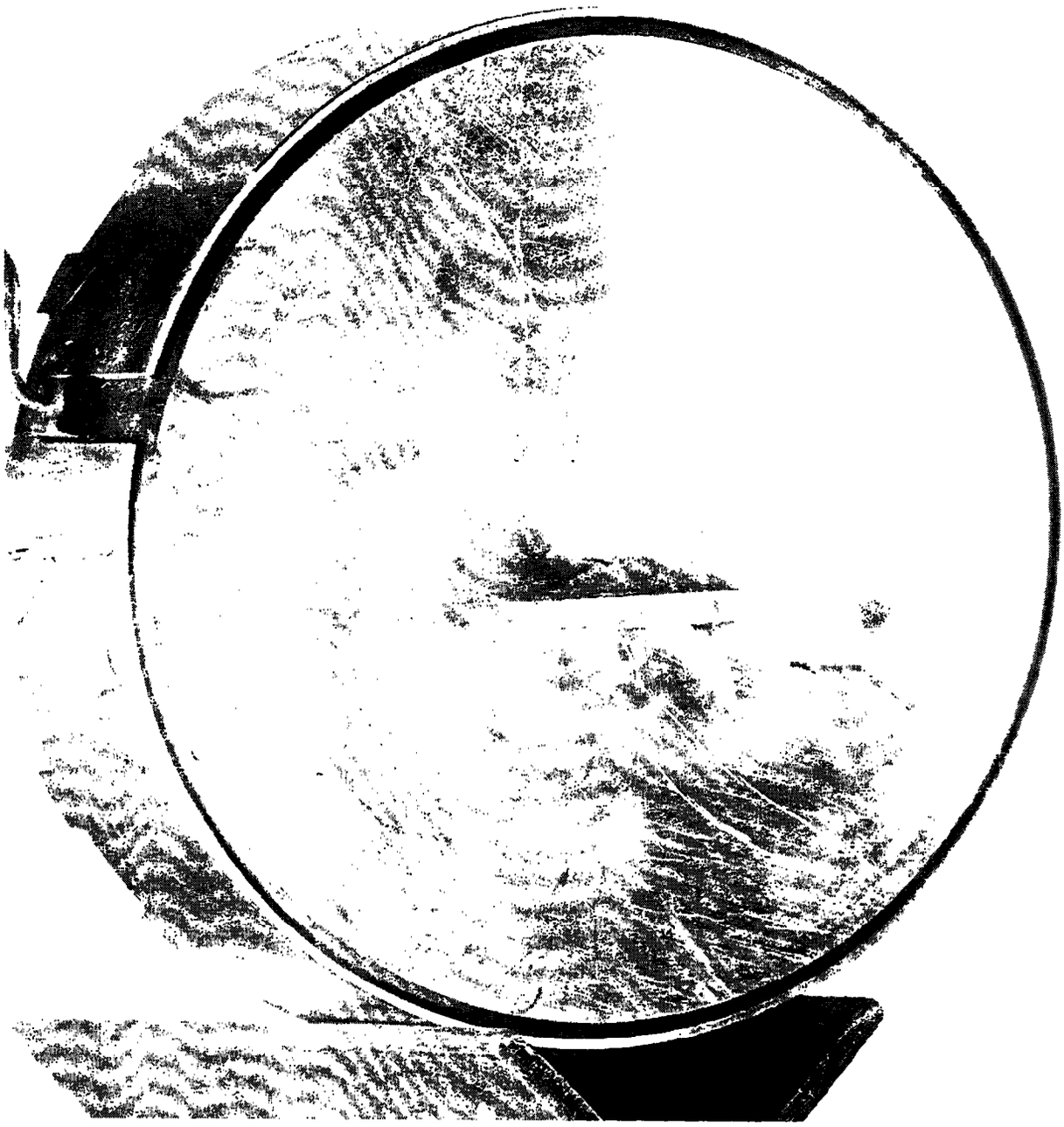

Figure 1. Rear Face of Disk #1.

2.1 Visual Examination

Both faces of all 8 disks were visually examined and photographed. The condition of the disks has been described by Carpenter and Hins[2]. That description with some modification is as follows: Witness of the flow channel guide bars (flow separators) was apparent on the faces of all the disks. The marks left by the flow separators result from reduced discoloration of the Zircaloy-2 cladding that was in contact with the spacers compared to the cladding exposed to the coolant. However, the spacers appear to have prevented expansion of the disk surface and to have produced sharply defined indentations across the center regions of the first three disks.

The front (upstream, toward the proton source) face of disk #1 shows a 25 mm-long crack running across the disk in the direction of the thermocouple. The crack occurs near the center of the disk and appears to be imbedded in a narrow depression channel that is visible on the disk surface. The depression channel extends from near the center of the disk to the thermocouple tube exit point (over 50 mm long). The central region of the disk appears to exhibit a general bulging (except under the coolant spacers). A pattern of wrinkles and apparent blistering about 50 mm diameter is also visible near the center of the disk.

Fig. 1 shows the rear face of disk #1. In this view the disk is still housed in the flow guide cup. A small blunt crack is present near the center of the disk on a outward projection (blister) of the surface. The imprint of a flow spacer is quite close to this defect. The dial indicator measurements indicate that the projection extends to about 2 mm above the plane of the face. Undulations in the surface occur randomly over the entire surface, but are most pronounced in the central region of the face. A wide depression channel is visible, which extends from the exit point of the thermocouple to the distorted central region, and a narrow depression channel extends diametrally from the central region to the edge in line with the thermocouple.

The front face of disk #2 shows a surface projection near its center that appears to coincide with the location of the projection on the back face of disk #1. No cracks were visible on either face of disk #2, but wrinkles were present near the center of these faces. These undulations appear to be less severe and cover a smaller area than those on disk #1. Both faces of disk #3 and the front face of disk #4 show some visual evidence of wrinkles in the central region. The disk faces further back in the target stack show very little evidence of surface distortion.

2.2 Dimensional Measurements

Diameter (0° [aligned with the thermocouple well direction] and 90° orientations) and thickness measurements (eight locations) were made on each of the disks using a micrometer. These measurements indicate that significant diameter changes occurred in disk #1 (~0.25 mm increase) and slight diameter changes occurred in disk #2 (~0.05 mm increase). The measurements also indicate significant thickness increases near the center of disk #1 (~0.5 mm) and slight increases near the center of disk #2 (~0.08 mm). A dial indicator was used to measure the maximum deviation across each face of the disk. These measurements showed maximum distortions of 1. mm and .025 mm on the front faces of disks #1 and #2, respectively. The maximum distortion was found on the back face of disk #1 at the short crack (2 mm).

2.3 Gamma Scans

Gross beta and gamma activity measurements at the front and back face of each disk show peak values at the back face of disk #1 (120 R/hr) with slightly lower values at the front of disk #1 and both faces of disk #2 (110 R/hr). The activity diminished progressively in the remaining disks (from 105 to 4 R/hr). Diametral scans across the disks were performed at four orientations and for several nuclides. Scans for ^{137}Cs and $^{95}Nb/Zr$ fission products at the front face of disk #1 are shown in Fig. 2. The shape of these curves reflects the distribution of fission events and shows that most of the damage occurred near the center of the disks (but not perfectly centered) in a roughly circular pattern. The activity outside a radius of about 20 mm was less than half the peak activity. The area of measurable gamma activity is in general agreement with the observation of distortion of the cladding in disks #1 and #2.

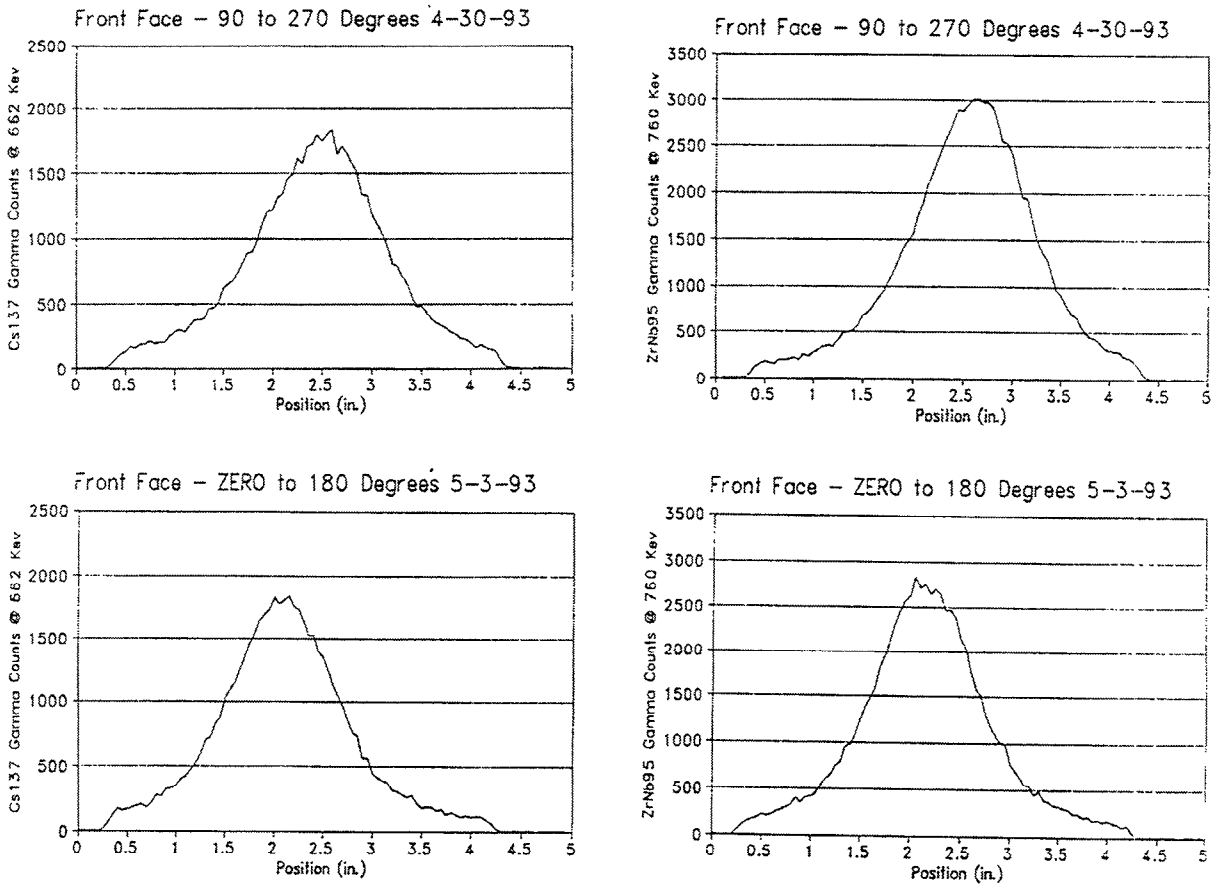

Figure 2. Gamma Activity Across the Diameter of Disk #1, Typical Shapes.

3. Destructive Examinations

3.1 Disk #1

Disk #1 was sectioned approximately perpendicular to the thermocouple about 12 mm from its centerline. The dominant feature revealed by the cut was a large crack through the core (uranium) at the thermocouple locations (Fig. 3) that was filled with powder.

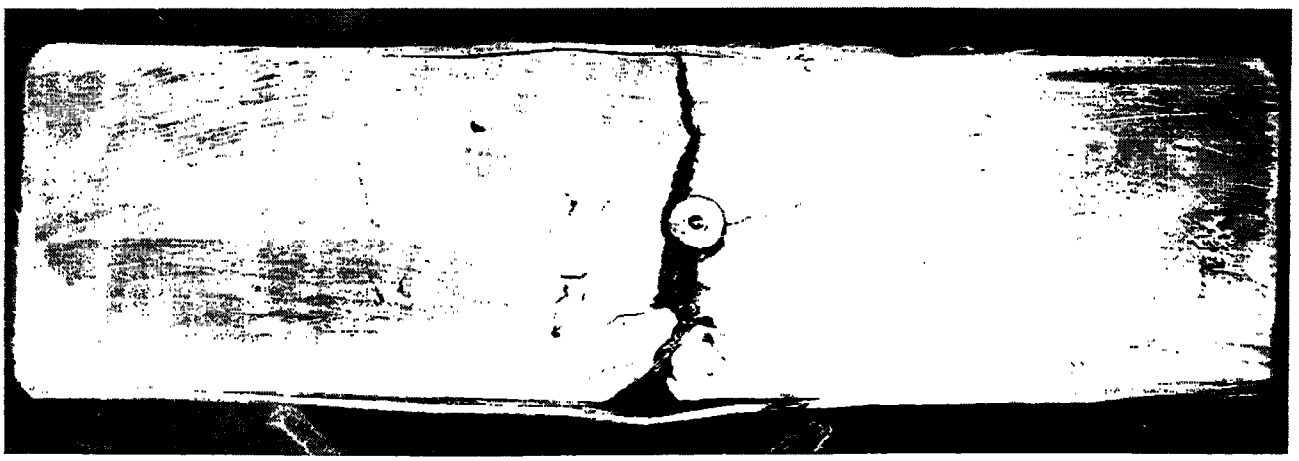

Figure 3. Section Perpendicular to the Thermocouple in Disk #1.

In addition to the major crack, smaller cracks radiate from the thermocouple location, and small cracks were visible at several other locations in the core material. The cladding was separated from the uranium near the major crack on both the front and back of the disk. Analysis of the material in the major crack with scanning electron microscopy (SEM) and neutron diffraction showed that it was primarily UO_2 (~70%) and UH_3 (~30%).

Figure 4. Micrographs of a Sample from Disk #1.

The powder in the major crack was assumed to be the result of interaction between the cooling water and the core material. The corrosion of uranium by water produces uranium oxides and under certain conditions uranium hydride. The formation of these reaction products results in large volume increases since the specific gravity of the most dense corrosion product (UO_2) is about 11 g/cm^3 compared to about 19 g/cm^3 for alpha phase uranium. We believe the volume increase of the relatively large amount of corrosion product to be the cause of the protrusion near the center of the back face of the failed disk. The location of the protrusion (with the short crack) of the cladding on the back face of the disk corresponds to the location with a large amount of the corrosion product.

A sample for optical microscopy was cut at a location 12 to 25 mm from the center of the disk. This sample was chosen because it included several smaller cracks, but was away from the major crack filled with corrosion product. Low magnification composite photographs of the sample from disk #1 show that the cladding has separated from the core material and a network of cracks is present in the uranium. Higher magnification photographs show that every crack examined contained a gray -colored material (Fig. 4) that is assumed to be corrosion product as a result of reaction between the uranium core material and the coolant water. In most areas the corrosion product appears to be a single phase, medium gray, monolithic material that is assumed to be uranium dioxide. At the end of cracks (where the crack is extending into the core material) the corrosion product appears to consist of two phases (the medium gray phase and a lighter gray phase). The lighter gray phase may be uranium hydride (if its not an optical illusion). The formation of hydride is promoted by high hydrogen partial pressure. The crack tip would tend to trap hydrogen and is a logical location for the formation of the hydride.

3.2 Disk #2

Reasoning that because corrosion had not taken place in the disk adjacent to the failed disk it must show cleaner evidence of the cause of failure than the failed disk, we performed a thorough destructive examination of disk #2. Disk #2 was initially sectioned through its center. Visual examination of the cut surfaces showed readily observable cracks in the core material at a distance of about 25 mm from the center. Two samples were cut from this area. A low magnification composite photograph of the first sample shows one large crack system in the uranium and several short cracks some distance from the main crack. Higher magnification micrographs (Inset in Fig. 5) revealed no evidence of corrosion products or other material in these cracks (the material that appears in the micrographs is epoxy that was used to fix the sample in a mount). The cracks in the uranium indicate that the failure of the cladding on the first disk initiated in the uranium. We conclude that the cracks in the uranium were the result of anisotropic swelling from a combination of thermal cycling and irradiation.

A second sample was cut that included the back face of disk #2. A low magnification composite micrograph, Fig. 6, of this sample shows that the main crack system extended through the entire thickness of Disk #2 to the back face. Again the cracks contained no corrosion product. At the intersection of the main crack with the cladding on the rear face of Disk #2, the core material appears to have pulled away from the cladding. The uranium on the two sides of the crack appear to be displaced from each other parallel to the direction of the crack. There appears to be a second phase present at the inner surface of the cladding in the region where the core material has separated from the cladding. Etching of the cladding indicates that the microstructure of the cladding is altered (the addition of fine precipitates) to a depth of about 150 μm in the region of the separation.

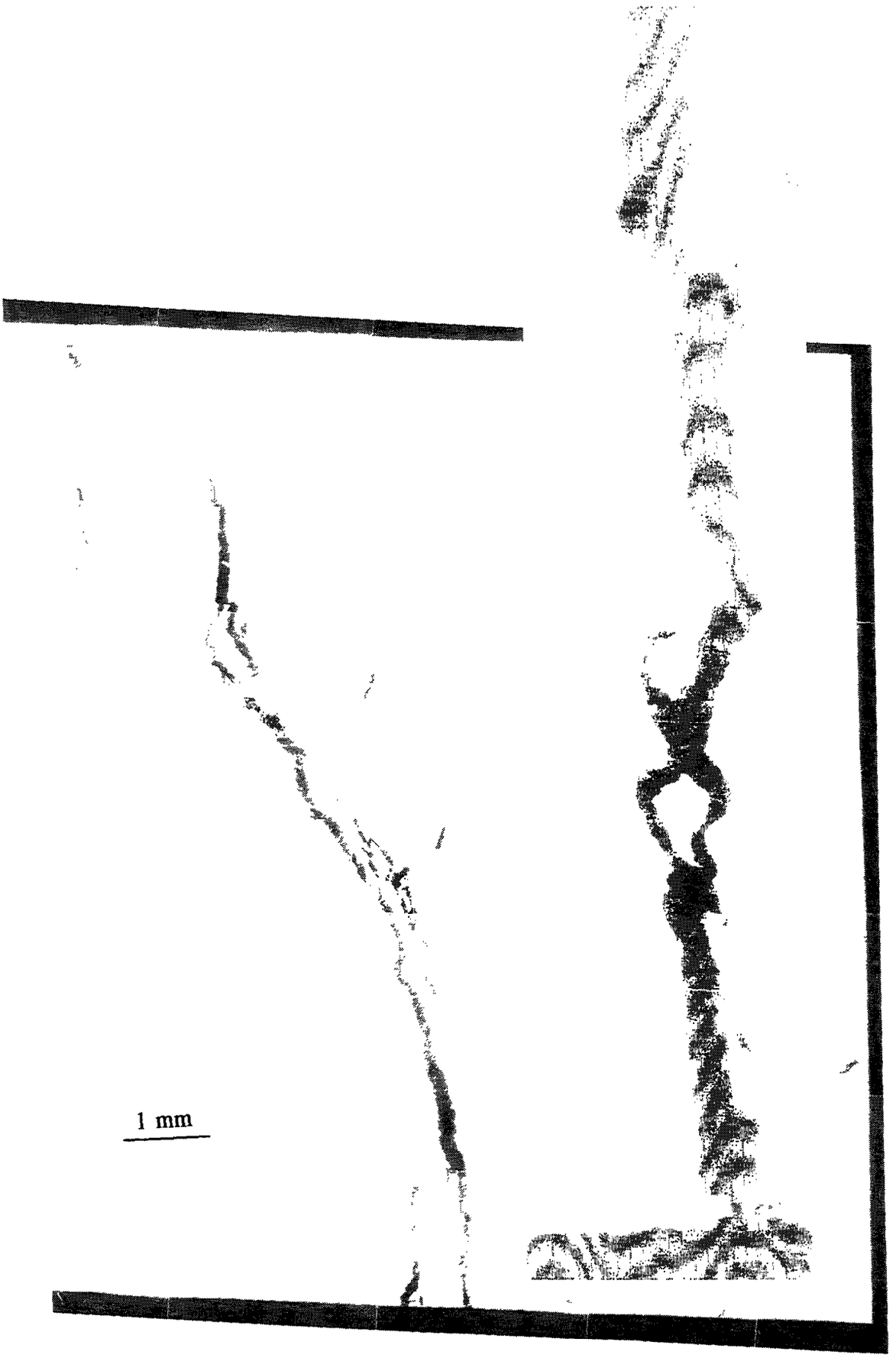

Figure 5. Cracks in the Core Material of Disk #2

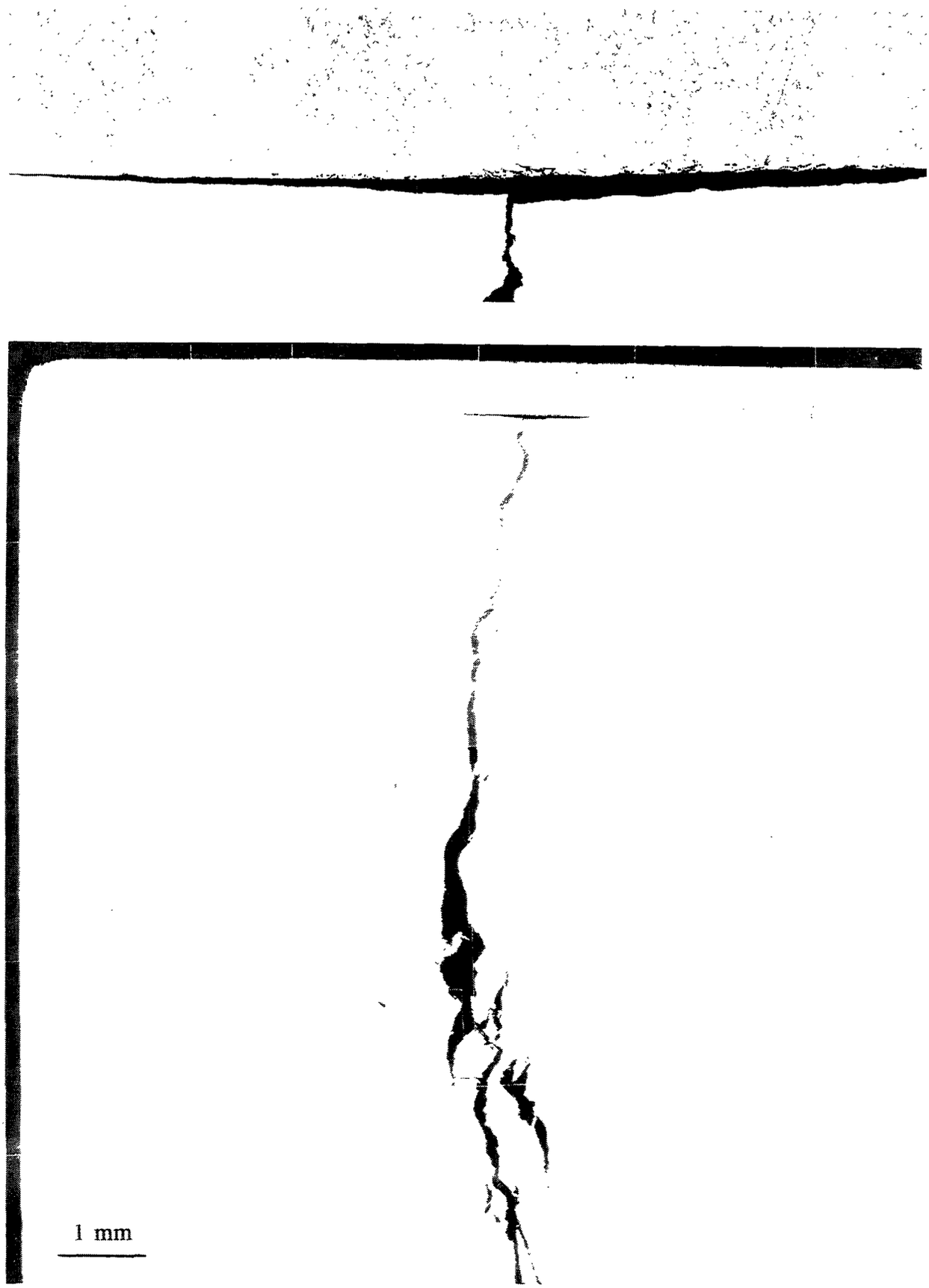

Figure 6. Intersection of a Crack in the Core Material with the Cladding, Disk #2.

4. Discussion of Results

Examination of the Zircaloy-clad uranium disks from the depleted uranium source showed that cracks were present in the cladding on the front and back face of the first disk. The faces of the first disk were distorted and measurable changes in the thickness of the disk had occurred. Observable distortion was also present on the front face of the second disk. Destructive examination of these disk showed cracking of the uranium in both disks. Corrosion products (UO_2 and UH_3) were present in the cracks in the first disk, but no corrosion products were present in the second disk. The results very strongly indicate that the cracking of the uranium preceded the cladding failure. The cracking of the uranium alloy appears to be in agreement with observation of distortion of uranium under conditions of irradiation and thermal cycling [3-5]. The presence of cracks in the uranium of disk #2 indicate that the thermocouple was not the initiator of the failure. The presence of corrosion products along the cracks, the relatively large amount of corrosion product found at the region of maximum cladding distortion, and the crack at the back face of disk #1 indicate that the reaction was limited by the availability of water in contact with the uranium. The thermocouple in the first disk may have exacerbated the corrosion by providing additional exposed surface area once water entered the cladding. The presence of hydride in the corrosion product indicates that the saturation temperature of the water was not exceeded.

5. Conclusions

Results of the detailed examination of the first two disks from the depleted uranium source assembly show that cracks occurred in the core material uranium before the cladding failed. These core material cracks were induced by anisotropic growth of the alpha-uranium caused by irradiation and thermal cycling at the operating temperature of the source. A second phase was present in the cladding at the core-cladding interface where a major crack in the uranium intersected the cladding in the second disk. If the second phase is an intermetallic compound, as was found in some cases during the manufacture of the disks[6], it is a brittle phase that could have resulted in an debonded condition. Such a bond failure could have contributed to the cracking of the cladding as a result of slightly greater amplitude of the thermal cycles, but a debond is not considered the root cause of the cracking of the core material. There was no evidence of failure of the circumferential seam weld or failure of the welds at the thermocouple well.

The widening of the cracks in the core material stressed the cladding and eventually led to its failure, probably a fatigue failure induced by the thermal cycling. Once the cladding failed, water entered through the crack in the cladding and found its way into the cracks in the core material. As the water reacted with the uranium it formed uranium dioxide and uranium hydride which have much lower densities that the metal. The volume expansion from these reactions was partially responsible for the distortion of the cladding that was observed for the first disk. The projection near the center of the back side of the first disk was caused by the formation of a pocket of corrosion product at that location. The thermocouple well in disk #1 appears to have weakened the disk structurally and enhanced the formation of corrosion product, once water had entered the cladding, by providing additional surface area in the core material.

The extensive formation of corrosion product in the core material cracks and the release characteristics of fission gas from uranium metal indicate that the source was operated for at least some time after the initial failure of the cladding with no adverse consequences. Measurable gas release is hypothesized to have occurred only after a significant amount of the corrosion products had formed.

These results are sufficient to indicate that the use of an alloy that stabilizes the uranium in the cubic (isotropic) gamma phase should greatly lengthen the useful life of the source. The examination also indicates that a second phase at the core-cladding interface may have played a secondary role in the failure of the cladding. Therefore, steps should be taken to avoid conditions that could result in the formation of intermetallic or other brittle phases at this interface.

6. References

[1] B. A. Loomis, H. R. Thresh, G. L. Fogle, and S. B. Gerber, "Design, Production, and Evaluation of a Zircaloy-clad Uranium Target for an Intense Pulsed Neutron Source Application", Nuclear Technology, Vol. 55 (December 1981), p. 617-627.

[2] J. M. Carpenter and A. G. Hins, "Experience with IPNS Targets", ICANS XII, Rutherford-Appleton Laboratory, May, 1993, Rutherford-Appleton Laboratory report 94-025, (1994), p. T-1 to T-11.

[3] L. T. Lloyd and R. M Mayfield, "Microstructural Changes of Uranium Upon Thermal Cycling", Transactions of the ASM, Vol. 50 (1957), p. 954-980,

[4] J. H. Kittel, "Preliminary Experiments on Irradiation Cycling and Partial Beta-Phase Irradiation of Uranium," ANL-5712 (April 1959)

[5] A. N. Holden, *Physical Metallurgy of Uranium,* Addison-Wesley Publishing Company, Inc., Reading, MA, p. 164-195

[6] A. G. Hins, et al., "A Study of Core/Cladding Bonding in IPNS Booster Target Discs," Proc. Second International Conference on Hot Isostatic Pressing, Gaithersburg, MD, June 9, 1989. p. 281-291

The submitted manuscript has been authored by a contractor of the U. S. Government under contract No. W-31-109-ENG-38. Accordingly, the U. S. Government retains a nonexclusive, royalty-free license to publish or reproduce the published form of this contribution, or allow others to do so, for U. S. Government purposes.

EUROPEAN SPALLATION SOURCE
General ESS Meeting
October 16-19, 1995
Weinfelden, CH

TARGET AND STRUCTURAL MATERIALS UNDER DUAL-BEAM IRRADIATION

Eric Camus, Nelja Wanderka and Heinrich Wollenberger

Hahn-Meitner-Institut Berlin GmbH, Glienicker Strasse 100, 14109 Berlin, Germany

The European Spallation Source (ESS) is planed to have a beam power of 5 MW (3.75 mA of 1.334 GeV protons). This is by a factor 30 higher than the available most powerful spallation source ISIS at Rutherford-Appleton Laboratory (RAL) in Great-Britain. This causes a damage rate of approx. 10 dpa (*displacements per atom*) per month in target materials (W or Ta) or structural materials (steels for beam windows, vessels). The high energetic protons produce, beside damage, high levels of transmutation products. One main characteristics of the spallation reaction is the simultaneous production of high levels of H and He. H and He are produced at rates of approx. 3000 appm/dpa and 200–300 appm/dpa, respectively. Both damage and transmutation products have detrimental effects on mechanical properties of target and structural materials.

The problem of radiation damage by high energy protons in different alloys has been recently reviewed by Ullmaier and Carsughi [1]. Main conclusion of this bibliographical work is that available data set is, as far, too small to allow any reliable prediction of lifetime of the different components.

At HMI, simulation irradiations using heavy ions and helium or hydrogen ions at the dual-beam facility are being carried out. The decisive advantages of such irradiation experiments are:

- (i) high damage levels and high helium or hydrogen contents can be produced within few hours. Such levels cannot be reached in a reasonnable time in any spallation facility;
- (ii) the irradiation parameters (damage rate, implantation rate, temperature) can be varied easily. Such fundamental study is indeed necessary. As shown in Fig. 1, displacement rates and He production rates are very different from one radiation field to another, even if one considers only spallation irradiations. It will be necessary to extrapolate existing data on the ESS typical irradiation field. Effect of changing the damage rate is generally well understood, as it has been investigated extensively, both theoretically and experimentally, in the Fusion Reactor Program. Such extensive studies are not available concerning the influence of helium/hydrogen implantation rate, especially in the low temperature region in which the spallation source is expected to operate;
- (iii) the irradiated specimens are not radioactive and can be analysed with the conventional methods available at HMI such as transmission electron microscopy.

Here, we report on some preliminary results obtained on tantalum as target material and on ferritic/martensitic steels (HT9 type steels or comparable steels), which are proposed to be used as structural materials. Goal of these investigations is to correlate the results with those obtained at spallation irradiated specimens and to investigate the unexplored field of simultaneous production of damage, helium and hydrogen at high levels.

1 Evolution of ferritic/martensitic steel under dual-beam irradiation

Ferritic/martensitic steels are under discussion for use as beam window material and confinement material for the ESS project. As discussed very extensively in a recent publication by Dai [2] (PSI, Switzerland), ferritic/martensitic steels of HT9 type (HT9 steel, German DIN 1.4970 steel, Manet steel or comparable German DIN 1.4926 steel) have excellent properties in terms of strength, thermal conductivity, thermal strength resistance, corrosion resistance, void swelling, and irradiation creep resistance, as compared to austenitic steels. The composition of the Manet steel (fusion program NET) and of the DIN 1.4926 steel (PSI beam window) are given in Table 1. For comparison, the composition of the F82H steel is given. This steel is now under consideration in the fusion program ITER as a low activation steel. It would be meaningful to investigate its possible use for ESS. In the expected service temperature region of interest for ESS (i. e. between 473 K and 773 K after G. Bauer [3]), only few experimental data are available on these steels. We have investigated the microstructural evolution of the HT9 type steel under dual-beam irradiation with two experimental techniques: (i) with field-ion microscopy with atom probe (FIM–AP) to get information on phase stability, and (ii) with transmission electron microscopy (TEM) to get information on helium bubble formation.

1.1 Phase stability

Concentration depth profiles of chromium as obtained by FIM–AP after dual-beam irradiation at temperatures between 673 K and 773 K are shown in Fig. 2. The samples were irradiated to a fluence of 50 dpa (displacement rate of 10^{-2}dpa s^{-1}) with a He/dpa implantation rate of 200 appm dpa^{-1}. In total, 1 at.% He were implanted. This corresponds to an ESS service time of approx. 1 year (full power). After irradiation at 673 K and 698 K, the chromium distribution is found to be statistically different from a random distribution we would expect for a solid solution. A detailed analysis yields a variation of the concentration amplitude ΔC of approx. 2.2 at.% to 2.8 at.%, respectively. At the temperatures of 723 K and 773 K, chromium clusters with diameters of about 4 nm with concentrations up to 25 at.% are observed. These results are reported extensively elsewhere [4]. We conclude from this study that the observed decomposition is caused by radiation-induced segregation in the lath structure of the annealed martensite. This effect has the detrimental consequence on mechanical properties to reduce the ductility and to increase the yield strength of the material [5,6].

1.2 Helium bubble formation

As helium is insoluble in metals, it will precipitate as bubbles. These bubbles, especially when they form at grain boundaries, have a detrimental effect on the mechanical properties and fatigue time of the materials. Experimental data on temperature dependencies of bubble densities observed under different experimental conditions have been compiled by Singh and Trinkaus [7] and demonstrate the key role of the helium generation rate for microstructural evolution. As the helium generation rate is different, even from one spallation environment to another, correlation of data is necessary. However, as pointed out by Singh and Trinkaus, lack of data in the low temperature regime, where ESS should operate, makes it impossible to confirm or infirm the prediction of theoretical models. This requires further studies. We have started respective investigations at HMI. Figure 3 contains, as examples, two TEM micrographs of the DIN 1.4926 steel implanted with He at 473 K and 773 K. Note that the size of the bubbles decreases as the temperature decreases. It renders such studies difficult as bubble size is at the limit of resolution of TEM. Investigations with high resolution electron microscopy (HREM) are planed, but are also difficult due to the high density of defects produced by the irradiation.

2 Hardness of tantalum and steel after helium implantation

Helium has been implanted at room temperature in both tantalum and DIN 1.4926 steel with energies up to 400 keV. The penetration depth of such ions is approx. 1 μm. Hence, the hardness must be measured with a nanoindenter (TU Berlin). The results are shown in Fig. 4, where the Vickers hardness is plotted as a function of the He concentration. In both cases, increase of the He concentration results in a drastic increase of the hardness of the specimens. This hardening might be interpreted in terms of a shift of the ductile-brittle transition temperature ΔDBTT. Such transition temperature appears in bcc alloys. It is possible to correlate the change in hardness with ΔDBTT. In the case of the HT9 type alloys, it has been done by Chen and Jung [8]. The observed increase in hardness of ΔHV= 150 would correspond to a shift ΔDBTT= 150 to 300 K. As the DBTT of such an unimplanted/unirradiated steel is just below room temperature, the DBTT under working condition would be around 400 to 570 K. Similar shifts have been observed under neutron irradiation [2].

3 Conclusion

The investigations carried out for environments which are different from the ESS spallation conditions (ISIS, Los Alamos, dual-beam irradiations) must be correlated to ESS conditions in order to be useful for the ESS design. Thus, the influence of the parameters, temperature, damage rate, implantation rate of helium and hydrogen, on bubble morphologies and, in turn, on the mechanical properties of the gas-containing materials must be investigated. It is clear from the

wt.%	ITER F82H steel	NET Manet steel DIN 1.4914	PSI window Steel DIN 1.4926
Cr	8.0	10.3	11.8
C	0.1	0.1	0.21
Si	0.1	0.14	0.36
Mn	0.1	0.75	0.47
P	0.005	0.005	0.016
S	0.002	0.0045	0.003
Ni	0.03	0.65	0.63
Mo	0.01	0.57	0.90
V	0.2	0.19	0.29
Nb	0.0002	0.14	<0.005
⋮			
W	2.0	—	0.02
Ta	0.04	—	—
Fe		bal	

Table 1: Composition of different Fe-Cr steels investigated in the fusion project and in the spallation project

experimental studies cited above that the combination of all damage sources, i.e. introduction of (i) defects, (ii) hydrogen, and (iii) helium at high levels and their interaction plays a determinant role in the evolution of the microstructure. In particular, the interaction of helium and hydrogen has to be studied [9]. Experiments at our dual-beam facility are in progress.

The morphologies and microstructures obtained under these simulation experiments must then be compared to the morphologies observed and to the mechanical properties of the spallation irradiated materials (investigations done at KFA Jülich by F. Carsughi and Prof. Ullmaier).

REFERENCES

[1] H. Ullmaier and F. Carsughi, Nucl. Instr. Meth. in Phys. Res. **B101**, 406 (1995).

[2] Y. Dai, Proceeding of the 13th Meeting of the International Collaboration on Advanced Neutron Sources (ICANS-XIII), October 11–14, 1995, PSI, Switzerland.

[3] G. Bauer, Liquid Metal Target Station, ESS-report 95–20–T (1995).

[4] N. Wanderka, E. Camus, V. Naundorf, C. Keilonat, S. Welzel, and H. Wollenberger, J. Nucl. Mater. (in press).

[5] K. K. Bae, K. Ehrlich, and A. Möslang, J. Nucl. Mater. **191–194**, 905 (1992).

[6] A. Kimura, L.A. Charlot, D.S. Gelles, and R.H. Jones, J. Nucl. Mater. **212–215**, 725 (1994).

[7] B.N. Singh and H. Trinkaus, J. Nucl. Mater. **186**, 153 (1992).

[8] Chen, and P. Jung, J. Nucl. Mater. , (1994).

[9] E. Camus, N. Wanderka, and H. Wollenberger, ESS-report 95–29–T (1995).

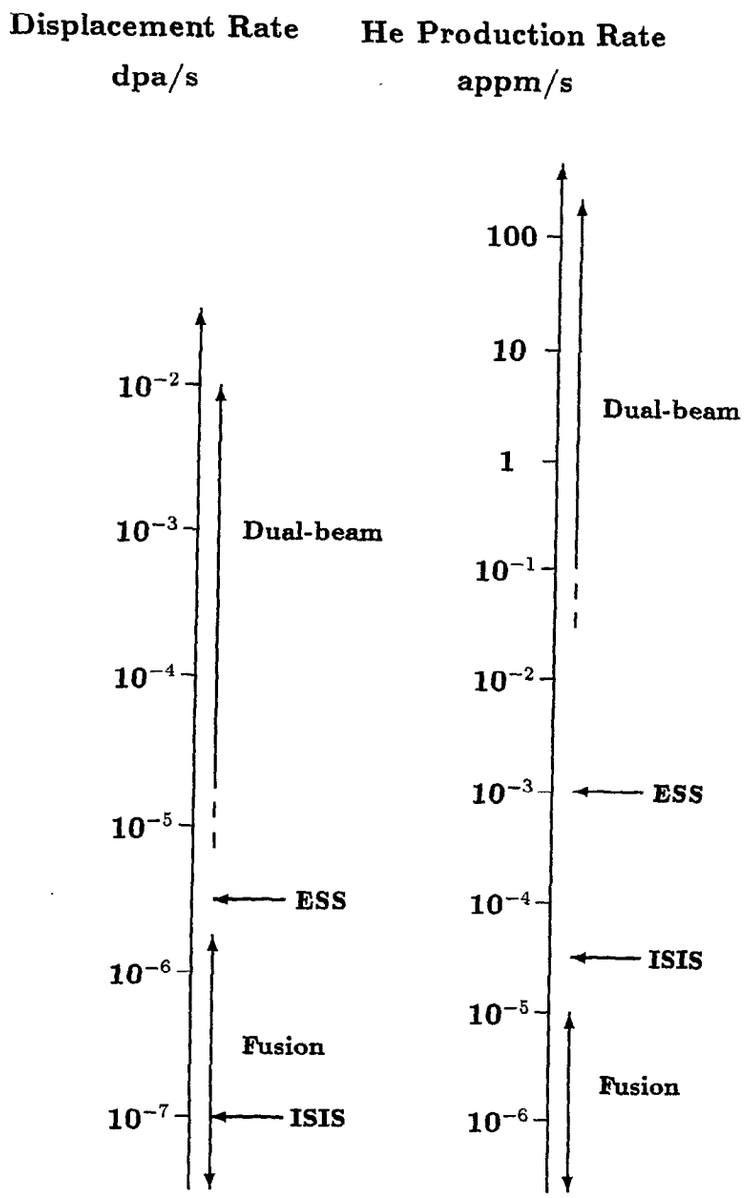

Figure 1: Comparison of different environments in terms of displacement rate and helium production rate (ESS: European Spallation Source; ISIS: Spallation Source at RAL).

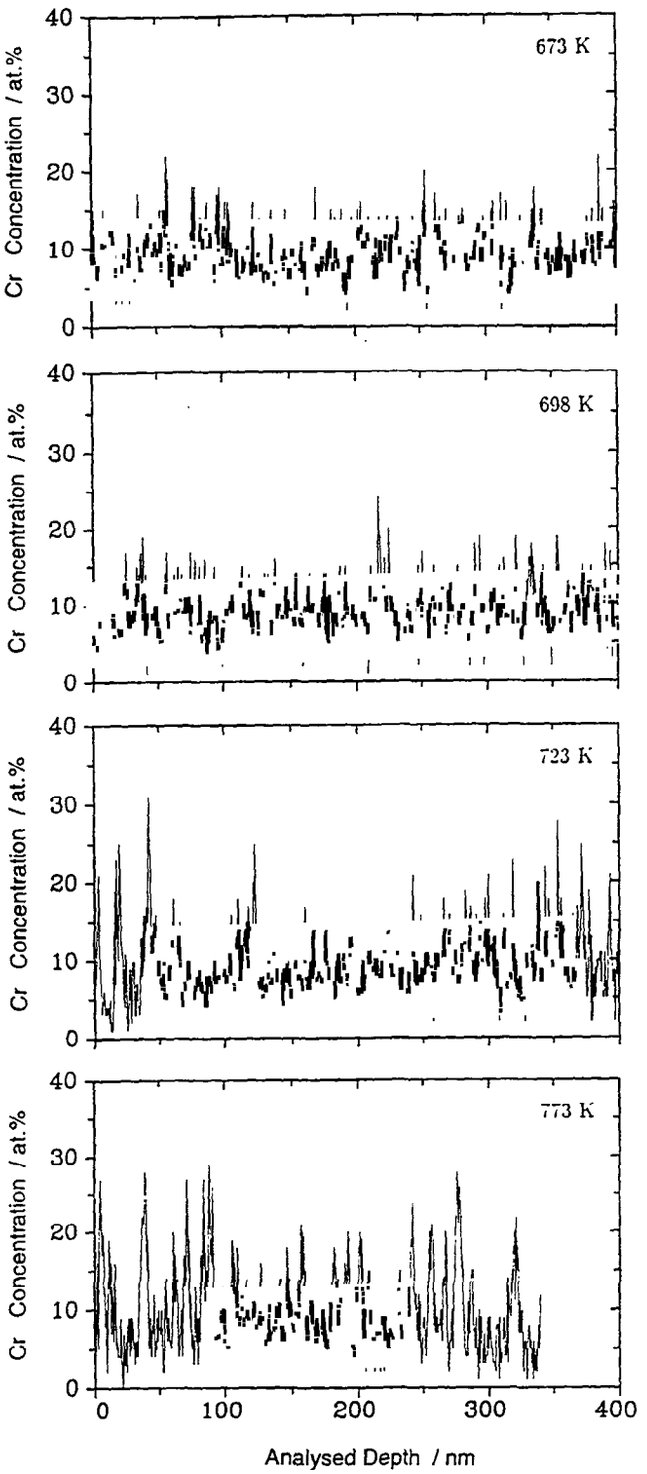

Figure 2: Chromium concentration profiles of Manet steel obtained after irradiation to 50 dpa implanted with 1 at.% helium with an implantation rate of 2 appm s^{-1} at temperatures between 400°C and 500°C. The implanted level of 1 at.% helium corresponds to approx. 1 year ESS service time (full power).

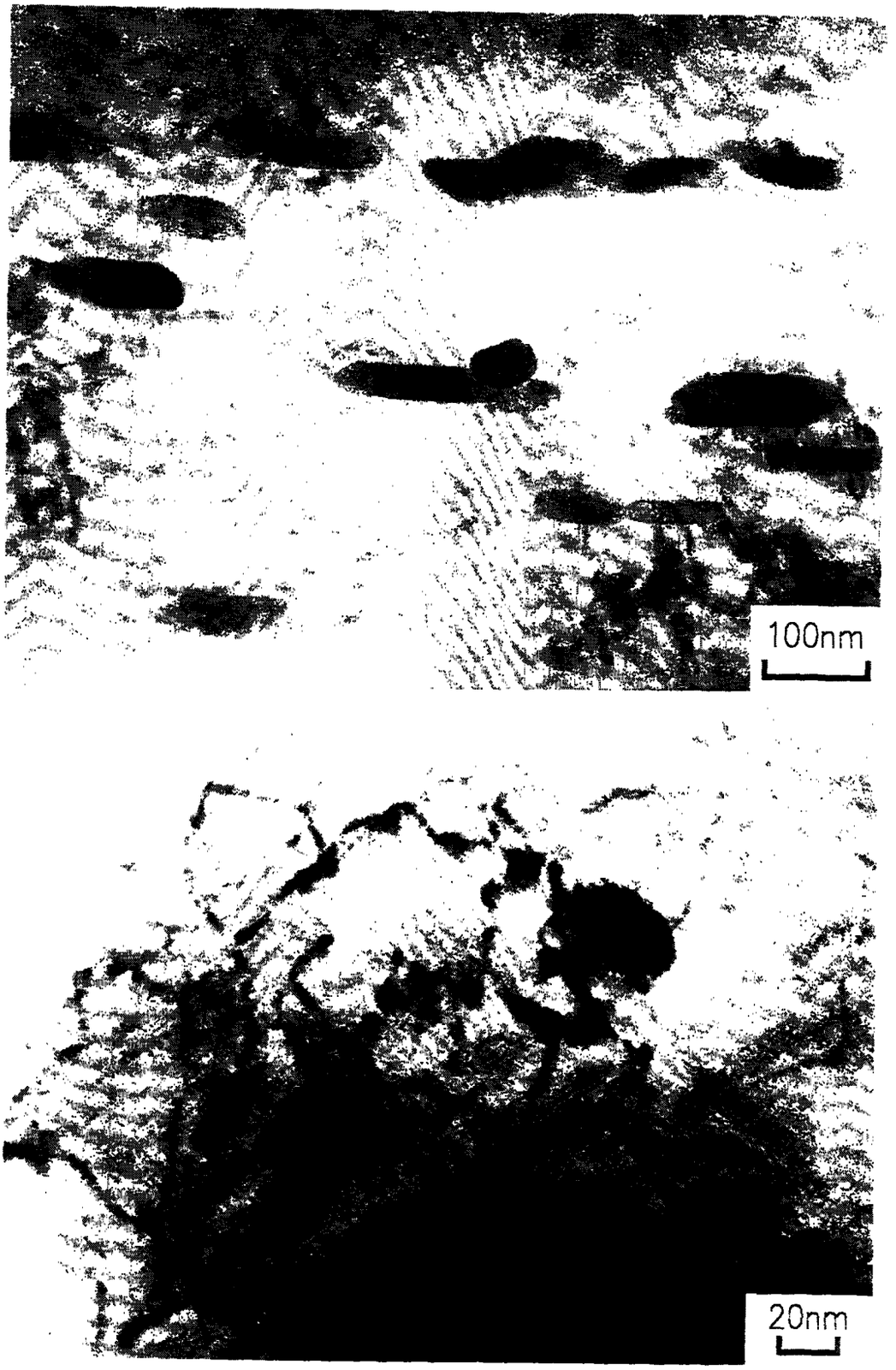

Figure 3: TEM micrographs of DIN 1.4926 steel obtained after irradiation to 30 dpa implanted with 0.6 at.% helium at a) 773 K and b) 473 K with an implantation rate of 2 appm s^{-1}. The implanted level of 0.6 at.% helium corresponds to approx. 6 months ESS service time (full power). In the upper image, helium bubbles are clearly visible and precipitate preferentially at grain boundaries, lath boundaries and precipitate/matrix interfaces. In the lower image, a high density of very small helium bubbles is visible.

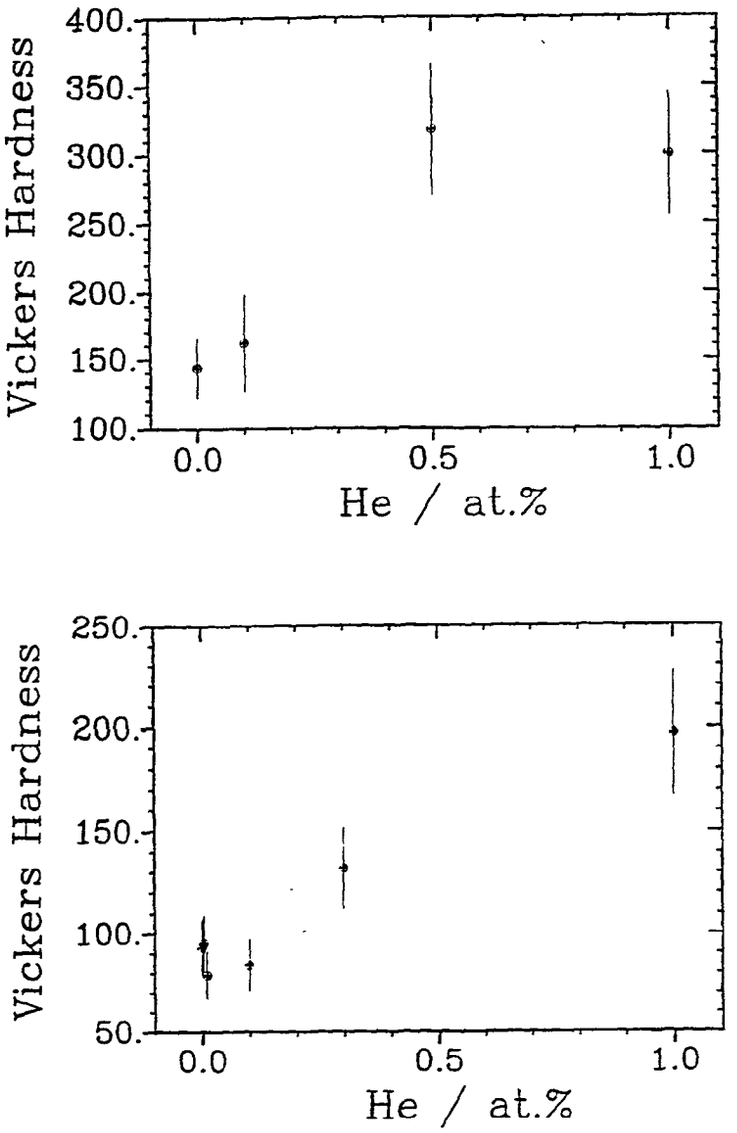

Figure 4: Vickers hardness of a) HT9 type steel and b) tantalum as a function of implanted He concentration. The materials were implanted at room temperature with an implantation rate of 10 to 50 appm s^{-1}. The implanted level of 1 at.% helium corresponds to approx. 1 year ESS service time (full power).

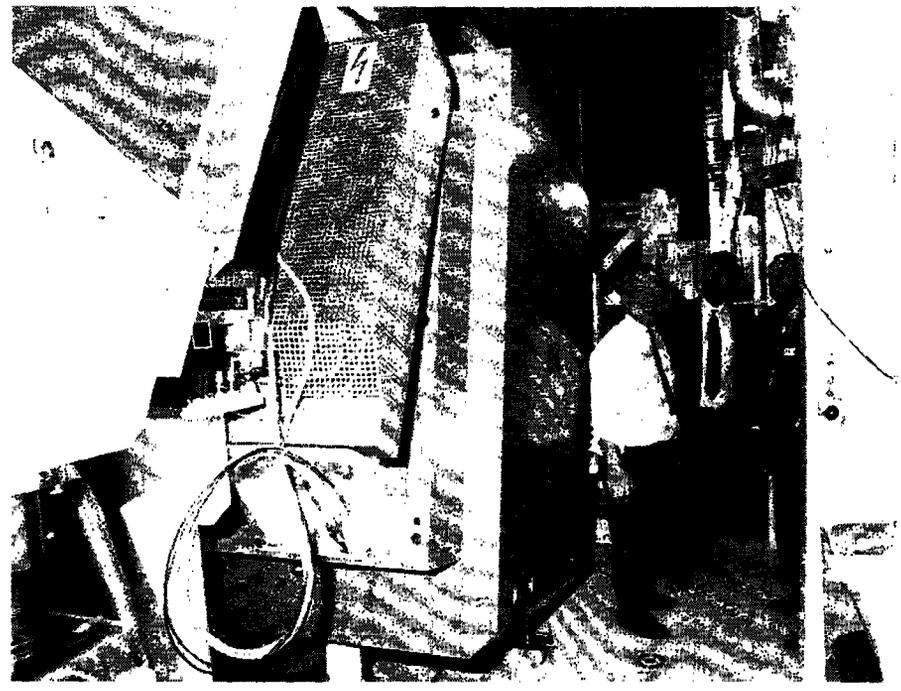

Accelerator Systems and Components

ICANS-XIII
13th Meeting of the International Collaboration on
Advanced Neutron Sources
October 11-14, 1995
Paul Scherrer Institut, 5232 Villigen PSI, Switzerland

THE LOS ALAMOS LONG-PULSE-SPALLATION-SOURCE DRIVER

Andrew J. Jason

Accelerator Technology Division
Los Alamos National Laboratory
Los Alamos, NM 87544

ABSTRACT

A Los Alamos study has investigated the possibility of adapting the LANSCE facility to a 1-MW Long-Pulse Spallation Source (LPSS) delivering H^+ beam to a new spallation target in 1-ms long pulses at a repetition rate of 60 Hz, while maintaining the present short-pulse capabilities. The study noted limitations of the LANSCE linac and has specified a scheme for high-reliability operation with low beam loss. Such an upgrade would provide a very inexpensive spallation source equivalent to a large reactor. Novel aspects of the scheme are stressed.

1. Background

A schematic diagram of the LAMPF linac is shown in Fig. 1. Ion sources placed in three Cockroft-Walton generators produce H^+, H^-, and P^- (polarized H^-) beams. The beams are bunched into a 201.25-MHz time structure and merged (as well as chopped in the case of H^-) in the (approximately 12-meter-long) Low Energy Beam Transport (LEBT) system at an energy of 750 keV. Injection into a four-tank, 201.25-MHz Drift-Tube Linac (DTL) and acceleration to 100 MeV then follows. The beam is then matched transversely to an 805-MHz side-coupled linac (SCL) by elements in the Transition Region (TR). The TR has two magnetically separated beam paths for separate transverse matching and longitudinal phasing of positive and negative species. The SCL accelerates to a nominal 800 MeV in 44 modules and constitutes over 90% of the linac length. The 201.25-MHz "micropulse" structure formed by the linac constitutes the substructure of nominally 1-ms-length "macropulses," delivered at up to twice the line frequency, 120 Hz. Beam is partitioned by a "Switchyard" to the delivery areas. Presently the beam is delivered to three facilities:

- Area A (primarily nuclear physics) with H^+ beam at somewhat less than a megawatt to 120 Hz. The exact pulse structure depends on user requirements and the needs of PSR and WNR of beam power and with ~13 mA or higher of peak current at repetition rates of up 120 Hz, twice the line frequency.
- The proton Storage Ring (PSR) with less than 100 kW of H^- beam power at 20 Hz. The PSR drives the LANSCE neutron-spallation source.

Keywords: LANSCE, Linac, Long-pulse

- Weapons Neutron Research (WNR) with 16.7-MHz-chopped H^- beam delivered with the H^+ macropulse.

The linac performs well under these circumstances and has tolerable activation and over 90% reliability. As this and other studies (along with operational experience) have found, appreciable increases in the peak power at these duty factors promote rapidly increasing beam losses and decreased reliability.

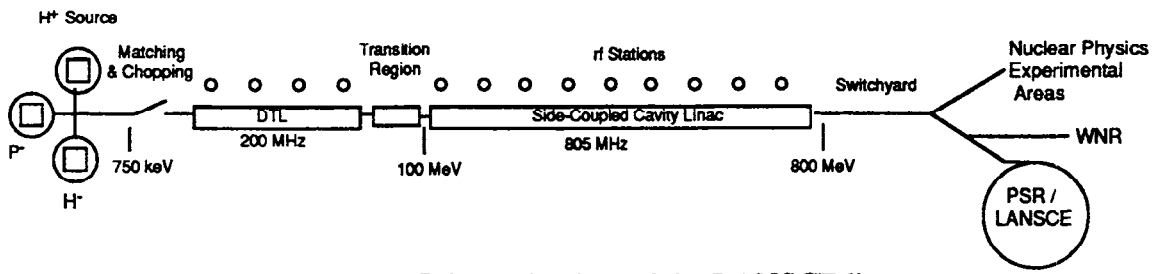

Fig.1. Schematic view of the LANSCE linac.

The LPSS requires 1-MW H^+ beam power delivered to the spallation target with macropulses of 1.0 ms length and 60 Hz repetition rate. This implies a peak output current of nearly 21 mA. Maintenance of interlaced PSR operation at from 20 to 60 Hz and WNR operation as requested is also required in the remaining 60 Hz.

2. Limitations of the present facility

Limitations of the LANSCE linac in achieving reliable operation with low equipment activation, under the LPSS beam requirements, stem from four major causes:

1) Limitations in the present 201.25-MHz rf system. The present system cannot provide the required peak power at the required duty factor.

2) The inability of the LEBT bunching system to provide a clean longitudinal match to the DTL causing subsequent losses in the TR and SCL. Such losses increase rapidly with peak current and would result in very high activation for the levels here proposed.

3) The lack of provision for longitudinal matching of the TR to the linac.

4) The speed of the 805-MHz control loops in the SCL rf system. Substantial loss is generated by the macropulse turn-on transient.

The first of these items relates to the limitations of the 7835 power triodes that constitute the final amplifiers of the 201.25 MHz DTL rf system. The maximum safe plate dissipation of the tubes is 250 kW. The DTL consists of four Alvarez tanks driven by four nearly identical RF power systems with energy gain in each tank of 4.64, 35.94, 31.39, and 27.28 MeV in that order. With present operating parameters, the peak rf loads approach 3 MW with plate dissipations hovering around the 250 kW limit. The increased LPSS current requires nearly 4- MW peak power that, combined with the PSR duty factor cause a plate dissipation of over 300 kW in three of the amplifiers. The higher peak powers also stress the present modulators tubes because of the higher plate voltage required. Additionally, it is feared that adequate replacements for the triodes will not be available in the future. A redesign of the rf system is needed for LPSS operation.

The second item, bunching in the LEBT, is done by a pair of 201.25-MHz resonant cavities at 750 keV. The single frequency cavities are inherently incapable of compressing the dc beam into a small region of longitudinal phase space. Hence, a substantial fraction of the particles (~25%) fall outside the DTL phase acceptance and are not accelerated, to be lost in tank 1. A further fraction (several percent) are injected into a nonlinear region of the DTL acceptance and cannot be longitudinally matched to the smaller SCL 850 MHz bucket. These particles are lost near the entrance of the SCL at 100 MeV and at a transition in the focusing lattice near 212 MeV. This picture is substantiated by the SCL activation pattern and loss monitor data as well as by beam dynamics simulations. Such loss increases rapidly with peak current. Hence, a better bunching scheme is required to implement the LPSS scheme.

The lack of a linear longitudinal match to the SCL also causes an appreciable part of the beam loss. This is distinct from the nonlinear phenomena described above, which cannot be aided by a better linear match.

It is to be noted that the SCL, which constitutes 90% of the linac, is very robust. Tests at 27-mA peak current (but with low duty factor) demonstrate the controllability and confirm its peak-current capacity despite heavy loading of the cavities.

3. Upgrade Recommendations

Several recommendations were made by the study to allow peak current increase to the LPSS levels and to maintain operation of WNR and PSR.

1) Replace the present injectors and DTL first tank with a 201.25-MHz Radio-Frequency Quadrupole (RFQ) linac to accelerate to an energy of 5.395 MeV. The H^+ and H^- beams are focused, chopped, and merged by a new LEBT at 100 keV before the RFQ. A two-buncher matching section is placed after the RFQ. This arrangement produces the appropriate transverse and longitudinal match to the second tank of the DTL.

2) Replace the 201.25 MHz rf system with a modern version that will produce adequate peak and average power.

3) Install an 805-MHz bunch rotator cavity in the TR that will provide a good longitudinal match to the SCL.

4) Upgrade the low-level rf-control system on SCL for removal of initial transient loss on the macropulse, and .operational ease.

5) An upgraded set of beam-diagnostic systems for better and more rapid machine tuning.
6) Provide transport to the LPSS target.

7) Install a laser-system that neutralizes H^- beam to provide for WNR operation.

8) A computer-control-system upgrade in support of the modifications.

With these modifications, a peak beam current of more than 25-mA can be supplied to the LPSS target to provide over 1.2 MW of beam power delivered at 60 Hz with a 1.0-ms macropulse length. A schematic drawing of the modified linac is shown in Fig. 2.

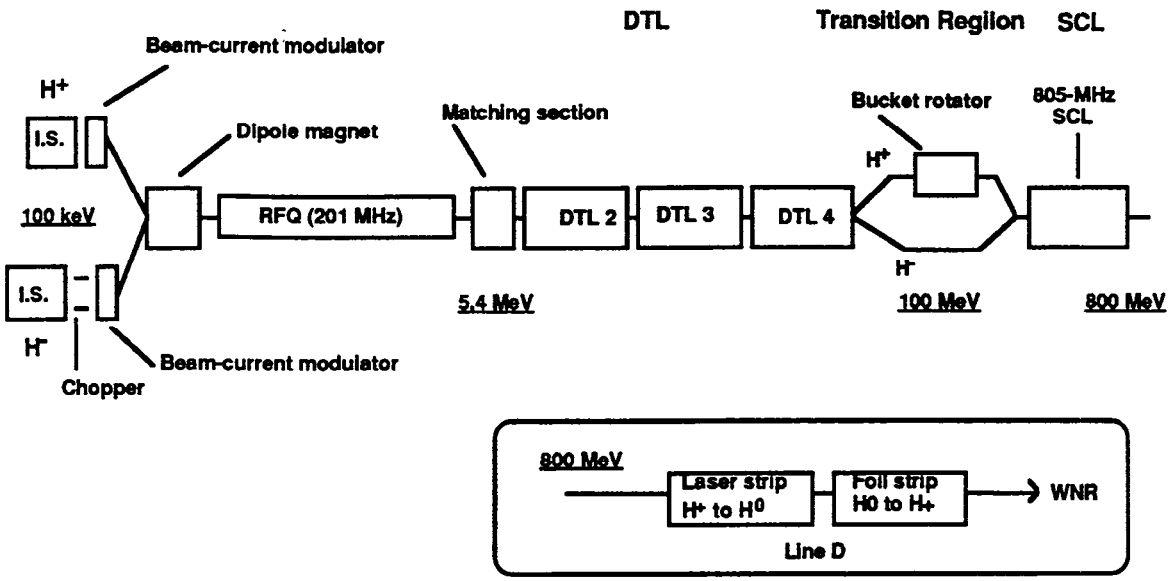

Fig. 2. Schematic of the LPSS linac upgrade

3.1 Injector and chopping

Adequate ion sources currently exist for both the H^- and H^+ beams. However, 2.8-MHz chopping at a duty factor of 75% for the 15-mA-peak-current H^- beam that supplies the PSR must be addressed. Currently, beam is chopped in the LEBT by a traveling-wave deflector that has a rise time of under 5 ns. Replacement of the LEBT by an RFQ requires a different chopping scheme. Post-RFQ chopping is quite feasible but would require an expensive installation. Chopping before the RFQ is seen as difficult because of the high beam neutralization and subsequent interaction between an oscillating positive-ion column and negative beam that distorts the transmitted beam, with a substantial emittance increase. This latter chopping scheme is believed to be feasible at a high energy (100 kV) and at the relatively low H^- currents needed.

We have devised an alternative pre-RFQ chopping method that removes beam neutralization by electrostatic focusing. To prevent neutralization in the deflector and maintain beam focusing, a novel quadrupole deflector is to be used. This traveling-wave structure is shown in Fig. 3. Undeflected beam is focused through a defining aperture by a constant quadrupole bias V on the side electrodes, with the deflector electrodes (upper electrodes in Fig. 3) set at ground potential. Activation of the deflector electrodes to $\pm V$, moves the beam off the defining slit, with substantial beam distortion by the sextupole field inherent in the deflecting arrangement. Despite this distortion the beam is completely chopped by the at the defining aperture.

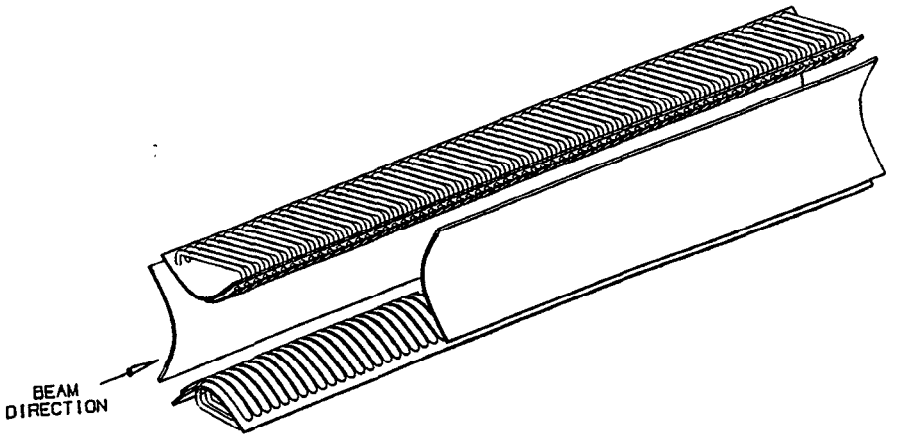

Fig. 3. Quadrupole traveling-wave deflector for use in an electrostatic LEBT. The device is 0.7-m long and sustains a deflecting voltage of just under a kilovolt across a gap of 19 cm.

The 2.6-m long line consists of an initial solenoid after the source, four electrostatic quadrupole matching lenses, the deflector, followed immediately by a defining aperture, and a final solenoid for matching into the RFQ. Simulations show that with a neutralized beam, substantial transmitted-beam distortion occurs. With the same simulation, using codes that have proven useful in linac design, the unneutralized case is adequately transported with currents over 30 mA. While the technique appears promising, experimental verification is needed.

3.2 RFQ

A 9.65-m long 201.25-MHz RFQ has been designed as the critical element in avoiding beam losses at the SCL entrance. The RFQ accelerates the beam from 100 kV to 5.4 MeV, replacing the LEBT and the first DTL tank. The less than 1-MW peak power required will be supplied by the original first-tank supply.

The RFQ provides excellent bunching. Beam dynamics results are summarized in Fig 4, which shows calculated results for the beam emerging from the DTL in the present configuration and with addition of the RFQ. Losses due the longitudinal tail in the present configuration are substantially reduced and DTL transmission increased. SCL losses for the LPSS are expected to decrease by a factor of over 300 from present nominal operation if longitudinal matching is done in the transition region. An alternative and less expensive scheme, using additional higher harmonics in the LEBT to enhance bunching can alleviate the loss somewhat.

3.3 201.25 MHz system

The main problem in the DTL-rf upgrade is the selection of an adequate final amplifier tube. A modern tetrode made by Thomson, the TH526, with many desirable features, is in production. Two such tubes in combination with a hybrid coupler would reliably supply the LPSS DTL at 18-mA peak current during development and commissioning. The final power amplifiers would later be upgraded to 6-MW peak power with a double-ended tetrode currently under development, the D28 Diacrode, having the same lower socket as the TH526.

Addition of a top slave cavity section would then be required. The present low-power portion of the system, recently upgraded, as well as the power supplies, would be used in this scheme.

Two options are under consideration for the rf window in each DTL tank. The present Rexolite windows function with rare arc overs at the present average power of over 350 kW. The upgrade requires a 33% increase in this average transmitted power, hence the window will be upgraded to a larger diameter with improved geometry and materials. Otherwise, the tank could be fed from two windows, with lower power requirements than at present, but tank retuning would be required.

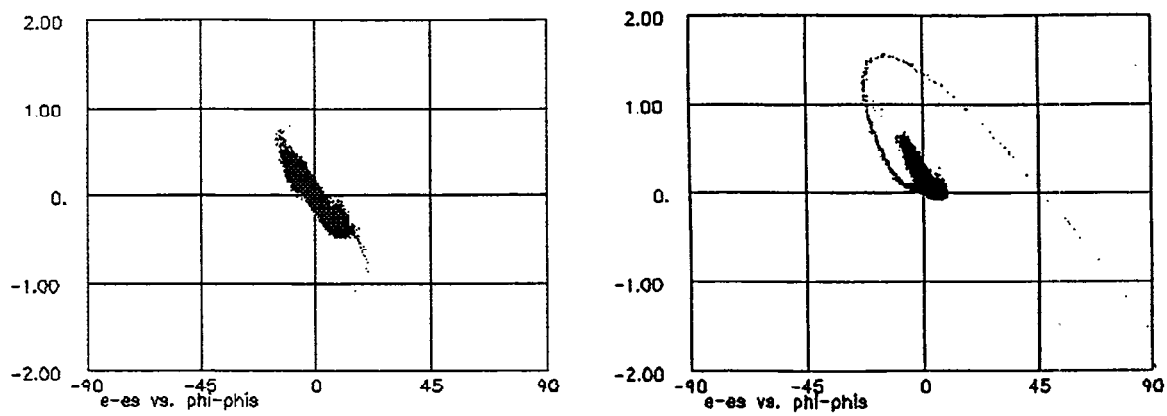

Fig. 4. Longitudinal phase space at 100 MeV for the present linac (left) and for the upgraded linac that utilizes an RFQ. Both plots are at 18 mA into the DTL. Vertical scales show energy in MeV while horizontal scales show phase in degrees

3.3 Transition region

The transition region contains two legs defined by dipole bends to form chicanes. Its purpose is to transversely match the 100-MeV H^- and H^+ beams to the SCL as well as providing a small path difference for the two species. Part of the beam that is not accelerated to full energy by the DTL is lost in the bends causing considerable activation. Addition of a single longitudinal cavity into the present configuration is ineffective in decreasing losses. With the upgrade, a single cavity dissipating 56 kW with an E_0TL of 1.0 MV provides good longitudinal matching. Whether or not to retain the present two-legged structure is to be determined; a straight-through configuration can serve both beams with proper rf phasing.

3.4 805-MHz system

A substantial fraction of the loss (as high as 40%) occurs due to the speed of the 805-MHz control and subsequent transient loss at the start of the macropulse. An adaptive feed-forward control system developed at Los Alamos appears promising in substantially reducing this loss. The 44 1-MW klystrons that drive the present are limited in peak output power to 1.25 MW. Allowing for a 10 % control margin, the maximum current that could be transported by the present rf system is near 30 mA.

3.5 Transport to target

The LPSS target is located in area A, a large shielded structure that presently contains several beam lines for nuclear physics programs. A long transport line exists that functions well in bringing beam to the area and needs only be augmented by an expander section. It is perhaps noteworthy that the gaussian-distributed beam can be well matched to the target by adding nonlinear elements to the expander. Fig 5 shows contour plots demonstrating the transverse confinement to the target with the proposed expander.

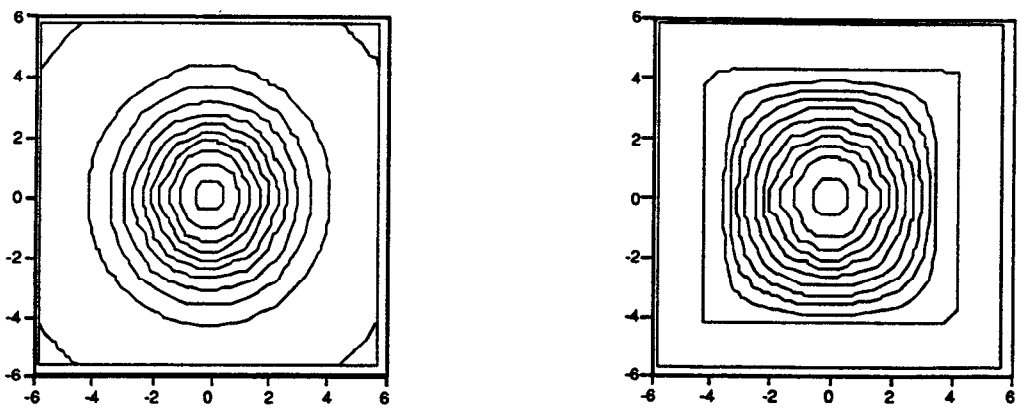

Fig. 5. Contours of beam intensity on the target for the linear expander (left) and the nonlinear expander (right).The contour lines are for relative intensities of 0.001, 0.1, 0.2,...1.0. The 1.0 contour corresponds to a current density of about 60 $\mu A/cm^2$ for a 1 MW beam. Dimensions are in cm.

3.6 Laser Chopping

The RFQ is incapable of accelerating single micropulses as required by WNR. The alternative scheme proposed uses a laser to neutralize single micropulses (~100 ps long) from the PSR beam at a rate of 555 kHz during the 800 ms macro pulse. The transport line to the PSR is configured so that such neutralized pulses will through a bend that directs the remainder of the beam into the ring. A thick stripper foil will then allow transport of the pulses to WNR.

Components that can be assembled to into a laser system exhibiting such performance are commercially available. A cw pumped mode-locked frequency-doubled Nd:YAG laser forms the driver for the system. Photon energy is 2.36 eV with 0.5 mJ per pulse for total laser power of 15 W. Transport of photons to the beam line may be stably accomplished by new fiber optics systems.

ACKNOWLEDGEMENTS

Work described here was performed by several individuals in AOT-Division. The support of the LANSCE ER office and the Los Alamos National Laboratory Directed Research and Development, under the auspices of the United States Department of Energy, is gratefully acknowledged.

PSI-Proc. 95-02

A-2

ICANS-XIII
13th Meeting of the International Collaboration on
Advanced Neutron Sources
October 11-14, 1995
Paul Scherrer Institut, 5232 Villigen PSI, Switzerland

MOSCOW MESON FACTORY LINAC FOR THE PULSED NEUTRON SOURCE

L. V. Kravchuk
Institute for Nuclear Research, Moscow 117312, Russia

Introduction

Pulsed Neutron Source IN-06 based on the Moscow Meson Factory (MMF) Linac is under construction now. The first stage of Neutron Source IN-06 is planned to be put into operation in 1996. The watercooled neutron target of silicious uranium will be exposed to the 500 MeV proton beam. The IN-06 disign parameters (thermal neutron peak flow of $5 \cdot 10^{15} n/cm^2 \cdot s$, 35 μs pulse, 50 Hz repetition rate, average flow of $8 \cdot 10^{12} n/cm^2 \cdot s$) may be achived after storage-compressor ring (PSR) comissioning in 1998.

We studied the possibilities of IN-06 upgrade by means of MMF Linac modernization using existing building areas, shielding and net power consumption. Our analyses have shown that peak flow of $10^{17} n/cm^2 \cdot s$ and average flow of $10^{14} n/cm^2 \cdot s$ could be achievd with the pulse length of 30 μs and repetition rate 25 Hz using PSR and neutron multiplication ion target. All necessary linac innovations are not overstep the limits of the contemporary state of art. To get the above mentioned parameters we need to increase the energy of the linac up to 700 MeV and beam pulse length up to 300 μs with repetition rate 25 Hz. Thus neutron multiplication target will be exposed to 10^{14} proton per pulse which corresponds to 10 MW power dissipation in target [1].

MMF Linac was designed with following parameters: maximum energy of protons and H^- ions 600 MeV; average beam current 500 μA; pulse current 50 mA; beam pulse length 100 μs; repetition rate 100 Hz. Recently the proton energy of 423 MeV was achived which is determined with the number of klystrons on hand which are used for DAW Linac RF power supply. By the end of 1995 6 more klystrons will be manufactured that provide the beam energy of 500 MeV. Regular linac operation take place with the average current of 60 μA (demonstrated 75 μA). Total beam losses are not exceed design value (0,1 $\div$ 0,2)% [2]. Beam pulse length of 70 μs; and repetition rate 50 Hz are determined with experimental requirements as well as with power consumption expenditures.

Linac Upgrade Possibilities

The following linac system must be upgrated to get 700 MeV proton energy and 300 μs beam pulse length [3]:

Accelerating system. RF pulse length increase up to 300 μs leads to thermal heat growth in DTL as well as in DAW (disk and washer) cavities. It seems that necessary heat transfer could be provided with the water flow increase as well as with water temperature lowering in the secondary loop. Addtional expenditure of electric power could be compensated due to elemination existing heaters and reduction of the water pumps number in the modernized cavity reso-

nant frequency control system.

Energy upgrade from 600 MeV to 700 MeV could be fulfilled due to addition of one more 4-section DAW module onto existing girder at the end of accelearting tunnel. This module has to provide the accelearting gradient of 7 MeV/m. Our experience shows that is fully guaranted in DAW accelerating structure.

DTL RF Power Supply. To meet 300 μs beam pulse we need to increase the modulator pulse length from 360 μs to 500 μs. It requires to increase the number of cells in delay line, to modify the pulsed transformer in the GMI-44A anode circuit, to increase the pulse length of the submodulator. Similar modifications have to be done in modulator of the powerful driver amplifier to increase its pulse length from 420 μs to 550 μs.

DAW Linac RF Power Supply. There are 28 991 MHz 4,75 MW power supply channels (one for each 4-section DAW cavity) in the DAW Linac. For 300 μs 50 mA beam pulse operation we need to modify the klystron driver amplifiuer together with its modulator as well as the output powerfull klystron itself. The number of cells in the delay line of the driver amplifier modulator must be increased twice. The pulsed transformer must be redesigned to eliminate the iron saturation due to longer pulse.

To provide 300 μs operation with the same net power consumptionand equipment sizes unchanged we have three options:

- powerfull klystron modulator is reconstructed using the same elements of the delay line. The KIU-40 old klystron may be utilized.
- powerfull klystron modulator is modified for the operation with low volatge (50 kV) high efficient 42 beam klystron "Atlant", which was developed recently by the scientific and technical firm "Thorium".
- completely new delay line has to be developed and constructed.

After some modelling and testing one of those three options has to be choosen taking into account its reliability. The RF channel for the last high accelearting gradient cavity differs from those regular ones significantly. It must be developed separately and needs additional net power.

Ingection system. Existing injectors on the base of accelerating tube and 750 kV pulsed transformer have to be substitutde with RFQ section designed to provide 50 mA in the pulse length of 300 μs with 25 Hz repetition rate. 198,2 MHz RFQ injector must be placed close to the first DTL cavity.

Conclusion

The fulfilment of the above mentioned steps of the MMF Linac upgrade together with PSR comissioning and neutron multiplication target insted of silicious uranium one instalation make the Pulsed Neutron Source based on the MMF Linac beam highly competitive.

Acknowlegment

The author is grateful to Drs. S. Esin, Yu. Stavisski, P. Ostroumov, A. Kvasha, V. Leontiev for their collaboration and helpful discussions.

References

[1] M. Grachev, L. Kravchuk, Yu. Stavisski. Moscow Meson Factory Pulsed Neutron Source. Possibilities of development. Proc. of PANS-II Conference, Dubna, Russia, 1994.

[2] S. Esin, L. Kravchuk, V. Matveev et al. Commissioning and operating of the Moscow Meson Factory Linac. Proc. of LINAC Conference, Tsukuba, Japan, 1994, p.31.

[3] S. Esin, L. Kravchuk, A. Kvasha et al. MMF Linac Upgrade Possibilities for the Pulsed Neutron Source. Proc. of 1995 Particle Accel. Conf., Dallas, USA, May 1995.

High Current Ion Source Development at Frankfurt

K. Volk, H. Klein, A. Lakatos, A. Maaser, M. Weber
Institut für Angewandte Physik, Universität Frankfurt

I. Introduction

The development of high current positive and negative ion sources is an essential issue for the next generation of high current linear accelerators. Especially, the design of the European Spallation Source facility (ESS) and the International Fusion Material Irradiation Test Facility (IFMIF) have increased the significance of high brightness hydrogen and deuterium sources. As an example, for the ESS facility, two H^--sources each delivering a 70 mA H^--beam in 1.45 ms pulses at a repetition rate of 50 Hz are necessary [1]. A low emittance ($\varepsilon_{rms,norm} \sim 0.1\pi$ mmmrad) is another important prerequisite. The source must operate, while meeting the performance requirements, with a constancy and reliability over an acceptable period of time. The present paper summarizes the progress achieved in ion sources development of intense, single charge, positive and negative ion beams.

II. Experimental setup

A. Description of the HIgh EFiciency Source

The **HI**gh **EF**ficiency Source (HIEFS) [2] is a compact high brilliance ion source designed to supply intense ion beams. It was optimized to generate nearly pure atomic ion beams with a single charge state only (e.g. He^+, N^+, O^+, Ar^+). By using Helium (Nitrogen) as operation gas, the 80% normalized 4rms-emittance was measured to 0.003π mmmrad (0.01π mmmrad), which corresponds to an ion temperature of 300 K (1480 K) only [3]. A schematic cross-sectional view of the HIEFS and the extractor is shown in Fig. 1. The plasma generator is made of a water-cooled cylindrical copper chamber whose dimensions are 6.0 cm in diameter by 10.5 cm depth. In the middle of the chamber, a tungsten cathode (1.8 mm diameter) is mounted. The front-end of the chamber is closed by the plasma electrode, which can be biased with respect to the anode. This arrangement serves to control the plasma potential near the plasma electrode. On the backside are the gas inlet and several rows of permanent magnets in cuspfield arrangement to reduce particle losses. A solenoid is surrounding the plasma chamber to confine the plasma in longitudinal direction (B_z). Near the plasma electrode an electro-magnet is installed as a filter, forming a transverse magnetic field (B_y) with a magnitude of about 100 G at axis.

For ion extraction, a single aperture accel-decel-system is used, designed for beam energies up to 30 keV. The diameter of the outlet aperture is variable from 3 mm to 8 mm. The distance between outlet and screening electrode is 6 mm. The screening electrode is on a negative potential of up to 3 kV with respect to the ground electrode and serves as a barrier for secondary electrons from the beam line. In case of negative ion extraction, the electron beam is deflected outside of the beam channel by means of the filter magnet field distribution in the extraction region. That way, the electrons are dumped on the screening electrode. All measurements were performed with the source and extraction system operated in dc-mode.

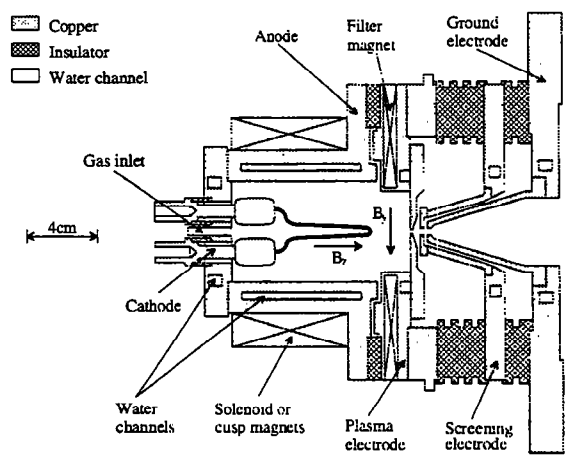

Fig. 1 Schematic drawing of the HIEFS.

B. Description of the H^--source

Based on the experimental results with the HIEFS, a more optimized version was built [4]. A schematic drawing of the this source is shown in Fig. 2. The source can be divided into three parts: the plasma generator, the extraction system and the dumping system. Because of the high heat conductivity, the discharge chamber is made of a water-cooled copper cylinder (12 cm depth, 10 cm diameter). For high reliability the plasma generation is done by rf drive. A high reliability and little fluctuations are essential to ensure a constant current from pulse to pulse. The rf-coupling

inductor is positioned on the cylinder axis. To optimize its z-position the antenna is movable. For the experiments transmitter from 1.7 to 27 MHz with up to 100 kW are available. This allows us to investigate the source at different frequencies. At the beginning the source will be driven without cesium. Later on cesium will be injected to enhance the H^- yield. Like the HIEFS, the plasma generator is equipped with a solenoid, cusp magnets on the back wall and a filter magnet on the front end.

For the ion beam formation a single aperture accel-decel system is used. The distance between the outlet aperture and the screening electrode is 7 mm, the extraction voltage up to 35 kV. The radius of the outlet aperture is a compromise to guarantee low gas flow and low beam emittance as well as a large ion current. For higher beam energies a 60 kV / 300 mA power supply is being ordered.

In this version of source, a dumping system will be used to dump the electrons. It consists of a bending magnet (mounted in the screening electrode) and a water cooled dumping tube. By means of the transverse magnetic field, the electrons will be deflected (40°) outside the H^--beam. In the electric field between the screening electrode and the dumping tube, the electron beam will be decelerated to few kV and finally annihilate in the tube.

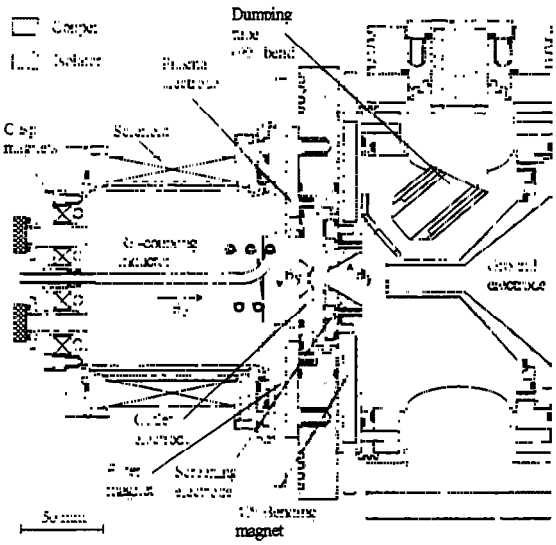

Fig. 2 Schematic drawing of the H^--source.

C. Description of the test stand

An experimental setup is depicted in Fig. 3. The beam diagnostics consist of a faraday cup, an emittance measurement device and a bending magnet to analyze the beam composition. The whole facility is placed in a vacuum chamber.

The moveable water-cooled high current faraday cup was designed for a maximum power density of 1 kW/cm^2. It is fabricated from stainless steal and equipped with a repeller electrode. The emittance measurement device works according to the slit grid principle. Due to the high beam power density, a new water cooled slit was built. Slit and grid are computer-controlled driven through the beam independently by stepping motors. Because of the quantization error of the emittance device, one has to use as high resolution as possible [5]. The maximum linear resolution is given by the slit height, in our case 0.1 mm. To increase the angular resolution, the feedthroughs for the slit and grid are mounted in different vacuum chambers. This allows to increase the slit-grid distance, and so the angular resolution as far as the full beam just hit the grid. Behind the slit, an electrostatic deflection system is installed. To determine the pure H^--beam emittance, we take away the H^0-beam emittance from the full beam emittance (H^0 + H^-) numerically. The pure H^0-beam emittance will be measured by deflection of the H^--beam between the slit and the grid. At the exit of the emittance measurement device a 75° bending magnet is installed to analyze the ion distribution.

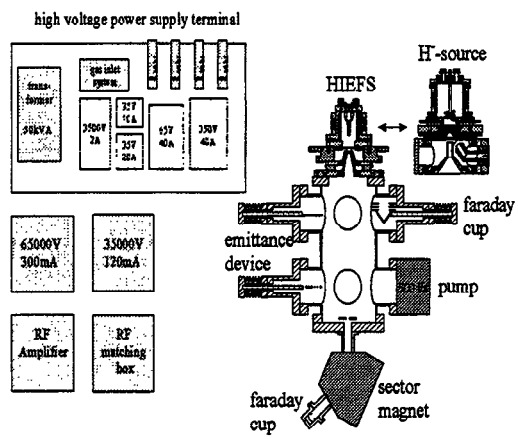

Fig. 3 Schematic drawing of the experimental setup.

III. Experimental results

A. Operation with H^-

Negative ion extraction is always accompanied by the extraction of electrons. According to the Child-Langmuir law, the space charge of the extracted electrons reduces the extractable H^--current. Consequently, for a given design current, the diameter of the outlet aperture has to be larger than for an extraction without electrons. This leads to a higher gas flow in the extractor, accompanied

by a higher rate of recombination, charge transfer and stripping of the extracted H^--ions. Furthermore, the electron beam has to be dumped and the beam power has to be deposited in the extractor. Therefore, a low electron to H^--ratio is essential for negative ion extraction. In order to determine the optimum conditions for generating high current H^--beams with a low electron to H^--ratio, the influence of the plasma parameter on the electron to H^--ratio and the current density were investigated.

We assumed that the relative position of the arc discharge with respect to the filter field might have an influence on the electron to H^--ratio. First of all, the polarity of the cathode was changed as it inverts the direction of the magnetic field that it produces itself. We found significant differences in the electron to H^--ratio and chose the configuration with the better yield for further operation. Then, both the angular position and the cathode length were varied and the effect on the electron to H^--ratio was studied.

The influence of the cathode length on the electron to H^--ratio is depicted in Fig. 4. The larger the distance between cathode and filter field, the better the ratio obtained. The reason is that the fast electrons intersect the magnetic field lines right away. Consequently, their fraction in the extraction region area is diminished. That way, with a cathode length of 10 mm, an electron to H^--ratio of eight was obtained. Additional flanges to enlarge the distance between cathode and filter field are under construction. From these experiments, we expect further improvement in the electron to H^--ratio.

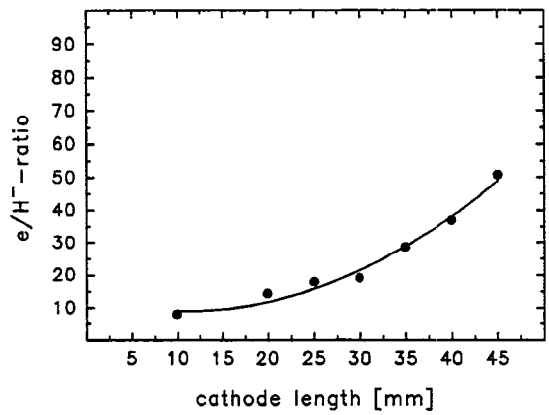

Fig. 4 Electron to H^--ratio as function of the cathode length.

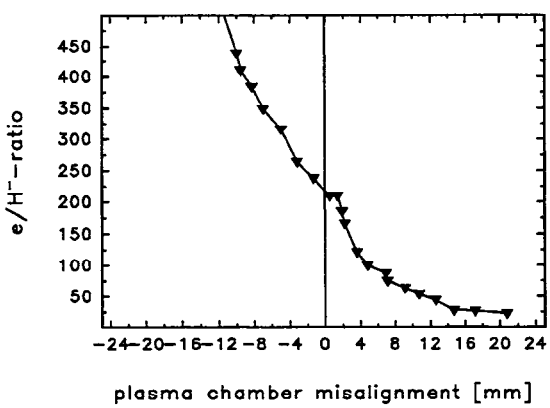

Fig. 5 Electron to H^--ratio as function of the plasma chamber misalignment.

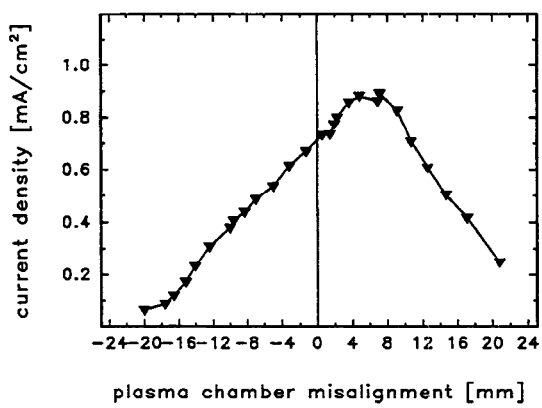

Fig. 6 H^--current density as function of the plasma chamber misalignment.

Due to the transverse filter field (B_y) and the potential distribution in the plasma column along the z-axis, the plasma column experiences a drift movement perpendicular to the electrical and magnetic field. That way, the center of the plasma column does not agree with the axis of the plasma chamber. Therefore, the electron to H^--ratio and the emission current density as function of the chamber misalignment (resp. the plasma column) were investigated. In Fig. 5 and 6, the results of these experiments are presented. On the x-axis, the distance between the plasma chamber axis and the plasma electrode axis (beam axis) is plotted. The zero-position means a symmetrical alignment of the plasma chamber. As shown in Fig. 5, positioning out of the middle decreases significantly the electron to H^--ratio, while the

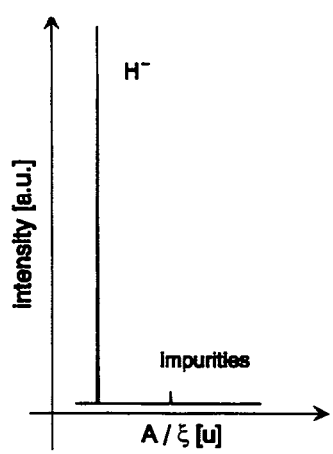

Fig. 7 H^--spectrum

extracted current density reaches a maximum, if the misalignment distance is about 7 mm. In that mode of operation, we obtained a current density of 10 mA/cm^2 for an arc power as small as 1 kW. Fig. 7 presents a mass spectrum taken at an extraction voltage of 8 kV only. The spectrum shows a 10 mA H^--beam with 1.8% of impurities. Note that we have not used cesium in the plasma chamber so far.

A key problem of negative ion extraction is the simultaneous extraction of ions and electrons. Without an e-dumping system inside the ion source, it is necessary to dump the electrons inside the LEBT or the RFQ, which leads to a higher technical effort.

In case of negative ion extraction the extracted H^--current will be reduced by the space charge of the extracted electrons. In order to calculate the extractable H^--current, the law of Child-Langmuir had to be modified. In Fig. 8 the calculated H^--current is shown under the condition of an extraction voltage of 35 kV and an aspect ratio of 0.357.

The dumping system consists of two parts. In the first part, the beam is decelerated with a designated dumping voltage which depends on the current of the electron beam in the front part of the system. Then, in the back part of the system, the electron beam spreads and will be dumped in the water cooled tube outside of the beam channel. An IGUN simulation [6] of the electron beam course in the dumping system is shown in Fig 9.

In this way, we can use a high perveance extractor. Due to the deceleration of the electron beam, we get low dumping power. Additionally, one achieves a high flexibility in the source handling and a low influence on the H^--beam emittance. The thermal stress of the dumping system material will be about 20 Watt/cm^2. This power density can be controlled by a water cooled catcher.

To optimize the electron to H^--ratio and the current density of the plasma generator we use a electrical dipole magnet as filter magnet. To minimize the magnetic field strength at the outlet aperture, the filter magnet and the bending magnet of the dumping system have the opposite polarity. In this way an undesired electron beam deflection in the accelerator gap is reduced and the negative influence of the resulting magnetic field at the plasma sheath is minimized. Fig. 10 shows a high resolution measurement of the resulting B_y-field. The negative region corresponds to the plasma chamber (filter magnet), and the positive region to the extractor (bending magnet). As the measurement shows, we get a minimized B_y field strength in the plasma sheath region.

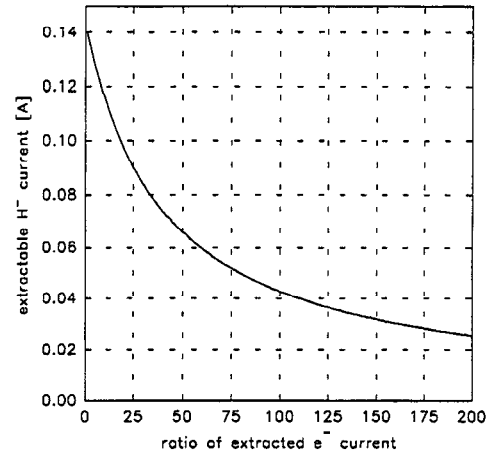

Fig. 8 Calculated extractable H^--current.

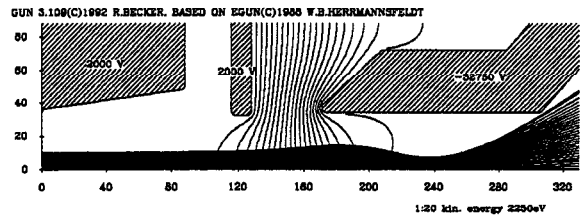

Fig. 9 Simulation of the dumping system.

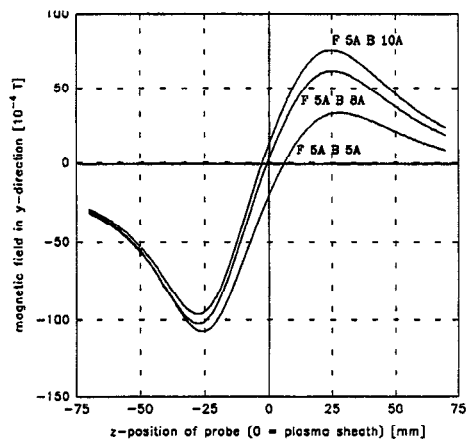

Fig. 10 B_y-field vs. z-position at the axis.

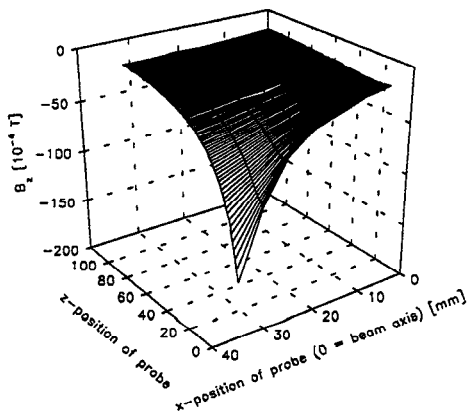

Fig. 11 B_y-field in the dumping region.

For ion optical calculations, the exact knowledge of the magnetic field course between the plasma sheath to the dumping tube is necessary. As an example, in Fig. 11 the B_Z-field is shown in the dumping region. The dumping system was built in our workshop and a dumping power supply (3500 V, 2 A) was delivered, a high voltage platform is being built.

B. Operation with H_2^+

The dependence of the extracted ion species on various discharge parameters were investigated to determine the optimal conditions for generating a high percentage of H_2^+ ions.

For the ion species percentage of the beam, the gas pressure in the source is an essential parameter. A graph of the ion species percentage in the extracted beam as a function of the gas pressure is shown in Fig. 12. The source is operated with a discharge voltage of 100 V, a discharge current of 1.5 A and a solenoid field of 12 mT. It can be seen that for low gas pressures the H_2^+-fraction increases beyond 85 %. At the same time, the H_3^+-fraction decreases while the atomic fraction does not change. This dependence is consistent with the known cross-section for H_3^+ production (via $H_2^+ + H_2 \Rightarrow H_3^+ + H$), which is the pre-dominant reaction in the plasma chamber. This way, raising the neutral gas pressure leads to an increase of the H_3^+- fraction.

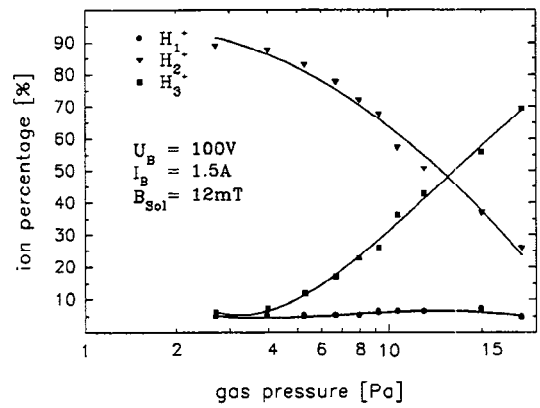

Fig. 12 Ion species ratio vs. gas pressure.

It is also observed that the amount of the H_2^+-fraction is a function of the arc voltage between cathode and anode. The arc voltage corresponds to the maximum electron energy in the plasma chamber. The result is plotted in Fig. 13 and shows, that for arc voltages in the range of 60 - 100 V the H_2^+ ion species percentage yield in a maximum. For higher arc voltages decrease the H_2^+-fraction, accompanied by an increase of the H_3^+-fraction. The H_1^+-percentage remains stable over a wide range. This behavior can be explained by the cross-section for the ionization of molecular hydrogen by electron impact ($e^- + H_2 \Rightarrow H_2^+ + 2e^-$). The cross-section shows, that electron energies between 50-100 eV yield a maximum production of H_2^+-ions. This means, that arc voltages, respectively electron energies, higher than 100 V or below 50 V leads to a reduction of the H_2^+ fraction. During source operation, arc voltages less then 60 V are impossible because the source does not operate in that range.

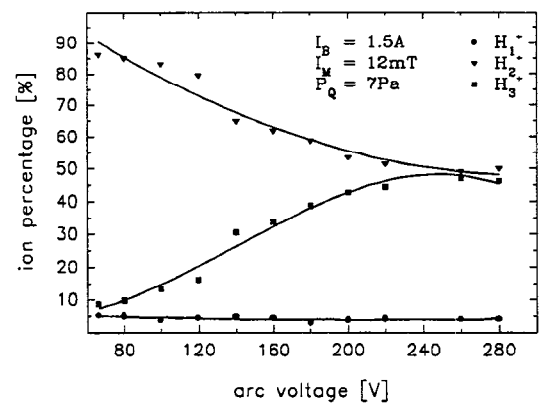

Fig. 13 Ion species ratio vs. arc voltage.

Further measurements have shown, that the H_2^+-fraction is independent on the arc current. On the other hand, the arc current is an essential parameter to reach high current densities. That way in a next step the source will be optimized for the extraction of high beam currents.

C. Operation with D^+

Usually, deuterium ion beams consist of three species: the atomic D_1^+, the molecular D_2^+ and D_3^+. In order to enhance the atomic yield, the influence of all essential plasma-parameters (including cathode length and position of the magnets) on the beam composition were investigated [7]. The experiments were initially carried out with hydrogen and then continued with deuterium. For identical plasma-parameters, the results of the ion species percentage were basically the same for both gases. In the case of deuterium, the atomic fraction is a few percent higher than for hydrogen. Subsequently, the main results for deuterium will be presented.

Fig. 14 illustrates the relationship between the ion species percentage and the arc current for a constant arc voltage of 55 V and a solenoid field of 24 mT. The source pressure is 9 Pa, and the plasma-electrode is on negative potential of 150 V with respect to the anode. The plot shows, that for high arc currents the atomic fraction exceeds 90 %. On the other hand, the D_3^+-fraction decreases while the D_2^+-fraction does not change.

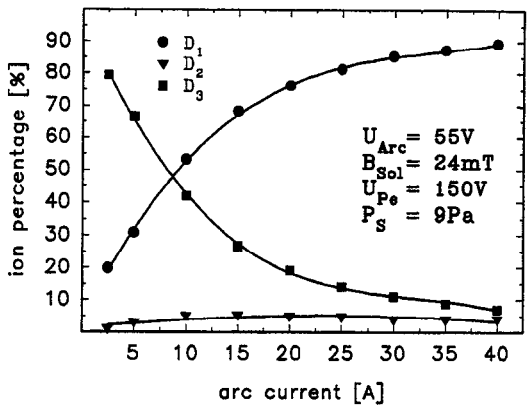

Fig. 14 Ion species ratio vs. arc current.

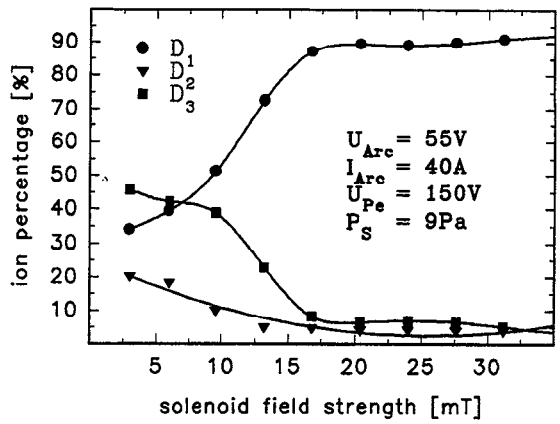

Fig. 15 Ion species ratio vs. solenoid field strength.

Furthermore, the atomic fraction is very sensitive to changes in the solenoid field. Only a strong magnetic field in combination with a high discharge power leads to a high percentage of the atomic fraction. According to the plot of the measured ion species percentage versus the magnetic field of the solenoid (Fig. 15), the atomic fraction has dropped for a rising magnetic field to 93 % while the D_2^+- and D_3^+-concentration has decreased to 4 % and 3 %, respectively.

As mentioned above, a high atomic fraction requires a high discharge power and a strong longitudinal magnetic field. Both parameters lead to a high current density. That way, a maximum emission current density of 210 mA/cm^2 has been achieved for a 1.5 mm aperture radius. Operating the source at 35 kV with a 4 mm aperture radius of the plasma electrode delivers 80 mA D^+.

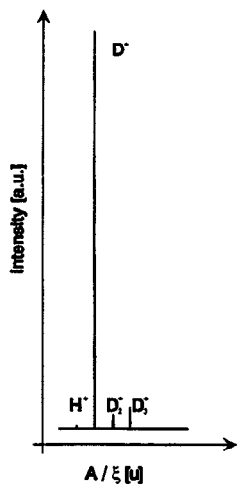

Fig. 16 D^+-Spectrum

Fig. 16 presents a typical spectrum taken at an arc current of 40 A and a solenoid field of 24 mT. The spectrum shows an atomic fraction of 91 %, 3 % for D_2^+ and 5 % for D_3^+. The fraction of impurities is about 1 %.

IV. Acknowledgments

The authors would like to thank G. Hausen and his team for their continued technical support.

V. References

[1] Klein, H., Linac design for the European Spallation Source, Proc. Int. Conf. on Accelator-Driven Transmutation and Application, Las Vegas, USA (1994)
[2] Volk, K. et. al., A Compact High Brilliance Ion Source For RFQ Injection, Proceedings of EPAC, London, 1438 (1994)
[3] Volk, K., Dissertation Univ. Frankfurt (1993)
[4] Volk, K. et. al., An H^--Source for ESS, Proceedings of the 6th International Conference on Ion Source, Whistler, Canada (1995)
[5] Ludwig, T., Quantization error of slit-grid emittance measurement devices, Proceedings of the 5th International Conference on Ion Source, Peking, China (1993)
[6] Becker, R., Herrmansfeldt W.B., Proceedings of the 4th International Conference on Ion Source, Bensheim, Germany (1991)
[7] Maaser A. et. al., Development of a D^+-Source in Frankfurt, Proceedings of the 6th International Conference on Ion Source, Whistler, Canada (1995)

LEBT Design Studies for ESS

J. Pozimski, P. Groß, R. Dölling, K. Reidelbach and H. Klein
Institut für Angewandte Physik der Johann Wolfgang Goethe Universität,
Postfach 111932, D-60054 Frankfurt am Main, Germany.

Introduction

For new applications of accelerator physics like ESS, high perveance ion beams have to be transported from the ion source to the first accelerator (see fig. 1). The requirements for such a Low Energy Beam Transport (LEBT) are high transmisson and low emittance growth. The transport properties of the section will be influenced strongly by the space charge of the beam. This can not be avoided in an electrostatic LEBT [1,2,3] and defines a limit of transportable beam current. It also increases the beam diameter drastically and therefore emittance growth due to higher aberrations occurs. In opposite magnetic LEBT sections (i.e. with solenoids) where the space charge can be compensated by particles of opposite sign avoid this problems. The compensation particles are usually produced by interaction of beam ions and residual gas atoms. In absence of external electric fields they are trapped in the potential well of the beam itself and reduce the net charge density. In spite of the fact that space charge compensated beam transport is used quite often, the theoretical models do not allow precise forecasts of the transport properties and the emittence growth.

1. Space charge compensation

For a beam of negative ions three different stages of space charge compensation can be characterized (shown in fig. 2). The gas (or self-) focusing stage is similar (concerning the radial potential distribution and the net charge density distribution) to a compensated positive ion beam. Therefore considerable experimental experiences and computer codes are available [4, 5]. The lower pressure limit for self focusing can be calculated by

$$p_{limit} = k_b\, T_{RGA} \frac{v_{RGI}}{r_b\, \sigma_{RGI}\, v_{BI}} \qquad (1)$$

and is for the given ESS parameters below $1*10^{-3}$ Pa. For this pressure the losses by charge exchange and stripping in the LEBT can be calculated (see fig. 3) for a 1 m LEBT to be below 5%. This is suitable for an ESS application. The minimum rise time for compensation is given by

$$\tau = \frac{1}{N_{RGA}\, \sigma_{RGI}\, v_{BI}} \qquad (2)$$

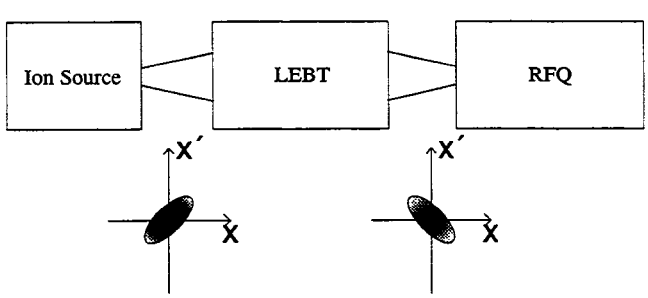

Fig. 1 : Schematic drawing of beam matching from ion source to first accelerator section (RFQ).

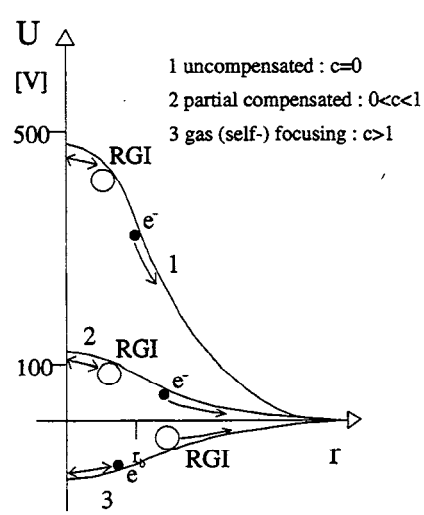

Fig. 2 : Schematic drawing of the three compensation stages for negative ion beams.

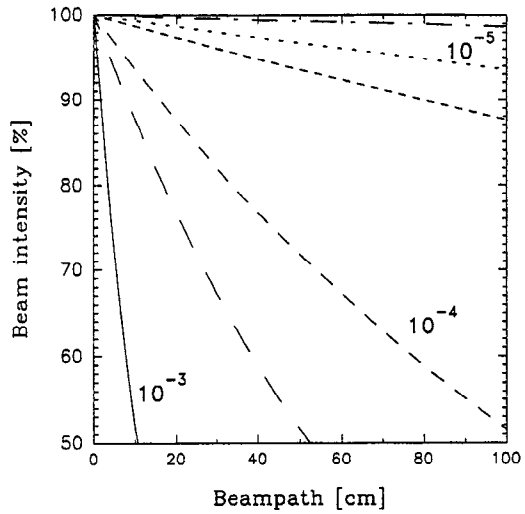

Fig. 3 : Transmission through LEBT as a function of LEBT lenght and residual gas pressure [hPa](H^-, 50 keV in Ar).

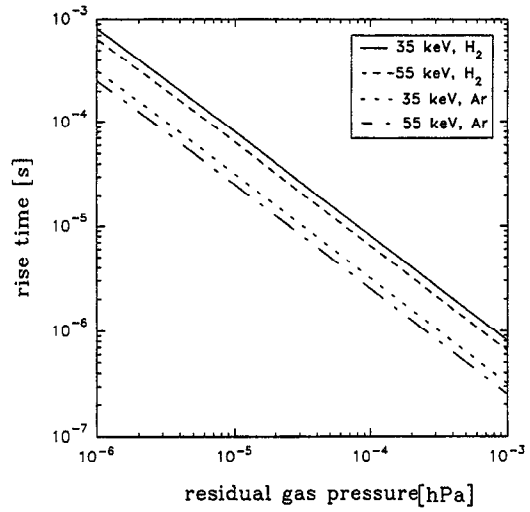

Fig. 4 : Minimum rise time of compensation as a function of residual gas pressure for different gases and ion energies.

For the lower pressure limit the rise time will be approx. 50 µs (see fig. 4). This seems to be appropriate for ESS application (pulse duration 1.2 ms). A simulation of different beam enveloppes for different degrees of compensation, where the magnetic field strength was altered for the same matching in parameters, is shown in fig. 5. Smaller beam radii are the clearly visible result of compensated transport. The influence of the RFQ fields are taken into account in one calculation (last 100 mm decompensated - worst case !).

2. Emittance growth

Two general sources of emittance growth can be determined. Aberrations of lenses (or other external devices) and the internal forces due to space charge. Both can be influenced by space charge compensation. Due to the lower inner fields the lens is filled to a lower degree by the beam and therefore the influence by the nonlineareties of the external fields on the beam is smaller. Numerical simulations [6] have shown that in drift regions the beam redistributes himself into a homogeneous net charge density distribution with minimum non linear field energy. Non linear field energy is transformed into non linear kinetic energy (emittance growth). Lower internal fields due to compensation of the space charge therefore directly influences the emittance growth. The final emittance after a drift region long enough to allow total redistribution can be calculated by

$$\varepsilon_{final} = \sqrt{\varepsilon_{initial}^2 + \frac{K\langle x^2\rangle f}{2}} \qquad (3)$$

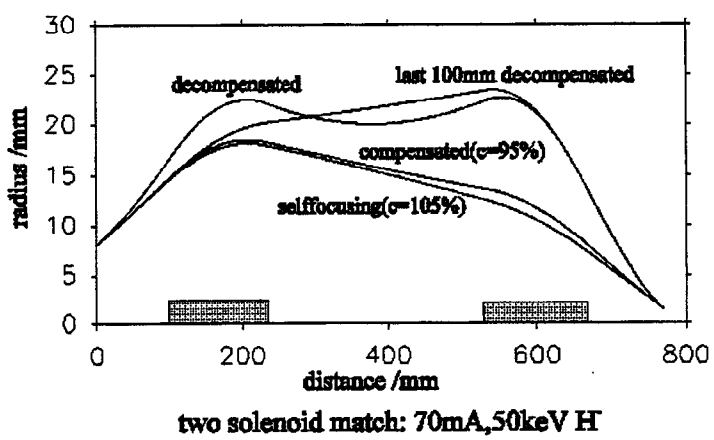

Fig. 5 : Calculation of beam enveloppe for different compensation degrees (and field strength from 0.3 to 0.6 T) in a two solenoid LEBT.

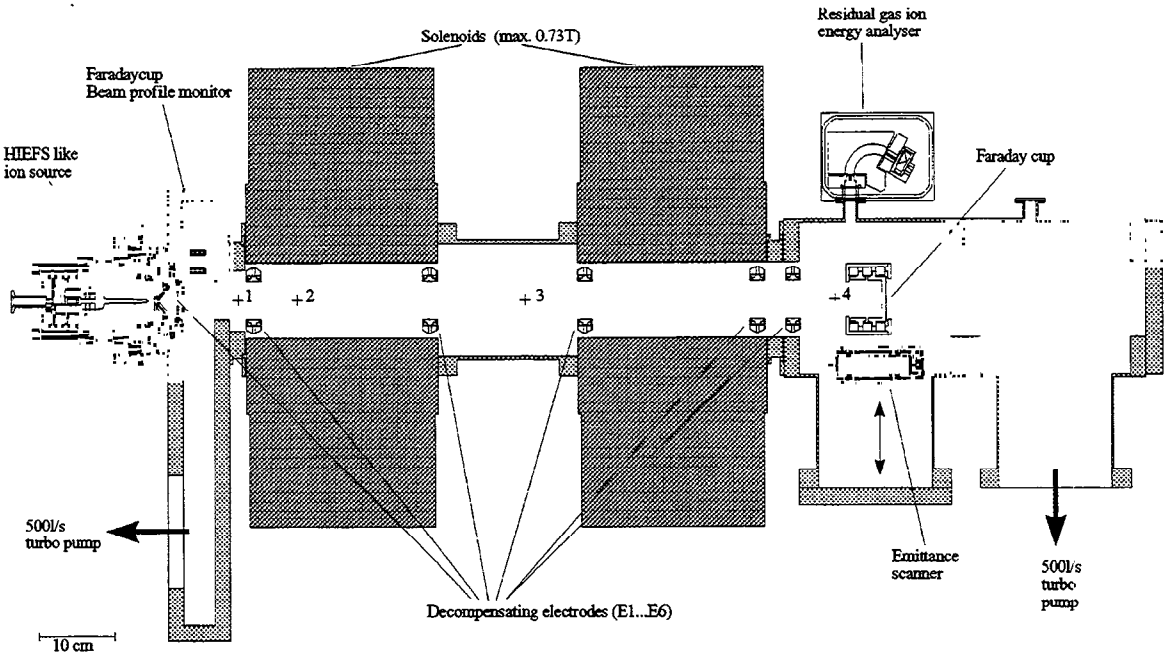

Fig. 6 : Schematic drawing of the experimental set up of the Frankfurt LEBT for ε growth measurements.

where K is the generalized perveance and f is the redistribution factor (0.0386 for Gauss into homogeneous). Whereas the perveance K is influenced positively by compensation, the Factor f might grow. A disadvantage of compensated transport is the fact that the net charge density distribution might change due to changing compensation degrees along z and therefore redistributions might occure more often. Also the unavoidable decompensation in front of the RFQ due to electric fields might add emittance growth. In the moment it is not possible to fully calculate the behavior of a compensated ion beam in a magnetic LEBT and therefore theoretical comparisons with other solutions are not possible, but the theoretical work might help to optimize an existing LEBT.

3. Experimental set up

In Frankfurt a magnetic LEBT similar to the proposed ESS LEBT (see fig. 6) has been set up. It consists of a HIEFS like ion source delivering a high perveance He^+ beam (comparable to the ESS perveance) with very low emittance (see fig. 7). This very low emittance yield high growth rates which is necessary to identify the sources of emittance growth [7] (aberrations and charge redistributions). Various cylindrical electrodes allow to influence the degreee of compensation

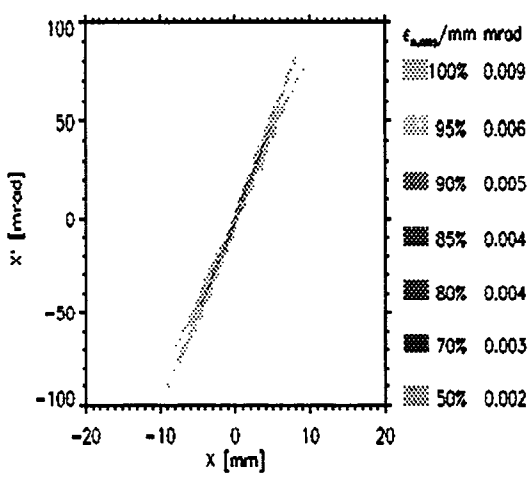

Fig. 7 : Initial emittance of a 10 keV, 2.5 mA He beam 11 cm behind extraction.

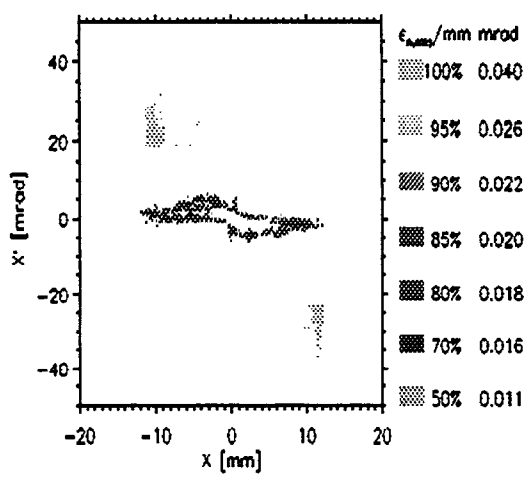

Fig. 8 : Emittance behind the LEBT for the same beam.

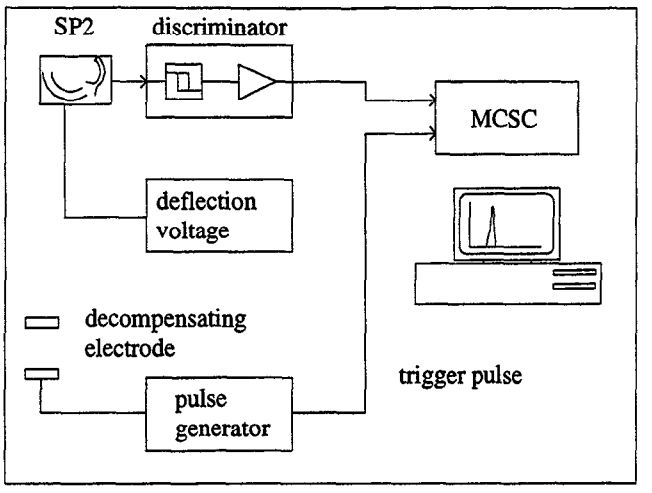

Fig. 9 : Schematic drawing of the experimental set up for measurements of the rise time.

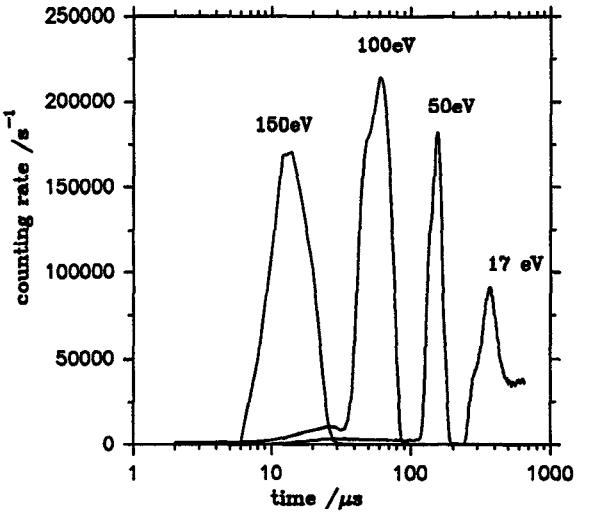

Fig. 10 : Time dependence of the occurence of certain RGI energies (t=0 start of compensation).

along the beampath. Fig. 8 shows the emittance behind the LEBT for fully compensated transport. The absolute growth of emittance is $\Delta\ \varepsilon$ = 0.017 πmmmrad (90 %, RMS). For ESS (ε=0.1 πmmmrad) this would give an growth rate of appr. 20 % including the growth in front of the RFQ. Various measurements have shown that disturbance of compensation will result an enormous emittance growth and fluctuations in the beam.

To get more information concerning the behavior of a pulsed compensated ion beam a upgrade program for the beam diagnostics has been started. A time resolved residual gas ion (RGI) energy analyser is already in use. Fig. 9 shows the experimental set up. With a single particle detector a time resolution of 2 µs has been achieved. Fig. 10 shows a first result, from which the rise time of compensation can be derived. The first measurements [8] indicated rise times of compensation below the theoretical minimum rise time. This might be due to secondary electrons.

4. Conclusions

Space charge compensated transport has many advantages. The LEBT has to be designed very carefully and flexible to allow optimization. The LEBT should be kept short to keep the beamradius small and there should be no irritating external electric fields. Still there is no way to exactly predict the behavior of the beam because there is no model available to forecast the density distribution of the compensating particles in r and z (for cylindrical symmetry). For pulsed beams the dynamic of the rise of space charge compensation makes the problem even worse. If the rise time of compensation is in the range of the rise time of the beam pulse itself if does not influence the focus shift substantial. Otherwise active compensation by encasement of the compensating particles in a Gabor Plasma Lens [9] might improve the rise time. Nevertheless optimization of the LEBT including the final version of the ion source is absolutely necessary and might benefit from the existing experimental and theoretical knowledge.

5. Reference

[1] Anderson et. al. Pac 1987
[2] C. Allen et. al., LINAC 1990
[3] Guharay et. al. PAC 1991
[4] R. Dölling, Dissertation, IAP, Frankfurt, 1994
[5] J. Pozimski et. al. , Il Nuovo Cimento 106 A (1993), 1713
[6] P. Groß et. al., Il Nuovo Cimento 106 a (1993), 1657
[7] P. Groß et. al., LINAC 1994
[8] K. Reidelbach et. al., EPAC 1994
[9] J. Pozimski, GSI Annual Report 94, GSI-95-06, 32

Chopping- and Funneling-Studies for ESS at Frankfurt

J. Madlung, A. Firjahn-Andersch, A. Schempp
Institut für Angewandte Physik, Johann Wolfgang Goethe-Universität
D-60054 Frankfurt/Main, Germany

Abstract

The front end of the ESS linac has to provide a bunched high current beam with a special time structure for injection into the following DTL [1]. Therefore the layout contents beam funneling and chopping. A new concept for beam funneling using a two-beam RFQ and a multi-gap funneling deflector and first calculations for a new layout of the chopping line will be presented.

1. Introduction

The ESS reference design requires a 1.334 GeV H^- linac beam optimized for injection into two compressor rings. The RFQ injector for the ESS linac provides a bunched beam of 107 mA at 5 MeV. This can be achieved by a system of two 175 MHz RFQ lines, each with a current of 54 mA, whose beams will be combined in a funnel section to a 107 mA beam with a bunch repetition rate of 350 MHz. For a proper operation of the compressor rings the linac beam must be chopped with a 60 % duty factor at the ring revolution frequency of 1.67 MHz which implies beam pulses of 360 ns and gaps of 240 ns during the macro pulse of 1.2 ms. The layout of the ESS linac is shown in figure 1.

In contrast to first funneling experiments with a system of discrete elements like quadrupole-doublets and -triplets, debunchers and deflectors [2,3,4], the first two-beam funneling experiment at the Institut für Angewandte Physik (IAP) in Frankfurt includes a two-beam RFQ where the beams are bunched and accelerated with a phase shift of 180° between each bunch. In the two-beam RFQ the beam separation is kept small. Therefore the rf-funneling deflector system can operate at low voltages.

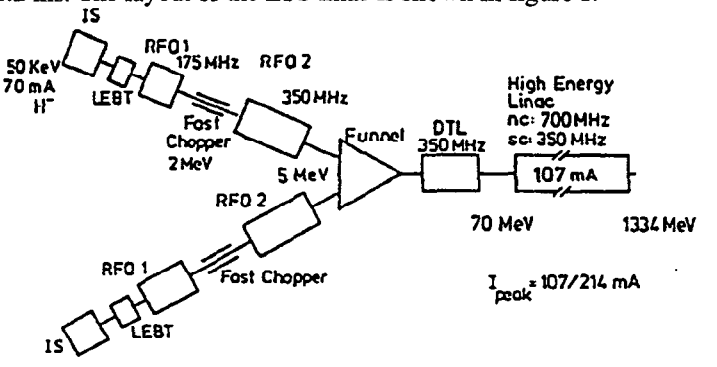

Fig. 1: Layout of the ESS linac.

A new concept, based on a resonator driven multi-gap deflector, where the ions are deflected several times, facilitates some constraints in beam funneling like the limitation of the electric field by rf-sparking. A combination of a two-beam-RFQ instead of the two single RFQs and such a multi-gap deflector could be used for the ESS linac.

Instead of earlier concepts with chopping in front of the first RFQ or even in the ion source the chopping of the ESS H^--beam will be done between the two RFQ stages at an energy of 2 MeV. Here a clean chopping can be achieved due to the unneutralised, bunched beam. A travelling-wave electrostatic chopper, based on the BNL design, will be used to produce the time structure [5].

2. The two-beam RFQ for funneling

To study the properties of the new two-beam RFQ resonator, different kinds of prototype resonators were built and tested [6]. Also calculations with the MAFIA-code were done for comparison with the low-level measurements.

A prototype resonator with a reduced length and parallel beam axis has been designed and mounted into the 2 m long rectangular vacuum chamber. The resonator consists of two pairs of electrodes with a length of 100 cm supported by four symmetric stems in linear arrangement (Figure 2).Low-level measurements were done with the bead perturbation method. In high power tests the maximum rf-input power in pulsed mode was limited to 12 kW by the rf-power amplifier. At this power an electrode voltage of 27 kV was measured.

A 2 m long two-beam RFQ with convergent beam axes is under construction where the inner electrodes merge at the end of the structure. With this RFQ two single ion sources instead of a difficult two-hole extraction from one ion source can be used. While the parallel beam axes of the first prototypes would need a parallel beam shift in the funneling element, with convergent beam axes out of the new two-beam RFQ a shorter rf funneling deflector, placed before the beam crossing, is possible. Here the convergent beams will be bent to the new common axis.

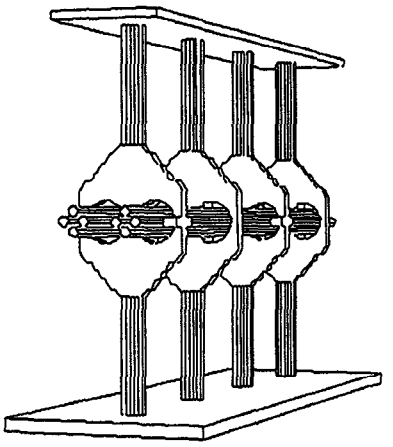

Fig. 2: MAFIA plot of the prototype two-beam RFQ structure.

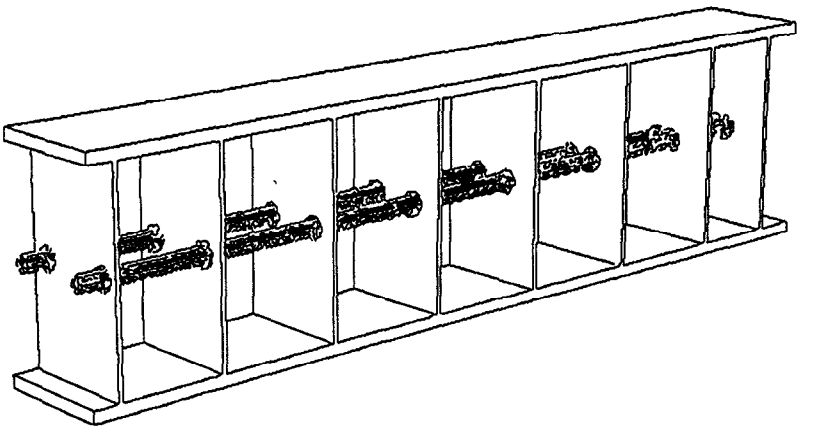

Fig. 3: MAFIA plot of the two-beam RFQ with convergent beam axes.

With an angle of 75 mrad between the beam axes the beam separation at the RFQ input will be more than 160 mm and 16 mm at the RFQ output. The electrodes are supported by eight flat stems. Figure 3 shows the resonator geometry as modelled by MAFIA. The RFQ electrode design with the use of the PARMTEQ code is in progress. For the phase shift of 180° between the bunches of each beam axis two different electrode designs with different electrode lengths are required.

3. The deflector geometry

The electrode geometry of the multi-gap deflector consists of some capacitors divided by spaces or sections with larger aperture with equal length. In this geometry the particles will see the deflecting field in one direction several times but the deflection in the opposite direction is always less. The length of the capacitors have to be proportional to the particle velocity and to the inverse of the frequency of the deflection system. The scheme of the multi-gap deflector electrode geometry and the behaviour of the particles along the deflector are shown in figure 4.

If the electric field is taken as a homogeneous and constant field over the cell length l, the single cells can be treated like separate rf-deflectors. For beam funneling the frequency of the deflector has to be the same as the accelerator frequency, so that the bunches from different beam axes will see opposite field directions, caused by the phase shift of 180° between each bunch. The advantage of the multi-gap deflector is a lower electric field than in single gaps. The field strength needed to bend a beam by 37.5 mrad is nearly 3 times less for a multi-gap deflector with 15 cells. Another option is to add focusing elements in the cells with larger aperture [7].

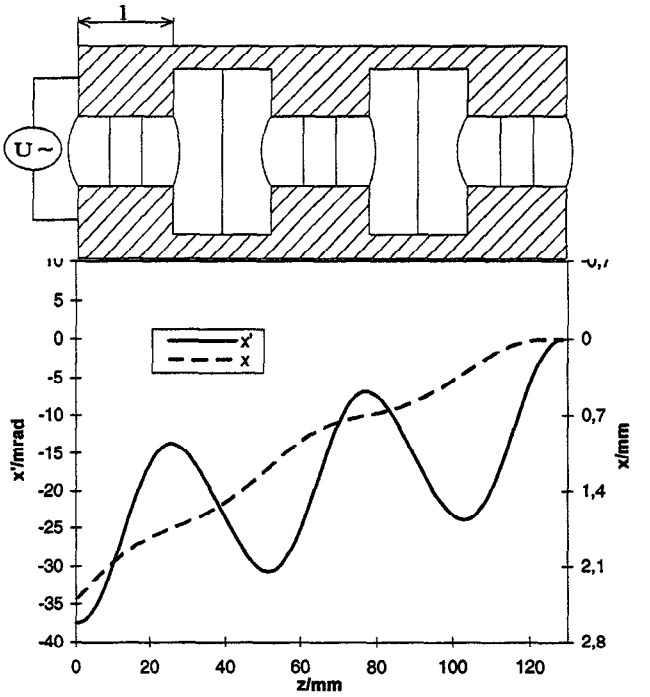

Fig. 4: Scheme of the multi-gap deflector electrode geometry and the behaviour of the deflection angle x' and the deflection x.

4. The funneling experiment

The funneling experiments will be carried out with He^+-ions to facilitate ion source operation and beam diagnostics. Two small multicusp ion-sources and electrostatic lenses, built by LBNL [8], will be used. The ion-sources and injection-lens will be attached directly on the front of the RFQ with an angle of 75 mrad. Behind the RFQ the funneling deflector will be placed before the beam crossing. Figure 5 shows the experimental setup of the funneling experiment. Beam diagnostics in front of and behind the RFQ and behind the funneling deflector are in preparation. The rf-resonator for the multi-gap deflector will be a structure as it is used for 4-Rod-RFQs with two stems. Each stem is electrically contacted with one of the deflector electrodes and will sustain the other electrode by a ceramic support. For longer electrodes it is possible to use an rf structure with more stems to preserve mechanical

stability. The resonator is under construction and a prototype for rf measurements has been finished. Figure 6a shows the output distribution of PARMTEQ calculations for the two-beam RFQ which are used as input for the particle simulations of the multi-gap deflector. In figure 6b the output is plotted. For an input distribution with displacement and angle in the opposite direction and a phase shift of 180° the results are the same. The bunch is bent 37.5 mrad to the common axis. These results show that such a system could be used for funneling. In table 1 the main parameters for the planned experiment with He^+ and design parameters for the ESS funnel are listed.

two-beam RFQ	He^+	H^-
f_0 [MHz]	54	350
T_{in} [keV]	4	2000
T_{out} [MeV]	0.205	5
Length [m]	2	5.5/2.9
Angle between beam axes [mrad]	75	75
rf-deflector		
f_0 [MHz]	54	175
Voltage [kV]	9.5	230
Length [cm]	44	133
Length [$\beta\lambda/2$]	15	15
Beam separation at input [mm]	16	50

Table 1: Main parameters of the planned experiment with He^+ and design parameters for H^-.

5. Beam chopping

The chopping line between the two RFQs has to provide a good matching in both the transversal and the longitudinal plane for the unchopped beam as well as a total beam loss of the chopped beam. A first layout for an ESS chopping line by K. Bongardt [9] is shown in figure 7. The transversal focusing is achieved by quadrupole triplets where the chopper will be placed in the drift between the first two triplets and the beam stopper in the following drift section. Bunchers in front of and behind each triplet provide the longitudinal focusing.

An alternative layout is shown in figure 8. Here the chopper and the beam dump are placed in the same drift section.

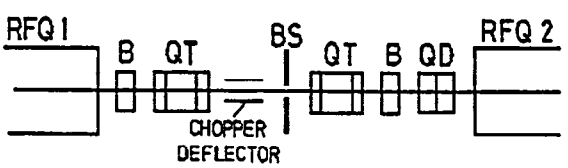

Fig. 8: Funneling line scheme by A. Schempp.

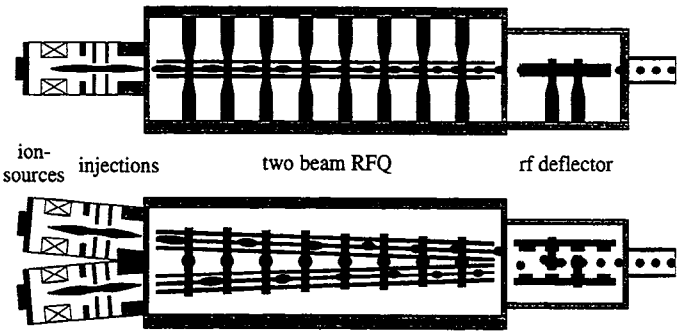

Fig. 5: Scheme of the planned experimental setup for funneling.

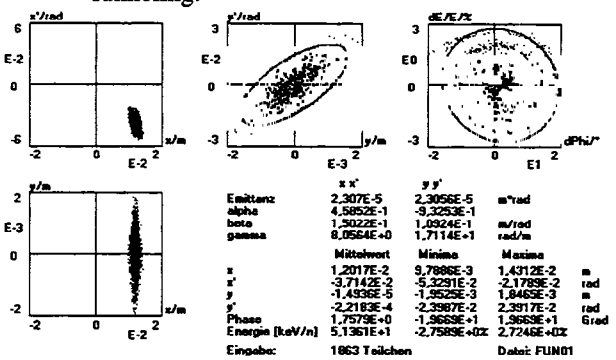

Fig. 6a: Input distribution for the funneling simulation.

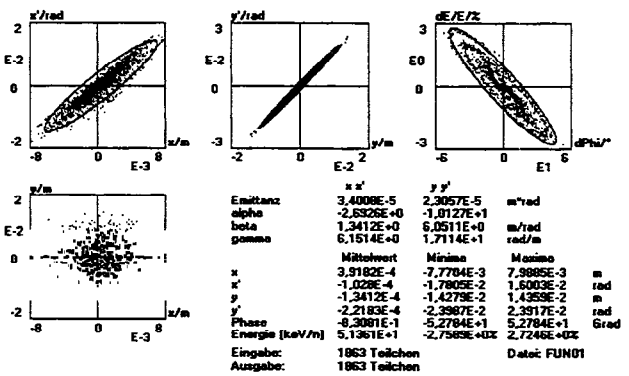

Fig. 6b: Output distribution of the funneling simulation.

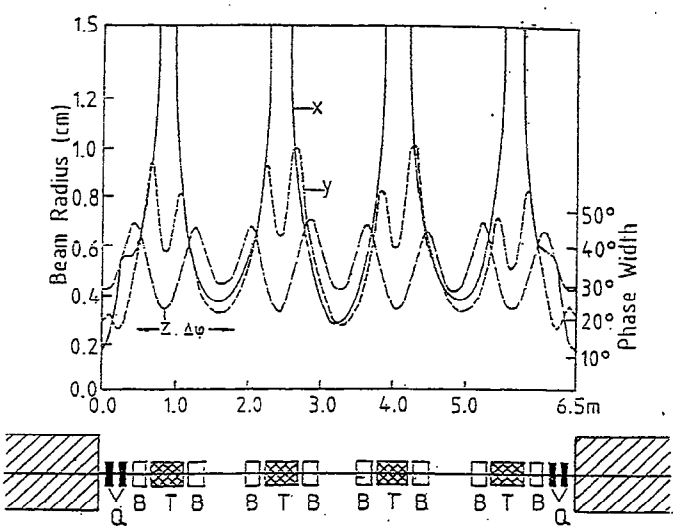

Fig. 7: Funneling line design by K. Bongardt.

Beam dynamics calculations for this layout were done with the PARMTRA-code. In figure 9 the transversal behaviour of the beam along the funneling line is shown both for the unchopped (a) and chopped (b) beam. For these calculations a quadrupole doublet has been added to match the beam from the first RFQ to the triplet and a deflection force as high as 100 kV/m has been used.

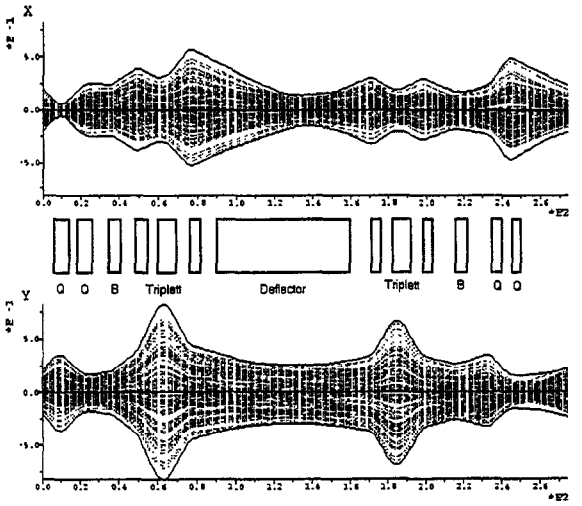

Fig. 9a: PARMTRA output of the chopping line simulation (chopper off).

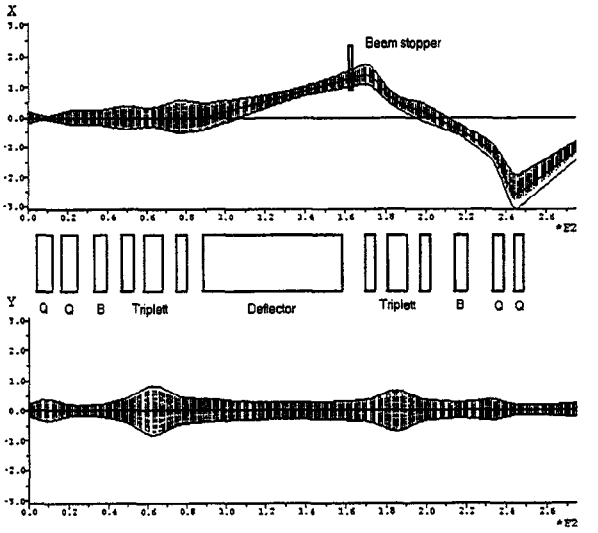

Fig. 9b: PARMTRA output of the chopping line simulation (chopper on).

For this layout the longitudinal focusing has to be investigated carefully. The beam power to be dumped is more than 2.5 kW, so that the beam dump has to be sufficiently cooled and probably more space has to be taken into account for the beam stopper.

The chopper will be a pulsed electrostatic deflector with deflection plates segmented into strips transversal to the beam direction. They are connected by coaxial delay lines, so that the pulse velocity along the beam direction is matched to the beam velocity. One set of strips above and below the beam will halve the magnitude of the voltage needed for deflection. In figure 10 a schematic drawing of the chopper is shown. For the ESS case the rise and fall time of the chopping voltage has to be less than 4.5 ns to reach a clean chopping.

6. References

[1] Outline Design of the European Spallation Neutron Source, Editors: I.S.K. Gardner, H. Lengeler, G.H. Rees, ESS/P1/95

[2] K. Bongardt and D. Sanitz, Funneling of Heavy Ion Beams, Primary Report, Kernforschungszentrum Karlsruhe, 11 04 02P14C (1982)

[3] J.F. Stovall, F.W. Guy, R.H. Stokes and T.P. Wangler, Beam Funneling Studies at Los Alamos, Nucl. Instr. and Meth. A278 (1989) 143

[4] K.F. Johnson, et al., A Beam Funneling Demonstration: Experiment and Simulation, Part. Acc. Vols. 37-38 (1992) 261-268

[5] J.M. Brennan, et al., A Fast Chopper for Programmed Population of the Longitudinal Phase Space of the AGS, BNL-41832, PAC89, IEEE CH2669 (1989) 1154

[6] A. Firjahn-Andersch, A. Schempp, C.Staschok, J. Madlung, A Two-Beam RFQ for Funneling of Ion Beams at Low Energies, GSI-Report, GSI-95-06 (1995) 25

[7] A. Schempp, Beiträge zur Entwicklung der Radiofrequenzquadrupol-(RFQ)-Ionenbeschleuniger, Habilitationsschrift, Universität Frankfurt am Main (1990)

[8] K.N. Leung, Multicusp Ion Sources, Proc. 5th Int. Conf. Ion Sources, Beijing, China (1993) 1165-1169

[9] K. Bongardt, Matching Problems between Linac and Compressor Ring, ESS-Report 94-8-L (1994)

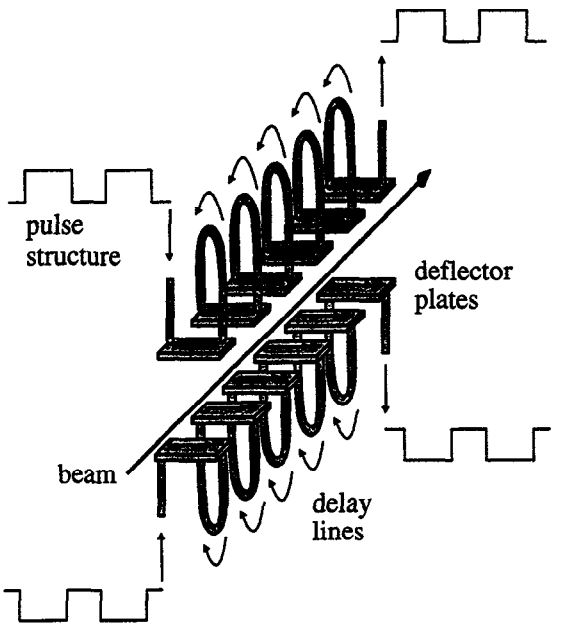

Fig. 10: Schematic drawing of the chopper.

Recent Development of a Closed Orbit Monitor System in the KEK Booster Synchrotron

H. Someya, D. Arakawa, J. Kishiro and I. Yamane

National Laboratory for High Energy Physics, KEK
1-1, Oho, Tsukuba, Ibaraki, Japan

Abstract

The KEK 500MeV booster synchrotron is now under operating to provide a high intensity proton beam to a medium energy nuclear/neutron physics experiments, and also used as an injector into the 12GeV main accelerator. The KEK accelerator complex is scheduled to serve an intense beam for a neutrino experiment and booster utility also foreseeing more intense protons to produce a high intensity neurons. The accelerator machine studies are going on in order to improve the current beam intensity as high as possible.

A new closed orbit distortion monitor system has been developed in the booster synchrotron to make more clear the beam orbit behavior during the acceleration period, during which the beam caused from some emittance blow up and preventing the intensity. The system consists of newly designed electrostatic beam position monitor(ESBPM), analogue to digital convertor(ADC) and a graphic display. The detail of this system is described in this paper.

1. Introduction

The KEK 500MeV booster is a combined function synchrotron having eight cells in a 12m diameter circumference and is operated with a rapid cycling of 50ms period (Fig. 1).

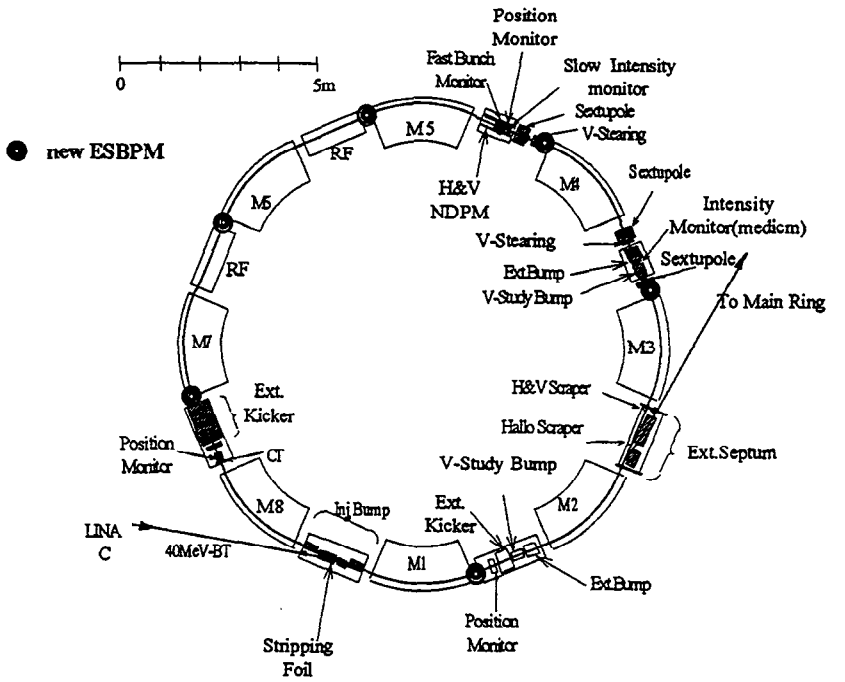

Figure 1. KEK 500MeV Booster Synchrotron and an installation of the new ESBPM.

Most of all the straight sections are already occupied by many equipments such as collection magnets, beam monitors *etc.* And the main bending magnets have a curved shape to provide a combined focusing function. So that there are no room for systematic beam orbit monitor installation. The beam orbit has been observed by only two monitors in the ring. However, recent accelerator machine study shows some transverse emittance blow up and a dynamic variation of the beam orbit in the booster ring during the acceleration period. A systematic beam orbit observation is strongly required.

A strictly small area are found to install the new beam position monitors between a bellow vacuum chamber in the main bending magnet and the short straight section, only 3cm in length is available.

2. Structure of the pick-up

By the strict installation condition, the beam position pick-up should have the length less than 3cm. The pick-up is the electrostatic pick-up, on which some electric charge are induced according to the beam bunch passed.

The outer case of the pick-up is just fit to the vacuum bellow cross section which is race track shape with the width of 150mm and height of 90mm. On the inner surface of the outer case, four thin stain-less steel electrodes are attached by using a ceramics pipe. The electrode and ceramics pipe are finely designed to fit the outer case shape in order to maximize the electric capacitance between the electrode and the outer case (Fig. 2). So as to make the gap between those small as possible, the ceramics pipe is a small tube designed to have the diameter of 1.2mm, and small stain-less steel tip is welded on the outer case. The gap is only 0.2mm and the electrode capacitance is typically 30pF. Each electrode is connected to a LEMO type vacuum feed through. The overview of the pick-up is shown in Fig. 3.

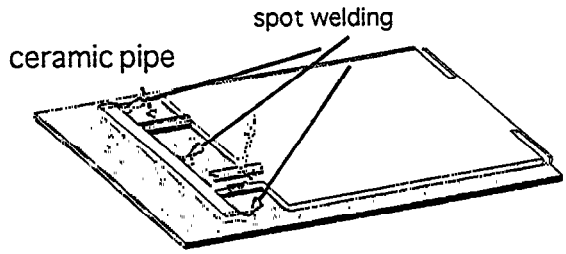

Figure 2. The electrode and support.

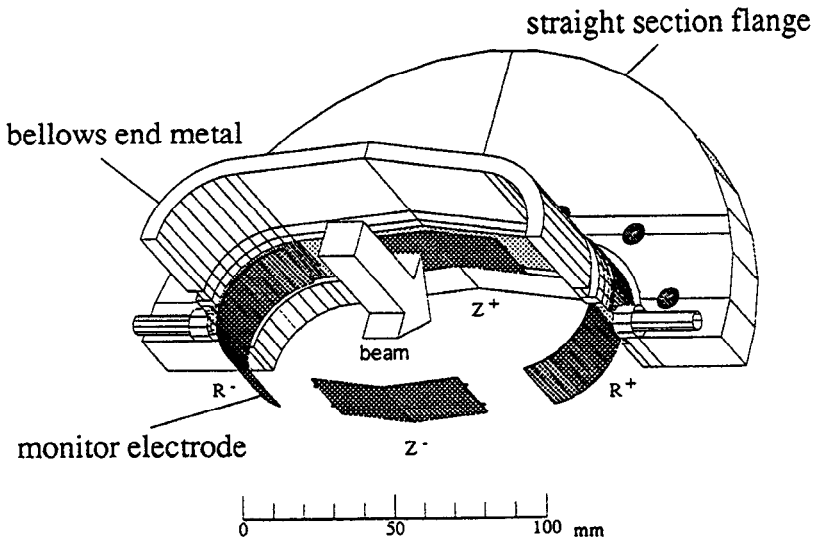

Figure 3. An overview of the position pick-up.

3. Calibration

The electrostatic pick-up is described equivalently as the circuit shown in Fig.4., and has a frequency characteristics like a high pass filter (equation 1).

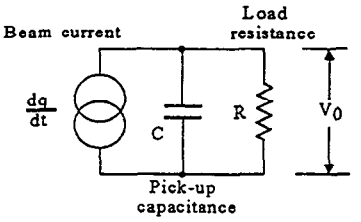

Figure 4. An equivalent circuit of the pick-up.

The transfer function from the beam current to the pick-up voltage is described as follow;

$$V_0 = \frac{S}{S + S_0} \frac{q}{C} \qquad (1)$$

Where S is the Laplace variable and S_0=1/CR.

The high cut off frequency is described as 1/CR, where C and R are the electrode capacitance and the load resistance, respectively. The high cut off frequency of our pick-up, about 660MHz, however, is too higher than the booster ring acceleration rf frequency which ranges from 4MHz to 6MHz. This wide band sweep causes some problems to detect the beam bunch signal, *i.e.*,the detected signal amplitude varies because of the variation of the frequency spectrum of the beam bunch. To avoid this difficulty, we put an additional capacitance of 2200pF on to the feed through, and it makes the high frequency cut off low enough to cover the lowest acceleration frequency.

A test pick-up was installed in the booster ring and carried out some examinations. An observation showed that there was a resonant characteristics around the frequency of 160MHz. So that the some spectrum of the beam revolution frequency disturb the pick-up signal when its frequency is just on the resonance of the pick-up. This resonance comes from the stray inductance of the feed through and is dumped by putting a small resistor in the connector. The dumping resistor is estimated by using a circuit simulation program "SPice" and the final results are shown in Fig. 5 and 6.

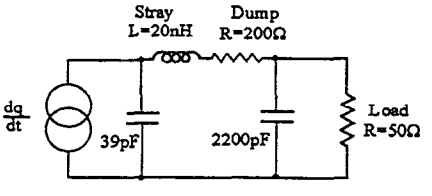

Figure 5. A dumped pick-up.

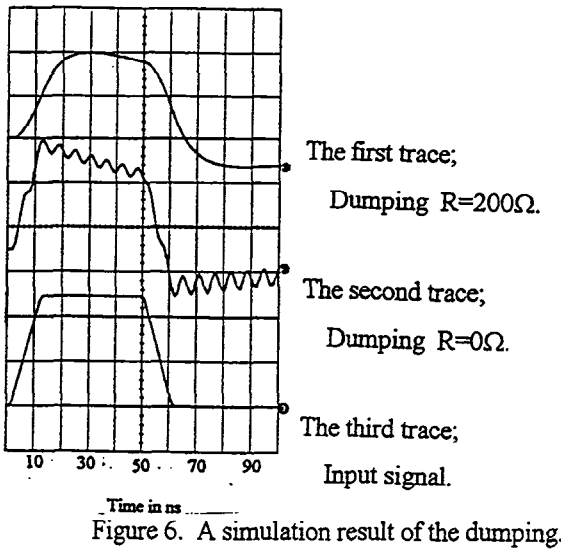

Figure 6. A simulation result of the dumping.

The electric field distribution in the pick-up is estimated to know the sensitivity of the pick-up to the beam orbit deviation. The field calculation is performed by a finite element method using a "Excel" program on an IBM PC compatible personal computer. Figure 7 shows an example of the calculation.

The cross section of the pick-up is a race track with low aspect ratio. It causes a large non-linearlity in the beam position sensitivity. So we developed a bench stand to measure the position dependence of the sensitivity. Each pick-up are calibrated by this bench stand measurement and typical result is shown in Fig. 8.

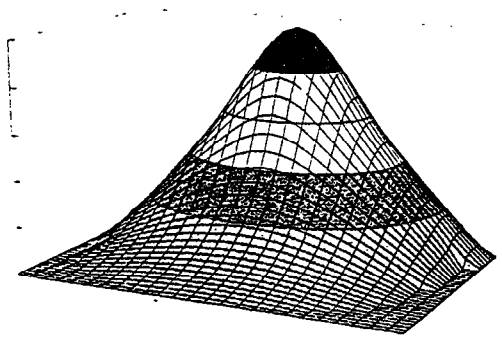

Figure 7. A calculated field distribution in the pick-up.

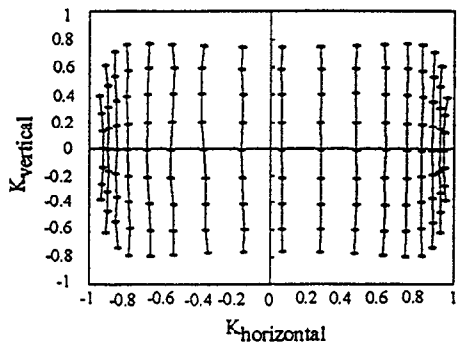

Figure 8. Mapping data of the pick-up. The point separation is 5mm.

4. Signal processing

Six pick-ups have been installed in the booster ring. The induced signal on each electrode is amplified immediately in the ring and diode detector is used in the amplifier to obtain a signal envelope. This process makes easy the signal transmission through a long distance, in which the signal disturbance coming from a high frequency noise can be avoidable. In the first stage of the test installation, the signal is directly transmitted to the control room. However, the position signals are disturbed by a stray acceleration rf power or the pulse noise caused from the kicker magnet *etc.* So that the bunch by bunch fast position monitor was difficult, then we put the diode detector in the ring and obtain only the low frequency envelope component, which makes easy to get the position accuracy of less than 0.5mm. The diagram of the signal processing is shown in Fig.9.

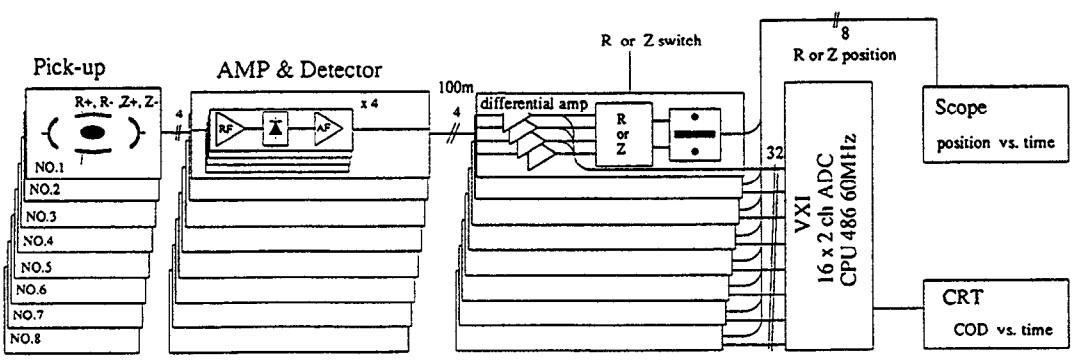

Figure 9. Circuit diagram of the system.

The beam position is displayed in two ways. The signal is divided into an analogue switch and to an analogue digital convertor (ADC). The switched signal is electrically normalized to obtain the beam position following the arithmetics as:

$$X = K \frac{V_{X+} - V_{X-}}{V_{X+} + V_{X-}}$$

where X and K are the beam position in the unit of mm and the calibration constant, respectively. This normalized signal shows the time variation of the beam position at the pick-up and displayed on a CRT scope (Fig. 10).

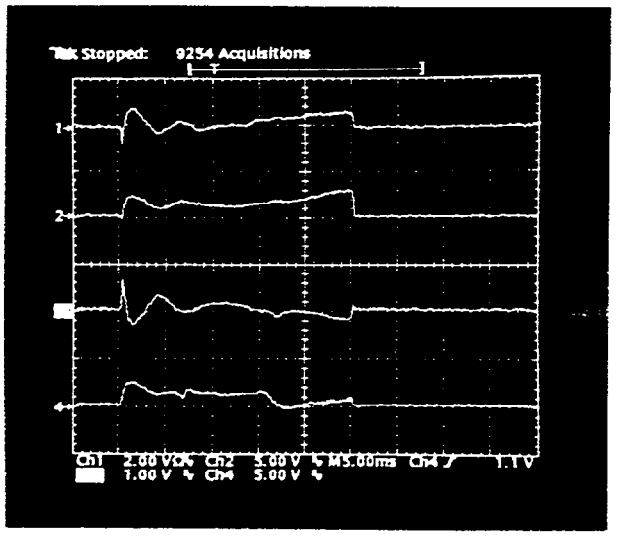

Figure 10. Analogue display of the COD.

However, the strong non-linearlity mentioned in the section 3 is too difficult to compensate in this electrical process.

While, the digitized signal is easy to proceed both the normalization and non-linearily compensation by using a computer. Two 16 channel ADC and a IBM PC compatible computer are installed in a VXI crate, and the digitized signal is transmitted via the VXI bus. The software programming is now going on.

Conclusion

A new closed orbit monitor system is developing for the KEK 500MeV Booster Synchrotron. The new electrostatic pick-up electrode and its support are designed. And the data acquisition system by using the VXI and computer is now developing to display the real time display of the detected beam orbit.

ICANS-XIII
13th Meeting of International Collaboration on
Advanced Neutron Sources
October 11-14, 1995
Paul Scherrer Institut, 5232 Villigen PSI, Switzerland

FFAG - OPTIONS FOR SPALLATION NEUTRON SOURCES

R. L. Kustom[1], S. Martin[2], P. F. Meads, Jr.[3], E. Zaplatine[4], K. Ziegler[4]

[1]ANL, 9700 South Cass Ave., Argonne Illinois 60439, USA
[2]KFA Jülich, IKP, D-52425 Jülich, Germany
[3]7053 Shirley Drive, Oakland, CA. 94611-1631 USA
[4]HMI Berlin GmbH, Glienicker Strasse 100, 14109 Berlin, Germany

ABSTRACT

The architecture of facilities needed to produce intense pulsed proton beams to obtain a high power pulsed neutron flux is described. We elaborate on one architecture and give reasons, why we think this combination is particularly suitable for a spallation neutron source. The ring accelerator we favour is an FFAG (Fixed Field Alternating Gradient) machine, known since the late fifties from studies at MURA. We describe several options for the FFAG machines, all producing a beam power of 5 MW. In conclusion an outlook on 'new' ideas concerning nonscaling FFAG's including nondispersive straight sections and their advantages is given.

1. Introduction

For the design of a pulsed spallation neutron source two architectures are feasible: a) a linear accelerator followed by a ring machine, with an orbit period of a little more than the required length of the proton pulse ($\sim$1 μs), or: b) an induction linac, which can produce the desired pulse length directly. As induction linacs for high power proton beams have never been built and operated and their estimated price appears high[1] compared to architecture option a), so far only this option has been investigated in more detail[2–5]. One of the major design criteria for high power accelerator facilities is the requirement of extremely low beam losses ($<10^{-5}$), in order to allow 'hands on' maintenance and repair, and to have remote handling facilities only at areas beforehand determined where the beam is disposed of in emergency or in a test period. Beam losses are the main reasons limiting the performance of the existing spallation sources at Rutherford Appleton Laboratories in England and Los Alamos Laboratories in the USA. In the linac-ring scenario there are unavoidable losses at injection into the ring, because the 'stripping injection method' used to modify the phase space density of the incoming beam through the non liouvillean stripping process. The stripping of the incoming H^- beam produces a charge

Keywords: Ring-Accelerator, Fixed-Field, Frequency Modulation, Intense Beams

state distribution of H^-, H^0 (in excited Rhydberg states), and of the desired protons, with the relative abundance of the charge states depending on thickness of the foil and energy of the incoming beam. The amount of the undesired H^- and the excited H^0 beam is of the order of one to two percent. We think therefore, that it is best to inject at an energy as low as possible, to minimize the damage produced by the particles lost during injection, because this damage is proportional to the power contained in the lost beam. Therefore the major part of the beam power should be rather gained in the ring accelerator, than in the injector linac.

2. The Fixed Field Alternating Gradient Accelerator

The ring accelerator we have looked at is a Fixed Field Alternating Gradient (FFAG)[6] machine, and we have studied three versions, all producing a beam power of 5 MW. The FFAG machine is a circular machine which has properties of a synchrocyclotron and of a synchrotron. It uses DC magnets but the frequency has to be modulated, just as in synchrocyclotrons, however for the FFAG generally only by 10–20% compared to the 40–50% for synchrocyclotrons. The working point in the tune diagram for a FFAG is fixed as in synchrotrons. The beam is injected into the FFAG at an inner radius, the injection radius, and then accelerated and spiraling out to the extraction radius, somewhere between 1 m to 4 m larger than the injection radius. This requires relatively large magnets, the price one has to pay for using DC-magnets. Inherently the FFAG is a pulsed machine, like the synchrocyclotron, and therefore well suited for the production of pulsed proton beams. At the extraction radius the beam is kicked out of the machine using a fast kicker, and then transported to the target. The beam quality of the FFAG, like in synchrocyclotrons, is not extremely high, but that is exactly what one wants for high power beams, because one needs large size beams at the target, in order not to destroy the targetwindow or the target. We will now describe several FFAG-options, all laid out for a beam power of 5 MW. The obvious advantage of an FFAG over a linac–storage ring option or a linac–synchrotron version is the possibility of using a higher repetition rate. Frequencies of 200 to 250 Hz are quite feasible, opening up the possibility to use multiple targets with repetition rates of e.g. 200Hz, 50Hz, and 10 Hz respectively. The FFAG options discussed below range in the repetition rate from 50 Hz to 200 Hz, with the higher repetition rate demanding more RF power in the FFAG and also a higher repetition rate for the linac injector.

2.1 The high energy 50 Hz FFAG-option

When the ESS study was initiated in 1991 in Simonskall one of the options considered, was a 430 MeV linac injecting into a 3.2 GeV FFAG at 50 Hz. We studied quite a range of machines for this option, varying magnetic field, number of sectors, field index k, as well as the radial and vertical tunes. Finally we looked into the feasibility of producing the required magnetic field, building the magnets, designing the RF-system, and looking at the dynamic aperture of the machines we considered. We had set the extraction radius to 45 m, and depending on the magnetic field data the injection radius varied between about 41.5 m and 42.3 m, giving a radial extent from 2.7 m to 3.5 m, obviously rather large magnets. Furthermore it became clear, that for a machine with such a high field index k, which we needed to avoid crossing γ_{tr} and to reduce the radial width, the dynamic aperture decreased dramatically with increasing vertical betatron amplitudes. Also an energy gain factor of about 7.5 seems rather large for a convenient FFAG machine, leading always to a rather large radial extent. When we looked into the cost of such a machine we concluded, that it would be a rather costly option for a 5 MW 50 Hz spallation source. In that case it would be less expensive to built a 50 Hz rapid cycling synchrotron, going from 430 MeV to 3.2 GeV, provided the multiturn injection and capture problem can be solved, as is indicated by the Argonne study[7]. The parameters of one version of a 430 MeV–3.2 GeV at 50 Hz are shown in Table 1, column 1.

2.2 A 50 Hz 800 MeV to 2.5 GeV FFAG-option

The study of this version was proposed at a meeting in Müden in December of 1993 by G. Bauer. It was to be compared with the 800 MeV – 3 compressor ring option proposed by our colleagues from RAL. We set the extraction radius of this machine to 38 m, and again varied the different field parameters to optimize radial width, mechanical dimensions, and dynamic aperture for the FFAG. We also had studied the magnetic field data and had come to the conclusion, that a maximum field of 5 T is quite feasible. The radial extend of this machine is 1.7 m, it has 24 sectors, and radial and vertical tunes of 4.78 and 3.29 respectively. This machine unfortunately does not use a low energy injection and it needs quite a detailed study to ensure the low losses required for the incoming 1.6 MW beam. The parameters for this machine are shown in table 1 column 2. A cost estimate of this machine has been given elsewhere[8] , and the investment cost for the FFAG including shielding and tunnel is 207 MDM. The cost per MW of beam power gained in the FFAG is approximately 66 MDM.

2.3 A 100 Hz 430 MeV to 1.6 GeV FFAG-option

This FFAG option was considered, when it appeared that the high energy version with an extraction energy of 3.2 GeV would not be competitive from cost considerations. We then set out to find the optimum parameters for a 5 MW machine. We set the extraction radius to 26 m with a maximum magnetic field of 4 T. The radial extent of this machine is 1.7 m and the field index $k = 11.8$. There are 16 sector magnets. The radial and vertical tunes are 4.26 and 3.26 respectively. There are 10 RF-cavities needed to produce the required energy gain per turn of 200 kV, each capable of delivering 26 kV. The RF-frequency modulation is 19%. The beam dynamics of this machine also are quite comfortable, giving a value of more than 83000 π·mm·mrad at zero vertical amplitude and 32000 at an amplitude of 5 cm. The technical requirements for this machine are quite conservative and can certainly be obtained. The parameters of this FFAG are given in table 1 column 3. We have studied the cost for this machine in more detail and conclude that the total cost for such an FFAG including shielding and tunnel, is estimated to be 180 MDM. The cost per MW of beam power gained in this FFAG is about 49 MDM. A cost breakdown is given in Table 2.

3. Cost Estimation Procedure

In order to get an idea of the relative cost of the different FFAG options we have looked at, we have set up a table calculation program, which gives us the estimated cost for the machine components. For instance to get the cost for a magnet, we calculate the total amount of steel needed for yoke and pole, and then use the cost for steel (3 DM/kG) and machining (3 DM/kG). For the vacuum chambers we estimated 300 TDM per magnet and for support and alignment 150 TDM per magnet. The cryogenic coils are estimated to 1.08 MDM per magnet. Clearly this estimates are based on a mixture of educated guesses and solid information. For comparisons of different FFAG-options as far as their price is concerned however it is quite reliable. Of course to estimate the cost of a linac–FFAG facility the varation of cost for the linac with linac energy and required beam current have to be looked at.

4. Conclusion and outlook

We have looked at the possibility of using an FFAG as ring accelerator for a high power pulsed spallation source. In most cases we limited ourselves to investigate so called 'scaling' machines, where the orbit are simple photographic images of each other at all energies. This means, that if one has found a solution for one energy, all other energies are outomatically stable also. This procedure is necessary when one wants to scan a large variation in the parameter

Table 1: FFAG-options for 5MW beam power.

	a	b	c	
Max Energy	3200	2500	1600	MeV
Inj Energy	430	800	430	MeV
Inj Radius	41.57	36.31	24.3065	m
Ext Radius	45.00	38.00	26	m
Max +B field	4.00	5.00	4.00	T
Min +B field	1.04	2.31	1.81	T
Max -B field	-3.00	-1.70	-2.0	T
Min -B field	-0.78	-0.79	-0.91	T
Field Index k	16.66	17.41	11.8	
Repetition Rate	50	50	100	Hz
Number of Sectors	24	24	16	
Azimuthal Cell Length	11.78	9.95	10.21	m
Straight Section Length	7.94	7.11	7.447	m
Average Current	1.56	2.00	3.13	mA
β=v/c max	0.97	0.96	0.93	
β=v/c min	0.73	0.85	0.73	
$B\rho$ max	13.44	11.03	7.87	T·m
$B\rho$ min	3.32	4.88	3.32	T·m
radial width	3.426	1.69	1.694	m
Ions Number/Pulse	1.95	2.50	1.95	$*10^{14}$
(+) Plateau Width	6.75	3.03	4.53	%
(-) Plateau Width	2	2.73	1.5	%
Approx. Magnet Width	3.84	2.29	2.76	m
Vert. Beam Size (95%)	33.84	99		mm
Spiral Angle	4.86	0	0	deg
Q_x	4.75	4.78	4.26	
Q_y	3.75	3.29	3.26	
x: phase adv/cell	71.25	71.70	95.85	deg
y: phase adv/cell	56.25	49.35	73.35	deg
W_x for z=0	453000	740239	83412	π·mm·mr
W_x for z/R=0.001	28183	59301	32219	π·mm·mr
Harmonic Number	1	2	1	
Max Acc. Time	0.018	0.018	0.009	sec
Energy Gain/turn	179.83	92.40	200.0	kV
Max RF Freq.	1.03	2.42	1.7052	MHz
Freq. Swing Ratio	1.27	1.09	1.1934	
Number of Cavities	11	6	10	

Table 2: FFAG Cost (type c)

All Magnets Cost	45	MDM	Total Shielding Cost	7	MDM
Total RF Cost	53	MDM	Total Diagnostic Cost	18	MDM
Instrumentation Cost	41	MDM	Tunnel Cost	15	MDM
			Investment Cost	179	MDM

space in order to find an optimum. However this also means, that there are further steps of optimization possible if one uses nonscaling machines with special insertions like non dispersive straight sections[9]. In that case however the machine has to be checked at each energy, as far as stability and dynamic aperture is concerned. The advantage of such nondispersive straight section is, that the beam goes through this section along the same orbit at all energies so relatively small RF cavities with accordingly high RF amplitudes can be used for the acceleration. It even appears to be possible to design the non scaling FFAG in such a way, that the necessary frequency modulation is so small, that even a constant frequency could be used with rather high RF amplitudes of several 100 kV, like for instance in the cavities of the PSI ring cyclotron[10], in which case the beam would be accelerated with a rather large energy gain and relatively few turns to the extraction radius and the question of getting close to resonances or even passing through a resonance will be quite alleviated. Further studies need to be made to investigate these questions, and we hope to report on the results shortly.

5. References

1. A. Faltens, *Proc. of the Workshop on Accelerators for future Spallation Neutron Sources*, Feb.16-20,1993, LA-UR-93-1356, Vol.IIB, p.1282.

2. H.Lengeler, *Proc. of the 4th European Particle Accelerator Conf.*, EPAC94, Vol.1, p.249, 1994.

3. IPNS Upgrade: A feasibility Study, Argonne National Laboratory, *ANL-95/13.*

4. 5 MW Pulsed Spallation Neutron Source, *Preconceptual Design Study*, Brookhaven National Labotatory, BNL60678, June 1994.

5. A. Jason, *Proc.of the Workshop on Accelerators for future Spallation Neutron Sources*, Feb. 16-20, 1993, LA-UR-93-1356, Vol. IIA, p.370, 1993.

6. F.T. Cole et al., *Rev. Sci. Instr.*, 1957.

7. E.S. Lessner, Y. Cho, *Proc. of the 1993 Particle Accelerator Conf.*, Vol.1, p.399, 1993.

8. H. Jungwirth et al., *Proc.of the XIV Conf. on Cyclotrons and their Appl.*, Cape Town, RSA, 1995, to be published by World Scientific, Singapore.

9. P.F.Meads Jr., *Proc. of the 1993 Particle Accelerator Conf., Washington*, May 17-20, p.3825.

10. P.K.Sigg et al., *Proc. of the XIV Conf. on Cyclotrons and their Appl.*, Cape Town, RSA, Oct. 1995, to be published by World Scientific, Singapore.

EUROPEAN SPALLATION SOURCE
General ESS Meeting
October 16-19, 1995
Weinfelden, CH

PULSED SPALLATION NEUTRON SOURCE WITH AN INDUCTION LINAC AND A FIXED-FIELD ALTERNATING-GRADIENT ACCELERATOR

A. G. Ruggiero [a], G. Bauer [b], A. Faltens [c], R. Kustom [d], S.A. Martin [e], P. Meads [f], and E. Zaplatin [g], K. Ziegler [g]

[a] Brookhaven National Laboratory, P.O. Box 5000, Upton, NY 11973
[b] Paul Scherrer Institut , 5232 Villigen PSI, Switzerland
[c] Lawrence Berkeley National Laboratory, One Cyclotron Road, Berkeley, CA 94720
[d] Argonne National Laboratory, 9700 So. Cass Avenue, Argonne, IL 60439
[e] KFA, Kernforschungsanlage Julich GmbH, 52425 Julich, Germany
[f] 7053 Shirley Drive, Oakland, CA 94611
[g] Hahn-Meiner-Institut, Glienicker Strasse 100, 14109 Berlin, Germany

ABSTRACT

The paper describes an accelerator scenario of a Pulsed Spallation Neutron Source made of an Induction Linac injecting into a Fixed-Field Alternating-Gradient Accelerator (FFAG). The motivations underlying the proposal deal with the concern of removing technical risks peculiar to other scenarios involving RF Linacs, Synchrotrons and Accumulator Rings, which originate, for example, from the need of developing intense negative-ion sources and of multi-turn injection into the Compressor Rings. The system proposed here makes use of a positive-ion source of very short pulse duration, and of single-turn transfer into the circular accelerator.

1. Introduction

There are basically two groups of accelerator architectures to be considered for the application of Pulsed Spallation Neutron Sources. One group makes use of RF Linear Accelerators, which inject into Compressor Rings, either Rapid-Cycling Synchrotrons or Accumulator Rings. The other group uses more exotic machines, that is, Induction Linacs and Fixed-Field Alternating-Gradient accelerators. In the following we review briefly the concepts underlining the first type of accelerator architectures and we shall expose some of their most fundamental technical risks, that is, development of high-intensity negative-ion sources and the control of very low level beam losses during injection into the Compressor Rings. We shall then describe, also briefly, the features of more exotic accelerators, namely, Induction Linacs and Fixed-Field Alternating-Gradient Accelerators. We then finally propose, for consideration of further studies, an architecture which is made of an Induction Linac injecting into a Fixed-Field Alternating-Gradient Accelerator. This combination should in principle eliminate those major technical risks we have mentioned above, peculiar to the first group of accelerators of Synchrotrons and Accumulator Rings.

Keywords: Induction Linac, FFAG Accelerator

2. General Considerations on Accumulators and Synchrotrons

In order to get a short and intense beam pulse, we need to "compress' the proton beam in one or more Compressor Rings [1-4]. The circumference of the Rings is adjusted to yield a revolution period comparable to the required pulse length. The beam intensity needed depends on the intensity of the negative-ion source and on the number of beam turns that is possible to inject. Finally, the average beam power, for a give repetition rate, is given by the product of the average beam current with the final beam kinetic energy. This approach is very simple and straightforward, and very easy to follow. Beam energy and beam current can, to some degree, be traded against each other.

The Compressor Ring can be either a constant-energy Accumulator Ring [1-2], where the beam is stored after it has been injected in many turns, until the final intensity has been reached, or a rapid-cycling Synchrotron where, after multi-turn injection, the beam is accelerated to the final energy. In the former case the beam power is totally produced by acceleration in the Linac, and the Accumulator Rings are needed only to compress the beam. Clearly in this approach the RF Linac becomes a crucial component for achieving the desired beam parameters, and considerable design effort is to be given to it. Rapid-Cycling Synchrotrons [3-4], on the other end, reduce the technical requirements on the performance of the injector. This method should permit high energies (2 - 10 GeV), and most of the beam power is obtained by acceleration in the Synchrotron.

All these accelerator architectures, which assume an RF Linac as injector, have considerable technical risks that can be summarized as follows. Negative-ion sources are required to allow multi-turn injection into the Compressor Rings by charge-exchange method. Considerable high-current sources of negative-ions are thus needed with performance well beyond the capability of the present technology. Very large number (about a thousand) of beam turns are to be injected in the Compressor Rings. This makes quite problematic the control of beam losses during transfer and injection to a level low enough to circumvent possible long-term activation problems caused by the same beam losses. These technical risks can be eliminated by considering different, less well publicized accelerator architectures that do not need negative-ion sources and multi-turn injection. The architecture that we like to propose here for further consideration is a combination of an Induction Linac followed by a Fixed-Field Alternating-Gradient Accelerator.

3. Induction Linacs

Induction Linacs [5] have the very interesting capability to accelerate microsecond-long, and even shorter pulses, at high repetition rate, and with relatively large accelerating gradient (1 MV/m). In principle they can accelerate large beam intensity, few tens of amperes, as directly derived from relatively low duty-cycle positive-ion sources. With an Induction Linac there is in principle no need of Compressor Rings, since beam pulses of the desired short length and power can be directly generated at the exit. Unfortunately, full-energy Induction Linacs are quite long and expensive. But the Linac, as it will be explained later, can also be used as an injector to a Rapid-Cycling Synchrotron, or an FFAG machine, by removing thus the concerns and the problems associated to the multiturn injection and to the development of negative-ion sources, since the positive-ion beam can be simply injected in one single turn. The major technical risk is the development of the (positive) ion source, which considering the large beam

intensity has also a large beam emittance, the early stage of acceleration, the overall length, and the cost. The technology, which is of old date, and by now very mature and sophisticated, is not that well known to the large majority of the accelerator expert community, who prefer working on Accumulators, Synchrotrons and RF Linacs. In the past there has been a tendency to dismiss prematurely the technology as a stand-alone application to Pulsed Spallation Neutron Sources. But we believe that if used as a low-energy injector to an FFAG accelerator, as explained below, has very attractive features to be exploited.

4. Fixed-Field Alternating-Gradient Accelerators

FFAG accelerators have also been proposed in the past as possible Spallation Neutron Sources [6-9]. They need an injector, usually a modest RF Linac, but they can provide otherwise most of the acceleration once the beam velocity has reached a large enough value. The good feature is that they provide acceleration in a constant (fixed) field environment. In the past the use of an FFAG was based on the idea to inject 300 to 500 turns pulse trains arriving from an injection linac. During that time the RF-system of the FFAG was turned off. When the DC-beam in the FFAG had reached the space charge limit, the RF was turned on slowly and the beam adiabatically captured into the RF-bucket. Then the beam was accelerated to full energy, spiraling out to the extraction radius, where it was then kicked out in one single shot, and directed onto the neutron production target. The output power of such a linac-FFAG combination is determined by the space charge limit at injection, the FFAG repetition rate and the output energy of the FFAG. The major technical difficulty for the past linac-FFAG combination was the low loss requirement for the multiturn injection, the lossfree adiabatic trapping of the injected beam, and the disposal of the excited H^0-states at a suitable beam stop. The design of the sector magnets and of the rf cavity is also not trivial. Most of these problems can be removed by using an Induction Linac as the injector. Because of the initial short beam pulse length, in this case, there is no need for multiturn injection, which simplifies considerably the design.

The technology of FFAG accelerators is also of old date, but recently has acquired maturity and has become quite sophisticated. Several new features can be incorporated [10]. For instance, long drift spaces can be inserted. To minimize the cost of the magnets, transverse focussing may be obtained not only with a conveniently chosen field profile, but also with the shaping of the entrance and exit angles of the bending magnets. With specially adjusted focussing elements, it is also possible to introduce isochronism and zero or small dispersion regions where to locate more compact rf cavities for acceleration.

5. A Scenario based on an Induction Linac injecting into a FFAG Accelerator

The scenario which makes use of the best combined features of the Induction Linac and of the FFAG accelerator is as outlined in Figure 1. The combination in sequence of the two types of accelerator complement each other's features, removes some of their major technical difficulties, and, most important, eliminates problems peculiar to negative-ion sources and multi-turn injection.

As a reference, we shall assume an average beam power of 5 MW at the repetition rate of 200 Hz. The final energy in exit of the FFAG accelerator is in the range 1-3 GeV, so that the average proton beam current will range between 0.42 and 1.25 mA, as shown in Table 1. A preliminary conceptual design of the Induction Linac [5] has shown that an intermediate energy of

260-600 MeV is possible with an initial accelerating gradient of 36 kV/m and a final gradient of 1 MV/m. The total length would be 380-720 m. These values are also shown in Table 1. The positive-ion source operates at the duty cycle of 0.04%, delivering a pulse length of 2 μs and a peak current of 4.2-12.5 A depending on the final energy of the facility.

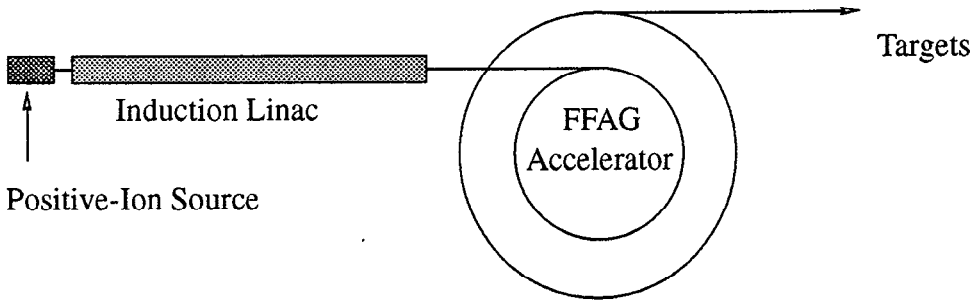

Figure 1. A Pulsed Spallation Source with an Induction Linac and a FFAG Accelerator

During acceleration the beam is compressed in length to 100-150 ns. In fact, higher accelerating gradients can be reached at the end of the Linac with a shorter beam pulse and when space-charge forces are less important. Typical normalized beam emittance is 10-30 π mm mrad. Total beam dimensions are thus of the order of few centimeters, whereas the inner core diameter can be made of 60 cm.

Table 1: Requirement and Induction Linac Parameters

Average Beam Power	5 MW	
Repetition Rate	200 Hz	
Final Energy	1 GeV	3 GeV
Average Beam Current	1.25 mA	0.42 mA
Positive-Ion Source		
Pulse Length	2 μs	
Duty Cycle	0.04 %	
Peak Current	12.5 A	4.2 A
Normalized Emittance	30 π mm mrad	10 π mm mrad
Induction Linac		
Final Energy	260 MeV	600 MeV
Final Pulse Length	0.15 μs	0.1 μs
Initial Accel. Gradient	36 kV/m	
Final Accel. Gradient	1 MV/m	
Total Length	380 m	720 m
Internal Core Diameter	60 cm	

The design, construction and operation of this Induction Linac should not present insurmountable difficulties. Also, considering the very short beam pulse length and the large ratio of inner core diameter to beam size, no problems of radiation activation due to latent beam losses are expected. Such a short beam pulse can be injected in one single turn in a circular accelerator for further acceleration. The circular accelerator could be a FFAG Accelerator because it avoids fast-ramping magnetic fields, as in the case of Synchrotrons, which require a complicated vacuum system and vacuum chamber, among other things, and limit the pulse repetition rate.

The actual value of the injection energy, between 260 and 600 MeV, can be chosen as a compromise between conflicting requirements. One would prefer a large value of the injection energy to avoid too severe space-charge effects, to reduce the cost of the FFAG accelerator, to narrow the required momentum acceptance and thus the size of the magnets. On the other end high-energy Induction Linacs are long and more costly. The optimum choice can be determined only after careful trade studies. Table 2 summarizes typical parameters of the FFAG accelerator for a range of injection and final energy values.

Table 2: FFAG Accelerator Parameters

Final Energy	1 GeV	3 GeV
Injection Energy	260 MeV	600 MeV
Circumference	200 m	200 m
Packing Factor	40 %	40 %
Bending Radius	12.74 m	12.74 m
Bending Field	1.95-4.44 kG	3.19-10.01 kG
Momentum Aperture	± 40 %	± 50 %
max. Dispersion	2.0 m	2.0 m
max. Beta Function	20 m	20 m
Magnet Aperture	1.6 m	2.0 m
Magnet Gap	30 cm	20 cm
Space-Charge $\Delta\nu$	0.3	0.3
Normalized Emittance	400 π mm mrad	220 π mm mrad
Acceleration Period	5 ms	5ms
Harmonic Number	1	1
rf Frequency	0.93-1.31 MHz	1.19-1.46 MHz
rf Peak Voltage	400 kV	600 kV

A preliminary design of the FFAG accelerator has been made which includes drifts of few meter length to accommodate equipment for injection and extraction, and zero-dispersion regions for rf cavities. It is to be noted that one single-turn transfer and extraction into and

from the FFAG accelerator can be made at a high confidence level, with high efficiency (99.99% or better).

6. A High-Performance Neutron Facility

For many years, indeed since the early days of the SNQ-project [11], the discussion on the "best" design parameters of a spallation neutron source have been going on and, as far as long pulses (or strongly coupled moderators yielding high average neutron flux) are concerned, have been revived recently. There are clear arguments for short pulse spallation neutron sources which allow to exploit hot and epithermal neutrons, and to perform powder diffraction, in an unparalleled way. Their most desirable parameters are proton pulses of a few hundred nanoseconds length and a repetition rate of about 50 Hz. Furthermore, pulsed spallation neutron sources have also been shown to be quite successful in the cold neutron regime, but, due to the long flight times of these neutrons, lower repetition rates, of the order of 10 Hz, are desirable. For this reason, almost all new spallation source proposals include two target stations. These concepts leave aside, however, a large and well developed suite of instruments which have proven extremely successful on reactors and which could benefit by an order of magnitude, on average, from a time structure of the neutron source [12-15]. The important point is that for these instruments, a low repetition rate of the source is not necessary; many of them can easily work with moderately long pulses (200 μs or so) and at 100 Hz or above [16]. (Thermal time-of-flight, triple axis spectrometers, multiplexing instruments, etc.).

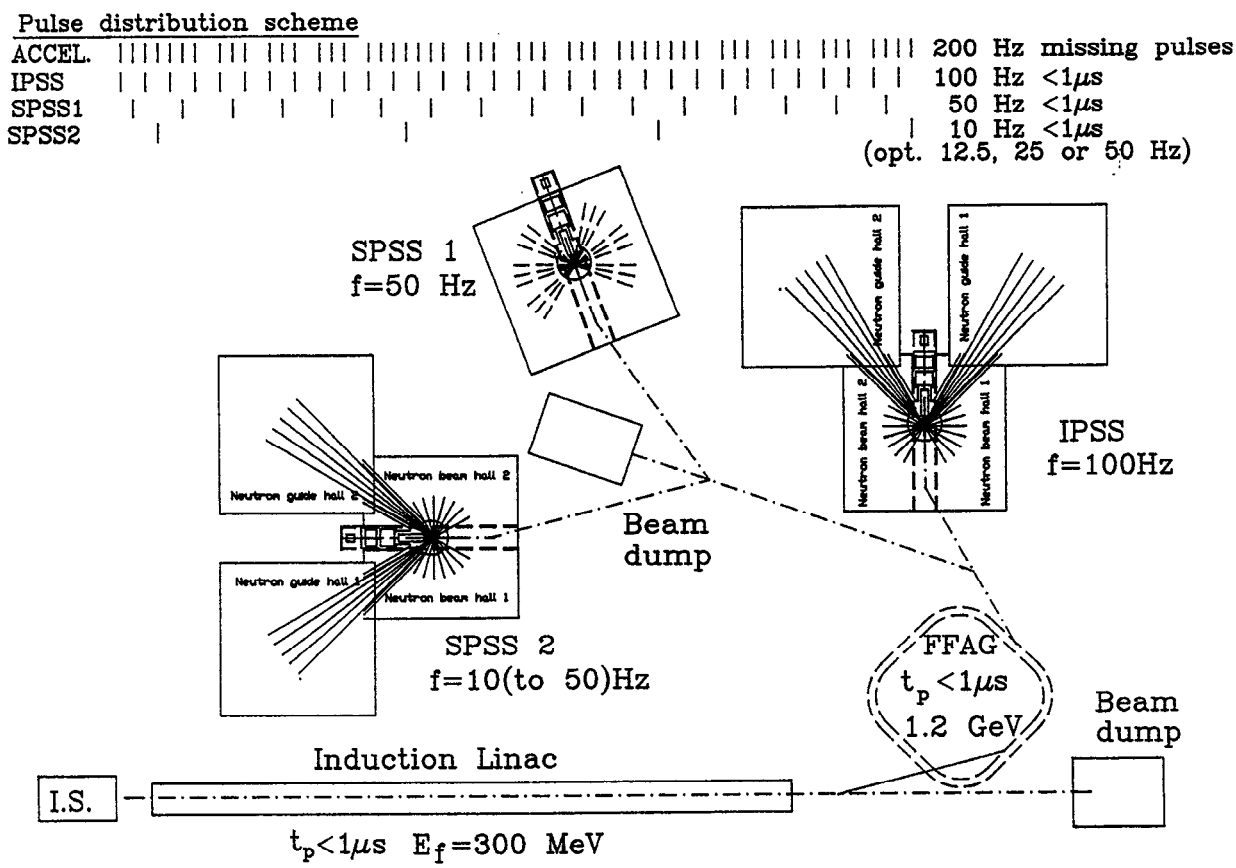

Figure 2: A High Performance Neutron Facility Based on a 200 Hz Short Pulse Accelerator System

If an accelerator system is available that can deliver pulses at 200 Hz, as the one described here, this offers a unique possibility to satisfy the needs of the traditional reactor user community and the short pulse users by supplying pulses to three target stations according to the scheme at the top of Figure 2. Every other pulse goes to the 100 Hz target, and 1 of 4 goes to the 50 Hz target. Of the remaining 50 cycles, 10 have protons and 40 are empty. These 10 pulses go to the 10 Hz - low rep rate target. (There are, of course, other options, e.g. 12.5 Hz, 25 Hz, etc., at corresponding beam average power). This combination, at a total beam power of about 5 MW (3 MW for the 100 Hz target, 1.5 MW for the 50 Hz target and 0.3 MW for the 10 Hz target) would make a unique world class facility which could serve about 100 neutron spectrometers with unprecedented performance, making the system very cost effective.

Due to the short proton pulse, slowing-down neutrons would be usable on all three targets. It should be noted that the power in each pulse is of the order of 30 kJ, less than one third of what is presently considered as feasible in the ESS-project. All three targets could be identical, differing only in their average power and their moderator-reflector systems.

7. Conclusion

We have described a Pulsed Spallation Neutron Source concept which is made of an Induction Linac and a FFAG accelerator, and serves 3 target stations of different design. Such project is feasible and has considerable attractive features which include the availability of high-intensity, low duty-cycle positive-ion sources, and the control of beam losses by eliminating the need of multi-turn injection. The short beam pulse, of sub-microsecond length, is beneficial to a sharp rising edge of the neutron pulse from the moderator. Due to the moderate pulse power of only 30 kJ, no serious problems in the target are anticipated.

8. References

[1] A.G. Ruggiero, BNL Feasibility Studies of Spallation Neutron Sources. Submitted to the Proceedings of the ICANS-XIII Conference, Villigen, Switzerland. October 1995.

[2] Outline Design of the European Spallation Neutron Source. ESS 95-30-M. Sept. 1995. Edited by I.S.K. Gardner, H. Lengeler, G.H. Rees.

[3] 5 MW Pulsed Spallation Neutron Source. Preconceptual Design Study. BNL 60678. Brookhaven National Laboratory. June 1994.

[4] IPNS UPgrade. A Feasibility Study. ANL-95/13. Argonne National Laboratory. April 1995.

[5] A. Faltens, Induction Linacs for Neutron Generation. Proceedings of the Workshop on Accelerators for Future Spallation Neutron Sources. Vol. II B, page 1284. Santa FE, NM. February 1993.

[6] P.F. Meads and G. Wustefeld, An FFAG-Compressor and Accelerator Ring studied for the German Spallation Neutron Source, IEEE Trans. Nucl. Sci., NS-32, p. 2637 (1985).

[7] S.A. Martin, et al., Study of FFAG-Options for a European Pulsed Neutron Source. Proceedings of the Workshop on Accelerators for Future Spallation Neutron Sources. Vol. II B, page 1252. Santa FE, NM. February 1993.

[8] R. Kustom, History of ANL 5 MW FFAG Design. Proceedings of the Workshop on Accelerators for Future Spallation Neutron Sources. Vol. II B, page 1264. Santa FE, NM February 1993.
[9] H. Jungwirth, et al., Design of Fixed Field Alternating Gradient Cyclotrons -- FFAG - as Accelerators for Intense Pulsed Proton Beams. Submitted to the Proc. of the 14th Int. Conf. on Cyclotrons and their Applications, Capetown, South Africa, Oct. 8-13, 1995.
[10] P. F. Meads, Proceedings of the Particle Accelerator Conference, Washington, 1993.
[11] G.S. Bauer, The general concept for a spallation neutron source in the Federal Republic of Germany; Atomkernenergie-Kerntechnik 41 (1982) p.234-242.
[12] B. Alefeld, G.S. Bauer, H. Conrad and H.H. Stiller, The SNQ Thermal Neutron Source DIANE and its Experimental Options; in "Neutron Scattering", Proc Int. Conf. Santa Fe, Physica 136B (1986), p 114-116 North Holland, Amsterdam.
[13] G. S. Bauer, R. Scherm, Forthcoming Instrument Developments for Improved Utilization of Neutron Beams; in "Neutron Scattering", Proc. Int. Conf. Santa Fe, Physica 136B (1986), p 80-86 North Holland, Amsterdam.
[14] R. Scherm, B. Alefeld; Instruments for High Flux Sources with Time Structure of Neutron Flux, paper IAEA-CN-46/80 in "Neutron Scattering in the 'Nineties", IAEA Conference Procceedings, Vienna, (1985) p. 247-259.
[15] G.S. Bauer, Some general reflections on long pulse neutron sources; in Proc. Int. Workshop on Long Pulse Spallation Sources Lawrence Berkeley Laboratory, 18-21 April 1995 to be published. Submitted to J.N.R.(1995).
[16] G.S. Bauer, Options for Neutron Scattering Instruments for Long Pulse Neutron Sources, Proc. ICANS-XIII, Paul Scherrer Insitut, PSI-Proceedings 95-02 (1995).

ICANS-XIII
13th Meeting of the International Collaboration on
Advanced Neutron Sources
October 11-14, 1995
Paul Scherrer Institut, 5232 Villigen PSI, Switzerland

A 10-GeV, 5-MW PROTON SOURCE FOR A PULSED SPALLATION SOURCE* +

Y. Cho, Y.-C. Chae, E. Crosbie, H. Friedsam, K. Harkay, D. Horan, R. Kustom, E. Lessner, W. McDowell, D. McGhee, H. Moe, R. Nielsen, G. Norek, K. J. Peterson, K. Primdahl, Y. L. Qian, K. Thompson, and M. White

Argonne National Laboratory, Argonne, IL 60439, USA

ABSTRACT

A feasibility study for a pulsed spallation source based on a 5-MW, 10-GeV rapid cycling proton synchrotron (RCS) is in progress. The integrated concept and performance parameters of the facility are discussed. The 10-GeV synchrotron uses as its injector the 2-GeV accelerator system of a 1-MW source described elsewhere [1-7]. The 1-MW source accelerator system consists of a 400-MeV H^- linac with 2.5 MeV energy spread in the 75% chopped (25% removed) beam, and a 30-Hz RCS that accelerates the 400-MeV beam to 2 GeV. The time-averaged current of the accelerator system is 0.5 mA, equivalent to 1.04×10^{14} protons per pulse. The 10-GeV RCS accepts the 2 GeV beam and accelerates it to 10 GeV. Beam transfer from the 2-GeV synchrotron to the 10-GeV machine utilizes highly efficient bunch-to-bucket injection, so that the transfer can be made without beam loss. The synchrotron lattice uses FODO cells of 90° phase advance. Dispersion-free straight sections are obtained using a missing magnet scheme. The synchrotron magnets are powered by dual-frequency resonant circuits. The magnets are excited at a 20-Hz rate and de-excited at 60-Hz, resulting in an effective 30-Hz rate. A key feature of the design of this accelerator system is that beam losses are minimized from injection to extraction, reducing activation to levels consistent with hands-on maintenance. Details of the study are presented.

I. Introduction

Proton beam power in the MW range with a pulse repetition rate of 30 to 60 Hz can be attained by several accelerator configurations; they can be divided into two basic categories.

In one category, a full-energy pulsed linear accelerator (linac) and pulse compressor ring or rings are used. A typical linac pulse length is of the order of 1 msec, and the compressor ring shortens the beam pulse length to the desired microsecond range. In general, a higher energy linac is expensive to construct and to operate. This is one reason that the highest energy proton linac built to date has less than 1-GeV energy. If the linac energy is chosen in a range around 1 GeV, a 5-mA beam current is required to obtain 5 MW of beam power. This is the low-energy, high-current option.

* Work supported by the U. S. Department of Energy, Office of Basic Energy Sciences under the Contract W-31-109-ENG-38.

+ Keywords: Accelerator, Synchrotron, Proton

In the other category, a low energy linac injects beam into a circular accelerator that provides most of the proton energy as a result of multiple revolutions around the ring. This combination of a low energy linac and a synchrotron to obtain high proton beam energy has been standard technology for decades. A typical synchrotron energy gain is about a factor of 10, thus the injector linac energy can be a factor of ten less than the final beam energy. If the final synchrotron energy is chosen to be 10 GeV, a beam current of 0.5 mA is required to produce 5 MW of beam power. This is the high-energy low-current option. A disadvantage of this method is that a synchrotron can accelerate a limited amount of beam. The most recent record for the number of protons accelerated per pulse is 6.3×10^{13}, set by the AGS at BNL. The 1×10^{14} protons/pulse requirement for 0.5 mA current at 30 Hz can be reached with appropriate R&D and design features.

One of the most important design considerations is the prevention of beam losses during all phases of transport and acceleration. Handling a smaller number of particles (lower current) should result in lower losses. Past experience has shown that the most likely time for beam losses to occur is during multi-turn injection into a ring. If there are injection losses, it is best that they occur at low energy to minimize activation. For these reasons, we propose to have the highest possible proton energy and lowest possible beam current for this source.

This study of a 10-GeV, 5-MW proton source is an extension of a feasibility study of a 1-MW 2-GeV 30-Hz pulsed neutron source to upgrade the ANL Intense Pulsed Neutron Source (IPNS) [1]. The harmonic number in the 2-GeV machine was increased from one to two in this 5-MW study. The 10-GeV synchrotron accepts the 2-GeV (0.5-mA) beam from the 1-MW source and accelerates it to 10 GeV. Beam transfer from the 2-GeV RCS (RCS-I) to the 10-GeV RCS (RCS-II) is performed using bunch-to-bucket transfer. A detailed study of this transfer showed that no-loss injection can be achieved.

The 1-MW facility design takes into account existing infrastructure in the former ZGS (12-GeV Zero Gradient Synchrotron) buildings, totaling about 50,000 m^2 of space. The accelerator configuration for the 1-MW facility consists of a 400-MeV injector linac and a 400-MeV to 2-GeV synchrotron. The 10-GeV accelerator system is housed in a new enclosure adjacent to the ZGS complex.

Geometric layouts of the 1-MW and 5-MW facilities are arranged such that construction of the 5-MW system does not interfere with operation of the 1-MW source except during the last minute link-up between the two accelerator systems. This geometric separation between the two accelerators enables the 5-MW facility to be constructed in stages without interfering with operations, and utilizes all previous investments. Figure 1 shows the layout of the proposed facility and clearly indicates the 5-MW addition.

II. Lattice

The required features of the 10-GeV lattice are similar to those of the 2-GeV lattice: 1) the transition energy must be larger than the extraction energy so that the lattice has a relatively large slip factor, $\eta = \left|\gamma^{-2} - \gamma_t^{-2}\right|$, 2) there must be enough straight-section length for the radio-frequency cavity system that could have a total length of $\approx$ 200 m, and 3) the straight sections should be dispersion-free so that the rf cavities can be placed in dispersion-free regions. In addition, the circumference of the 10-GeV ring should be a multiple of that of the 2-GeV ring

in order to have a harmonic relationship between the two synchrotron rf systems during bunch transfer from one machine to the other.

One way to satisfy requirement 1) above is for the lattice to have a large horizontal tune, since the transition energy, γ_t, is proportional to the horizontal tune. A FODO cell lattice with a phase advance of approximately 90° in both transverse planes was chosen for the normal cell in order to obtain a higher tune.

Additional advantages of the 90° FODO cells are: 1) Dispersion suppression can be obtained by removing a dipole from a normal cell. 2) Normal cells without both dipoles can be used to construct the straight-section cells. 3) Focusing quadrupoles in the normal cells, the dispersion-suppressor-cells and the straight-section cells have the same strength, and therefore only one power supply is needed for the quadrupole family. Similarly, defocusing quadrupoles in the ring can also be powered by a single power supply.

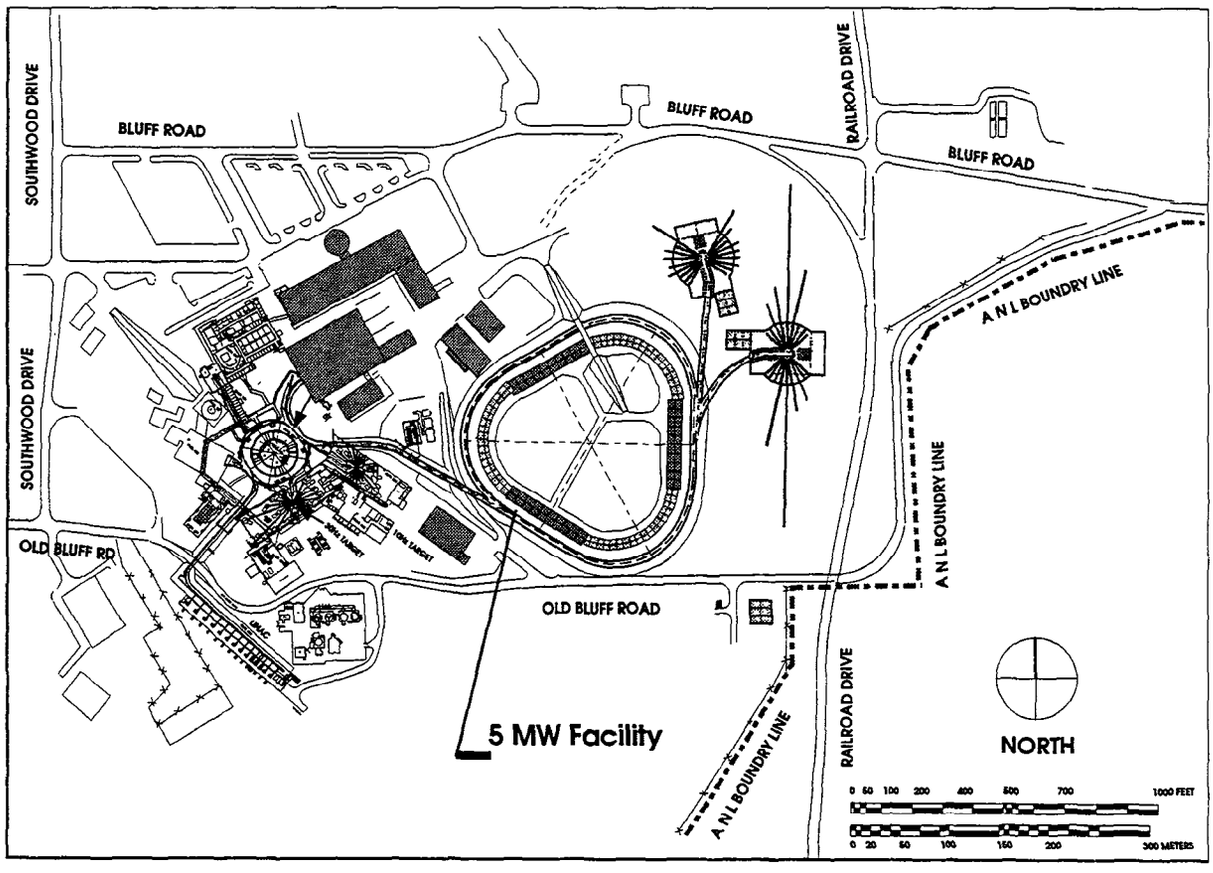

Figure 1: Site Layout Showing the Location of the 5-MW Facility.

Figure 2 shows 1/2 of a super period with reflective symmetry at both ends. Each cell of the FODO structure has a phase advance of ~ 90° in both transverse planes. The normal cells, dispersion-suppressor cell and the straight-section cells are evident in the figure. Dispersion suppression is achieved by removing a dipole from a normal cell. The missing dipole scheme suppresses the dispersion function when the vertical phase advance is slightly less than 90° while maintaining a horizontal phase advance of 90°. A benefit of this arrangement is that the horizontal tune is about one unit higher than the vertical tune, which is a good feature. Further study of this lattice showed that the lattice tunes can be adjusted to within ± 1/2 unit while

maintaining the tune difference of one unit and a vanishing dispersion function through the straight sections.

The circumference ratio between the 10-GeV ring and the 2-GeV ring is four, giving RCS-II a circumference of 761.6 m. The superperiodicity of the 10-GeV ring was chosen to be three, so that the ring fits into the available space and reduces the required number of dispersion-suppressor cells. Table 1 shows the normal cell parameters. The overall lattice parameters are shown in Table 2.

Table 1: Normal Cell Parameters for RCS-II
(10 GeV, B ρ = 36.352 T·m, Cell Length 10.155 m)

Elements	Length (m)	Strength	Units
QD	0.4	-13.086	T/m
DQS	0.2		
SD	0.4	-1.299	m^{-2}
DSB	0.675		
B	1.72735	1.377	T
DBQ	1.275		
QF	0.8	13.536	T/m
DQS	0.2		
SF	0.4	0.867	m^{-2}
DSB	0.675		
B	1.72735	1.377	T
DBQ	1.275		
QD	0.4	-13.086	T/m

III. Apertures

The 2-GeV beam from RCS-I has a transverse emittance of 128 π mm mr. The beam-stay-clear (BSC) acceptance of the 10-GeV ring is defined by twice the emittance and $\pm$ 1 % of the momentum spread of the incoming beam. This method is similar to that used in the 2-GeV ring. Figure 3 shows a vacuum chamber cross-section at a focusing quadruple indicating the BSC and the injected beam envelope in RCS-II.

IV. Dynamic Aperture

The natural tune of the 90° FODO lattice is 18.75 in both transverse planes. The working point must be chosen taking a large tune spread due to space charge into account, since the lattice has to provide a large enough dynamic aperture to contain the beam. The space charge effects are greatest during the low energy injection, where the maximum tune shift was estimated to be about 0.18 in each plane. In addition to the space-charge induced tune spread, there is a tune spread due to the momentum spread. If we assume a beam with $\Delta p/p = 1\%$, the chromatic tune spread is larger than the space-charge tune spread. Thus chromaticity correction is necessary, especially during injection.

In order to find the optimum working point, the tune region where the dynamic apertures are largest was searched. As a result of extensive tracking studies, the optimal tune range was found to be $19 < \nu_x < 19.25$ and $18 < \nu_y < 18.25$ to provide enough dynamic aperture to contain the beam at injection. We chose the lattice tunes to be $\nu_x = 19.20$ and $\nu_y = 18.19$. The

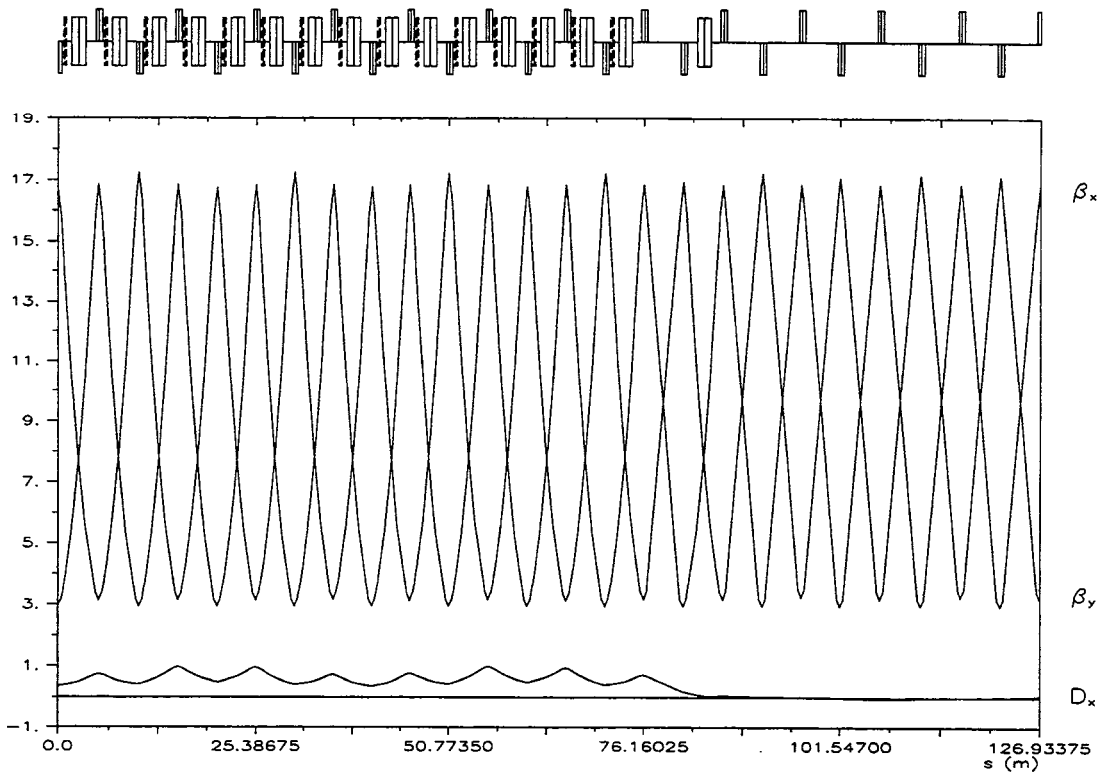

Figure 2: Lattice Functions for 1/2 Super-Period.

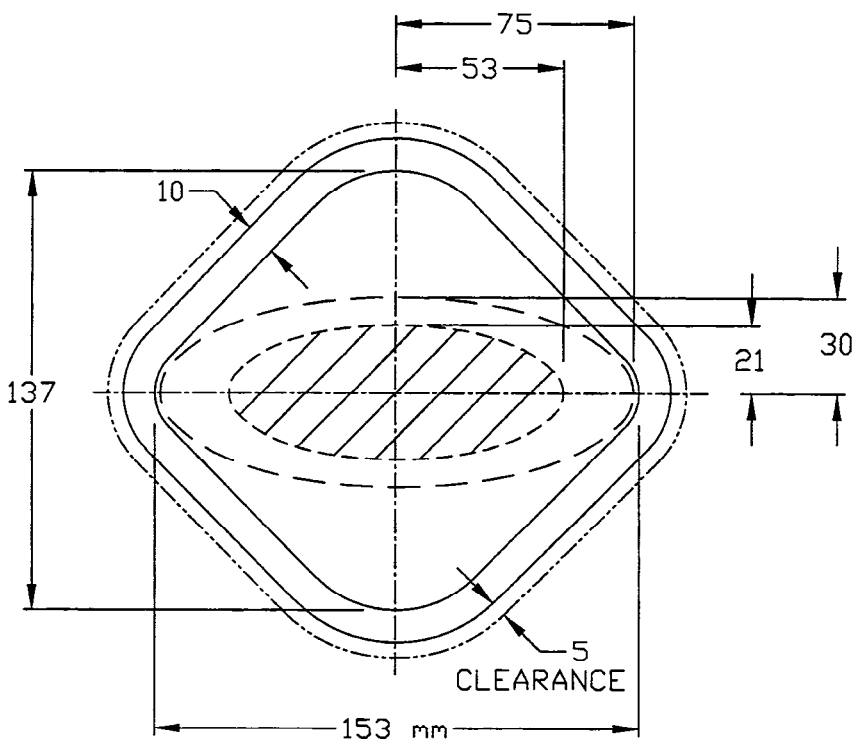

Figure 3: Focusing Quadrupole Vacuum Chamber Cross Section Showing Beam-Stay-Clear (dashed line) and Beam Envelope (area containing diagonal lines).

working point, including the space-charge tune spread, is clear of structure resonances and is shown in the tune diagram in Figure 4.

The lattice dynamic apertures at the design tune and at the depressed tune are shown in Figure 5. The beam size at injection and the BSC are also shown. In Figure 5(a), we show the dynamic apertures at the chromaticities $\xi_{x,y} = 0$ and -5. The operating range of the chromaticity is expected to be close to $\xi_{x,y} = -5$, where the dynamic aperture is shown to be larger than the BSC. In Figure 5(b), we show the dynamic aperture when the lattice is adjusted to the space-charge depressed tune.

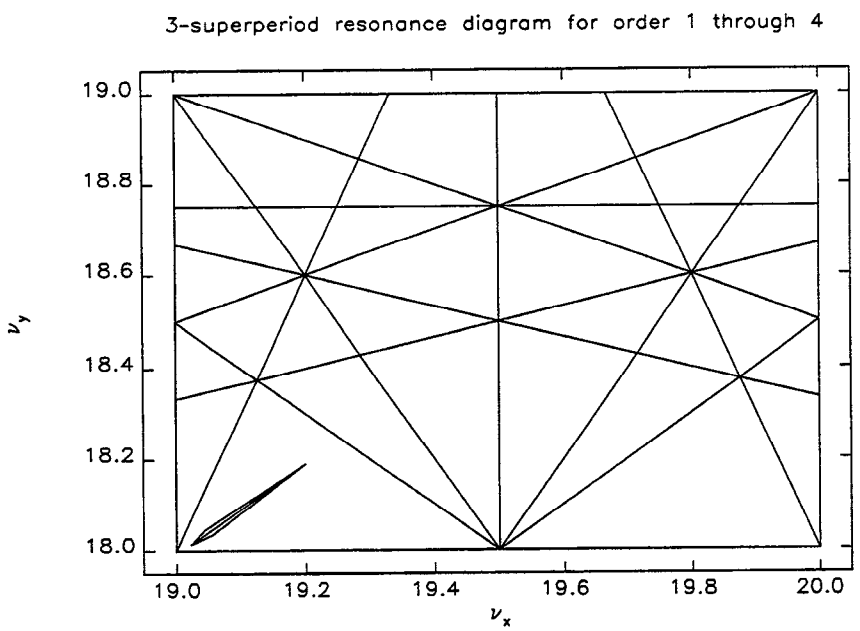

Figure 4: 1st through 4th Order Resonance Diagram Including Working Point and Tune Spread.

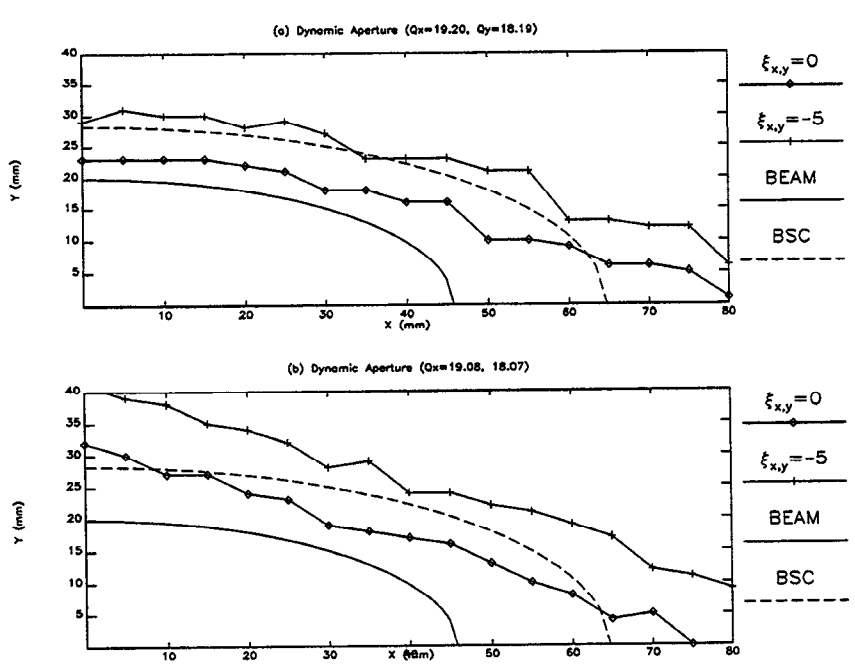

Figure 5: Dynamic Aperture of the Lattice at Different Chromaticities. (a) Lattice at the Design Tune $\nu_x = 19.20$ and $\nu_y = 18.19$. (b) Lattice at the Depressed Tune $\nu_x = 19.08$ and $\nu_y = 18.07$, Where a Uniform Charge Distribution is Assumed.

Since the particle at the edge of the beam is oscillating with large amplitude at this tune, the dynamic aperture is critical. This consideration is already taken into account in choosing the working point, resulting in the large aperture at the depressed tune, shown in Figure 5(b).

Table 2: Lattice Parameters for RCS-II.
(10 GeV, B ρ = 36.352 T·m)

Parameters	Value	Units
Circumference	761.6	m
Superperiodicity	3	
Total Number of Cells	75	
Number of Normal Cells	45	
Number of Dispersion-suppressor Cells	6	
Number of Straight-section Cells	24	
Nominal Length of Cell	10.155	m
Nominal Length of Straight Section	4.277	m
Bending Radius	26.392	m
Number of Dipole Magnets	96	
Dipole Magnets Effective Length	1.72735	m
Dipole Field Strength at Extraction (10 GeV)	1.377	T
Dipole Field Strength at Injection (2 GeV)	0.352	T
Number of Quadrupole Magnets	150	
Quadrupole Magnet Effective Length	0.8	m
Maximum Quadrupole Gradient (B′)	13.54	T/m
Number of Sextupole Magnets (F)	42	
Number of Sextupole Magnets (D)	48	
Sextupole Magnet Effective Length	0.4	m
Sextupole Field Coefficient (B″)	118.1	T/m^2
Transition Energy γ_t	14.83	
Horizontal Tune, ν_x	19.20	
Vertical Tune, ν_y	18.19	
Natural Chromaticity, $\xi_x = (\Delta\nu)_x/(\Delta p/p)$	−23.90	
Natural Chromaticity, $\xi_y = (\Delta\nu)_y/(\Delta p/p)$	−23.06	
Maximum β_x	16.84	m
Maximum β_y	17.26	m
Maximum Dispersion Function	1.0	m

V. Injection

Each pulse of the 2-GeV extracted beam from RCS-I contains two bunches separated by 332 nsec. Each bunch contains 5×10^{13} protons, and has an area of 3.7 eV·sec. The rf frequency of RCS-I at extraction is 3 MHz, with a harmonic number of 2.

The two bunches from each RCS-I pulse are transferred into waiting RCS-II buckets. Two RCS-I bunches at 3 MHz are injected into two buckets of the 6-MHz RCS-II rf system. As a consequence of this change in the rf frequency and the ratio of circumferences of the machines, RCS-II has 16 buckets (harmonic number = 16) of which only two are occupied by the beam, separated by an empty bucket.

VI. Rf Voltage Program

The key feature of the design studies for both the 1- and 5-MW machines was to determine the rf programming such that there is no beam loss from injection to extraction. Such programming was obtained using a Monte Carlo method to track the particles from injection to extraction [8].

VI.1 Rf Voltage at Injection:

The 2-GeV beam from RCS-I has a single bunch area of 3.7 eV sec; this bunch is injected into a slightly larger waiting bucket in RCS-II. Matching between the bunch and the bucket is performed using the following algorithm. The rf voltage at the extraction of the 2-GeV beam determines the energy spread, ΔE, and length, Δt, of the bunch. The energy spread and bunch length of the incoming beam are matched to a phase space contour of the waiting bucket. The space charge suppression of the phase space area is taken into account in these considerations to prevent mismatching and consequent dilution of the beam. Figure 6(a) shows the rf bucket and the bunch population in RCS-I at extraction. Figure 6(b) shows the bunch injected into the waiting bucket of RCS-II. The dashed line in Figure 6(b) represents the Hamiltonian contour whose height, ΔE, and whose enclosed area are equal to those of the injected beam. This shows that the 3.7 eV sec bunch is matched to a contour of a 3.7 eV sec phase space area within a 5.8 eV sec bucket. The required rf voltage at this time is 0.7 MV.

VI.2 Rf Voltage Program During Acceleration:

The rf voltage program for the accelerating cycle is depicted in Figure 7(a). The time variation of the bucket and bunch area is shown in Figure 7(b).

During the first eight msec of acceleration the rf voltage is raised to maintain the 5.8 eV sec bucket area determined by the previously described procedure. The rf voltage increases from 0.7 MV to 1.9 MV, and reaches a maximum at 8 msec. From this time to the end of acceleration, the voltage is decreased gradually from 1.9 MV to 1.7 MV. The bucket area grows from 5.8 eV sec to 106.3 eV sec. The voltage for the latter part of the cycle is maintained high to ensure a synchrotron frequency fast enough to allow the particles in the bunch to follow the rapid change of the synchronous phase near extraction. The bunch area is 3.7 eV sec throughout the cycle. At extraction, the bunch height is ± 102.5 MeV and the bunch length is ± 11.3 nsec. The final bunch length can be tailored to a longer or shorter length by rf manipulations, as is explained in detail in the following subsection.

The rf voltage program is able to capture and accelerate 1×10^{14} particles per pulse with no loss of particles during the beam transfer and acceleration processes.

VI.3 Rf Voltage Manipulation to Adjust the Bunch Length:

The RCS-II bunch length at extraction can be tailored to the specific application through rf manipulations. The typical full bunch length at extraction without any manipulations is between 22 and 25 nsec. The bunches can be shortened through bunch rotation prior to extraction. Using a combination of bunch rotation and debunching, the bunches can be lengthened. An overlap of the two bunches can be achieved in about 3.5 msec, if there is a flat-top in the ring magnetic field.

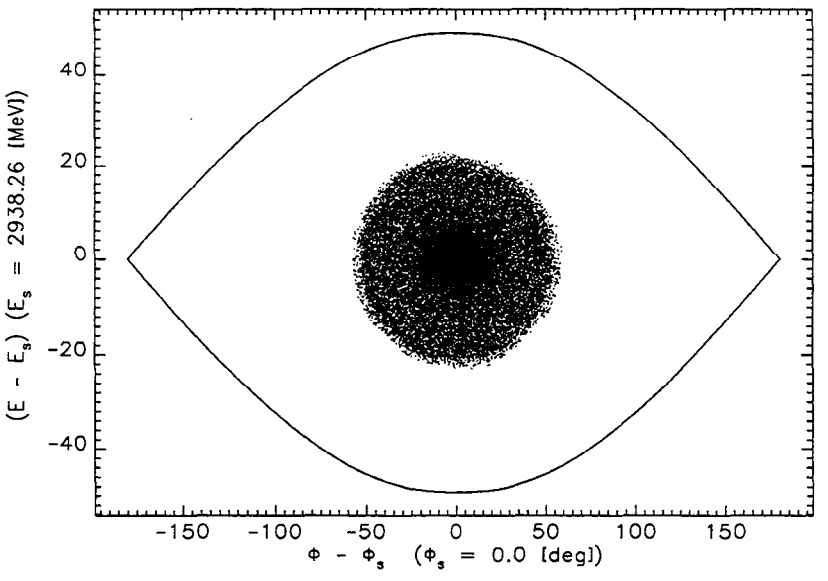

Figure 6(a): Rf Bucket and Phase Space Distribution at Extraction in RCS-I.

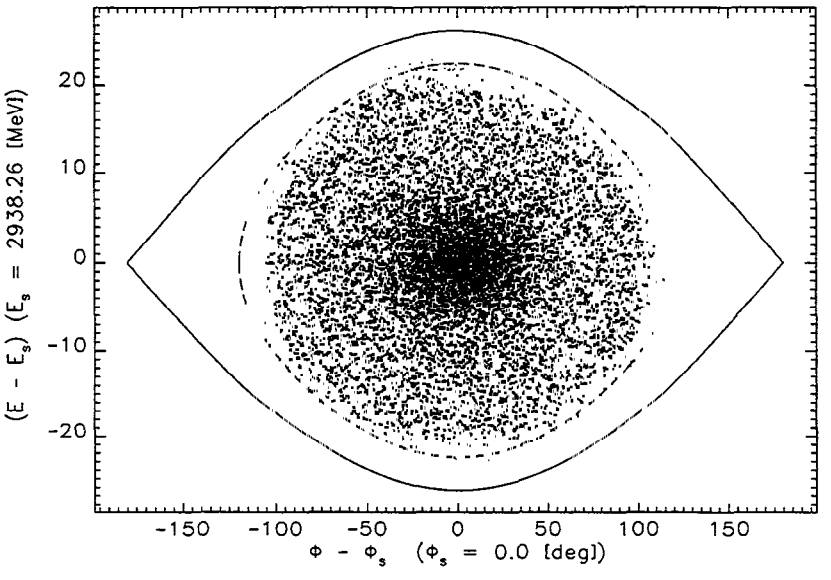

Figure 6(b): Rf Bucket and Phase Space Distribution at Injection in the RCS-II. The Dotted Line Indicates the Contour Enclosing an Area of 3.7 eV sec.

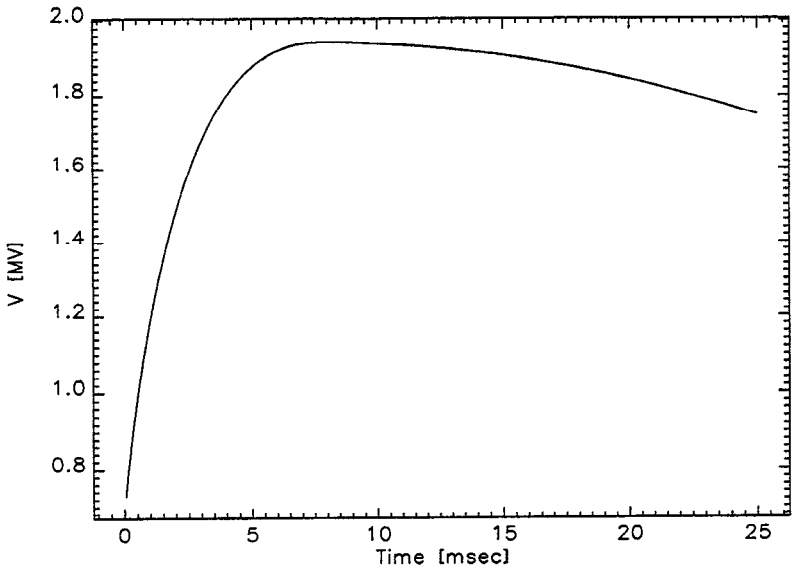

Figure 7(a): Rf Voltage Program for the Acceleration Cycle.

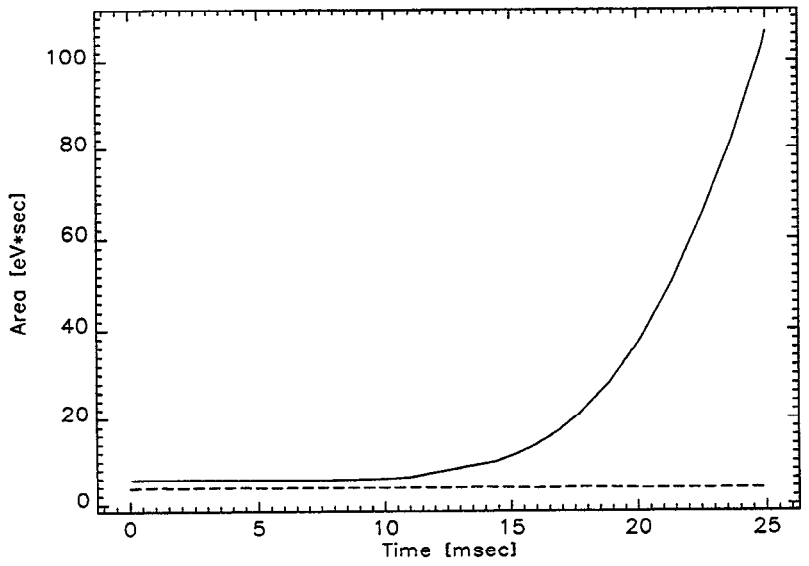

Figure 7(b): Time Evolution of the Bucket (solid line) and Bunch (dotted line) Areas During the Acceleration Cycle.

For bunch rotation to shorten the bunch, the voltage step, V_1, is related to the final, desired half-bunch length in radians, ϕ_1, and initial energy spread, ΔE_0, through

$$V_1 = \frac{\pi h|\eta|}{2\beta^2 E_s} \frac{\Delta E_0^2}{e\sin^2(\phi_1/2)}.$$

Longitudinal particle tracking results using several rf voltage steps and two initial bunch lengths agree well with this relationship. In the tracking study, the voltage is increased in 50 μsec. The voltage V_1 can be minimized by starting with a long bunch. When the bunch length at the start of rotation is 25 nsec and the $\Delta p/p$ is 0.9% (V_{rf} = 1.25 MV), a voltage V_1 = 3.2 MV results in a bunch length of 15 nsec and $\Delta p/p$ of 1.5% after 0.45 msec (1/4 synchrotron period). The phase space distribution of the bunch at the end of rotation from the Monte Carlo studies is shown in Figure 8(a). Note that the bunch length has changed from 25 nsec to 15 nsec.

A combination of bunch rotation and debunching can be used to increase the bunch length. The rf voltage is set to zero at the end of the ramp, with or without first rotating the bunch, and the beam is allowed to drift on a flat-top. The new full bunch length, τ_1, is related to the drift time, t, and the full bunch length at the beginning of the drift, τ_0, through

$$\tau_1 = 2|\eta|\frac{\Delta p}{p}t + \tau_0,$$

where τ_1 and τ_0 have units of time. Without first rotating the bunch and starting with $\Delta p/p$=0.9% (τ_0 = 25 nsec), the bunch length increases by about 50 nsec for every 1 msec of drift. After rotating the bunch to $\Delta p/p$ = 1.5% (τ_0 = 15 nsec), the bunch length increases by about 90 nsec for every 1 msec of drift. The resulting phase space distribution after 1.5 msec drift from Monte Carlo studies is shown in Figure 8(b). At extraction, the rf frequency is 6.3 MHz; therefore, the bunches are separated by 320 nsec. Complete decoherence, or just overlapping of both bunches, can be achieved in the latter example after about 3.5 msec of drift. This results in a single bunch with length ≥ 640 nsec.

VII. Impedance and Collective Instabilities

Longitudinal and transverse instability thresholds were obtained after the coupling impedances were estimated. The transverse impedance is dominated by space charge. The contribution to the longitudinal impedance from space charge is comparable to that from the broadband rf cavity impedance. Beam parameters such as $\Delta p/p$ and peak current were obtained through Monte Carlo studies of beam capture and acceleration using a longitudinal tracking code that includes the effects of space charge [8]. The analysis lead to an rf voltage profile and beam parameters that minimize the instabilities as well as beam losses.

RCS-II operates below the transition energy, thus the longitudinal microwave instability is not expected to occur unless there is a large resistive component. However, a conservative approach was adopted to ensure that the momentum spread is sufficient to satisfy the Keil-Schnell (KS) stability criterion. The space charge impedance is smaller in RCS-II than in RCS-I by a factor of between 5 and 10. Therefore, a contour-following rf shield, such as that used in the RCS-I and ISIS [9], is not required. The vacuum chamber is constructed of ceramic with a fixed-position wire rf shield. The KS criterion is difficult to satisfy in RCS-II because the threshold is dominated by the high peak current and a small slip factor. Studies were performed to choose an rf voltage profile that provides adequate bucket area and momentum spread. Tracking studies show that the beam remains in the stable region through most of the acceleration, where, at extraction energy, the $\Delta p/p$ is about 1% and the bunching factor (peak/circulating current) is about 0.01. The peak current is 160 A at injection and < 800 A at extraction.

In the transverse plane, the head-tail instability was analyzed. The growth rate is proportional to the resistive wall and kicker impedance. With a chromaticity corrected to zero and estimating the kicker impedance to be < 60 kΩ/m, the fastest growth rate is < 120 sec^{-1}. The head-tail modes are stabilized at a slightly negative chromaticity. The threshold tune spread for transverse microwave instability is 0.11. Given a Δp/p of 1%, stability is satisfied by a chromaticity $\xi \leq -1$.

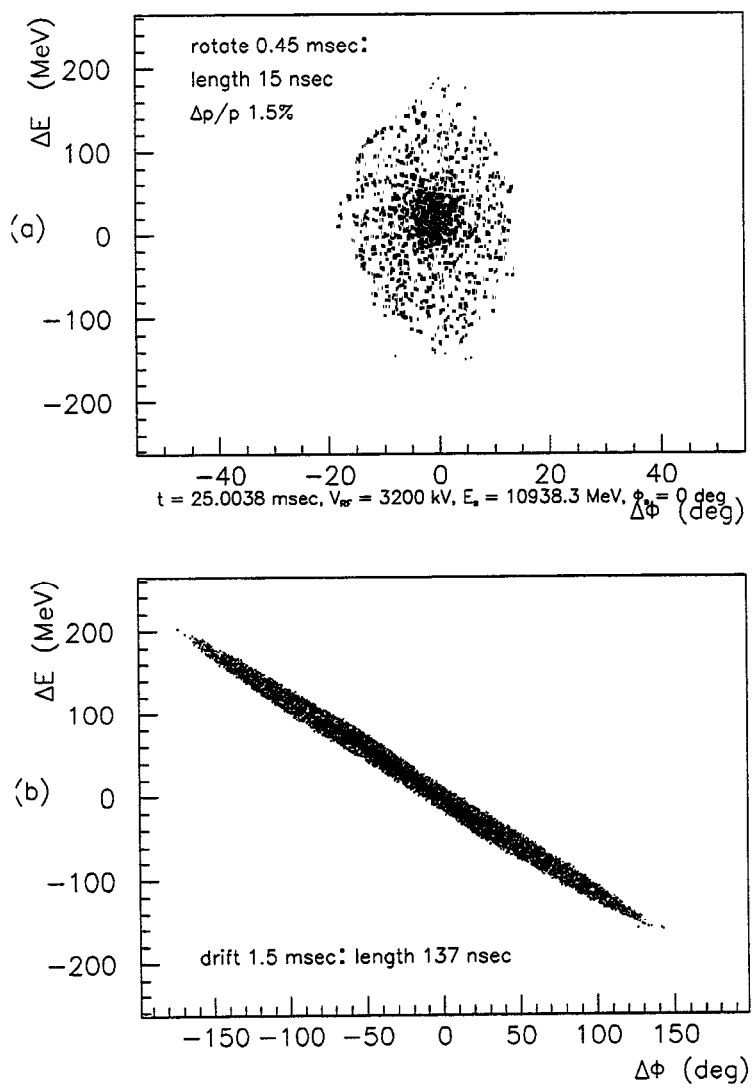

Figure 8: Effect of Rf Manipulations on Bunch: (a) Bunch Rotation with Rf Voltage of 3.2 MV and (b) Debunching with Zero Rf Voltage.

VIII. Synchrotron Hardware

The following is a short summary of the RCS-II hardware systems.

VIII.1 Synchrotron Magnets

The dipole, quadrupole and sextupole magnets for the synchrotron are designed for nominal beam energies of 10 GeV but are capable of handling a maximum value of 11 GeV. The gap geometries were scaled down from the corresponding magnets in the RCS-I ring to fit the smaller vacuum chambers. Calculated field qualities for the RCS-II magnets are, therefore, nearly identical to the RCS-I values.

Some of the major parameters for each of the synchrotron ring magnets are listed in Table 3. The rms currents listed there are based on a simple 30-Hz biased excitation, and not on the dual-frequency excitation described in Section VIII.2. An end-view of a quadrupole is shown in Figure 9.

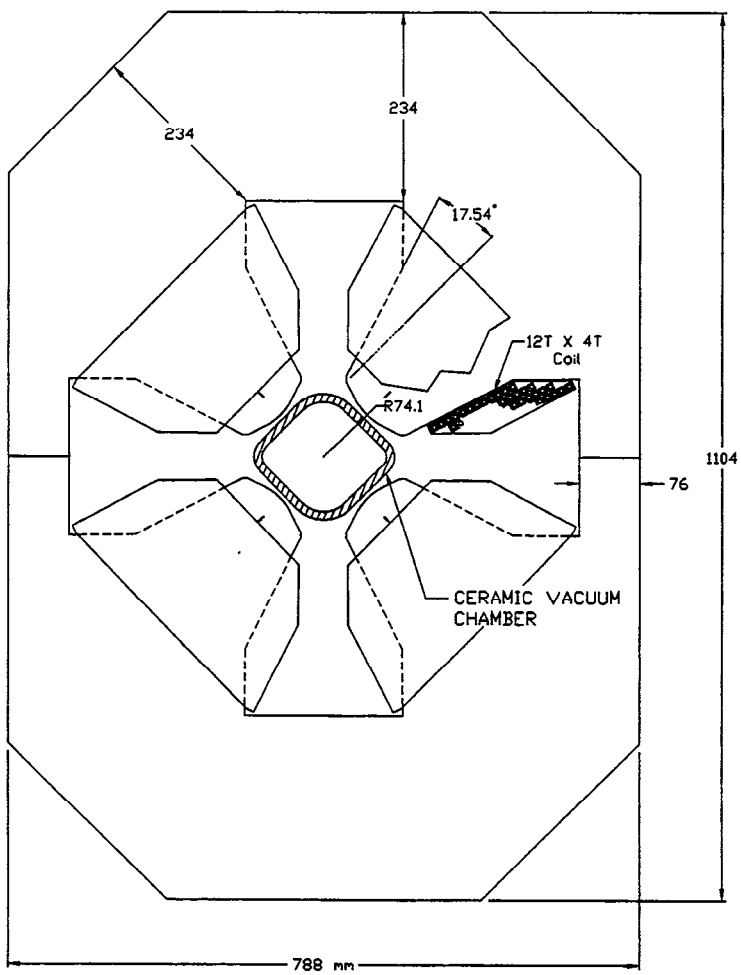

Figure 9: End View of a Synchrotron Quadrupole Magnet.

The cores of these magnets are parallel stacks of low-silicon steel laminations that are 0.36-mm thick. Each consists of 2 or 3 sections, allowing it to be assembled around the vacuum chamber. Bonded end-packs at the ends of each section contain the special contouring required to control field shapes at the ends. Each core section is held under compression by welded tie-bars and insulated tie-rods. The pole taper-angles keep the flux densities on the pole axes below saturation, and the average flux densities in the yokes are between 1.0 and 1.2 T.

The coils for these magnets contain hollow copper conductor that is insulated with polyimide film, fiberglass tape, mica tape and vacuum-impregnated, heat-cured epoxy. Although the insulating materials are radiation resistant, radiation exposures of the coils are further reduced by locating them well away from the midplanes. Parallel electrical paths are used to allow the use of smaller conductors to control eddy current losses and to keep the peak voltages across a series-connected group of magnets at manageable levels. The parallel circuits extend around pairs of poles for a given magnet so as to equalize the impedances of all paths. Magnet cooling is provided by deionized water with a maximum supply temperature of 32°C and a pressure gradient of 6.9 bars across all magnets.

Table 3: Parameters for the Synchrotron Ring Magnets

Parameters		Dipole	Quadrupole	Sextupole	Units
Number Required		90	150	90	
Peak Strength at 10.0 GeV		1.38 T	13.54 T/m	118.1 T/m^2	
Effective Length		1.73	0.8	0.40	m
Gap Height or Diameter		131.4	148.2	166.6	mm
Total Mass of Magnet		16000	3750	720	kg
Conductor	Height	8.9	8.9	7.3	mm
	Width	8.9	8.9	7.3	mm
	Hole Diameter	4.9	5.3	4.1	mm
Number Turns per Pole		10	8	16	
Number of Parallel		40	6	2	
Total Inductance		2.5	1.8	7.8	mH
Total Resistance		0.74	3.5	21	mW
Supply Current	Max.	7264	3877	590	A
	Min.	1856	991	151	A
	rms	4945	2639	402	A
Power Losses		32.3	28.0	3.6	kW
Total Water Flow		1.13	0.77	0.19	l/sec
Water Temp. Rise		7	9	5	°C

VIII.2 Power Supplies

The RCS ring magnets are energized with dual-frequency resonant power supplies, that excite the ring at a 20-Hz rate and de-energize it at a 60-Hz rate. This method, similar to that proposed in the 1-MW source [1,7] results in an overall repetition rate of 30 Hz, and reduces the peak rf voltage required for acceleration by one third.

VIII.3 Vacuum Chamber System

The vacuum chambers through the RCS ring magnets are 99.7% pure alumina ceramic similar to those used in RCS-I [1,7]. There are rf shields close to the inside surface of each chamber section. Figure 3 shows a cross section of the chambers in the quadrupole and sextupole magnets.

VIII.4 Radio-Frequency System

The design of the cavities for the 10-GeV ring uses type 4M2 ferrite, the same ferrite used on the ISIS RCS [10] and for which extensive measurements were made at BNL [11]. Each cavity is built in a double-cell configuration similar to the ISIS cavities. The physical length of the full cavity from flange-to-flange is 3.46 m. A ground plane separates the cavity into two cells, each of which has 40 ferrite rings and a single-ended ceramic accelerating gap. The cavity is in air and only the beam pipe is under vacuum. Each ferrite ring is 0.0254 m thick and has inner/outer radii of 0.125/0.25 m. Based on measurements in [11], it appears that a safe operating field of 0.0049 T is possible at 6 MHz without thermal runaway problems. This means that each ring can generate 583 volts and each cavity can generate 23.5 kV/cell and 47 kV/cavity. A 3-mm-thick cooling plate is clamped between ferrite rings. The ferrite rings are mounted together in groups of 20 and a figure-8 bias winding is wound around two groups of 20 ferrites per cell to provide dc excitation with rf cancellation at the input.

The two cells are connected together by a rigid coaxial line that is directly connected to the ceramic gaps. A single amplifier tube excites the two gaps in parallel as is done on the ISIS RCS. A total of 43 cavities are needed to provide the required peak accelerating voltage of 2MV per turn. The cathode-follower amplifier is planned to compensate for and control beam loading problems. It is expected that feed-forward will be needed to handle the initial shock caused by the one-turn injection from the 2-GeV ring.

VIII.5 Control System

The control system design is similar to that planned for the 1-MW source, described in [1]. High-performance workstations act as operator consoles, distributed microprocessors control the equipment interfacing and preprocess data, and a network connects the system together. The control system is a direct application of EPICS, the Experimental Physics and Industrial Control System, described in [12] and the references therein.

VIII.6 Beam Diagnostic Instrumentation - RCS-II and Transport Lines

Diagnostic instrumentation is used to monitor beam position, profile, current, and beam losses in RCS-II and in its associated transport lines. The types of beam diagnostics provided for RCS-II and the transport lines include beam position monitors, current monitors, and loss monitors. Specialized diagnostic instrumentation, such as moving wire scanners and Faraday cups, is provided for beam studies. Interlocked target protection secondary emission monitors are also provided.

IX. Summary

A feasibility study for a pulsed spallation source based on a 5-MW, 10-GeV rapid cycling proton synchrotron (RCS) is in progress. The 10-GeV synchrotron uses as its injector the 2-GeV accelerator system from a 1-MW source [1-7]. The 1-MW source accelerator system consists of a 400-MeV proton linac with 2.5 MeV energy spread in the 75% chopped beam, and a 30-Hz RCS that accelerates the 400-MeV beam to 2 GeV. The 10-GeV RCS accepts and accelerates the 0.5 mA of beam at 2 GeV to 10 GeV. Beam transfer from the 2-GeV synchrotron to the 10-GeV machine utilizes highly efficient bunch-to-bucket injection, so that

the transfer can be made without beam loss. The synchrotron lattice uses FODO cells of 90° phase advance. Dispersion-free straight sections are obtained using a missing magnet scheme. The synchrotron magnets are powered by a dual-frequency resonant circuit. The magnets are excited at a 20-Hz rate and de-excited at 60-Hz, resulting in an effective 30-Hz rate. A key feature of the design of this accelerator system is that beam losses are minimized from injection to extraction, reducing activation to levels consistent with hands-on maintenance. The low losses are achieved by providing large dynamic aperture in the transverse plane and sufficient bucket area in the longitudinal plane.

X. References

[1] "IPNS Upgrade - A Feasibility Study", ANL Report ANL-95/13 (April, 1995).

[2] E. Lessner, Y.-C. Chae, and S. Kim, "Effects of Imperfections on Dynamic Aperture and Orbit Functions of the IPNS Upgrade Synchrotron," Proc. of the 1995 Particle Accelerator Conference, Dallas, Texas, May 1995, to be published.

[3] Y.-C. Chae and Y. Cho, "Study of Field Ionization in Charge Exchange Injection for the IPNS Upgrade," Proc. of the 1995 Particle Accelerator Conference, Dallas, Texas, May 1995, to be published.

[4] E. Crosbie and K. Symon, "Injecting a Kapchinskij-Vladimirskij Distribution into a Proton Synchrotron," Proc. of the 1995 Particle Accelerator Conference, Dallas, Texas, May 1995, to be published.

[5] K. Harkay, Y. Cho, and E. Lessner, "Longitudinal Instability Analysis for the IPNS Upgrade," Proc. of the 1995 Particle Accelerator Conference, Dallas, Texas, May 1995, to be published.

[6] K. Harkay and Y. Cho, "Transverse Instabilities Analysis for the IPNS Upgrade," Proc. of the 1995 Particle Accelerator Conference, Dallas, Texas, May 1995, to be published.

[7] Y. Cho, et al., "Feasibility Study of a 1-MW Pulsed Spallation Source," these proceedings.

[8] Y. Cho, E. Lessner, and K. Symon, "Injection and Capture Simulations for a High Intensity Proton Synchrotron," Proc. of the European Particle Accelerator Conference, page 1228 (1994).

[9] G. H. Rees, "Status Report on ISIS," Proc. of the IEEE Particle Accelerator Conference (March 16-19, 1987).

[10] G. H. Rees, "Status of the SNS," IEEE Transactions on Nuclear Science, Vol. NS-30, No. 4, August 1983.

[11] M. A. Goldman, et al., "Studies Of Ferrite Materials For The AGS Booster Synchrotron", Proc. of the IEEE Accelerator Conference, Chicago, IL, March 20-23, 1989.

[12] McDowell, et al., "Status of the Advanced Photon Source and its Accelerator Control System," Nucl. Instrum. and Methods **A 352** 13 (1994).

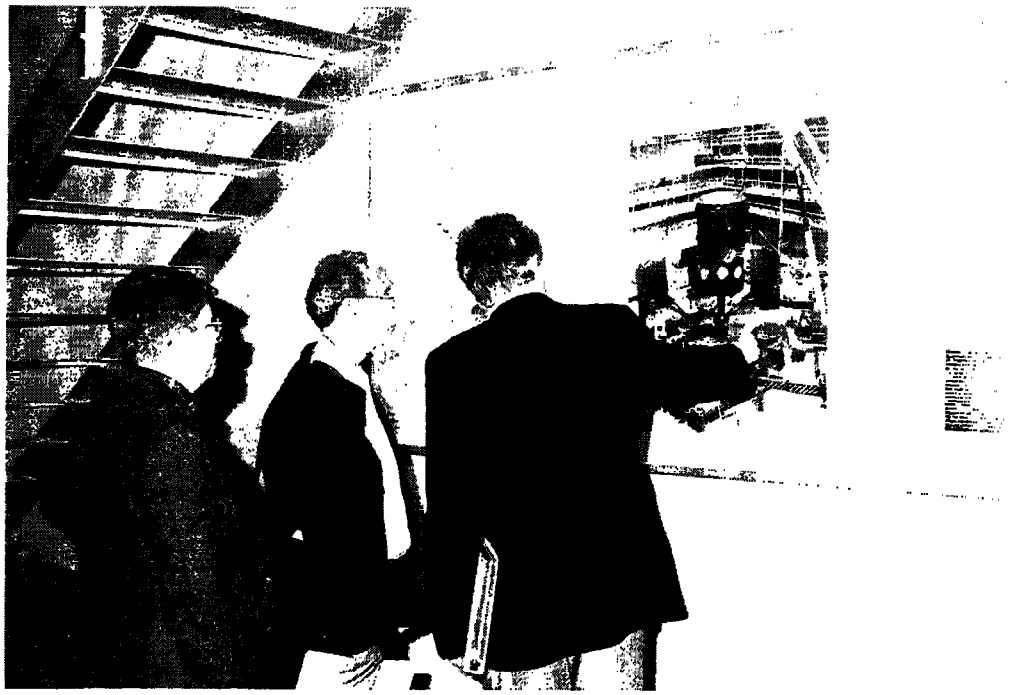

Project Studies

ICANS-XIII
13th Meeting of the International Collaboration on
Advanced Neutron Sources
October 11-14, 1995
Paul Scherrer Institut, 5232 Villigen PSI, Switzerland

FEASIBILITY STUDY FOR THE IPNS UPGRADE, A 1-MW PULSED SPALLATION NEUTRON SOURCE TARGET STATIONS

John M. Carpenter
for the IPNS Upgrade Target Station Design Group

Intense Pulsed Neutron Source, Argonne National Laboratory
Argonne, IL 60439, USA

ABSTRACT

This paper describes the design of target stations for the IPNS Upgrade Pulsed Spallation Neutron Source.

1. Background

In 1992, the U. S. Department of Energy commissioned a Panel on Neutron Sources chaired by Walter Kohn, to provide advice on the future of neutron sources and the related scientific and technological applications in the United States. Under Panel auspices, a Review of Neutron Sources and Applications was held at Oak Brook, Illinois in September 1992. About seventy experts convened to (1) review the status of advanced research reactors and spallation sources and (2) provide an update on scientific, technological and medical applications. The Panel's recommendations were published in January 1993[1] and the report of the Panel's findings was published in January 1994[2]. The Panel recommended:

> 1: Complete the design and construction of the Advanced Neutron Source[a] according to the schedule proposed by the project.
> 2: Immediately authorize the development of competitive proposals for the cost-effective design and construction of a 1-MW PSS ... .

The recommendation for studies of 1-MW Pulsed Spallation Sources (PSS) followed consideration of technical problems, costs and opportunities relating to accelerators and targets, and of accessible scientific applications.

After the Panel discussions, two workshops further evaluated accelerator prospects (Santa Fe, February 1993)[3] and scientific applications of a 1-MW PSS (Argonne, May 1993)[4]. In early 1993, the DOE asked Lawrence Berkeley Laboratory to host a design study for a 1-MW PSS, but major funding for this study has not yet been authorized. In early 1994, the Neutron

[a] The Advanced Neutron Source (ANS) at Oak Ridge National Laboratory was to produce neutron fluxes 5 times those at ILL (Grenoble) and provide facilities for isotope production and materials irradiation at least as good as those at the existing Oak Ridge HFIR reactor. Although the conceptual design has been completed and documented, funding of the program has been terminated. The Total Project Cost of the ANS would have been about $3.0 B.

Keywords: Argonne, Upgrade, Pulsed Neutron Source, Targets

Scattering Society of America established a subcommittee to oversee the studies and nominated a steering group to guide the efforts.

Site-specific studies of 1-MW PSSs begun in 1992 are continuing under local laboratory sponsorship at Argonne National Laboratory[5] and Los Alamos National Laboratory[6] in response to the Panel recommendations. These are feasibility studies, a step preceding full-blown conceptual design studies, which normally follow DOE decision and higher-level funding. Both studies have been documented and have undergone review.

Brookhaven National Laboratory[7] has launched a study of a "green field" 5-MW source, which is at an early stage. Most of that work is on accelerator questions. The system includes a 600 MeV linear accelerator feeding two 3.6 GeV Rapid Cycling Synchrotrons operating at 30 Hz each and delivering pulses shorter than 3 μsec at 10 and 60 Hz.

Recently, in early 1995, the Department of Energy designated Oak Ridge National Laboratory the "preferred alternative site" for a 1-MW pulsed spallation source and requested funds to pursue its conceptual design.

2. IPNS Upgrade Feasibility Study

The development of the design and the preparation of the Feasibility Study greatly benefited from the expertise in the Advanced Photon Source project. The methodologies used for this study were essentially identical to those used for the APS document[8] which we believe greatly enhance the quality and reliability of this study. The study required about three years.

The Upgrade uses buildings and infrastructure of the former high energy physics Zero Gradient Synchrotron (ZGS) at Argonne. The ZGS Ring Building houses the synchrotron, about 200 meters in circumference, and has adequate radiation shielding to accommodate the 1-MW accelerator system. Two of the former high-energy physics experimental buildings house the two target stations and associated neutron scattering instruments. It is estimated that the use of existing buildings saves about $175 million in construction costs.

The Feasibility Study document is complete[9].

The IPNS Upgrade will be the fourth in a series of pulsed spallation sources constructed at Argonne. The ZGS Intense Neutron Generator Prototype (ZING-P), built in 1973, was a test in which all the essential components of the pulsed spallation neutron source came together for the first time. Based on the ZGS 200-MeV prototype Booster-I synchrotron, ZING-P eked out a beam power of 100 W. ZING-P', a second prototype that used the present IPNS 450 MeV Rapid Cycling Synchrotron, operated very productively from 1977 through 1980. It achieved 2 kW of beam power. The IPNS, operational since 1981, produces 7 kW of beam power incident on uranium or enriched uranium targets.

3. Accelerator and Target Station Parameters

The IPNS Upgrade uses a 2 GeV rapid cycling synchrotron (RCS) delivering a time-average beam power of 1 MW. The choice of proton beam energy is determined by several factors, including neutron yield, heat removal from the target, ease of machine construction and serviceability, and available space in the ZGS Ring Building. The design is also influenced by the distribution of the deposited heat and the distribution of produced neutrons. Most experience to date has been confined to energies below 1 GeV. Monte Carlo studies[10] show that the power density distribution, neutron production distribution, and total yield of neutrons favor energies higher than 1 GeV, at least up to about 3 GeV, the code-imposed limit of the study. The calculations confirm that the neutron production rate for constant beam power is approximately proportional to the proton beam power within the range of

proton energies studied. Additional studies show that higher energies are preferable due to the lower peak power density at the upstream end of the target for a given beam power. These calculations indicate that proton energies above 1.5 GeV are equivalent with respect to the thermal and neutronic design of the target and moderator systems.

The choice of 30 Hz as the source repetition frequency was based upon a survey of scientific requirements and an evaluation of preliminary designs for neutron scattering instruments for a 1-MW pulsed source. Two categories of instruments emerged from the study of scattering instruments, those for which 30 Hz is preferable, and those that require a lower frequency, for which 10 Hz is satisfactory. Few of the instruments we considered could efficiently use frequencies higher than 30 Hz. Two targets that operate at different frequencies provide the flexibility to serve both classes of instruments and double the available number of beamlines and instruments. The accelerator delivers one out of three pulses to the low-frequency station at 10 Hz, and the high-frequency station receives the remaining two pulses of the 30-Hz pulse train. The high-frequency target is capable of using the full 1 MW of beam power, that is, all the pulses of the 30-Hz pulse train.

Our preference is to have the highest possible energy and lowest possible current to minimize the impact of beam losses at synchrotron injection. This does not affect the neutron production rate, since the rate is proportional to the proton beam power. We chose a linac delivering 400-MeV H^- beam for injection into the rapid cycling synchrotron (RCS). The synchrotron accelerates a time-average proton beam current of 0.5 mA to 2 GeV. Figure 1 shows a general view of the IPNS Upgrade.

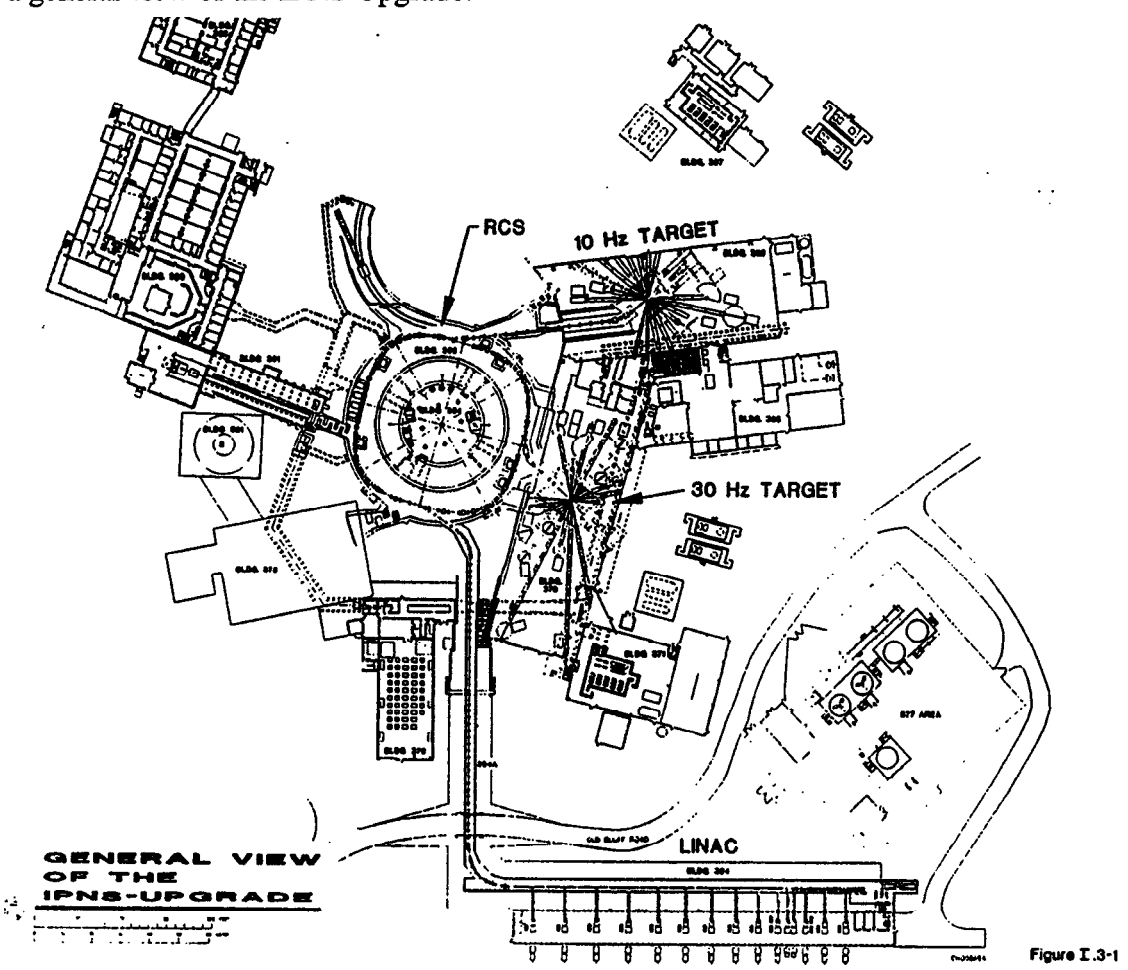

Figure 1. General view of the IPNS Upgrade

4. Accelerator Systems

The accelerator system is the subject of another paper in this conference. Table I summarizes the parameters of the IPNS Upgrade accelerator system.

Table I Accelerator Parameters

Parameters	Values	Units
Beam energy at extraction	2	GeV
Maximum beam energy attainable	2.2	GeV
Beam energy at injection	400	MeV
Beam average current	0.5	mA
Beam power	1.0	MW
Beam pulse length	< 1	μsec
Synchrotron repetition rate	30	Hz
Synchrotron circumference	~200	m
Number of external proton beams	2	-
Number of extraction lines	2	-
Linac beam energy	400	MeV
Linac energy spread (95%)	±2.5	MeV
Linac repetition rate	30	Hz
Linac pulse current	44	mA
Linac pulse length	0.5	msec
Linac emittance (rms normalized)[a]	$1.0 \times 10^{-6}\ \pi$	m

5. Neutron Scattering Capabilities

Shielded proton beam transport lines carry two extracted proton beams to the two target stations. Each station contains a neutron-producing target consisting of water-cooled tungsten plates in two sections. Water, liquid methane, and liquid hydrogen moderators positioned close to each target slow down neutrons from the primary source energies (about 1 MeV) to useful energies (less than about 10 eV). Reflectors of beryllium metal or of beryllium and heavy metal surround the moderators to enhance the intensities of the neutron beams. Decouplers and heterogeneous poisons within the moderator-reflector system tailor the spectra and pulse characteristics of the neutron beams. Massive steel and concrete shields surround the targets and moderators and provide multiple levels of confinement of radioactive materials within. Because some components of the target have finite lifetimes and because changes need to be made over the years to accommodate changing demands of the instruments, each target station is equipped with a hot cell and remote handling equipment designed to facilitate moving and servicing the internal components. Figure 2 shows the target stations of the IPNS Upgrade.

Irradiation facilities for neutron activation and fast neutron materials irradiation applications are arranged close to the targets. These irradiation facilities do not interfere with the neutron scattering application. The irradiation facilities are accessible during operation.

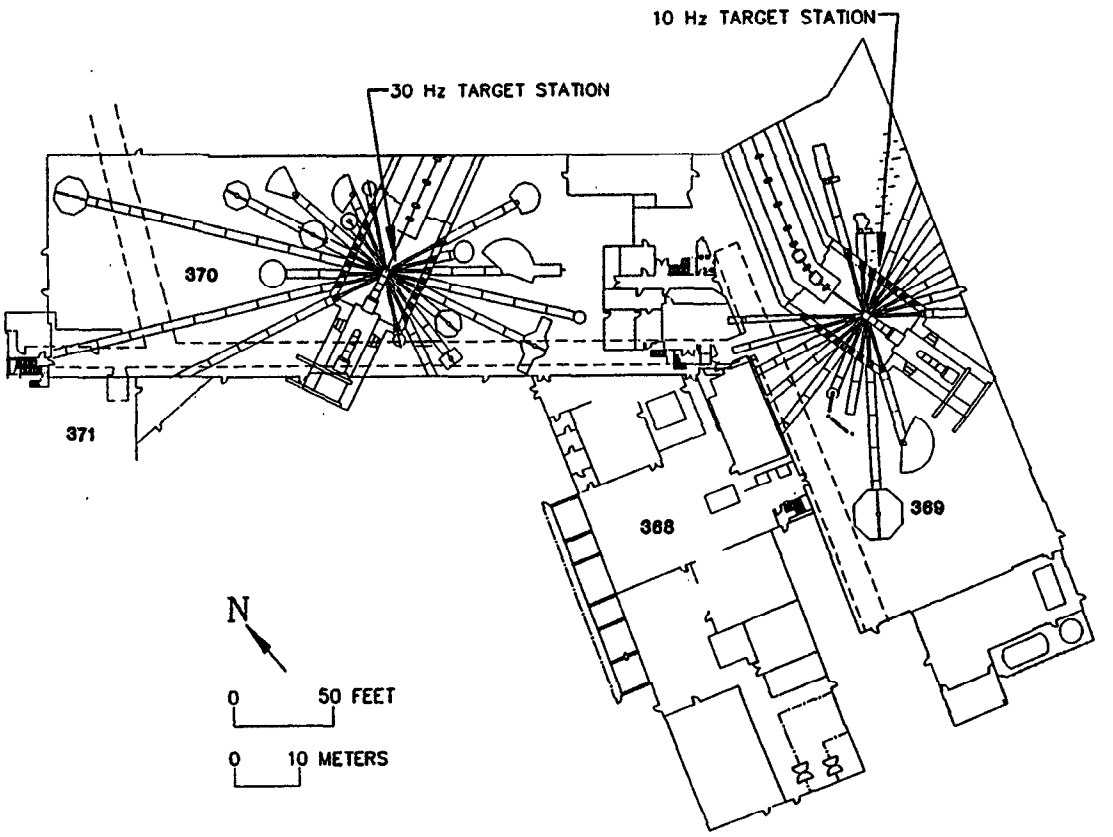

Figure 2. Target Stations and Reference Set of Instruments of the IPNS Upgrade

The IPNS Upgrade provides 36 beam ports for neutron scattering instruments, 18 each at the 30-Hz and 10-Hz target stations. Neutron beams for more than one instrument are extracted from a single beam port in some cases, so more than 36 neutron scattering instruments can be supported at this facility. There are a total of 12 moderators, one for every three beam ports, so the moderator characteristics can be optimized to the requirements of the individual instruments. The IPNS Upgrade provides 27 instruments for 24 of these 36 beam ports. The remaining 12 un-instrumented beam ports are available for later development and installation of new state-of-the-art instruments, as well as for the installation of specialized instruments developed by Participating Research Teams (PRTs). Chapter V of the IPNS Upgrade Feasibility Study outlines a reference set of 27 instruments that provide a well-balanced initial instrumentation complement. Tables II AND III briefly describe this reference set of instruments and indicate the wide range of neutron scattering science possible. This reference set of instruments has been used to select the target station parameters, lay out the locations of the target stations within the experiment halls, and provide the cost estimates. Up to 10 of the instruments that are presently operating at the IPNS would be refurbished and transferred to the IPNS Upgrade as part of this initial instrument complement. This approach provides a core of proven instruments ready for operation at startup. The neutron scattering instruments are located in existing experiment halls that provide internal space for beamlines up to 50 m long, as shown in Figure 1. Longer beamlines can be extended outside the buildings if necessary.

Most of the neutron scattering instruments use the neutron time-of-flight (TOF) principle for determination of neutron wavelengths. Of these instruments, the majority require good wavelength resolution. For such instruments, the IPNS Upgrade target stations provide 25-50 times the intensity available at the IPNS. However, for those instruments that do not require good wavelength resolution (for example, small-angle-scattering instruments), coupled liquid hydrogen moderators are used that provide 100-200 times the intensity available at the IPNS.

Table II Reference Set of Diffractometers and Reflectometers

Powder Diffractometers		Target	Moderator[a]	Range for d (Å)	Best Δ d/d (%)
VSPD	Very small samples (10-100 mg)	30-Hz	CH_4	0.2-17	0.35
SEPD[b]	High intensity	30-Hz	H_2O	0.2-17	0.35
GPPD[c]	Medium resolution (excellent at 90°)	30-Hz	H_2O	0.2-9	0.2
HRPD	High resolution	30-Hz	H_2O	0.2-5	0.08
RSD	Residual stress (12-m position)	30-Hz	H_2O	0.3-6	0.55
	(25-m position)	30-Hz	H_2O	0.2-3	0.30

Small-Angle Diffractometers		Target	Moderator[a]	Q_{min} ($Å^{-1}$)	Q_{max} ($Å^{-1}$)
SAND[b]	General purpose (wide Q range)	10-Hz	C-H_2	0.002	2
HRSAND	High resolution	10-Hz	C-H_2	0.0005	0.4
SPSAND	Re configurable for special purposes	10-Hz	C-H_2	Variable	Variable

Amorphous Materials Diffractometer		Target	Moderator[a]	Range for Q ($Å^{-1}$)	ΔQ/Q (%)
GLAD[b]	Liquids and glasses	30-Hz	CH_4	0.07-120	1.2-10

Single-Crystal Diffractometers		Target	Moderator[a]	Range for Q ($Å^{-1}$)	ΔQ/Q (%)
SCD[b]	General purpose	30-Hz	CH_4	0.9-17	0.6-0.9
HQSCD	High real-space resolution	30-Hz	H_2O	2-30	0.4

Reflectometers		Target	Moderator[a]	Sample	Minimum Reflectivity
POSY-I[c]	Polarized neutrons	10-Hz	H_2	Vertical	10^{-6}
POSY-II[c]	General purpose	10-Hz	H_2	Horizontal	10^{-7}
HIREF	High intensity	10-Hz	H_2	Horizontal	10^{-4}
GREF	Grazing incidence	10-Hz	H_2	Horizontal	10^{-7}

[a] Moderators are water at ~320 K (H_2O), liquid methane at ~95 K (CH_4), decoupled liquid hydrogen at ~18 K (H_2), and coupled liquid hydrogen at ~18 K (C-H_2). Moderator performance is shown in Figure I.2.2-1.

[b] Transferred from IPNS with little change.

[c] Transferred from IPNS with some modification.

The IPNS Upgrade source is sufficiently intense that it is no longer necessary that all instruments be based on TOF techniques. With moderators optimized for total neutron output rather than for sharp neutron pulse structure, time-averaged thermal or cold neutron fluxes are equivalent to those at a medium flux reactor. The reactor-equivalent cold neutron flux has been calculated to be ~5 x 10^{13} n/cm^2-sec for one of the liquid hydrogen moderators at the upgraded source. Thus, any instrument that works at a medium-flux reactor can be made to work at least as well at the IPNS Upgrade. Furthermore, even a moderator optimized for high time-averaged flux has a pulse width of less than one millisecond, and so has a duty factor of 1:30 or less at the IPNS Upgrade. This time structure can be used to significant advantage even on nominally steady-state instruments; for example, it can be used to reduce background and eliminate unwanted orders from crystal monochromators. A cold-neutron triple-axis spectrometer operating in this "quasi-steady-state" (QSS) mode is proposed as one instrument for the initial complement of IPNS Upgrade instruments.

Table III Reference Set of Inelastic Scattering Instruments and Component Development Instruments

Chopper Spectrometers		Target	Moderator[a]	Range for E_{inc} (meV)	$\Delta E/E_i$ (%)
HRMECS[b]	High-resolution general purpose	30-Hz	CH_4	4-2000	2-4
LRMECS[c]	Low-resolution general purpose	30-Hz	CH_4	3-2000	4-7
CNCS	High-resolution low energy	10-Hz	H_2	0.3-20	<1
SCCS	Excitations in single crystals	30-Hz	H_2O	50-2000	~1
Crystal-Analyzer Spectrometers		**Target**	**Moderator[a]**	**Range for E (meV)**	**ΔE (meV)**
TFCA	General purpose	30-Hz	CH_4	0-1000	0.5-30
QENS[c]	Quasielastic, medium resolution	30-Hz	CH_4	0-150	0.05-3
HRBS	Micro volt resolution	10-Hz	H_2	0-10	0.005-0.06
MICAS	Survey of single-crystal excitations	30-Hz	CH_4	0-20	variable
QSTAXC	Cold-neutron triple axis (QSS)[d]	30-Hz	C-H_2	variable	variable
Spin-Echo Spectrometer		**Target**	**Moderator[a]**	**Resolution (meV)**	**ΔQ/Q (%)**
TOFNSE	TOF spin-echo, cylindrical geometry	10-Hz	C-H_2	10^{-6} to 10^{-1}	1.5
Component Development Instruments		**Target**	**Moderator[a]**		
REFD	Reflectometer development	10-Hz	H_2		
DEVEL	General purpose development	10-Hz	H_2		

[a] Moderators are water at ~320 K (H_2O), liquid methane at ~95 K (CH_4), decoupled liquid hydrogen at ~18 K (H_2), and coupled liquid hydrogen at ~18 K (C-H_2). Moderator performance is shown in Figure I.2.2-1.

[b] Transferred from IPNS with some modification.

[c] Transferred from IPNS with little change.

[d] Quasi-steady-state.

The facilities can be expanded to allow for a number of other research opportunities — including radiation damage studies, isotope production, neutron activation analysis, neutron radiography and tomography, muon spin rotation studies for materials science research, and neutrino physics — with minimum interference to operation as a dedicated neutron scattering source. These possibilities are discussed briefly in the IPNS Upgrade Feasibility Study Chapter V and Appendix C. Facilities for radiation damage studies, isotope production, and neutron activation analysis are included within the scope of the IPNS Upgrade project.

6. Targets, Moderators, Reflectors and Shields

The targets and shielding, and the reflector and moderator layouts are identical in the 10 Hz and 30 Hz stations, but moderators differ according to purpose. The targets are of split design, as shown schematically in Figure 3, but in a single piece. The split target, with the horizontal proton beam configuration, allows for "tall" moderators in the flux trap position, especially effective for powder diffractometer applications, and accommodates six differently tailored moderators.

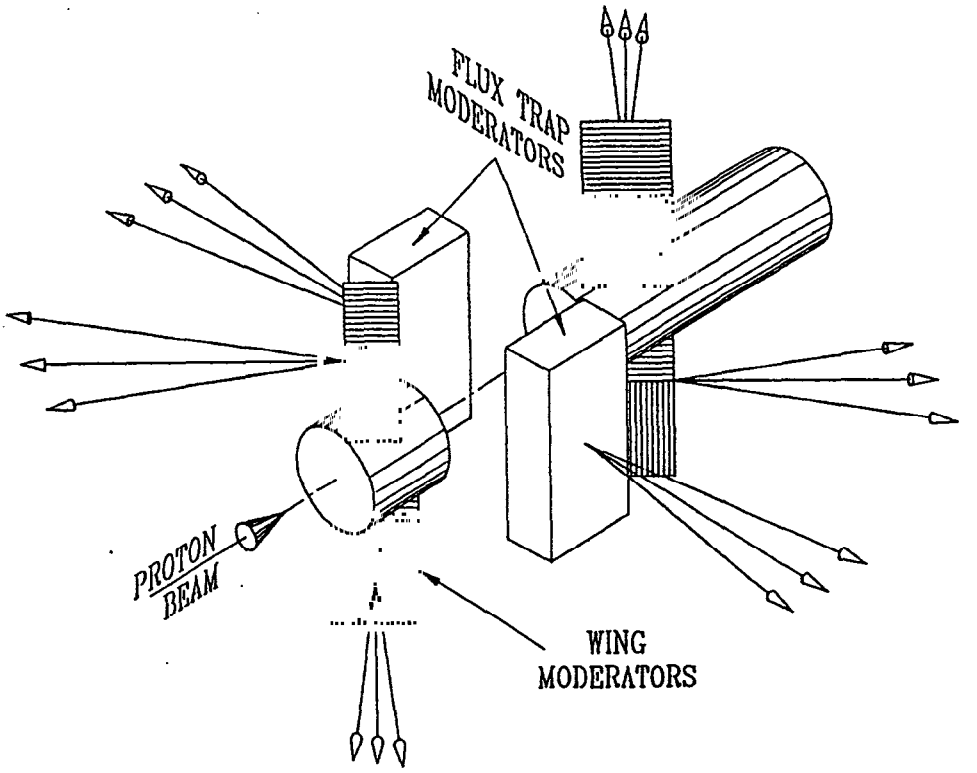

Figure 3. Schematic illustration of the split target and six moderators.

Figure 4 shows the one-piece split target. Water channels spanning the flux trap gap can serve as premoderators in some applications.

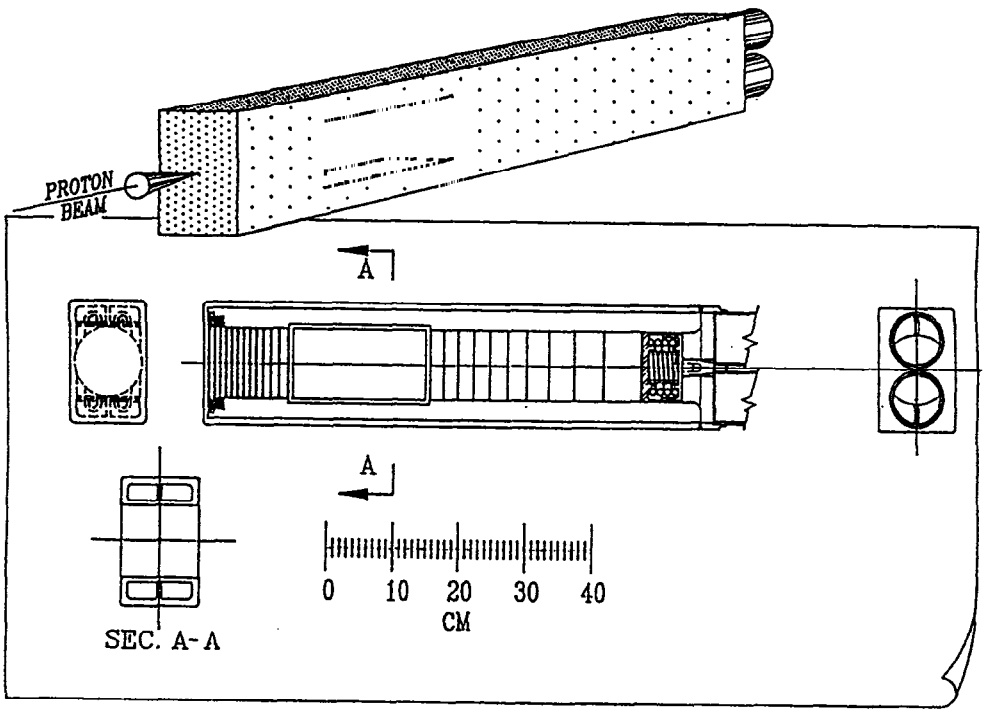

Figure 4. The one-piece split target.

Figure 5 shows how targets and moderators fit within the reflector. The arrangement allows the removal of parts for changes with minimal disturbance of other parts. The target moderator reflector assembly and attached shield roll downstream into a hot cell for servicing. The target module rests within a sealed aluminum tank filled with helium during operation.

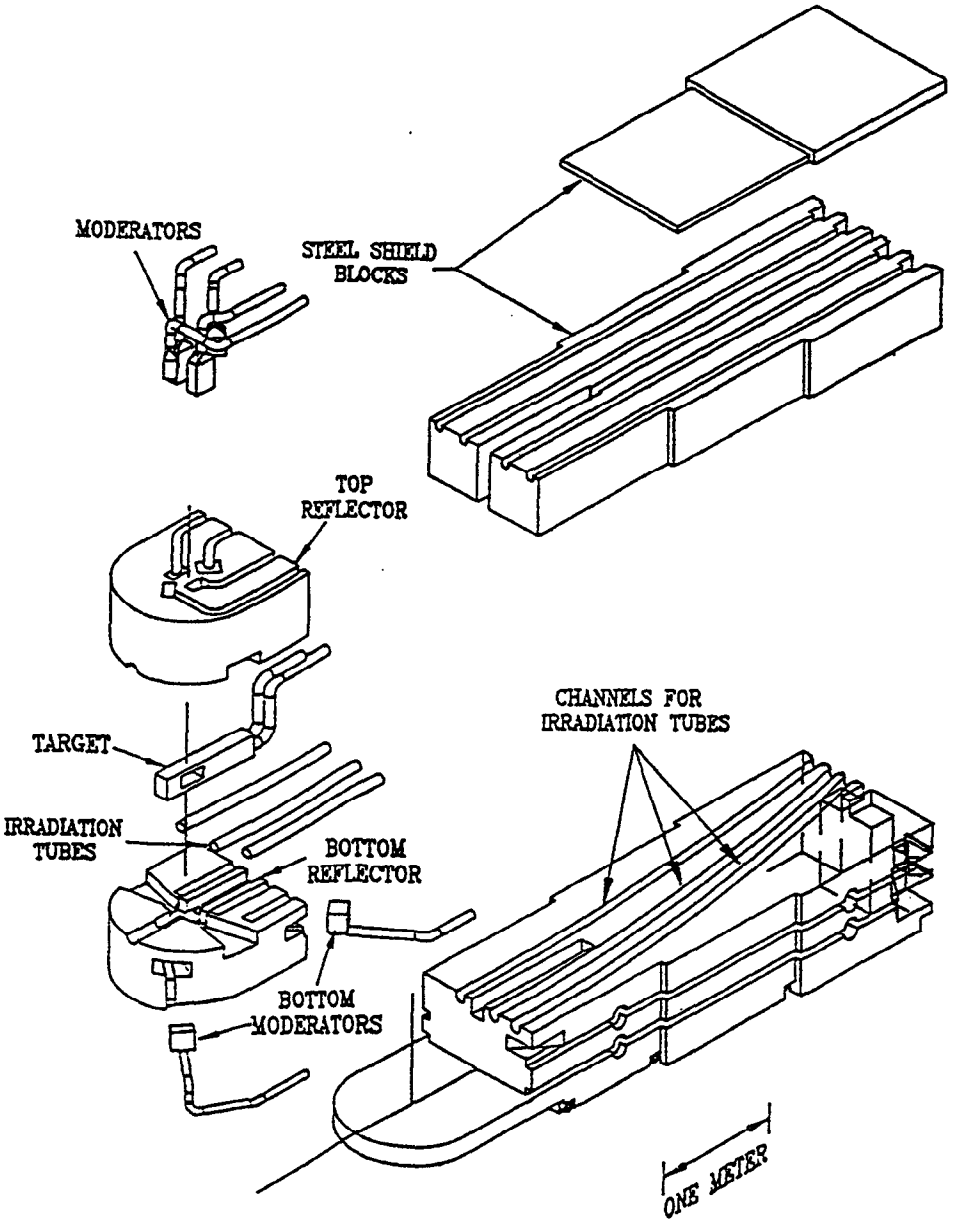

Figure 5. Target-moderator-reflector-shield assembly.

Figure 6 shows a cross sectional view of the shield. The shield consists of about 10,000 tonnes of stacked iron, approximately 5.5 meters thick, with 1 meter of exterior concrete. Two-meter-thick gates slide with precise alignment, driven by hydraulic actuators. The gates may contain guide sections or collimating elements. The core of the shield is sealed within an enclosure for confinement of radioactive gases. The shield rests on driven pilings set on bedrock about 30 meters below grade.

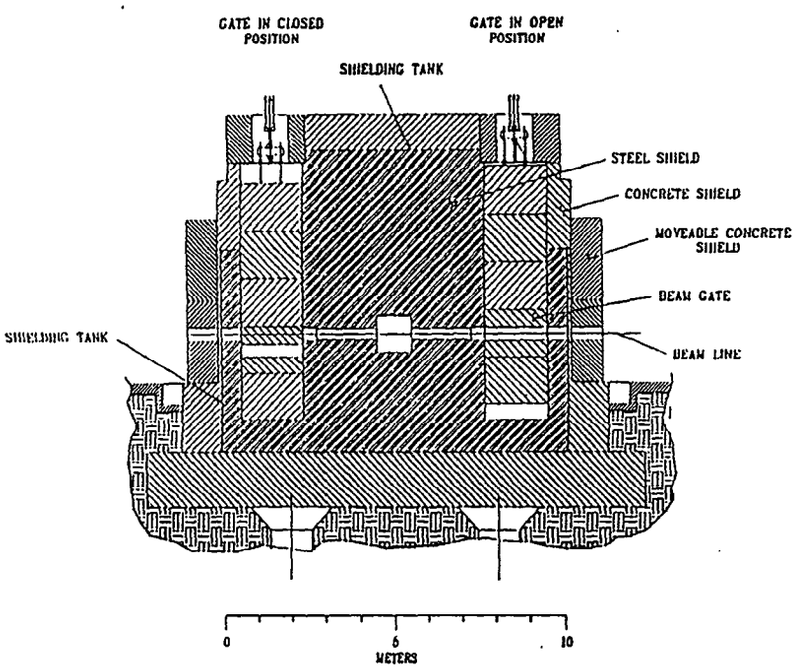

Figure 6. Cross sectional view of the shield taken perpendicular to the proton beam direction.

Figure 7 shows a plan view of the shield, beam tubes, gates, and hot cell. The proton beam enters horizontally through a water-cooled double-walled window and cooled tube, which can be dismounted from the accelerator side. Seals that isolate the target atmosphere and the inner shield atmosphere from the surroundings are made at the proton beam entry tube and at a seal sheet at the downstream end of the target train. Hands-on bayonet connectors provide for water, gas and cryogenic flows, accessible from behind the seal sheet.

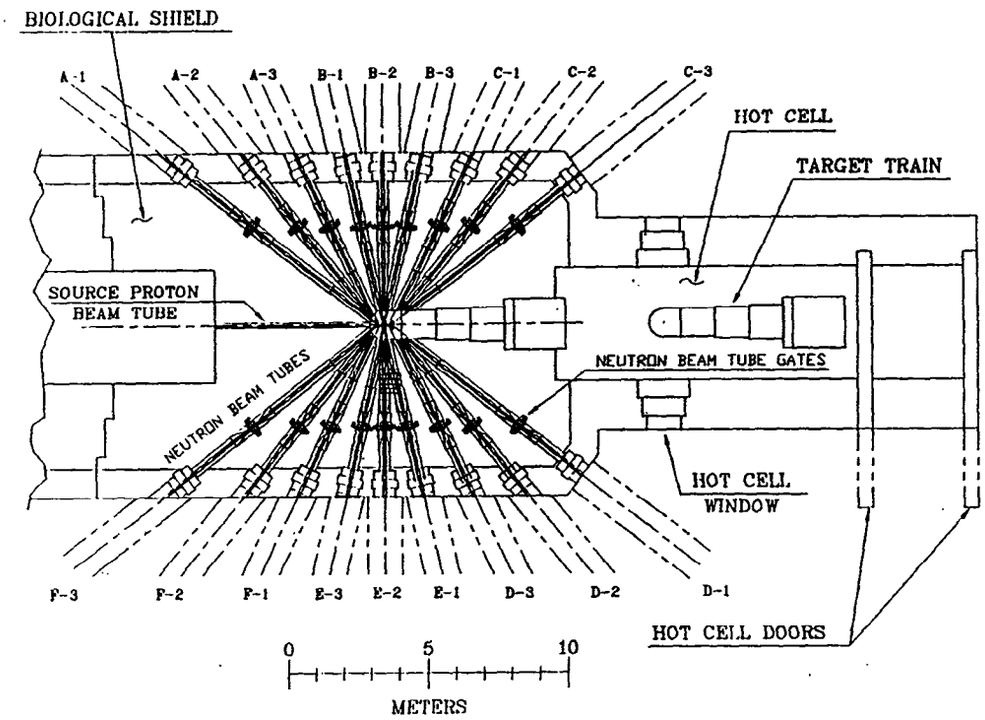

Figure 7. Plan view of the target station, showing the target train in the hot cell..

7. Summary Project Description

The major components of the IPNS Upgrade facility described here are an accelerator system, two target stations, and neutron scattering instruments. The accelerator system consists of a new, 400-MeV H^- linac and a new, 2-GeV rapid-cycling proton synchrotron (RCS). The RCS has a circumference of about 200 m and delivers a time-averaged proton current of 0.5 mA, for a total time-averaged power of 1.0 MW.

The 400-MeV injector linac, along with its associated technical equipment, is housed in a new building and tunnel. The 400-MeV linac beam is transported by a low-energy transport (LET) line to the RCS. The linac tunnel and klystron gallery are the only new buildings to be built for the IPNS Upgrade project. An extensive study was undertaken to choose a location for the new injector that would avoid interruption of present IPNS operation. A brief interruption of IPNS operation allows moving IPNS instruments to the IPNS Upgrade facility.

All other technical components are housed in approximately 55,000 m^2 of the former ZGS-complex space and use existing infrastructure. The synchrotron is located in the existing ZGS Ring Building. The power supplies for the RCS magnets, rf system, and beam transport systems are housed in the Center Building and other adjacent buildings. The target stations and instruments are located in existing large buildings that previously housed high-energy experiments at the ZGS, a use very similar to the new use. System control rooms, maintenance facilities, and a considerable amount of laboratory and office space for resident personnel and visitors are provided in existing buildings. The project uses water systems, cooling towers, main power and transformer systems, roads, sewers, and general infrastructure items that already exist. There is little need for constructing new conventional facilities. The cost estimate includes an allowance for refurbishing these existing buildings and facilities. Use of these existing buildings results in a very large savings in cost and construction time.

We expect that there is no need for land-use studies, such as wetlands accommodation and archaeological investigations, because construction takes place within existing buildings and in areas such as parking lots that are already graded. Altogether, these factors effect considerable cost and time savings.

If the project is initiated in FY 1997, the total estimated construction cost (TEC) is $478 million (in 1995 dollars), or $559 million in inflated dollars for the year in which they are spent. The facility commissioning is to start at the beginning of FY 2001. Construction of new components and refurbishment of existing facilities will not interfere with the present IPNS operations, except for reworking and relocation of the scattering instruments. An interval as short as a few months will be required to rework the scattering instruments and install them in their new locations. The accelerator commissioning period will be followed by commissioning of the target stations and instruments. Details of the cost and schedule appear in the IPNS Upgrade Feasibility Study document.

8. Upgrade ability

The IPNS Upgrade is a 1-MW source that can easily be upgraded to 5-MW by injecting the beam from the 2-GeV RCS into a 10-GeV RCS. Studies on this option have been underway since the 1-MW Feasibility Study was completed and a feasible concept, including siting, has been developed, the details of which are been worked on at the present time. This design has the large advantage of permitting full operation of the 1-MW source while the 10-GeV ring and target areas are under construction. Connecting the 2- and 10-GeV rings can be done quickly. In addition, no additional capabilities need to be built into the 1-MW facility for

future enhancement to 5-MW, thereby avoiding any extra costs for the 1-MW source. The 10 GeV, 5-MW upgrade is the subject of a separate paper in this conference.

9. References

[1] *Neutron Sources for America's Future* , DOE Report ER-0576P. January, 1993.
[2] J. J. Rush and D. L. Price, editors, *Neutron Sources and Applications,* Report of a review held at Oak Brook, Illinois September 8-10, 1992, DOE Report ER-0607P. January, 1994.
[3] R. J. Macek and H. A. Thiessen, editors, *Proceedings of the Workshop on Accelerators for Future Spallation Neutron sources*, Santa Fe. February 16-20, 1993. Three volumes. Los Alamos Report LA-UR-93-1356. 1993.
[4] G. Aeppli and B. S. Brown, *Technology and Science at a High Power Spallation Source,* Proceedings of a Workshop held at Argonne National Laboratory, May 13-16, 1993, Argonne internal report. February, 1994.
[5] B. S. Brown, et al, Proceedings of the XIIth Meeting of the International Collaboration on Advanced Neutron Sources, (ICANS XII) Rutherford-Appleton Laboratory Report 94-025, Vol. 2, (1994), p 13.
[6]R. Pynn, ibid., p 7.
[7]A. van Steenbergen, ed., *5 MW Pulsed Spallation Neutron Source*, Brookhaven National Laboratory Report 60678 (June, 1994).
[8] *7-GeV Advanced Photon Source Conceptual Design Report*, Argonne National Laboratory Report ANL-87-15 (Apr. 1987).
[9] *IPNS Upgrade Feasibility Study,* Argonne National Report ANL-95/13 (Apr. 1995).
[10] D. W. Jerng and J. M. Carpenter, *Heat Generation and Neutron Beam Characteristics in a High Power Pulsed Spallation Neutron Source,* submitted to IEEE Transactions in Nuclear Science, 1994.

The submitted manuscript has been authored by a contractor of the U. S. Government under contract No. W-31-109-ENG-38. Accordingly, the U. S. Government retains a nonexclusive, royalty-free license to publish or reproduce the published form of this contribution, or allow others to do so, for U. S. Government purposes.

ICANS-XIII
13th Meeting of the International Collaboration on
Advanced Neutron Sources
October 11-14, 1995
Paul Scherrer Institut, 5232 Villigen PSI, Switzerland

FEASIBILITY STUDY OF A 1-MW PULSED SPALLATION SOURCE*+

Y. Cho, Y.-C. Chae, E. Crosbie, H. Friedsam, K. Harkay, D. Horan, S. Kim, R. Kustom, E. Lessner, W. McDowell, D. McGhee, F. Mills, H. Moe, R. Nielsen, G. Norek, K. J. Peterson, K. Primdahl, A. Rauchas, K. Symon, K. Thompson, and M. White

Argonne National Laboratory, Argonne, IL 60439, USA

ABSTRACT

A feasibility study of a 1-MW pulsed spallation source based on a rapidly cycling proton synchrotron (RCS) has been completed. The facility consists of a 400-MeV H^- linac, a 30-Hz RCS that accelerates the 400-MeV beam to 2 GeV, and two neutron-generating target stations. The design time-averaged current of the accelerator system is 0.5 mA, or 1.04×10^{14} protons per pulse. The linac system consists of an H^- ion source, a 2-MeV RFQ, a 70-MeV DTL and a 330-MeV CCL. Transverse phase space painting to achieve a Kapchinskij-Vladimirskij (K-V) distribution of the injected particles in the RCS is accomplished by charge exchange injection and programming of the closed orbit during injection. The synchrotron lattice uses FODO cells of $\approx 90°$ phase advance. Dispersion-free straight sections are obtained by using a missing magnet scheme. Synchrotron magnets are powered by a dual-frequency resonant circuit that excites the magnets at a 20-Hz rate and de-excites them at a 60-Hz rate, resulting in an effective rate of 30 Hz, and reducing the required peak rf voltage by 1/3. A key feature of the design of this accelerator system is that beam losses are minimized from injection to extraction, reducing activation to levels consistent with hands-on maintenance. Details of the study are presented.

I. Introduction

A proton synchrotron system capable of delivering 1 MW of beam power was designed for the Intense Pulsed Neutron Source (IPNS) Upgrade Feasibility Study at Argonne National Laboratory (ANL) [1]. The RCS and associated research facilities are housed in the 50,000 m^2 of space in the former 12-GeV Zero Gradient Synchrotron (ZGS) area. The ZGS Ring Building houses a 190-m circumference, 2-GeV RCS. Two adjoining experiment halls house two neutron generating target stations, each serving 18 neutron beamlines and instruments. Figure 1 shows the proposed facility layout. Enclosures for the linac and low energy transport line (LET) are the only new conventional facility construction, and are also shown in Figure 1. The choice of 30 Hz as the repetition rate of the fast cycling synchrotron was based on preferences expressed by the users.

II. Lattice

Required features of the lattice are: 1) to have a large transition energy so that the lattice has a relatively large slip factor, $\eta = \left|\gamma^{-2} - \gamma_t^{-2}\right|$, 2) to have enough straight section length for a radio-

* Work supported by the U. S. Department of Energy, Office of Basic Energy Sciences under the Contract W-31-109-ENG-38.
+ Keywords: Accelerator, Synchrotron, Proton

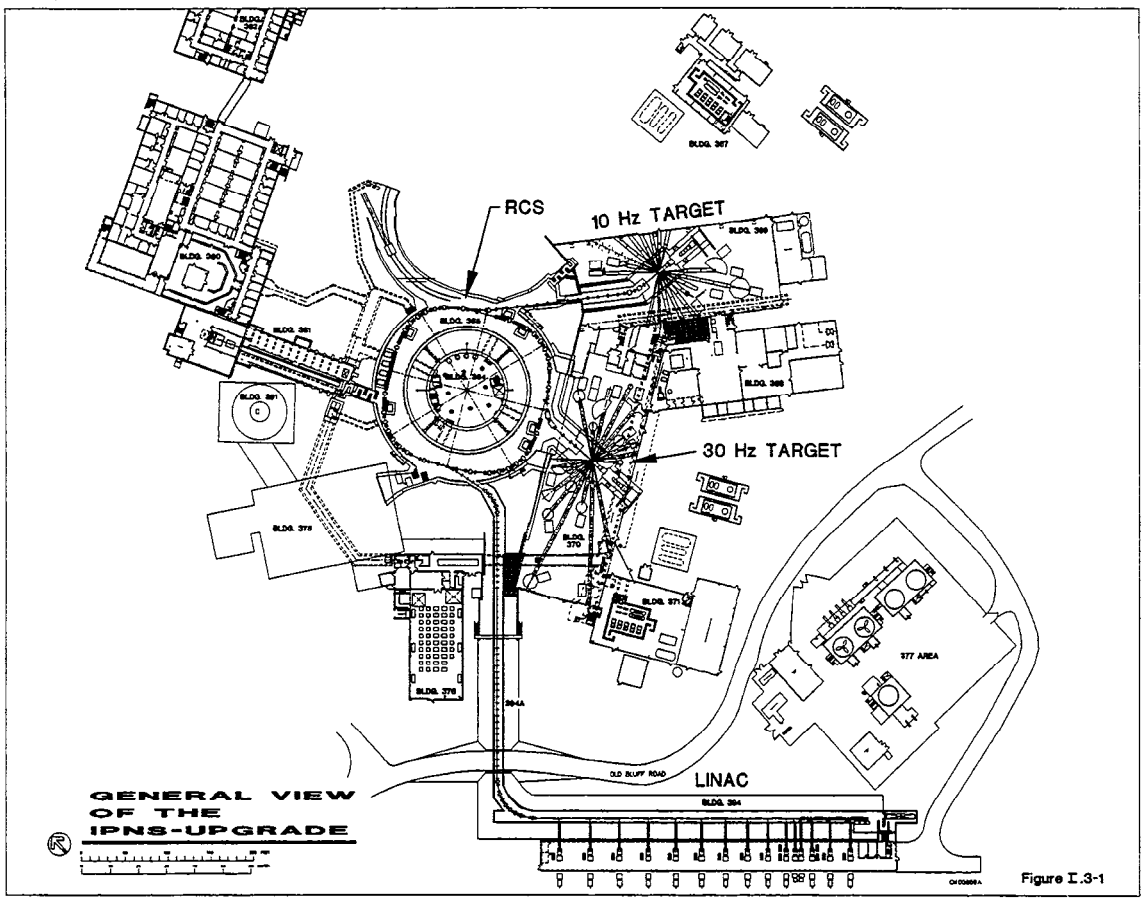

Figure 1: IPNS Upgrade Facility Layout.

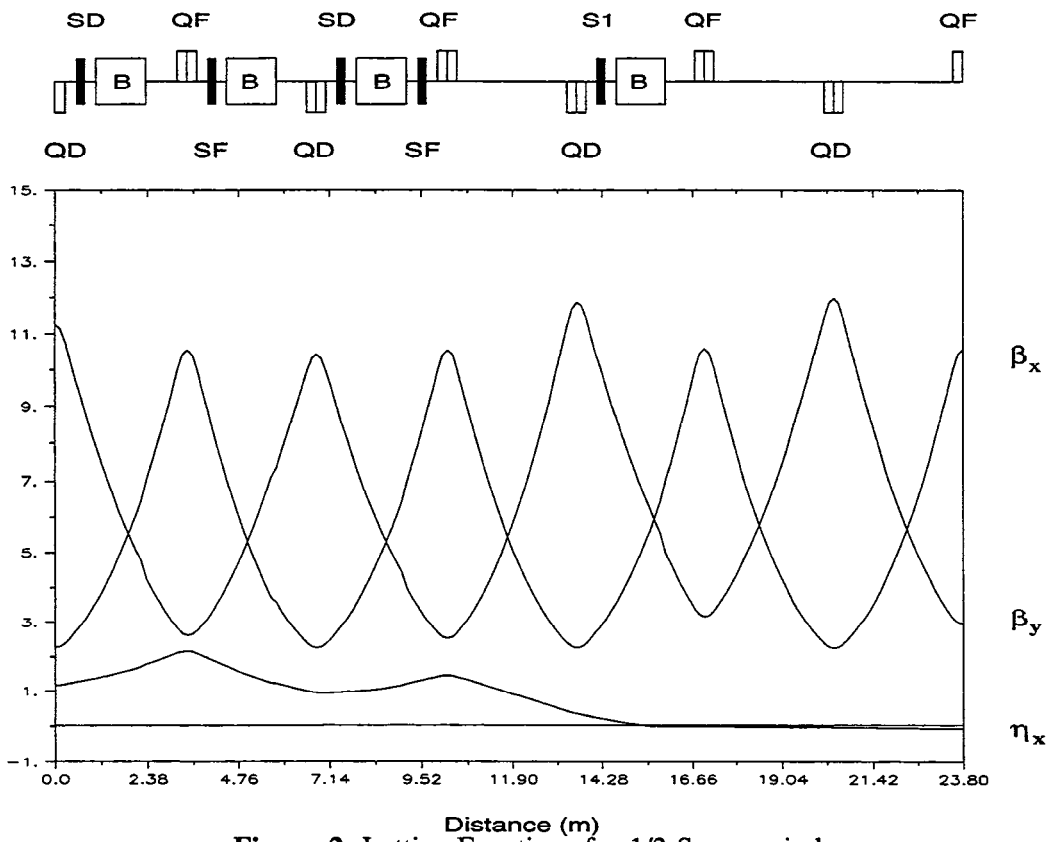

Figure 2: Lattice Functions for 1/2 Superperiod.

frequency cavity system that could have a total length of 20-30 m, and 3) the straight sections should be dispersion-free for implementation of charge-exchange injection. Figure 2 shows 1/2 of a super period with reflective symmetry at both ends. Each cell of the FODO structure has a phase advance of ~ 90° in both transverse planes. The normal cells, dispersion-suppressor cell and the straight-section cells are evident in the figure. The dispersion-suppressor cell is made by removing a dipole from a 90° phase advance cell. When the vertical phase advance is slightly less than 90° but the horizontal phase advance is maintained at 90°, the missing dipole scheme suppresses the dispersion function. An advantage of this arrangement is that the horizontal tune is about one unit higher than the vertical. The dynamic aperture study took alignment and construction imperfections into account, and the results are presented elsewhere [2]. Table 1 shows parameters of the normal cell. Table 2 is a summary of the main RCS parameters.

Table 1: Normal Cell Parameters
(2.2 GeV, B ρ = 9.989 Tm)

Elements	Length (m)	Strength	Units
QD	0.25	-7.276	T/m
D1	0.3		
SD	0.2	-0.843	m^{-2}
D1	0.3		
B	1.3	1.5088	T
D2	0.8		
QF	0.5	8.267	T/m
D1	0.3		
SF	0.2	0.612	m^{-2}
D1	0.3		
B	1.3	1.5088	T
D2	0.8		
QD	0.25	-7.276	T/m

III. Injection

The injection energy was determined by the incoherent space charge limit of the lattice and the defined acceptance of the synchrotron. If the injected beam stack has an emittance of 375 π mm mr in both transverse planes, the bunching factor is 0.4, and the allowed tune shift due to space charge is 0.15, an injection energy of 400 MeV is sufficient to allow a time-averaged current of 0.5 mA with a repetition rate of 30 Hz.

The 400-MeV H^- ion injector linac design for this feasibility study was performed by the industrial firm, AccSys Technology, Inc. The linac design specification includes: 1) an rms normalized emittance $\leq 1\pi$ mm mr, 2) an energy spread of less than $\pm$ 2.5 MeV, 3) a beam pulse length of 0.5 msec, and 4) beam chopping capability near the ion source so that the beam can be injected into a waiting synchrotron rf bucket.

Phase space painting in both transverse planes is used to stack 561 turns in the synchrotron. Four bumper magnets provide radial closed orbit displacement, and both injection position and angle can be radially adjusted as shown in Figure 3. A fast vertical steering magnet allows adjustment of the vertical injection angle. Unique features of this injection system include: 1) Trajectories of incoming H^- ions and of the circulating protons are combined by one of the ring focusing quadrupole magnets rather than by the customary dipole magnets. This focusing quadrupole has the added advantage that it acts as a defocusing quadrupole for the incoming H^-

Table 2: Main Parameters of the RCS.

Parameters	Values	Units
Circumference	190.4	m
Super-periodicity	4	-
Total number of cells	28	-
Number of normal cells	12	-
Number of dispersion-suppressor cells	8	-
Number of straight-section cells	8	-
Nominal straight-section length	2.9	m
Injection energy	400	MeV
Injection field	0.463	T
Nominal extraction energy	2.0	GeV
Maximum design energy	2.2	GeV
Dipole field at 2.2 GeV	1.5088	T
Bending radius	6.6207	m
Dipole length	1.3	m
Dipole good field region	0.45	m
Dipole gap height	0.182	m
Number of dipoles	32	-
Number of quadrupoles	56	-
Quadrupole length	0.5	m
Quadrupole aperture radius	0.1185	m
Maximum quadrupole gradient	8.8	T/m
Number of sextupoles (F)	16	-
Number of sextupoles (D)	16	-
Number of harmonic sextupoles	8	-
Maximum sextupole strength	1.2	m^{-2}
Sextupole length	0.2	m
Sextupole aperture radius	0.13	m
Horizontal tune, ν_x	6.821	-
Vertical tune, ν_y	5.731	-
Normalized transition energy, γ_t	5.40	-
Natural chromaticity, $\xi_x = (\Delta\nu)_x/(\Delta p/p)$	-7.23	-
Natural chromaticity, $\xi_y = (\Delta\nu)_y/(\Delta p/p)$	-6.88	-
Maximum β function	12	m
Minimum β function	2.2	m
Maximum η function	2.2	m
Minimum η function	-0.06	m
Revolution period at injection	890.1	nsec
Revolution period at extraction	665.1	nsec
$\dot{B}_{max}$	64.5	T/sec
Maximum energy gain/turn	81.4	keV

beam, and it provides an additional bend for the H^- particles. There is ample separation between the incoming beam and the circulating beam. 2) Since each cell has 90° phase advance, the bumper magnets, B1 and B4, shown in Figure 3, can displace and restore the closed orbit. However, B2 and B3 are needed to adjust the injection angle of the H^- ions so that H^o particles emerging from the stripping foil can be collected in a catcher. A discussion of the H^- and H^o particles associated with this injection system is given in reference [3].

Using the bumper system together with the vertical steering magnet in the transport line, the injected beam can be stacked in a K-V distribution [4].

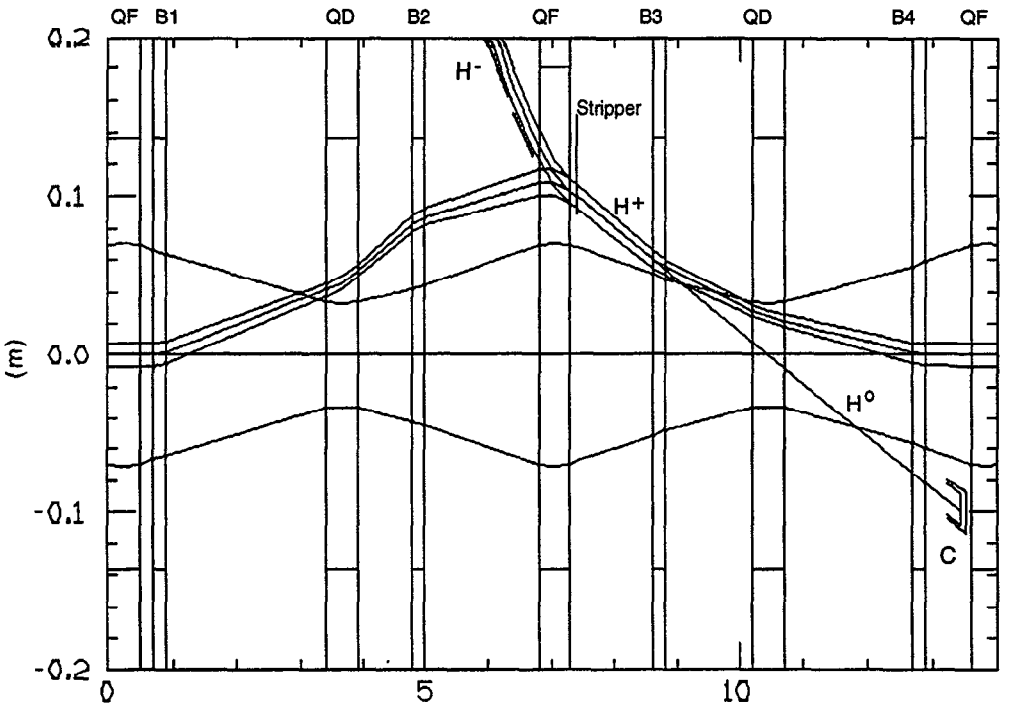

Figure 3: Bumped Orbit Injection, Showing the H^o Catcher (C).

IV. Rf and the Rf Voltage Program

The RCS rf system has 10 single-ended ferrite-loaded cavities to generate the required 180 kV. There is one cavity per straight section and a total of ten straight sections dedicated for the installation of the cavities. A change in resonant frequency from 1.12 MHz at injection to 1.50 MHz at extraction is accomplished by changing the dc current in the bias windings that are wound around the ferrite. A section of the rf cavity is shown in Figure 4.

A key goal of the design study was to devise an rf program that prevents beam loss from injection through acceleration to extraction. The rf program was obtained using a Monte Carlo program that tracked the particles from injection to extraction. The tracking study also provided information on optimum chopping of the incoming beam. In the context of bunch rotation, chopping is related to the energy spread of the injected beam. Figure 5 shows the rf voltage program and the corresponding bucket and bunch areas. When the first turn arrives at the start of injection, 40 kV is required to contain the linac beam that is 75% chopped (25% removed) and has a 2.5 MeV energy spread. The injected beam has a bunch area of 3.3 eV sec, and the

waiting bucket has an area of 7.3 eV sec, thus the initial dilution of the area is a factor of 2.2. During injection the voltage is raised to 69 kV to compensate for space charge effects and to give a somewhat larger bucket of 9 eV sec. Soon after injection, the bunch is well formed. The 9 eV sec bucket area is maintained for the next 7.5 msec. The bucket area beyond that point in time is made larger as indicated in Figure 5, for two reasons. The first is to make the momentum spread of the circulating beam large enough to stay below instability thresholds [5,6], and the second is to provide a synchrotron frequency large enough so that the particles in the bunch can follow the rapidly changing synchronous phase angle near the time of extraction.

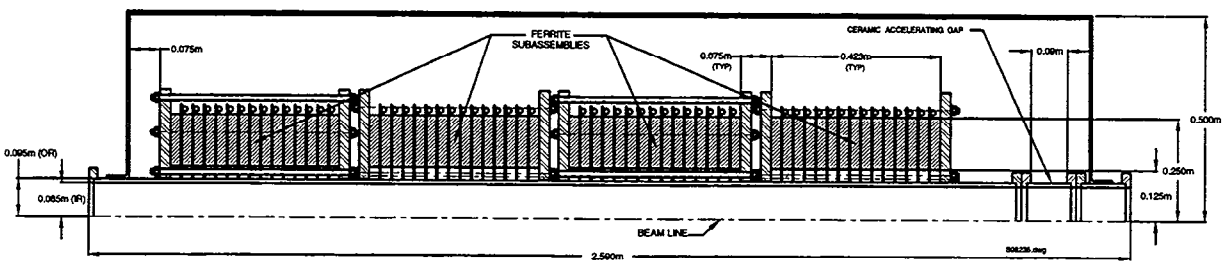

Figure 4: Quarter Sector of Single Ended Rf Cavity with Four Ferrite Sub-assemblies.

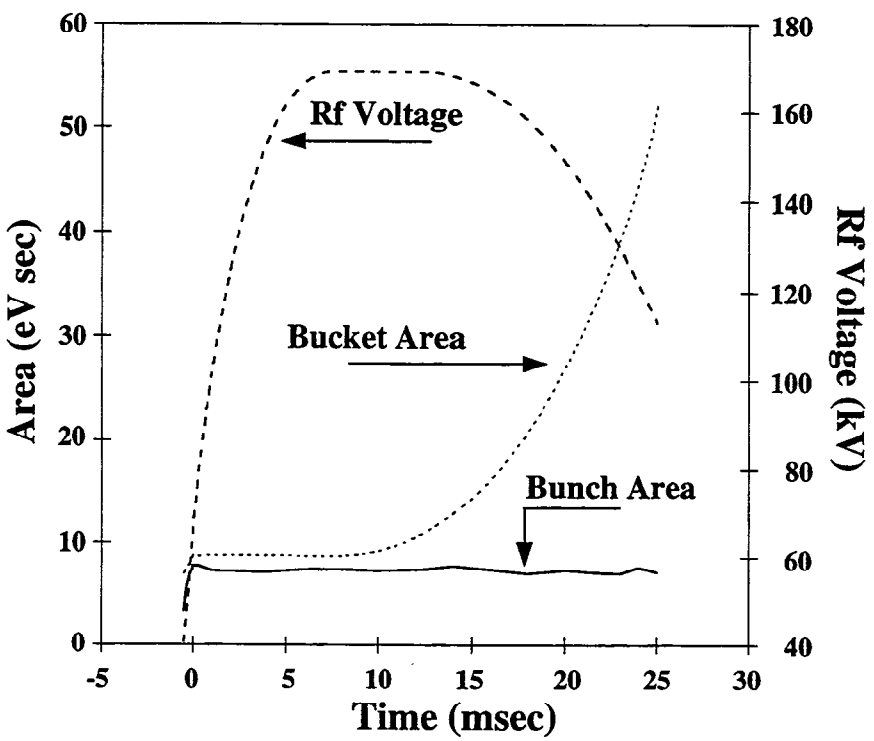

Figure 5: The Rf Voltage Program, Showing Bunch and Bucket Areas Over the Complete Cycle.

V. Impedance and Instabilities

The coupling impedance of the RCS is dominated by space charge which is capacitive for both the longitudinal and transverse components. The RCS operates below the transition energy, and is not expected to have longitudinal microwave instability. A detailed study of longitudinal impedance and instability was performed and results are presented in reference [5]. Similarly, the transverse impedance and instabilities were analyzed and details are presented in reference [6]. These studies showed that the machine can be operated stably.

VI. Synchrotron Hardware

The dipole, quadrupole, and sextupole magnets for the synchrotron are designed for a nominal beam energy of 2 GeV, but are capable of handling a maximum value of 2.2 GeV. An end view of a synchrotron quadrupole magnet is shown in Figure 6.

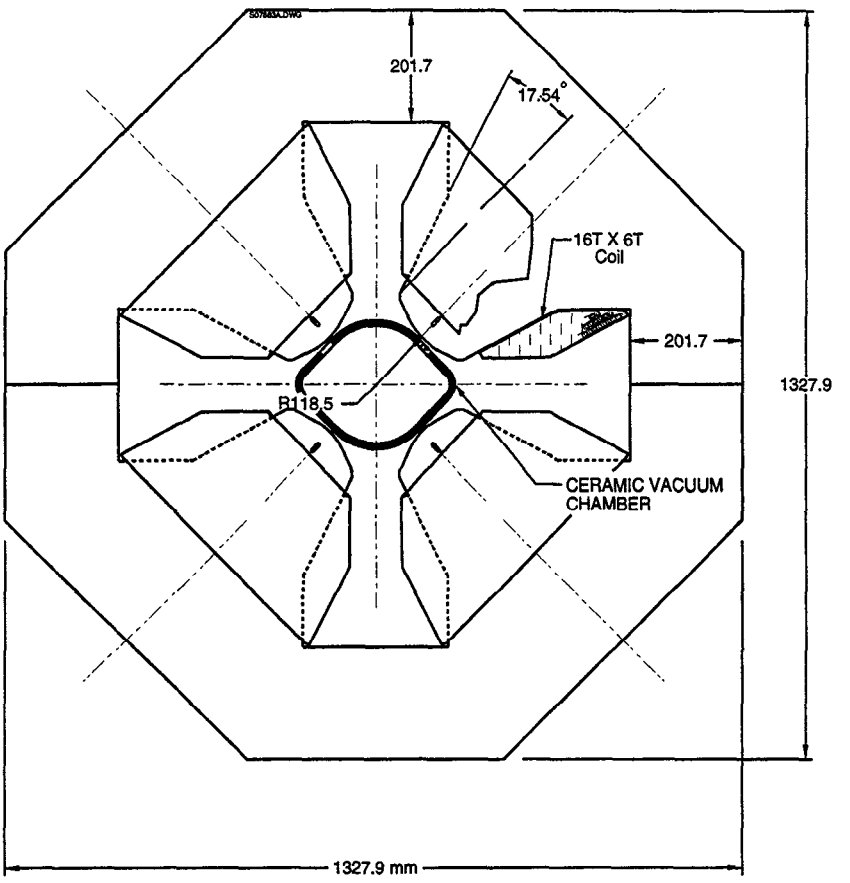

Figure 6: End View of a Synchrotron Quadrupole Magnet.

The RCS has ceramic vacuum chambers to avoid eddy currents. They are equipped with contour-following rf shields constructed of conducting wires to reduce the impedance due to space charge. The system is similar to that used at the ISIS facility at Rutherford-Appleton Laboratory [7].

The RCS ring magnets are energized with dual frequency resonant power supplies that excite the ring at a 20-Hz rate and de-energize it at a 60-Hz rate. This method results in an overall repetition rate of 30 Hz, and reduces the required peak rf accelerating voltage by 1/3. Figure 7 shows voltage and current waveforms for dual-frequency operation. Detailed descriptions of the hardware can be found in [1].

The vacuum chamber is constructed in sections made of 99.7% pure alumina ceramic. A typical quadrupole/sextupole chamber is 2.5 meters long and is constructed of individual 60-cm-long sections that are fused together. A typical cell is shown in Figure 8.

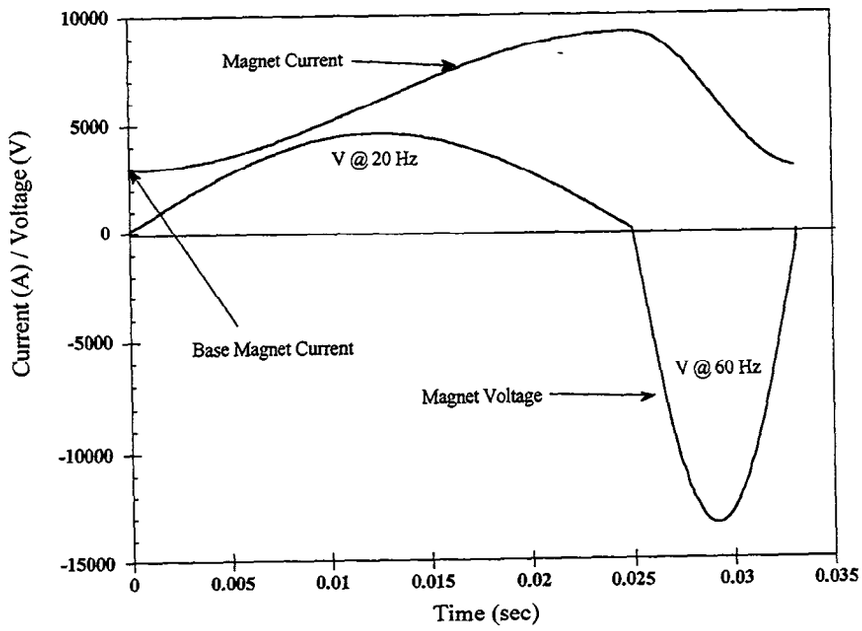

Figure 7: Dipole Magnet Current and Voltage Waveforms for Dual Frequency Operation.

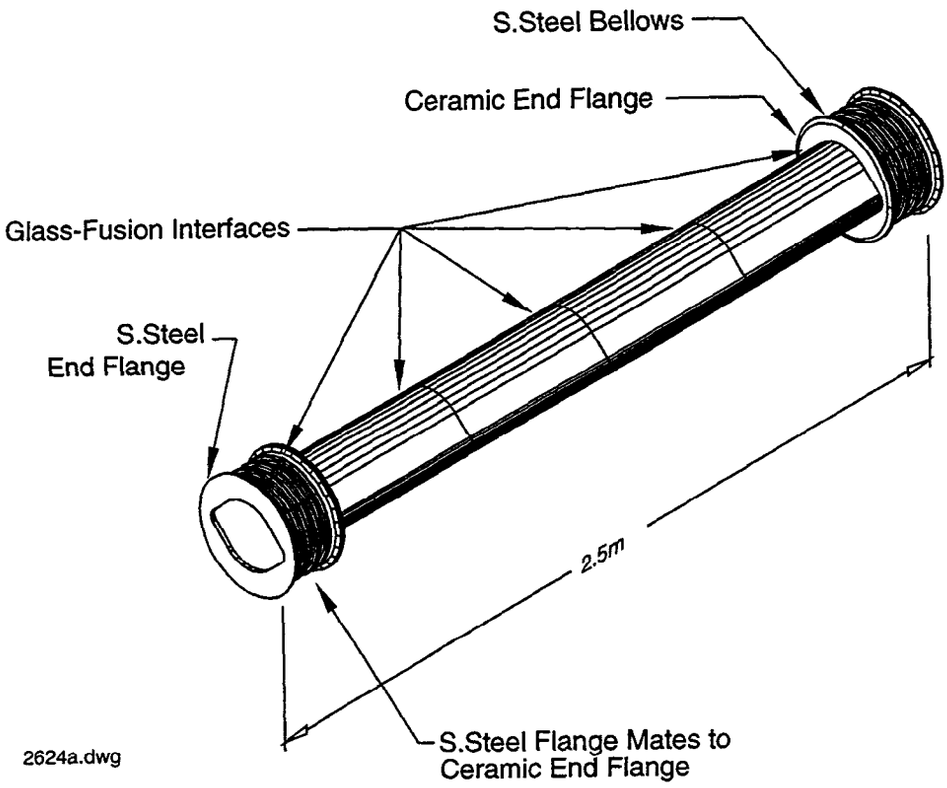

Figure 8: Typical Quadrupole/Sextupole Ceramic Chamber Cell.

VII. Summary

The IPNS Upgrade Feasibility Study resulted in the design of an accelerator system capable of producing 1 MW of proton beam power, while maintaining low losses. The full power can either be delivered to one of the two neutron generating targets, or can be split between them. A scheme of phase-space painting using charge exchange allows injection of 561 turns into the machine. Low losses are critical to assure hands-on maintenance of the machine, and are achieved by providing large dynamic aperture in the transverse plane and sufficient bucket area in the longitudinal plane.

Acknowledgments

We acknowledge D. Haid for help in manipulation of computer graphics and H. Rihel for drawings.

VIII. References

[1] "IPNS Upgrade - A Feasibility Study," ANL Report ANL-95/13 (April, 1995).
[2] E. Lessner, Y.-C. Chae, and S. Kim, "Effects of Imperfections on Dynamic Aperture and Closed Orbit of the IPNS Upgrade Synchrotron," Proceedings of the 1995 Particle Accelerator Conference, Dallas, Texas, May 1995, to be published.
[3] Y.-C. Chae and Y. Cho, "Study of Field Ionization in Charge Exchange Injection for the IPNS Upgrade," Proceedings of the 1995 Particle Accelerator Conference, Dallas, Texas, May 1995, to be published.
[4] E. Crosbie and K. Symon, "Injecting a Kapchinskij-Vladimirskij Distribution into a Proton Synchrotron," Proceedings of the 1995 Particle Accelerator Conference, Dallas, Texas, May 1995, to be published.
[5] K. Harkay, Y. Cho, and E. Lessner, "Longitudinal Instability Analysis for the IPNS Upgrade," Proceedings of the 1995 Particle Accelerator Conference, Dallas, Texas, May 1995, to be published.
[6] K. Harkay and Y. Cho, "Transverse Instabilities Analysis for the IPNS Upgrade," Proceedings of the 1995 Particle Accelerator Conference, Dallas, Texas, May 1995, to be published.
[7] G. H. Rees, "Status report on ISIS," in Proceedings of the IEEE Particle Accelerator Conference, Washington, DC, (March 16-19, 1987).

ICANS-XIII
13th Meeting of the International Collaboration on
Advanced Neutron Sources
October 11-14, 1995
Paul Scherrer Institut, 5232 Villigen PSI, Switzerland

A PROPOSAL FOR A LONG-PULSE SPALLATION SOURCE AT LOS ALAMOS NATIONAL LABORATORY

Roger Pynn and Dan Weinacht
Los Alamos National Laboratory, Los Alamos, New Mexico 87545, USA

ABSTRACT

Los Alamos National Laboratory is proposing a new spallation neutron source that will provide the U.S. with an internationally competitive facility for neutron science and technology that can be built in approximately three years for less than $100 million. The establishment of a 1-MW long-pulse spallation source (LPSS) at the Los Alamos Neutron Science Center (LANSCE) will meet many of the present needs of scientists in the neutron scattering community and provide a significant boost to neutron research in the U.S. The new facility will support the development of a future, more intense spallation neutron source, that is planned by DOE's Office of Energy Research. Together with the existing short pulse spallation source (SPSS) at the Manual Lujan, Jr. Neutron Scattering Center (MLNSC) at Los Alamos, the new LPSS will provide U.S. scientists with a complementary pair of high-performance neutron sources to rival the world's leading facilities in Europe.

1. World Class Performance in Several Areas

It has been recognised for over a decade that the U.S. needs new neutron sources and instrumentation if it is to carry out forefront neutron scattering research and compete in this arena with its international competitors in Europe and Japan. The 1 MW LPSS proposed by Los Alamos National Laboratory will provide advanced capabilities for neutron scattering and support the application of neutron scattering techniques to basic and applied research in disciplines such as materials science, structural biology, engineering, chemistry, and polymer science. Operating as a user facility, the proposed LPSS will provide U.S. universities, National Laboratories and industries with capabilities that will contribute strongly to the U.S. Department of Energy vision of being a major partner in world-class science and technology.

The principal focus of the LPSS will be on neutron scattering investigations that require cold or thermal neutrons. In many areas of neutron scattering research that use this part of the neutron spectrum — such as high resolution spectroscopy, reflectometry, moderate resolution powder diffraction, multiplexed backscattering, and Fourier methods — a 1 MW LPSS will outperform the ILL by a factor of between 3 and 4. In other areas — neutron spin echo, small angle scattering, and Laue diffraction, for example — performance similar to that of the ILL is anticipated. In a few areas — notably three-axis spectroscopy that concentrates on single points in Q,E space — the 1 MW LPSS will not perform as well as the ILL. The anticipated instrument performance, which has been documented at a recent workshop [1] held at Lawrence Berkeley National laboratory, will support a scientific program oriented towards macromolecular and

Keywords: Long-Pulse Spallation Source

soft-condensed matter science, areas which have grown significantly in the past few years and are expected to be of continuing importance.

The LPSS facility will establish the only high-intensity, ultracold neutron (UCN) source in the U.S. The importance of such a source has been acknowledged in long-range plans by the Nuclear Science Advisory Committee. UCNs are critical for our understanding of such issues as the origin of parity violation in elementary particle and nuclear interactions and the detailed nature of time reversal nonconservation. The precise measurement of neutron lifetime using UCNs is also critical for a number of issues in astrophysics and cosmology, such as the relative abundance of light elements predicted by the "Big Bang" theory. Installation of a UCN source at the LPSS will project the U.S. into an immediate position of leadership in this exciting area of fundamental research.

Science-based stockpile stewardship is a Department of Energy program that will ensure the safety, security, and reliability of the nuclear weapons stockpile without nuclear testing. The LPSS will provide high-energy neutrons for tomographic surveillance of nuclear weapons as well as long-wavelength neutrons for other types of non-destructive evaluation such as cold neutron radiography and depth profiling. By providing enhanced capability for examining issues such as explosive safety, polymer aging, and surface corrosion, the LPSS will make important contributions to understanding materials aging that will occur as nuclear weapons remain in the stockpile beyond their design lifetime.

Of the 15 beam lines envisaged for the new LPSS, 14 will be available for neutron scattering research and one will be equipped for high-energy neutron radiography. In addition to an intense source of ultracold neutrons, the facility will include a cell for testing new spallation neutron target systems, and a materials irradiation capability. If required, the facility could be used to produce neutron-rich radioisotopes, such as ^{99}Mo, for medical diagnostic or industrial applications. The LANSCE linac also has sufficient capacity to continue producing neutron-deficient isotopes at or above its present rate after the LPSS is installed.

2. Cost Effectiveness and Timeliness

Preliminary cost estimates indicate that the LPSS can be designed and constructed at Los Alamos for approximately $72M. At this stage, the project contingency is estimated at 30%, implying a Total Estimated Cost (TEC) of $95M. The facility is a cost-effective method for obtaining an advanced neutron scattering capability in the U.S., the necessity for which has been recognised by the scientific community and the DOE for over a decade. We estimate that the LPSS facility can be brought on-line quickly, with a design and construction time of three years. The facility thus provides a means of meeting the immediate need for a more powerful neutron source in the U.S. In addition, with its target testing and irradiation facilities and the experience it will provide with the operation of a 1 MW spallation target system, the proposed LPSS will provide important data to support future development of spallation technology for neutron production.

The cost and schedule estimates are based on our prior experience with spallation sources at the MLNSC and our Weapons Neutron Research (WNR) facility, and with our experience in constructing and commissioning accelerators. We can provide the LPSS capability at this cost by using an existing proton accelerator which produces the world's most powerful beam of protons. In addition, we will capitalize on our existing buildings and structures and use proven technologies. Operation of the facility also will be cost effective (at a marginal cost of $11M per year for eight months of operation) because the accelerator is already run by the DOE Office of Defense Programs at low power for the MLNSC and the WNR facility.

The existing linear accelerator is already capable of delivering about 750 kW of proton beam to an LPSS target and simultaneously accelerating the H^- ions needed for the existing short-pulse spallation source. Modifications to the linac will ensure that it can provide the additional 250

kW required to reach 1 MW in a reliable manner. Most importantly, these modifications are sufficiently minor that no extensive facility commissioning will be required. When one considers the history of spallation neutron sources and the time which has been required to bring their performance up to design specification, the real advantage of using an existing accelerator becomes very clear.

3. Existing Infrastructure

Los Alamos can provide an LPSS in a timely and cost-effective manner by using existing buildings and equipment with a replacement value of $38M, proven technology, experienced personnel, current resources, and Laboratory infrastructure. The LPSS target, shielding monolith, and support systems will be housed in an existing building at the end of the 800-MeV proton linear accelerator already operational at LANSCE. The facility is already equipped with utilities and ancillary support systems including lifting cranes; water cooling systems; vacuum, cryogenic, and air handling systems; waste treatment and disposal facilities; an electrical substation with transformers that can provide power for experiments; remote handling manipulators and control systems that can be used to handle targets and other radioactive components; and existing shielding. These systems constitute a considerable infrastructural investment and will be used to the fullest extent possible to support the LPSS.

As many of the presentations at this meeting have demonstrated, Los Alamos has in place the core of the team which will be needed to design the target for a new spallation source. In addition this team has many of the tools it will need, ranging from a powerful suite of Monte Carlo codes for simulating target performance, to irradiation facilities for qualifying materials, and a place to test the performance of mocked up targets in a proton beam. In addition, we are beginning to gain experience with simulations of neutron spectrometers so that the true merits of long pulses can be determined.

4. Looking to the Future

Neutron science has contributed to many advanced technologies and underpins U.S. economic competitiveness in vitally important industrial sectors such as automotive, aerospace, electronics, biotechnology, pharmaceuticals, materials, chemicals, and petrochemicals. The proposed LPSS is an important tool for continued contributions in many of these areas.

In addition to providing a powerful tool in the short term, the proposed LPSS will also support the development of future neutron sources in the U.S. by serving as a technological test-bed. The target test cell included in the LPSS shielding monolith will aid in the study and optimization of new spallation target concepts and the development of new designs for target systems for advanced spallation neutron sources. The materials irradiation capabilities of the LPSS will be employed for materials characterization experiments that support future spallation target designs, the nuclear weapons program, and the domestic fusion program. Data provided by the LPSS will support the National Ignition Facility (NIF) design efforts at Lawrence Livermore National Laboratory.

With spallation technology serving as the basis for future neutron sources in the U.S., the neutron scattering community will need to obtain more experience using time-of-flight methods by designing, building and using instrumentation at a high-power pulsed spallation neutron source. The proposed LPSS facility will enable scientists at the national laboratories and other members of the neutron scattering community to gain this valuable experience. This knowledge will support projects to build and operate even more powerful spallation neutron sources in the future.

Technical obstacles that may limit the ultimate performance obtainable with a SPSS are already apparent. The accelerator rings which provide the short proton pulses needed at an SPSS have a limited capacity to store protons, and thermal shocks make spallation target

technology more difficult with short pulses. A LPSS is an alternative path towards future neutron sources that avoids these limitations. The proposed new facility provides a cost-effective way of exploring the LPSS technology and evaluating its potential for future neutron sources.

5. Acknowledgments

This work was supported by the U.S. Department of Energy under contract W-7405-ENG-36 with the University of California.

6. References

[1] Proceedings of a workshop on Neutron Instrumentation for a Long-Pulse Spallation Source, held at Lawrence Berkeley National Laboratory, April 18-21, 1995.

ICANS-XIII
13th Meeting of the International Collaboration on
Advanced Neutron Sources
October 11-14, 1995
Paul Scherrer Institut, 5232 Villigen PSI, Switzerland

BNL FEASIBILITY STUDIES OF SPALLATION NEUTRON SOURCES

Y.Y. Lee, A.G. Ruggiero, A. Van Steenbergen, W.T. Weng

Brookhaven National Laboratory, PO Box 5000, Upton, NY 11973

ABSTRACT

This paper is the summary of conceptual design studies of a 5 MW Pulsed Spallation Neutron Source (PSNS) conducted by an interdepartmental study group at Brookhaven National Laboratory. The study was made of two periods. First, a scenario based on the use of a 600 MeV Linac followed by two fast-cycling 3.6 GeV Synchrotrons was investigated. Then, in a subsequent period, the attention of the study was directed toward an Accumulator scenario with two options: i) a 1.25 GeV normal conducting Linac followed by two Accumulator Rings, and ii) a 2.4 GeV superconducting Linac followed by a single Accumulator Ring. The study did not make any reference to a specific site.

1. Introduction

Since the beam power can be expressed as the product of beam kinetic energy and beam intensity, the design goal of 5 MW average beam power can be obtained by trading proton beam intensity for proton energy. Depending on the relative balance between these two parameters, two basic approaches, for the design of the PSNS facility may be considered. One choice is a relatively low proton energy accompanied by a higher beam intensity, which can be realized with a full-energy linac followed by a number (one or more) of constant energy accumulator rings. This approach has the advantage of a cheaper circular component (the accumulator ring) which may be also easier to design and to operate. The disadvantage is an expensive linac and higher beam intensity with consequences on cost, reliability and safety of the whole facility. The second choice is a higher proton energy accompanied by a commensurate lower beam current. Higher beam energy could be obtained with a linear accelerator, for example, with superconducting cavities; the cost, however, would be high and reliable operation difficult. At the present stage only fast-cycling synchrotrons seem appropriate for proton acceleration to high energy, with high average beam intensity. The two basic approaches: a full-energy linac followed by accumulator rings, and a low-energy linac followed by a fast-cycling synchrotron have been considered in various design proposals for similar PSNS facilities [1-5]. They have a layout schematically shown in Figure 1.

Initially, we have considered a scenario [6,7] based on the use of a 600 MeV Linac injector followed by two 3.6 GeV Rapid-Cycling Synchrotrons (RCS). The choice of design energy influ-

Keywords: Rapid-Cycling Synchrotrons, Accumulator Rings, Linear Accelerators

ences directly the proton to neutron yield and design of the target system. Higher beam energy was preferred because it eases many design considerations regarding beam performance. The synchrotron scenario alleviates considerably the design considerations of the injector linac, but requires careful examination of design issues which are peculiar to synchrotrons and not to accumulator rings. At the conclusion of the first period of studies, it was determined that a 5 MW synchrotron scenario holds several difficult technical issues. We thus initiated a second phase of studies for an accumulator scenario. At the end of the comparison, this was indeed proven to be less difficult, with only marginal cost differential. In the accumulator scenario, the beam energy choice is an open parameter, and two options have then been investigated: one at 1.25 GeV which can be obtained with either a normal- or a super-conducting linac, and the other at 2.4 GeV, definitively with a superconducting linac.

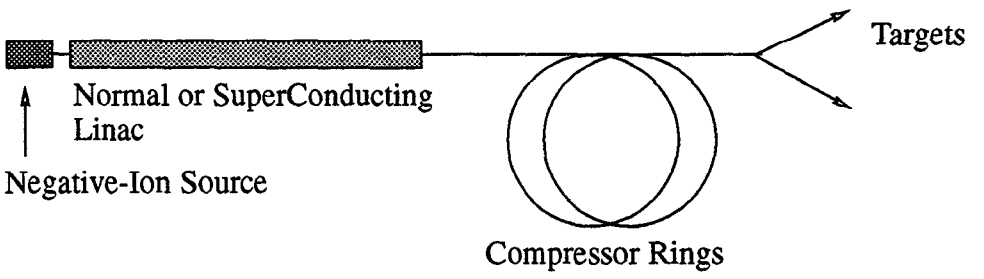

Figure 1. A Pulsed Spallation Source with Linac and Compressor Rings

Though which of the two energy and linac options to be preferred are still left to be determined, at Brookhaven we have nonetheless at the moment a preference for the accumulator scenario as the PSNS facility.

2. The Rapid-Cycling Synchrotron Scenario

The most important issue of the synchrotron scenario is the choice of the linac energy. One might suggest as low a beam energy as possible, with most of the energy increase to take place in the synchrotron in order to favor linac reliability and minimum cost. Yet the low-energy injection into the synchrotrons creates a bottleneck in the beam performance because of the space charge effects. These can be reduced either by raising the final energy, so that the total amount of beam intensity is lowered, or by increasing the injection energy. The scenario we have investigated takes as a compromise one 600 Mev Linac followed by two 3.6 GeV Synchrotrons.

The number of synchrotrons (two) is driven by two additional considerations. One is again space charge: two synchrotrons, running in parallel, need half of the total amount of beam current and therefore half of the amount of space charge effects. A second consideration is that the overall repetition rate of 60 beam pulses to the target per second is better achieved with two synchrotrons each running 180° out of phase at the repetition rate of 30 Hz.

A list of the most important issues relevant to the design of high beam intensity rapid-cycling synchrotrons is as follows: space charge effects at injection; RF capture during injection; RF acceleration; ramping of the guide field; and, vacuum.

Space charge effects are particular important to synchrotrons because of the low injection energy. The indicative parameter is the depression $\Delta\nu$ of the betatron tune given by

$$\Delta\nu = Nr_p / 2B\beta^2\gamma^3 \varepsilon \tag{1}$$

where N is the total number of protons circulating, $r_p = 1.535 \times 10^{-18}$ m, B the bunching factor which during the early part of the acceleration cycle is about 0.3, β and γ are the usual relativistic factors, and ε is the beam emittance. We have adopted the limit $\Delta\nu = 0.25$. Thus Eq. (1) relates closely injection energy, beam intensity and beam dimension, which also determines the gap of the magnets and therefore their feasibility and cost. The choice of two 3.6 GeV synchrotrons together with the 600 MeV linac requires a magnet gap close to 15 cm, which is technically and financially acceptable.

The scenario works as follows. Beam pulses of negative ion sources are accelerated to 600 MeV in the linac at the repetition rate of 60 Hz. The pulse duration is long enough to allow injection of many turns in one synchrotron at the time. Injection occurs by charge exchange, letting the beam cross a stripping foil. The beam is then accelerated to 3.6 GeV and immediately extracted and transported to one of two experimental targets. As the beam is being extracted from the first synchrotron, the second synchrotron is being filled with a linac beam pulse of the same duration and intensity which it accelerates to the same final energy and at same repetition rate. The procedure then repeats periodically alternating filling and acceleration from one synchrotron to the other, thus creating a beam pulse sequence at the repetition rate of 60 Hz.

It was determined that rf capture and multiturn injection is difficult to control in a rapid-cycling synchrotron because of the fast ramping of the guide field. It is important to control the total beam losses to a low level (about 10^{-4}) during the entire acceleration cycle. In particular, it is crucial to demonstrate capability of controlling beam losses to a 10^{-5} level during multi-turn injection and rf capture. This was proven to be difficult, and eventually with no more than 300 beam turns. This required a low linac duty cycle (3%) and a large ion source beam current (in excess of 100 mA). General linac parameters are shown in Table 1.

Other problems also appeared in the synchrotron scenario. The rf system for acceleration had to provide a peak power of 7 MW, with a total voltage of 0.8 MV at 1 - 1.5 MHz. The bending field were ramped at the large rate of 50 T/s. The vacuum system was complex, made of a sophisticated and costly ceramic vacuum chamber with screening metallic wires.

3. The Accumulator Scenario

The accumulator scenario was proven to have less technical difficulties, at least during the feasibility study, than the synchrotron scenario. Moreover, since no substantial cost difference was found, it is the currently preferred scenario at Brookhaven. The required beam power is entirely generated in the linear accelerator, and thus the linac is the most crucial component which requires special care and attention during design. On the other end, the design of the accumulator ring is simplified, and expected to be less critical. Because of the lower energy, in principle the accumulator scenario requires larger average beam current. Again the largest energy value and the largest number of beam turns injected are preferred, since they would lead to a lower beam current and thus a less demanding ion source. There are two possible

options, which have indeed been investigated: a normal conducting linac which cannot exceed the energy of 1.25 GeV because of cost, and a superconducting linac that can reach an energy as high as 2.4 GeV. In the first option one needs two accumulator rings, whereas only one should suffice for the large energy option.

With the accumulator scenario several technical problems disappear or become less important. For instance, the vacuum system is greatly simplified, by adopting a solid metallic vacuum chamber. The rf system is needed only to compress the beam in one single bunch, and not for acceleration. At most, a peak voltage of 30 kV is needed at the frequency of about 1 MHz. Similarly the operation of the accumulator ring is at constant field without pulsed excitation.

Though the injection energy is larger, nevertheless space charge effects are still important and determine the performance of multi-turn injection as well as beam dimension and magnet aperture. Numerical simulations have demonstrated that it is possible to control beam losses to an acceptable level also with one thousand (or more) turns injected. Also, it was possible to prove that multi-turn injection by charge exchange is feasible, essentially without appreciable negative ion stripping due to crossing of magnetic fields, also [8] at the injection energy of 2.4 GeV.

The scenario works as follows. A long beam pulse is generated by the linac at the repetition rate of 60 Hz. Half of the pulse is injected in one accumulator ring, and the second half in the second ring. Both beam pulses are compressed to a length of 400 ns, simultaneously in the corresponding rings, and then extracted in sequence with a 200 ns interval. The overall pulse on the target is thus about 1 ms long. In the 2.4 GeV option, the total beam pulse can be directed, if desired, to a single accumulator ring.

4. Linac Configurations

The accumulator scenario sets clearly the priority and the emphasis of the design to the linear accelerator. Five different linac structures are summarized in Table 1. The first column (A) is the 600 MeV normal conducting linac used in the study of the synchrotron scenario. The other four columns (B to D) describe possible linac configurations for the accumulator scenario.

A schematic layout of the linac is given in Figure 2. It is made of a front-end, a low-energy section, and a high-energy section.

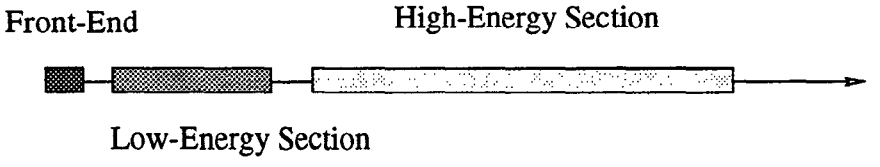

Figure 2. Schematic Layout of the Linear Accelerator

The front-end is made of a negative-ion source on a 50-kV platform, followed by either a single 2.5-MeV, 350-MHz RFQ (options A to C) or by a sequence of two 350-MHz RFQ's at energies 2 and 5 MeV (options D and E). The low-energy section is in all cases a normal-conducting 700-MHz Drift Tube Linac with the output energy of 70 MeV for cases A to C, and 100 MeV for cases D and E. The high-energy section is a 700-MHz Cavity-Coupled Linac for

options A to C, and a 700 MHz superconducting linac for options D and E. The final energy varies from one option to the other.

Table 1: Comparison of few Linac Configurations

	A	B	C	D	E
PSNS Scenario	Synchr.	Accumul.	Accumul.	Accumul.	Accumul.
Beam Power, MW	0.84	1.0	5.0	5.0	5.0
Final Energy, GeV	0.6	0.8	1.25	1.25	2.4
H^- Source Current, mA	120	70	120	120	30
Pulse Length, ms	0.360	0.533	1.024	1.111	2.315
Duty Cycle, %	2.2	3.2	6.1	6.7	13.9
Chopping Factor, %	65	65	65	60	60
Beam Current, mA	100	60	100	100	25
Beam Turns injected	236	747	770	1000	1000
RFQ, frequency, MHz	350	350	350	350	350
RFQ, energy, MeV	2.5	2.5	2.5	2 - 5	2 - 5
DTL, MHz / MeV	700 / 70	700 / 70	700 / 70	700 / 100	700 / 100
CCL, MHz / MeV	700 / 600	700 / 800	700 / 1250	--	--
Superc. Section, GeV	--	--	--	0.1-1.25	0.1-2.4
Peak Power, MW	90	30	135	125	60
Length, m	290	390	650	480	850

Configurations B and C apply to a phased mode of construction for the accumulator scenario. In a first phase the linac provides only 1 MW of average beam power, at the energy of 800 MeV, and it is followed by one single accumulator ring. In a second phase, the linac energy is raised to 1.25 GeV, and a second accumulator is added. At the same time the ion source intensity is increased to obtain a 5 MW beam power. Clearly, option beam B requires less beam current. If the number of turns injected is increased to one thousand, the required source current is 50 mA. Configuration D is the superconducting option of the 1.25-GeV, 5-MW linac, and it should be compared to option C. Though the length of the superconducting version is shorter, nevertheless a preliminary estimate has shown that they have comparable cost.

Finally, the high-energy superconducting option E, explores the possibility of larger energies with the intent of minimizing development of negative-ion source [8, 9]. As it is shown in the Table 1, the energy of 2.4 GeV would match to an accelerated beam current of 25 mA, and thus to an ion source peak current of 30 mA. Of course, this may require a longer pulse length, and eventually, two accumulator rings. Nevertheless, the high-energy superconducting option is perceived as the most flexible since would allow adjustments in case higher intensity ion

sources should be developed, or in case of funneling two ion sources in one DTL.

5. Conclusion

We have described the results of feasibility studies done at Brookhaven for a Pulsed Spallation Neutron Source. We have compared two scenarios: one which makes use of Rapid-Cycling Synchrotrons, and the other of Accumulator Rings. We have determined that the Synchrotron scenario present some technical difficulties at the level of 5 MW beam average power, and that the Accumulator scenario is to be preferred. This conclusion is supported by the fact that there was no major cost estimated difference between the two approaches. Nonetheless, the Accumulator scenario requires a more careful and detailed study and design of the linear accelerator, which provides the entire beam power. In our opinion technical risks are still represented by the development of the negative-ion source, which can be mitigated with a high-energy superconducting linac, and by the feasibility of thousand-turns injection by charge exchange. These options require more careful evaluation and more numerical simulations.

6. References

[1] F. Baumann et al., The Accelerators for the AUSTRON Spallation Source. Proceedings of EPAC 94, Vol. 3, page 2675. London, June 27 - July 1, 1994.

[2] G. Voronin et al., Development of Intense Neutron Generator SNEG-13. Proceedings of EPAC 94, Vol. 3, page 2678. London, June 27 - July 1, 1994.

[3] A. J. Jason and R. Woods, The Los Alamos Study for a Next-Generation Spallation-Neutron Source Driver. Proceedings of EPAC 94, Vol. 3, page 2684. London, June 27 - July 1, 1994.

[4] IPNS Upgrade. A Feasibility Study. ANL-95/13. Argonne National Laboratory. April 1995.

[5] Outline Design of the European Spallation Neutron Source. ESS 95-30-M. Sept. 1995. Edited by I.S.K. Gardner, H. Lengeler, G.H. Rees.

[6] 5 MW Pulsed Spallation Neutron Source. Preconceptual Design Study. BNL 60678. Brookhaven National Laboratory. June 1994.

[7] A. G. Ruggiero, Study of a Spallation Neutron Source based on Fast-Cycling Synchrotrons. Proceedings of EPAC 94, Vol. 3, page 2681. London, June 27 - July 1, 1994.

[8] A.G. Ruggiero, Negative-Ion Injection by Charge Exchange at 2.4 GeV.BNL - 62310. Brookhaven National Laboratory. September 1995.

[9] A.G. Ruggiero, Design Considerations on a Proton Superconducting Linac. BNL - 62312. Brookhaven National Laboratory. August 1995.

7. Acknowledgments

The work described in this report has been done by a BNL interdepartmental study group, which included staff members of the Alternating Gradient Synchrotron, the National Synchrotron Light Source departments, and the department of Advanced Technologies.

ICANS-XIII
13th Meeting of the International Collaboration on
Advanced Neutron Sources
October 11-14, 1995
Paul Scherrer Institute, 5232 Villigen PSI, Switzerland

STATUS OF PULSED SPALLATION NEUTRON SOURCE TARGET WORK AT BROOKHAVEN NATIONAL LABORATORY

H. Ludewig, M. Todosow, and J. Powell
Department of Advanced Technology, Brookhaven National Laboratory, Upton, NY 11973

ABSTRACT

This paper outlines work carried out at BNL on the Pulsed Spallation Neutron Source (PSNS) target, since the ICANS-XII meeting. A target, reflector, and moderator assembly was designed consistent with a 1.25 GeV proton beam energy. This target consisted of two modules containing randomly packed tungsten spheres and one flux trap. In addition, a study was carried out of the variation of neutron pulse length with proton pulse length for various reflector/pre-moderator configurations. It was found that:

- The amplitude of the neutron pulses increases with decreasing proton pulse length,
- Long proton pulses overlap the neutron pulse developing in the moderator, while shorter proton pulses are complete before the neutron pulse develops in the moderator
- Reflector/pre-moderators which slow neutrons by inelastic scattering result in neutron pulses which are narrower, and have shorter tails.

1. Introduction

A pulsed spallation neutron source (PSNS) study has been undertaken at Brookhaven National Laboratory (BNL) over the past two years. The results of this study have been outlined in a report[1], and have been reported on at the ICANS-XII meeting [2]. The parameters of this study were as follows:

- Average power of the proton beam 5MW
- Proton energy 3.6 GeV
- Two target stations operating at 10 Hz and 50 Hz
- Proton pulse width 1.2 μs.

The target associated with this design consisted of a three section/two flux trap arrangement. Due to the high proton energy three separate target sections could be used. "Wing", "back scatter", and "flux trap" moderator arrangements were employed in this target, making sixteen beam tubes possible. The neutron production volumes are surrounded by a beryllium reflector.

Keywords: Particle Bed Target, Lead Fluoride Reflector, Pulse Length

In this paper a target arrangement operating with a 1.25 GeV proton beam will be outlined. This proton energy is consistent with an accelerator system which consists of an accumulator ring rather than a synchrotron ring following the LINAC. In addition, a study of the dependence of moderator neutron pulse length as a function of reflector type and proton pulse length will be outlined. This study will be carried out on a simple target arrangement, rather than the more realistic targets described above.

2. Target Consistent with 1.25 GeV Proton Beam

The reduced range of 1.25 GeV protons implies a target which consists of two elements and one flux trap. The target elements consist of tungsten in the form of particles cooled by heavy water. The coolant flows at right angles to the direction of the proton beam through the particle bed. Two porous walls (frits) and four solid walls contain each of the particle beds. Two of the solid walls are in the proton beam, and are cooled on one side of the particle coolant. The frits separate the particle beds from inlet and outlet plena. The coolant flows along the inlet plenum, through the inlet frit, through the particle bed, and out the outlet frit and outlet plenum. Due to the extremely high heat transfer area per unit volume of the particle bed it is possible to remove well in excess of 3MW/L from the bed. Experimental results [3] have shown that it is possible to remove 3MW/L from a water cooled particle bed at ambient pressure before coolant boiling commences. Thus, with a moderate amount of system pressurization it should be possible to remove all the heat deposited in the bed. Furthermore, since the bed will be a tightly packed (no relative motion between particles), random arrangement of spheres, it is expected that the void fraction will be approximately 35%. Thus the average tungsten density in the target will be ~ 12.5 gm/cc. In order to minimize the pressure drop across the bed, the bed cross section will be rectangular with the flow traversing the shortest distance. The tungsten sphere OD was determined by the following four requirements:

- Increasing the OD will reduce the pressure drop
- Decreasing the OD will increase the area per unit volume, and thus heat removal ability
- Decreasing the OD will reduce the effect of thermal-mechanical induced shock stress enhancement
- The bed thickness in the direction of the coolant flow should be greater than 10 - 15 particle diameters, to avoid transients in the average particle bed void distribution.

Based on the above four requirements a particle OD of 2 mm has been chosen. This particle size results in an acceptable pressure drop, thermal performance, and essentially no stress enhancement due to thermal-mechanical shock.

All material structures of the target are of Inconel. This material has been used as window material at LAMPF, and shown to withstand substantial radiation exposures without unacceptable loss of integrity. An alternate material of construction with a low thermal expansion coefficient is also being considered. Since the thermal stress is proportional to the coefficient, a low cyclic stress would be implied. The target modules are surrounded by a beryllium neutron pre-moderator and multiplier zone 5 cm thick. This zone consists of beryllium spheres and is cooled by heavy water. The beryllium thus has a density of ~.73gm/cc and the heavy water density is ~.35 gm/cc. Finally, both light water and liquid hydrogen moderators are considered. It is

expected that these moderators will yield peak neutron fluxes in the thermal range (~ 0.0253 eV) and the cryogenic range (~0.004 eV). Currently no poisoning and de-coupling of the moderators has been investigated.

3. Proton Pulse Length Implications

In this section the effect of the proton pulse length and reflector type on the moderator neutron pulse length and relative amplitude will be outlined. In order to carry out this study a simple target arrangement will be considered. It will consist of the following components:

- Cylindrical tungsten heavy metal target 15cm OD x 100-cm L
- Cylindrical reflectors surrounding tungsten 50cm ODx100cm L
- Two moderators (light water and liquid hydrogen) embedded in the reflector

The proton energy in all cases will be 2 GeV. Gaussian pulse shapes in time, with widths varying from 1.2 (-6) s - 1.0 (-3) s are assumed. The four different reflector/pre-moderators assessed in this study are:

- Lead Fluoride (PbF_2)
- Beryllium Fluoride (BeF_2)
- Heavy Water (D_2O)
- Light Water (H_2O)

The neutron slowing down mechanism in this selection of reflectors varies from essentially all inelastic scattering (PbF_2), to purely elastic scattering (D_2O and H_2O). Beryllium fluoride uses a mixture of both inelastic and elastic scattering for neutron slowing down. The inelastic scattering cross section for fluroine is shown on Figure 1. The inelastic scattering cross section for lead has a value of approximately 2.0 barns from 3 MeV to 10 MeV. Thus, the inelastic scattering cross section for PbF_2 is significant over an energy range from 0.1 MeV to 10.0 MeV. Neutron slowing down due to elastic scattering with PbF_2 is not very efficient, and is not expected to contribute much to the slowing down spectrum. Light water is the most efficient at slowing neutrons down by elastic scattering of the reflectors being considered.

Results of the anaylses are shown in Table 1. From these results the following conclusions can be drawn:

- The shortest proton pulses result in neutron pulses in the moderators with the largest amplitudes for the H_2O moderator, regardless of reflector

- In the case of the liquid hydrogen moderator there is an optimum proton pulse length longer than the shortest one considered at which the neutron pulse amplitude is a maximum

- Lead fluoride reflector/pre-moderator results in the largest neutron pulse amplitude, for both moderators considered

The neutron pulse widths at half maximum for the light water moderator are shown on Table 2. These results show that the PbF_2 reflector results in a neutron pulse width which is approximatley 75% as narrow as those for the D_2O reflector/pre-moderator. The fractional difference between

the pulses corresponding to a PbF_2 reflector and a D_2O reflector for the light water moderator are shown on Figure 2. The fractional change is positive up to 1.0(-4) s, and then becomes negative, approaching -1.0. This result shows that the pulse corresponding to the PbF_2 reflector rises faster than that corresponding to the D_2O reflector. In addition, the result indicates that the pulse corresponding to the PbF_2 moderator dies away faster than the one corresponding to the D_2O reflector. Finally, a study was carried out of the effect of poisoning (^{10}B) the moderator, on the neutron pulse width and the corresponding pulse amplitude. These results are shown on Table 2 and Figure 3.

Table 2 shows the variation in the width, amplitude, and time of the peak with the increased addition of ^{10}B. The amount of ^{10}B added to the light water moderator is measured in units of water absorption. Thus, enough ^{10}B is added to the moderator to equal ten times and fifty times the original absorption cross section of light water. It is seen that the pulse width can be reduced from 8.0(-5) s to 1.0(-5) s. However, the pulse amplitude is reduced by approximately a factor of five at the same time.

The neutron energy spectrum in the target (tungsten), reflector (lead fluoride), and moderators are also considered. It is seen that in the tungsten target the neutron energy spectrum peaks at approximately .44 MeV with a tail extending to 20.0 Mev. The spectrum in the reflector peaks at .022 Mev - .066 MeV with a lesser peak at 1.2 MeV. However, its fairly tight structure in energy is the result of the inelastic slowing down mechanism characteristic of this reflector. In the light water moderator there is a broad peak at approximately 0.057 eV. Finally, in the liquid hydrogen moderator there is a pronounced peak at 0.009 eV.

Finally, the time of the maximum amplitude in the various components was determined for two proton pulses (1.2(-6) s and 1.0(-3) s)). It was seen that for the short pulse the pulse in the heavy metal target and the reflector are clearly separated from the pulses in the moderators. In the case of the long proton pulse the neutron pulses in the heavy metal target and light water moderator essentially overlap.

4. Conclusions

The following conclusions can be drawn from this comparative study of proton pulse lengths and their effects on the neutron pulses:

- The result of using a short proton pulse length (~ 1.0(-6) s) are:
  - Moderator neutron pulses with larger amplitudes
  - Neutron pulses which have a narrower width at half maximum; and which rise faster, and die away faster,
  - Neutron pulses in the heavy metal target and reflector which do not overlap the neutron pulse in the moderator.

- The use of longer proton pulses (~ 1.0(-3) s) are:
  - Removal of the thermal-mechanical shock enhanced stresses in the target components,
  - Potentially more reliable operation and the possibility of a larger number of target design options.

5. References

[1] Powell, J.R., et al."The BNL 5 MW Pulsed Spallation Neutron Source", This Conference.

[2] Blumberg, L.N., "Preliminary Report on the BNL Spallation Neutron Source Design Study", 12th International Collaboration on Advanced Neutron Sources - ICANS XII, Abingdon, Oxfordshire, U.K. (May 1993).

[3] Katscher, W., Nuclear Technology, Vol. 35, p.557, (1977).

TABLE 1. NEUTRON PULSE HEIGHT
(Relative Unites) / P

Proton Pulse (s)	H_2O (0.0253 eV)	LH_2 (0.00405 eV)
LEAD FLUORIDE REFLECTOR		
	MODERATOR	
1.2 (-6)	3.5	0.59
5.0 (-5)	2.9	0.62
5.0 (-4)	0.96	0.29
1.0 (-3)	0.53	0.18
BERYLLIUM FLUORIDE REFLECTOR		
	MODERATOR	
Proton Pulse (s)	H_2O (0.0253 eV)	LH_2 (0.00405 eV)
1.2 (-6)	2.4	0.56
5.0 (-5)	2.2	0.56
1.0 (-3)	0.43	0.18
HEAVY WATER REFLECTOR		
	MODERATOR	
Proton Pulse (s)	H_2O (0.0253 eV)	LH_2 (0.00405 eV)
1.2 (-6)	1.6	0.48
5.0 (-5)	1.5	0.49
1.0 (-3)	0.38	0.25

* 1.2 (-6) = 1.2×10^{-6}

TABLE 2. NEUTRON PULSE WIDTH AT HALF MAXIMUM
(s)

Proton Pulse Width	Lead Fluoride	Heavy Water
LIGHT WATER MODERATOR		
	REFLECTOR	
1.2 (-6)	8.0 (-5)	1.3 (-4)
1.0 (-3)	6.2 (-4)	8.0 (-4)

EFFECT OF POISON ON MODERATOR PERFORMANCE
LEAD FLUORIDE REFLECTOR
LIGHT WATER MODERATOR

Poison Concentration (In multiples of H_2O abs.)	Width (s)	Relative Amplitude	Time of Peak (s)
1.0	8.0 (-5)	3.5	1.9 (-5)
10.0	2.5 (-5)	2.3	1.3 (-5)
50.0	1.0 (-5)	0.8	7.6 (-6)

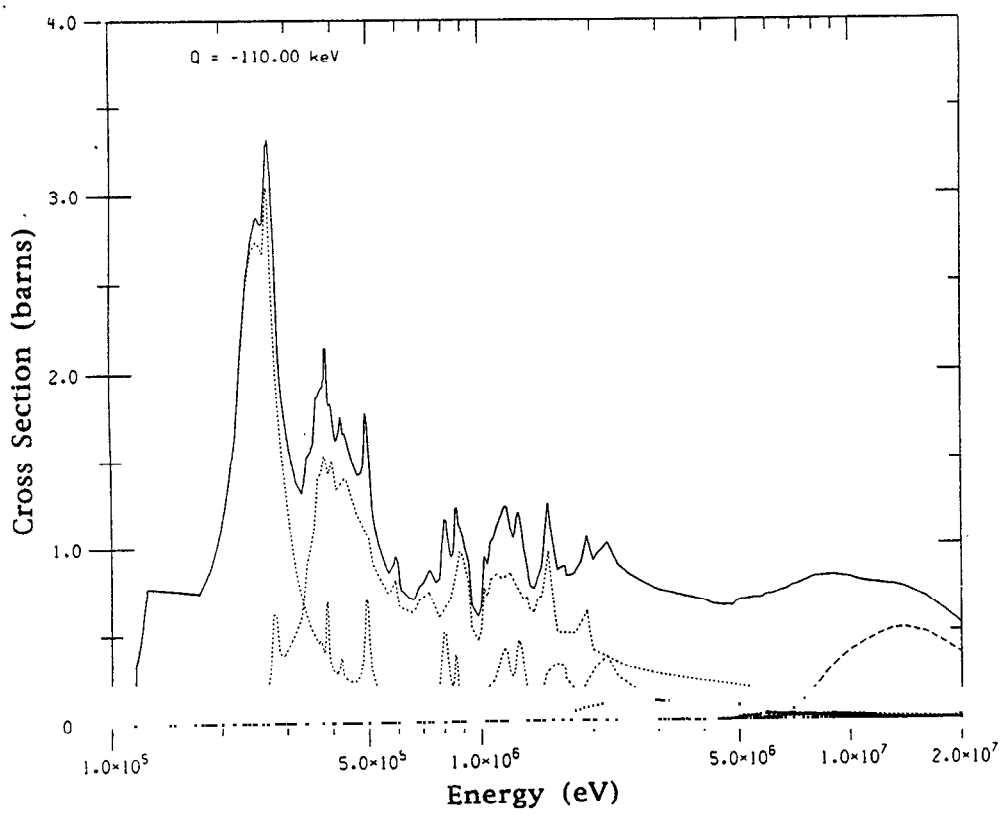

Figure 1 - Inelastic Scattering Cross Section for Fluorine

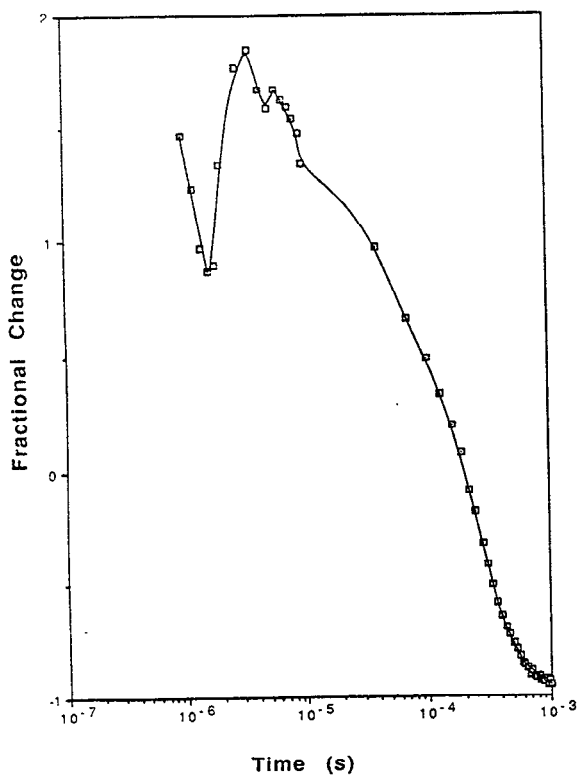

Figure 2 - Fractional Change in Pulse Amplitude

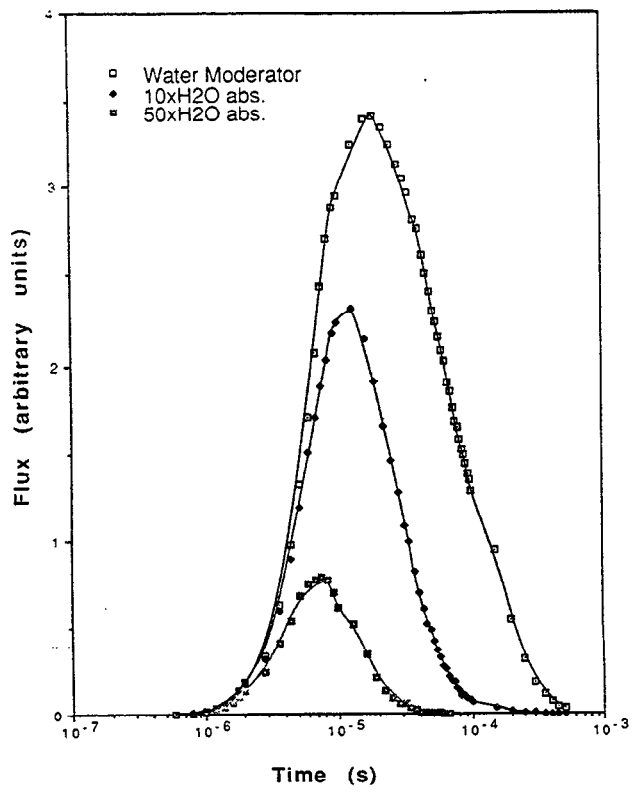

Figure 3 - Neutron Pulse in Light Water Moderator

ICANS XIII - ESS PM4
Thirteenth International Conference on Advanced Neutron Sources
October 11-13, 1995
Paul Scherrer Institute
Villigen, Switzerland

STATUS OF THE OAK RIDGE SPALLATION NEUTRON SOURCE (ORSNS) PROJECT

Bill R. Appleton
Oak Ridge National Laboratory
Oak Ridge, Tennessee 37831
USA

ABSTRACT

The current status and future plans of the Oak Ridge Spallation Neutron Source (ORSNS) are reviewed. The ORSNS is a new project initiated by the U.S. Department of Energy (DOE) beginning October 1, 1995, to prepare the conceptual design for a new spallation neutron source.

INTRODUCTION

There have been numerous studies in the United States and Europe detailing the need for a next-generation neutron source. Assessments in the U.S. date from the early 1970s with the most recent being the U.S. Department of Energy's Basic Energy Sciences Advisory Committee (BESAC) report *Neutron Sources for America's Future* (so-called Kohn Panel report). The first recommendation of this report was construction of the Advanced Neutron Source (ANS), a steady state research reactor, and the second recommendation was to initiate conceptual design for a complementary pulsed spallation neutron source. Because of cost and other considerations, the ANS project was cancelled and the DOE has now concluded that design and construction of a pulsed spallation neutron source will be the department's top priority for a new neutron source. In light of these changes, the BESAC has been charged by the DOE to complete a follow-up study to identify the scope and trade-offs for such a project that could be built for about one billion dollars. In addition, BESAC will assess upgrades to the existing DOE neutron sources that are necessary to maintain the U.S. neutron capability while this new source is being built.

The Oak Ridge National Laboratory has been identified as the preferred site for the spallation neutron source and has been asked to perform the conceptual design and R&D by the DOE. Design and R&D are proceeding for a high power, pulsed spallation neutron source that can be built in stages to accommodate evolving neutron science needs and available funds. These efforts will be carried out to achieve the performance goals set by the neutron science community and reflected in the upcoming BESAC assessment and will involve broad ranging collaborations with other DOE laboratories, industries, universities, and the international community.

ORNL TECHNOLOGY APPROACH

In their initial assessment, the scientific community, through the BESAC report *Neutron Sources for America's Future*, considered the long-term consequences if the ANS were not built and concluded:

"If the ANS is not built, a 5-MW PSS would be needed to basically cover its capabilities in neutron scattering. Other essential capabilities of the ANS would not be available.

"Thus, an approach that would combine a possible future 5-MW PSS (if successfully developed) with a new HFIR reactor would provide capabilities comparable overall to the ANS alone (e.g., much better at high energies but considerably worse for a number of important beam research

areas, particularly with cold neutrons), but at a considerably greater estimated cost of construction and operation. . . . ."

Extrapolating from this guidance, the ORNL is pursuing a two-phased approach to meeting the future needs of the U.S. neutron science community.

1. Design and construction of ORSNS
   - Design a 5 MW pulsed (μs) spallation neutron source that can be constructed in stages.
   - Align the technology choices with performance criteria established by the neutron users (BESAC assessment).
   - Design and construct the first stage at a power consistent with available technology and funds, and upgrade in the future as technology and funding allow.

2. Complementary upgrade of the High Flux Isotope Reactor (HFIR).
   - Upgrade the HFIR to maintain U.S. neutron science capabilities in areas such as isotope production, materials irradiation and testing, neutron activation analysis, and continuous neutron beams that cannot be provided by a spallation neutron source.

STATUS AND FUTURE PLANS

CURRENT STATUS OF ORSNS

The ORNL received funds to begin conceptual design and R&D on ORSNS in the fourth quarter of Fiscal Year 1995. Progress to date includes initiation of the following tasks:

1. Target Design

   The target needed to accommodate an energetic pulsed proton beam delivering 5 MW of power presents formidable challenges as documented in these proceedings. As a result, initial design efforts have focused on both solid and liquid target concepts. The results from these efforts will be reported when they are more complete, but the work so far has been in the nature of scoping studies to identify the needs for R&D and technology development. Studies underway include the following:

   - Solid targets. The materials being considered are W, Ta and Pb in various configurations including rods, packed beds, and monoliths with cooling channels.
   - Liquid targets. The systems being considered are Hg and Pb/Bi.
   - Neutronics calculations. Neutronics calculations have been done for various target/moderator systems to establish the spatial, temporal, directional, and energy dependent particle and neutron fluxes. In addition, the correlated spatial and temporal energy deposition distributions, damage profiles, gas production, and activation products are being calculated to assist in damage assessments and materials selection.

In these investigations, both continuous and pulsed beam spallation sources are being simulated. A combination of Monte Carlo and discrete ordinates codes are necessary and those used are:

- CALOR95. Monte Carlo Hadronic/Electromagnetic Transport Code System (HETC95, EGS4, SPECT95, MORSE/MICAP/MCNP)
- HETC95. Monte Carlo Hadronic Transport Code (~20 MeV <E <20 TeV)
- EGS4. Monte Carlo Electromagnetic Transport Code (~.01 MeV <E <1 TeV)
- MORSE/MICAP/MCNP. Monte Carlo Neutron and Gamma-Ray Transport Codes (E <20 MeV)
- ANISN/DORT/TORT. 1-D/2-D/3-D Discrete Ordinates Neutron and Gamma-Ray Transport Codes (E <20 MeV)

All of these codes with the exception of MCNP and EGS4 have been developed by ORNL for various applications over the years and have been widely adapted and used by many other institutions.

2. Materials qualification

   Materials issues important for target, moderator, windows, etc., include radiation effects, compatibility, corrosion, thermal shock, and fatigue. Materials of interest include a range of alloys and liquid metals. Initial goals are to evaluate irradiation responses based on relevant existing data and calculations/extrapolations, examine existing high energy/dose irradiated materials that are available, participate in international efforts assessing spallation neutron source materials, and perform reactor and high energy irradiations to fill in gaps. Qualification of liquid metal targets will require building prototypes and test stands for direct tests.

   It is already clear that spallation irradiation conditions for solid targets in particular are outside the existing experience base acquired for fission and fusion applications. Spallation materials will experience higher transmutation gas and solid impurity production rates, proton radiation damage, particle energies, pulsed damage delivery schedule, and possible synergistic effects. These anticipated severe materials problems are also a motivation for considering liquid metal targets.

3. Thermal hydraulics

   The heat transfer group and test facilities developed for the ANS project have been adapted to SNS needs to evaluate heat removal schemes for the target/moderator designs thermal shock/cycling effects, transient heat flux effects, and average energy deposition effects.

4. Design-to-cost model

   A design-to-cost model is being constructed as a project management tool to assist in making technical choices, and calculating the performance, cost, and project risk associated with these choices. This model will be validated using data from other spallation source designs and related projects. This approach to making technical choices is necessitated by the need to design a facility capable of meeting the future needs of the neutron science community but one whose first stage can be constructed for about one billion dollars.

5. Cooperative projects

   - A cooperative effort with Brookhaven National Laboratory (BNL) was started to cost validate the BNL design for a 5 MW pulsed spallation source using rapid cycling synchrotrons (RCS). This design could be built in stages and will help validate the design-to-cost model.

   - A cooperative effort for similar purposes with BNL was started to consider accumulator rings instead of RCS for their 5 MW source and to assess superconducting linac alternatives to conventional linacs.

   - A cooperative effort with the Rutherford Appleton Laboratory ISIS facility was started to evaluate the effects of background radiation that occur during the proton pulse at various instrument locations and shielding configurations. This study is important to assess the feasibility of continuous spallation sources as well as target/shielding/moderator designs and instrument development at pulsed sources.

   - Project structure. Those project management and technical programs that were developed for the ANS project, and are applicable to ORSNS, have been transferred.

FUTURE ORSNS PLANS AND COLLABORATIONS

The receipt of funding for the ORSNS project in the FY 1996 budget will allow the full R&D and design group to be completed. The target and other design activities started in FY 1995 will continue at full pace. An accelerator design effort will be put in place to facilitate selection of the technologies that will be used to design a spallation neutron source. These technology choices will be aligned with guidance received from the DOE as a result of the BESAC assessments concerning scope, trade-offs, and budget constraints.

It is anticipated that a high power short-pulse, 5 MW, spallation neutron source will be needed to ensure that the U.S. remains competitive in neutron scattering in the future. Budget and technology constraints will likely require that a 5 MW source be designed that is capable of being built in stages. The first stage would be a fully operational source that could be constructed with available technology and consistent with the current budget constraints. However, the design would allow subsequent upgrades to full performance.

The ORSNS project will take full advantage of the work that has been done at various laboratories around the world in developing spallation neutron sources. The technology evaluations and feasibility studies that have been performed by the other DOE laboratories in the U.S., and studies in Europe and Japan will be evaluated and utilized. The ORSNS R&D design and construction efforts will utilize the existing expertise of these same laboratories as well as those currently operating spallation neutron sources. Because of the similarity in design activities and goals, the ORSNS will maintain close cooperation with the European Spallation Source project and its member laboratories. This will include collaborations on mutually beneficial R&D, science and technology, instrumentation development, and personnel exchanges. In short, ORSNS will be a highly collaborative team effort involving national and international partners directed toward a high-intensity, next generation neutron source to serve the U.S. community.

HFIR UPGRADES

The second part of the ORNL technology approach is to upgrade the HFIR steady state research reactor to address those needs of the neutron science community that cannot be performed at a spallation neutron source. ORNL is planning a three phased approach to HFIR improvements.

1. Phase I: Improvements within existing funds
   - Request to the DOE to operate at 100 MW again based on improved techniques for fuel plate inspection/selection.
   - Improve irradiation and neutron activation analysis facilities.
   - Develop a new gamma irradiation facility.
   - Develop new neutron scattering instruments and layout for more effective use of existing beams.
   - Improve beam part for neutron tomography and radiography.

2. Improvements requiring additional funds
   New funds (Scientific Facilities Initiative) have been requested in the FY 1996 Budget by the DOE Office of Energy Research to improve operation of DOE user facilities. These and other DOE funds will be used to make several improvements to HFIR.
   - Install a new liquid hydrogen cold source in an existing HFIR beamport with a brightness equivalent to the ILL vertical cold source (two years estimated completion).
   - Develop new instruments in collaboration with HFIR users and collaborators.
   - Propose a new guide hall for cold neutron research.
   - Extend core life and thus greater availability through use of an improved fuel developed for ANS.

3. Full upgrade of HFIR[2]
   The beryllium reflector at HFIR must be replaced at or before the end of its lifetime in ~1999. This presents the opportunity to upgrade the HFIR and greatly improve its lifetime and performance.
   - The beryllium reflector would be replaced with a thin-walled, annular tank of heavy water surrounding the core.
   - An aluminum, steel, or zircalloy sleeve would be placed between the core and the present reactor vessel; the present vessel would then no longer be a pressure boundary and its embrittlement would be of no consequence.
   - A new, large cold source would be added in the heavy water tank, located in a thermal neutron flux about three times higher than the vertical cold source at ILL.
   - Several new beam tubes and more guide hall space would be added.
   - Irradiation and activation facilities would be improved as well as reactor controls and instrumentation.

ACKNOWLEDGMENTS
I gratefully acknowledge my colleagues at ORNL who have been an integral part of the formation and planning of the ORSNS project.

REFERENCES

1. Neutron Sources for America's Future. Report of the Basic Energy Sciences Advisory Committee Panel on Neutron Sources, U.S.D.O.E. Office of Energy Research, DOE/ER-0576P, January 1993.
2. High Flux Isotope Reactor Futures Group Report. ORNL/TM-13002, 1995.

ICANS-XIII
13th Meeting of the International Collaboration on
Advanced Neutron Sources
October 11-14, 1995
Paul Scherrer Institut, 5232 Villigen PSI, Switzerland

THE EUROPEAN SPALLATION SOURCE STUDY (ESS)

H. Lengeler

CERN and ESS Study Group

ABSTRACT

The present status of the ESS study is described. A reference layout has been fixed including a 1.334 GeV H^- injector linac, two proton accumulator rings operated in parallel and two target stations fed with μs proton pulses: one at 50 Hz up to a beam power of 5 MW, the second one at 10 Hz with 1 MW beam power. The study of a mercury target has been given first priority.

1. Preface

In 1990 the need for a next generation pulsed European neutron source was identified by the "Large Installation Plan's Panel" of the European Community (CEC). In a series of workshops, neutron experimentalists together with accelerator experts and target designers have explored possibilities for such a next generation neutron source, resulting in the proposal for an accelerator driven, pulsed spallation source with the following design parameters:
- Average proton beam power up to 5 MW
- Repetition rate of 50 Hz
- Proton pulse length at the targets of ~ 1 μs
- Two target stations, one operated at 50 Hz up to 5 MW beam power and the second one operated at 10 Hz at 1 MW beam power

In June 1993 a conceptual design study was initiated and supported by seven European countries. Since December 1994 it is also supported by CEC and it is continued as a two year, site independent study. A reference design has been fixed (Fig. 1 and Table 1) and more detailed studies will be continued to establish its potential and a project costing at the 20 % precision level. R+D work has already been started to asses the feasibility of some accelerator components and to investigate target material problems. Neutron scattering instrumentation and technique development is the subject of a parallel European-wide programme under the same initiative. A first intermediate outline report has been issued in September 1995 [1]. The final report will be ready in October 1996.

2. Accelerator issues

At the start of the study a proton energy range of 0,8 to 3 GeV had been recommended. There are a number of ways to meet the source specifications given above. With present day technologies the combination of a linear (injector) accelerator and compressor or accelerator rings is favoured for achieving a time compression of the proton beam into 1 μs pulses. Various combinations have been considered namely (in ascending order of proton energy or decreasing average current):

Keywords: Spallation Neutron Sources; H^-linear accelerators, Proton Accumulator rings, Targets for Spallation Sources.

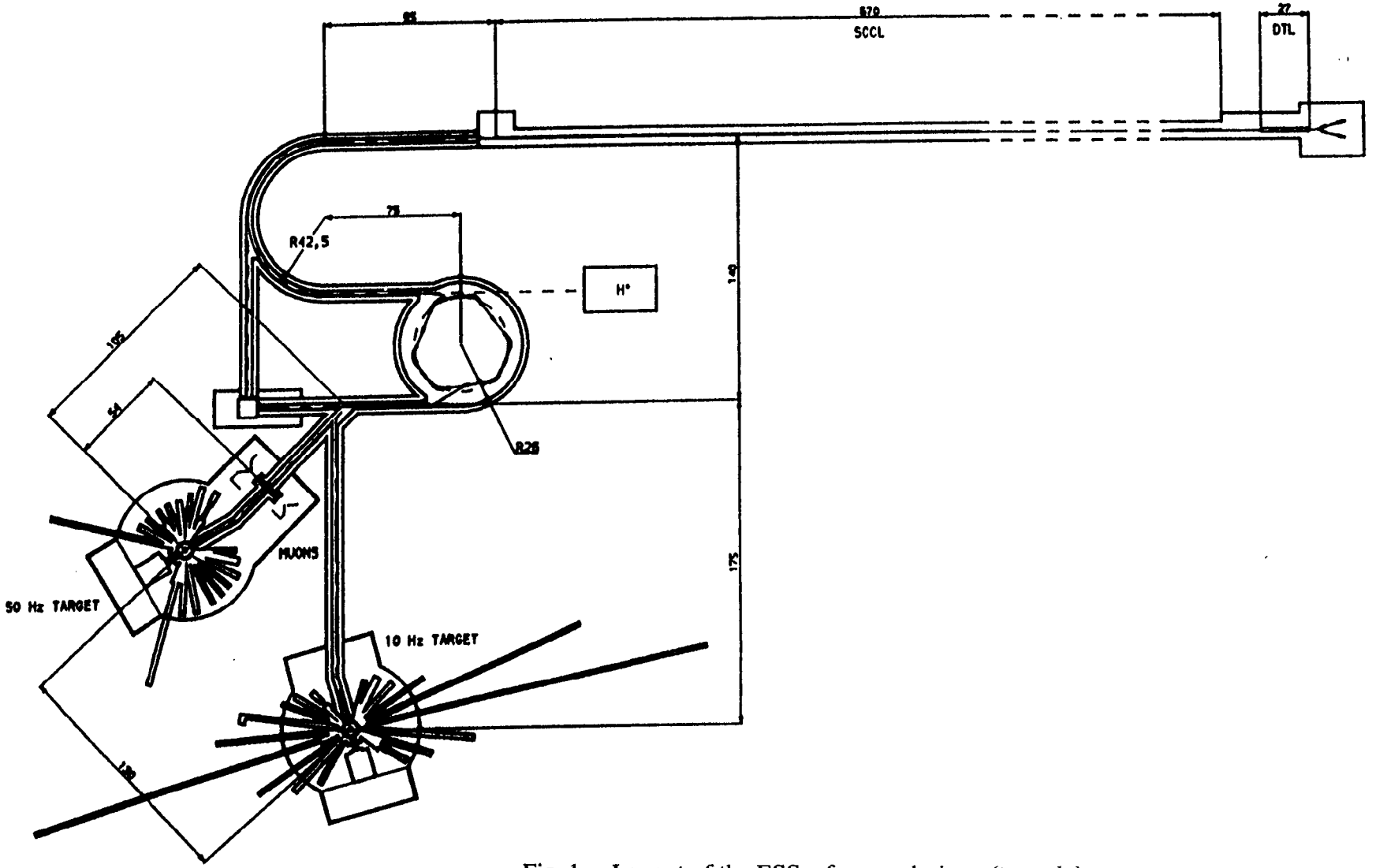

Fig. 1 Layout of the ESS reference design (to scale)

Linac		
Linac beam energy	1.334 GeV	
Linac beam power	5 MW	
Linac average / peak current	3.8 / 107 mA	
Linac repetition rate	50 Hz	
Linac beam pulse duration	2 x 0,6 ms	
Linac beam duty cycle	6.0 %	
Linac length (80 % filling factor)	~ 700 m	
Two accumulator rings		
Mean radius of rings	26.0 m	
Frequency of parallel operation	50 Hz	
Number of circulating protons per ring	2.34×10^{14}	
Bunch length / ring at ejection	0.4 µsec	
Two target stations	**1**	**2**
Energy of protons	1.334 Gev	1.334 GeV
Energy content of combined p-pulses	100 kJ	100 kJ
Proton beam diameter at target (parabolic 2D-density distribution)	200 x 60 mm^2	200 x 60 mm^2
Target	liquid, Hg, unsplit, horizontal injection	
Time structure	2 x 0.4 µs	2 x 0.4 µs
Beam power	4 or 5 MW	1 MW
Repetition Rate	50 Hz	10 Hz
Moderators	room temperature and cold	cold

Table 1 General Parameters of the Reference Design

1. A 0.8 GeV H^- linac and three accumulator (compressor) rings;
2. A 1.334 GeV H^- linac and two accumulator rings;
3. A 2.4 GeV H^- linac and one accumulator ring;
4. A 0.8 GeV H^- linac and two 3 GeV, 25 Hz proton synchrotrons (RCS);
5. A 0.8 GeV H^- linac and a single 3 GeV FFAG accelerator.

Priority has been given to a 1.334 GeV linac (Fig. 2), developing the full beam power of 5 MW at 50 Hz and followed by two accumulator rings operated in parallel (Fig. 3).

This combination has been preferred because of:

- an energy choice presenting a reasonable compromise between the size and cost of accelerators and the energy density produced by the proton pulses at the target

- a simple and reliable layout of rings with constant magnetic fields, a relatively small rf-system only used for particle bunching and lower ring space charge levels than option 1

A key issue and the dominating design principle for the accelerators are low beam losses, allowing "hands on" maintenance and repair on short notice. At high energy this corresponds to beam losses in the linac below 1 nA/m. The linac is also optimised for low loss injection into the accumulator rings and this fixes almost completely its most important parameters. A charge exchange injection ($H^- \rightarrow H^+$) is used and as a consequence H^--ions have to be accelerated in the linac. The time compression of the linac beam into 1 μs pulses is obtained by multiturn injection into the rings and by a fast one turn ejection. As a compromise between linac peak currents and a limited injection time (2 x 0,6 ms or 2 x 900 turns) a linac pulse length of 1,2 ms has been chosen.

Each ring delivers a 0,4 μs proton pulse with a 0,2 μs gap inbetween to the targets. In order to avoid beam losses during the rise time of the ejection kicker the linac beam has to be chopped with a beam-on time of 400 ns and a beam-off time 270 nsec (60 % chopping efficiency). Together with a 50 Hz operation this leads for the linac to a beam duty cycle of 6 %, an average current of 3,75 mA and a peak current of 107 mA, well below the space charge limit of the linac. For a well designed high current linac less than 10^{-3} particles are outside 20 times the r.m.s. emittance [2]. The proposed linac layout is shown in Fig. 2 and a few more parameters are given in Table 1. A special feature of the high intensity linac is the double front end. This layout has been adopted for two reasons [1]:
- State of the art H^- sources do not yet reach the combination of 100 mA peak currents, 6 % d.c. and low emittance, therefore it seemed advisable to use two H^--sources in parallel with reduced currents.
- Emittance increase with the concomitant enlarged beam losses can be kept smaller by the use of a double front end with subsequent combination of beams in a funnel.

Behind the funnel a classical drift tube linac (DTL) and side coupled accelerating structures of the type pioneered at Los Alamos are used. For the reference linac design, normal-conducting side coupled cavities have been preferred to superconducting disk loaded cavities. Superconducting cavities have been retained as an option with the advantage of a larger acceleration efficiency, higher acceleration fields resulting in a shorter linac and large beam openings decreasing the risk of cavity activation by beam losses. However at the present state it has to be seen if these advantages do not outweigh the disadvantages of greater complexity and more complex rf-control systems.

The dominant requirement for the accumulator rings (Fig. 3) 1 is to minimise and localise the beam losses, especially at the injection and ejection region. Design values for uncollected losses are set at less than 2×10^{-4} which corresponds to less than 500 W per ring. The quality of the injected linac beam and the layout of the injection region are crucial for achieving this limit. A

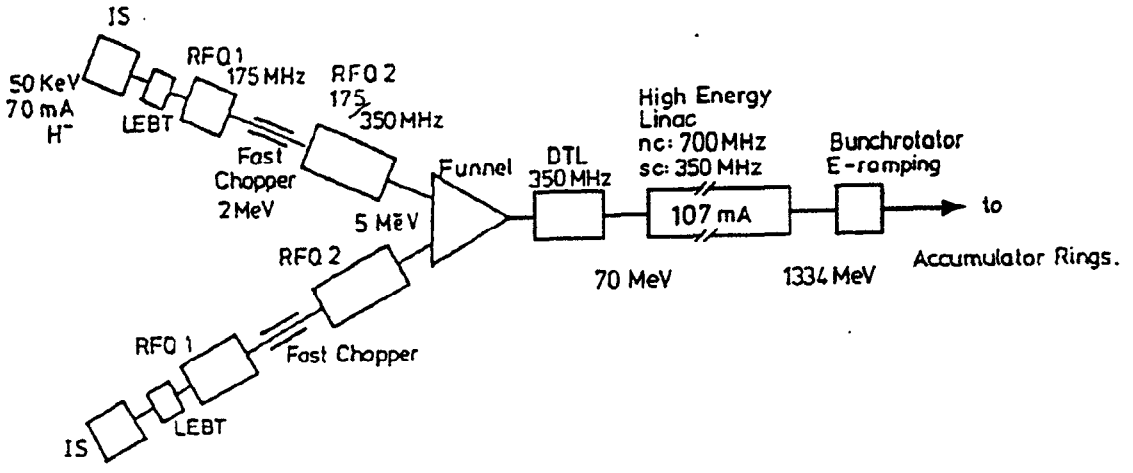

Fig. 2 Schematic Layout of the ESS linac

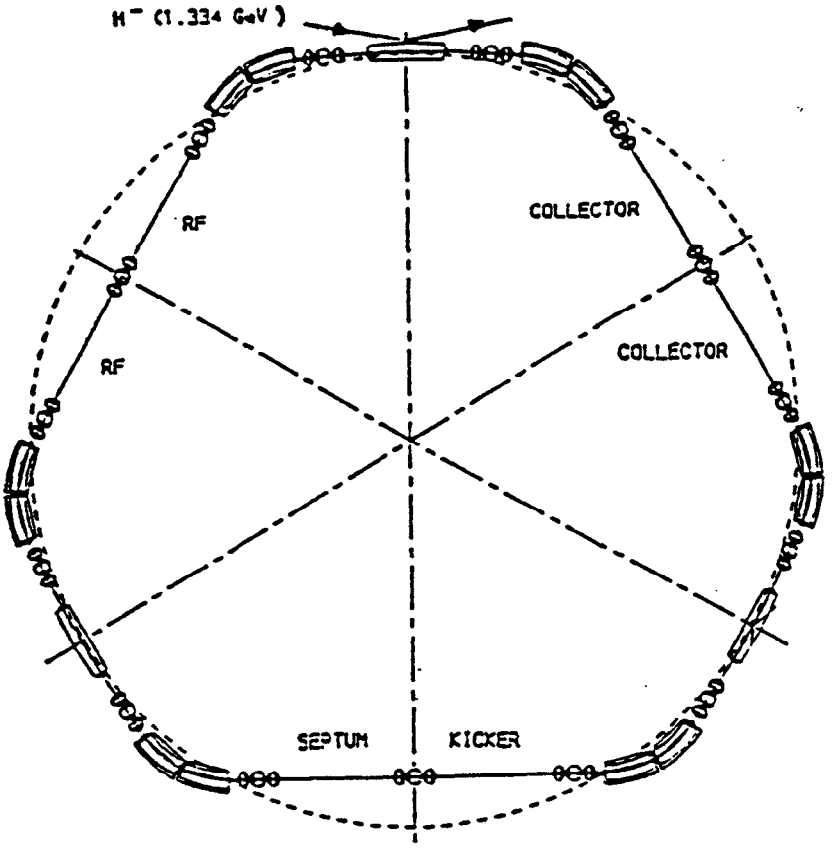

Fig. 3 Layout of the 1,334 GeV accumulator (compressor) rings.

lattice with three superperiods containing separate straight-sections for betatron collimation, extraction and rf-systems is used. An important feature is a long straight section for the charge exchange injection using a thin stripping foil located inside a low field dipole. The field value of this dipole has been chosen to give negligible pre-stripping of H^-ions ahead of the foil, to minimise delayed stripping of (partly stripped) H° atoms and to provide a bending radius for electrons large enough for direct collection. For the accumulator rings a field level of 0,177 T and an injection energy of 1.334 GeV have been chosen. An Al_2O_3 stripping foil of 345 $\mu g/cm^2$ thickness is proposed. It will strip 98,5 % of the injected H^--beam. The rest is mainly partially stripped H° atoms leaving the foil in a range of excited quantum states with different lifetimes. The H° beam will have a power of about 75 kW and could be used for instance as a powerful source for a muon beam with a pulse time structure of 400/270 ns and a pulse length of 1,2 ms.

The injection scheme will use simultaneous "painting" in the longitudinal and transverse phase planes and will reduce the average number of foil traversals (an important source of injection losses) below 10 [3]. For sufficiently low injection losses the halo of the injected H^- beam has to be carefully controlled and removed [2]. It is planned to introduce a 180° achromat bend for momentum and transverse collimation in the transfer line between linac and rings (Fig. 1). This line has in addition to provide some energy ramping and a vertical separation into two matching sections for the rings, which will be located one above the other at a distance of ~ 1,5 m.

A schematic view of the transfer lines between the two accumulator rings and the two target stations is shown in Fig. 1. After passing vertically separated transfer sections, the beam is combined in a common external line including a septum and a fast kicker magnet. The following switchyard allows to channel the proton pulses either to one of the 2 targets or to a 5 MW beam dump, common for the linac and the ring beams. In front of the two target stations a horizontal bend of 11° is foreseen; it should shield upstream beam components against backstreaming fast neutrons from the target and it will increase somewhat the distance between the two target stations. At the target an elliptical beam cross-section (200 x 60 mm^2) with a parabolic intensity distribution is proposed. An adequate distance and shielding of target stations as well as of beam stoppers and accelerators is still under discussion. This issue can influence considerably the cost of the target and transfer line areas. More information from existing spallation sources on the behaviour of skyshine and groundshine neutron background will be needed for fixing a final layout.

Besides the detailed accumulator ring studies some work is also devoted to the option of two rapid cycling synchrotons (RCS) accelerating protons in 25 Hz alternance from 0,8 to 3 GeV.

3. Target issues

At the beginning of the ESS study a number of options for the target stations had been considered [1]:

1. A stationary, solid, unsplit target;
2. A stationary, solid, split target;
3. A rotating target;
4. A liquid metal target (Pb-Bi);

and variants of the above with horizontal and vertical injection and different target materials.

At its June 1995 meeting, the target group has proposed and given priority to an unsplit mercury target with horizontal injection. The decision for replacing the initial liquid material candidate Pb-Bi by Hg had been taken after an assessment of the mechanical, thermal and neutronic properties of Hg which indicate its basic feasibility for a 5 MW, 1 μs pulsed target [4].

There exist many arguments in favour of a liquid metal target. One may mention:

- Radiation damage confined essentially to the target window and target container where some flexibility of design is possible.

- Convective heat removel from the proton reaction zone by flowing liquid metal.

- Reduced neutron absorption, radiolysis and tritium production due to the absence of cooling water.

- Low specific activation and afterheat of the target material.

- Good self shielding.

- Very long lifetime of target material.

- Larger potential for higher beam power.

Neutronically, mercury is characterised by a large thermal neutron absorption cross section of 263 barns as compared to Ta with 15 barns and W with 12,5 barns. This excludes Hg for a system with full moderation to thermal energies but allows its use in a pulsed system with short neutron pulses where moderators are usually decoupled against thermal neutron return from their surrounding. Resonance absorption in the slowing down region is less severe in Hg than in Ta and W (Hg: 73 barns; Ta: 710 barns; W: 352 barns) and neutrons will leave the surface of the Hg target without significant energy loss and with little absorption. The hard spectrum of neutrons may influence the configuration of moderator- reflector layouts as compared to watercooled Ta or W-targets. In Fig. 4 the neutron flux leaving a 5 MW Hg and a watercooled, W- or Ta-target is shown [5]. A target of 14 x 14 x 60 cm^3 dimension and surrounded by a large Pb-reflector is assumed. In this approximation the high energy neutron fluxes of W and Hg are comparable. In Fig. 5 the calculated time behaviour of afterheat for three target materials is compared. An irradiation of 1 year at 5 MW is assumed [5]. Obviously W and Hg are again comparable and typically a factor 5 to 10 smaller than for Ta during the first 3 years of decay.

The problem of pressure waves induced in the Hg by the μs, 100 kJ proton pulses has been considered [6] and it is expected that the dynamic stress on the container will be too close to the recommended design values of the container material (e.g. Manet HT 9 steel [7]). It has been proposed to increase the compressibility of the Hg target by introducing a small amount of He-gas (e.g. 3 % [6]). Theoretical investigations suggest that dynamical stresses are decreased by two orders of magnitude. More theoretical and practical work is under preparation on this issue. In summary the work carried out so far has not identified "show stoppers" for the Hg-target.

Up to now some detailed work had been devoted to the layout of a solid, unsplit, Ta plate target and should be mentioned here although it is considered as a second priority option [1]. In Fig. 6 a possible layout for a watercooled Ta-target with partly integrated Ni-reflector is shown. The cooling and hydrodynamic conditions for pulsed 5 MW operation can be handled but more experimental work will be needed to assess the lifetime of the target and the target window under heavy irradiation and stress wave conditions. R and D work for these issues using electron pulses at 100 MeV with pulse durations and energy contents comparable to the ones of the ESS proton beam are under preparation. Similarily a long term investigations on heavy irradiation damage is actively pursued.

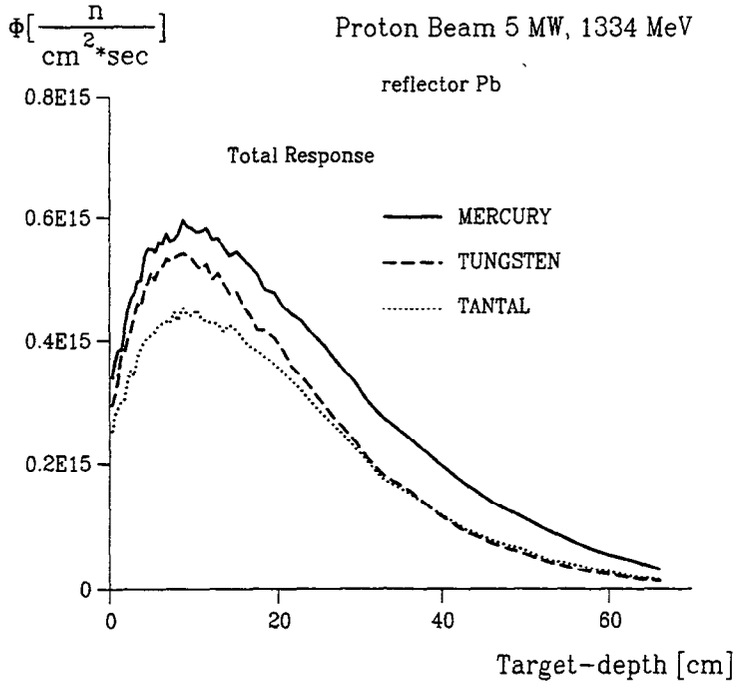

Fig. 4 Leakage distribution for neutrons below 20 MeV and a target with Pb-reflector

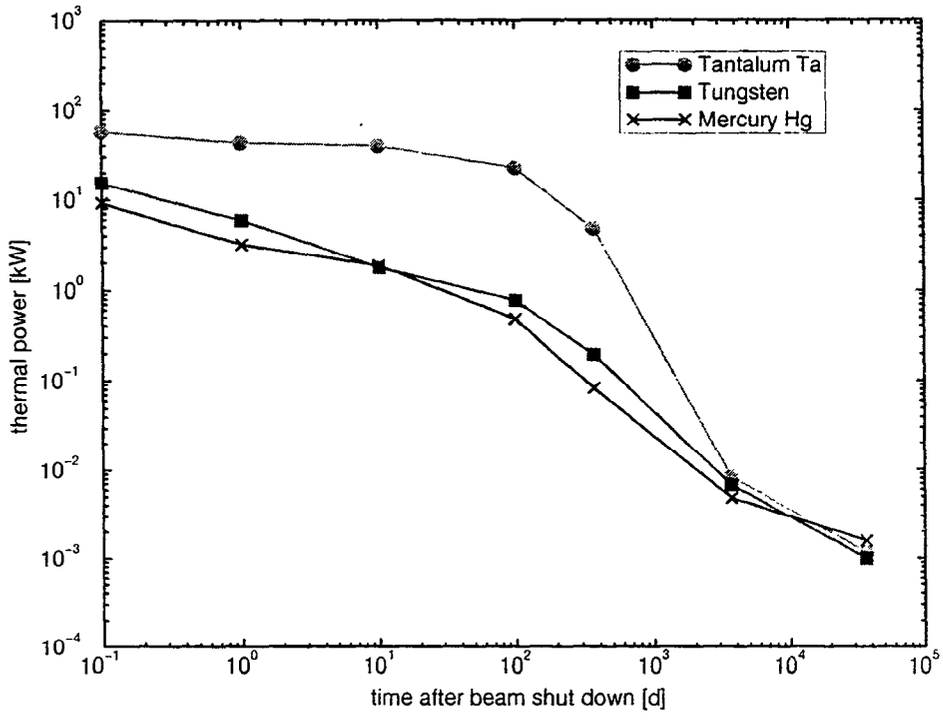

Fig. 5 Time behaviour of afterheat in a target after 1 year full power operation.

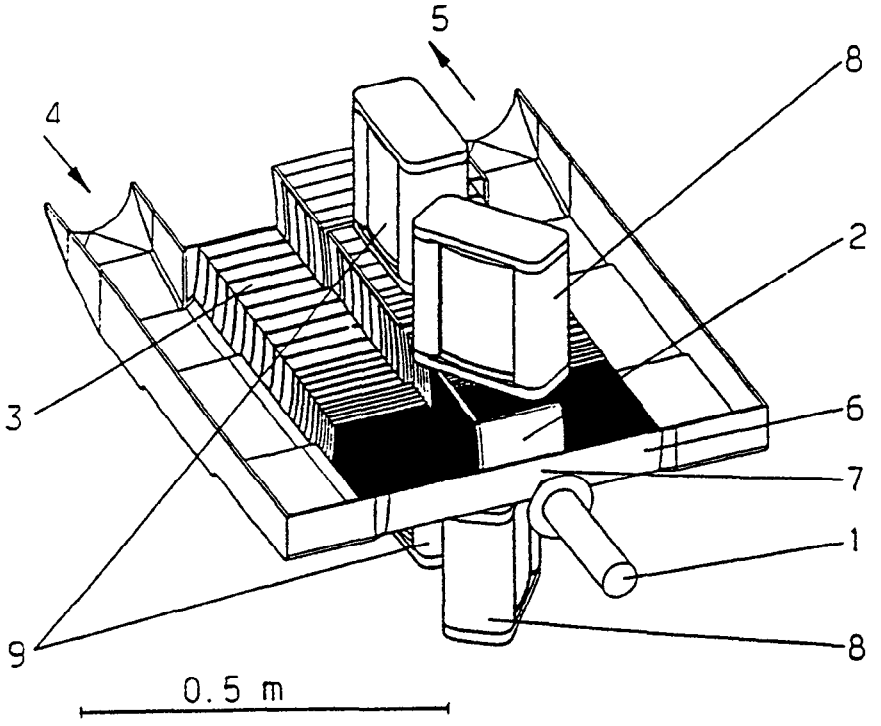

Fig. 6 A 5 MW Ta-target with moderators and cooling water supply (cut away view). 1: proton beam, 2: target plates, 3. wing reflector plates (half cut), 4: coolant inlet, 5: coolant outlet, 6: target vessel, 7: beam entrance window, 8: cold wing moderator, 9: room temperature wing moderator.

A modular layout for the target stations has been fixed (Fig. 7 and 8). The 5 MW and 1 MW should be made as similar as possible. A layout with horizontal removal of the target including its cooling circuits and a vertical upward removal of the moderator-reflector units have been retained. This layout limits the position of neutron beam tubes to an angle of about 2 x 120°. A total of 18 beam holes, some equipped with neutron guides, are considered for each target station.
4 basic types of moderators have been suggested, namely:
a high intensity room temperature moderator
a high resolution (fast) room temperature moderator
a high intensity cold moderator
a high resolution cold moderator.

With a beam power up to 5 MW liquid water and liquid H_2 are considered as moderator materials. Besides these basic types, a low intensity, 100°K moderator optimised for a wavelength range around 3 Å has been proposed by some users. The number and type of moderators for the two target stations has to fixed after more discussions with the users.
Detailed engineering of a layout where the inner parts of the target block can be either a Hg target or a solid, unsplit Ta plate target has been started. In Fig. 8 a conceptual layout of the Hg target with its auxiliaries is shown. The Hg target will presumably be operated at a few hundred °C in a forced flow mode [8] . Classical heat exchangers [9] or heat pipes [10] are considered for cooling. On line purification and trapping of gaseous spallation products are foreseen. A separately cooled security hull and a separated beam window are under study. At present two options for removing the target complex are under discussion and have to be worked out in detail: a removable trolley with the whole liquid metal circuit and its shielding or a "plug" containing only the target, the safety hull and their corresponding feeder lines (Fig. 9) [11]. Work on the diagnostics for liquid metal target system is also going on [12].

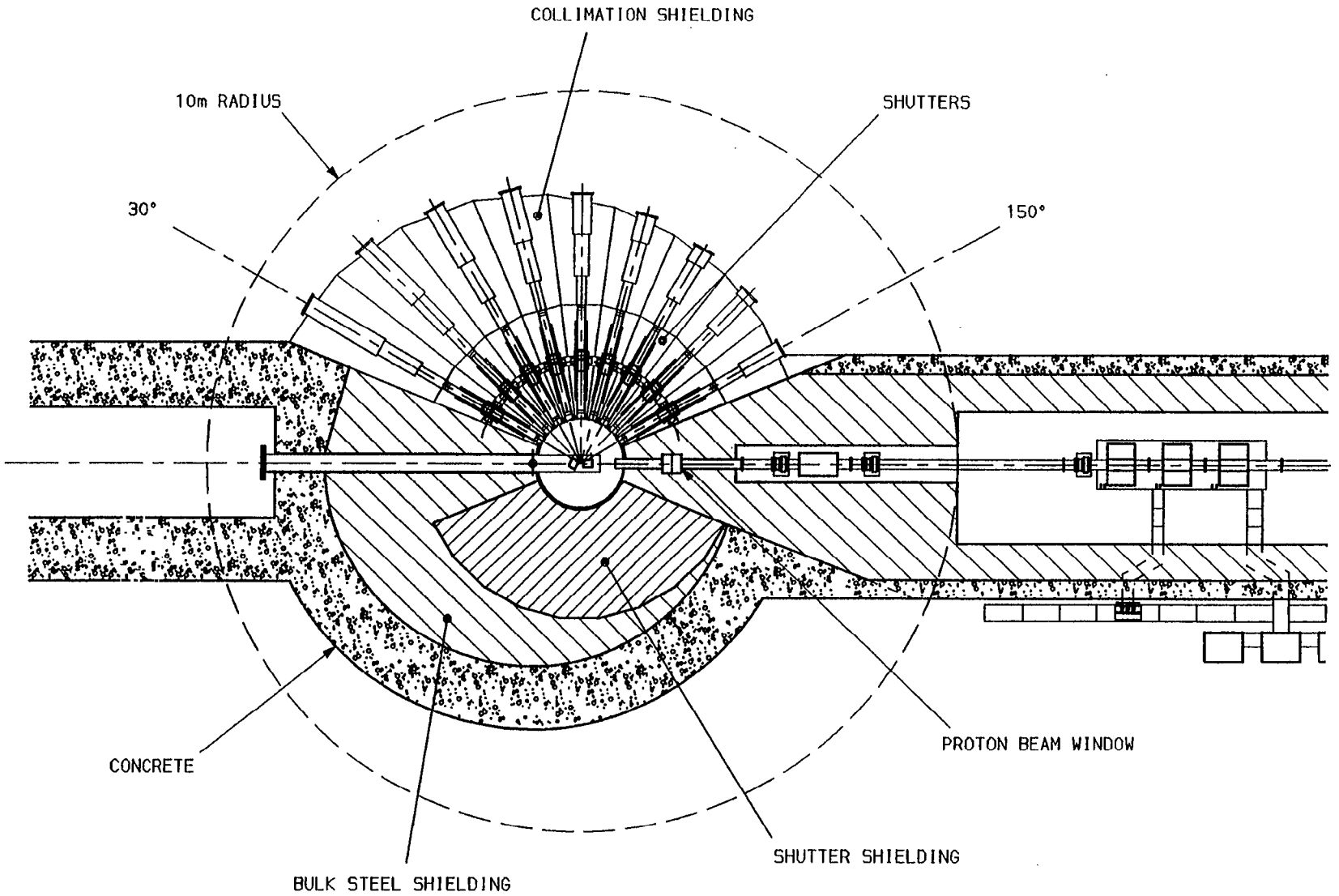

Fig. 7 Schematic layout of a ESS target station

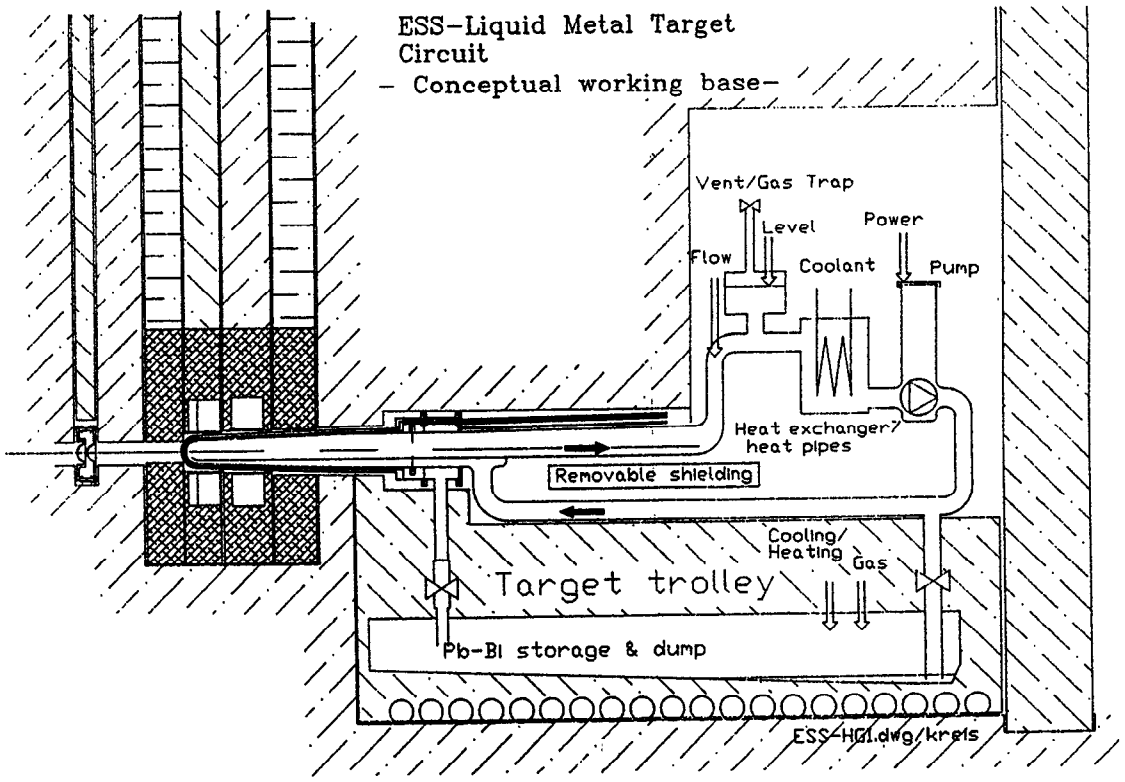

Fig. 8 Concept of liquid metal circuit with safety hull around the beam interaction zone with leakage return flow tube located behind the reflector unit.

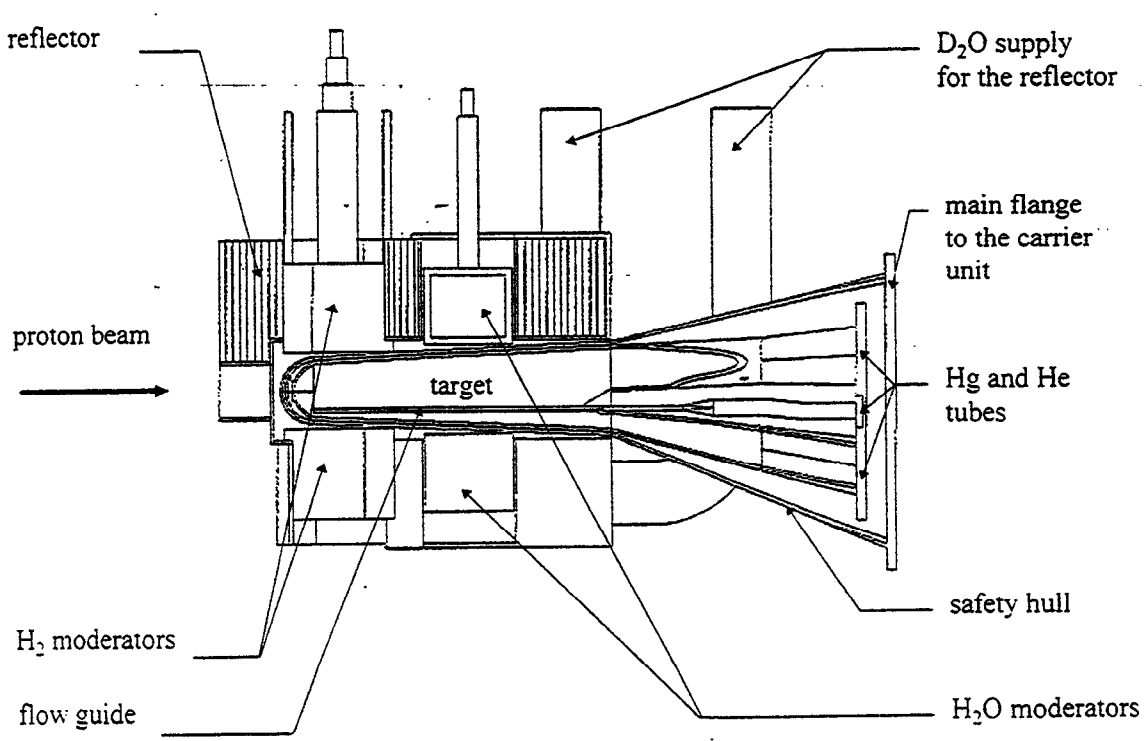

Fig. 9 Crosscut through the reflector-moderator assembly with the Hg target inserted.

4. Other uses of ESS

A number of add-on facilities could be integrated in the ESS design; however they will not be worked but in detail nor costed.

- Muons may be producedin a transmission target in front of the 5 MW target station (Fig. 1). It is suggested to use 0,4 % of the proton beam (~ 20 kW) with the time structure of 2 x 0,4 μs at 50 Hz. Obviously the muon target area has to be heavily shielded to keep the background in the neutron target once sufficiently low. Muons may also be generated by the H° beam emerging from the stripping foil inside the accumulator rings. A beam power of 75 kW with the linac bam time structure (60 % chopping) and emittance would be available.

For a neutrino detector a shielded cave could be located below the high power target. It would then extend at least 20 m below ground level and has to support a target block of about 12000 t weight.

- Irradiation facilities, as developed for SINQ, are expected to be in demand at ESS but are at present not considered in the target layout.
- A radioactive beam facility could be developed around the H° beam (also considered for muon pruduction). This could produce beams much more powerful than CERN's Isolde facility.

The philosophy adopted for the ESS study is not to design away recognised future uses.

Acknowledgements

I would like to thank all members of the ESS study group for their contributions to this report.

5. References

[1] Outline Design of the European Spallation Neutron Source, *ESS Report ESS 95-30-M* (1995) Editors I.S.K. Gardner, H. Lengeler and G.H. Rees
A large number of references can be found in this report.

[2] M. Pabst, K. Bongardt and A. Latchford to be published in: *Proc. Workshop on advanced beam dynamics studies*, Bloomington, IN, USA, October 1995

[3] C. Prior in reference [2]

[4] G.S. Bauer "Mercury as a Target Material for Pulsed (Fast) Spallation Neutron Sources Systems", " *Proc. ICANS-XIII, Paul Scherrer Insitut*, PSI-Proceedings 95-02 (1995)

[5] D. Filges, R.D. Neef and H. Schaal "Nuclear Studies of Different Target Systems for the European Spallation Source (ESS)" *Proc. ICANS-XIII, Paul Scherrer Insitut*, PSI-Proceedings 95-02 (1995)

[6] K. Skala and G.S. Bauer, "On the Pressure Wave Problem in Liquid Metal Targets for Pulsed Spallation Neutron Sources" *Proc. ICANS-XIII, Paul Scherrer Insitut*, PSI-Proceedings 95-02 (1995)

[7] Y. Dai, "Suitability of Steels as ESS Mercury Target Container Materials" *Proc. ICANS-XIII, Paul Scherrer Insitut*, PSI-Proceedings 95-02 (1995)

[8] B.L. Smith, "Thermal Hydraulics of the ESS Liquid Metal Target" *Proc. ICANS-XIII, Paul Scherrer Insitut*, PSI-Proceedings 95-02 (1995)

[9] L. Griesser and B. Sigg, "Mercury Circuit and Cooling System Using an Intermediate Water Loop" in: ESS-Liquid Metal Taget Studies / 2nd Status Report;

[10] M.T. North, J.H. Rosenfeld, D.B. Sarraf, G.S. Bauer and Y. Takeda, " Water/Monel Heat Pipes for Cooling of Liquid Metal Targets For SINQ and ESS" *Proc. ICANS-XIII, Paul Scherrer Insitut*, PSI-Proceedings 95-02 (1995)

[11] B. Guttek, to be published as ESS internal report

[12] Y. Takeda "Metrology for diagnostics of liquid metal target system" in: ESS-Liquid Metal Taget Studies / 2nd Status Report

Status of the AUSTRON-Project

M. Schuster*, P. Bryant#

* Austron Office c/o Atominstitut der Österreichischen Universitäten, Schüttelstraße 115 A-1020 Wien, Austria
# The Austron Accelerator Study Group, CERN, CH-1211 Geneva 23, Switzerland

ABSTRACT

This paper discusses the status of the AUSTRON-project especially highlighting the progress made since the finalization of the feasibility study in November 1994.

1. Introduction

At the end of 1994 the feasibility study for the AUSTRON-project was completed [1]. Subsequently, studies concerning the losses inside the accelerator complex and a further increase of the proton beam power (up to 0.5 MW) have been made. Additionally, recent studies propose a target design for a 0.5 MW proton beam and a detailed study of the medical facility of AUSTRON has just started.

2. Accelerator complex

Figure 1 shows a schematic layout of the AUSTRON accelerator complex. The injection chain has two ion sources each with its own RFQ and these two sources feed into a common drift-tube linac. The rapid-cycling synchrotron (RCS) has a single injection insertion and a single extraction insertion. The injection insertion is for charge-exchange injection with negative hydrogen ions. The extraction insertion employs the classic scheme of a full-aperture fast kicker with a current-wall septum. The beam transport lines and the RCS are basically classical in design, but the operational requirements impose some demanding technological solutions. The injection line with a short dump line totals about 100 m. The RCS is 213 m in circumference and the various extraction lines total nearly 450 m in the final stage. The light ions are transferred after the linac to a dedicated medical accelerator with a slow extraction system for conformal cancer therapy.

The implementation of the AUSTRON spallation source is foreseen in two stages (the original AUSTRON I stage with only 100 kW is no longer considered):

AUSTRON II
Injection energy 130 MeV, a top energy of 1.6 GeV, 3.2 x 10^{13} particle/cycle, 25 Hz repetition rate, 205 kW (further improvement to 250 kW seems to be feasible) delivered to a single spallation target and the capability to accelerate light ions in the linac.

AUSTRON III
Injection energy of 130 MeV, a top energy of 1.6 GeV, 3.2 x 10^{13} particle/cycle, 50 Hz repetition rate, 410 kW (further improvement to 0.5 MW seems to be feasible). The doubling of the repetition rate will bring the machine elements to their design and technological limits.

Keywords: Neutron Source, Spallation Source, AUSTRON Project

The medical ring can be added at any stage. The light ions have a maximum nominal intensity of 5 x 10^8 ions/fill and a maximum nominal energy of 425 MeV/nucleon. Depending on the ion source and the injection system it may be possible to exceed the nominal intensity.

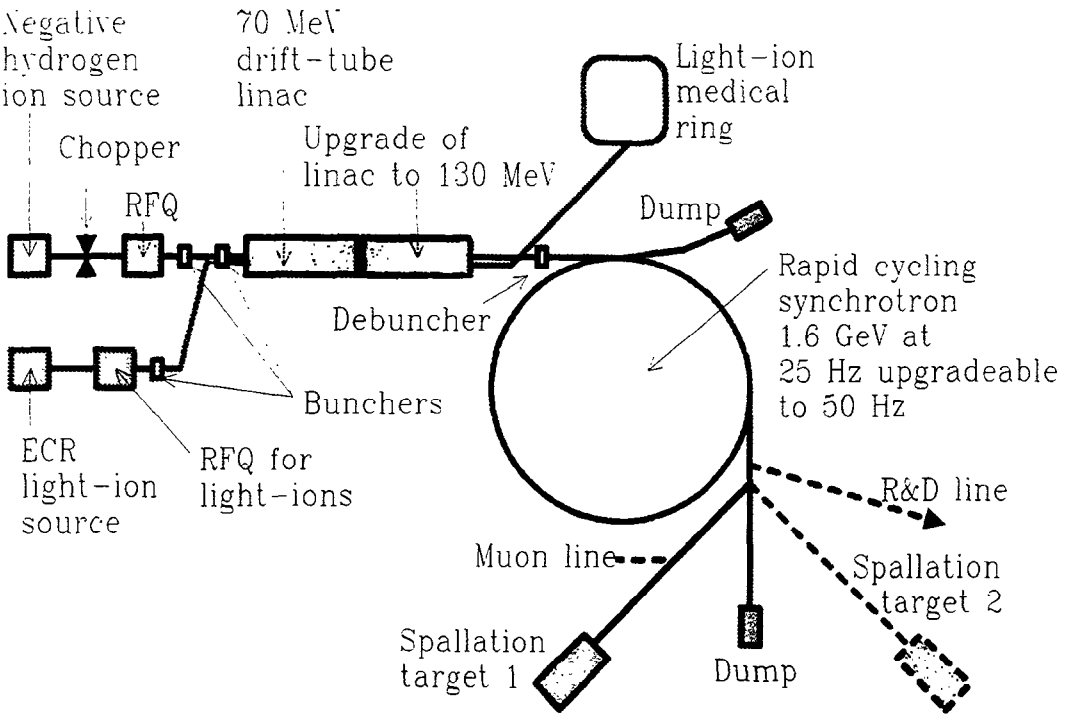

Figure 1 Schematic layout of the AUSTRON Facility

2.1 Injection chain

The drift-tube linac will be optimised to accelerate both negative hydrogen ions and light ions ('light' is defined as any ion up to neon, but carbon will probably be preferred). This has been demonstrated in the CERN linac, but the AUSTRON linac will be unique in being optimised for this purpose from the design stage. Only partially stripped light ions will be accelerated in the linac and, before injection into the RCS, these ions will be fully stripped by a foil in the transfer line. The extremely low intensity of the ion beam means that there is no problem with activation in the foil region, or with foil lifetime. In contrast, the negative hydrogen will be at a far higher intensity and the stripping foil in the RCS injection will become extremely active and will require remote handling equipment. Operation with the negative hydrogen ions is dominated by losses and activation at all stages. For this reason, 'chopping' is being considered after the RFQ. By physically chopping gaps in the beam that will overlap in the RCS, a pre-bunching of the beam is achieved before the RF is applied. This reduces the RF trapping losses and trades them for increased losses in the transfer line, but at a much lower energy so that the induced activity is reduced overall. A debunching cavity will be used to reduce the momentum spread of the beam to a minimum. Minimum momentum spread is essential if the chopping is to be efficient. To remove any halo generated in the linac and tails from the chopper, the beam will be collimated before injection to reduce uncontrolled losses on the injection equipment. There will also be full diagnostics for emittance measurements and an external dump for setting up the injection chain. Recent simulations of the injection and trapping process suggest that at 25 Hz the injection will be cleaner than assumed in the Feasibility Study and at 50 Hz the assumed losses can be respected or bettered.

In the final stage, the RCS will operate at 50 Hz. Although the main dipoles, main F-quadrupoles and main D-quadrupoles have separate resonant power supplies, the voltages on the coils will still be of the order of 10 kV to ground. For this reason, the coil surfaces will be coated with a conducting varnish and earthed to prevent corona discharge. The high voltages are necessary because the lattice is designed with a small number of superperiods customised for specific machine requirements, rather than having a large number of identical cells, as has been used in earlier machines of this type. The magnets will be laminated and have specially shaped ends to reduce eddy currents. Eddy currents are also a factor in the coil conductor design. The dipole magnets and their coils will be curved to follow the central beam trajectory. If this were not done it would be necessary to have much larger magnet apertures and higher power consumptions. The curved ceramic vacuum chambers for the dipoles also represent a considerable technological challenge. Particle losses will be a major preoccupation in the operation of the machine. At full intensity and 50 Hz, the radiation resistance of the coil insulation, the epoxy bonding between the laminations, the hoses etc. will be marginal with respect to the projected losses in some critical areas in the complex.

2.2 Extraction

The large aperture of the proton beam and the short rise time makes the extraction kicker a very substantial magnet. Extraction can also be lossy and at 1.6 GeV the particle losses are particularly critical. The first defence is to apply collimation just before extraction to remove any halo or tail caused by blow-up on non-linear resonances or by instabilities during acceleration. This will be achieved by making an extraction bump that brings the extracted beam against the limit set by the envelope of the beam at injection, both in the extraction straight section and in the following straight section where the betatron collimators will be mounted. In this way, the same collimators can be used at injection and then again before extraction, albeit with a slightly increased clearance and lower efficiency. The second defence will be preventative. The fast kicker will be pushed to its limit to provide the maximum clearance for the extraction septum. This space will then be used to increase magnetic shielding of the stray field from the current wall of the septum, since this can cause resonance excitation and beam loss.

2.3 Light-ion medical ring

The light-ion ring will have a circumference of about 70 m. The slow extraction from this ring will need to be stable and precise. This requirement will be the main design consideration.

3. The Target

In the feasibility study [1] two (only edge cooled) target designs with edge-cooling only [2] - a flat monolithic target and a cylindrical split target - for a 200 kW proton beam have been studied. The present aim is to make a target design capable of being loaded with a beam power of up to 0.5 MW and we try to improve the target (-reflector-moderator) efficiency [3] i.e. to increase the thermal neutron yield at the surface of the moderators.

The flat target concept is more appropriate for increased beam powers. This is because one can use a rather wide beam (large cross section) without loosing much of the efficiency of the target. Concerning the two designs simulated in the feasibility study the thermal load at the hottest spot of the split target is about 32 W/cm^3 whereas the corresponding number for the flat target is 12 W/cm^3 (200 kW proton beam). The beam intensity profile for the split target was

assumed to be of the Gaussian type with a standard deviation σ of 1.5 cm, for the flat target it was described according to

$$I(x,y) \propto \exp[-x^2/\sigma_x^2] \exp[-y^2/\sigma_y^2]$$

with $\sigma_x^2 = 20$ cm^2 and $\sigma_y^2 = 1.2$ cm^2. The corresponding maximum temperature rise during the proton pulse in the flat target is only about 2.5°C (200 kW proton beam, 25 Hz). Nevertheless a single flat target with edge cooling only does not seem to be a realistic target design due to the extensive stresses that will occur inside the target [1]. A possible solution to this problem might be to share the thermal load between two flat targets as shown in Fig. 2. This can be achieved by a switching magnet that directs the proton beam alternating to one of the two target plates. Thus such a system consists of two 25 Hz targets (each loaded with a proton beam up to 250 kW) with probably 3 moderators in between. Additional moderators can be placed above and below this sandwich-like system. Therefore there is a lot of space for various types of moderators (may be even coupled moderators for NAA and for irradiation of samples) that see basically (concerning the thermal load) only one 25 Hz target. Thus these 25 Hz moderator positions are especially suited for cold moderators. A major draw back of that system is that the high energy neutrons produced in both targets will generate significant cross talk in the 25 Hz moderators. Nevertheless considering the significant cost of a second target station it might be a reasonable first step target configuration for a 50 Hz, 0.5 MW machine. And after building a second target station (with a low frequency 10 Hz target) - as proposed in the feasibility study - it could be used as the high frequency (40 Hz) target.

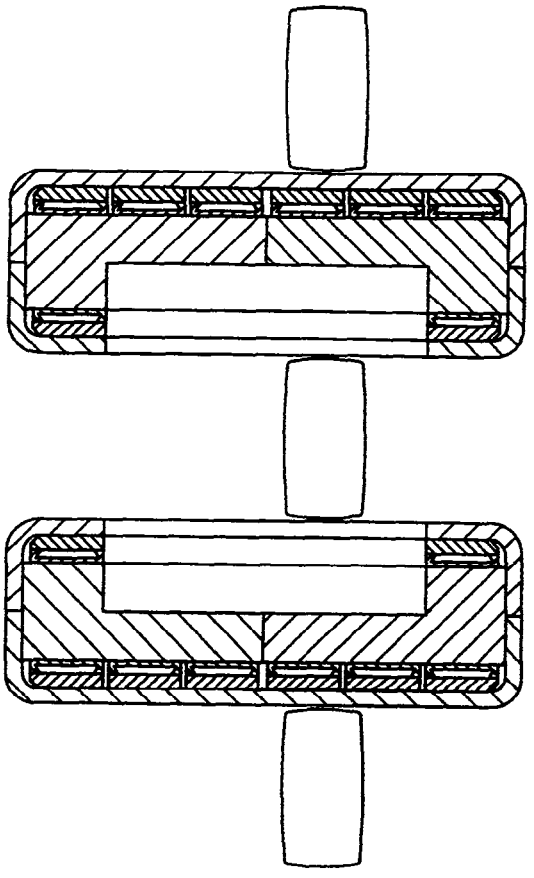

Figure 2 A schematic view of a sandwich like target system - two flat targets with three moderators

To improve the efficiency of the target a grooved flat target has been considered as shown in Fig. 3. This target design increases the area that provides high neutron flux for the moderators. This is indicated by the preliminary results of Monte Carlo simulations obtained so far.

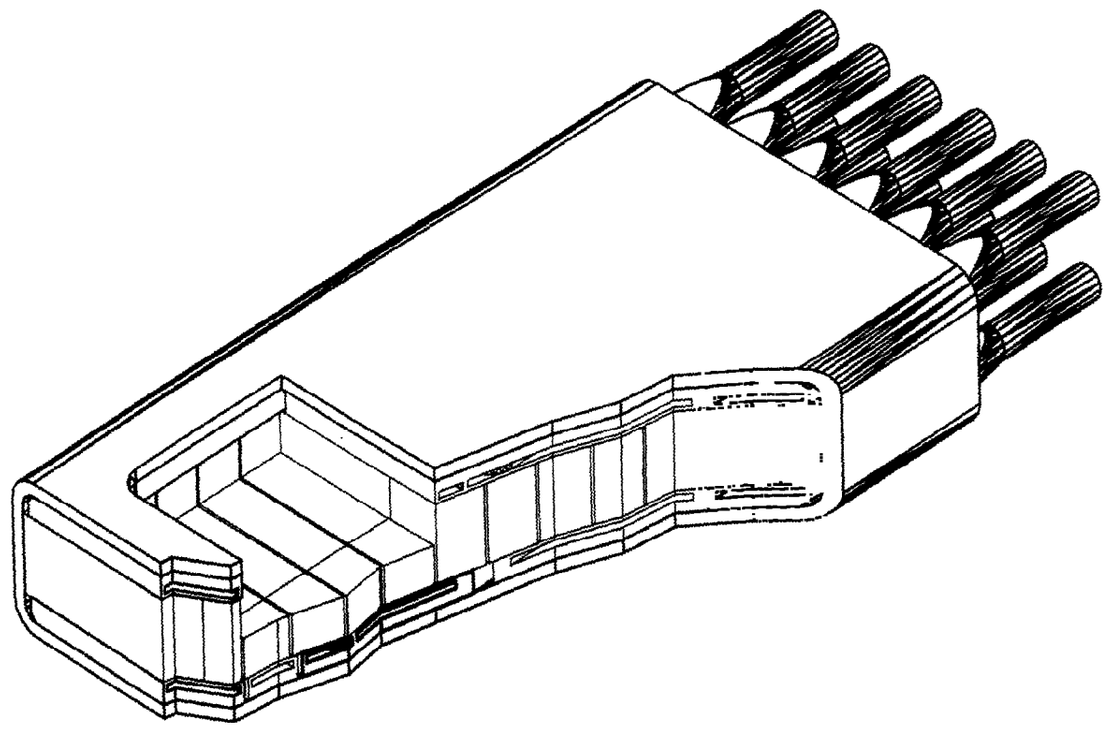

Figure 3 A grooved flat target (tarbet block: 60 x 30 x 6 cm^3)

4. Conclusion

It seems to be feasible to develop AUSTRON towards a 0.5 MW neutron spallation source with a thermal neutron flux which would be 2.5 to 3 times that of the ISIS facility which is currently best source in the world. In order to keep investment cost reasonably low one could consider starting with just one target station.

5. Acknowledgements

The authors would like to thank the Research Centre Seibersdorf for providing the drawings of the target designs.

5. Literature

[1] P. Bryant, M. Regler, M. Schuster eds. *AUSTRON Feasibility Study* (Austron Planning Office c/o Atominstitut, A-1020 Vienna, 1994)

[2] M. Schuster, J. Casta, R. Dobrozemsky, G. Muhrer, W. Ninaus, E. Schachinger, T. Schmeskal, I. Smid, G. Weimann, Physica B 213&214 (1995) 851

[3] G. Muhrer, W. Ninaus, E. Schachinger, „The AUSTRON-Target: The Neutron Flux of Decoupled an Poisoned Moderators", Proceedings of the ICANS XIII Meeting

ICANS-XIII
13th Meeting of the International Collaboration on
Advanced Neutron Sources
October 11-14, 1995
Paul Scherrer Institut, 5232 Villigen PSI, Switzerland

Current status of JHP N-arena

M. Furusaka, H. Ikeda, N-arena working group and JHP accelerator group

BSF, National Laboratory for High Energy Physics, 1-1 Oho, Tsukuba 305, Japan

ABSTRACT

Japanese Hadron Project (JHP) consisted of four facilities, namely, N-arena (a high power pulsed spallation neutron source), M-arena (meson science), E-arena (unstable nuclear beam) and K-arena (nuclear and particle physics). JHP is based on a 200 MeV, 400 μA linac, a 3 GeV, 200 μA, 0.6 (1.2) MW rapid cycle synchrotron and a 50 GeV, 5 (10) μA synchrotron. Conceptual design of N-arena, for example, a target station, a target-moderator-refletor-assembly (TMRA) and instruments is underway now. Systematic research and development of high efficiency TMRA is also underway.

1. Outline of JHP

1.1 History of JHP

In 1983, soon after the successful startup of KENS-I, we already had a project KENS-II, aimed to be a 0.4 MW pulsed spallation neutron source (SNS). In 1986, KENS-II was merged into the original Japanese Hadron Project (JHP), which comprised a 1 GeV, 400 μA linac and a 200 μA compressor/stretcher ring. JHP consisted of four facilities, namely, N-arena (neutron scattering), M-arena (meson science), E-arena (unstable nuclear beam) and K-arena (nuclear and particle physics). It was a phased program and K-arena was for second phase.

The site for the project had not been decided at that stage, but a site south to the KEK was a strong candidate. Since we do not have any buildings, tunnels, and infrastructures like roads, electricity, water supply and so on at that site, the total cost of the project was considered to be rather expensive.

1.2 Updated JHP

In June, this year, all the parameters were reconsidered, taking into account that there were several plans to build megawatt class SNSs in Europe and in USA. After the discussions, the requirements for N-arena were summarized as follows: i) proton beam power: 1-MW class, ii) energy: between 1 and 3 GeV, iii) repetition rate: between 10 and 50 Hz, and iv) harmonics number: do not care.

We also decided to build the whole array of accelerators and facilities at the current KEK site, using tunnels for the current proton accelerators and experimental halls for nuclear and particle physics as shown in Fig. 1. By using existing tunnels and facilities, it was shown that

Keywords: Spallation neutron, moderator, accelerator

we could build the whole facilities including a 50 GeV accelerator and the K-arena with almost the same budget as the previous plan.

Some compromises were made among the requirements for M-arena, E-arena, K-arena and the accelerators. Eventually, the energy has been decided to be 3 GeV (Injection to the 50 GeV ring and M-arena prefer higher energy.), the repetition rate to be 25 Hz and the harmonic number to be four. The parameters for the accelerators have been decided to be 200 MeV and 400 μA for the linac, 3 GeV, 200 μA and 25 Hz for the rapid cycle synchrotron, i.e. 0.6 MW, and a 50 GeV, 5 μA synchrotron for the K-arena. By adding RF cavities to the 3 GeV synchrotron in the future, we could increase the frequency to 50 Hz and hence upgrade to 1.2 MW. An alternative idea is to extend the linac to 400 MeV and increase the current to 400 μA to upgrade to 1 MW, keeping the long repetition rate.

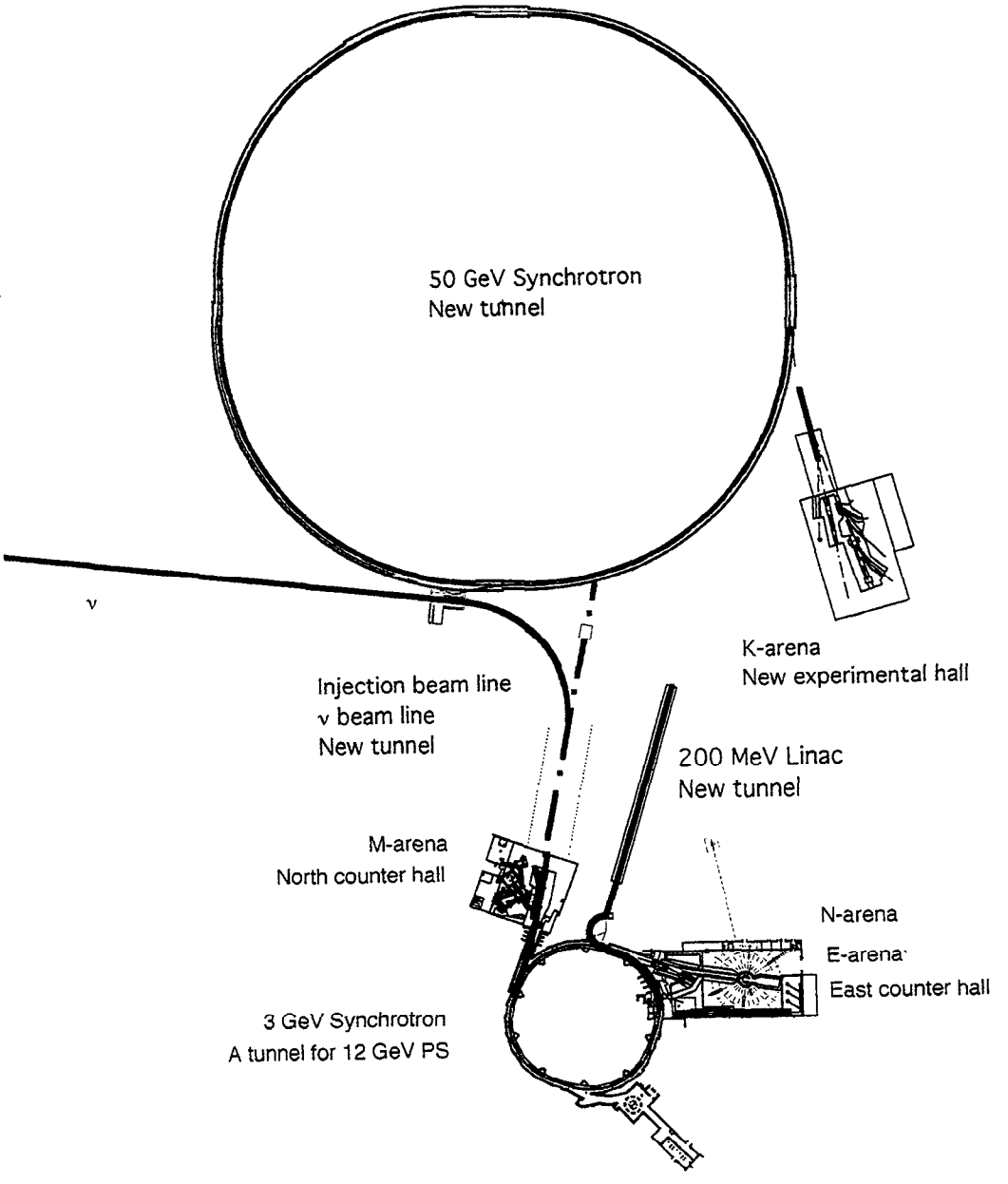

Fig. 1. Layout of the JHP accelerators and experimental facilities.

The updated parameters for the accelerators are summarized in table 1-3.

Table 1. Parameters of proton linac (updated JHP)

Energy	200 MeV
Repetition rate	25 Hz (50 MHz in future)
Beam Pulse Length	400 μs
Chopping Rate	70 %
RFQ, DTL Frequency	324 MHz
Peak Current	30 mA
Linac Average Current	300 μA
	(600 μA in future)
Average Current after chopping	200 μA
	(400 μA in future)
Total Length	150 m
H- Ion Source	
Type	Volume-Production Type
Peak Current	32 mA
Normalized Emittance	1.5 π mm·mrad
Extraction Energy	50 kV
RFQ	
Energy	3 MeV
Frequency	324 MHz
DTL	
Energy	200 MeV
Frequency	324 MHz
Focusing Quadrupole Magnet	Electromagnet
(After a few 10 MeV, the quadrupole magnets are located outside tanks-"Separated DTL (SDTL)")	
Total Tank Length	135 m
The Number of Tanks	16
RF Sources	
The Number of Klystrons	17
Total RF Power	26 MW

Table 2. Parameters of 3 GeV Synchrotron (updated JHP)

Energy	3 GeV
Beam Intensity	5×10^{13} ppp
Repetition rate	25 Hz (50 Hz in future)
Average Beam Current	200 μA
	(400 μA in future)
Beam Power	0.6 MW
	(1.2 MW in future)
Circumference	339.36 m
Magnetic Rigidity	2.15 ~ 12.76 Tm
Lattice Cell Structure	FODO

Tune	(7.3, 4.3)
Natural Chromaticity	-8.4, -6.3
Transition energy : γ_t	7
(no transition below 3 GeV)	
Total Number of Cells	24
Number of Bending Magnets	48
Length of Bending Magnets	1.75 m
Magnetic Field	0.161 ~ 0.954 T
Number of Quadrupoles	48
Length of Quadrupole Magnets	0.5 m
Maximum Field Gradient	5.4 T/m
Revolution Frequency	0.50 ~ 0.86 MHz
Harmonic Number	4
RF Frequency	1.99 ~ 3.43 MHz
Bunch Length	88 ns (B = 0.3)
Average Circulating Beam Current	3.98 ~ 6.83 A
RF Voltage	389 kV
RF Voltage per Cavity	40 kV (20 kV/gap)
The Number of RF Cavities	10
RF Power	5 MW
Beam Emittance at Injection	320 π mm·mrad
Beam Emittance at Ejection	53.9 π mm·mrad

Table 3. Parameters of 50 GeV Synchrotron (updated JHP)

Energy	50 GeV
Beam Intensity	2×10^{14} ppp
	(4×10^{14} ppp in future)
Repetition period	6 s
Average Beam Current	5 μA (10 μA in future)
Circumference	1442 m
Average Radius	229.5 m
Magnetic Rigidity	12.76 ~ 170 Tm
Lattice Cell Structure	3-Cell DOFO x 6 module
	+ 4-Straight Cell
Tune	(24.25, 20.7)
Transition energy : γ_t	27 i (imaginary)
Total Number of Cells	88
The Number of Bending Magnets	96 (6.2 m)
Maximum Bending Magnetic Field	1.8 T
The Number of Quadrupoles	176 (1.5 m and 2 m)
Maximum Field Gradient	25 T/m
Revolution Frequency	0.21334 ~ 0.21966 MHz
Harmonic Number	16 (32)
RF Frequency	3.42 ~ 3.52 MHz
	(6.83 ~ 7.03 MHz)
Bunch Length	95 ns (47 ns) (B = 0.3)
Average Circulating Beam Current	6.83 (13.70) A
RF Voltage	200 kV
RF Voltage per Cavity	40 kV (20 kV/gap)
The Number of RF Cavities	5

RF Power	3(6) MW
Beam Emittance at Injection	53.9 π mm·mrad
Beam Emittance at Ejection	4.1 π mm·mrad

1.3 Schedule

We already have a panel in the Ministry of Education, Science, Sports and Culture (Monbusho) established this fiscal year which is now discussing a unification of National Laboratory for High Energy Physics, KEK and Institute for Nuclear Study, University of Tokyo to form a new research institute organization. The reorganization will very likely be happening in 1997. JHP is planned to start in either 1997 or 1998 and finish construction in five years, expecting first beam around 2003.

2. Current status of N-arena

2.1 N-arena basic schemes

Since we use an existing experimental hall for the target station, basic concepts have to be modified. In the original plan, a vertical injection scheme was employed, in preference for a larger number of neutron beam lines. That scheme had to be abandoned and a horizontal scheme employed because the beam line from the accelerator is now above ground level.

The concept of two TMRA's in one target station was also abandoned, mainly because of the horizontal injection. It was also shown that the gain of having two TMRA's compared with only one is only 10 to 20 %. The gain depends on a repetition rate and a harmonic number of the synchrotron and a pulse delivering scheme. If each TMRA has a separate target station, the number of neutron beamlines is doubled, result in a big gain, but with only one target station, we can not increase the number of beamlines. The effect of cross talk between the TMRS's is also a drawback.

2.2 N-arena experimental hall

A preliminary layout of the N-arena is shown in Fig. 2, together with a schematic layout of instruments and a possible moderator arrangement in the inset. The experimental hall which already exists is called "East counter hall", and is now used for nuclear and particle physics experiments. It has a dimension of 108 m by 50 m with three story high attached rooms. The E-arena target is shown at the middle of the left hand side of the figure. Unstable nuclei produced there will be mass-separated, and accelerated by a heavy ion linac which is shown at the bottom of the figure.

2.3 TMRA R&D

Although the proton power for the JHP is only 0.6 MW for the first stage, the N-arena would become a very powerful SNS, because of the improved performance in TMRA, because of the results of the recent research and development. Continuing efforts searching for better TMRA arrangements are still continuing, by mockup experiments using an electron linac facility in Hokkaido University and by computer simulation.

The first big improvement was achieved in 1990 by a coupled hydrogen moderator with a premoderator[1]: Six times higher flux has been achieved compared with a conventional decoupled hydrogen moderator. The moderator is best for the instruments which are not affected by a neutron pulse width, like small-angle scattering instruments and reflectometers. For these instruments, the size of moderator surface viewed from the sample should be small, due to the requirement of the incident beam collimation. The recent study showed that a gain

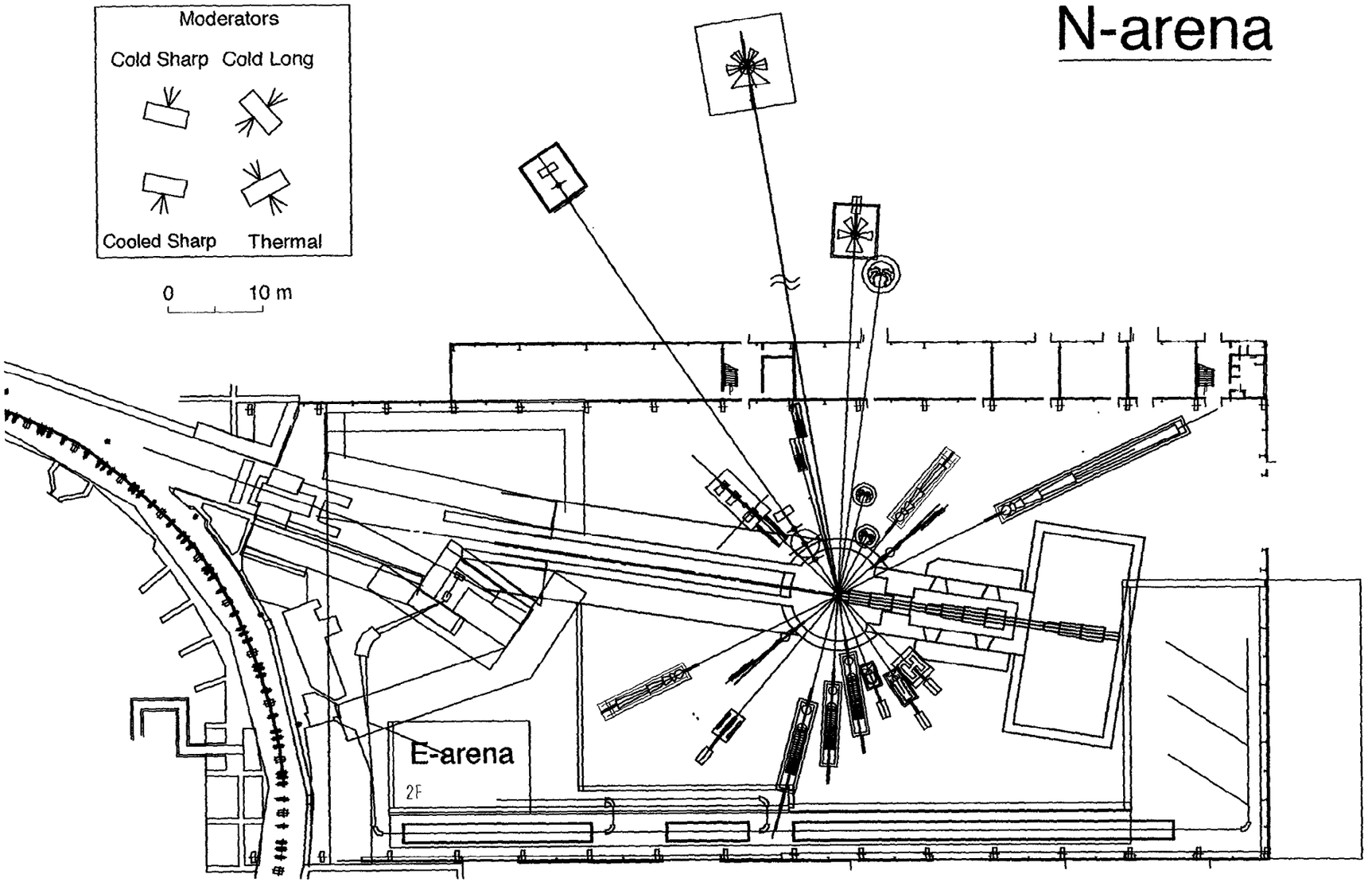

Fig. 2. Preliminary layout of the N-arena experimental hall.

of about 12 % could be achieved, by narrowing a neutron beam extraction hole [2].

A decoupled hydrogen moderator with a premoderator has been developed for instruments which require higher time resolution, hence narrower pulse width. It is intended for instruments like μeV spectrometers and high resolution powder diffractometers. Recently, a poisoned premoderator instead of the decoupled premoderator has been tested, and it showed slightly narrower pulse width than simple premoderators [3].

A decoupled hydrogen moderator with cooled zirconium hydride premoderator was developed [4] as a replacement for a liquid methane moderator, but further research and development is needed for such a moderator. Development of this kind of moderator is crucial for the high power SNS like N-arena, because methane can not be used for the moderator material because of radiation damage problem.

A systematic study of the effect of poisoning especially for room temperature water moderator is also underway.

3. References

[1] Y. Kiyanagi, N. Watanabe and H. Iwasa: Nucl. Instrum. and Meth., A312, 561-570 (1992)

[2] Y. Kiyanagi, N. Watanabe et al., "Further optimization of coupled liquid hydrogen moderator for intense pulsed neutron sources" in this proc.

[3] Y. Kiyanagi, N. Watanabe et al., "High efficiency cryogenic moderator system for short pulse cold neutron use" in this proc.

[4] Y. Kiyanagi, N. Watanabe and H. Iwasa: Nucl. Instrum. and Meth., A343, 558-562 (1994)

ICANS-XIII
13th Meeting of the International Collaboration on
Advanced Neutron Sources
October 11-14, 1995
Paul Scherrer Institute, 5232 Villigen PSI, Switzerland

USE OF COLD SOURCE AND LARGE REFLECTOR MIRROR GUIDE FOR NEUTRON–ANTINEUTRON OSCILLATION SEARCH (PROPOSAL)

Yu. Kamyshkov[a], W. Bugg[b], H. Cohn[b], G. Condo[b], Yu. Efremenko[a], S. Lamoreaux[c], R. Lillie[a], F. Plasil[a], S. Raman[a], M. Rennich[a], K. Shmakov[b], R. Wilson[d], G. Young[a]

[a] Oak Ridge National Laboratory, Oak Ridge, TN
[b] University of Tennessee, Knoxville, TN
[c] University of Washington, Seattle, WA
[d] Harvard University, Cambridge, MA

ABSTRACT

An ORNL-UTK-UW-Harvard group is exploring the possibility of performing a new experiment to search for neutron-antineutron oscillations either at the ORNL HFIR reactor or at the proposed neutron spallation source. The advanced layout, based on a large mirror focusing reflector, proposed for this experiment should allow improving the discovery potential of an $n \rightarrow \bar{n}$ transition search by 3-4 orders of magnitude, as compared to the most recent similar experiment at ILL-Grenoble, and to reach the limit of the characteristic transition time of $\tau_{n\bar{n}} > 10^{10}$ seconds. Use of a cold neutron moderator operating at temperatures lower than conventional moderators can further enhance the discovery potential of an $n \rightarrow \bar{n}$ search provided that neutrons can be thermalized at these lower temperatures. The latter assumption is an open question.

1. $n - \bar{n}$ Experiment

Experiments which search for neutron-antineutron oscillations can provide important information on the "baryon asymmetry" of the universe [1] and on baryon number nonconservation expected in some GUT models [2]. The most recent review of theoretical models related to neutron-antineutron transitions can be found in reference [3]. Present lower limit on characteristic $n \rightarrow \bar{n}$ transition time of $\tau_{n\bar{n}} > 8.6 \cdot 10^7$s is set by an experiment [4] performed at ILL-Grenoble with free-flying neutrons. Although the limit for $\tau_{n\bar{n}}$ extracted from baryon-number-violating intranuclear transition searches [5] (including uncertainties of nuclear model calculations [6]) is higher ($\tau_{n\bar{n}} > 1.2 \cdot 10^8$s), experiments with free neutrons have a higher potential for improvement. The ORNL-UTK-UW- Harvard [7] group is exploring the possibility to perform an experiment either at the HFIR reactor at ORNL or at a newly-proposed, powerful spallation neutron source [8], with the goal of improving the discovery potential for an $n \rightarrow \bar{n}$ search by 3–4 orders of magnitude or of setting a new limit of $\tau_{n\bar{n}} > 3 \cdot 10^9 - 1 \cdot 10^{10}$ s. Earlier we proposed an $n \rightarrow \bar{n}$ search experiment for the proposed ANS reactor in which, due to the larger flux of neutrons, the discovery potential could have been even higher. Unfortunately, the ANS project was discontinued.

Keywords: Focusing, Moderator, Oscillation, Experiment

Since the transition probability of $n \rightarrow \bar{n}$ in vacuum in the absence of external fields (earth magnetic field can be compensated for down to a sufficient level of few nanotesla [4]) is

$$P_{n\bar{n}} = \left(\frac{t}{\tau_{n\bar{n}}}\right)^2, \qquad (1)$$

where t is the neutron flight time; the discovery potential (D.P.) is proportional to $N \cdot t^2$, where N is the number of neutrons per second crossing the target at the end of the flight path. (Antineutrons would be observed via their annihilation in the target.) To maximize the discovery potential for an experiment with a given geometry, the highest flux of neutrons with the coldest possible spectrum (large t) is required at the target. If no focusing device is used between the source of neutrons and the annihilation target, the discovery potential will not be dependent on the distance L between source and target. Indeed, the neutron flux will decrease in proportion to the solid angle which decreases with increasing L. This decrease will be compensated by an increase of neutron flight time with increasing L. (We assume that the size of the neutron source and the size of the annihilation target are sufficiently large and fixed by practical constraints.) Use of a focusing reflector which concentrates neutrons on the target is an efficient way that can dramatically improve the discovery potential.

2. Large Focusing Mirror Reflector

The large focusing mirror reflector proposed for our experiment is a further development of the idea of neutron beam focusing used in an experiment [4 and 9] at ILL-Grenoble, which allows the optimization of both N and t. Indeed, if the neutrons emitted from the source within a fixed solid angle around the beam axis can be focused onto the target, the solid angle reduction with increase of L is eliminated and L in the experiment can be chosen as large as practically possible, thus enhancing the discovery potential via the increase of $t^2 = L^2 / V^2$ (V is the neutron velocity). Since the unperturbed coherence of n and $\bar{n}$ wave functions is required [10] for the unsuppressed transition, any scattering, including focusing scattering in the mirror reflector, will "reset the clock" which counts t^2. Therefore, the focusing scattering should occur as close to the source of neutrons as possible. Qualitatively the discovery potential can be expressed as

$$\text{D.P.} \sim A_{mod} \cdot \Delta\Omega \cdot L^2 / T_n , \qquad (2)$$

where A_{mod} is the effective luminous area of the cold moderator, $\Delta\Omega$ is the solid angle effectively intercepted by the focusing reflector, and T_n is the temperature corresponding to the average energy of the neutron spectrum. Only those neutrons within $\Delta\Omega$ with transverse velocity components at reflection point $< V_{crit}$ are reflected. Practically, V_{crit} can be in range of ~5–7 m/s [11]. This fraction will increase when the neutron spectrum temperature T_n is lowered. In addition, when T_n is lowered, the solid angle $\Delta\Omega$ can be increased by reoptimization of the shape of the focusing mirror to accept larger incident angles for reflection. Thus, the distance L and the neutron spectrum temperature T_n are the most effective parameters to increase the discovery potential of the experiment. A_{mod} will be maximized if the focusing reflector installed close to a cold moderator and is of the type similar to the one with a large luminous area proposed for the ANS reactor [12]. The proposed experimental setup for HFIR is shown schematically in Figure 1.

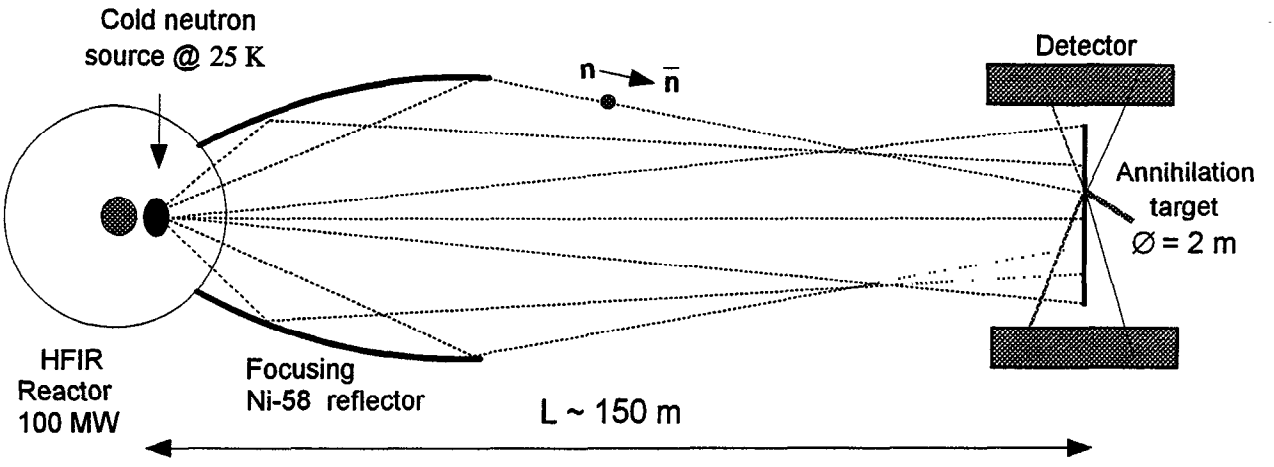

Fig. 1 Conceptual layout of $n\bar{n}$ - search experiment proposed for Oak Ridge HFIR reactor (not to scale)

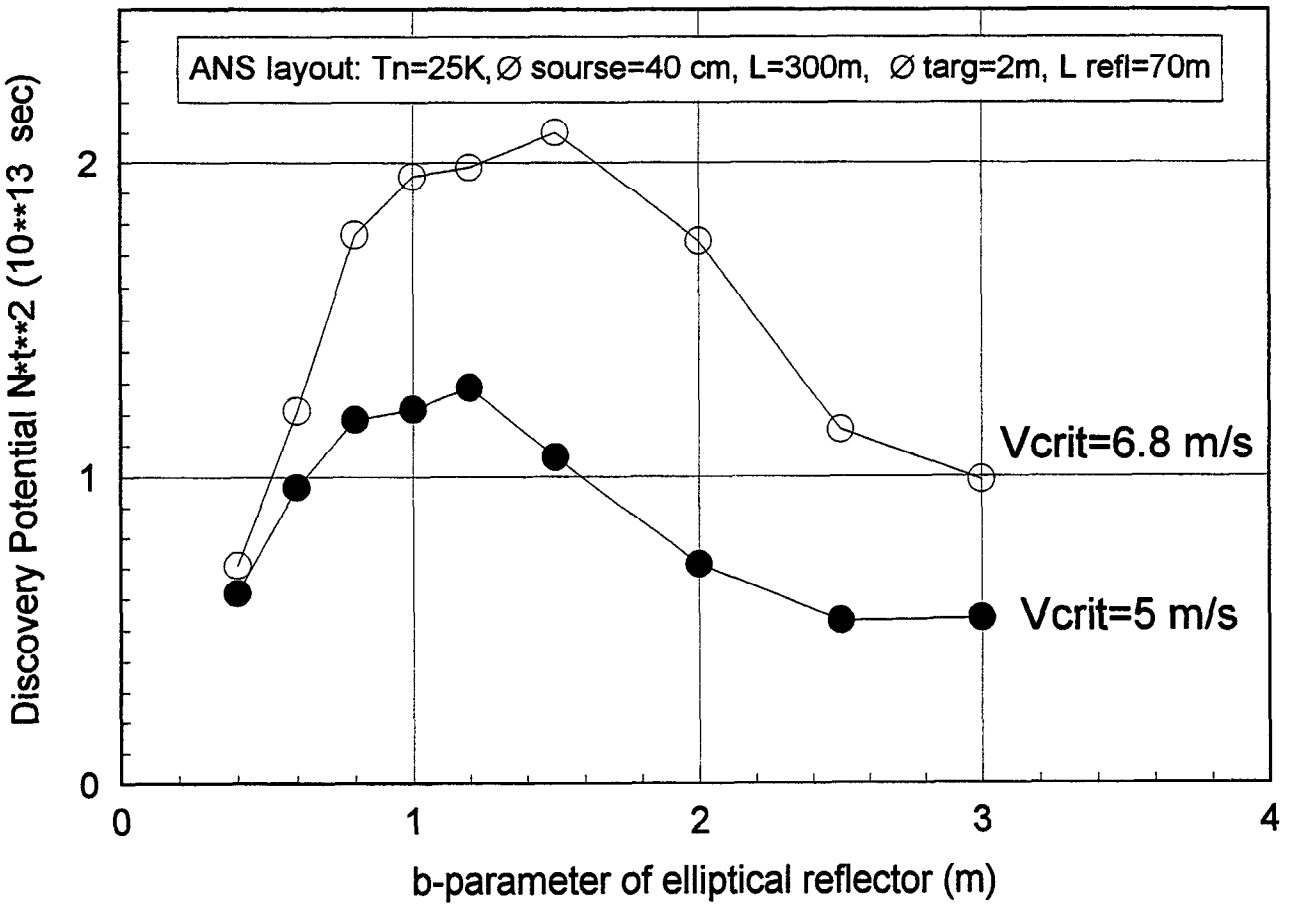

Fig. 2 Monte Carlo optimization of b-parameter of elliptical reflector

When large L and low T_n values are used, the effects of gravity play an important role in neutron propagation. To simulate accurately all of the above-mentioned effects and parameters, we have developed a Monte Carlo code for the neutron transport. In the Monte Carlo procedure, neutrons originated in a cold moderator with spectra deduced from more detailed simulations [13]. The radial variation of the effective temperature of neutrons produced in the cold moderator was taken into account. Neutrons emitted from the surface of the cold moderator were propagated in the gravitational field through the focusing mirror reflector, experiencing reflections when appropriate conditions were satisfied. Various focusing reflector shapes were tried (conical, parabolic, cylindrical). The best results were obtained with an ellipsoidal reflector where the cold moderator was positioned at one focus of the ellipsoid and the annihilation target was placed at the other focus. In the simulations the reflector typically started at ~3 m from the center of the cold moderator and extended to a distance of 50-100 m, while the distance to the annihilation target was in the range of 150-300 m. Simulated data were normalized to the expected flux of cold neutrons obtained from more detailed simulations of the reactor-cold moderator system [13]. Figure 2 shows the discovery potential versus parameter b (b is the small half-axis of the ellipsoid) simulated by the Monte Carlo program for two different assumptions of reflector coating in the scenario of the ANS experiment. At the optimum, the discovery potential of $D.P. = N \cdot t^2 \sim 2 \cdot 10^{13}$ s corresponds to the maximum diameter of the ellipsoid tube of 2–2.4 m. Similar calculations were performed for different possible options of a HFIR-based experiment, depending on various scenarios of reactor upgrade. These options with corresponding discovery potential gains are described in Table 1. The maximum discovery potential gain at HFIR can be obtained when cold neutron moderators are used. We assumed that either the solid methane moderator (pellet technique as was discussed in [14] at this meeting) or a large-size liquid deuterium moderator (design developed for the ANS [12]) can be implemented at HFIR.

Table 1. Experimental Options for Neutron-Antineutron Transition Search. The discovery potential of ILL-Grenoble reactor experiment was taken as 1. All HFIR-based experiment options are assumed to have a horizontal layout. SCNM stands for super-cold neutron moderator as explained below in the text.

1	Neutron source	Neutron moderator	Discovery potential gain for one year of operation
2	ILL'94 *completed experiment*	Liq D_2 @ 25 K	× 1
3	ANS *discontinued project*	Large Liq D_2 @ 25 K	× 13,000
4	HFIR *present*	Be @ 342 K	× 50
5	HFIR *present*	Small CH_4 @ 20 K	× 300
6	HFIR modified *with new Be reflector*	Large CH_4 @ 20 K	× 1000
7	HFIR upgraded *with D_2O reflector*	Large Liq D_2 @ 25 K	× 5,000
8	HFIR upgraded *with D_2O reflector*	SCNM @ 1 K	× 23,000
9	5-MW spallation source *horizontal layout*	SCNM @ 1 K	× 10,000
10	5-MW spallation source *vertical layout*	SCNM @ 1 K	× 80,000

In Table 2 a more detailed comparisons of the parameters of one of the HFIR-based experiment options (HFIR upgraded with a D_2O reflector and with a large liquid-deuterium source of the ANS type) with those of the experiment [4] performed at ILL-Grenoble are given. Also shown in the table are the parameters of an experiment proposed for the discontinued ANS project and those of an experiment proposed at ORNL in 1982 for the ORR reactor [15].

Table 2. Comparison of neutron-antineutron search experiments. The upgraded HFIR configuration shown in this table corresponds to the option of row 7 in Table 1.

Neutron source	ILL' 94	ORR' 82	ANS	HFIR (upgraded)
Status	Completed experiment	Rejected proposal	Discontinued project	New proposal
Power (MW)	57	30	330	100
Max. thermal neutron flux (n/cm²/s)	$1.5 \cdot 10^{15}$	$(7 \cdot 10^{13})$	$7 \cdot 10^{15}$	$2 \cdot 10^{15}$
Moderator	Liq. D_2 @ 25 K	D_2O @ 300 K	Liq. D_2 @ 25 K	Liq. D_2 @ 25 K
Source area	6×12 cm²	Ø 42 cm	Ø 40 cm	Ø 40 cm
$\varnothing_{det}$ (m)	1.1 m	1.0 m	2.0 m	2.0 m
L_{free} (m)	76	20	~300	~150
n/s @ target	$1.25 \cdot 10^{11}$	$2 \cdot 10^{13}$	$4.4 \cdot 10^{13}$	$5.1 \cdot 10^{13}$
$\sqrt{<t^2>}$ (s)	0.109	0.01	0.672	0.384
Detector efficiency	0.48	~ 0.5	~ 0.5	~ 0.5
Run time (s)	$2.4 \cdot 10^7$	$3 \cdot 10^7$	$3 \cdot 10^7$	$9 \cdot 10^7$
Discovery potential $N \cdot \langle t^2 \rangle$ (s)	$1.5 \cdot 10^9$	$2 \cdot 10^9$	$2 \cdot 10^{13}$	$0.75 \cdot 10^{13}$
$\tau_{n\bar{n}}$ limit, s (90% CL)	$8.6 \cdot 10^7$	$1.1 \cdot 10^8$	$1.1 \cdot 10^{10}$	$1.0 \cdot 10^{10}$

The discovery potential for the HFIR-based option shown in Table 2, for three years of operation, would be a factor of ~10,000 higher than the discovery potential of the completed experiment at the ILL-Grenoble reactor [4]. This factor is made up of the following contributions: higher reactor power (× 1.75); larger cold source area (× 16); larger detector area (× 3.3); focusing reflector and optimized layout (× 50); and three years of running time (× 3). Advantages of the focusing reflector are clearly seen in Table 1, where a considerable gain is indicated even for the option without a cold moderator (row 4).

3. Colder Sources of Neutrons?

As we saw from formula (2) and from the discussion thereafter, a cold neutron moderator allowing the lowest possible temperature, T_n, of the neutron spectrum would be the most advantageous for an increase of the discovery potential of the $n \rightarrow \bar{n}$ search. In previous discussions we assumed that in large-size moderators, neutrons can be thermalized down to the temperature of the moderator substance (~25K). This assumption may not be valid, even for such well-studied systems as liquid deuterium moderators, and needs more careful comparisons of detailed Monte Carlo simulations with measured neutron spectra. The situation is even less clear if the temperature of the moderator is lowered to helium temperatures. All moderators of practical interest, except helium proper, (i.e., D_2, H_2, CH_4, and CD_4) are solid at these temperatures. Inelastic scattering of cold neutrons with excitation of translational and vibrational modes of the moderator media plays an important role in the moderation process, while elastic scattering becomes less efficient when the neutron wavelength exceeds interatomic distances in the moderator.

Although a considerable amount of experimental and theoretical information on cold moderators can be found in the literature, the following question remains unanswered both at an experimental level and at the level of simulations: *what is the lowest temperature that the neutron maxwellian spectrum can be moderated to?* The answer to this question can open new possibilities in the search for $n \rightarrow \bar{n}$ transitions. If we assume that a super-cold neutron moderator (SCNM) can be build (for example, based on deuterium or methane pellets [14] immersed in super-fluid helium-4) with neutron spectra thermalized down to 1K, a further gain in the discovery potential can be obtained as indicated in row 8 of Table 1. The average velocity of 1K neutrons is about 150 m/s and, in ~150-m-long horizontal layout of a possible experiment, the gravity effect would modify the trajectories of the neutrons and substantially destroy the focusing effect of the elliptical reflector. A vertical layout of the experiment would minimize the negative effects of gravity and would allow the use of the full advantage of a SCNM in the $n \rightarrow \bar{n}$ search. It is rather unlikely that a long vertical layout can be used in the reactor environment where many services and safety features are located in the lower part of the reactor. A vertical layout is, however, suitable for an experiment designed for the spallation neutron source (SNS). Table 1 shows the discovery potential gain for both a horizontal (row 9) and a vertical (row 10) layout of the experiment, based on 5-MW SNS. In the calculations it was assumed that the maximum thermal flux for a 5-MW SNS will be as high as ~ $1 \cdot 10^{15}$ n/cm^2/s.

4. Conclusions

We have shown that with existing and future generation of neutron sources, it is possible to increase the discovery potential of the $n \rightarrow \bar{n}$ search by 3 to 4 orders of magnitude relative to present experiments. The key element of the proposed setup is a large focusing reflector installed close to the cold moderator. Further increases of the discovery potential will be possible if neutrons can be moderated down to lower temperatures (ultimately to 1K) with a super-cold neutron moderator. Whether this is a practical future option remains to be demonstrated both experimentally and via simulations.

This research was sponsored by the Laboratory Directed Research and Development Program of the Oak Ridge National Laboratory, managed for the U.S. Department of Energy by Lockheed Martin Energy Systems, Inc., under Contract No. DE-AC05-84OR21400.

5. References

[1] A. Sakharov, JETP Lett. **5** (1967) 24;
V. Kuz'min, Письма в ЖЭТФ, **13** (1970) 5;
V. Kuz'min, Изв. АН СССР сер. физ. **35** (1971) 2088;
V. Kuz'min, P. Lebedev, Preprint IYAI P–0116, P–0140 (1979).

[2] S. Glashow, Harvard preprint, HUTP-79/A059 and 79/A079 (1979);
R. Marshak and R. Mohapatra, Phys. Rev. Lett. **44** (1980) 1316;
D. Chang, R. Mohapatra et al, Phys. Rev. D **31** (1985) 1718;
V. Kuz'min et al., Phys. Lett. **102B** (1981) 397;
G. Segrè et al., Phys. Rev. Lett. **44** (1980) 1737.

[3] R. Mohapatra, Nucl. Instr. and Meth. A **294** (1989) 1-8.

[4] M. Baldo-Ceolin et al., Z. Phys. C **63** (1994) 409-416.

[5] Ch. Berger et al., (FREJUS), Phys. Lett. B **240** (1990) 237;
M. Takita et al., (KAMIOKANDE), Phys. Rev. D **34** (1986) 902.

[6] K. Chetyrkin et al., Phys. Lett. B **99** (1981) 358-360;
C. Dover et al., Phys. Lett. B **344** (1995) 433-435;
W. Alberico et al., Nucl. Phys. A **523** (1991) 488-498.

[7] W. Bugg et al., Prospects for Neutron → Antineutron Transition Search; Paper submitted to 4th International Workshop TAUP'95, Toledo, September 17-21, 1995.

[8] B. Appleton, Status report on ORNL–study, Paper O3-3 presented at this meeting.

[9] T. Bitter et al., Nucl. Instr. and Meth A **321** (1992) 284-290.

[10] Proceedings of the Informal Workshop on Neutron-Antineutron Oscillations, Harvard University, April 30 – May 1, 1992.

[11] See, for example, in R. Golub, D. Richardson, S.K. Lamoreaux, "Ultra–Cold Neutrons", Adam Hilger IOP Publishing Ltd 1991; J. Byrne, "Neutrons, Nuclei and Matter", IOP Publishing Ltd, 1994.

[12] ANS close-out document on CD-ROM, ORNL/M-4674.

[13] R.G. Alsmiller, Jr., and R.A. Lillie, Nucl. Instr. and Meth. **A295** (1990) 147-154.

[14] A. T. Lucas, G. B. Bauer, C.D. Sulfredge, A Pelletized Solid Methane Moderator for a Short Pulsed Neutron Source, Paper G1D-3 presented at this meeting.

[15] M.S. Goodman et al., A Sensitive Search for Neutron-Antineutron Transitions, Proposal of Harvard University–ORNL–University of Tennessee, 1982, ORNL/PHYS-82/1

Our Sponsors

CILAS

OPTRONICS AND LASERS

French company CILAS (Companie Industrielle des LASers) is held by French aeronautics and defense firm Aerospatiale (63%) and by CEA-Industrie (37%). CILAS specialises in defense laser equipment, in high-power lasers for industrial and research nuclear applications and in laboratory and neutron instrumentation. The company also has research and development capacities in the field of systems, laser sources, detection devices and fine optics, in particular adaptive optics which are used in synchrotron radiation applications.

Neutron Guide System for the Paul Scherrer Institut (PSI)

First introduced in 1963 by Prof. Maier Leibnitz, the concept of total reflexion in neutron guide systems has become essential to neutron beam transportation at modern research neutron sources. For the last 25 years, CILAS Neutron Guides Department has produced and installed more than 4000m of neutron guides. CILAS neutron guides with boron containing glass are both of high transmittance and low background and have become a respected international standard. The latest neutron guide system installed at the continuous spallation source of the Paul Scherrer Institute incorporates a generation of experience to bring higher levels of performance and neutron flux into the laboratory.

CILAS has made an ongoing effort in product research and development with R&D expenses as high as 13% of sales turnover during the last five years. Since 1992, CILAS has developed a range of so-called Super Mirror coatings with a remarkable array of features, large critical angle, high reflectivity, repeatability and stability under high neutron and Gamma flux.

Complete services are offered including design studies, manufacturing and installation. The application engineering staff is always ready to assist users for special applications worldwide.

For any questions and comments please contact:

Dr. Klaus AL USTA
Neutron Guide Department - CILAS
Route de Nozay, B.P. 27 - 91460, MARCOUSSIS, France
Phone: +33 1 64 54 48 00 - FAX: +33 1 69 01 37 39

descote

High Integrity Valves

Headoffice
descote S.A.
9 Avenue Jean Jaurès
69320 FEYZIN
FRANCE
Phone : (33) 78 70 80 85
Fax : (33) 78 67 78 85
Contact: J.P.RICHER

Subsidiary USA
descote Inc.
11529 Sun Belt Court
BATON ROUGE
LOUISIANA
Phone : (1) 504 756 5082
Fax : (1) 504 751 0130
Contact: M. FUCICH

Subsidiary Germany
descote GmbH
Postfach 18 01 03
Täppken 1
D-42626 SOLINGEN
Phone : (49) 0 212 59 8645
Fax : (49) 0 212 59 2407
Contact: J.C. COCU

Subsidiary Benelux
descote B.V.
Erichemsekade 18
4117 ERICHEM
Phone : (31) 344 57 13 90
Fax : (31) 344 57 14 90
Contact: H. CRONE

Subsidiary Taiwan
descote Asia Co. Ltd
13F n358,
Chung Hsiao E. Road, Sec.5
TAIPEI
Phone : (886) 2 720 9683
Fax :(886) 2 722 7406
Contact: G. OUANG

ISO 9001

What deserves to be done deserves to be well done

Manufacturing programme

. bellows sealed globe valves
. gland packed globe valves
. parallel slide gate valves
. manifold
. manual and actuated valves
. lift check valves
. 3 way valves
. transportation valves
. control valves
. specialty valves
. bellows sealed needle valves for instrumentation

Materials

. Carbon steels from 100°C to +450°C
. Stainless steels and duplex
. Monel®, Inconel®
. Hastelloy®, Nickel®
. Titanium, Tantalium, etc.

Chemical applications

Chlorine, HF, HCl, Phosgene, TDI, MDI, NH3, H2S, SO3, VCM, HCN, Ethylen oxyd...and any toxic, hazardous, noxious, corrosive and unuasually dangerous media.

Nuclear applications

Heavy water, UF6, radioactive and contaminated media

Products delivered at SINQ Unit

. Stainless steel manual shut-off and control bellows sealed globe valves for light and heavy radioactive water circulation systems and its gas supplying systems
. colmonoy seat
. radiation resistance 10^6 Gy
. external tightness:
  10^{-9} atm.cm3.s^{-1}
. internal tightness:
  10^{-6} atm.cm3.s^{-1}

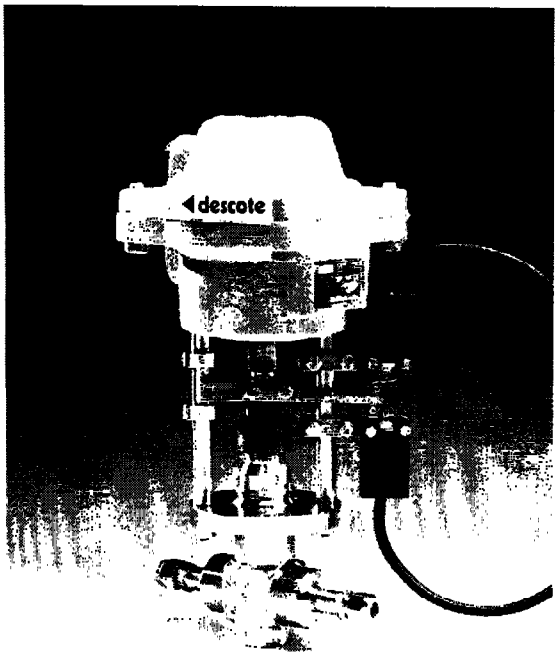

Your Partner for Development of Products

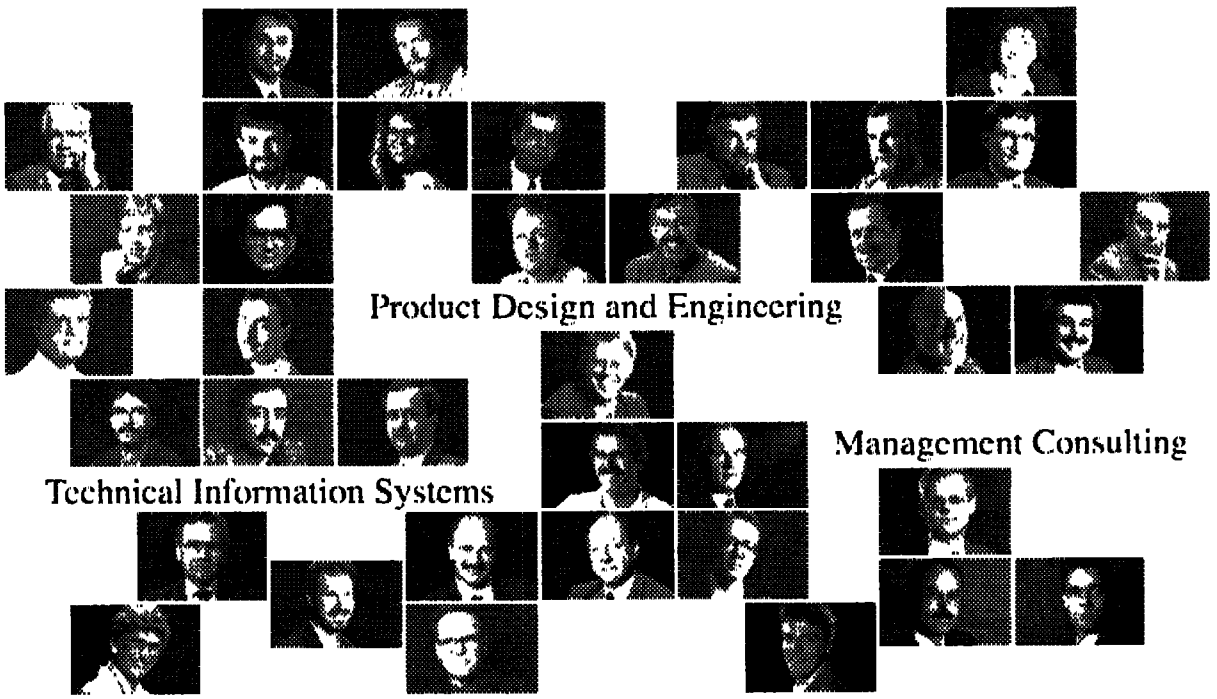

Services by Helbling Technik for PSI SINQ Moderator Tank

- Detail design of D_2O-tank for safe operation over 30 years
- Dimensioning of all critical parts
- Load Cases:
  Normal Operation, Earthquake, Impact by Aircraft, Leakage Test, Transport
- Verification of stresses, buckling and eigenfrequencies by Finite Element Analyses according to SVTI standards
- Complete set of drawings based on 3D CAD
- 3D data transfer for five axis milling
- Data for tools and operating material
- Assembly plan

Helbling Technik AG
Hohlstrasse 610, CH-8048 Zürich
Phone +41 1 438 17 11, Fax +41 1 438 17 10

helbling Technik

Im Schörli 5, 8600 Dübendorf

KIWI Systemingenieure und Berater AG

Hr. P. Antipovic / 01/821 98 00

- Gesamtplanung/Totalunternehmung Gebäudetechnik
  - Elektrotechnik
  - Heiz.-/Lüft.-/Klima-/Kälte-/Energietechnik
  - Fachkoordination Gebäudetechnik
- Integrale Gebäudeautomatisierung
  - Kommunikation
  - Sicherheit
  - Heiz.-/Lüft.-/Klima-/Kälte-/Elektro-/Energietechnik

Wir sind eine dynamische, flexible Ingenieurunternehmung und erbringen qualitativ hochstehende Leistungen im Bereich der Gebäudeautomatisierung und Gebäudetechnik. Unser Team besteht aus qualifizierten, erfahrenen Ingenieuren unterschiedlicher Fachrichtungen. Durch unsere interdisziplinäre Zusammensetzung sind wir besonders geeignet, unkonventionelle, komplexe Spezialprojekte zu planen und zu realisieren. Für Spezialanlagen und Sanierungen technischer Anlagen übernehmen wir die Gesamtplanung (Technik). Auf Wunsch des Kunden leisten wir zusätzlich auch Garantie für Kosten, Qualität und Termine als verantwortlicher Totalunternehmer. Umfangreiche Bauvorhaben mit überwiegendem Bauanteil realisieren wir in Zusammenarbeit mit Architekten und qualifizierten Generalunternehmungen. *Mitarbeiter (Stand 1995):* 17 qualifizierte Mitarbeiter mit Ausbildung in den Fachgebieten Elektro/HLK-Technik, Informatik

Leistungsübersicht Gebäudetechnik (Spezialprojekte)

- Planung komplexer Gebäudetechnikanlagen, umfassend Elektro-/Klima-/Lüftungs-/Kälte-/Heizungsanlagen für Bauten der Industrie, Chemie, Forschung, Verwaltung, Banken, Versicherungen, EDV, Kommunikation
- Systemneutrale Planung integraler Gebäudeautomationssysteme
- Projektmanagement und technische Gesamtkoordination für die Planung und Ausführung umfangreicher Gebäudetechnikprojekte
- Energiekonzepte, Expertisen, Durchführbarkeitsstudien, Wirtschaftlichkeitsanalysen, Betriebskonzept

Leistungsübersicht Gebäudeautomatisierung

- Neutrale Beratung, Projektierung und Integration von vernetzten Systemen, herstellerunabhängig und systemübergreifend, mit Schwerpunkt auf dem Gebiet der Gebäude-/Prozessautomatisierung
- Studien, Konzepte, Expertisen, Analysen, Evaluationen
- Problemanalyse, Projektierung, Pflichtenheft, Ausschreibung, Software-Design, Software-Implementierung, Dokumentation, Systemintegration, Inbetriebnahme, Optimierung, Schulung, Wartung

Projekt: Paul Scherrer Institut, Würenlingen/Villigen, Neutronenhalle, Lüftungs-/Klimasystem für die Spallationsquelle

Bearbeitete Fachgebiete durch KIWI: ➤ Aktiv-Lüftungsanlage ➤ Steuer-/Regelsystem ➤ Datenkommunikation zum best. Leitsystem

Leistungen der KIWI:
- Erstellung des techn. Sicherheitskonzeptes
- Vorprojekt, Projekt, Ausführung, Abnahme (100% Teilleistung nach SIA 108)

Nutzen für den Kunden:
- Min. Koordinationsaufwand durch interdisziplinäre Bearbeitung der Prozesstechnik, des Steuer-/Regelsyst. u. Datenkommunikat.
- Sicherstellen einer hohen Betriebssicherheit
- Min. Aufwand für Betriebsführung durch Integration in das Gesamtleitsystem

Projektspezifisches:
- Strenge Anforderungen an die aerodynamischen Verhältnisse und Betriebssicherheit
- Weltweit einmaliges Projekt, keine bisherigen Erfahrungen für die Planung und Ausführung vorhanden

LINDE KRYOTECHNIK AG
Dättlikonerstrasse 5, P.O. Box 167
CH-8422 Pfungen / Switzerland

Dr. B. Ziegler	Man. Director	Phone	41 52 31 05 12
A.-E. Senn	Man. Sales	Phone	41 52 31 05 18
		Fax	41 52 31 05 50

LINDE KRYOTECHNIK AG is a subsidiary division of LINDE AG, Germany. The activities of this division cover the field of Helium refrigerators / liquefiers and Hydrogen liquefiers, in the range of a few litres up to several thousand litres per hour. As an international group we perform on engineering, contracting, manufacturing, installation, operation and services based on facilities in Switzerland, Great Britain and Germany.

For the SINQ project we were awarded the contract for the cryogenic Helium refrigeration plant to cool and maintain the D_2-condensor at operating conditions. In tight collaboration with the SINQ project team we established the interfaces and procedures for the integration of an automated refrigeration system to the project. The refrigeration plant consists of two main groups; the Helium compression station with gas management and utilities, and the refrigeration cold box with the plant control system. After test trials in the external test position the cold box with control system will be installed at their final position in the SINQ experiment area.

LINDE KRYOTECHNIK AG, formerly SULZER CRYOGENICS, has provided various similar plants for Cold Neutron Source cooling as well as for cryogenic isotope separation, all in the range of 15 ... 25 K operating temperature. Extensive know how became established and outstanding operational flexibility and reliability were recorded. The main products are related to Helium liquefaction resp. refrigeration in the 4.5 K temperature range. All plants built are based on the outstanding technology of turboexpanders, which feature high reliability, excellent flexibility and maintenance free operation over years. Several hundred units of turboexpanders are in operation and have accumulated millions of hours to customers satisfaction. Their main application is in

- Helium liquefiers 10 ..... 5'000 l/h
- Helium refrigerators 20 ..... 20'000 W
- Hydrogen liquefiers 20 ..... 12'000 l/h

and other special, customer tailored plants. The customers are served worldwide through our Linde subsidiaries and with local partners.

LOOSLI FORMTECH AG
CAD/CAM-Modell- und Formenbau, Stereolithographie, Formteile

Die Firma Loosli FORMTECH AG hat 40 Jahre Erfahrung in Modell- und Formenbau, Kunststoffformteile und Mechanik und arbeitete in früheren Jahren nach alten traditionellen Techniken.
Mit dem Aufkommen der CNC-Technik (der computergesteuerten Maschinenbearbeitung) eröffnete sich dem traditionellen Werkzeug-, Formen- und Modellbau neue Wege in der Be- und Verarbeitung von Materialien. Der Einzug der Computertechnik erfordert ein inovatives und flexibles Denken. Die Loosli FORMTECH AG hat diesem Zeitschritt Rechnung getragen. Sie hat sich mit modernsten Fertigungsmitteln eingedeckt, wie z.B. 3-5-Achsen Fräsmaschinen mit Verfahrwegen bis zu 5300 mm, Stereolithographie, CNC-Drehbank bis D 500 mm, welche von CAD/CAM-Systemen wie CATIA, PRO-ENGINEER, PRO-CAT programmiert werden. Ein direkter ISDN-Telefonanschluss lässt den Kunden "fast" direkt auf die Geräte zugreifen.

Die Firma Loosli FORMTECH AG erhielt den Auftrag die Innenteile des Moderator-Tanks aus vorgeschmiedeten, vollen ALU- Klötzen zu fräsen. Die Daten für die Bearbeitung wurden direkt auf CATIA übertragen, und somit war es möglich ohne Zwischenschritte die komplexen ALU-Teile 5-achsig zu fräsen.
Das grösste Teil hatte ein Rohgewicht von ca. 1'200 kg und brachte nach der Bearbeitung noch ein Gewicht von ca. 50 kg auf die Waage. Es erforderte demzufolge eine spezielle Arbeitstechnik um solch grosse, dünnwandige Teile herzustellen.

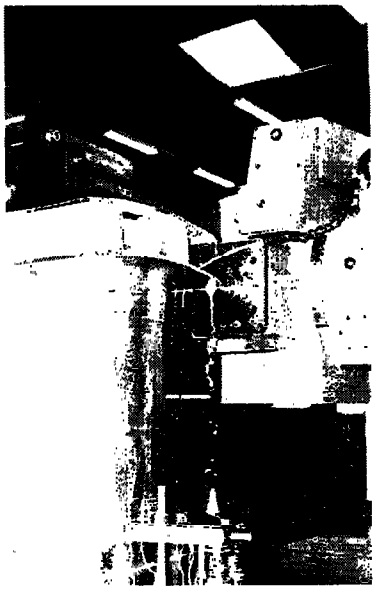

Loosli FORMTECH AG

Die Loosli FORMTECH AG, Derendingenstrasse 60,
4562 Biberist
Tel: 065/41 53 41 / Fax: 065/42 59 67
Tel. ISDN Anschluss 065/41 53 45
gliedert sich heute in drei Abteilungen

Modellbau: Technischer Modellbau, Giessereimodelle, Anschauungsmodelle, Designstudien, Prototypenbau, Funktionsmodelle, Stereolithographie

Kunststoffformteile: PUR-, Epoxidharz-, GFK-, Silikonteile für Klein- bis Grossserien

CAD/CAM-Werkzeugbau/Mechanik: Giesserei-, Press-, Umform-, Biege- und Spezialwerkzeuge, Spezialteilebau, Abdigitalisieren, CAD/CAM CATIA, PRO-ENGINEER, PRO-CAD.

NOELL GmbH
Gerd Edler / Dept. V29
Alfred-Nobel-Strasse 20

Telephone: ++49 931 903 1318
Fax: ++49 931 903 1016

D-97080 Würzburg

NOELL was established in Würzburg in 1824 and is a subsidiary of PREUSSAG AG, Hanover today. Employing approximately 8,000 persons - 4,000 of whom are engineers and technicians - NOELL is active in the fields of environmental engineering, hydropower plants, systems engineering and nuclear engineering.
In the field of **nuclear engineering** the product range has changed substantially over the past few years. Following a tradition as a supplier of components for nuclear power plants, NOELL is one of the leading companies in the decommissioning of nuclear power plants today. The complete dismantling and decommissioning of the Niederaichbach nuclear power plant in August 1995 was the first "return to the green fields" in history.
NOELL also supplies turnkey plants such as the pilot conditioning plants for spent fuel elements in Gorleben.
The NOELL **Advanced Technologies** department, a nuclear engineering subdivision, supplies components for accelerators (LHC, LEP, HERA) and fusion experiments (JET, TFTR, W VII X, CIEMAT) - in particular super-conducting magnets and handling equipment.
NOELL has supplied the **Shielded Target Transport Cask** for SINQ. This transport device for targets, weighing approx. 60 t, basically consists of

- tight shielding enclosure
- safety hoist with grab
- tight shielding valve and
- various accessories (plugs, windows, etc.)

The shielded target transport cask is transferred by means of the workshop crane and operates in the vertical as well as in the horizontal position.
A particular problem in the design was to accommodate all required safety and control devices within the limited space available.

PIER FOLIEN- & TOPSEAL - SICHERHEITSVENTILE

Ein bedeutender Anteil der Sicherheitsventile zur Absicherung der Kühlkreisläufe der SINQ-Anlage wurde durch die Firma PIER-Armaturen GmbH in Hattersheim, Tel. 06190 99080 - Fax. 06190 8725 geliefert (Schweizer Vertretung Zürcher-Technik in Sissach, Tel. 061 9717777 - Fax. 061 9717010).

Die Sicherheitsventile der Firma PIER-Armaturen GmbH sind seit vielen Jahren u.a. in kerntechnischen Anlagen, in der chemischen Industrie, der Verfahrenstechnik der Reinstgastechnik usw. erfolgreich im Einsatz. Die spezifischen Einsatzbedingungen der SINQ-Anlagen, insbesondere die hohe, permanente Strahlenbelastung von bis zu 35 Gy/h stellen an die PIER Sicherheitsventile hohe Anforderungen:

- Konstruktive und fertigungstechnische Ausführung
- Auswahl der Werkstoffe
- Dichtheit der Ventile nach aussen und im Durchgang
- Erzielung hoher Standzeiten
- Leichte Dekontaminierbarkeit

In den Kühlbereichen Target- und Targetfensterkühlung, belasteter H_2O-Kreislauf sowie im Moderationssystem kommen ***FOLIEN-Sicherheitsventile*** (Proportionaltyp) jeweils in der Nenndruckstufe PN 40 mit Metallfaltenbalg zum Einsatz. ***FOLIEN-Sicherheitsventile*** besitzen als besonderes Konstruktionsmerkmal zusätzlich zu der geläppten Metall / Metalldichtfläche eine dem Sitz nachgeschaltete Folie, die dem Ventil eine Leckrate im Bereich < 10^{-7} mbar/ls im Durchgang verleiht.

Beim Ansprechvorgang des Ventils wird diese Folie zunächst durchstanzt. Das Ventil bläst dann wie ein normales Sicherheitsventil ab, schliesst nach der Druckabsenkung und dichtet über die geläppten Metalldichtflächen ab. Die ursprüngliche Dichtheit von < 10^{-7} mbar/ls wird nach Einbau einer neuen Folie wiederhergestellt. Für die übrigen Einsatzfälle wurden PIER Sicherheitsventile der ***TOPSEAL***-Baureihe (Kegel mit gekammerter strahlungsbeständiger Weichdichtung) ebenfalls in Metallbalgausführung geliefert. Alle gelieferten Ventile sind mit einem strahlenbeständigen Microschalter zur Registrierung der Ansprechvorgänge ausgerüstet.

TECHNIQE FOR YOUR HIGHEST REQUIREMENTS

Perfect Solutions of Sealing- and Clamp- Systems in following fields of application:

- **Vacuum Technology**
- **Nuclear Industry**
- **Accelerator Technology**
- **Cryogenics**
- **Vast fields of Industrial Service**

Metal Seals for Flange-Systems

- *HELICOFLEX Seals*
- *KENOL Assemblies*
- *Quick Disconnect Systems*

Example of Application in the SINQ-Project:

- *HELICOFLEX Seals with Silver-Lining for Heavy-Water circuits; DN 16-150, DN 300, DN 400, DN 500, DN 600*
- *HELICOFLEX Seals with Alu-Lining for Vacuum Sealing up to DN 800, Seal Types HN / HNV*
- *Double-Section HELICOFLEX Type HND 229; DN 150-900*
- *HNV Type HELICOFLEX Seals with Alu and Nickel Lining*

Membrane Bellows and Assemblies

- *Edge-Welded Bellows and Assemblies*
- *Actuators and Feed-Throughs*

Example of Application in the SINQ-Project:

- *SINQ-Target-Unit: 8 off Coaxial-Compensator-Units DN 700 / DN 600 as transition from the Helium+Nitrogen Tank to the Beam-duct housing. Sealing level ≤ 10 (-9) mbar.l/s He Vacuum to 4 bar delta P in case of accident*

Conical Flange-Systems using Clamp-Chains

- *PNEUROP KF: DN 10 - 63*
- *ISO-tubing: DN 63 - 1000*
- *KFCF: DN 16 - 50*
- *CF: DN 35 - 250*
- *Elastomer Seals, Metal Seals*

Example of Application in the SINQ-Project:

- *A wide range of Conical Flange-Systems according KF and ISO Standard.*
- *Special designed Clamp-Systems up to DN 550*
- *Various mechanical components, realized according to the specific requirements of PSI*

Fail-save System Service -- Optimizing the Operating data -- Enhancement on working time - the basis to apply our Know-How uncompromisingly.

FL-9491 RUGGELL / FÜRSTENTUM LIECHTENSTEIN
Industriestrasse 416, P.O. Box 414
Phone (075) 3771570, Fax (075) 3771575

Prophysik Aktiengesellschaft

Schär Engineering AG

Schär Engineering AG
Lachen 7
8416 Flaach

Telefon 052 42 18 26/36
Telefax 052 42 10 39

Ansprechpartner: Hugo Schär, Geschäftsleiter
David Bächtold, Projektleiter Nuklearmedizin und Nukleartechnik

Tätigkeit der Firma Schär Engineering AG

Schär Engineering AG führt Studien, wenn nötig mit Vorversuchen, aus und erarbeitet auf Grund dieser Erkenntnisse Konzepte für Maschinen oder gesamte Anlagen.

Schär Engineering AG plant und konstruiert, beschafft Fabrikations- und Kaufteile, montiert die einzelnen Komponenten und nimmt die Anlagen in Betrieb.

Die Wünsche der Kunden werden unter Berücksichtigung von technischen und wirtschaftlichen Aspekten eingearbeitet und die Anlagen nach den gängigen Normen realisiert.

Schär Engineering AG integriert das Kunden- Know How und pflegt enge Beziehungen zu unzähligen Spezialisten in den verschiedensten Fachgebieten.

Schär Engineering AG ist damit in der Lage, auf höchstem technischem Niveau kundenspezifische Anlagen wirtschaftlich und termingerecht zu erstellen.

Arbeiten am Projekt SINQ

Bei der Beschaffung der Wechseleinrichtung SINQ wurden folgende Arbeiten ausgeführt:

- Mithilfe bei der Evaluation eines Lieferanten
- Ueberwachung von Konstruktion, Fabrikation und Montage
- Ueberwachung der Termine
- Ueberwachung der Inbetriebnahme
- Für die Ausrüstung der Hotzelle zur Demontage des Targets wurde in einer Studie die Machbarkeit abgeklärt, ein Pflichtenheft erarbeitet und ein Konzept aufgezeichnet. Momentan wird die Detailkonstruktion dieser Ausrüstungskomponenten von Schär Engineering AG ausgeführt.

Weitere realisierte Projekte

- Nuklearmedizin: Therapiesimulator mit 18 Positionierantrieben, komplette Mechanik für Protonentherapie (PSI-Gantry), Mechanik C-Arm
- Nuklearindustrie: Prüfmaschinen für atomare Brennstäbe
- Nahrungsmittelindustrie: Hochleistungs-Siegelanlage mit Abfüllstrecke, Qualitätssicherungsanlage für Kunststoffschalen, Maschinen zur Dosenfertigung
- Automobilindustrie: Dynamische 5-Achsen-Schweissroboter für Treibstofftanks
- Werkzeugmaschinen: Planung und Fertigung von vollautomatischen Anlagen für die Produktion von Linearführungen

SULZER CHEMTECH

Sulzer Chemtech Ltd
P.O. Box 65
CH-8404 Winterthur, Switzerland

Richard Zmasek
Telephone 052-262 37 62, Telefax 052-262 00 77

Sulzer Chemtech Ltd has supplied for the Spallation Neutron Source at Villigen, Switzerland:

Design and Engineering for

- Heavy Water Loop
- Helium Loop
- Nitrogen Loop

Sulzer Chemtech Ltd is a recognized supplier of:

Design, Engineering and Hardware for

- Heavy Water Enriching Plants
- Heavy Water Production Plants
- Tritium Extraction Plants
- Isotope Separation Plants for Hydrogen, Deuterium, Tritium, Boron, Nitrogen etc.

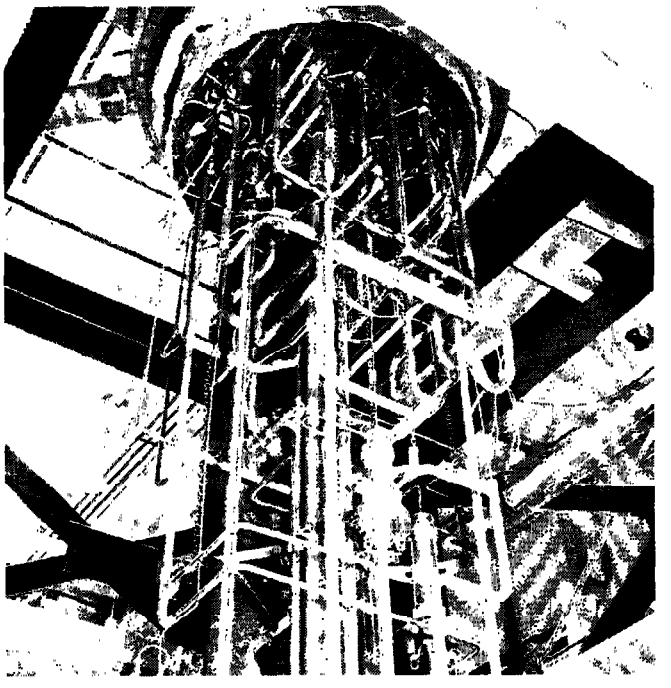

Joint European Torus
Hydrogen Isotope Separation System
View of the Cold Box before final assembly

TENSOL SA

CH-6776 PIOTTA

Tel. 091/868 15 28
Fax. 091/868 11 29

Ansprechpartner: Herren H.R. KNECHT (Werksdirektor)
P. VOGEL (Direktor Marketing / Verkauf)

TENSOL - LIEFERUNGEN für SINQ:

1.) Herstellung von kobaltarmen Eisenstrukturen (Totalgewicht 2500 Tonnen) bestehend aus Platten in den verschiedensten Dicken und Konturen, unterhalb und rund um den Moderatorbehälter angeordnet für die Abschirmung in der Spallationsneutronenquelle SINQ.

2.) Herstellung von kobaltarmen Eisenstrukturen (Totalgewicht 100 Tonnen) bestehend aus 19 Stück kreisförmigen Platten mit einem Durchmesser von 2,5 Meter und unterschiedlichen Dicken, zentral oberhalb dem Moderatorbehälter angeordnet, ebenfalls für die Abschirmung in der Spallationsneutronenquelle SINQ. Die ersten fünf, über dem Moderatorbehälter angeordneten Platten sind mit je zwei unabhängigen Kühlschlangensystemen, zwecks Wasserkühlung versehen.

3.) Herstellung des Neutronenleiter - Einschubwagens (Totalgewicht 25 Tonnen) inkl. Radsätzen, Führungsrollen, Antriebskupplung, Strahl - Justierfüsse und Drehpunkte, demontierbare Wagenabschirmungen mit Führungsbolzen, Kastenabschirmungen und Kastendeckel.

4.) Herstellung von mechanischen Komponenten für das Neutronenleitersystem wie Stahlträger, Aluminiumträger, Supporte, Ständer u.s.w. inkl. Oberflächenbehandlungen: Glasperlen gestrahlt, grundiert und endlackiert.

TENSOL - Lieferprogramm / Tätigkeitsgebiet:

- Eisenbahn - Oberbaumaterialien
- Masten- und Antennenträgerbau
- Abkantmaschinen für die Blechbearbeitung
- Herstellung mechanischer Einzelteile

VAT Vakuumventile AG
CH - 9469 Haag, Switzerland

Tel. xx41-81-771 61 61
Fax xx41-81-771 48 30

Sales Manager: Georg Öhri

VAT Vacuum Valves and the SIN-Q Project at the PSI

VAT offers by far the largest choice of vacuum valves worldwide! A variety of more than 1000 standard valves can be ordered from our catalogue.

Key factors such as high quality products and top service helped to establish an ongoing excellent relationship between the Paul Scherrer Institute of Switzerland and VAT. VAT has been involved in many different projects at the PSI including the SIN-Q project.

The following VAT products are part of the SIN-Q equipment:

- gate valves series 01 and series 10.8 for the beamline
- two customized fast-closing shutters DN 200 for protection of the main beamline in case of an accident within the SIN-Q experiment
- angle valves series 28 and special gate valves based on series 14 and series 10.1 for the deuterium handling system; these valves are exposed to conditions from high vacuum until several bar of over-pressure
- gate valve DN 630 series 12 with special flange, in front of the huge neutron scattering chamber
- several angle valves series 26 and gate valves series 12 for the forevacuum lines

We wish all participants of the ICANS-VIII conference lots of success with their work!

Von Roll Maschinen und Fördertechnik AG

Fabrikstrasse 2
CH - 3012 Bern

Werner Gartmann, Leitung Bearbeitungstechnologie
Telephon: 031 308 52 37
Telefax: 031 302 55 04

Von Roll ist ein international tätiger, diversivizierter Industriekonzern, der sich auf die vier Geschäftsbereiche Umwelttechnik, Elektroisolations-Systeme, Stahl für die Bauwirtschaft sowie Gussprodukte und Maschinen konzentriert.

Die durch die langjährige Erfahrung und technische Kompetenz erworbenen Kernfähigkeiten werden eingesetzt, um technologisch zukunftsgerichtete Produkte von hohem Kundennutzen herzustellen.

Zum Projekt Spallations-Neutronenquelle SINQ durften wir im Auftrage des Paul Scherrer Institutes, folgende anspruchsvolle Komponenten in unseren Werkstätten in Bern herstellen und liefern:

- Ablenkmagnet
- Strahlkanalgehäuse
- Quellengehäuse
- Neutronenleiter- und Strahlkanaleinschübe
- Hochenergiestrahlverschlüsse mit Verschlusstrommeln
- Blindeinschübe
- Wechselplatteneinheit, Doppelschlitten und andere mechanische Komponenten.

Wir sind stolz, mit den von uns gelieferten Komponenten ebenfalls einen Beitrag zur Realisierung der Spallations-Neutronenquelle SINQ des Paul Scherrer Institutes geleistet zu haben.

Romabau AG

Fohlenweide
CH-8570 Weinfelden
Tel. 072 - 21 95 95
Fax 072 - 22 21 32

Ein Unternehmen der ROMABAU-Gruppe
A Company of the ROMABAU Holding

Zertifizierter Bereich/ Tätigkeitsgebiet	**Ganzes Unternehmen**
Certificated field/ Company activities	**Entire Company**
Normmodell Specification	**ISO 9001/EN 29001**
Reg.-Nr. Reg. No	**11033-01**
Erteilung Assessment	**1994-03-24**
Gültig bis Valid until	**1997-03-23**

- Gesellschaftsform: Aktiengesellschaft
- Gründung: 1961
- Aktienkapital: Fr. 2,4 Mio
- Bilanzsumme 1993: Fr. 10 Mio
- Anzahl Beschäftigte: 72
- Geschäftssprachen: Deutsch, Französisch, Englisch

- Qualitäts-Beauftragter des Managements: R. Klingler

- Geschäftsleitung: Rudolf Klingler
- Produktion: Rudolf Klingler
- Marketing: Johann Kortje
- Verkauf: Johann Kortje

- Legal status: Joint-stock company
- Year of foundation: 1961
- Share capital: SFr. 2.4 Mio
- Balance 1993: SFr. 10 Mio
- Number of employees: 72
- Business languages: German, French, English

- Management delegate for quality control: R. Klingler

- Management: Rudolf Klingler
- Production: Rudolf Klingler
- Marketing: Johann Kortje
- Sales: Johann Kortje

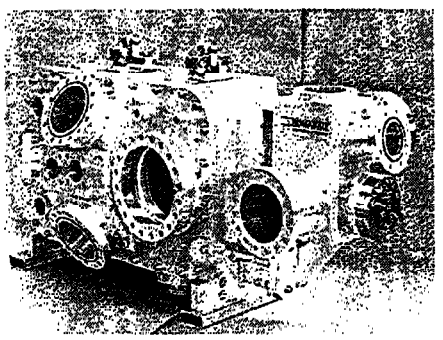

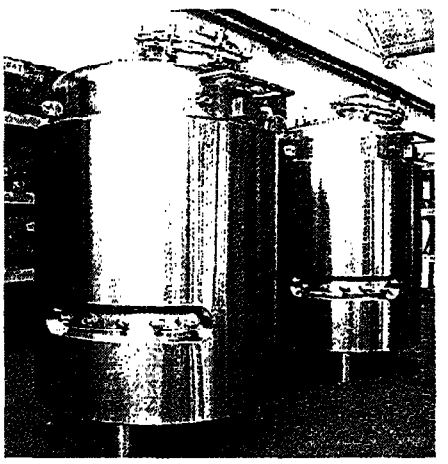

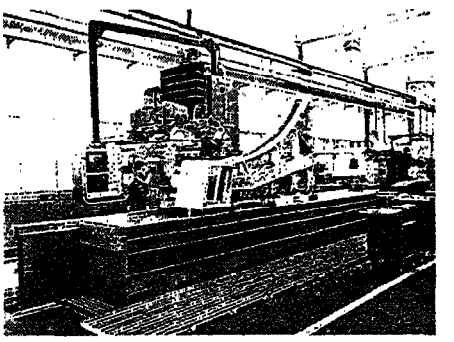

Partner der Industrie

Seit über 30 Jahren ist die Romabau AG ein zuverlässiger Partner der Industrie im europäischen Raum. Seit seiner Gründung widmet sich das Unternehmen der Herstellung komplexer Maschinen, Apparate und Anlagenteile nach den jeweiligen Kundenwünschen.

Maschinen und Apparate aus korrosionsfesten Materialien

Die Verarbeitung von rostfreien Stählen, Nickelbasislegierungen, Aluminium, Kupfer und seinen Legierungen, Titan und weiteren Spezialwerkstoffen ist seit jeher die Kernstärke unseres Unternehmens. Wir formen, verbinden und bearbeiten diese mit modernen Verfahren und Einrichtungen zu dem von Ihnen gewünschten Produkt.

Engineering

Unsere umfassende schweiss- und bearbeitungstechnische Erfahrung erlaubt uns, Fertigung einschliesslich zugehörigem Engineering entsprechend höchsten Qualitätsanforderungen anbieten zu können.

Produktionsbereiche

- Engineering und Produktion
- Rostfreier Maschinen- und Apparatebau für die chemische, pharmazeutische und Nahrungsmittelindustrie
- Druck- und Vakuumbehälterbau
- Hochvakuum- und UHV-Technik
- Komponenten für Forschung und Entwicklung
- Plasmabrennschneiden und Beizen
- Kundenarbeiten auf Grossbearbeitungsmaschinen

Range of Products

- Engineering and Manufacturing
- Machinery and Equipment from corrosion proof materials for the chemical, pharmaceutical and food industry
- Pressure and Vacuum vessels
- High vacuum and UHV Technology
- Components for Research and Development
- Plasma cutting and Pickling Services
- Machining Services on large machine tools

A partner for industry

Since more than 30 years, Romabau acts as a reliable partner for the European industry. Our company is dedicated to the manufacturing of sophisticated machinery, welded equipment and parts made according the requirements of our clients.

Machinery and equipment from corrosion resistant materials

Since the very beginnings, our company has concentrated in the perfect mastering of manufacturing processes for stainless steels, nickel base materials, aluminium, copper, and its alloys as well as titanium and other sophisticated construction materials. We form, join and machine these materials to the desired product, using modern processes and equipment.

Engineering

Our extensive experience in welding and machining allows us to accept the manufacturing and engineering of the most demanding parts and equipments according to high quality standards.

ROMABAU

FLEXWELL CRYOGENIC LINES

The main technical component is a thin corrugated stainless steel tube which can be produced continuously in long length by a process and equipment developed by Alcatel Kabel AG & Co. This corrugated tube was originally designed as a watertight cable sheath. Later is has been used as an insulated tube for transport of hot water.

Since about 1967 an arrangement of several concentric tubes has been used as a cryogenic transferline for cryogenic fluids. We have got experience with LN_2, LHe, LOX, LH_2, LAr. The terminations are designed based on our long lasting experience. These designs have proofed well at several International Institutes like CERN, JET and others.

The advantages of our design are:

- **long lengths without joints**
- **complete fabrication, testing and evacuation in the factory**
- **easy and quick installation because of the flexibility of the tube (installation similar to power cable)**
- **high reliability**

Alcatel Kabel AG & Co.
Kabelkamp 20
D-30179 Hannover
Tel.: 0049/511/676 2046
Fax.: 0049/511/676 3777

Dr.-Ing. D. Gerth

Daimler-Benz Aerospace
Dornier
88039 Friedrichshafen, Germany

Hugo Betzold

TEL +49-7545-82596 FAX +49-7545-82693

NEUTRON VELOCITY SELECTOR FOR SINQ-SANS

Incorporated in the Daimler-Benz Aerospace, Dornier is one of the leading high-tech companies in Germany.

In the field of advanced technolgies Dornier developed neutron velocity selectors which reaches the utmost limit of what is technically feasible today.
The unique feature of this SANS neutron velocity selector is the use of carbon fibre epoxy material for the very thin, helically twisted rotor lamellae which are coated with ^{10}B or Gd_2O_3 as absorbing material. This novel design allows rotor speeds of up to 28,300 rpm (= 430 m/s pheripheral velocity).

Based on this technology Dornier is a partner for:

- neutron velocity selectors (monochromotors)
- higher-order neutron filters (harmonic filters)
- disk choppers
- FERMI choppers
- components for FERMI choppers (slats, etc.)

as well as for software and peripheric instrumentation, e.g. as:

- control systems (PC based)
- monitoring systems for choppers and selectors
- interface to a host.

The successful use in many laboratories world-wide reflects the fact that Dornier's neutron research related instruments and components meet high experimental requirements and allows a broad versatility of applications.

References: **GKSS,** Geesthacht; **HMI,** Berlin; **ILL,** Grenoble; **ISSP,** Tokyo; **KFA,** Jülich; **LANL,** Los Alamos; **NIST,** Gaithersburg; **PSI,** Villigen; **PTB,** Braunschweig; **SERC,** Didcot

Alusuisse Road & Rail AG

Buckhauserstrasse 11
CH-8048 Zurich
Telephone 01 497 44 22
Fax 01 497 45 85

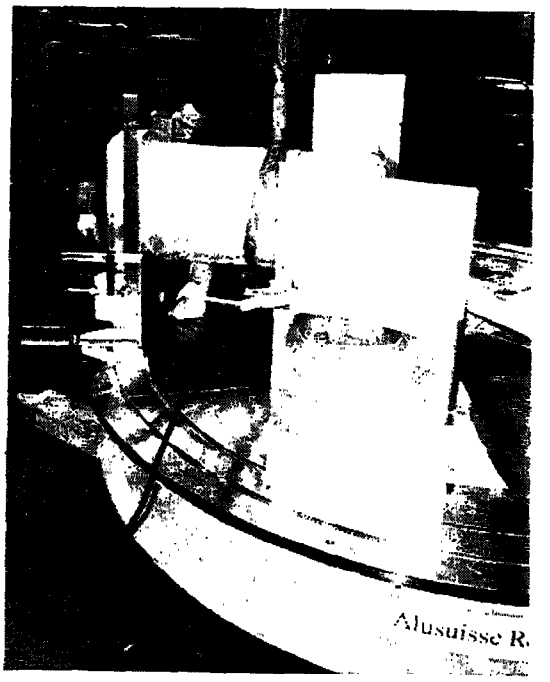

Alusuisse Road & Rail AG ist ein Engineering-Unternehmen innerhalb des Bereichs Alusuisse der Alusuisse-Lonza Gruppe.

Die Aktivitäten von Road & Rail konzentrieren sich auf die Projektierung von Wagenkasten-Strukturen aus Aluminium und Verbundwerkstoffen für Schienenfahrzeuge und Busse.

Im Rahmen des SINQ-Projektes hat das Paul Scherrer Institut einen verlässlichen Partner für den Bau des Moderator-Tanks gesucht. Dank der langjährigen Erfahrung in der Verarbeitung des Werkstoffes Aluminium ist die Wahl zur Ausführung dieses delikaten Projektes auf Alusuisse Road & Rail AG gefallen.

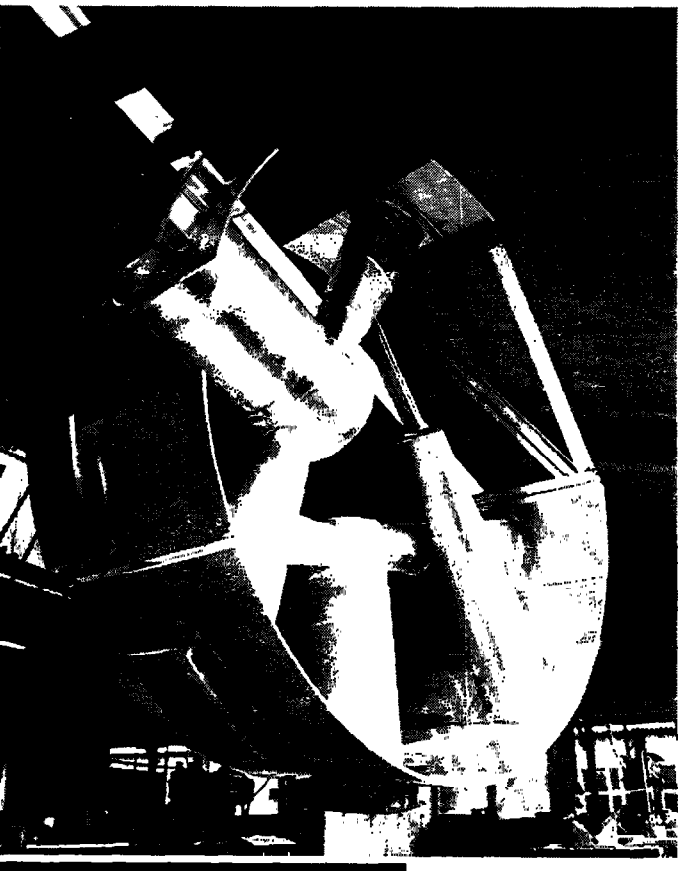

Nebenstehend einige Schnappschüsse von verschiedenen Bauphasen des Moderator-Tank, der in der hauseigenen Prototypen-Werkstatt von Alusuisse Road & Rail AG hergestellt wird.

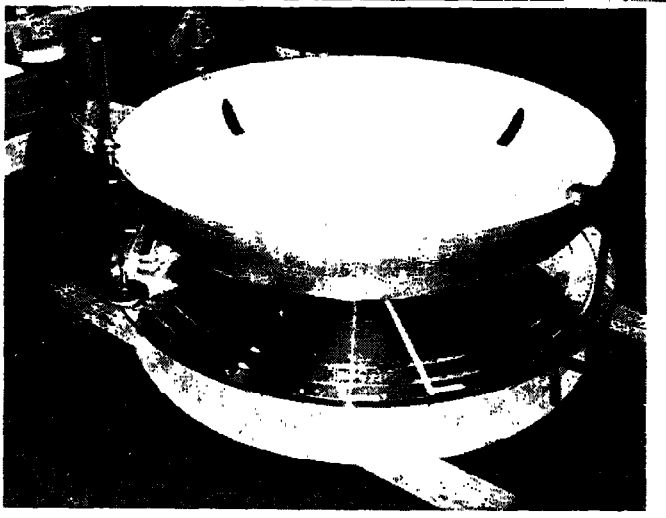

Indices

ICANS-XIII
13th Meeting of the International Collaboration on
Advanced Neutron Sources
October 11-14, 1995
Paul Scherrer Institut, 5232 Villigen PSI, Switzerland

List of Authors

Aksenov V.L.	S-4, I-2, I-11, I-17, N-5
Appleton, B.R.	P-6
Arai, M.	S-1
Arakawa, D.	A-6
Astakhov, Yu.A.	I-15
Balagurov, A.M.	I-2, I-17
Bauer, G.S.	L-3, T-12, T-13, T-17, T-19, A-8
Belushkin, A.V.	I-8
Beynon, T.D.	T-10
Boenig, H. J.	I-25
Bogdzel, A.A.	I-15
Böni, P.	I-22, I-27
Böttger, G.	I-23
Broome, T.A.	S-6, T-10, T-18
Brown, B.S.	N-2
Bryant, P.	P-8
Bucknall, D.G.	I-5
Bugg, W.	P-10
Camus, E.	T-26
Carpenter, J.M.	G-1, I-12, T-25, P-1
Catherall, R.	T-15
Chae, Y.-C.	A-9, P-2
Chernyshov, D.Yu.	I-20
Chiba, S.	T-2
Cho, Y.	A-9, P-2
Clemens, D.	I-22, I-27
Cohn, H.	P-10
Condo, G.	P-10
Conrad, H.	S-10, L-4
Crawford, R. K.	I-3
Crosbie, E.	A-9, P-2
Cser, L.	S-2, I-21
Daemen, L.	I-26, L-2, L-7
Dai, Y.	T-16
Dementyev, A.V.	T-1, T-4
Dickinson, E	I-5
Dölling, R.	A-4
Dönni, A.	I-23
Drumm, P.	T-15
Eckert, J.	L-7
Efremenko, Yu.	P-10
Ehrat, J.	T-24
Engels, R.	I-24
Epperson, J. E.	I-3
Evensen, A.	T-15
Eyssa, Y. M.	I-25
Faltens, A.	A-8
Ferguson, P.	L-1, T-7, T-8
Filges, D.	S-5, T-11
Firjahn-Andersch, A.	A-5
Fischer, P.	I-23
Fischer, S.	I-23
Fischer, W.E.	N-7
Fitzsimmons, M. R.	L-6
Fletcher, P	I-5
Friedsam, H.	A-9, P-2
Furusaka, M.	T-20, T-21, T-22, P-9
Geick, R.	I-6, I-13
Glazkov, V.P.	I-2
Grimm, H.	I-13
Grimmer, H.	I-22

Gross, P. A-4
Guttek, B. T-9
Hagen, M. I-9
Hahn, W. I-27
Harkay, K. A-9, P-2
Harnmonds, John P. G-1
Hempelmann, R. I-7
Higgins, JS I-5
Hiismäki, P. I-16, I-17
Hiraga, F. T-22
Hjelm, Rex P. S-8, I-26, L-5
Holitzner, L. I-7
Horan, D. A-9, P-2
Horisberger, M. I-23, I-27
Ignatiev, S.V. T-6
Ikeda, H. N-4, P-9
Ishibashi, K. T-2
Iwasa, H. T-20, T-22
Jansen, E. I-1, I-24
Janssen, S. I-7
Jason, A.J. A-1
Jones, R.A.L I-5
Jonsson, O. T-15
Kamyshkov, Yu. P-10
Kazimirov, V.Yu. I-8
Kim, S. P-2
Kishiro, J. A-6
Kiyanagi, Y. T-20, T-21, T-22
Kleb, R. I-3
Klein, H. A-3, A-4
Koch, M. I-23
Kockelmann, W. I-1
Kolesov, V.F. T-3
Konovalov, I.I. T-4
Kosugi, N. T-20, T-22
Kravchuk, L.V. A-2
Kugler, E. T-15
Kustom, R.L. A-7, A-8, A-9, P-2
Lakatos, A. A-3
Lamoreaux, S. P-10
Leach, D. I-3
Lebedev, S.G. T-1
Lengeler, H. P-7
Lessner, E. A-9
Lessner, E. P-2
Lettry, J. T-15
Levchanovsky, F.V. I-15
Likhachev, Y.N. T-3
Lillie, R. P-10
Lucas, A.T. T-19
Ludewig, H. P-5
Maaser, A. A-3
Macek, R. J. N-3
Madlung, J. A-5
Maehata, K. T-2
Martin, S. A-7, A-8
Maslov, A.A. T-4
Matsufuji, N. T-2
McDowell, W. A-9, P-2
McEwen, Keith I-10
McGhee, D. A-9, P-2
Meads, P.F. A-7, A-8
Medarde, M. I-23
Meigo, S. T-2
Mesot, J. I-7
Mezei, F. L-8
Michaelis, B. I-15
Mills, F. P-2
Miroshnichenko, V.G. T-3, T-4
Moe, H. A-9, P-2
Muhrer, G. T-5
Müller, K.D. I-24

Müller, K.D. I-24
Nakamoto, T. T-2
Naumov, I.V. I-2
Neef, R D. T-11
Nielsen, R. A-9, P-2
Nikitenko, Yu.V. I-11
Ninaus, W. T-5
Norek, G. A-9, P-2
North, Mark T. T-17
Novozhilov, V.E. I-15
Numajiri, M. T-2
Obert, J. T-15
Ogawa, Y. T-20, T-22
Olah, Glenn A. L-5
Ostrovnoy, A.I. I-15
Pankratov, D.V. T-6
Penfold, J I-5
Peterson, K.J. A-9, P-2
Petrillo, C. I-9
Picton, D.J. T-10
Pitcher, Eric L-1, T-7, T-8
Plasil, F. P-10
Platonov, S.L. I-2
Powell, J. P-5
Pozimski, J. A-4
Prager, M. I-7
Priesmeyer, H.G. I-18
Prikhodko, V.I. I-15
Primdahl, K. A-9, P-2
Putaux, J.C. T-15
Pynn, R. L-2, L-6, L-7, P-3
Qian, Y.L. A-9
Raman, S. P-10
Rauchas, A. P-2
Ravn, H. T-15
Reidelbach, K. A-4
Reinartz, R. I-24
Rennich, M. P-10
Rennie, A I-5
Rezaev, V.E. I-15
Richardson, RM I-5
Richter, D. I-7
Robinson, R. A. I-25
Rogov, A.D. T-4
Rosenfeld, J.H. T-17
Roser, S I-5
Ruggiero, A.G. A-8, P-4
Russell, G.J. S-9, L-1, T-7, T-8
Sacchetti, F. I-9
Sarraf, D. B. T-17
Sauvage, J. T-15
Savenko, B.N. I-2
Schaal, H. T-11
Schachinger, E. T-5
Schäfer, W. I-1, I-24
Schefer, J. I-23
Schempp, A. A-5
Schmidt, W. I-6, I-13
Schneider-Muntau, H. J. I-25
Schubert-Bischoff, P. I-27
Schuster, M. P-8
Seeger, P.A. S-7, I-14, I-26, L-1, L-5, L-7
Serdyuk, I. I-4
Shabalin, E.P. T-3
Sheptyakov, D.V. I-2
Shigyo, N. T-2
Shmakov, K. P-10
Sidorkin, S.F. T-3, T-4
Sirotin, A.P. I-15
Skala, K. T-13
Smirnova, O.N. T-1

Smith, B. L. T-14
Sobolevsky, N.M. T-1, T-4
Somenkov, V.A. I-2
Someya, H. A-6
Staub, U. I-23
Stavissky, Yu.Ya. T-1, T-3, T-4, N-6
Steigenberger, U. S-3, I-9, I-10
Stendal, K. T-23
Strain, R. V. T-25
Sukhomlinov, G.A. I-15
Sulfredge, C.D. T-19
Symon, K. P-2
Syrykh, G.F. I-2
Takada, H. T-2, T-17
Taylor, A. N-1
Thelliez, T. I-26
Thiyagarajan, P. I-3
Thomas, R.K. I-5
Thompson, K. A-9, P-2
Thut, R. I-23
Tietze-Jaensch, H. I-1, I-6, I-13
Todosow, M. P-5
Toulemonde, M. T-15
Tretyakov, I.T. T-4
Trounov, V. A. I-17, I-19
Trouw, F. I-3
Trushkin, V.I. T-4
Van Steenbergen, A. P-4
Van Swygenhoven, H. I-22
Vananti, A. I-27
Volk, K. A-3
Volkov, Yu.A. I-15
Wagner, W. T-24
Wakuta, Y. T-2
Wanderka, N. T-26
Watanabe, Y. T-2, T-20, T-21, T-22
Weber, M. A-3
Webster, J.R.P. I-5
Weinacht, D. P-3
Weng, W.T. P-4
White, M. A-9, P-2
Will, G. I-1, I-6, I-13, I-24
Wilson, R. P-10
Wollenberger, H. T-26
Wozniak, D I-3
Yamane, I. A-6
Yefimov, E.I. T-6
Young, G. P-10
Zaplatine, E. A-7, A-8
Zarbakhsh, A I-5
Ziegler, K. A-7, A-8

ICANS-XIII
13th Meeting of the International Collaboration on
Advanced Neutron Sources
October 11-14, 1995
Paul Scherrer Institut, 5232 Villigen PSI, Switzerland

List of Keywords

0.5 and 1.5 GeV	T-2
Accelerator	P-9, A-9, P-2
Accelerator design	I-12
Accelerator Ring	P-4
Activated inserts	T-24
Anvil	I-2
Argonne	P-1, T-25
AUSTRON Project	P-8, T-5
Beam port inserts	T-24
Beam transport	A-4
CERN-ISOLDE	T-15
Charge redistribution	A-4
Cold moderator	T-19
Cold moderator handling	T-24
Cold neutrons	T-20, T-22
Collimation	I-3
Complementarity	L-8
Composite	I-23
Composite Reflector	L-1
Conceptual design and R&D	P-6
Cooling	T-17
Corrosion	T-4
Coupled Moderator	L-1
Cryogenic moderator	T-21
Data acquisition	I-15, I-24
Data treatment	I-12
Deconvolution	I-12
Differential gain	L-4
Diffraction	I-16, I-19
Direct methods	I-4
Dual beam irradiation	T-26
Electron dumping system	A-3
Electronics	I-15
Emittance growth	A-4
Energy deposition	T-1

ESS T-9, T-10
ESS-Targets T-11
Experiment P-10
Extraction system A-3
Fermi Chopper I-7
FFAG Accelerator A-8
Figure of Merit L-2
Fissile target T-3
Fixed-Field A-7
Focusing I-7, P-10
Fourier I-16
Frequency Modulation A-7
Germanium I-23
Glass I-22
H^--linear accelerator P-7
Handling devices T-24
Heat pipe T-17
Helium cooling T-9
High current emittance measurements device A-3
High intensity moderator L-4
High pressure I-2
High-current low-energy beams A-5
High-Engery Protons T-6
History G-1
ICANS G-1
Inelastic scattering I-8
Instrument I-3, I-14, I-26, N-1, L-3
Instrumentation N-5
Intense Beams A-7
Intensity T-20
International cooperation P-6
Introduction Linacs A-8
Inverse geometry I-8
Ion source A-3
ISIS T-18, N-1
LANSCE A-1, T-8
LANSCE Upgrade Project N-3
Lead Fluoride Reflector P-5
Linac A-1
Linear detectors I-24

Liquid hydrogen	T-8, T-20, T-22
Liquid Metal	T-12, T-15, T-17
Liquid metal coolant	T-3
Liquid target	T-13
Long Pulse	L-3, L-5, A-1
Long pulse source	L-4, L-8
Long Pulse Spallation Source	L-1, L-2, P-3
Macromolecules	I-4
MCLIB	I-14, I-26, L-1, L-5, L-6
Meetings	G-1
Mercury	T-12, T-13
Metallurgy	T-25
Methane	T-19
Moderator	S-1, P-9, P-10, T-7, T-8, T-5, T-10, T-18
Monochromators	I-23
Monte Carlo	I-14, I-26, T-1, L-5
Multiplexing	L-3
Networks	I-15
Neutron	I-19
Neutron diffraction	I-23
Neutron guide	I-22
Neutron Pulse	T-5
Neutron Scattering	I-4
Neutron Source	P-8, L-6
Neutron spectrum	T-2
Neutron yield	T-1
NMTC/JAERI	T-2
Oscillation	P-10
Particle Bed Target	P-5
PC-system	I-24
Pellets	T-19
Performance	L-6
Phase error	I-20
Phonons	I-16
Polarization	I-21
Polarizer	I-27
Pole-figure scanning	I-1
Powder diffraction	L-8
Pressure waves	T-13
Proceedings	G-1

Proton A-9, P-2
Proton Accumulator ring P-7
Pseudo statistical modulation I-21
Pulse broadening I-12
Pulse length P-5
Pulse pauses A-5
Pulse Shape L-2
Pulsed Neutron T-20, T-21, T-22
Pulsed Neutron Source P-1
Pulsed reactor N-5
Pulsed Spallation Source N-1
Radiation effects T-19
Radioactive Halogens T-6
Reflectometry L-6
Reflector S-1, T-7
Resolution function I-13
Reverse TOF I-16
RFQ accelerators A-5
Ring-Accelerator A-7
ROTAX I-1
Roughness I-22
RTOF I-20
Sample absorption I-20
SANS L-4, L-5
Science N-1
Shock-waves T-15
Short pulses T-22
Simulation I-14, I-26, T-11, L-5
SINQ I-7, N-7
Small-angle I-3
Solenoid lenses A-4
Solubility T-12
Space charge compensation A-4
Spallation T-10, T-11
Spallation neutron P-9
Spallation neutron source P-6, P-7, P-8, T-5
Spallation Target T-17
Steels T-26
Stress T-13
Structure material T-26

Structure properties	I-19
Superconducting Linac	P-4
Supermirror	I-22, I-27
Supply system for Cold Neutron Sources	T-23
Synchrotron	A-9, P-2
Synchrotron Ring	P-4
Tantalum	T-9
Target	S-1, T-1, T-4, T-6, T-7, T-9, T-10, T-15, P-1, T-18, T-25
Target material	T-26
Target-System	S-1, T-7
Targets for Spallation Sources	P-7
Texture diffratometer	I-1
Thermal shock	T-3
Time of flight	L-3, I-2, I-13
Time of flight and unfolding technique	T-2
Time-of-flight Spectrometer	I-7
TOF spectroscopy	L-8
TOF-diffraction	I-1, I-24,
Triple-axis	I-13
Tungsten	T-4, T-6
Two beam RFQ	A-5
Upgrade	P-1
Uranium	T-4, T-25
User Interface	I-26
Vapour Pressure	T-12
Water	T-8
Water cooling	T-9
Workstations	I-15
Yields	T-6

List of Participants

ICANS-XIII
13th Meeting of the International Collaboration on
Advanced Neutron Sources
October 11-14, 1995
Paul Scherrer Institut, 5232 Villigen PSI, Switzerland

List of Participants

Kazuya Aizawa Department of Material Science and Engineering Japan Atomic Reserarch Institute Tokai-mura Naka-gun 319-11 Ibaraki Japan Tel. 0081 29 282 6830 Fax. 0081 29 282 6716 E-mail AIZAWA@KOTAI3.TOKAI.JAERI.GO.JP	Victor I. Aksenov Frank Laboratory of Neutron Physics JINR 141980 Dubna Moscow region Russia Tel. 007 09621 63387 Fax. 007 09621 65085 E-mail AKSENOV@LNP11.JINR.DUBNA.SU	Klaus Al Usta Compagnie Industrielle des Lasers CILAS Route de Nozay B.P. 27 91460 Marcoussis France Tel. 0033 1 64 54 48 15 Fax. 0033 1 64 54 48 17 E-mail
Peter Allenspach Paul Scherrer Institut ODRA/118 5232 Villigen PSI Switzerland Tel. 0041 56 310 2527 Fax. 0041 56 310 2646 E-mail	Bill Appleton Oak Ridge National Laboratory P.O Box 2008 Bldg. 4500N MS 6240 37831-6240 Oak Ridge TN USA Tel. 001 615 574 4321 Fax. 001 615 574 0323 E-mail GXB@ORNL.GOV	Masatoshi Arai Kobe University Department of Physics 1-1 Rokkodai, Nada 657 Kobe Japan Tel. 0081 78 803 0533 Fax. 0081 78 803 0722 E-mail ARAI@KEKVAX.KEK.JP
Francis Atchison Paul Scherrer Institut OVGA/305 5232 Villigen PSI Switzerland Tel. 0041 56 310 3256 Fax. 0041 56 315 2679 E-mail	Anatoli Balagurov Joint Institute for Nuclear Research Laboratory for Neutron Physics 141980 Dubna Moscow Region Russia Tel. 007 09621 65803 Fax. 007 09621 65882 E-mail BALA@NFSUN7.JINR.DUBNA.SU	Günter Bauer Paul Scherrer Institut WLGA/D12 5232 Villigen PSI Switzerland Tel. 0041 56 310 2524 Fax. 0041 56 310 3131 E-mail BAUER@PSI.CH
Alexandre Belushkin Frank Laboratory of Neutron Physics JINR 141980 Dubna Moscow region Russia Tel. 007 09621 65657 Fax. 007 09621 65429 E-mail BELUSHK@NFSUN.JINR.DUBNA.SU	Richard Benjamin Westinghouse Savannah River Co. 29808 Aiken SC USA Tel. 001 803 279 2560 Fax. 001 803 725 5103 E-mail RICHARD.BENJAMIN@SRS.GOV	Renate Bercher Paul Scherrer Institut WLGA/D12 5232 Villigen PSI Switzerland Tel. 0041 56 310 3402 Fax. 0041 56 310 3131 E-mail BERCHER@PSI.CH
Hugo Betzold Dornier GmbH 88039 Friedrichshafen Germany Tel. 0049 745 82596 Fax. 0049 7545 82693 E-mail	Peter Böni Paul Scherrer Institut ODRA/119 5232 Villigen PSI Switzerland Tel. 0041 56 310 2518 Fax. 0041 56 310 2849 E-mail BONI@PSI.CH	Grit Böttger Paul Scherrer Institut OBBA/6 5232 Villigen PSI Switzerland Tel. 0041 56 310 2091 Fax. 0041 56 310 2939 E-mail
Zoe Bowden Rutherford Appleton Laboratory Chilton, Didcot OX11 0QX Oxon UK Tel. 0044 1235 44 5683 Fax. 0044 1235 44 5720 E-mail Z.A.BOWDEN@RUTHERFORD.AC.UK	Tim Broome Rutherford Appleton Laboratory Chilton, Didcot OX11 0QX Oxon UK Tel. 0044 1235 44 6255 Fax. 0044 1235 44 5607 E-mail TIM.BROOME@RUTHERFORD.AC.UK	Bruce Brown Argonne National Laboratory IPNS 60539 Argonne IL USA Tel. 001 708 252 4999 Fax. 001 708 252 4163 E-mail BSBROWN@ANL.GOV

David Bucknall Rutherford Appleton Laboratory Chilton, Didcot OX11 0QX Oxon UK Tel. 0044 1235 44 5871 Fax. 0044 1235 44 5720 E-mail DGB @UK.AC.RUTHERFORD.ISISE	Stefano Buono CERN 1211 Geneva Switzerland Tel. 0041 22 767 9382 Fax. 0041 22 767 7555 E-mail Stefano_BUONO@EET.CERN.CH	John Carpenter Argonne National Laboratory 9700 South Avenue Cass. 60439 Argonne, IL USA Tel. 001 708 252 5519 Fax. 001 708 252 4163 E-mail JUCARPENTER@ANL.GOV
Flavio Carsughi Forschungszentrum Jülich Institut für Festkörperforschung Postfach 19 13 52425 Jülich Germany Tel. 0049 2461 61 2473 Fax. 0049 2461 61 3160 E-mail F.CARSUGHI@KFA-JUELICH.DE	D.Yu. Chernyshow St. Petersburg Nuclear Physics Institute Leningrad Area 188350 Gatchina Russia Tel. 007 8127130173 Fax. 007 81271 36051 E-mail TROUNOV@LNPI.SPB.SU	Yanglai Cho Argonne National Laboratory 360 ANL 60439 Argonne IL USA Tel. 001 708 252 6616 Fax. 001 708 252 4599 E-mail YC@APS.ANL.GOV
Daniel Clemens Paul Scherrer Institut ODRA/117 5232 Villigen PSI Switzerland Tel. 0041 56 310 2925 Fax. 0041 56 310 2849 E-mail DANIEL.CLEMENS@PSI.CH	Richard Coleman Rutherford Appleton Laboratory Chilton, Didcot OX11 0QX Oxon UK Tel. 0044 1235 44 Fax. 0044 1235 44 5720 E-mail	Harald Conrad Forschungszentrum Jülich IFF Postfach 19 13 52425 Jülich Germany Tel. 0049 2461 616740 Fax. 0049 2461 612610 E-mail
R.K. Crawford Argonne National Laboratory IPNS 9700 South Cass. Ave. 60439 Argonne IL USA Tel. 001 708 252 7269 Fax. 001 708 252 4163 E-mail CRAWFORD@ANLPNS.PNS.ANL.GOV	Laszlo Cser Research Institute for Solid State Physics P.O. Box 49 1525 Budapest Hungary Tel. 0036 1699 1526 Fax. 0036 1699 7128 E-mail CSER@IIF.KFKI.HU	Yong Dai Paul Scherrer Institut OVGA/4 5232 Villigen PSI Switzerland Tel. 0041 56 310 4171 Fax. 0041 56 310 2199 E-mail DAI@PSI.CH
L.A. de Graaf IRI Delft University of Technology Mekelweg 15 2629 JB Delft The Netherlands Tel. 0031 15 785545 Fax. 0031 15 786422 E-mail	Andreas Dönni Paul Scherrer Institut OBBA/4 5232 Villigen PSI Switzerland Tel. 0041 56 310 4007 Fax. 0041 56 310 2939 E-mail	Jürgen Duppich Paul Scherrer Institut WMHA/C9 5232 Villigen PSI Switzerland Tel. 0041 56 310 33 20 Fax. 0041 56 310 3717 E-mail DUPPICH@PSI.CH
Trevor Dury Paul Scherrer Institut OVGA/417 5232 Villigen PSI Switzerland Tel. 0041 56 310 2734 Fax. 0041 56 310 4411 E-mail	Yasuo Endoh Tohoku University Faculty of Science 980 Sendai Japan Tel. 0081 22 217 6495 Fax. 0081 22 217 6489 E-mail	Bernard Farnoux DSM CEA Saclay Orme des Merisiers 91191 Gif sur Yvette France Tel. 0033 1 69 082635 Fax. 0033 1 69 083816 E-mail FARNOUX@DSMDIR.CEA.FR
Detlef Filges Forschungszentrum Jülich IKP Postfach 19 13 52425 Jülich Germany Tel. 0049 2461 61 5232 Fax. 0049 2461 61 3930 E-mail	Peter Fischer Paul Scherrer Institut ETH Zürich OBBA/9 5232 Villigen PSI Switzerland Tel. 0041 56 310 2094 Fax. 0041 56 310 2939 E-mail	Walter Fischer Paul Scherrer Institut WLGA/D23 5232 Villigen PSI Switzerland Tel. 0041 56 310 3412 Fax. 0041 56 310 3131 E-mail BERCHER@PSI.CH

Albert Furrer Paul Scherrer Institut OBBA/3 5232 Villigen PSI Switzerland Tel. 0041 56 310 2088 Fax. 0041 56 310 2939 E-mail	**Michihiro Furusaka** Natl. Laboratory for High Energy Physics BSF 1-1 Oho 305 Tsukuba Japan Tel. 0081 298 64 5618 Fax. 0081 298 64 3202 E-mail FURUSAKA@kekvax.kek.jp	**Roland Gähler** Technische Universität München Fakultät für Physik E21 James-Franck-Strasse 85747 Garching Germany Tel. 0049 89 3209 2111 Fax. 0049 89 3209 2112 E-mail
Ian Gardner Rutherford Appleton Laboratory Chilton, Didcot OX11 0QX Oxon UK Tel. 0044 1235 44 5609 Fax. 0044 1235 44 5607 E-mail IAN.GARDNER@RL.AC.UK	**Klaus Gobrecht** Technische Universität München Projektgruppe FRM-II Reaktorstation 85747 Garching Germany Tel. 0049 89 3209 2116 Fax. 0049 89 3209 2112 E-mail KGOBRECH@PHYSIC.TU-MUENCHEN.DE	**M.I. Grachev** Institute for Nuclear Research RAS 60th October Anniversary prospect 7 a 117312 Moscow Russia Tel. 007095 334 0186 Fax. 007095 334 0184 E-mail
Mathias Gutmann Paul Scherrer Institut OBBA/7 5232 Villigen PSI Switzerland Tel. 0041 56 310 2092 Fax. 0041 56 310 2939 E-mail	**Bernd Guttek** Forschungszentrum Jülich Postfach 19 13 52425 Jülich Germany Tel. 0049 2461 61 3578 Fax. 0049 2461 61 6816 E-mail GUTTEK@EINSTEIN.ZAT.KFA-JUELICH.DE	**Markus Häfeli** Paul Scherrer Institut WMHA/B22 5232 Villigen PSI Switzerland Tel. 0041 56 310 4106 Fax. 0041 56 310 3294 E-mail
Pekka Hiismäki VTT Reactor Laboratory P.O. Box 200 2151 Espoo Finland Tel. 00358 0456 6320 Fax. 00358 0456 6390 E-mail PEKKA.HIISMAKI@VTT.FI	**Rex Hjelm** Los Alamos National Laboratory LANSCE H805 87545 Los Alamos NM USA Tel. 001 505 665 2372 Fax. 001 505 665 2676 E-mail HJELM@LANL.GOV	**Tom Holden** Neutron and Condensed Matter Science Branch Chalk River Nuclear Laboratories Chalk River KOJ 1JO Ontario Canada Tel. 001 613 584 3991 Fax. 001 613 584 4040 E-mail
Sviatoslav Ignatiev Institut of Physics and Power Engineering 249020 Bondarenko Sq. 1 Obninsk, Kaluga Region Russia Tel. Fax. 007 095 8833112 E-mail	**Hironobu Ikeda** BSF National Laboratory for High Energy Physics Oho 1-1 305 Tsukuba Japan Tel. 0081 298 64 5602 Fax. 0081 298 64 3202 E-mail HIKEDA@KEKVAX.KEK.JP	**Yoshiro Irie** National Laboratory for High Energy Physics KEK 1-1 Oho 305 Tsukuba Japan Tel. 0081 298 64 5292 Fax. 0081 298 64 3182 E-mail IRIEY@KEKVAX.KEK.JP
Stefan Janßen Paul Scherrer Institut ODRA/120a 5232 Villigen PSI Switzerland Tel. 0041 56 310 2875 Fax. 0041 56 310 2849 E-mail STEFAN.JANSSEN@PSI.CH	**Mike Johnson** Rutherford Appleton Laboratory Chilton Didcot OX11 0QX Oxon UK Tel. 0044 1235 5418 Fax. 0044 1235 44 5383 E-mail M.W.JOHNSON@RL.AC.UK	**Harry Jones** Rutherford Appleton Laboratory Chilton, Didcot OX11 0QX Oxon UK Tel. 0044 1235 44 5182 Fax. 0044 1235 44 5607 E-mail HJJ@RUTHERFORD.AC.UK
James Jorgensen Argonne National Laboratory Materials Science Division, Bldg 223 60439 Argonne IL USA Tel. 001 708 252 5513 Fax. 001 708 252 7777 E-mail JIM_JORGENSEN@QMGATE.ANL.GOV	**Yacine Kadi** CERN 1211 Geneva Switzerland Tel. 0041 22 767 9569 Fax. 0041 22 767 7555 E-mail YACINE_KADI@EET.cern.ch	**Iouri Kamyshkov** Oak Ridge National Laboratory Physics Division Build. 6003, MS 6372 37831 Oak Ridge, TN USA Tel. 001 615 576 6914 Fax. 001 615 576 2822 E-mail KAMYSHKOV@ORPH01.PHY.ORNL.GOV

Viatcheslav Kazimirov Institute for Nuclear Research RAS Joint Institute for Nuclear Research 141980 Dubna, Moscow region Russia Tel. 007 09621 62498 Fax. 007 09621 65882 E-mail KAZIMIR@NF.JINR.DUBNA.SU	Jun-ichi Kishiro Natl. Laboratory for High Energy Physics 1-1 Oho Ibaraki 305 Tsukuba Japan Tel. 0081 298 64 5273 Fax. 0081 298 64 3182 E-mail KISHIRO@KEKVAX.KEK.JP	Yoshiaki Kiyanagi Hokaido University Department of Nuclear Engineering Fakulty of Engineering Kita-13, Nishi-8 60 Kita-ku, Sapporo Japan Tel. 0081 11 706 6651 Fax. 0081 11 706 7896 E-mail KIYANAGI@HUNE.HOKUDAI.AC.JP
L.V. Kravchuk Institute for Nuclear Research RAS 60th October Anniversary prospect 7 a 117312 Moscow Russia Tel. 007095 334 0061 Fax. 007095 135 2268 E-mail KRAVCHUK@INR.MSK.SU	Alan Leadbetter Institute Laue Langevin BP 156 X 38042 Grenoble France Tel. 0033 7620 7100 Fax. 0033 76 96 1195 E-mail	Yong Lee Brookhaven National Laboratory Bldg. 911B 11973 Upton, NY USA Tel. 001 516 282 4663 Fax. 001 516 282 5954 E-mail YYLEE@BNL.GOV
Eberhard Lehmann Paul Scherrer Institut OSRA/007 5232 Villigen PSI Switzerland Tel. 0041 56 310 2963 Fax. E-mail	Herbert Lengeler Forschungszentrum Jülich ESS-Büro Postfach 19 13 52524 Jülich Germany Tel. 0049 2461 61 2305 Fax. 0049 2461 61 2470 E-mail ESS@KFA-JUELICH.DE	Jacques Lettry CERN 1211 Genf Switzerland Tel. 0041 22 767 2658 Fax. 0041 22 767 8990 E-mail
Paul Lisowski Los Alamos National Laboratory MS H813 87545 Los Alamos USA Tel. 001 505 665 5523 Fax. 001 505 667 4344 E-mail LISOWSKI@LANL.GOV	Helena Loner Paul Scherrer Institut OFLA/007A 5232 Villigen PSI Switzerland Tel. 0041 56 310 4428 Fax. 0041 56 310 2199 E-mail	Trevor Lucas Oak Ridge National Laboratory Lockheed Martin P.O. Box 2009 37831-8045 Oak Ridge USA Tel. 001 615 576 3586 Fax. 001 615 574 2032 E-mail
Hans Ludewig Brookhaven National Laboratory 11973 Upton, NY USA Tel. 001 516 282 2624 Fax. 001 516 282 7650 E-mail	Robert Macek Los Alamos National Laboratory P.O.Box 1663 MS H848 87545 Los Alamos, NM USA Tel. 001 505 667 8877 Fax. 001 505 665 8604 E-mail MACEK@LANL.GOV	Alexander Malik Paul Scherrer Institut WMHA/C44 5232 Villigen PSI Switzerland Tel. 0041 56 310 3076 Fax. 0041 56 310 3294 E-mail
Willi Marti Paul Scherrer Institut OBBA/7 5232 Villigen PSI Switzerland Tel. 0041 56 310 2092 Fax. 0041 56 310 2939 E-mail	Yasuhiro Masuda Natl. Laboratory for High Energy Physics KEK 1-1 Oho 305 Tsukuba Japan Tel. 0081 298 64 1171 Fax. 0081 298 64 3202 E-mail MASUDA@kekvax.kek.jp	Philip Meads 7053 Shirley Drive 94611-1631 Oakland USA Tel. 001 510 531 8171 Fax. 001 510 531 8172 E-mail MEADS@CCNET.COM
Shin-ichiro Meigo Japan Atomic Energy Research Institute Tokai-mura, Naka-gun 319-11 Ibaraki-ken Japan Tel. 0081 29 282 5356 Fax. 0081 29 282 5663 E-mail MEIGO@LINAC.TOKAI.JAERI.GO.JP	Joël Mesot Paul Scherrer Institut ODRA/120a 5232 Villigen PSI Switzerland Tel. 0041 56 310 4029 Fax. 0041 56 310 2646 E-mail MESOT@PSI.CH	Ferenc Mezei Hahn-Meitner-Institut BENSC Glienicker Strasse 100 14109 Berlin Germany Tel. 0049 30 8062 2322 Fax. 0049 30 8062 2523 E-mail

V. Miroshnichenko Institute for Nuclear Research RAS 60th October Anniversary prospect 7 a 117312 Moscow Russia Tel. 007095 334 0712 Fax. 007095 334 0184 E-mail	Ralf-Dieter Neef Forschungszentrum Jülich IKP Postfach 19 13 52425 Jülich Germany Tel. 0049 2461 61 6224 Fax. 0049 2461 61 3930 E-mail	Liping Ni Paul Scherrer Institut OTLA/103 5232 Villigen PSI Switzerland Tel. 0041 56 310 4453 Fax. 0041 56 310 2546 E-mail
Yu.V. Nikitenko Joint Institute for Nuclear Research JINR 141980 Dubna, Moscow region Russia Tel. 007 0959243914 Fax. 007 09621 65085 E-mail NIKIS@LNFVX2.JINR.DUBNA.SU	Waldemar Ninaus Institut für Theoretische Physik Technische Universität Graz Petersgasse 16 8010 Graz Austria Tel. 0043 316 873 8181 Fax. 0043 316 873 8199 E-mail	Charles Perret Paul Scherrer Institut WLGA/D17 5232 Villigen PSI Switzerland Tel. 0041 56 310 3318 Fax. 0041 56 310 3131 E-mail PERRET@PSI.CH
Dave Picton School of Physics and Space Research The University of Birminghamg B15 2TT Birmingham UK Tel. 0044 121 4696 Fax. 0044 121 4725 E-mail D.J. PICTON@BHAM.AC.UK	Eric Pitcher Los Alamos National Laboratory LANSCE P.O.Box 1663MS H848 87545 Los Alamos, NM USA Tel. 001 505 665 0651 Fax. 001 505 665 2676 E-mail PITCHER@LANL.GOV	Hans Priesmeyer Christian Albrechts Universität Institut für Kernphysik Otto-Hahn-Platz 24118 Kiel Germany Tel. 0049 4152 871315 Fax. 0049 431 880 1647 E-mail HANS-GEORG.PRIESMEYER@GKSS.DE
Valentin Prikhodko Joint Institute for Nuclear Research 141980 Dubna, Moscow region Russia Tel. 007 09621 65362 Fax. 007 09621 65164 E-mail NIKIS@LNFVX2.JINR.DUBNA.SU	Roger Pynn Los Alamos National Laboratory P.O. Box 1663 LANSCE H805 87545 Los Alamos NM USA Tel. 001 505 667 8842 Fax. 001 505 665 2676 E-mail PYNN@LANL.GOV	John Rosenfeld Thermacore Inc. 780 Eden Road 17601 Lancaster USA Tel. 001 717 569 6651 Fax. 001 717 569 4797 E-mail ROSENFELD@THERMACORE.COM
Gary J. Russell Los Alamos National Laboratory LANSCE MS H805 87545 Los Alamos NM USA Tel. 001 505 667 2937 Fax. 001 505 665 2676 E-mail RUSSELL@LANL.GOV	William Ruzicka Argonne National Laboratory IPNS 60539 Argonne, IL USA Tel. 001 708 252 6834 Fax. 001 708 252 4163 E-mail WGRUZICKA@ANL.GOV	E. Sackmann TU München Physik-Department E22 85748 Garching Germany Tel. 0049 89 3209 2471 Fax. 0049 89 3209 2469 E-mail SACKMANN@PHYSIK.TU-MUENCHEN.DE
Francois Samuel Compagnie Industrielle des Lasers CILAS Route de Nozay B.P. 27 91460 Marcoussis France Tel. 0033 1 64 54 48 15 Fax. 0033 1 64 54 48 17 E-mail	Hartwig Schaal Forschungszentrum Jülich IKP Postfach 19 13 52425 Jülich Germany Tel. 0049 2461 61 4004 Fax. 0049 2461 61 3930 E-mail	Wolfgang Schäfer Forschungszentrum Jülich MIN/ZFR (Univ. Bonn) Postfach 19 13 52428 Jülich Germany Tel. 0049 2461 61 6024 Fax. 0049 2461 61 3841 E-mail IFF080@DJUKFA11
Jürg Schefer Paul Scherrer Institut ODRA/118 5232 Villigen PSI Switzerland Tel. 0041 56 310 4347 Fax. 0041 56 310 2646 E-mail SCHEFER@PSI.CH	Wolfgang Schmidt Institute Laue Langevin BP 156 30842 Grenoble France Tel. Fax. E-mail	Jürgen Schreiber Fraunhofer Institut IzfP-EADQ Dresden Krügerstrasse 22 1326 Dresden Germany Tel. 0049 351 3748251 Fax. 0049 351 3748218 E-mail SCHREIBE@EADG.IZFP.FHG.DE

Reinhard Schulze Paul Scherrer Institut WLGA/D17 5232 Villigen PSI Switzerland Tel. 0041 56 310 3595 Fax. 0041 56 310 3131 E-mail	Martin Schuster Atominstitut AUSTRON Office Schüttelstrasse 115 1020 Wien Austria Tel. 0043 1 72 701 297 Fax. 0043 1 72 89 220 E-mail SCHUSTER@ATI.AC.AT	Philip Seeger Consultant Loma del Escolar 87544 Los Alamos NM USA Tel. 001 505 662 7163 Fax. E-mail PASEEGER@AOL.COM
I.N. Serdyuk Joint Institute for Nuclear Research 141980 Dubna, Moscow region Russia Tel. 007 09243914 Fax. 007 09621 65085 E-mail	Denis Sheptyakov Joint Institute for Nuclear Research 141980 Dubna, Moscow region Russia Tel. 007 09621 62498 Fax. 007 09621 65882 E-mail SAVENKO@NFSUN1.JINR.DUBNA.SU	Hiroyuki Shibazaki Kobe University Department of Physics 1-1 Rokkodai, Nada 657 Kobe Japan Tel. 0081 78 803 0533 Fax. 081 78 803 0722 E-mail SHIBAZAKI@KBUAR1.PHYS.KOBE-U.AC.JP
Stanislav Sidorkin Institute for Nuclear Research RAS 60th October Anniversary prospect 7 a 117312 Moscow Russia Tel. 007095 334 0712 Fax. 007095 135 2268 E-mail SIDORKIN@INR.MSK.SU	Karel Skala Paul Scherrer Institut ODRA/103 5232 Villigen PSI Switzerland Tel. 0041 56 310 2930 Fax. 0041 56 310 2549 E-mail	Brian Smith Paul Scherrer Institut OVGA/417 5232 Villigen PSI Switzerland Tel. 0041 56 310 2726 Fax. 0041 56 310 4411 E-mail
N.U. Sobolevsky Institute for Nuclear Research RAS 60th October Anniversary prospect 7 a 117312 Moscow Russia Tel. 007095 334 0714 Fax. 007095 135 2268 E-mail	Hirohi Someya Natl. Laboratory for High Energy Physics KEK 1-1 Oho Ibaraki-ken 305 Tsukuba-shi Japan Tel. 0081 298 64 5266 Fax. 0081 298 64 3182 E-mail	Walt Sommer Los Alamos National Laboratory Materials Science and Technology Division P.O. Box 1663, MS H805 87545 Los Alamos NM USA Tel. 001 505 665 8806 Fax. 001 505 665 2676 E-mail SOMMER@ESA.LANL.GOV
Yuri Stavissky Institute for Nuclear Research RAS 60th October Anniversary prospect 7 a 117312 Moscow Russia Tel. 007095 334 0191 Fax. 007095 135 2268 E-mail STAV@INR.MSK.SU	Uschi Steigenberger Rutherford Appleton Laboratory ISIS Chilton, Didcot OX11 0QX Oxon UK Tel. 0044 1235 445145 Fax. 0044 1235 445383 E-mail USM@ISISE.RL.AC.UK	Karsten Stendal Riso National Laboratories Postbox 49 Riso 4000 Roskilde Denmark Tel. 0045 4677 5581 Fax. 0045 4237 3993 E-mail
Yasushi Takeda Paul Scherrer Institut WMHA/B22 5232 Villigen PSI Switzerland Tel. 0041 56 99 3568 Fax. 0041 56 310 3294 E-mail TAKEDA@PSI.CH	Andrew Taylor Rutherford Appleton Laboratory Chilton, Didcot OX11 0QX Oxon UK Tel. 0044 1235 44 6681 Fax. 0044 1235 44 5383 E-mail ADT@ISISE.RL.AC.UK	Gary Thomas Rutherford Appleton Laboratory Chilton, Didcot OX11 0QX Oxon UK Tel. 0044 1235 44 5232 Fax. 0044 1235 44 5607 E-mail G.THOMAS@RUTHERFORD.AC.UK
Iran Thomas Basic Energy Sciences Acting Associate Director 19901 Germantown Road 20874-1290 Germantown MD USA Tel. Fax. E-mail	Holger Tietze-Jaensch Rutherford Appleton Laboratory ISIS Chilton, Didcot OX11 0QX Oxon UK Tel. 0044 1235 445685 Fax. 0044 1235 445720 E-mail HTJ@UK.AC.RL.ISISE	Vitali Trounov Russian Academy of Sciences Petersubrg Nuclear Physics Institut Gatchina 188350 St. Petersburg Russia Tel. 007 0812 2949129 Fax. 007 0812 71 31347 E-mail TROUNOV@LNPI.SPS.SU

Frans Trouw Argonne National Laboratory IPNS 9700 S.Cass. Av. 60439 Argonne IL USA Tel. 001 708 252 7665 Fax. 001 708 252 4163 E-mail TRUOW@ANL.GOV	**Colin Uden** Rutherford Appleton Laboratory Chilton, Didcot OX11 0QX Oxon UK Tel. 0044 1235 44 6606 Fax. 0044 1235 44 5607 E-mail CNU@RL.AC.UK	**Luc Van den Durpel** SCK-CEN ADONIS-project Boeretang 200 2400 Mol Belgium Tel. 0032 14 332196 Fax. 0032 14 321529 E-mail VDDURPEL@SCKCEN.BE
Werner Wagner Paul Scherrer Institut ODRA/120 5232 Villigen PSI Switzerland Tel. 0041 56 310 2517 Fax. 0041 56 310 2646 E-mail	**Noboru Watanabe** Nat. Laboratory for High Energy Physics KEK Booster Synchrotron Utilization Facility 1-1 Oho 305 Tsukuba Japan Tel. 0081 298 64 5602 Fax. 0081 298 64 3202 E-mail	**Marion White** Argonne National Laboratory ANL-ASD 9700 South Cass. Ave. 60439 Argonne, IL USA Tel. 001 708 252 5552 Fax. 001 708 252 4599 E-mail MWHITE@APS.ANL.GOV
Gavin Williams Rutherford Appleton Laboratory ISIS Facility Chilton Didcot OX11 0QX Oxon UK Tel. 0044 1235 44 5599 Fax. 0044 1235 44 5642 E-mail W.C.WILLIAMS@ISISE.RL.AC.UK	**Kazuyoshi Yamada** Tohoku University Department of Physics Aramaki, Aoba 980-77 Sendai Japan Tel. 0081 22 217 6486 Fax. 0081 22 217 6489 E-mail YAMADA@IIYO.PHYS.TOHOKU.AC.JP	**Max Zaslawsky** US Department of Energy DP 25; GA-045 1000 Independence Ave. S.W. 20585 Washington, D.C. USA Tel. 001 202 586 5114 Fax. 001 202 586 1217 E-mail MAX.ZASLAWSKY@DP.DOE.GOV
Klaus Ziegler Hahn-Meitner-Institut Glienicker Strasse 100 14109 Berlin Germany Tel. 0049 30 8062 2498 Fax. 0049 30 8062 2293 E-mail ZIEGLER@VAX.HMI.D400.DE		

EUROPEAN SPALLATION SOURCE
General ESS Meeting
October 16-19, 1995
Weinfelden, Switzerland

List of Participants

Abildskov, Finn Institute for Synchrotron Radiation Aarhus University DK-8000 Aarhus C	Appleton, Bill, R. Oak Ridge National Laboratory PO Box 2008 Bldg 4500N, MS 6240 Oak Ridge TN, 37831-6240 U S A	Balagurov, Anatoli Frank Lab. of Neutron Physics JINR 141980 Dubna, Mosc. reg. RUSSIA
Barocchi, Fabrizio Dipartimento die Fisica Largo E. Fermi 2 I-50125 Firenze ITALY	Bauer, G. Paul Scherrer Institut SINQ-Project, LG/D12 CH-5232 Villigen	Belushkin, Alexandre Frank Laboratory of Neutron Physics, JINR 141980 Dubna, Moscow region RUSSIA
Benjamin, Richard Walter Westinghouse Svannah River Co. Savannah River Sife Aiken SC 29808 U S A	Boehne, Dieter GSI Darmstadt Postfach 110552 Planckstr.1 64291 Darmstadt	Bongardt Forschungszentrum Jülich Postfach 1913 52425 Jülich Deutschland
Bothe, Werner c/o DESY-MKK Notkestraße 85 22603 Hamburg	Broome, Tim Rutherford Appleton Laboratory ISIS Facility, Bldg. R2 Chilton Didcot Oxon, OX11 0QX UK	Brown, Bruce IPNS Bldg. 360 Argonne National Laboratory Argonne, IL 60439 USA
Bryant, P. PS Division CERN CH-1211 Genève 23	Camus, Eric Hahn-Meitner-Institut Glienicker Str. 100 D-14109 Berlin	Carlile, Colin J. Rutherford Appleton Laboratory ISIS Facility, Bldg. R2 Chilton Didcot Oxon, OX11 0QX UK
Carpenter, John M. IPNS Division, Buildg. 360 Argonne National Laboratory 9700 South Cass Avenue Argonne, IL 60439 U S A	Carsughi, Flavio Forschungszentrum Jülich Postfach 1913 52425 Jülich Deutschland	Cho, Yanglai Advanced Photon Source Bldg. 360, F225 Argonne National Laboratory 9700 S. Cass Ave. Argonne, Ill. 60439 USA
Clausen, Kurt, N. Solid State Physics Department RisØ National Laboratory DK-4000 Roskilde	Conrad, Harald Forschungszentrum Jülich Postfach 1913 52425 Jülich Deutschland	Craddock, Mike K. Triumf 4004 Westbrook Mall Vancouver BC CANADA VGT 2A3

Cser, László Research Institute for Solid State Physics POB 49 H-1525 Budapest HUNGARY	Dai, Yong Paul Scherrer Institut Geb. 21/8 CH-5232 Villigen SCHWEIZ	Deitinghoff, Dr. Institut f. Angewandte Physik Universität Frankfurt a.M. Robert-Mayer-Straße 2 - 4 D-60325 Frankfurt a. Main
Dubbers, Dirk Physikalisches Institut der Universität Heidelberg Philosophenweg 12 69120 Heidelberg	Duppich, Jürgen Paul Scherrer Institut PSI CH 5232 Villigen SCHWEIZ	Dury, Trevor Paul Scherrer Institut PSI CH 5232 Villigen SCHWEIZ
Filges, Detlef Forschungszentrum Jülich Postfach 1913 52425 Jülich Deutschland	Finney, J. Dept. of Physics and Astronomy University College London Gower Street London WC1E 68T UK	Firjahn-Andersch, Arne Institut f. Angewandte Physik Universität Frankfurt a.M. Robert-Mayer-Straße 2 - 4 D-60325 Frankfurt a. Main
Furusaka, Michihiro BSF, National Laboratory for High Energy Physics 1-1 Oho, Tsukuba, 305 JAPAN	Gardner, Ian S.K. SERC Rutherford Appleton Laboratory ISIS Facility, Bldg. R2 Chilton Didcot Oxon, OX11 0QX UK	Guttek, Bernd Forschungszentrum Jülich Postfach 1913 52425 Jülich Deutschland
Harold, Mike R. Rutherford Appleton Laboratory ISIS Facility, Bldg. R2 Chilton Didcot Oxon, OX11 0QX UK	Hjelm, Rex P. Los Alamos National Laboratory H 805 Los Alamos, NM 87545 U S A	Hudina, Marjan Paul Scherrer Institut PSI CH 5232 Villigen SCHWEIZ
Irie, Yoshiro KEK National Laboratory for High Energy Physics Oho 1-1, Tsukuba Ibaraki 305 JAPAN	Jason, Andy AOT-1, MS H808 Los Alamos National Laboratory P.O. Box 1663 Los Alamos, NM 87545 U S A	Johnsen, Kjell c/o CERN Bldg. 584 CH-1211 Geneva 23 SWITZERLAND
Jones, Henry, John Rutherford Appleton Laboratory ISIS Facility, Bldg. R2 Chilton Didcot Oxon, OX11 0QX UK	Kishiro, Ju. National Laboratory for High Energy Physics, KEK 1-1, Oho, Tsukuba Ibaraki JAPAN	Kiyanagi, Yoshiaka Dept. of Nuclear Eng. Faculty of Eng. Hokkaido University kita-ku, kita-13, Nishi-8 Sapporo 060 JAPAN
Kjems, Joergen Chairman ESS Council Risø National Laboratory PO Box 49 DK-4000 Roskilde	Klein, Horst, Prof. Institut f. Angewandte Physik Universität Frankfurt a.M. Robert-Mayer-Straße 2 - 4 D-60325 Frankfurt a. Main	Kustom, R.L. Argonne National Laboratory ASD--RF, Bldg. 371T 9700 South Cass Av. Argonne, IL 60439 U S A

Lakatos, Andreas Institut f. Angewandte Physik Universität Frankfurt a.M. Robert-Mayer-Straße 2 - 4 D-60054 Frankfurt a. Main	Lehmann, Mogens, S. Institut Laue-Langevin Av. Des Martyrs B.P. 156 X F-38042 Grenoble Cedex 9	Lengeler, Herbert Forschungszentrum Jülich Postfach 1913 52425 Jülich Deutschland
Letchford, Alan Rutherford Appleton Laboratory ISIS Facility, Bldg. R2 Chilton Didcot Oxon, OX11 0QX UK	Lisowski, Paul William APT Project Office MS H813 Los Alamos National Laboratory Los Alamos, NM 87545 U S A	Lucas, Albert, T. Lockheed Martin Energy Systems Mallstop 8045 Y 12 Plant Oak Ridge, TN 37831 U S A
Ludewig, Hans Brookhaven National Laboratory Building 475 B PO Box 5000 Upton, NY 11973-5000 U S A	Maaser, Andreas Institut f. Angewandte Physik Universität Frankfurt a.M. Robert-Mayer-Straße 2 - 4 D-60325 Frankfurt a. Main	Macek, Robert J. Los Alamos National Laboratory MS H848 Los Alamos, NM 87545 U S A
Madlung, J. Institut f. Angewandte Physik Universität Frankfurt a.M. Robert-Mayer-Straße 2 - 4 D-60325 Frankfurt a. Main	Masullo, Maria Rosaria INFN Sezione di Napoli Mostra d'oltremare, pad. 20 80125 NApoli Italy	McGreevy, Robert, L. NFL Studsvik S-611 82 Nyköping SWEDEN
Meads, Ph. F. 7053 Shirley Drive Oakland, California 94611-1631 U S A	Mezei, Ferenc Hahn-Meitner-Institut BENSC Glienicker Strasse 100 D-14109 Berlin	Møller, Søren, P. Institute for Synchrotron Radiation Aarhus University DK-8000 Aarhus C
Ni, Liping Paul Scherrer Institut PSI CH 5232 Villigen SCHWEIZ	Nilsson, Leif The Svedberg Laboratory Uppsala University Box 533 S-751 21 Uppsala SWEDEN	Ninaus, Waldemar Institut für Theoretische Physik Steyrergasse 17 A-8010 Graz ÖSTERREICH
Ohmori, Chihiro Rutherford Appleton Lab Buildg. R2 Chilton Didcot OXON OX11 OQX ENGLAND	Papst, Forschungszentrum Jülich Postfach 1913 52425 Jülich Deutschland	Penfold, J. Rutherford Appleton Laboratory ISIS Facility, Bldg. R2 Chilton Didcot Oxon, OX11 0QX UK
Pichler, Stephan 10 ch. de l'Epenontaz CH- 1213 ONEX	Picton, D.J. School of Physics and Space Res. The University of Birmingham Birmingham B15 2TT ENGLAND	Piel, Helmut Fachbereich Physik Bergische Universität - Gesamthochschule Wuppertal Gaußstr. 20 D-42097 Wuppertal

Planner, Charles, W. Rutherford Appleton Laboratory ISIS Facility, Bldg. R2 Chilton Didcot Oxon, OX11 0QX UK	Prior, Chris, R. Rutherford Appleton Laboratory ISIS Facility, Bldg. R2 Chilton Didcot Oxon, OX11 0QX UK	Pynn, Roger Los Alamos National Laboratory LANSCE MS H805 Los Alamos, New Mexico 87545 U S A
Rees, Graham, H. Rutherford Appleton Laboratory ISIS Facility, Bldg. R2 Chilton Didcot Oxon, OX11 0QX UK	Reistad, Dag V. The Svedberg Laboratory, Box 533 75121 Uppsala SWEDEN	Rodriguez-Carvajal, Juan Laboratoire Leon Brillouin (CEA-CNRS). CE Saclay F-91191 Gif sur Yvette, Cedex FRANCE
Ruggiero, Alessandro Brookhaven National Laboratory Building 475 B PO Box 5000 Upton, NY 11973-5000 U S A	Russell, Gary J. LANSCE, MSH 805 Los Alamos National Laboratory P.O. Box 1663 Los Alamos, NM 87545 U S A	Schaal, Hartiwg Forschungszentrum Jülich Postfach 1913 52425 Jülich Deutschland
Schenck, Alex Paul Scherrer Institut PSI CH 5232 Villigen SCHWEIZ	Sigg, Beat Paul Scherrer Institut PSI CH 5232 Villigen SCHWEIZ	Simonsson, Ansgar Manne Siegbahn Laboratory Frescativagen 24 S-104 05 STOCKHOLM SWEDEN
Smith, Brian L. Paul Scherrer Institut PSI CH 5232 Villigen SCHWEIZ	Someya, Hi. National Laboratory for High Energy Physics, KEK 1-1, Oho, Tsukuba Ibaraki JAPAN	Sommer, Walt LANSCE, H805 Los Alamos National Laboratory Los Alamos, New Mexico 87544 U S A
Spatzek, Margret Forschungszentrum Jülich Postfach 1913 52425 Jülich Deutschland	Springer, Tasso Forschungszentrum Jülich Postfach 1913 52425 Jülich Deutschland	Stålnacke, Carl-Söran The Svedberg Laboratory, Box 533 S-75121 Uppsala SWEDEN
Stechemesser, Horst Forschungszentrum Jülich Postfach 1913 52425 Jülich Deutschland	Steigenberger, Uschi Rutherford Appleton Laboratory ISIS Facility, Bldg. R2 Chilton Didcot Oxon, OX11 0QX UK	Stendal, Karsten Risø National Laboratories Box 49 4000 Roskilde DENMARK
Takeda, Yasushi Paul Scherrer Institut Würenlingen u. Villigen CH-5232 Villigen SCHWEIZ	Taylor, Andrew Rutherford Appleton Laboratory ISIS Facility, Bldg. R2 Chilton Didcot Oxon, OX11 0QX UK	Thomas, G. Rutherford Appleton Laboratory ISIS Facility, Bldg. R2 Chilton Didcot Oxon, OX11 0QX UK

Thomas, Iran, L. US Department of Energy ER-10, GTN 19901 Germantown Road Germantown, MD 20874-1290 U S A	Timmins, Peter Institut Laue Langevin BP 156 F-38042 Grenoble Cedex 9 FRANCE	Torell, Lena, M. Dept. of Physikcs Chalmers University of Technology S-412 96 Göteborg SCHWEDEN
Vaccaro, Vittorio Departimento di Scienze Fisiche Universita di Napoli Mostra d'Oltremare Pad 20 Napoli ITALY	Volk, Klaus Institut für Angewandte Physik der J.W. Goethe Universität Robert-Mayer-Str. 2-4 60054 Frankfurt	Warsop, Chris Rutherford Appleton Laboratory ISIS Facility, Bldg. R2 Chilton Didcot Oxon, OX11 0QX UK
Watanabe, Noboru 4-18-3 Shogen Izumi-ku, Sendai, 981-31 JAPAN	Weber, Manfred Institut f. Angewandte Physik Universität Frankfurt a.M. Robert-Mayer-Straße 2 - 4 D-60325 Frankfurt a. Main	Whithers, Phil University of Cambridge Dept. of Material Science and Metallurgy Pembroke Street Cambridge CB2 3Q2 ENGLAND
Yamazaki, Yoshihi PS Division Accelerator Dept. National Lab. for High Energy Phys Oho-cho 1-1, Tsukuba-shi, Ibaraki-ken 305 JAPAN	Zaplatin, Eugenii Hahn-Meitner Inst. Berlin GmbH Glienicker Str. 100 D-14109 Berlin 39	Zaslawsky, Max Forrestal Building US Dept. of Energy 1000 Independence Ave, SW Washington, D.C. 20585 U S A
Ziegler, Klaus Hahn-Meitner Inst. Berlin GmbH Glienicker Str. 100 D-14109 Berlin 39		

A Taste of Appenzell

PAUL SCHERRER INSTITUT

Paul Scherrer Institut
CH-5232 Villigen PSI

Phone 056 310 21 11
Fax 056 310 21 99